Warner Marzocchi and Aldo Zollo (Editors)
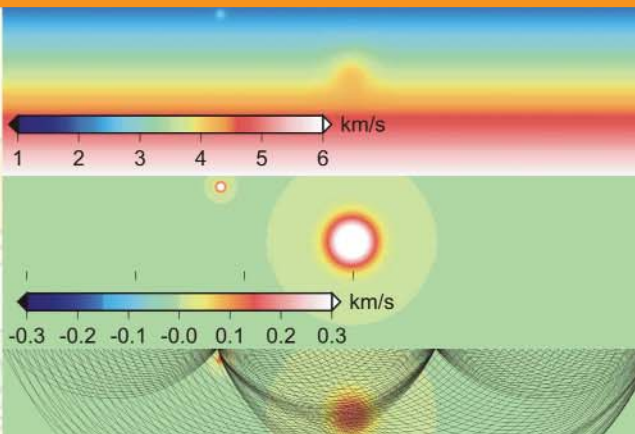
Conception, verification and application of innovative techniques to study active volcanoes

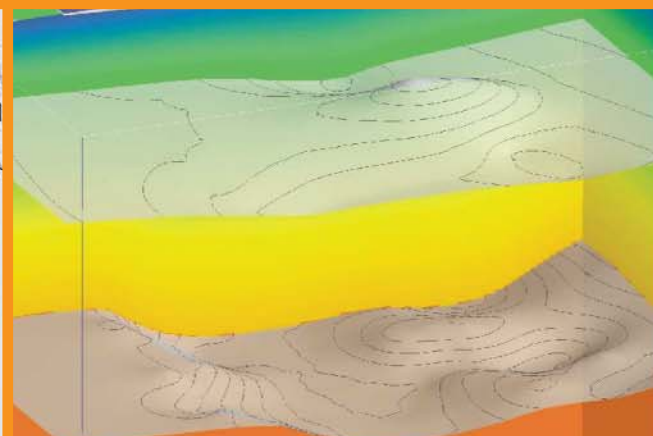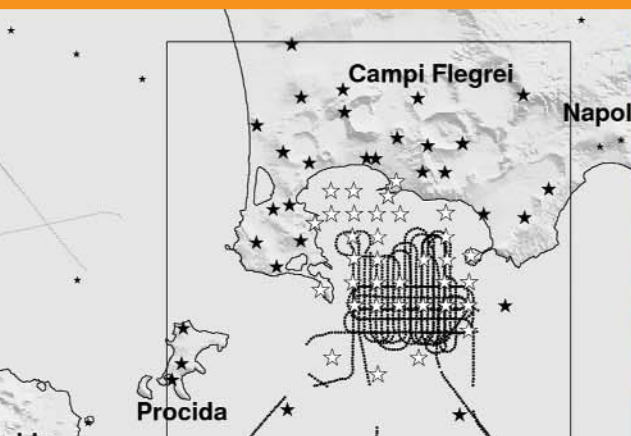**Istituto Nazionale di Geofisica e Vulcanologia**

Dipartimento della Protezione Civile

Conception, verification and application of innovative techniques to study active volcanoes

Edited by

Warner Marzocchi
Istituto Nazionale di Geofisica e Vulcanologia, Bologna, Italy

Aldo Zollo
Dipartimento di Scienze Fisiche, Università Federico II, Napoli, Italy

Contents

Task 2
HIGH RESOLUTION SEISMIC IMAGING OF VOLCANIC STRUCTURES   99

Contents

Task 3
REAL TIME OBSERVATIONS AND MEASUREMENTS — 361

Contents

Preface

The Agreement between the Italian Dipartimento della Protezione Civile – DPC and the Istituto Nazionale di Geofisica e Vulcanologia – INGV for the period 2004-2006 included the execution of five projects in Volcanology. One of these projects was led by the Editors and had the title of this book. The papers in the book are written by the project participants, and illustrate the Project developments and achievements.

This book testifies of the rapid and great advances of the science of volcanoes during last years. More and more, volcanoes are being investigated through the development of innovative techniques which rest on a solid physical and mathematical basis. Volcanoes are extremely complex systems, and their investigation is made even more difficult by the fact that the major processes occurring within them, and leading to volcanic eruptions, are not directly accessible to observation. Nonetheless, volcanoes deserve great attention not only for the intriguing aspects of their physics, but also – mostly – for the great concern they bring about due to their potentially enormous destructive power. This is especially true in Italy, where some of the most dangerous volcanoes in the world – Vesuvius and Campi Flegrei – represent a menace for more than 1 million people, and where other volcanoes – Etna and Stromboli are among the world-wide well-known examples – frequently erupt generating serious damages and giving origin to severe social issues.

The thirty-eight papers in this book offer a top-level perspective of some of the most advanced methods to estimate the volcanic hazard, image the volcanic structures, and obtain in real-time relevant volcano and eruption parameters. Most of the science in the book is being published or will be published in international specialized journals, making the book a very qualified update of the methods and techniques described. It is easy to predict that many of the advancements reported here will have a relevant influence in the way active volcanoes are monitored and the volcanic hazard is evaluated, and will become routine in volcano surveillance activities.

Paolo Papale

Introduction

The development of innovative and quantitative methods is one of the main ingredients for future progresses in volcanic risk assessment and management at long- and short- term time scales.

The complexity of volcanic systems originates from the strong heterogeneity of their internal structure (in terms of spatial variation of physical rock properties) and the large variety of thermomechanical processes which may precede and accompany the magma rise and eruption. The most comprehensive understanding of volcanic processes necessarily calls for a multi-disciplinary, integrated approach of data acquisition, analysis and modeling.

During the past three decades, we have been witnessing a strong technological development leading to a rapid growth of multidisciplinary studies of volcanoes. The controlled, repeatable experimentation is nowadays replaced by dense monitoring surveys, where the analysis strategy is often dictated afterwards, depending on the data produced. Volcano monitoring networks (geophysical, geochemical, geodetical, …) produce terabytes of data, only a small fraction of them is practically used for research and/or survey purposes.

It comes out the need for implementing new strategies of data management able to analyze and mine in the near-real-time huge data flows, having the targets 1/ to exploit the whole available information, 2/ identify and measure quantitative risk indicators useful for volcanic risk monitoring and emergency management and 3/ develop advanced tools for process simulation and event prediction based on the real time analysis and modeling of observed data.

Due to the multi-disciplinary nature of the object under study, innovative approaches and techniques for volcano monitoring may concern an ultra-wide disciplinary domain (geophysics, geochemistry, geology, remote sensing, …).

The collection of articles in this volume represents an exhaustive description of the main outcomes of the INGV-DPC V4 project "Conception, verification, and application of innovative techniques to study active volcanoes" that we have coordinated during 2005-2007 and which has seen the participation of 14 national and international research units.

In the project development the innovation has been focussed on a restricted number of tasks which were believed to be prior in terms of needed scientific effort and development and possible gain of knowledge about volcanic processes.

The **Task 1** of the project (*Probabilistic volcanic hazard estimation*) was aimed at the estimation of volcanic hazard based on probabilistic techniques and eruption forecasting. In this framework the research activity was devoted to developments of prototypes of software/codes, strategies for the development of quantitative tools to analyze multivariate seismic database, find precursory patterns of volcanic eruptions, and define probabilistic rules to quantify short-term volcanic hazard, applications to case studies.

The main issue in project **Task 2** (*High resolution seismic imaging of volcanic structures*) was the analysis and modelling of seismic waves propagating through the complex volcanic medium with the aim to extract relevant information about structure, depth location and geometry of the feeding system.

Since the initial TOMOVES experiments around Mt Vesuvius in 1993 till the SERAPIS project in Campi Flegrei bay area in 2001, the active exploration tools have demonstrated to well complement passive observations standardly performed by volcanological observatories. In this task most of applications have been devoted to a better understanding of the Campi Flegrei caldera structure through the adaptation of existing tools to the complexity of acquisition and modelling in volcanic environments, while new tools have been developed, especially for the imaging of local elastic/anelastic properties of the volcanic medium.

The main objectives of **Task 3**, was the development, implementation and testing of new tools for realtime analysis of seismic and thermal monitoring data, and to design and test of a prototype, sea-bottom multi-parametric station integrated to an on-land existing monitoring network. Automatic techniques for real-time detection and location estimation of seismic events have been developed and made able to work in 3D heterogeneous volcanic structures. Concerning the experimentation of prototypes for data acquisition in hostile environments it has been developed and tested a sea bottom seismic station with real time transmission connected to the monitoring system of Neapolitan volcanic area. New instruments for thermal monitoring have been conceived along with tools to analyze thermal images in near real-time.

The researches and results described in this volume follow the new trend of modern volcanology, where the multi-disciplinary observation is combined with advanced modelling tools and innovative technologies for monitoring of volcanic processes.

We hope this book can represent an useful reference for volcano researchers and technology developers.

Aldo Zollo and Warner Marzocchi

Task 1

Estimation of the volcanic hazard based on probabilistic techniques, and eruptions forecasting

Joint inversion of geodetic data in a layered medium: a preliminary application to the Campi Flegrei caldera (Italy)

A. Amoruso, L. Crescentini

Dipartimento di Fisica, Università di Salerno, Italy

Abstract: One of the most promising ways of studying volcanic phenomena is the use of high-precision deformation and gravity data, and gravity measurements are usually considered the best tool to constrain the nature of the source responsible for the observed unrest. The effects of a mass-less expanding source, given by the addition of vertical movement effects free air effect) and subsurface mass redistribution (deformation effect) are subtracted from the observed gravity changes, obtaining the gravity residuals. If the source can be approximated by an oblate spheroid (to a major extent a degenerate one, i. e. a penny-shaped crack) and is embedded in a homogeneous half-space, the deformation effect is positive and so large as to be comparable with gravity residuals.

By inverting ground deformation and gravity data for a penny-shaped crack in a homogeneous half-space, Battaglia et al. [2006] obtained 600 kg/m³ as best-fit intrusion density for the 1982-1984 Campi Flegrei unrest, excluded the intrusion of magma, and ascribed ground deformation and consequent unrest to the migration of fluid to and from the caldera hydrothermal system. Our preliminary results show that neglecting crustal layering leads to strong density underestimation and consequently to a possibly incorrect assessment of volcanic hazard at Campi Flegrei, while taking into account layering leads to higher intrusion densities (2200 to 2700 kg/m³, depending on the misfit function minimized in the inversions). Our results do not support hydrothermal fluid intrusion as the primary cause of the Campi Flegrei 1982-1984 unrest, indicating an effective role of magma.

INTRODUCTION

Mogi [1958] applied solutions for a point spherical pressure source to surface displacement data to show that, for eruptive activity at Sakurajiima and Kilauea, such observations provided constraints on the reservoir location. Despite the simplicity of the model, surface displacements associated with volcanic activity could be very well explained in terms of a point spherical

source at a determined depth in a homogeneous half-space. This model continues to enjoy widespread use and success, especially since commonly the sparsity of data available for investigating volcanic activity generally requires that only solutions with the fewest number of parameters can be considered. In most settings, the only available measurements derive from GPS observations and levelling service.

Subsequent work has resulted in several refinements in the modeling: analytic expressions and numeric techniques have been developed for ellipsoidal point sources [Davis, 1986], finite prolate spheroids [Yang et al., 1988] and finite horizontal cracks [Fialko et al., 2001] embedded in a homogeneous half-space.

Fernandez et al. [1997] developed a numerical code able to compute gravity changes and deformation due to a point mass and a center of expansion, embedded in a layered elastic-gravitational Earth model; the medium consists of up to four distinct layers overlaying a half-space. More recently, Wang et al. [2006] presented a numerical code, PSGRN, calculating the time-dependent Green functions of a given layered viscoelastic-gravitational half-space for four fundamental dislocation sources (the strike-slip double-couple, the dip-slip double-couple, the compensated linear vertical dipole, CLVD, and the point inflation) at different depths. The code considers the coupling between the deformation and the Earth's gravity field, so that its output includes the complete deformation field and the geoid and gravity changes.

We use Green's function computed by PSGRN inside a new nonlinear inversion code (ANGELA, Crescentini et al., 2007) able to invert deformation and gravity data for point spheroidal sources and finite cracks.

The presence of soft superficial layers affects the deformation pattern, giving an apparent shallower source if layering is not taken into account [e. g. Amoruso et al., 2004; Trasatti et al., 2005]. Effects of layering are larger on horizontal displacements than vertical ones, so the ratio of horizontal to vertical displacements is increased with respect to models in homogeneous half-space [e.g. Crescentini and Amoruso, 2007]. For a fixed source location, this ratio is larger for a finite prolate spheroid than for a finite oblate spheroid, thus neglecting layering in joint inversions of horizontal and vertical displacements could also bias the source shape.

Intrusion density, which can be affected by subsurface mass redistribution (deformation effect), is obtained from gravity measurements. The deformation effect is strongly dependent on the shape of the expanding source. If the source (embedded in a homogeneous elastic half-space) can be approximated by a sphere or a prolate spheroid, the deformation effect is null or negligible, but if the source can be approximated by an oblate spheroid (to a major extent a degenerate one, i. e. a penny-shaped crack) it is positive and so large as to dominate residual gravity changes [Battaglia et al. 2006]. Soft superficial layers affect the subsurface mass redistribution effects on gravity changes. Retrieved

intrusion density is biased toward very low values if the source is modeled as a penny-shaped crack (point and finite) in a homogeneous half-space and the resulting density misestimate can lead to a possibly incorrect assessment of volcanic hazard.

As an application, we present preliminary results for the 1982-1984 Campi Flegrei unrest. The Campi Flegrei caldera is located in a densely populated area close to Naples (Southern Italy) renowned as a site of continual slow vertical movements. It is a nested caldera structure generally ascribed to two main collapses at about 37 and 12 kyr BC [Rosi et al., 1983], and hosted numerous smaller explosive eruptions during the last 10kyr.

Secular ground movements at Campi Flegrei have been reconstructed by Dvorak and Mastrolorenzo [1991], and integrated by Morhange et al. [1999, 2006] back to 200 yr BC. For at least 2000 years the caldera is slowly deflating, at a rate of 1.5-1.7 cm/year, but episodes of rapid uplifts occurred in the early 1500s (up to 8 m, culminating in the Monte Nuovo eruption in 1538) in 1969-1973 and in 1982-1984. These last two episodes, showing at peak rate of 1 m/year, have resulted in a net uplift of 3.5 m, were accompanied by microseismicity but did not lead to an eruption.

While post-1985 deflation is usually ascribed to changes in the sub-surface hydrothermal system, a long-standing controversy accompanies the interpretation of geodetic data recorded during the 1982-1984 rapid uplift episode. Deformation and gravity changes were interpreted to result from the sub-surface magmatic reservoir by some authors, the hydrothermal system by others, or hybrid sources involving both magmatic and hydrothermal systems by others [e. g. Berrino et al., 1984; Berrino, 1994; De Natale et al., 1991, 2001; Bonafede, 1991; Gaeta et al., 1998; Bonafede and Mazzanti, 1998; Chiodini et al., 2003; Battaglia et al., 2006; Gottsman et al., 2006abc]. The controversy is of major importance in the framework of the Campi Flegrei volcanic hazard, because distinguishing between magmatic and hydrothermal sources of volcanic unrest is the first node of any volcanic hazard tree. In particular, Battaglia et al. [2006] obtained 600 kg/m³ as best-fit intrusion density for a finite crack source embedded in a homogeneous half-space when taking into account the deformation effect on measured gravity changes.

Intrusion density inferred for spherical sources was > 3000 kg/m³ both for the single source model in Battaglia et al. [2006] and the deeper of the two spherical sources in Gottsmann et al. [2006b].

Here we show preliminary results of joint inversion of geodetic data (leveling, EDM and gravity data) collected at Campi Flegrei caldera, during the 1980-1984 inflation, in a layered medium appropriate for the area. We show that the large discrepancy between densities of spherical and penny-shaped sources, given in the literature and obtained inverting ground displacement and gravity data in a homogeneous half-space, is a consequence of the homogeneous half-space assumption.

METHODS

We assume that the source is either a point spheroid or a finite crack, and is identified by its horizontal projection (x_s, y_s), depth (z_s), potency (i. e. volume change ΔV), aspect ratio (point source) or radius (finite crack).

The problem of computing deformation due to a finite horizontal crack embedded in a homogeneous half space has been solved by Fialko et al. [2001]. No solution is available in the case of a horizontally layered elastic medium, but a point crack (PC) is a good approximation of a finite crack (FC) only if source depth to radius exceeds 5. We find that a regular distribution of PCs over the FC mid-plane gives quite the same ground displacements in a homogeneous half-space as those computed using the code by Fialko et al. [2001] if source depth to radius exceeds 0.8 [Crescentini and Amoruso, 2007] (see Figure 1). Potency of each PC is proportional to $[1-(r/R)^4]$, where r is dis-
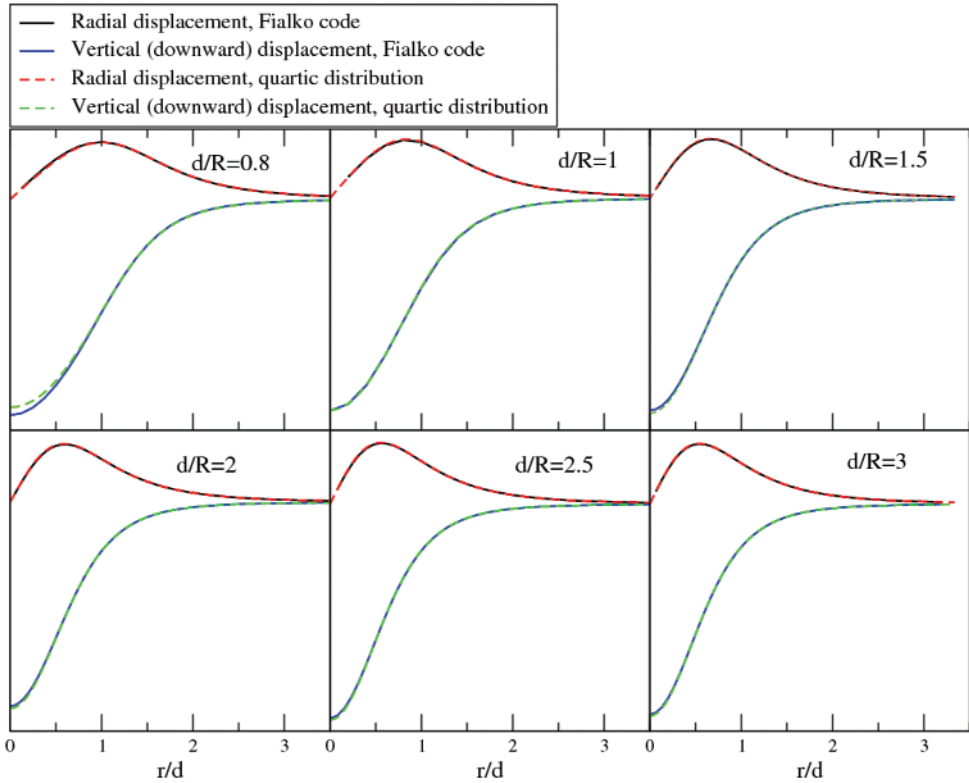
Fig. 1. Surface displacements due to a finite horizontal crack embedded in a homogeneous half-space. Solid lines, exact expressions from Fialko et al. [2001]. Dashed lines, quartic distribution of point sources over the crack mid-plane [Crescentini and Amoruso, 2007]. R, crack radius; d, crack depth; r, distance from the crack axis.

tance from the crack axis and R is the crack radius. PC spacing is (source depth)/10. We approximate the FC with the same PC distribution in the layered half-space also.

Following the approach in the work by Davis [1986] far-field deformation due to inflation of a mass-less pressurized vertical spheroid is obtained by a weighted combination of an isotropic point source (IPS) and a compensated linear vertical dipole (CLVD). Weights depend on the source aspect ratio. We compute Green's functions for ground displacements and gravity changes due to mass-less IPS ($\mathbf{G}^{IPS}$) and CLVD ($\mathbf{G}^{CLVD}$) using PSGRN code [Wang et al., 2006]. As an example, the seismic moment of a PC is given by $\mathbf{M}^{PC}=\Delta V$ ($\mathbf{G}^{IPS}+4\ \mathbf{G}^{CLVD}\ /3$).

As regards the layered medium, we use recent V_p [Judenherc and Zollo, 2004] and 3D V_p/V_s [Chiarabba et al., 2006] models and the Nafe-Drake curve to infer density and elastic parameters (layered model LM1). To test the sensitivity of results to details of elastic parameter layering and to take into account the drained response of the medium (more appropriate to study slow ground deformation) we also consider two additional layering models (LM2 and LM3). Density profile is the same in LM1, LM2, and LM3. In case of LM2, we use the same V_s profile as in LM1, and $\lambda=\mu$. In case of LM3, we use the same V_p profile as in LM1, and $\lambda=\mu$. Layering models are listed in Figure 2. Values for intermediate depths are obtained by linear interpolation between adjacent listed depths.

Layered models (LMs)

Velocity model (from CF tomography)			LM1 (velocity model and Nafe-Drake)				LM2 (Vs from velocity model; λ=μ)			LHS3 (Vp from velocity model; λ=μ)		
depth (km)	Vp (km/s)	Vs (km/s)	depth (km)	density (kg/m³)	λ (Gpa)	μ (GPa)	depth (km)	density (kg/m³)	λ(μ) (Gpa)	depth (km)	density (kg/m³)	λ(μ) (Gpa)
0.00	1.60	0.85	0.00	1800	2.00	1.30	0.00	1800	1.30	0.00	1800	1.54
0.62	2.50	1.35	0.62	2100	5.47	3.83	0.62	2100	3.83	0.62	2100	4.38
1.40	3.20	1.78	1.40	2270	8.86	7.19	1.40	2270	7.19	1.40	2270	7.75
1.55	3.90	2.17	1.55	2380	13.79	11.21	1.55	2380	11.21	1.55	2380	12.07
2.73	3.95	2.32	2.73	2400	11.61	12.92	2.73	2400	12.92	2.73	2400	12.48
3.92	5.20	3.25	3.92	2580	15.26	27.25	3.92	2580	27.25	3.92	2580	23.25
4.03	5.92	3.42	4.03	2700	31.46	31.58	4.03	2700	31.58	4.03	2700	31.54

Fig. 2. Velocity and elastic parameter models.

Layering effects are larger on horizontal ground displacements (H) than vertical ones (V). We already suggested that if synthetics are generated in a layered half-space (LHS) and inverted in a homogeneous half-space (HHS), retrieved source parameters depend on the relative weight of horizontal and vertical displacement data in the misfit function, and it is impossible to fit H and V simul-

taneously [Crescentini and Amoruso, 2007]. Figure 3 shows H and H/V due to a point crack embedded in the layered medium used in this work (see below for details). We have tried to reproduce the same data set by using a point spheroidal source or a finite crack embedded in a homogeneous half space. Figure 3 shows that if H is fitted, H/V is underestimated, while if H/V is fitted, H maximum is too close to the source axis or H pattern is wrong. Since vertical displacement data are usually more numerous and reliable than horizontal displacement data, predictions of the best-fit model fit vertical displacement data better than horizontal displacement data [e. g., Battaglia et al., 2006; Gottsmann et al., 2006a].
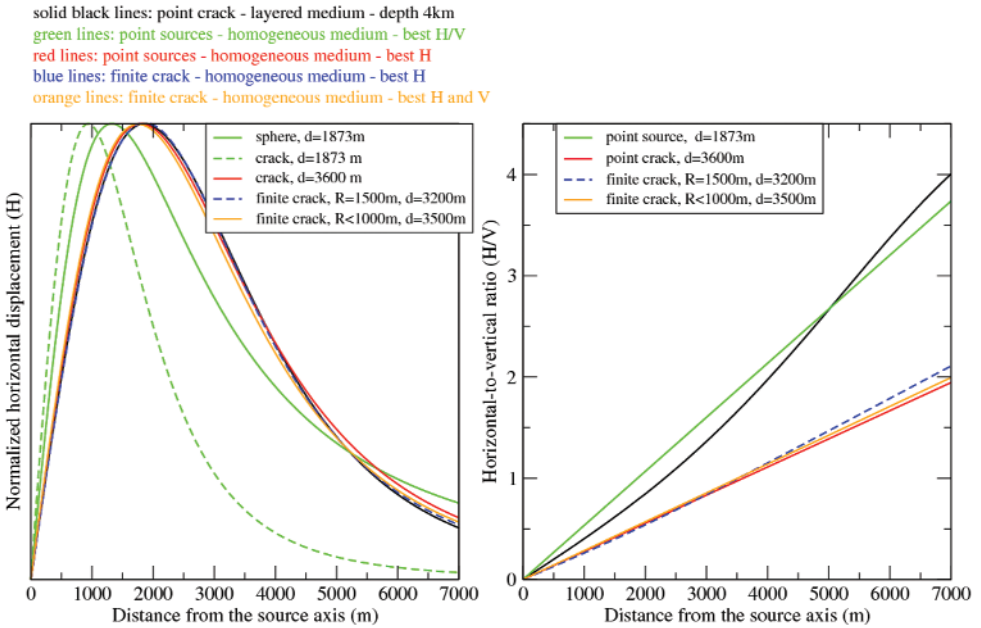
Fig. 3. Horizontal displacement (H) and horizontal to vertical ratio (H/V) for different sources embedded in a homogeneous medium and in the layered medium.

The effects of a mass-less expanding source, given by the addition of vertical movement effects (free air effect) and subsurface mass redistribution (deformation effect)[e.g., Walsh and Rice, 1979] are subtracted from the observed gravity changes, obtaining the gravity residuals. If the background gravity noise due to water table fluctuations is negligible, the gravity residuals are finally used to infer the intrusion density, after fixing the geometry, potency (i.e., volume change) and depth of the source, based on the ground deformation data.

In case of a finite crack, gravity changes due to the intrusion mass are computed from the gravity potential due to a homogeneous triaxial ellipsoid [Landau and Lifsits, 1975].

Data inversion leads to minimizing a cost function which measures the disagreement between model and observations adjusting a suitable set of model parameters. The cost function is obtained from maximum-likelihood arguments according to the statistical distribution of the residuals, i.e. of the differences between data and model predictions. We use two different cost functions, namely the mean squared deviation of residuals (chi-square fitting, M_2, proper for normally distributed errors) and the mean absolute deviation of residuals (M_1, proper for two-sided-exponentially distributed errors and commonly used for robust fitting). The cost function M_1 is less sensitive to the presence of outliers, which can prevent accurate determination of model parameters if M_2 is minimized [e.g. Amoruso et al., 2002].

Residuals are due to random measurement errors as well as to non-measurement errors, mainly caused by benchmark instabilities and the use of an inadequate model (e. g. a simple shape of the intrusion). We consider the complete covariance matrix for each different data set, obtained by combining the covariance matrix due to measurement errors and the covariance matrix due to non-measurement errors, under the simple hypothesis of lack of correlation among bench marks for non-measurement errors.

The complete covariance matrix for each data set (e. g. correlated measurement errors and uncorrelated non-measurement errors in the case of levelings) is not diagonal, but is symmetric and is reduced to diagonal form by means of a rotation matrix. The same rotation transforms the data to independent form (i. e. into a set of statistically independent data, which are linear combinations of the measured data set). The eigenvalues of the complete covariance matrix give the uncertainties of the transformed independent data [Amoruso and Crescentini, 2007]. This procedure can be used also in case of non-normal distribution of errors. Misfit is written in terms of the transformed independent data set. To minimize misfit we use two different codes.

Adaptive simulating annealing [ASA, Ingber 1993] finds the best global fit of a non-linear non-convex cost-function over a D-dimensional space. Different parameters have different finite ranges, annealing schedules and annealing-time-dependent sensitivities. Even if success in finding the global minimum is never guaranteed and inversions from different starting points and/or different cooling parameters often lead to different endpoints, after running a proper number of inversions the distribution of retrieved endpoints allows the identification of the region containing models of acceptable data fit.

Neighbourhood Algorithm [NA, Sambridge, 1999] generates ensembles of models which preferentially sample the the good data-fitting regions of the parameter space, rather than seeking a single optimal model. The algorithm makes use of only the rank of a data fit criterion rather than the numerical

value, so all difficulties associated with the scaling of a data misfit function are avoided, and any combination of data fit criteria can be used.

Assessment of parameter uncertainties is performed using NAB, that makes quantitative inferences from the entire ensemble produced by any direct search method (in our case ASA or NA) without any assumption and allows measures of resolution and trade-offs, within a Bayesian framework. The input ensemble is used to construct a multidimensional interpolant (based on Voronoi cells) of the data to measure, or more generally the posterior probability density function (PPD).

DATA

The data set includes leveling, EDM and gravity data. We consider the period September 1980-September 1983 in order to have the maximum amount of different data (Figure 4); measurement errors and data have been kindly provided by G. Berrino (personal communication). The data set has already been used in the past [e. g. Dvorak and Berrino, 1991; Gottsmann et al., 2003; Battaglia et al., 2006 and references therein].

Precision levelings have been carried out according to the first order optical leveling standards. While measurement errors can be a-priori evaluated, it is difficult to estimate non-measurement errors. As we have already shown, if measurement errors have been correctly evaluated, average non-measurement
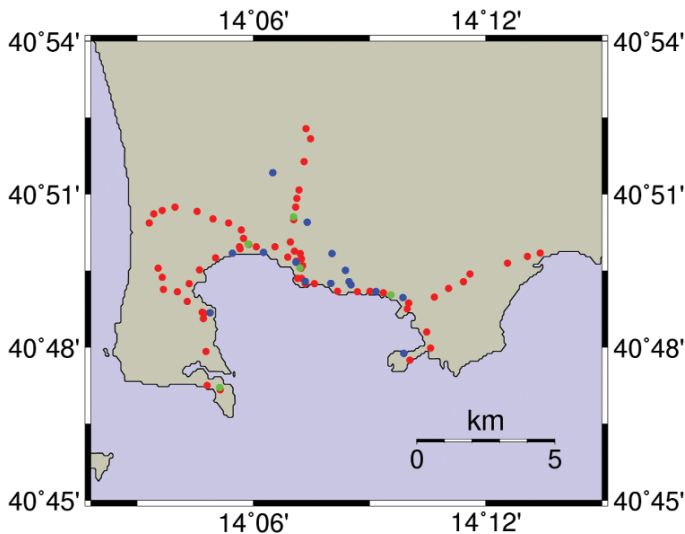
Fig. 4. Map of the Campi Flegrei area, showing location of geodetic bench marks. Red circles, leveling bench marks; green circles, EDM monuments; blue circles, gravity stations.

errors can be estimated by choosing their weight inside the covariance matrix so that the ratio between the total square residual for the χ^2 best-fit model and the number of degrees of freedom is about one. This result holds even if non-measurement errors are different from bench mark to bench mark and/or not normally distributed [Amoruso and Crescentini, 2007].

MODELING

We invert the whole data set for source center location (x_s, y_s, z_s), potency (ΔV), aspect ratio (a.r.=(polar radius)/(equatorial radius), point source) or radius (R, finite crack), and intrusion density (ρ).

Best-fit model parameters obtained using ASA and NA are quite similar and here we show what obtained using ASA (see Table 1 for a point spheroidal source and Table 2 for an extended crack).

We compute marginal probability density functions (PDFs) of all model parameters. Figure 5 shows PDFs for a finite crack embedded in LM3 (i. e., the model with the lowest misfit), obtained sampling the parameter space

Tab. 1. Best-fit models for a point spheroidal source.

Earth model	Misfit	Misfit value	z_s (m)	$\Delta V (m^3)$	ρ (kg/m^3)	a.r.
HHS	M_2	328	4000	3.5×10^7	1200	0.4
LM1	M_2	548	4700	3.2×10^7	2300	0
LM2	M_2	503	4700	3.0×10^7	2700	0
LM3	M_2	451	4700	2.9×10^7	2800	0
HHS	M_1	110	4000	3.9×10^7	1300	0.5
LM1	M_1	139	4700	3.2×10^7	1600	0
LM2	M_1	134	4800	3.1×10^7	2000	0
LM3	M_1	132	4800	3.1×10^7	2000	0

Tab. 2. Best-fit models for a finite crack.

Earth model	Misfit	Misfit value	z_s (m)	$\Delta V (m^3)$	ρ (kg/m^3)	R (m)
HHS	M_2	323	3600	3.0×10^7	900	1800
LM1	M_2	240	2700	2.3×10^7	2400	2900
LM2	M_2	235	2800	2.2×10^7	2700	2900
LM3	M_2	229	2900	2.2×10^7	2700	2800
HHS	M_1	113	3700	3.3×10^7	900	1900
LM1	M_1	103	2800	2.3×10^7	2200	2800
LM2	M_1	102	2900	2.2×10^7	2500	2800
LM3	M_1	101	3000	2.2×10^7	2500	2800

using NA and misfit M_1. As expected, density is the least defined parameter, but its PDF is completely inconsistent with hydrothermal fluids and is peaked at values consistent with a (at least partially) magmatic intrusion.

It is interesting to note that 2D marginal PDF of depth and density does not indicate the presence of trade-off (see Figure 6).

Marginal probability density functions
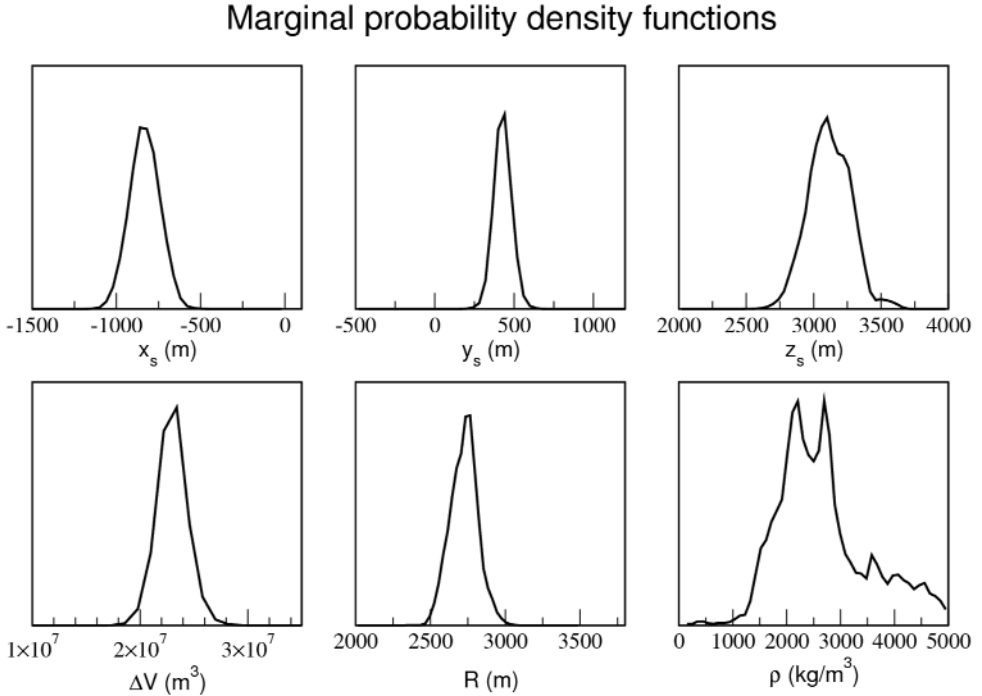
Fig. 5. Marginal probability density functions of model parameters, in case of a finite crack embedded in LM3. Parameter space was sampled using NA and misfit M_1.

CONCLUSIONS

Assessment of volcanic hazard can be dramatically affected by inferred intrusion densities. By inverting ground deformation and gravity data for a penny-shaped crack in a homogeneous half-space, Battaglia et al. [2006] obtained 600 kg/m³ as best-fit intrusion density for the 1982-1984 CF unrest. This value of the intrusion density is in strong disagreement with the intrusion density inferred for spherical sources, which is >3000 kg/m³ both for the single source model in the work by Battaglia et al. [2006] (rejected because of its large χ^2 and the deeper of the two spherical sources in the work by Gottsmann et al. [2006b]. Results for a penny-shaped crack lead Battaglia et al. [2006] definitely to exclu-
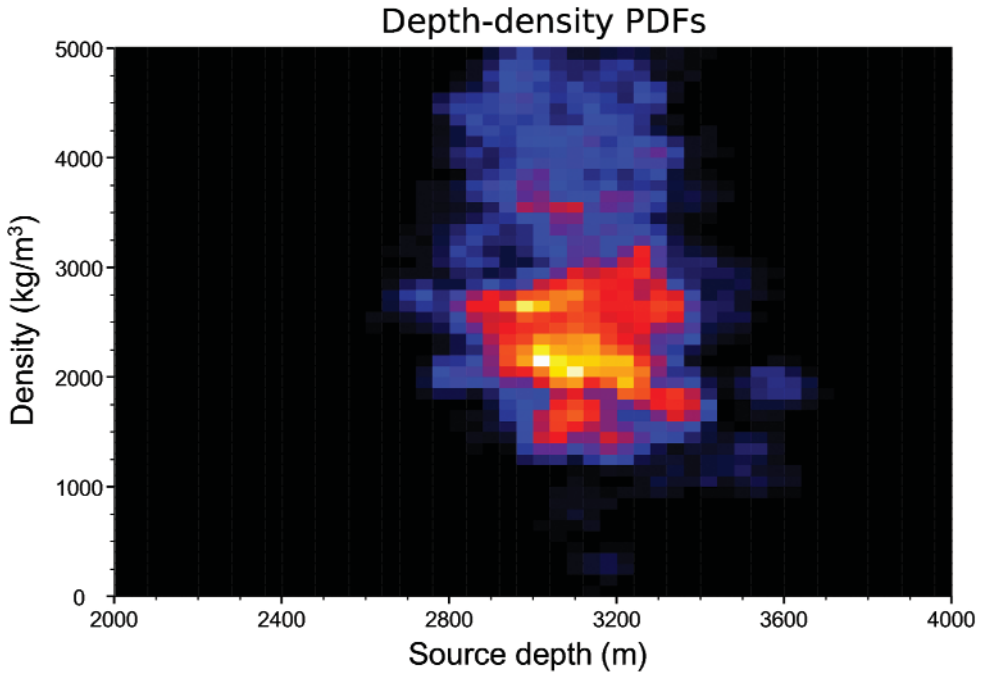
Fig. 6. 2D marginal probability density function of source depth and density, in case of a finite crack embedded in LM3. Parameter space was sampled using NA and misfit M_1.

de the intrusion of magma, and ascribe ground deformation and consequent unrest to the migration of fluid to and from the caldera hydrothermal system. Results shown here are still to be considered preliminary, but they prove that neglecting crustal layering leads to strong density underestimation and consequently to a possibly incorrect assessment of volcanic hazard at CF and other similar calderas. When neglecting layering, we obtain results very similar to those in the work by Battaglia et al. [2006]. In particular, the preferred expansion source is a finite crack, with an intrusion density too low to be ascribable to magma. Taking into account layering lowers misfit (because of a better fit of horizontal displacements) and leads to higher intrusion densities (2200 to 2700 kg/m³, depending on the misfit function minimized in the inversions). Our results do not support hydrothermal fluid intrusion as the primary cause of the Campi Flegrei 1982-1984 unrest, indicating an effective role of magma.

REFERENCES

Amoruso, A., L. Crescentini, and R. Scarpa, J. Geophys. Res.,107, B4, 2080, doi:10.1029/2001JB000434, 2002.

Amoruso, A., L. Crescentini, and C. Fidani, Geophys. J. Int., 159, 353-364, 2004.

Amoruso, A., and L. Crescentini, Geophys. J. Int., in press, 2007.

Battaglia, M., C. Troise, F. Obrizzo, F. Pingue, and G. De Natale, Geophys. Res. Lett., 33, doi:10.1029/2005GL024904, 2006.

Berrino, G., G. Corrado, G. Luongo, and B. Toro, Bull. Volcanol., 44, 187-200, 1984.

Berrino, G., J. Volcanol. Geotherm. Res., 61, 293-309, 1994.

Bonafede, M., J. Volcanol. Geotherm. Res., 48, 187-197, 1991.

Bonafede, M., and M. Mazzanti, J. Volcanol. Geotherm. Res., 81, 137-157, 1998.

Chiarabba, C., M. Moretti, and P. De Gori, in Geophysical Exploration of the Campi Flegrei (Southern Italy) Caldera Interiors: Data, Methods, and Results, edited by A. Zollo et al., pp. 34-37, Doppiavoce, Napoli, Italy, 2006.

Chiodini, G., M. Todesco, S. Caliro, C. Del Gaudio, G. Macedonio, and M. Russo, Geophys. Res. Lett., 30(8), 1434, doi:10.1029/2002GL016790, 2003.

Crescentini, L., and A. Amoruso, Geophys. Res. Lett., 34, L09303, doi:10.1029/2007GL029919, 2007.

Crescentini, L., A. Amoruso, and M. Carpentieri, this issue, 2007.

Davis, P.M., J. Geophys. Res., 91, 7429-7438, 1986.

De Natale, G., F. Pingue, P. Allard, and A. Zollo, J. Volcanol. Geotherm. Res., 48, 199-222, 1991.

De Natale, G., C. Troise, and F. Pingue, J. Geodyn., 32, 487-517, 2001.

Dvorak J.J., and G. Berrino, J. Geophys. Res., 96, B2, 2309-2323, 1991.

Dvorak, J. J., and G. Mastrolorenzo, U.S. Geol. Surv. Spec. Pap., 263, 1-47, 1991.

Gaeta, F. S., G. De Natale, F. Peluso, G. Mastrolorenzo, D. Castagnolo, C. Troise, F. Pingue, D. G. Mita, and S. Rossano, J. Geophys. Res., 103, 20,921-20,933, 1998.

Gottsmann, J., G. Berrino, H. Rymer, and G. Williams-Jones, Earth Planet. Sci. Lett., 211, 295-309, 2003.

Gottsmann, J., H. Rymer, and G. Berrino, J. Volcanol Geotherm. Res., 150,132-145, 2006.

Gottsmann, J., A. Folch, and H. Rymer, J. Geophys. Res., 111, B07203, doi:10.1029/2005JB003745, 2006.

Gottsmann, J., A.G. Camacho, K.F. Tiampo, and J. Fernandez, Geophys. J. Int., 167, 1089-1096, doi: 10.1111/j.1365-246X.2006.03157.x, 2006.

Fernandez, J., J.B. Rundle, R.D.R. Granell, and T.-T. Yu, Computers & Geosciences, 23, 3, 231-249, 1997.

Fialko, Y., Y. Khazan, and M. Simons, Geophys. J. Int., 146, 181-190, 2001.

Ingber, L., Math. Comput. Modell., 18, 29-57, 1993.

Judenherc, S., and A. Zollo, J. Geophys. Res., 109, B10312, doi:10.1029/2003JB002876, 2004.

Landau, L. D., and E. M. Lifsits, The classical theory of fields, Pergamon Press, 1975.

Mogi, K., Bull. Earthq. Res. Inst. Univ. Tkyo, 36, 99.134, 1958.

Morhange, C., M. Bourcier, J. Laborel, C. Giallanella, J. P. Goiran, L. Crimaco, and L. Vecchi, Phys. Chem. Earth, Part A, 24, 349-354, 1999.

Morhange, C., N. Marriner, J. Laborel, M. Todesco, and C. Oberlin, Geology, 34, 93-96, 2006.

Rosi, M., A. Sbrana, and C. Principe, J. Volcanol. Geotherm. Res., 17, 273-288, 1983.

Sambridge, M., Geophys. J. Int., 138, 479-494, 1999.

Trasatti, E., C. Giunchi, and M. Bonafede, J. Volcanol. Geotherm. Res., 144, 105 -118, 2005.

Yang, X.-M., P.M. Davis, and J.H. Dieterich, J. Geophys. Res., 93, 4249-4257, 1988.

Walsh, J. B., and J. R. Rice, J. Geophys. Res., 84, 156-170, 1979.

Wang, R., F. Lorenzo Martin, and F. Roth, Computers & Geosciences, 32, 527-541, 2006.

Dynamical and stochastic techniques

R. Carniel[1], O. Jaquet[2], M. Tárraga[3]

[1] *Dipartimento di Georisorse e Territorio, Università di Udine, Italy*

[2] *In2Earth Modelling Ltd, Basel, Switzerland*

[3] *Departamento de Volcanología. Museo Nacional de Ciencias Naturales, CSIC, Madrid, Spain*

with acknowledgements to:

W. Aspinall, F. Barazza, E. Del Pin, F. Fattori Speranza, A. García, C. Pshenichny, A. Quintero Oliveros, R. Ortiz.

INTRODUCTION

In the evaluation of the volcanic hazard, several time scales can be taken into account, from the minute to the thousands of years (Carniel et al., 2007a). For each time scale, several independent approaches can be followed while analyzing raw data, and the combination of the results in a bayesian sense is a noteworthy problem on its own (Aspinall et al., 2003; 2006), as the combination of the single results is as important as the methods used to generate them. In other words, the single methodologies constitute a "data reduction" stage to generate the input for the final evaluation stage. These data reduction methodologies can include methods completely based on heuristics, such as the artificial neural networks, others completely deterministic, such as those based on the theory of non linear dynamical systems and the embedding, and others based on a stochastic approach. One of the most informative geophysical time series that can be recorded on a volcano is the continuous seismic noise, that approaching an eruptive phase must show a growing self-organization as it transforms into what is more properly called "volcanic tremor", that has been recognized as extremely information-rich more than 30 years ago (Schick and Riuscetti, 1973).

THE STOCHASTIC APPROACH

A stochastic methodology for the estimation of volcanic hazards at short term was developed using multi-parameter seismic data from monitoring. Specific time series were analysed from different volcanoes using a geostatistical multivariate approach (Jaquet and Carniel, 2006). This stochastic approach was expanded for the integration of several seismic variables, and parameters considered over various periods of time and sampled at different rates (minutely,

hourly to daily) which were monitored at Etna, Stromboli and Teide volcanoes. This development has led to the creation of an integrated multivariate methodology combining stochastic and spectral methods with dynamic systems theory. Results obtained for various periods of time, such as daily sampling summarizing data recorded over many years at Etna, minute data recorded over weeks (Etna) or monthly data (Teide and Stromboli), have enabled the estimation of time scales quantifying the memory intrinsic to volcanic systems. This stage has important implications for the identification of precursors, since it must be based on seismic parameters (or parameters derived from spectral and dynamical analysis) with a sufficient degree of persistence.

Then, the geostatistical multivariate approach was extended in the space-time domain in order to include spatial correlation related to volcano-tectonic events (VT) at Etna. These events are characterised in terms of location, occurrence, magnitude and strain release. It enables the detection of spatial patterns varying in time and likely to occur before the onset of eruptive events. By monitoring the depth and the magnitude of VT distribution, evidence of different correlated behaviours in space was detected and monitored. Such finding has some interesting consequences, because such detection based on time varying patterns leads to the identification of precursory behaviours with added information content, since they integrate the spatial variability of volcanic effects.

The origin of the continuous seismic noise recorded during the last few years in the volcanic island of Tenerife (Canary Islands, Spain) is under debate, also due to the important implications in terms of hazard. The seismic noise is strongly affected by anthropogenic contamination but several works have shown that nevertheless a significant fraction of this noise has a natural origin, an origin that appears to be related also to the generation of local tectonic events within or close to the island (see later in this report). In Carniel et al. (2007c), the variogram tool was used to characterize the so called "persistence" of the seismic noise. This has important implications in terms of how informative the recorded noise can be about its future evolution, and this in turn puts important constraints on how likely it is for the seismic noise to be the source of potential precursors highlighting variations in the volcanic activity that is supposed to generate (part of) this seismic noise. In particular, the memory characterization can help to distinguish the naturally generated seismic noise from the anthropogenic contamination. Although only few clear examples were observed until now, the possibility that this memory can be affected by the occurrence of local tectonic events is also discussed by Carniel et al. (2007c).

FAILURE FORECAST METHOD

Several authors have observed an increase in the rate of change of observables, such as ground deformation, seismicity and gas emission, at different

time scales before an eruption. The first example is probably the one of Bezymyanny volcano in Kamchatka, Russia, where an increase was observed in the rate of seismic energy release ahead of 13 eruptions in October 1959, April 1957 and March 1961 (Tokarev, 1963). Several more examples are presented by Carniel et al. (2007a).

The Material Failure Forecast Method (which we now apply to forecast eruptions) was originally developed to study the mechanics of landslides, with several experimental data acquisitions and subsequent modelling by different authors, starting from the pioneering work of Fukuzono (1985), where analogue models were presented where soil layers deposited at different angles on inclined planes were subjected to an increasing load due to artificial rain. After a given time the surface displacement of the layers with different slopes increased, and material failure was observed after several hours. Empirically, the increase of the logarithm of acceleration was observed to be proportional to the logarithm of displacement velocity immediately before failure.

Voight (1988) proposed a general law of material failure governed by accelerating creep in order to characterise precursory phenomena of volcanic eruptions. This gave birth to the Material Failure Forecast Method (FFM) as we now know it. The underlying hypothesis of this methodology is that deterministic models can be applied to volcanic systems. Pressurisation of a magma reservoir results in material failure, due to fracturing of the host rock. Voight's (1988) original approach has subsequently been applied and further developed in a number of studies in order to forecast eruptions or volcano-related seismic events at a number of different volcanoes. An extensive description of the method, its advantages and drawbacks, together with application case studies can be found in Tárraga et al., 2007a.

The FFM methodology was recently applied to the case of Tenerife (Tárraga et al., 2006a). The island of Tenerife (Canary Islands, Spain), is in fact showing possible signs of reawakening after its last basaltic strombolian eruption, dated 1909 at Chinyero. The main concern relates to the central active volcanic complex Teide-Pico Viejo, which poses serious hazards to the properties and population of the island of Tenerife, and which has erupted several times during the last 5000 years, including a subplinian phonolitic eruption (Montaña Blanca) about 2000 years ago. Tárraga et al. (2006a) show the presence of low frequency seismic noise which possibly includes tremor of volcanic origin and investigate the feasibility of using it to forecast, via the material failure forecast method, the time of occurrence of discrete events that could be called Volcano-Tectonic or simply Tectonic (i.e. non volcanic) on the basis of their relationship to volcanic activity. In order to avoid subjectivity in the forecast procedure, an automatic program has been developed to generate forecasts, validated by Bayes theorem. A parameter called "forecast gain" measures (for the first time quantitatively) what is gained in probabilistic terms by applying the (automatic) failure forecast method. The correlation between the obtained forecasts and the occurrence of (Volcano-)Tectonic events – a

clear indication of a relationship between the continuous seismic noise and the discrete seismic events – is the explanation for the high value of this "forecast gain" in both 2004 and 2005 and an indication that the events are Volcano-Tectonic rather than purely Tectonic (Tárraga et al., 2006a).

DYNAMICAL SYSTEMS APPROACH

It is now recognized that volcanoes are complex dynamical systems controlled by the interaction of many processes that can show non-linear behaviour and therefore techniques derived from dynamical systems theory can be used to characterize them and follow their evolution (Carniel and Di Cecca, 1999).

In the dynamical systems approach, the idea is to reconstruct a multidimensional state from a monodimensional time series using a time delay. Each series is an observable of the state of the system which evolves with time, so that it carries information about all the time history of the volcanic system and can be used, alone, to forecast its future evolution. Two parameters are needed (Carniel and Di Cecca, 1999): the optimal "delay-time" is the one that maximizes the coordinates independence, and the optimal "embedding dimension" is the first one that guarantees that all the system dynamics is completely unfolded. Other related techniques include the Detrended Fluctuation Analysis (Del Pin et al., 2006) and the Singular Spectrum Analysis or Singular Value Decomposion (e.g. Carniel et al., 2006a). The dynamical methodology has been applied to different volcanoes at different timescales. At Stromboli volcano, a long-term analysis (1992-96) had already allowed Carniel and Di Cecca (1999) to identify distinct eruptive phases, the transitions between them and the relationships with the occurrence of paroxysmal phases. During this project, at a shorter timescale, the method has been applied to characterize the period preceding the catastrophic explosion of 5 April 2003, also in combination with the Failure Forecast Method (Carniel et al., 2006a).

The well known strombolian activity at Stromboli volcano is occasionally interrupted by rarer episodes of paroxysmal activity which can lead to considerable hazard for Stromboli inhabitants and tourists. On 5 April 2003 a powerful explosion, which can be compared in size with the latest one of 1930, covered with bombs a good part of the normally tourist-accessible summit area. This explosion was not forecasted, although the island was by then effectively monitored by a dense deployment of instruments. After having tackled in a first paper (Carniel et al., 2006a) the problem of highlighting the timescale of preparation of this event, Carniel et al. (2006b) investigated the possibility of highlighting precursors in the volcanic tremor continuously recorded by a short period summit seismic station. Carniel et al. (2006b) showed that a promising candidate at the hours timescale is found by examining the degree of coupling between successive singular values that result from the Singular Spectrum Analysis of the raw seismic data.

At a slightly longer timescale, the method has been used to investigate the effects of the regional tectonic events on the volcanic dynamics of Stromboli. The occurrence of a tectonic event sufficiently close to a volcano and/or sufficiently energetic can trigger a change in its eruptive activity. One of the first examples examined by the group was the one of Ambrym (Vanuatu), where tectonic earthquakes have triggered a significant increase of the permanent lava lakes activity, as highlighted by spectral and dynamical parameters (Carniel et al., 2003). Tectonic events in the area around Stromboli are rare and no evidence of a local tectonic event changing the characteristics of the tremor was previously known (Falsaperla et al., 2003). In April and May, 2006 a swarm of tectonic events was recorded, located very close to the island of Stromboli, possibly within the same volcanic edifice. Carniel and Tárraga (2006) analyzed the time evolution of several dynamical parameters computed on the volcanic tremor and show examples where abrupt transitions can be associated to the occurrence of such local tectonic events.

One important issue when trying to compare the occurrence of tectonic events with the occurrence of transitions in the volcano dynamics is to find a way to define when a transition objectively exists or not within a time series. In fact, no serious attempt has been carried out so far to formalize the identification of these structural changes with a statistical approach. Only recently, the problem was tackled by Fattori Speranza and Carniel (2007), where a statistical approach is applied to test for structural changes in volcanic tremor recorded at Stromboli from April to July, 2006. Different fluctuation type tests using the free source package strucchange in R language were considered and again Stromboli was chosen as a particularly interesting case of study, because previous works (Falsaperla et al., 2003) had suggested that tectonic events have no influence on volcanic activity, while most recent results (Carniel and Tárraga, 2006) suggest that they can have it. Fattori Speranza and Carniel (2007) found that there was at least one structural change associated to every earthquake recorded between April to July 2006, even in the cases for which the previous analysis of Carniel and Tárraga (2006) could not see any convincing variations.

The dynamical methodology has also been applied to Tenerife (Canary Islands, Spain), again together with FFM and again tackling the important issue of the interaction between tectonic and volcanic activity. Also at Tenerife results show that tectonic events can cause significant transitions in the volcanic system dynamics of Teide-Pico Viejo volcanic complex (Carniel et al., 2007b). In particular, the continuous seismic noise recorded in the volcanic island of Tenerife was considered as raw data. The origin of this noise, strongly augmented by anthropogenic contamination, is still under debate, as mentioned above. Transitions were sought by Carniel et al. (2007b) in the time evolution of dynamical parameters computed on the seismic noise, and examples were shown where abrupt transitions can be associated to the occurrence of tectonic events. This information, together with the fact that seismic

noise contains information about the next tectonic events, as we have seen presenting the FFM methodology (Tárraga et al., 2006a), gives further evidence in favor of a possible unique process generating the continuous seismic noise and the tectonic events recorded in or close to the Las Cañadas caldera. The analysis of data recorded between May and December 2004 with tools such as Hidden Markov Models and Bayesian Belief Networks also support the existence of a bidirectional relationship between volcano-tectonic events and the background seismic noise – in particular its frequency content (Quintero-Oliveros et al., 2006).

Although Villarrica volcano in Chile is one of the most active in the southern Andes, the literature studying its seismic activity is relatively scarce. An interesting problem recently tackled is once again the possibility for a regional tectonic event to trigger a change in the volcanic activity of this basaltic to basaltic-andesitic volcano, which is in turn reflected in the time evolution of the properly volcanic seismicity, especially in the form of a continuous volcanic tremor. Tárraga et al. (2006b) conducted a spectral, dynamical and statistical analysis of the tremor recorded during September and October 2000, in order to characterize the anomalous behaviour of the volcano following a tectonic event recorded on 20th September 2000. The observed dynamical transitions are compared with remote sensing and visual observations describing the changes in the eruptive style of the volcano.

Conclusions

Probabilistic methodologies using stochastic methods and dynamical techniques were developed for the characterisation and analysis of multi-parameter data set monitored at active volcanoes. Using these methods enables the modelling of space-time patterns for seismic parameters corresponding to precursors likely to occur before the beginning of an eruption. The monitoring of these (modelled) seismic patterns delivers valuable information together with its uncertainty about current and future states of volcanic activity. Such results provide the type of input as required by probabilistic risk assessments. In particular, they could be used as input to the BET_EF model (Marzocchi et al., 2006) that applies a Bayesian procedure for the forecasting of volcanic eruptions.

The identification of the time scale at which precursory behaviours are expected to occur is of prime importance for civil protection purposes. Decision making during volcanic crisis requires in fact the analysis of behaviours that exhibit patterns with significant persistence before the onset of an eruption. Only these are likely to provide useful information in relation to changes in the states of the volcanic system. Therefore, the developed approach offers an efficient way for the selection and analysis of various monitoring parameters, potentially relevant for the (probabilistic) forecasting of eruptive events.

REFERENCES

Aspinall W.P., Woo G., Voight B., Baxter P.J. 2003. Evidence based volcanology: application to eruption crises. J. Volcanol. Geotherm. Res. 128 (1-3), 273- 285.

Aspinall W., Carniel R., Jaquet O., Woo G., Hincks T. 2006. Using Hidden Multi-state Markov models with multi-parameter volcanic data to provide empirical evidence for alert level decision-support, Journal of Volcanology and Geothermal Research, 153, 1-2, 112-124, DOI 10.1016/j.jvolgeores.2005.08.010.

Carniel R., Di Cecca, M., 1999. Dynamical tools for the analysis of long term evolution of volcanic tremor at Stromboli, Annali di Geofisica, 42, 3: 483-495.

Carniel R., Tárraga M. 2006. Can tectonic events change volcanic tremor at Stromboli?, Geophysical Research Letters, Vol. 33, L20321, doi:10.1029/2006GL027690.

Carniel R., Ortiz R. and Di Cecca M., 2006a Spectral and dynamical hints on the time scale of preparation of the 5 April 2003 explosion at Stromboli volcano, Canadian J. Earth Sciences 43 (1), 41-55.

Carniel R., F. Barazza, M. Tárraga, R. Ortiz, 2006b. On the singular values decoupling in the Singular Spectrum Analysis of volcanic tremor at Stromboli, EGU Natural Hazards and Earth System Sciences, 6, 903-909, 16-10-2006 http://www.copernicus.org/EGU/nhess.

Carniel R., Di Cecca M., Rouland D. 2003. Ambrym, Vanuatu (July-August 2000): spectral and dynamic transitions on the hours-to-days timescale. J. Volcanol. Geotherm. Res.128, 1-13.

Carniel R., Jaquet, O., Tárraga M., 2007a. Perspectives on the application of the geostatistical approach to volcano forecasting at different time scales. In: Gottsmann, J. and Marti, J (eds.): Caldera volcanism: Analysis, modelling and response, Developments in Volcanology, Elsevier, 2007, in press.

Carniel R., Tárraga M., Barazza F., García, A., 2007b. Possible interaction between tectonic events and seismic noise at Las Cañadas volcanic caldera, Tenerife, Spain. Bull. Volc., doi:10.1007/s00445-007-0193-7.

Carniel R., Tárraga M., Jaquet O., Ortiz R., García, A., 2007c. The seismic noise at Las Cañadas volcanic caldera, Tenerife, Spain: Persistence characterization, and possible relationship with regional tectonic events. J. Volcanology Geothermal Research, doi:10.1016/j.jvolgeores.2007.12.044.

Del Pin E., Carniel R., Tárraga M., 2006. Event recognition by detrended fluctuation analysis: An application to Teide-Pico Viejo volcanic complex, Tenerife, Spain. Chaos, Solitons and Fractals, Elsevier, Available online 26 September 2006, . doi:10.1016/j.chaos.2006.07.044

Falsaperla S., Alparone S., Spampinato S. 2003. Seismic features of the June 1999 tectonic swarms in the Stromboli volcano region, Italy. J. Volcanol. Geotherm. Res., 125(1-2), 121-136.

Fattori Speranza F., Carniel R. 2007. Structural Changes of Volcanic Tremor at Stromboli Volcano. Journal of Volcanology and Geothermal Research, Available online 17 November 2007. doi:10.1016/j.jvolgeores.2007.11.003.

Fukuzono T. 1985. A new method for predicting the failure time of a slope. In: Proc IV International Conference and Field Workshop on Landslides, Tokyo.

Jaquet O., Carniel R. 2006. Estimation of volcanic hazards using geostatistical models, Statistics in Volcanology, edited by H.M. Mader, S.G. Coles, C.B. Connor and L.J. Connor, IAVCEI Publications, Geological Society of London.

Marzocchi W., Sandri L., Furlan C. 2006. A quantitative model for volcanic hazard assessment, Statistics in Volcanology, edited by H.M. Mader, S.G. Coles, C.B. Connor and L.J. Connor, IAVCEI Publications, Geological Society of London.

Quintero Oliveros A., Carniel R., Tárraga M., W. Aspinall, 2006. On the application of Hidden Markov Model and Bayesian Belief Network to seismic noise at Las Cañadas Caldera, Tenerife, Spain. Chaos, Solitons and Fractals, Elsevier, Available online, 13 November 2006., doi:10.1016/j.chaos.2006.09.073

Schick R., Riuscetti M. 1973. An analysis of volcanic tremor at South-Italian volcanoes. Zeit. Geophysik, 39, 262-274.

Tarraga M., Carniel R., Ortiz R., Marrero J.M., Garcia A. 2006a. On the predictability of volcano-tectonic events by low frequency seismic noise analysis at Teide-Pico Viejo volcanic complex, Canary Islands, EGU Natural Hazards and Earth System Science, 6, 365-376, 15-5-2006. http://www.copernicus.org/EGU/nhess

Tárraga M., Carniel R., Ortiz R., García A., Moreno H. 2006b. A dynamical analysis of the seismic activity of Villarrica volcano (Chile) during September-October 2000. Chaos, Solitons and Fractals, Elsevier, Available online 18 December 2006, .doi:10.1016/j.chaos.2006.10.062

Tárraga M., Carniel R., Ortiz R., García A. 2007a. The Failure Forecast Method. Review and application for the realtime detection of precursory patterns at reawakening volcanoes. In: Gottsmann, J. and Marti, J (eds.): Caldera volcanism: Analysis, modelling and response, Developments in Volcanology, Elsevier, 2007, in press.

Tokarev P.I. 1963. On a possibility of forecasting of Bezymianny volcano eruptions according to seismic data. Bull. Volcanol 26:379-386.

ANGELA:
a new package for the near-real-time inversion of geodetic data in layered media

L. Crescentini, A. Amoruso, M. Carpentieri

Dipartimento di Fisica, Università di Salerno, Italy

Abstract: One of the most promising ways of studying volcanic phenomena is the use of high-precision deformation and gravity data. Crustal layering affects the deformation pattern (giving an apparent shallower source if layering is not taken into account), the ratio of horizontal to vertical displacements (biasing the source shape), and the subsurface mass redistribution effects on gravity changes. We have developed a new numerical package (ANGELA, ANalysis of GEodetic data in Layered media) which can be used to invert geodetic data for different kinds of sources embedded in an elastic layered half-space. Model sources are represented as linear combination of four fundamental point sources. Forward computations are performed by discrete convolution of the linear combination coefficients and stored 2-D Green's functions, which depend on layering details. The code is fast enough to be suitable for near real-time applications in alert systems even using a single PC.

INTRODUCTION

One of the most promising ways of studying volcanic phenomena is the use of high-precision deformation and gravity data. In the framework of an alert system, it is essential that near real-time inversion of data could be performed. Critical stages prior to a volcanic eruption are usually investigated in the framework of linear elastostatic analyzes developed from the study of volcanic unrest in terms of mechanical models and the overpressure in magma chambers and conduits.

Mogi [1958] applied solutions for a point spherical pressure source to surface displacement data to show that, for eruptive activity at Sakurajiima and Kilauea, such observations provided constraints on the reservoir location. This model continues to enjoy widespread use, especially since commonly the sparsity of data available for investigating volcanic activity generally requires that only solutions with the fewest number of parameters can be considered. In most settings, the only available measurements derive from GPS observations and levelling service. On the other hand, it is intrinsically unrealistic to

model the magma chamber as a point source of volume change and a dike as an opening-mode dislocation, assuming that the earth is a homogeneous, isotropic, elastic half-space. This approach often poses difficulties in simultaneously modeling observed horizontal and vertical displacements and gravity changes at calderas and other volcanic areas. If the effects on the intrusion are not due primarily to pressure changes in the intrusion, but instead there is a considerable amount of magma recharge, elastic-gravitational models should be used [e. g. Tiampo et al., 2004]. The presence of inelastic (e.g. Maxwell viscoelastic) layers can produce large signal amplifications [e. g. Fernandez et al., 2001]. The effects of elastic layering are larger on horizontal ground displacements than vertical ones [e. g. Crescentini and Amoruso, 2007].

The inversion of geodetic and seismic data is intrinsically nonlinear and results in cost functions with a rough landscape and several local minima. Local optimization techniques can fall into a local minimum, which depends strongly on the starting model. Among the global optimization techniques, we have used ASA (adaptive simulating annealing) to invert geodetic and seismic data for the sources of strong Italian earthquakes occurred last century [e. g. Amoruso et al., 2002]. Others [e. g. Tiampo et al., 2004] have used GA (genetic algorithm) to determine the parameters of a volcanic intrusion. Finite element modeling allows to incorporate realistic features, such as the topography and the 3D heterogeneities inferred from seismic tomography, in the computation of ground deformation [e.g. Trasatti et al., 2005] but as global optimization techniques require to solve many forward problems, time-consuming techniques like 3D finite-element modeling can not be integrated in the inversion codes, and are unsuitable for near real-time applications in alert systems.

We have developed a new numerical package (ANGELA, ANalysis of Geodetic data in LAyered media) which can be used to invert geodetic data for different kinds of sources embedded in an elastic layered half-space, in a reasonably short time.

CONFIGURATION (REQUESTED RESOURCES)

ANGELA has been tested on Pentium-4 PCs running Linux. It is written in C and Fortran and has been compiled using GNU compilers (>4.0.2, http://gcc.gnu.org). All subroutines included in ANGELA can be freely downloaded from the web (ASA from http://www.ingber.com, GRAVW4 from http://www.iamg.org) or obtained from the authors upon request (NA and NAB from M. Sambridge, http://wwwrses.anu.edu.au/~malcolm; PSGRN v.4.4 from R. Wang, http://www.gfz-potsdam.de). Even if it could be easily modified for parallel processing, ANGELA presently runs on single processor platforms. Extensive use of dynamic memory allocation and storing of Green's functions actually required by each inversion reduce memory request to what really necessary for each run. In our tests, memory usage never exceeded few

ten Mbytes. Run time for a single point source is a few minutes. In case of a single finite crack, run time can be as long as a couple of hours. In any case, it is suitable for near real-time applications in alert systems even using a single PC.

CODE BASICS

Data inversion usually leads to minimizing a cost function which measures the disagreement between model and observations adjusting a suitable set of model parameters. The cost function is obtained from maximum-likelihood arguments according to the statistical distribution of the residuals, i.e. of the differences between data and model predictions.

In linear problems it is common to use χ^2 as cost function. The main reason of this widespread use is its simplicity: it leads to least squares techniques and an ellipsoidal cost function in parameter space; cost function minimization reduces to matrix inversion. In nonlinear problems most linearized inversion techniques correspond to a gradient-based optimization algorithm (i. g. steepest descent, conjugate gradients, and Newton-Raphson). Linearized inversion techniques can be applied to weakly nonlinear problems, but, in case of highly nonlinear ones, a good enough guess at the solution must be available in advance, because of multimodal cost functions. In this case an even greater problem relates to what data inversion means. The model corresponding to the global minimum is of little use by itself, and inference should be based on the class of all acceptable models.

Since geodetic data do not depend linearly on model parameters, there is no advantage in using χ^2 as cost function. Besides the mean squared deviation of residuals (χ^2-fitting, M_2, proper for normally distributed errors) we also use the mean absolute deviation of residuals (M_1, proper for two-sided-exponentially distributed errors and commonly used for robust fitting). The cost function M_1 is less sensitive to the presence of outliers, which can prevent accurate determination of model parameters if M_2 is minimized [e.g. Amoruso et al., 2002]. Residuals are due to random measurement errors as well as to non-measurement errors, mainly caused by benchmark instabilities and the use of an inadequate model (e. g. a too simple source shape). We consider the complete covariance matrix for each different data set, obtained by combining the covariance matrix due to measurement errors and the covariance matrix due to non-measurement errors, under the simple hypothesis of lack of correlation among bench marks for non-measurement errors.

The complete covariance matrix for each data set (e. g. correlated measurement errors and uncorrelated non-measurement errors in the case of levelings) is not diagonal, but is symmetric and is reduced to diagonal form by means of a rotation matrix. The same rotation transforms the data to independent form (i. e. into a set of statistically independent data, which are linear combinations of the measured data set). The eigenvalues of the complete covariance matrix give the uncertainties of the transformed independent data

[Amoruso and Crescentini, 2007a]. This procedure can be used also in case of non-normal distribution of errors. Misfit is written in terms of the transformed independent data set, namely:

$$\mathcal{M}_1 = \sum_{j=1}^{M} w_j \sum_{i=1}^{N_j} \left| \frac{x_i - f_i(\mathbf{a})}{\sigma_i} \right|$$

$$\mathcal{M}_2 = \sum_{j=1}^{M} w_j \sum_{i=1}^{N_j} \left(\frac{x_i - f_i(\mathbf{a})}{\sigma_i} \right)^2$$

where j=1,...,M indicates different data sets, w_j is the weight of each data set in the cost function, i=1,...,N_j indicates different rotated independent data (x_i) in each data set, $f_i(\mathbf{a})$ is model prediction of x_i, and σ_i is uncertainty of x_i.

To invert data we use two different codes, the former aims to find the global minimum of the cost function, the latter is multi-dimensional parameter space search algorithm. Adaptive simulating annealing [ASA, Ingber 1993] finds the best global fit of a non-linear non-convex cost-function over a D-dimensional space. Different parameters have different finite ranges, annealing schedules and annealing-time-dependent sensitivities. Even if success in finding the global minimum is never guaranteed and inversions from different starting points and/or different cooling parameters often lead to different endpoints, after running a proper number of inversions the distribution of retrieved endpoints allows the identification of the region containing models of acceptable data fit. Neighbourhood Algorithm [NA-sampler, Sambridge, 1999] generates ensembles of models which preferentially sample the good data-fitting regions of the parameter space, rather than seeking a single optimal model. The algorithm makes use of only the rank of a data fit criterion rather than the numerical value, so all difficulties associated with the scaling of a data misfit function are avoided, and any combination of data fit criteria can be used.

Assessment of parameter uncertainties is performed using NAB, that makes quantitative inferences from the entire ensemble produced by any direct search method (in our case ASA or NA) without any assumption and allows measures of resolution and trade-offs, within a Bayesian framework. The input ensemble is used to construct a multidimensional interpolant (based on Voronoi cells) of the data to measure, or more generally the posterior probability density function (PPD).

At present, ANGELA can invert leveling, dilatometric, EDM, GPS, gravity data, and sea level changes, using models including one or more double-couple sources (uniform slipping extended rectangular faults, possibly divided into a small number of sub-faults), expansion sources (point spheroids and finite horizontal cracks), mass intrusions (point masses and finite horizontal cracks) embedded in a layered half-space.

Model sources are represented as linear combination of four fundamental point sources, namely the strike-slip double-couple, the dip-slip double-

couple, the compensated linear vertical dipole (CLVD), and the isotropic inflation. Following the approach in the work by Davis [1986] far-field deformation due to inflation of a mass-less pressurized vertical spheroid is obtained by a weighted combination of an isotropic point source and a CLVD. Weights depend on the source aspect ratio. As regards a finite horizontal crack, a regular distribution of point cracks over the finite-crack mid-plane gives quite the same ground displacements in a homogeneous half-space as those computed using the code by Fialko et al. [2001] if source depth to radius exceeds 0.8 [Crescentini and Amoruso, 2007]. We approximate the finite crack with the same point crack distribution in a layered half-space also.

Forward computations are performed by discrete convolution of the linear combination coefficients and stored 2-D Green's functions, which depend on layering details.

In case of mass-less sources, time-dependent Green's functions of a given layered viscoelastic-gravitational half-space for the four fundamental dislocation sources at different depths are computed using PSGRN [Wang et al., 2006]. PSGRN considers the coupling between the deformation and the Earth's gravity field; it computes the complete deformation field (three displacement components, six stress components and two tilt components), and the geoid and gravity changes. When possible, results have been compared with those obtained following Pollitz [1997] and Fernandez et al. [1997].

As regards point mass intrusions, the user can take into account elastic-gravitational coupling by computing Green's functions of a given four-layered elastic-gravitational half-space for a point mass at different depths using an *ad hoc* modified version of GRAVW4 [Fernandez et al., 2006]. It computes the three displacement components and the geoid and gravity changes.

In case of an extended intrusion mass (finite horizontal crack) elastic-gravitational coupling can not be taken into account by ANGELA. Gravity changes in (x, y, z) are computed from the gravity potential due to a homogeneous triaxial ellipsoid (semi-axes a, b, c) centered in the coordinate system origin [Landau and Lifsits, 1975], i. e.

$$\Phi = -\pi\rho abcG \int_{\xi}^{\infty} \left(1 - \frac{x^2}{a^2+s} - \frac{y^2}{b^2+s} - \frac{z^2}{c^2+s} \right) \frac{\mathrm{d}s}{R_s}$$

where

$$R_s = \sqrt{(a^2+s)(b^2+s)(c^2+s)}$$

and ξ is the positive root of the equation

$$\frac{x^2}{a^2+\xi} + \frac{y^2}{b^2+\xi} + \frac{z^2}{c^2+\xi} = 1.$$

Near future improvements of the package include additional data (SAR), sources (variable-slip rectangular faults, point scalene ellipsoids with any orientation, finite prolate spheroids), and uncertainty estimation techniques (bootstrapping).

THE ANGELA PACKAGE

Parameters of the elastic layered medium are chosen *a priori* on the basis of seismic tomography and/or geological information, and proper Green's functions are generated as previously described and stored for future use.

ANGELA consists of more than 50 functions. The program is controlled by five ASCII input files, in which tunable parameters and other options (like data file names and number and kind of model sources) are set. Experimental data are changes of some measured quantity between two surveys, and are provided in the form of one file for each data set. Each data file includes location of measurement points and uncorrelated and, when necessary, correlated errors and begins with a header describing the kind of data, the weight of the data set in the cost function, and survey times. Adjustable model parameters include start time of each source in addition to location, geometry, potency, and intrusion density. The output is in the form of a few files giving details on parameter space sampling, partial misfit of each data set, best-fit model predictions, PPDs.

Apart from Green's function generation, a typical ANGELA session consists of five steps:
1. generation of data files;
2. generation of option files (misfit function, annealing parameters for ASA, etc.);
3. data inversion using ASA (to search for the misfit global minimum);
4. parameter space sampling using NA;
5. 1D and 2D marginal PPD estimation using NAB.

EXAMPLES

We have validated the code running several tests on synthetic data. Each test consists of three steps:
1. generation of synthetics, given a layered medium, a set of model parameters and a set of measurement points;
2. addition of random (correlated and uncorrelated) noise to synthetics;
3. inversion of noisy synthetics using ANGELA.

For the sake of conciseness, here we show only one example, chosen because of its relation to the preliminary application of ANGELA to the 1982-1984 Campi Flegrei unrest [Amoruso and Crescentini, 2007b].

Parameters of the proper layered medium are listed in Table 1. Source model consists of a finite horizontal crack embedded in the layered medium. We generate synthetics for EDM, leveling, and gravity measurements (Figure 1).

Tab. 1. Campi Flegrei multilayer model used in this work.

Depth (km)	Density (kg/m^3)	λ, μ (GPa)
0.00	1800	1.54
0.62	2100	4.38
1.40	2270	7.75
1.55	2380	12.07
2.73	2400	12.48
3.92	2580	23.25
4.03	2700	31.54
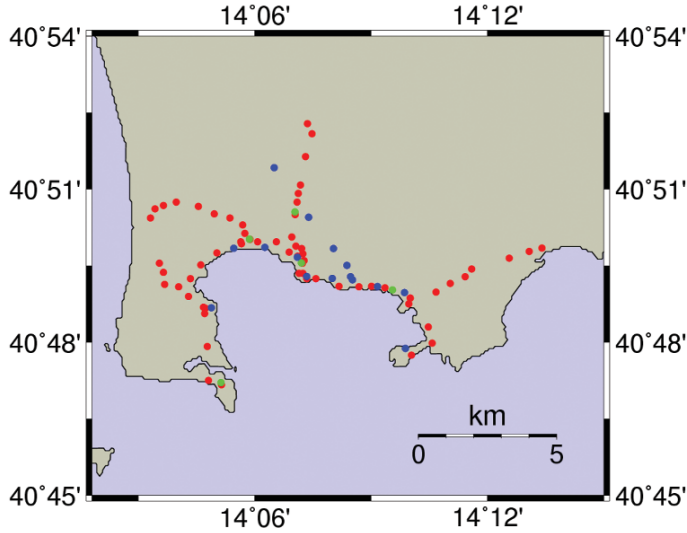
Fig. 1. Map of the Campi Flegrei area, showing location of geodetic bench marks. Red circles, leveling bench marks; green circles, EDM monuments; blue circles, gravity stations.

As regards levelings, we simulate correlated measurement errors adding a zero-mean gaussian noise (standard deviation = 0.24 cm/√km) to computed section height differences and uncorrelated errors adding a zero-mean double-sided exponential noise (mean absolute value = 1 cm) to vertical displacements. As regards EDM and gravity data, we add a zero-mean gaussian noise (standard deviation = 5x10^{-8} m/s^2 for gravity; 0.6x√(1+L^2) cm for EDM, where L is baseline length in km).

We invert the whole data set for source center location (x_s, y_s, z_s), potency (ΔV), aspect ratio (a.r.=(polar radius)/(equatorial radius), point source) or radius (R, finite crack), and intrusion density (ρ).

Best-fit misfits for a point spheroidal source or an extended crack, embedded in a homogeneous half-space or in the layered half-space, are shown in Table 2. An extended crack embedded in the layered half-space gives the lowest misfit, both using M_1 and M_2, showing the capability of ANGELA to discriminate between competing source and Earth models.

We compute marginal probability density functions (PDFs) of all model parameters. Figures 2 and 3 show PDFs for a finite crack embedded in the layered medium (i. e., the model with the lowest misfit), obtained sampling the parameter space using NA and misfits M_1 and M_2 respectively. As expected, density is the least defined parameter, but its PDF allows discriminating between hydrothermal fluids and magmatic intrusions.

Tab. 2. Best-fit misfits for point and extended sources embedded in a homogeneous half-space and in the layered half-space.

Earth model	Cost function	Misfit value point spheroid	Misfit value extended crack
Homogeneous	M_2	362	326
Layered	M_2	352	149
Homogeneous	M_1	132	125
Layered	M_1	122	81
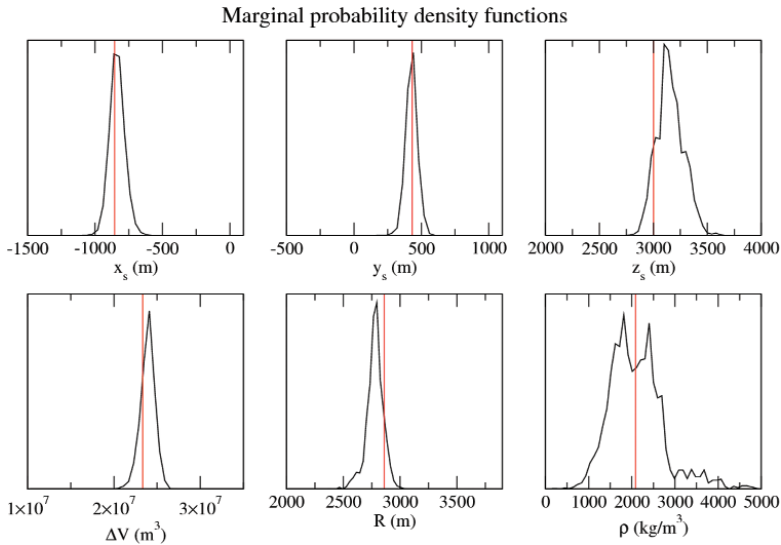
Fig. 2. Marginal probability density functions of model parameters, in case of a finite crack embedded in the layered medium. Parameter space was sampled using NA and misfit} M_1. Red lines indicate forward model parameters.
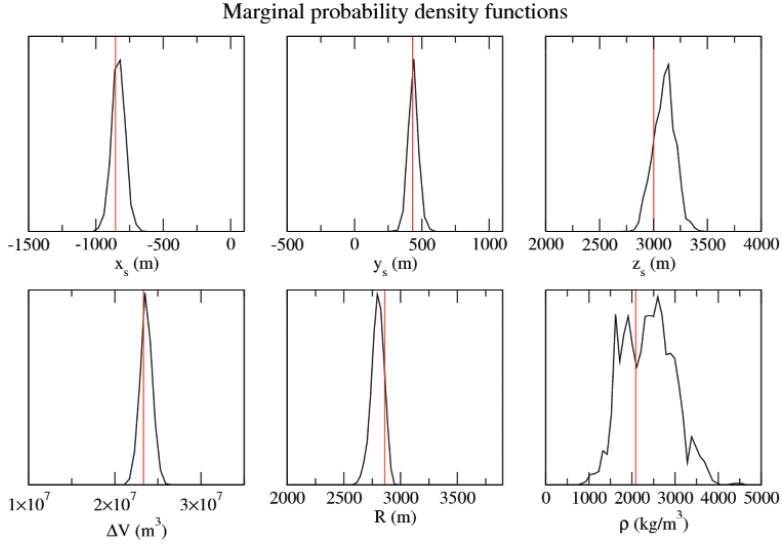
Fig. 3. Marginal probability density functions of model parameters, in case of a finite crack embedded in the layered medium. Parameter space was sampled using NA and misfit M_2. Red lines indicate forward model parameters.

2D marginal PDFs of depth and density are shown in Figure 4.
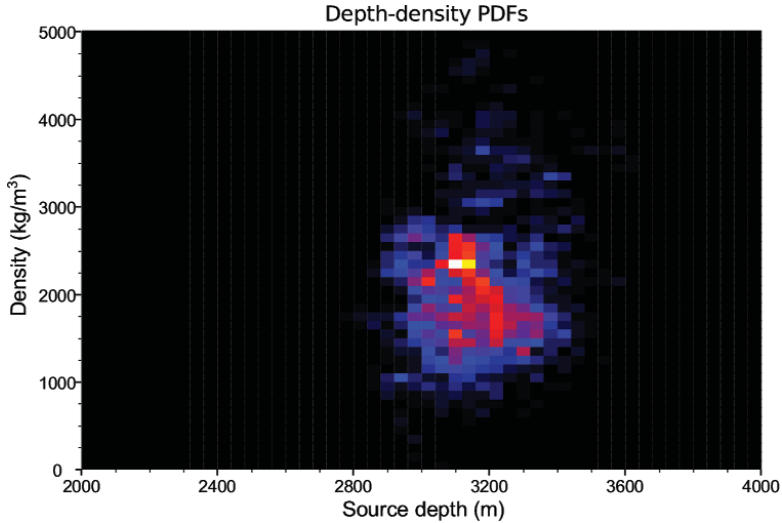
Fig. 4. 2D marginal probability density function of source depth and density, in case of a finite crack embedded in the layered medium. Parameter space was sampled using NA and misfit M_1.

REFERENCES

Amoruso, A., L. Crescentini, and R. Scarpa, J. Geophys. Res.,107, B4, 2080, doi:10.1029/2001JB000434, 2002.

Amoruso, A., and L. Crescentini, Geophys. J. Int., in press, 2007a.

Amoruso, A., and L. Crescentini, this issue, 2007b.

Crescentini, L., and A. Amoruso, Geophys. Res. Lett., 34, L09303, doi:10.1029/2007GL029919, 2007.

Davis, P.M., J. Geophys. Res., 91, 7429-7438, 1986.

Fernandez, J., J.B. Rundle, R.D.R. Granell, and T.-T. Yu, Computers & Geosciences, 23, 3, 231-249, 1997.

Fernandez, J., K. F. Tiampo, and J. B. Rundle, Geophys. J. Int., 146, 155-170, 2001.

Fernandez, J., M. Charco, J. B. Rundle, and K. F. Tiampo, Computers & Geosciences, 32, 275-281, 2006.

Fialko, Y., Y. Khazan, and M. Simons, Geophys. J. Int., 146, 181-190, 2001.

Ingber, L., Math. Comput. Modell., 18, 29-57, 1993.

Landau, L. D., and E. M. Lifsits, The classical theory of fields, Pergamon Press, 1975.

Mogi, K., Bull. Earthq. Res. Inst. Univ. Tkyo, 36, 99.134, 1958.

Pollitz, F. F., J. Geophys. Res., 102, 17921-17941, 1997.

Sambridge, M., Geophys. J. Int., 138, 479-494, 1999.

Tiampo, K. F. , J. Fernandez, G. Jentzsch, M. Charco, and J. B. Rundle, Computers & Geosciences, 30, 985-1001, 2004.

Trasatti, E., C. Giunchi, and M. Bonafede, J. Volcanol. Geotherm. Res., 144, 105 -118, 2005.

Wang, R., F. Lorenzo Martin, and F. Roth, Computers & Geosciences, 32, 527-541, 2006.

Tremor source location
based on amplitude decay

S. Falsaperla, G. Di Grazia, H. Langer

Istituto Nazionale di Geofisica e Vulcanologia, Sezione di Catania, Catania, Italy

Abstract: A 3D grid search method for the location of the volcanic tremor source was applied to data recorded at Mt. Etna in 2004 [Di Grazia et al., 2006]. The aim of that application was to highlight changes in time and space of the location of the tremor source, heralding the onset of a lava emission on 7 September, 2004. The time span investigated ranged from January to November 2004. The method exploits the amplitude decay of the seismic signal recorded at permanent stations used for monitoring purposes. Consequently, it does not require any additional set up of temporary, mobile stations. We present here the results of that application, which was followed in the autumn of 2006 by the successful implementation of the method we named TREMLOC, as an automated and continuous near real time analysis for the location of volcanic tremor at the *Istituto Nazionale di Geofisica e Vulcanologia* (INGV) – Sezione di Catania.

INTRODUCTION

Volcanic tremor is commonly addressed to as the root-mean-square (RMS) amplitude of the seismic signal measured over a time span within a defined frequency band [e.g., Falsaperla et al., 1998]. On basaltic volcanoes with persistent activity, such as Mt. Etna [Patanè et al., 2004], Kilawea [Ferrazzini et al., 1991], and Kliuchevskoi [Gordeev et al., 1990], volcanic tremor is recorded as a persistent signal with no clearly identifiable seismic phases. Consequently, traditional event location methods fail in the attempt to locate its source. Studies dealing with this problem attribute a key role to the amplitude distribution [e.g., Hofstetter and Malone, 1986; Métaxian et al., 1997; Gottschämmer and Surono, 2000; Aki and Ferrazzini, 2000; Battaglia and Aki, 2003, Battaglia et al., 2003].

In agreement with the aforementioned studies, Di Grazia et al. [2006] tackled the problem using the spatial tremor amplitude distribution at Mt. Etna, and estimated the source location using a simplified attenuation law. In this study, we present the results Di Grazia et al. [2006] obtained from the first application of TREMLOC, a robust method to monitor the migration of tremor sources.

Data

The time span considered by Di Grazia et al. [2006] ranged from January to November 2004. It covered eight months of the pre-effusive and three months of the effusive phase, which started at Mt. Etna on 7 September, 2004 and ended on 8 March, 2005. Throughout the eruption, the lava flows stemmed from an eruptive fracture opened in the upper part of the Valle del Bove, far away from inhabited areas (Figure 1). The volcano unrest was characterized by a small effusion rate (2.3-4.1 m³/s) and a slow progression of the lava flows reported by volcanologists [Burton et al., 2005].
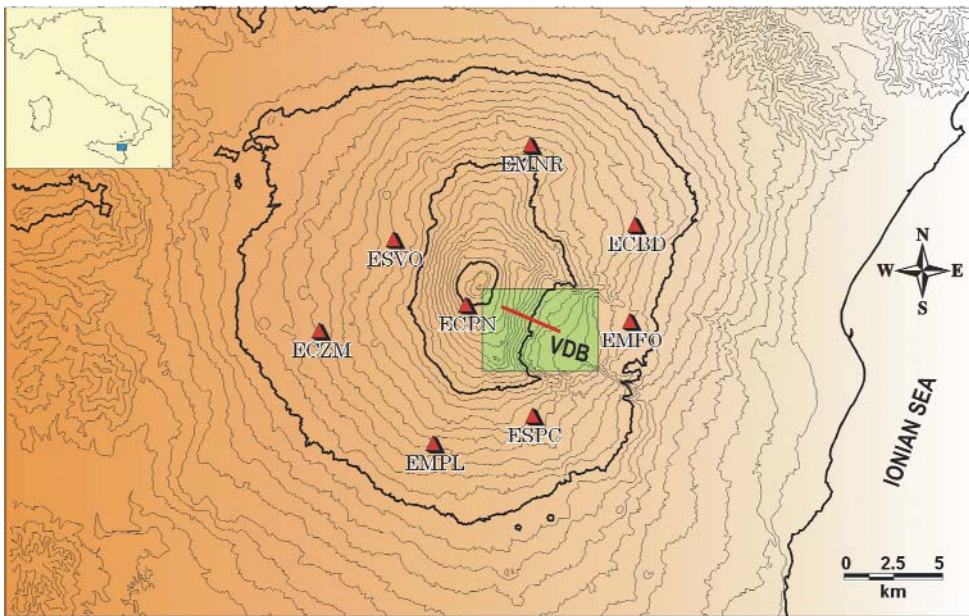
Fig. 1. Configuration of the seismic stations (solid red triangles) and eruptive fracture (red line). VDB stands for Valle del Bove. The green rectangle highlights the zone affected by lava flows.

Unlike other recent eruptions (1989, 1991-1993, 1999, 2001, 2002-2003, 2006), the volcano unrest in 2004 was neither heralded nor accompanied by earthquake seismicity (Figure 2). Volcanic tremor held the same lack of changes, even though it was affected by temporary changes in amplitude and frequency content starting from a couple of weeks after the onset of the effusive phase (Figures 3, 4).
To analyze volcanic tremor and provide the source location of this signal, the amplitude decay at eight stations of the permanent seismic network of Mt.
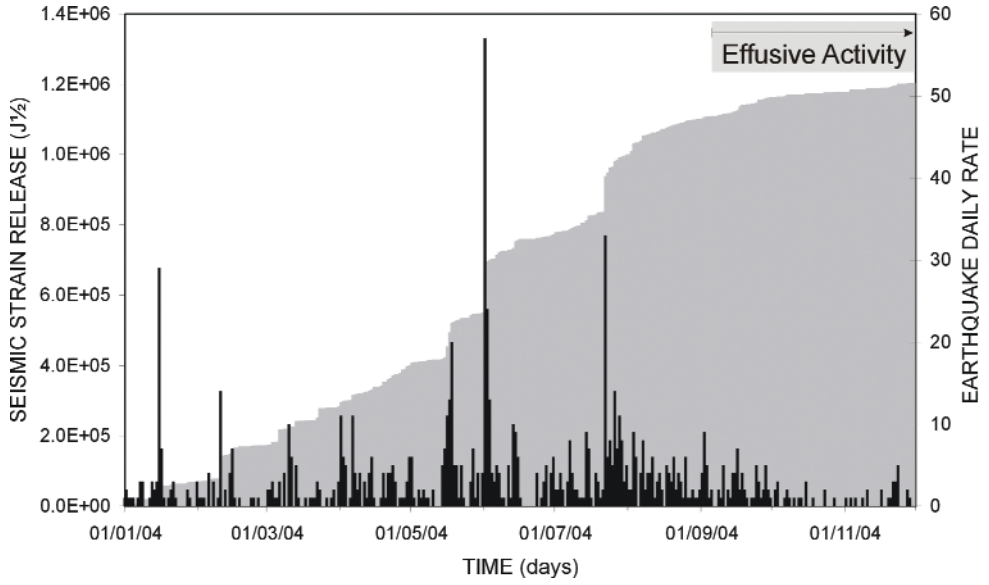
Fig. 2. Earthquake daily rate and seismic strain release from 1 January to 30 November, 2004.
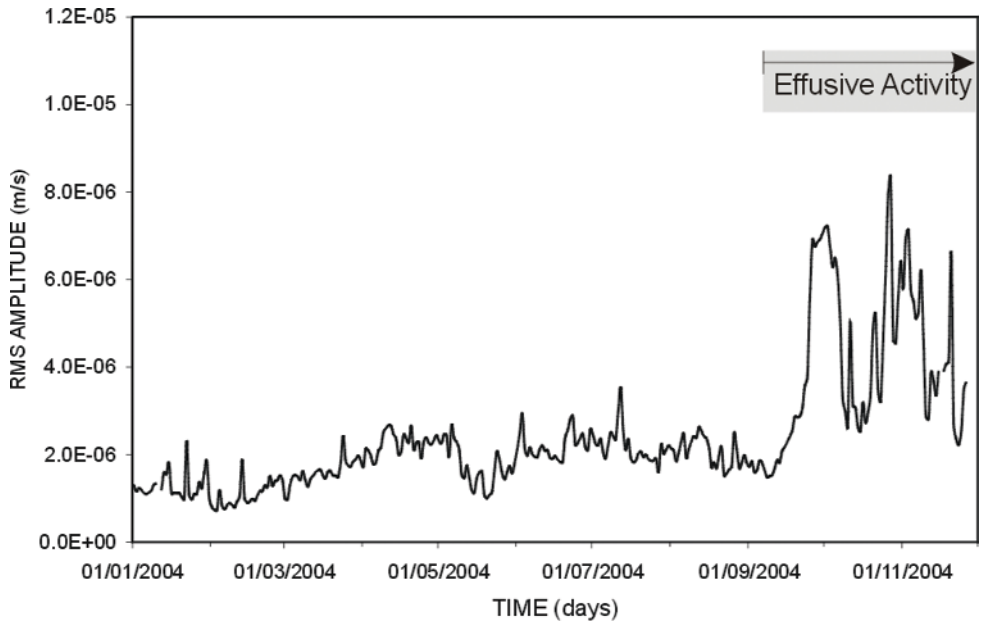
Fig. 3. RMS amplitudes of the 25th percentile of the signal at the vertical component of ECPN from 1 January to 30 November, 2004.
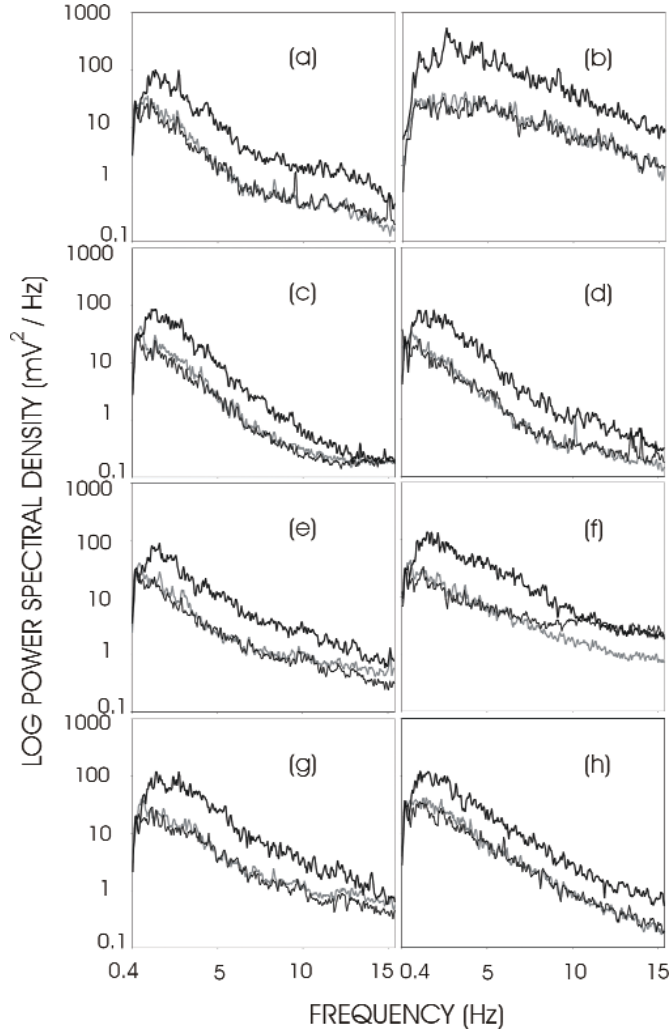
Fig. 4. Power spectral density of the signal at the vertical component of the stations considered in this study: **(a)** ECBD, **(b)** ECPN, **(c)** ECZM, **(d)** EMFO, **(e)** EMNR, **(f)** EMPL, **(g)** ESPC, **(h)** ESVO. For the station location see Figure 1. The stack of consecutive spectra calculated for each station is depicted in three time spans: on 6 (gray line) and 7 September (light black line) and 2 October, 2004 (thick black line). This spectral analysis highlighted that changes in shape and energy of the signal occurred well after the beginning of the effusive phase. Modified from Di Grazia et al. [2006].

Etna was taken into account. The stations used were all equipped with three components, broadband seismometers (Trillium 40 s cut off period sensors, Nanometrics™), and were located within 8 km distance from the summit craters (Figure 1). The choice of these stations was optimal for: their proximity to the summit craters and the zone affected by the eruptive fractures (Figure

1), the excellent signal-to-noise ratio, and the homogeneity of the instrumental chain, which allowed a fast comparison of the signals. Seismic data were acquired with a dynamic range of 24 bit; they were sampled at a frequency of 100 Hz, and transmitted to the data center in Catania via 4 Cygnus VSAT units deployed around Mt. Etna.

METHOD AND RESULTS

Similar to Hofstetter and Malone [1986], Di Grazia et al. [2006] tackled the problem of locating the source of volcanic tremor on the basis of the distance-dependent amplitude decay. Accordingly, the source location was estimated using the seismic amplitude distributions, assuming a seismic amplitude decay with the distance based on the general law

$$\ln A_i + \alpha \, s_i = a - b \ln s_i$$

where A_i is the RMS amplitude measured at the i-th station, a and b are constants, α is the frequency-dependent absorption coefficient, and s_i is the corresponding source-to-receiver distance. A key aspect in this assumption concerned the role of absorption, a factor expressing the loss of energy as seismic waves propagates. It was verified that the frequency-dependent absorption causes only a small deviation from a linear relationship between $\ln A_i$ and $\ln s_i$. Indeed, Di Grazia et al. [2006] found out that even assuming a constant Q-factor as low as 30 [De Gori et al., 2005] and typical frequencies of between 1 and 3 Hz, the linear fit theoretically yields a degree of explained variance over 99% with respect to the total variance. Site correction factors were also taken into account, calculating station corrections based on the residuals of measured amplitudes with respect to the ones predicted by the fit. No a-priori assumption about the characteristics of the radiated waves (i.e., body or surface waves) was made, due to the different wavefield characteristics at each station, the long time window analyzed, and the possibility of concurrent activity of different sources each with its peculiar shape and extension.
The daily amplitude distribution was calculated in the night-time to minimize the effects of external noise. In addition, the 25th percentile was preferred to the mean amplitude of the signal, as the corresponding value gets rid of undesired transient events (e.g., earthquakes, explosion quakes, etc.). The tremor source location was identified on the basis of the goodness of the regression fit (hereafter R^2) obtained for each point of a 3D grid with center underneath the craters. The grid had an extension of 6 km in horizontal and 3 km in vertical direction, with spacing of 500 m. In Figure 5 we depict the results obtained from this application. The results matched two conditions, that is R^2 greater than/equal to 0.95, and at least seven stations available for the calculation. The source locations in Figure 5 are marked with two different colors, distin-

guishing between the pre-effusive phase (yellow) and effusive phase (red). A jackknifing procedure [e.g., Efron, 1982] was applied to assess the stability of the centroid locations. In doing so, first the location was repeated several times using 7 out of 8 stations and changing the left out station each time. Second, the deviations of these locations with respect to the original ones were calculated. Based on this jackknifing procedure, the median values of the deviations were equal to 447 m for latitude, 412 m for longitude, and 747 m for depth.
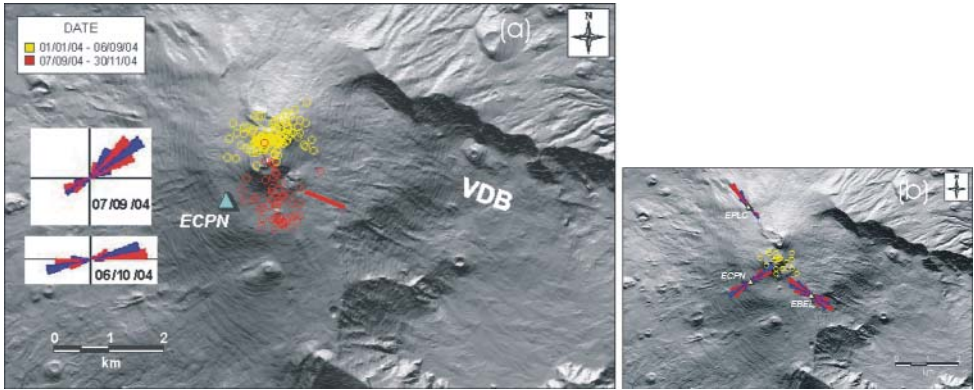
Fig. 5. (a) Map of Mt. Etna and location of the centroid of the tremor source. Colored open circles mark the centroid in two different time spans: pre-eruptive (yellow) and eruptive (red). The red line sketches the fracture system from which the lava emission stemmed. The results of polarization analysis at ECPN (blue triangle) on 7 September and 6 October are depicted on the left. VDB stands for Valle del Bove. **(b)** Results of polarization analysis for three stations of the permanent seismic network on 30 August, 2005. Yellow open circles mark the centroid located using the amplitude decay method. Modified from Di Grazia et al. [2006].

The results depicted in Figure 5a show that with the beginning of the lava effusion, the source locations neatly prevailed south of the summit craters, reaching a maximum distance from them of ca. 2 km. The depths of the source locations were all superficial and within the volcano edifice, i.e., between 1698 m and 2387 m a.s.l. Depths close to the maximum values (1698 m a.s.l.) were found only in the first months of 2004. The source locations had distances of 2 km both from the summit craters as well as the theatre of the volcano unrest (Figures 1, 5a). Independent evidence of this southward migration came from the principal directions of the polarization analysis of the seismic signal (Figures 5a, 5b). Additionally, in the effusive phase, the source locations laid within a region with low Qp anomalies revealed by 3D seismic attenuation tomographic images based on earthquakes recorded from 1994 to April 2001 [De Gori et al., 2005]. Based on these overall results and in agreement with volcanological data [e.g., Burton et al., 2005], Di Grazia et al. [2006]

interpreted the volcano unrest as due to a superficial phenomenon, with weak or no links to the deep internal dynamics of the magma feeder.

DISCUSSION AND CONCLUSIONS

In the application of the 3D grid search method we present here and described in more detail in Di Grazia et al. [2006], we followed a heuristic approach for assessing the location of the tremor sources. Given the well known complex structure of volcanic zones and shallow source depth of tremor at Mt. Etna, we voluntarily refrained from defining physical attenuation and seismic wave propagation models, as whatever assumption would be questionable. In this light, we made no a-priori assumptions either about the source or the properties of the medium. Notwithstanding the simplicity of our method, we found that – for the range of distances of interest in our location problem – the theoretical relation for the amplitude-distance decay could be fitted fairly well by a straight line. Indeed, in our locations we encountered pretty high scores for the goodness of R^2 fit, being on the order of 0.97-0.98 in most cases.

Our location method refers to the position of the centroid of the tremor sources, without separating the single contributions. Consequently, multiple sources (e.g., central conduit, dykes) – concurrently acting within the volcano feeder – might affect the result of the calculation. Even so, however, the solution is an average result which does not necessarily coincide with fixed points in the 3D grid.

The results obtained from the processing of the seismic data recorded in 2004 pointed out that even at the beginning of such a *silent* eruption there were changes in the tremor source location, despite the absence of other geophysical and/or geochemical signals heralding the impending eruptive activity. The use of permanent stations of the seismic network for the calculation of the amplitude decay provided additional value to the method, as it did not require any additional logistic effort.

After the application described in Di Grazia et al. [2006], the 3D grid search method was implemented as a routine procedure in the automated and continuous monitoring system of INGV-Sezione Catania. TREMLOC, as we named it, has been processing seismic data recorded at Mt. Etna in near real time from the autumn of 2006. Ever since, it has proved to be an efficient monitoring tool for volcanic surveillance, and contributes in answering the compelling question of how internal volcanic dynamics at Mt. Etna affects changes of the tremor source in time and space.

Improved versions of the method are in progress to couple with enlarged, variable geometries of the seismic network, and look promising for implementations on different volcanoes where information on the tremor source can positively contribute in volcanic hazard evaluation and risk assessment.

REFERENCES

Aki, K. and V. Ferrazzini, Seismic monitoring and modeling of an active volcano for prediction, J. Geophys. Res., 105, 16617-16640, 2000.

Battaglia J. and K. Aki, Location of seismic events and eruptive fissures on the Piton de la Fournaise volcano using seismic amplitudes, J. Geophys. Res., 108, 2364, 10.1029/2002JB002193, 2003.

Battaglia, J., J.L. Got, P. Okubo, Location of long-period events below Kilawea volcano using seismic amplitudes and accurate relative relocation, J. Geophys. Res., 108, 2553, 10.1029/2003JB002517, 2003.

Burton, M.R., M. Neri, D. Andronico, S. Branca, T. Caltabiano, S. Calvari, R.A. Corsaro, P. Del Carlo, G. Lanzafame, L. Lodato, L. Miraglia, G. Salerno, L. Spampinato, Etna 2004-2005: an archetype for geodynamically-controlled effusive eruptions, Geophys. Res. Letters, 32, L09303, 2005.

De Gori, P., C. Chiarabba, D. Patanè, Qp structure of Mt. Etna: constraints for the physics of the plumbing system, J. Geophys. Res., 110, B05303, 2005.

Di Grazia G., S. Falsaperla, H. Langer, Volcanic tremor location during the 2004 Mount Etna lava effusion. Geophys. Res. Letters, 33, L04304, doi:10.1029/2005GL025177, 2006.

Efron, B., The Jackknife, the Bootstrap and other resampling plans, SIAM, Philadelphia, PA, 1982.

Falsaperla, S., H. Langer and S. Spampinato, Statistical analyses and characteristics of volcanic tremor on Stromboli volcano (Italy), Bull. Volcanol., 60, 75-88, 1998.

Ferrazzini, V., K. Aki and B. Chouet, Characteristics of seismic waves composing Hawaiian volcanic tremor and gas-piston events observed by a near source array, J. Geophys. Res., 96, 6199-6209, 1991.

Gordeev, E.I., V.A. Saltykov, V.I. Sinitsyn and V.N. Chebrov, Temporal and spatial characteristics of volcanic tremor wave fields, J. Volcanol. Geoth. Res., 40, 89-101, 1990.

Gottschämmer, E. and I. Surono, Locating tremor and shock sources recorded at Bromo volcano, J. Volcanol. Geoth. Res.,101, 199-209, 2000.

Hoffstetter, A. and S. Malone, Observations of volcanic tremor at Mount St. Helens in April and May 1980, Bull. Seism. Soc. Am., 76, 923-938, 1986.

Métaxian, J.P., P. Lesage, J. Dorel, Permanent tremor of Masaya volcano, Nicaragua: wave field analysis and source location, J. Geophys. Res., 102, 22529-22545, 1997.

Patanè, D., O. Cocina, S. Falsaperla, E. Privitera, S. Spampinato, Mt Etna volcano: a seismological framework, in A. Bonaccorso, S. Calvari, M. Coltelli, C. Del Negro, S. Falsaperla (eds), Mt. Etna: Volcano Laboratory, AGU Monograph 148, 147-165, 2004.

Can flank instability at Stromboli volcano provide insights into precursory patterns of eruptions?

S. Falsaperla, M. Neri, E. Pecora, S. Spampinato

Istituto Nazionale di Geofisica e Vulcanologia, Sezione di Catania, Catania, Italy

Abstract: By 30 December, 2002 a flank collapse affected the Sciara del Fuoco on the western slope of Stromboli volcano, Italy. To characterize this landslide-prone area for hazard mitigation purposes, Falsaperla et al. [2006] followed a multidisciplinary approach, merging geo-structural observations with visual images (taken by a video-camera surveillance network and vertical ortho-photos) and seismic data recorded throughout the continuous monitoring of the volcano. The study combined these different data types in a complementary framework to assess how and where the Sciara del Fuoco morphology changed. The time span investigated ranged from 2002 to 2004. We present here the results of that study, which identified the zones affected by sliding episodes and highlighted their changes in time. The evidence of the regression of the upper landslide scarp toward the summit craters over the years leads us to speculate about precursory patterns of eruptive activity linked to the progression of flank instability.

INTRODUCTION

The 28 December, 2002 marked the beginning of one of the most peculiar eruptive episodes at Stromboli over the last decades [Ripepe et al., 2005]. A flank collapse occurred two days after the onset of the lava emission [Bonaccorso et al., 2003; La Rocca et al., 2004; Calvari et al., 2005; Acocella et al., 2006], and affected both the subaerial and submarine part of the Sciara del Fuoco (hereafter SDF), a deep scar located in the western side of the Stromboli island. The collapse yielded two huge landslides associated with tsunami waves, which ravaged part of the island and swept the coasts of Sicily and Calabria. The landslides involved over 30 X 10^6 m^3 of material, ~2/3 of which below sea level [Bonaccorso et al., 2003; Pino et al., 2004]. Minor sliding episodes continued throughout the lava emission, which lasted 206 days. Landslides, flowing debris, and rockfalls commonly occur in several volcanic areas. A compelling question which rises when similar exogenous phenomena occur is whether they can cause changes that affect the magma feeder. This

question is the subject of intensive studies on andesitic volcanoes, such as for example Soufrière Hills, Montserrat [e.g., Calder et al., 2002]. Nevertheless, even for a basaltic volcano like Stromboli, the potential high risk of large failure events [e.g., Tibaldi, 2001] poses a significant hazard for the local population. SDF is prone to phenomena of flank instability, and therefore the possibility that events similar to or even larger than those of 30 December, 2002 might affect the volcano feeder became one of the major concerns of Italian Civil Defense and volcanologists ever since.

We present here the results of a multidisciplinary study by Falsaperla et al. [2006], which took into account geostructural data, ortho- and video-images, and seismic records at Stromboli volcano. The study provided an overview of the sliding phenomena at SDF between 2002 and 2004. In the light of the results obtained, we outline potential links between flank instability and endogenous changes, which might impinge upon volcanic activity.

DATA AND ANALYSIS

In the multidisciplinary study proposed by Falsaperla et al. [2006], structural field surveys and aerial, digital ortho-photos (courtesy of M. Marsella) allowed reconstructing the morpho-structural evolution of SDF between 2002 and 2004. Figure 1 depicts the changes over these years. The landslide phenomena of 30 December, 2002 deeply eroded the SDF, creating a depression that in some points reached depths of several tens of meters. Afterwards, a reshape process began through other minor erosive episodes and the deposition of lavas. The latter were erupted within a part of the collapsed/eroded zone, until the end of the eruption on 21 July, 2003. The lava effusion contributed to fill the depression, stabilizing a wide portion (more than 50 percent) of it and approaching a new gravitational equilibrium. Conversely, erosive phenomena continued in the zone of the landslides not reached by the lavas, as evident from the progressive regression of the erosive rim, which approached the crater zone (Figure 2). These phenomena yielded several rockfalls and flowing debris, which involved a rock volume estimated at $\sim 5 \times 10^5$ m^3 [Falsaperla et al., 2006]. A comparative analysis of these sliding processes was based on seismic signals and video images covering the time span from March to October, 2004. The seismic signals were recorded at three seismic stations (Table 1) in continuous acquisition mode. The stations belonged to the permanent seismic network of *Istituto Nazionale di Geofisica e Vulcanologia* (INGV), and were located between a few hundreds meters and 1.8 km from SDF (ISTR, STR3 and STR8 in Figure 1). The images came from two live-cams, which recorded in the visible and IR band. The live-cams were set up in October, 2003 at 374 m a.s.l., and at a distance of 1042 m from SDF (LC in Figure 1). For the thermal live-cam, vertical and horizontal viewing was 18° and 24°, respectively. Video signals were digitalized to 640 X 480 pixels, and a GPS time-code added date

and time to each frame. Both seismic and live-cam equipment was run by INGV, and continuously monitored the volcano in the framework of surveillance activities to reduce volcanic hazard.
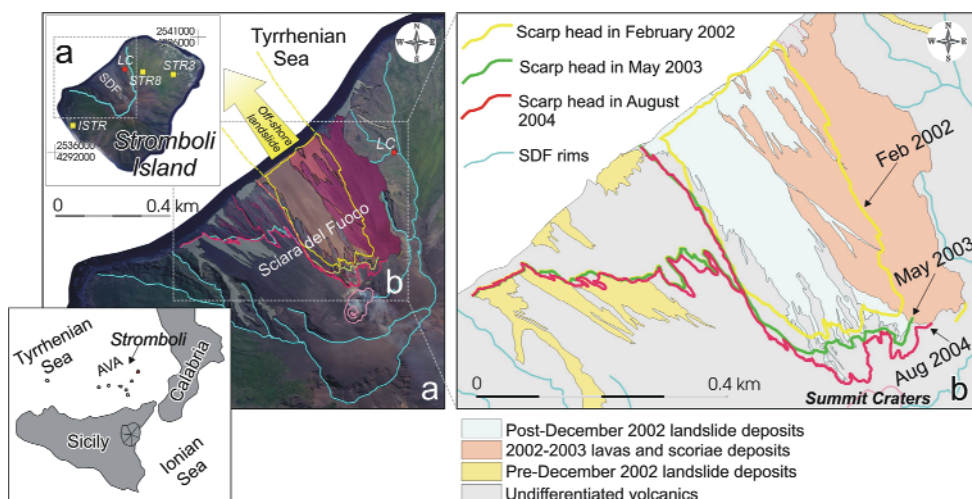
Fig. 1. Morpho-structural evolution of SDF between 2002 and 2004 (modified from Falsaperla et al., 2006). **(a)** Location of the studied area and ortho-photo in August 2004, with projection of the landslide margins, main displaced materials, lava flows, and SDF rim. AVA = Aeolian volcanic arc; LC = Thermal and visual live-cameras; ISTR, STR3, STR8 = seismic stations. **(b)** Morphological details of the landslide area.

Tab. 1. Instrumental characteristics of the seismic stations.

Station	Seismometer	Sampling frequency	Latitude	Longitude	Altitude (m)
ISTR	Geothech S-13	100 Hz	38N47.04	15E11.58	70
STR3	Guralp CMG40T	50 Hz	38N47.57	15E13.50	236
STR8	Guralp CMG40T	50 Hz	38N47.58	15E13.07	569

The data set consisted of 49 episodes, which were taken in daytime (Table 2). In so doing, the comparative analysis of video images and seismic records provided the opportunity to detect the sliding episodes in space and time. The search of each episode was fixed from the beginning of the digital readings on the seismic records.
Landslides, rockfalls, and flowing debris have a typical seismic signature [e.g., McNutt, 2000], which allowed a simple identifications of these signals from events of other origin, such as earthquakes and explosion quakes (Figure 3a). Their frequency content was characteristic as well (Figure 3b), and ranged bet-
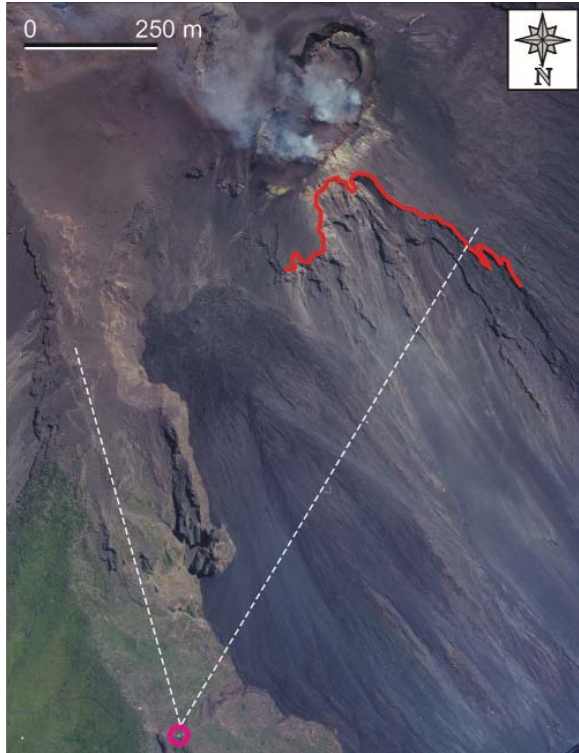
Fig. 2. Close-up view of an aerial snapshot taken on 4 August, 2004, showing the zone of SDF affected by 23 sliding episodes documented by visual images. The red circle and white dashed lines mark the position and visual field of the INGV live-cams. The red line marks the upper landslide scarp close to the summit craters. Image credit: M. Marsella, University of Rome 1.

ween 1 Hz and 20 Hz with small differences from station to station. Amplitude and duration of the episodes analyzed on the seismic records had no linear relationship. Consequently, no estimate of the source volume involved in the sliding process could be done from seismograms.

Overall, 23 out of 49 episodes had a documented visual record (Table 2). The remnant 26 episodes were not distinguishable as: i) they occurred during cloudy and/or bad weather conditions which might have hindered their occurrence (22 cases); ii) the weather conditions were fine, but there was no trace of them (4 cases). It is likely that the four unseen episodes stemmed from a zone outside the visual field of the video cameras, which covered only the upper-medium slope of SDF. The comparison between seismic records and timing of the images for the 23 documented episodes highlighted that the start of the visual phenomenon was almost concurrent with the beginning of the seismic record (Figure 4). The delay was of the order of a couple of seconds, i.e., within the scale of the resolution on the frames.
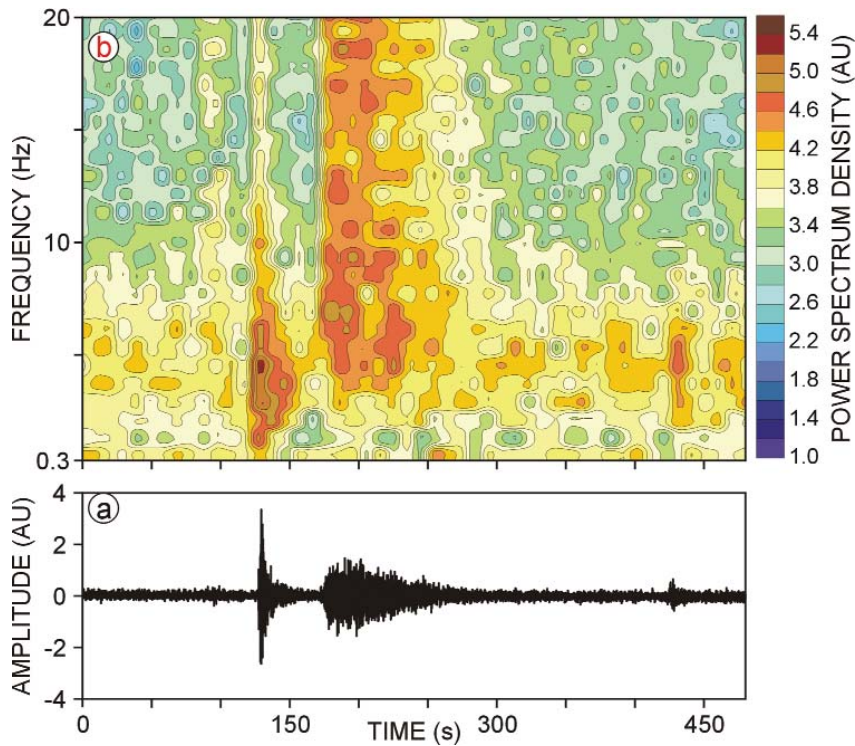
Fig. 3. Seismogram **(a)** and relative spectrogram **(b)** of a time series recorded at the vertical component of STR8 on 27 August, 2004. An explosion quake shortly precedes a rockfall episode. The spectrogram is calculated applying the Fast Fourier Transform to successive time series of 2.56 s with an overlap of 50%, and depicting the results as consecutive spectra. The frequency content of the rockfall is outstandingly higher than that of the explosion quake.

The 23 episodes documented by images shed some light on trigger mechanisms of seismic shaking. In spite of the absence of earthquakes preceding the sliding processes, the comparative analysis allowed documenting explosion quakes and Strombolian explosions conducive to shaking instability. There were 14 out of 49 episodes preceded by an explosion quake in a time span around two minutes before the onset on seismogram. An example is given in Figure 5, which includes a thermal image of the live-cam in IR band. The thermal image shows a typical Strombolian explosion at the summit craters – with ejection of ash, lapilli, and hot gas – followed by a rockfall episode. It is worth noting that the inspection of the thermal images excluded the presence of hot components within the material involved in the rockfalls.

Flowing debris and rockfalls yielded no evident distinction on the seismic record. On the other hand, since the video footage was limited, the mechanism of motion could not be wholly traced by the images. The boost of the

Tab. 2.

Date and time (yyyymmdd hh.mm.ss)	Visual observations and index (I) of resolution from 1 (poor) to 5 (good)	Time onset of:	
		visible explosion	explosion quake
20040329 09.39.38	Cloudy, hard to distinguish anything		
20040329 12.27.52	Cloudy, hard to distinguish anything		12.26.55
20040401 12.08.38	Cloudy, hard to distinguish anything		
20040403 17.41.36	Fine weather, no event		
20040410 05.33.16	I2		
20040413 15.56.35	Strong wind and ash, hard to distinguish anything		15.55.04
20040413 17.03.40	Strong wind and ash, hard to distinguish anything		17.03.19
20040414 07.35.06	Foggy, hard to distinguish anything		
20040414 08.32.49	Strong wind and ash, hard to distinguish anything		
20040414 12.20.14	Foggy, hard to distinguish anything		
20040415 07.43.55	I3		07.43.39
20040415 10.07.58	I4		
20040415 15.48.19	Foggy, hard to distinguish anything		
20040417 06.38.07	Strong wind and ash, hard to distinguish anything		
20040610 14.05.31	Strong wind and ash, hard to distinguish anything		14.05.12
20040628 09.44.56	Strong wind and ash, hard to distinguish anything		
20040630 13.09.55	Strong wind and ash, hard to distinguish anything		
20040722 17.35.29	Fine weather, no event		
20040723 16.02.31	Strong wind and ash, hard to distinguish anything		
20040723 16.21.33	Strong wind and ash, hard to distinguish anything		
20040723 16.29.34	Strong wind and ash, hard to distinguish anything		16.28.37
20040724 17.22.26	Strong wind and ash, hard to distinguish anything		17.21.22
20040725 09.26.14	I3		09.24.28
20040725 09.37.38	I2		
20040725 13.58.33	Cloudy, hard to distinguish anything		
20040727 13.44.02	I2		
20040727 14.47.20	Foggy, hard to distinguish anything		
20040802 07.24.31	I1		
20040802 17.19.27	I4-5	17.17.49	17.17.23
20040806 17.04.59	Fair visibility, no event		
20040807 06.37.58	Fair visibility, no event		06.37.26
20040810 18.12.28	I2		
20040811 07.38.57	I2		
20040813 16.18.29	I4		16.17.29
20040813 17.44.41	I5		
20040816 09.20.23	I5		
20040816 09.42.49	I5		
20040827 16.30.50	I4	16.30.08	16.30.06
20040827 16.48.01	I3		
20040830 08.55.03	I3		
20040830 13.45.49	I2		13.43.40
20040830 14.55.07	I2		
20040830 15.12.47	Cloudy, hard to distinguish anything		
20040830 15.31.42	I3		
20040905 07.57.41	I3	07.56.34	07.56.04
20040906 11.43.31	I3		
20040906 11.57.49	I3		
20041010 09.04.49	Cloudy, hard to distinguish anything		
20041013 11.02.49	Cloudy, hard to distinguish anything		
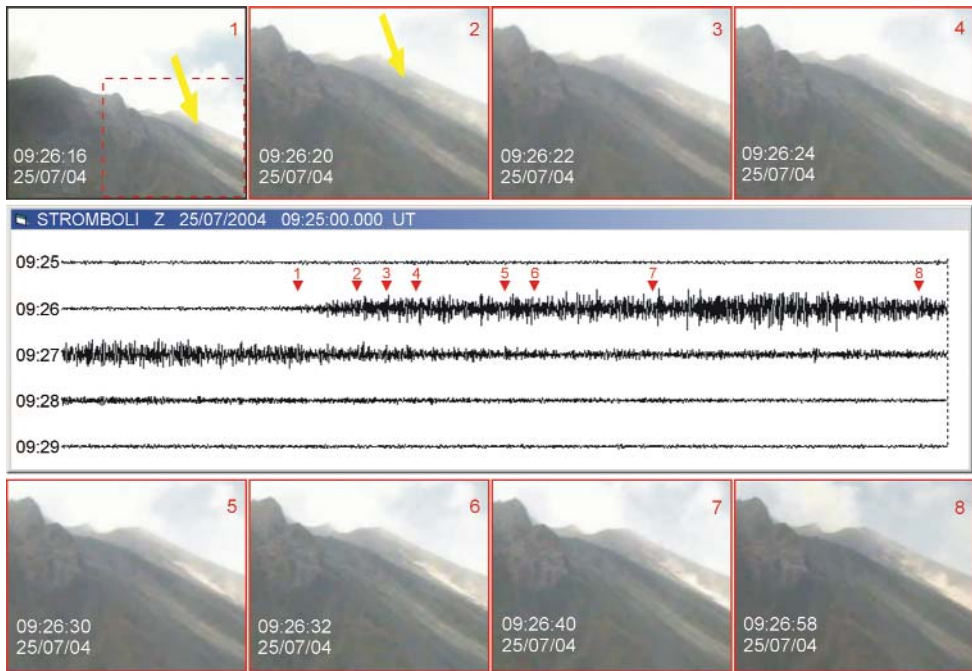
Fig. 4. Seismogram of a rockfall episode at the Sciara del Fuoco and concurrent snapshots (1-8) at the INGV live-cam in the visible band. The yellow arrow marks the beginning of the rockfall in the snapshots. The numbered red triangles from 1 to 8 on the seismogram match the sequence of video frames, which are a close-up view of the red dashed rectangle in frame 1.

live-cam network – in the wake of a renewal of effusive activity in spring 2007 – might shed more light on the variety of the mechanisms of motion and the zone from which they stem.

DISCUSSION AND CONCLUSIONS

Apart from the two huge landslides and concurrent tsunami on 30 December, 2002 – two days after the renewal of effusive activity – the island of Stromboli was not affected by as large sliding episodes ever since. However, whilst the lava flows emplaced along the slope of SDF had a stabilizing effect, numerous flowing debris and rockfalls continued in the zones which were not covered by lavas during and well after the end of the lava effusion in July, 2003. This evidence supported the hypothesis that the flank collapse of 30 December enhanced the latent instability of SDF [Falsaperla et al., 2006]. The observation that 14 out of 49 sliding episodes shortly (about 120 s) occurred after moderate explosion quakes / Strombolian explosions (Figure 5) further corroborated this hypothesis.
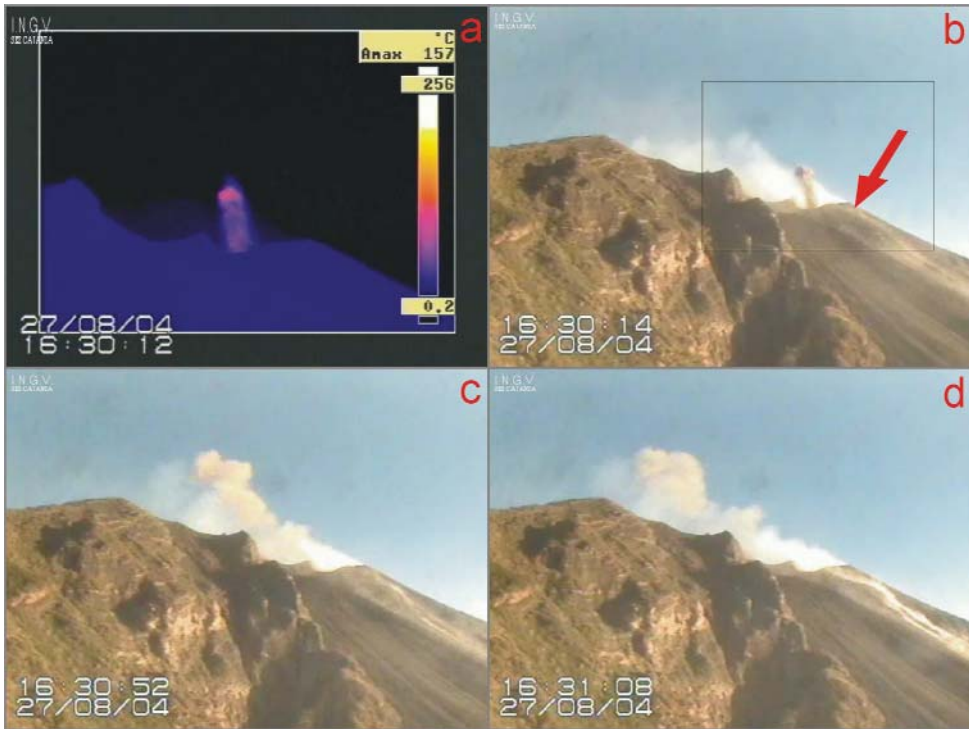
Fig. 5. Thermal image **(a)** and snapshots **(b-d)** taken from the INGV video cameras for a rockfall episode of our data set, which was shortly preceded by a Strombolian explosion. The red arrow marks the beginning of the rockfall in the snapshots. The frame in **(a)** is a close-up view of the black rectangle in **(b)**.

Falsaperla et al. [2006] identified the zones affected by the sliding episodes between 2002 and 2004 (Figure 1). The most active zone was located in the upper part of the SDF, close to the niche of detachment of the landslides of 30 December, 2002 (Figure 2). In August, 2004 this niche was only 125 m distant from the summit craters, showing to be still active. Reporting this finding, Falsaperla et al. [2006] concluded that if progressive degradation continued toward the craters, then a change in eruptive behavior cannot be excluded due to a possible sudden depressurization of the volcano feeder. In this light, even neglecting the hypothesis of large failure events, unrelenting sliding episodes close to the craters might represent a potential hazard due to the consequences on the impinging eruptive activity. On the other hand, there is a mutable remodeling process of the SDF slopes, which is the result of contra posed actions between the welding effect of new lava flows and erosive phenomena. For example, the renewal of lava effusions in spring 2007 once again changed the morpho-structural characteristics of the SDF, leading the balance of the two actions in favor of the stabilizing effect. In that occasion, an effusive frac-

ture propagated downslope in the SDF, reaching a minimum elevation of about 400 m asl. During the propagation of the dike, the highest portion of the fracture system collapsed, forming a graben (Neri et al., 2007). But the major morpho-structural changes happened in the summit area: the internal walls of the central conduit collapsed, causing the enlargement of the summit crater area and the partial obstruction of the conduit which triggered some explosive events due to the overpressure inside the system.

Therefore, only a continuous multidisciplinary monitoring of the volcano can provide valuable information to evaluate the on-going assessment and contribute in reducing the hazard of this landslide-prone area.

ACKNOWLEDGMENTS

REFERENCES

Acocella V., M. Neri, and P. Scarlato (2006), Understanding shallow magma emplacement at volcanoes: Orthogonal feeder dikes during the 2002-2003 Stromboli (Italy) eruption. Geophys. Res. Lett., 33, L17310, doi:10.1029/2006GL026862.

Bonaccorso, A., S. Calvari, G. Garfì, L. Lodato, and D. Patanè (2003), Dynamics of the December 2003 flank failure and tsunami at Stromboli volcano inferred by volcanological and geophysical observations, Geophys. Res. Lett., 30, 18, 1941, doi: 10.1029/2003GL17702.

Calder, E.S., R. Luckett, R.S.J. Sparks, and B. Voight (2002), Mechanisms of lava dome instability and generation of rockfalls and pyroclastic flows at Soufrière Hills Volcano, Montserrat, In: Druitt, T.H. and Kolelaar, B.P. (eds) The eruption of Soufrière Hills Volcano, Montserrat, from 1995 to 1999, Geological Society, London, Memoirs, 21, 173-190.

Calvari S., L. Spampinato, L. Lodato, A.J.L. Harris, M.R. Patrick, J. Dehn, M.R. Burton, and D. Andronico (2005), Chronology and complex volcanic processes during the 2002-2003 flank eruption at Stromboli volcano (Italy) reconstructed from direct observations and surveys with a handheld thermal camera, J. Geophys. Res., 110, 1029/2004JB003129.

Falsaperla, S., M. Neri, E. Pecora, and S. Spampinato (2006), Multidisciplinary Study of Flank Instability Phenomena at Stromboli Volcano, Italy. Geophys. Res. Letters, 33, L09304, doi:10.1029/2006GL025940.

La Rocca, M., D. Galluzzo, G. Saccorotti, S. Tinti, G.B. Cimini, and E. Del Pezzo (2004), Seismic signals associated with landslides and with a tsunami at Stromboli volcano, Italy, Bull. Seism. Soc. Am., 94(5), 1850-1867.

McNutt, S.R. (2000), Volcanic Seismicity, in Encyclopedia of Volcanoes, edited by H. Sigurdsson, B. Houghton, S.R. McNutt, H. Rymer, and J. Stix, pp. 1095-1119, Academic Press.

Neri, M., A. Tibaldi, G. Giordano, M. Porreca and V. Acocella (2007), Stromboli 2007: Shallow dyke propagation, fracturing and conduit collapse. In: The 2007 Eruption of Stromboli (Italy), XXIV IUGG General Assembly, Perugia (Italy) 2-16 July 2007.

Pino, N.A., M. Ripepe, and G.B. Cimini (2004), The Stromboli volcano landslides of December 2002: a seismological description, Geophys. Res. Lett., 31, L02605, doi: 10.1029/2003GL18385.

Ripepe M., E. Marchetti, G. Ulivieri, A.J.L. Harris, J. Dehn, M. Burton, T. Caltabiano, and G. Salerno (2005), Effusive to explosive transition during the 2003 eruption of Stromboli volcano, Geology, 33, 341-344.

Tibaldi, A. (2001), Multiple sector collapses at Stromboli volcano, Italy: how they work, Bull. Volcanol., 63, 112-125.

Automatic classification of volcanic tremor using Support Vector Machine

M. Masotti[1], S. Falsaperla[2], H. Langer[2], S. Spampinato[2], R. Campanini[1]

[1] *Medical Imaging Group, Department of Physics, University of Bologna, Bologna, Italy*

[2] *Istituto Nazionale di Geofisica e Vulcanologia, Sezione di Catania, Catania, Italy*

Abstract: A system for automatic recognition of different volcanic activity regimes based on supervised classification of volcanic tremor is proposed. Spectrograms are calculated from volcanic tremor time-series, separated into four classes, each assumed as representative of a different state of volcanic activity, i.e., pre-eruptive, eruptive, lava fountains, and post-eruptive. As classification features, the spectral profiles obtained by averaging each spectrogram along its rows are chosen. As supervised classification strategy, the Support Vector Machine (SVM) classifier is adopted. Evaluation of the system performance is carried out on volcanic tremor data recorded at Mt Etna during the eruptive episodes of July-August 2001. The leave-one-out classification accuracy achieved is of about 94%.

INTRODUCTION

In basaltic volcanoes, volcanic tremor is known to be a continuous seismic signal whose characteristics can be related to the activity regime of the volcano. Owing to its close relationship to the state of the volcano, volcanic tremor provides reliable information for alerting governmental authorities in case, for instance, of transition from a pre-eruptive to an eruptive regime. Furthermore, volcanic tremor monitoring yields information about the state of the volcano in time even when visual observation is hindered because of unfavorable weather conditions, or when direct access to the eruptive theatre is too risky. However, a huge amount of data is accumulated during continuous recording of volcanic tremor, posing severe difficulties for the human operator to handle these data masses on-line as well as off-line.

We propose automatic classification as a way to tackle those problems. Besides, automatic procedures are based on formalized data processing schemes, which render them reproducible. We thus can avoid the use expert's opinions which is always arbitrary to some degree. A scheme of the system proposed here is depicted in Figure 1. Data are represented by volcanic tremor time-series and their associated labels, namely, integer tags identifying the vol-

| Data Time–series and Labels | → | Features Averaged Spectrograms | → | Classification Support Vector Machine |

Fig. 1. Scheme of the proposed system.

canic activity regime during which they are recorded. Previous investigations highlighted that spectral analysis of tremor is particularly informative to discriminate different styles of volcanic activity [Falsaperla et al., 2005]. Therefore, we apply the Fourier transform to each time-series and calculate corresponding spectrograms using a gliding window scheme. The rows of each spectrogram are then averaged, thus ending up with patterns made up of average spectral values. For the classification of these patterns we adopted the Support Vector Machine (SVM) classifier [Vapnik, 1998]. Following a supervised learning scheme, during the SVM training phase the classifier learns how to discriminate the labelled pattern according to the extracted spectrogram-based features; then, during the test phase, its performance is evaluated on patterns not used during the training phase, but supposed to belong to the same parent population of the training set.

We present the application of the SVM classifier using the volcanic tremor data related to the 2001 Mt Etna flank eruption (Figure 2), which is one of the
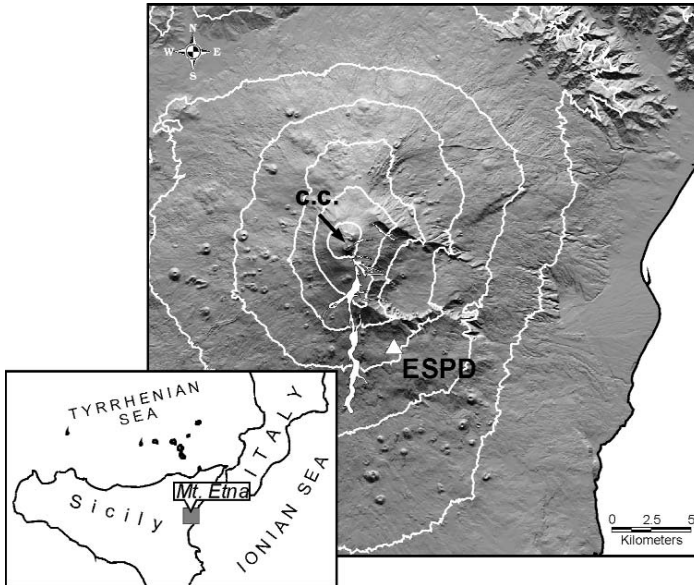
Fig. 2. Eruptive field at Mt Etna in 2001. C.C. stands for central craters. The white triangle marks the location of the seismic station ESPD.

most powerful ones occurred in recent years and for which a considerable amount of data is available.

DATA: THE CASE STUDY OF VOLCANIC TREMOR RECORDED DURING MT ETNA'S 2001 ERUPTION

On July 17, 2001, a volcanic unrest began at Mt Etna, with episodes of lava fountains preceding and accompanying the onset of lava effusion. The effusive activity stopped on August 9, 2001.

To develop and evaluate the proposed system, a time-span covering 16 days before the onset and 7 days after the end of the eruption was chosen, i.e., July 1-August 15, 2001 (Figure 3). The volcanic tremor time-series recorded by the three component digital station ESPD, located at a distance of about 6 km from the summit craters (Figure 2), were considered. To each time-series we assigned a-priori labels depending on the recording date, namely: pre-eruptive (PRE) if data were recorded between 1 and 16 July; eruptive (ERU) if recorded between July, 17 and August, 8; post-eruptive (POS) if recorded between 9 and 15 August; lava fountain (FON) if recorded during lava fountain episodes. The latter ones occurred both during the pre-eruptive (July, 4, 5, 7, 12, 13, and 16) and eruptive stages (July, 17). The resulting dataset was composed of 153 PRE, 55 FON, 180 ERU, and 37 POS time-series.
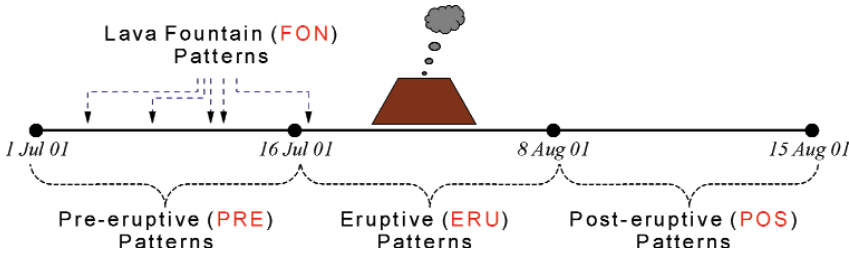
Fig. 3. Data. Scheme of the time-spans considered for Mt Etna's 2001 eruption.

FEATURES: AVERAGED SPECTROGRAMS

For each time-series, the short time Fourier transform [Oppenheim and Schafer, 1989] was calculated using time-windows of 1024 points with 50% of overlap. We extracted 62 frequency bins in the frequency range between 0.24 and ca. 15 Hz. The rows of each spectrogram were then averaged, so that the resulting patterns are made up by vectors of 62 average spectral values. These values were used as classification features. Figure 4 depicts a typical seismogram, spectrogram, and averaged spectrogram for each class.
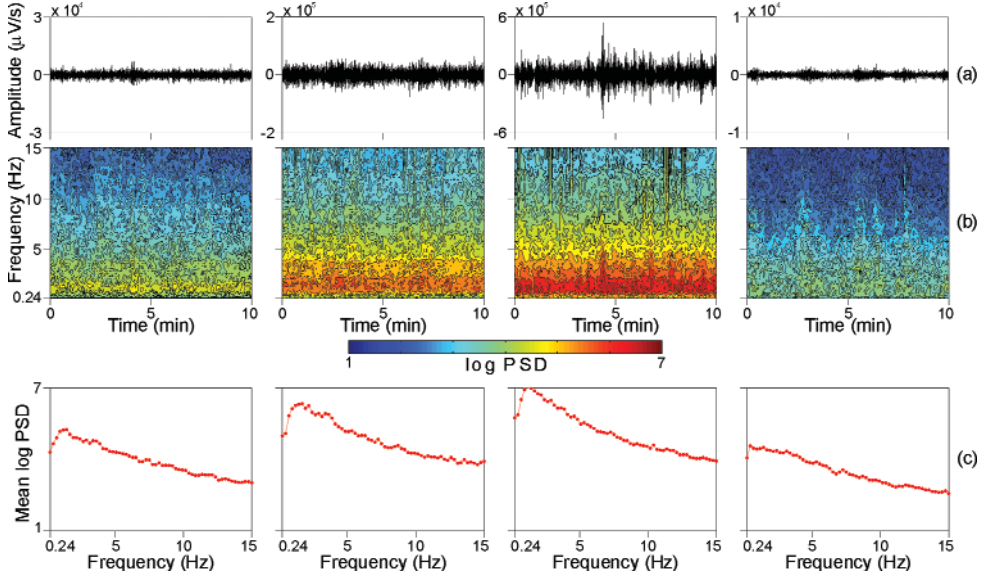
Fig. 4. Features. From left to right, examples of pre-eruptive, lava fountain, eruptive, and post-eruptive patterns: **(a)** time series, **(b)** spectrograms, and **(c)** corresponding 62-dimensional averaged spectrogram. PSD stands for power spectral density [from Masotti et al., 2006].

CLASSIFICATION: SUPPORT VECTOR MACHINE

Each averaged spectrogram was then automatically classified as belonging to a specific class by means of a SVM classifier [Vapnik, 1998].

For a two-class classification problem, given a set of $i = 1, …, l$ labeled patterns $(x_i, y_i) \in \mathbf{R}^N \times \{1; -1\}$, where x_i is the N-dimensional feature vector associated with the i-th pattern, and y_i the integer a-priori label assigned to its class membership, SVM training consists in finding the decision function $f: \mathbf{R}^N \to \{1; -1\}$ which causes the largest separation between itself and the border of the two classes under consideration (Figure 5a). This decision function, also known as maximal margin hyperplane, is calculated in terms of some scalars α_i and b by solving a quadratic programming problem and is defined by few patterns, the so-called support vectors [Vapnik, 1998]:

$$f(x) = sgn(w \cdot x + b) = sgn\left(\sum_{Support Vectors} y_i \alpha_i (x \cdot x_i) + b \right) \tag{1}$$

As the maximal margin hyperplane calculated by SVM is the farthest from the classes in the training set, it is also robust in presence of previously unseen patterns, achieving excellent generalization capabilities. Once SVM training is
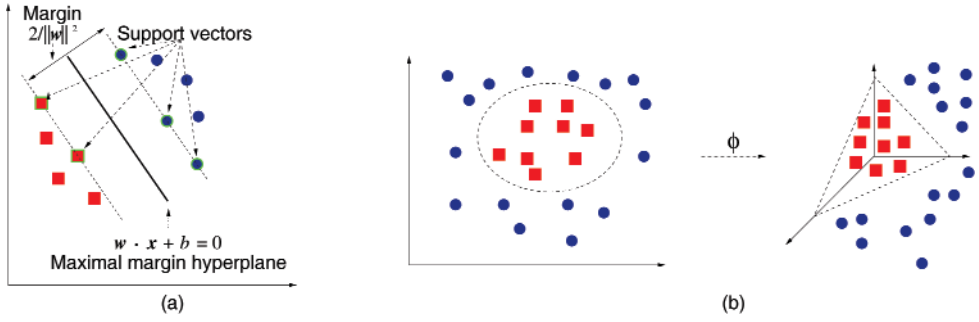
Fig. 5. Classification. Maximal margin hyperplane found by SVM **(a)**; the green bordered patterns on the two margins are called support vectors and are the only ones contributing to the determination of the hyperplane. Transformation of a non-linear classification problem into a linear one applying the kernel function ϕ **(b)**.

completed, SVM testing consists in assigning a label to a pattern x not used for training according to its position, in the feature space, with respect to the maximal margin hyperplane. SVM performance is hence evaluated by comparing the a-priori label of each pattern used for test with that assigned to it by the classifier.

The two-class approach described above can be extended to any k-class classification problem by adopting methods such as the one-against-all or the one-against-one, which basically construct a k-class SVM classifier by combining several two-class SVM classifiers [Weston and Watkins, 1999]. In this work, the one-against-one approach was used, namely, SVM classifier was trained six times, each time on averaged spectrograms x_i from two classes only, i.e., PRE vs. FON, PRE vs. ERU, PRE vs. POS, FON vs. ERU, FON vs. POS, and ERU vs. POS. A test pattern x was then associated with the class to which it was more often associated by the different SVM classifiers.

When patterns are not linearly separable in the feature space, a non-linear transformation $\phi(x)$ is used to map feature vectors into a higher dimensional feature space where they are linearly separable [Vapnik, 1998]. With this approach, classification problems which appear quite complex in the original feature space can be tackled by using simple decision functions, namely, hyperplanes(Figure 5b). To implement this mapping, the dot products $x \cdot x_i$ of Eq. 1 are substituted by a non-linear function $K(x, x_i) \equiv \phi(x) \cdot \phi(x_i)$ named kernel. Admissible and typical kernels are:

$$
\begin{aligned}
K(x, x_i) &= x \cdot x_i && \text{Linear} \\
K(x, x_i) &= (\gamma x \cdot x_i + r)^d && \text{Polynomial} \\
K(x, x_i) &= \exp(-\gamma \|x - x_i\|^2) && \text{Radial Basis Function}
\end{aligned} \tag{2}
$$

where γ, r, and d are kernel parameters selected manually.

RESULTS AND DISCUSSION

SVM performance was evaluated using a leave-one-out strategy [Efron and Tibshirani, 1993] singularly over the patterns associated with each component: EW, NS, and Z. Hence, for each component, the classifier was trained exclusively with all patterns, except one used for test, belonging to that component. By changing the test pattern in a round-robin manner, training and test were repeated a number of times equal to the number of patterns of that component. Classification performance was then obtained as the sum over the three components of correctly classified test patterns. The classification results achieved by adopting a polynomial SVM kernel with $d = 3$, $\gamma = 10$, and $r = 0$ are depicted in Figure 6; here, colors represent the a-priori class memberships, whereas values on the *y*-axis the assigned ones. The choice for the SVM parameters is the result of some initial trial-and-error experiments. We summarize the results of our classification with a confusion matrix (Table 1). Rows and columns of this matrix are read as the a-priori and assigned class membership, respectively. Diagonal elements represent correctly classified test patterns whereas the off-diagonal elements are misclassifications. It turns out that the class membership assigned by SVM for a test pattern matches its a-priori class membership in 400 out of 425 cases, corresponding to a success of 94.1%. Namely, PRE patterns are correctly classified with a score of 145/153 = 94.8%, FON patterns 42/55 = 76.4%, ERU patterns 177/180 = 98.3%, and POS patterns 36/37 = 97.3%.
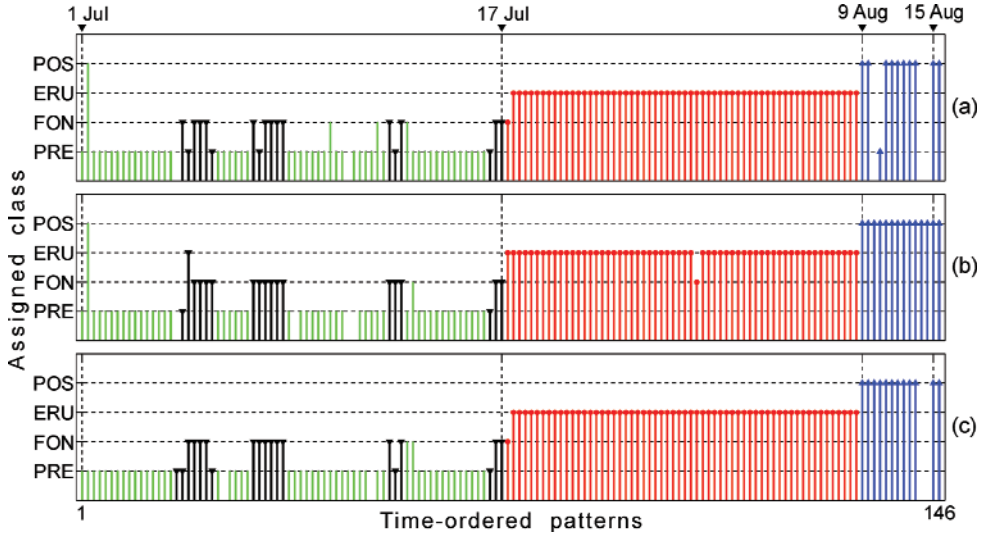
Fig. 6. Leave-one-out classification results for SVM over the patterns associated to each single component: EW **(a)**, NS **(b)**, and Z **(c)**. Colors represent the a-priori class membership: PRE (green), FON (black), ERU (red), and POS (blue). Patterns are time-ordered. Gaps correspond to missing data. Arrows on top are time markers [from Masotti et al., 2006].

Tab. 1. Confusion matrix for SVM classification.

		Assigned class			
		PRE	FON	ERU	POS
A-priori class	PRE	145	6	0	2
	FON	12	42	1	0
	ERU	0	3	177	0
	POS	1	0	0	36

Looking at Figure 6, it is evident that misclassifications are mostly concentrated near class transitions, particularly between PRE and FON, but also between FON and ERU. This is the case, for example, of misclassifications associated with the transition between PRE and the first (or third) FON, as well as those associated with the first ERU pattern. A possible reason for that may be the intrinsic fuzziness in the transition from one regime to the other. This yields a non-null intra-class variability likely responsible for the misclassifications afore-mentioned. In particular, by looking at the different spectrograms, it is evident that the intra-class variability of PRE and FON is quite high, (Figures 7a, 7b), with a high number of PRE very similar to FON and vice versa. Conversely, the intra-class variability of ERU and POS is much lower (Figures 7c, 7d), with just a few ERU similar to FON and very few POS similar to PRE.

(a)　　　　　　　　　　　　(b)

(c)　　　　　　　　　　　　(d)
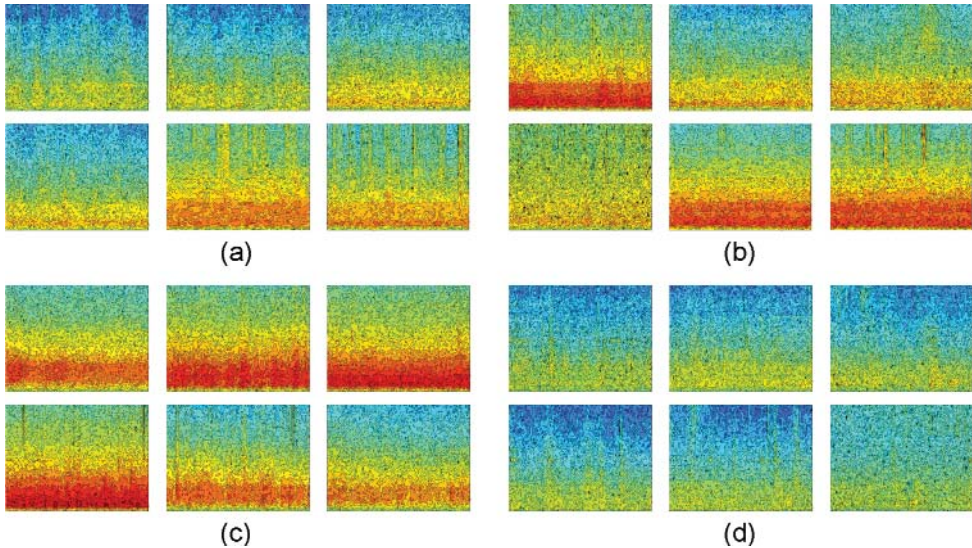
Fig. 7. Intra-class variability. Examples of PRE **(a)**, FON **(b)**, ERU **(c)**, and POS **(d)** spectrograms.

Fig. 8. TREMOrEC.

Conclusions

A system able to automatically recognize different volcanic activity regimes by means of supervised classification of the associated volcanic tremor was pro-

posed. Classification was performed using SVM as classifier and the averaged spectrograms of the original volcanic tremor time-series as features. By achieving less than 6% of classification error on volcanic tremor data recorded during Mt Etna's 2001 eruption, the performance of the proposed system results to be interesting. Useful applications can be envisaged for off-line classification of volcanic tremor datasets in search for precursors or in-depth investigation on the regime transitions. The developed approach can also be applied in other volcanic areas, where additional regimes may be taken into account or the same regimes may be associated with different volcanic tremor patterns.

The results presented in this report refer to the first test performed for this system [Masotti et al., 2006a; Masotti et al., 2006b]. However, to explore its generalization capabilities, further tests were performed on different eruptions, namely those occurred in 2002 and 2006 [Masotti et al., 2007a; Masotti et al., 2007c]. The obtained results showed good robustness of the system. Also, the performance of the SVM classifier was compared to that of artificial neural networks [Masotti et al., 2006c], showing outperforming results of the former. Finally, owing to the high classification performance achieved, and with the purpose of releasing a tool useful for the Italian Department of Civil Protection and scientific community, the initial Matlab implementation of the system was translated into a stand-alone software package (i.e., TREMOrEC, see Figure 8) developed in Visual C++ as an executable for Microsoft Windows systems [Masotti et al., 2007b].

REFERENCES

Efron, B., and Tibshirani, R. J., (1993), An Introduction to the Bootstrap, Chapman & Hall, New York.

Falsaperla, S., Alparone, S., D'Amico, S., Grazia, G., Ferrari, F., Langer, H., Sgroi, T., and Spampinato, S., (2005), Volcanic tremor at Mt. Etna, Italy, preceding and accompanying the eruption of July-August, 2001, Pure Applied Geophysics, 162, 2111-2132.

Masotti, M., Falsaperla, S., Langer, H., Spampinato, S., Campanini, R., (2006a), A new automatic pattern recognition approach for the classification of volcanic tremor at Mount Etna, Italy, EGU 2006, Vienna, Austria, April 02-07, 2006, (Abstract: EGU06-A-05780).

Masotti, M., Falsaperla, S., Langer, H., Spampinato, S., Campanini, R., (2006b), Application of Support Vector Machine to the classification of volcanic tremor at Etna, Italy, Geophysical Research Letters, 33, 20, L20304.

Masotti, M., Falsaperla, S., Langer, H., Spampinato, S., Campanini, R., (2006c), Supervised and unsupervised automatic classification methods applied to volcanic tremor data at Mt Etna, Italy, AGU 2006, San Francisco, USA, December 11-15, 2006, (Abstract: S13B-0228).

Masotti, M., Falsaperla, S., Langer, H., Spampinato, S., Campanini, R., (2007a), Activity regimes inferred from automatic classification of volcanic tremor at Mt. Etna, Italy, EGU 2007, Vienna, Austria, April 15-20, 2007, (Abstract: EGU2007-A-02970).

Masotti, M., Campanini, R., Mazzacurati, L., Falsaperla, S., Langer, H., Spampinato, S., (2007b), TREMOrEC: a software utility for automatic classification of volcanic tremor, EGU 2007, Vienna, Austria, April 15-20, 2007, (Abstract: EGU2007-A-05120).

Masotti, M., Falsaperla, S., Langer, H., Spampinato, S., Campanini, R., (2007c), Generalization capabilities of support vector machine for volcanic tremor classification at Mt. Etna, Italy, IUGG 2007, Perugia, Italy, July 02-13, 2007.

Oppenheim, A., V., and Schafer, R. W., (1989), Discrete-Time Signal Processing, Prentice-Hall, Englewood Cliffs, New York.

Vapnik, V., (1998), Statistical Learning Theory, Wiley, New York.

Weston, J., and Watkins, C., (1999), Multi-class support vector machines, In Proceedings of ESANN99, edited by M. Verleysen. pp. 219-224, D. Facto Press, Brussels.

Probabilistic volcanic hazard assessment and eruption forecasting: the Bayesian Event Tree approach

W. Marzocchi, J. Selva, L. Sandri

INGV, Bologna, Italy

PURPOSE

The purpose of this report is to discuss in detail the importance and prerogatives of quantitative volcanic hazard assessment and to describe the main features of a Bayesian model designed to achieve this goal. Ideas, models and results come out from the work made in the framework of the INGV-DPC V4 project, and partially from the application of the technique to Campi Flegrei (V3_2) and Vesuvius (V3_4). Here, we examine in depth the practical and philosophical implications of the approach, and report only a brief summary of the technical details that can be found on the cited literature.

GENERAL FEATURES OF PROBABILISTIC VOLCANIC HAZARD ASSESSMENT (PVHA)

One of the major goals of modern volcanology is to set up a sound risk-based decision making in land use planning and emergency management.
Despite different scientific disciplines attribute disparate definition to the term "risk", in volcanology the most used definition reads (e.g., UNESCO, 1972; Fournier d'Albe, 1979)

risk = hazard x value x vulnerability

where *hazard* is the probability of any particular area being affected by a destructive volcanic event within a given period of time; the *value* is the number of human lives at stake, or the capital value (land, buildings, etc.), or the productive capacity (factories, power plants, highways, etc.) exposed to the destructive events; the *vulnerability* is a measure of the proportion of the value which is likely to be lost as a result of a given event.
The above equation points out that risk assessment involves different scientific expertise. As a matter of fact, any risk-based decision/action taken from authorities in charge to manage volcanic emergencies and/or risk mitigation

strategies has to account also for complex inter-plays between social and economic needs, and infrastructure capability to sustain them. In particular, it is necessary to evaluate the vulnerability of exposed infrastructure, facilities and property, the impact of eruptions on human beings, costs vs. benefits of proposed mitigation measures, and the level of "acceptable risk" for society. In addition, we need educational programs to improve the "risk perception" of the people living around volcanoes, and improved ways to communicate risk and associated uncertainties to those people, mass media, and local authorities. In this compound framework, the role of volcanology is mostly focused on providing a reliable volcanic hazard assessment.

As for the term *risk*, also the term *hazard* can lead to some misunderstanding. In English, *hazard* has the generic meaning "potential source of danger", but, as mentioned before, for more than thirty years (e.g., Fournier d'Albe, 1979), *hazard* has been also used in a more quantitative way, that reads: "the probability of a certain hazardous event in a specific time-space window". However, many volcanologists still use "*hazard*" and "*volcanic hazard*" in purely descriptive and subjective ways. For this reason, in order to minimize ambiguities, many researchers have recently proposed that a more suitable term for the estimation of quantitative hazard is "Probabilistic Volcanic Hazard Assessment" (PVHA, hereinafter; see Marzocchi et al., 2007).

Despite the still large use of "qualitative" and "subjective" volcanic hazard assessment, PVHA has undoubtedly many pivotal advantages:

a. A quantitative hazard assessment moves this branch of volcanology from pure (and mere) "speculations" into a "scientific" domain, because only quantitative hypothesis can be tested and compared.

b. A reliable PVHA becomes the rational basis for critical quantitative and transparent decision-making for safety and mitigating volcanic risk to communities, in the long-term, prior to onset of volcanic unrest, and, in the short-term, during volcanic activity and during "volcano crises". For instance, Woo (2007), and Marzocchi and Woo (2007) proposed a quantitative strategy to link PVHA with a cost/benefit analysis for calling an evacuation during an emergency. This approach sharply contrasts with the current common practice, where mitigation actions are usually based on subjective decisions of one or few researchers.

c. The description in terms of probability is particularly suitable for eruptive processes, as well as for any generic complex systems, that are intrinsically unpredictable from a deterministic point of view (at least over time intervals longer than hours/few days). Beyond the extreme complexity, nonlinearities, and the large number of degrees of freedom of a volcanic system (the so-called *aleatory* uncertainty), also our still limited knowledge of the process involved (the so-called *epistemic* uncertainty) make deterministic prediction of the evolution of volcanic processes practically impossible.

d. The probabilistic definition has also the merit to be quite general, therefore it allows a large variety of possible destructive phenomena, such as pyro-

clastic and lava flows, tephra, lahars, gas emission, ground deformation, volcano-seismic events, and so on, to be encompassed by PVHA. For instance, PVHA also includes the definition of Eruption Forecasting (EF), if the destructive event is the occurrence of a volcanic eruption (without considering the ensuing effects on the territory). In other words, EF can be seen as a branch of the more general problem of PVHA.

We conclude this paragraph giving emphasis to a couple of important issues. First, PVHA does not reduce in any way the importance of deterministic studies and the analysis of specific scenarios. The simultaneous use of physical models and data contrasts with what is sometimes encountered in seismic risk analysis, where deterministic and probabilistic approaches are often considered irreconcilable (e.g., Castanos and Lomnitz, 2002). In seismic hazard assessment, the terms "probabilistic" and "deterministic", contained in acronyms PSHA and DSHA, reflect the kind of strategy adopted, mostly evidence-based for PSHA and mostly based on physical models for DSHA. In volcanology, we do not see this conflict; we attempt to use all the information we have (models, data, and expert beliefs), and the term "probabilistic" in PVHA only emphasizes that the quantification of volcanic hazard takes account of associated uncertainties.

Second, we remark that the great importance of this scientific issue is due to its practical implications for society; in this perspective, no matter what probabilistic approach is used, it is fundamental that PVHA is "accurate" (i.e., without significant biases), because a biased estimation would be useless in practice. On the other hand, PVHA may have a low "precision" (i.e., a large uncertainty) that would reflect our scarce knowledge of some physical processes involved, from the preparation of an eruption to the derived impact on the ground of a specific threatening event (e.g., pyroclastic flow, lahars, etc.). An accurate PVHA can be realistically achieved by using some sort of "best picture" of the shared state-of-the-art, and by including all the existing uncertainties. This approach allows the potential bias associated to personal convictions and to lacks of knowledge to be minimized. In particular, we caution against the use of even sophisticated models that are not yet properly tested, because they certainly increase the precision, but they can introduce a significant bias making the estimation highly inaccurate.

Eruption Forecasting

As mentioned before, EF can be seen as a specific branch of PVHA. EF deserves to be considered separately because it is the main drive for important risk mitigation actions like evacuation of the people living in the surrounding of a volcano.

Despite some recent researches on short-term forecasting (from hours to few days) are based on a deterministic approach (e.g., Voight and Cornelius, 1991; Kilburn, 2003; see also Hill et al., 2001), the presence of complex and different precursory patterns for distinct eruptions, as well as the exigency to consider the possibility that a precursory pattern not necessarily leads to an eruption, suggest that a probabilistic approach could be more efficient in EF (e.g., Sparks, 2003). At this purpose, it is worth remarking that the probabilistic approach is not incompatible with the deterministic approach, because the former can include deterministic rules as limit cases, i.e., when the probability tends to one. In other words, the probabilistic approach is certainly more general, and it has also the merit to be applicable at different time scales; for instance, during a quiet period of the volcano, EF is estimated by accounting for the past activity of the volcano (long-term EF; see, e.g., Marzocchi and Zaccarelli, 2006); conversely, during an unrest, the method allows mid- to short-term EF to be estimated by considering different patterns of pre-eruptive phenomena (e.g., Newhall and Hoblitt, 2002; Aspinall and Woo, 1994; Aspinall et al., 2003; and Marzocchi et al., 2004, 2008).

The concept of short/long-term EF/PVHA deserves further explanations. The terms "short" and "long" are referred to the expected characteristic time in which the process shows significant variations; in brief, during an unrest the time variations occur on time scales much shorter than the changes expected during a quiet phase of the volcano. On the other hand, these terms are not linked to the forecasting time window (for instance, we can use a forecasting time window of one day, both for short- and long-term EF). The distinction between these two time scales, besides to reflect a difference in the physical state of the volcano (quiescence and unrest), is also important in a practical perspective; in fact, for example, the long-term PVHA (years to decades) allows different kinds of hazards (volcanic, seismic, industrial, floods, etc.) in the same area to be compared, which is very useful for cost/benefit analysis of risk mitigation actions, and for appropriate land-use planning and location of settlements. In contrast, monitoring on mid- to short-time scales assists with actions for immediate vulnerability (and risk) reduction, for instance through evacuation of people from danger areas (Fournier d'Albe, 1979).

As a general thought, we can say that a realistic EF is usually entangled by the scarce number of data, and by the relatively poor knowledge of the physical pre-eruptive processes. This makes any EF hypothesis/model hardly testable also in a backward analysis, overall for explosive volcanoes. On the other hand, the extreme risk posed by many volcanoes pushes us to be pragmatic and attempt to solve the problem from an "engineering" point of view: by this, we mean that the devastating potential of volcanoes close to urbanized areas forces the scientific community to address the issue as precisely as possible. This strategy can be summarized quoting Toffler (1990) that said "it is better to have a general and incomplete (*we add: general and incomplete, but precise!*) map, subject to revision and correction, than to have no map at all".

This goal can be achieved at best by treating scientific uncertainty in a fully structured manner, and, in this respect, Bayesian statistics is a suitable framework for producing an EF/PVHA in a rational, probabilistic form (e.g., UNESCO, 1972; Gelman et al., 1995). Basically, the Bayesian approach described here starts from modeling the statistical distribution using our basic knowledge (or complete ignorance), and then it refines the distribution as long as new information come in as in a sort of "data assimilation" procedure.

As last remark, nevertheless the probabilistic tool used, we argue that only real data can reduce (epistemic) uncertainties in forecasting. The large uncertainty in EF is mostly due to the fact that the average level of knowledge of pre-eruptive phases is significantly lower than for syn- and post-eruptive phases. The most obvious reason is that all pre-eruptive processes occur deep inside the volcano, inaccessible to direct observation and, historically, early signs of impending eruption may have been marginal and not documented. Our eruption forecasting ability overall, and especially for long-quiescent explosive volcanoes, is still rather poor. Initiatives like the WOVOdat project (http://www.wovo.org/wovodat) will improve our capabilities. WOVOdat is a fledgling database that will serve as the primary resource for a new field of "volcano epidemiology" and will also aid associated research into how volcanoes prepare to erupt. During volcanic crises, it can be used to make queries such as "where else have X,Y,Z been observed and what happened?" or, more quantitatively, "how much do the given observations increase the probability of eruption today, tomorrow, and in the future?"

THE BAYESIAN EVENT TREE (BET) APPLIED TO PVHA

General features

In this section, we describe a possible strategy for PVHA based on Bayesian Event Tree (BET hereinafter). Basically

BET translates volcanological input into probability of any possible volcano-related event.

The "volcanological input" is every types of information relevant for the event under study. It ranges from models (i.e., ash fall model), to historical/volcanological information (i.e., eruptive catalogs), to monitoring measures (i.e., detecting magma movement), and so on…

A detailed description of the procedure can be found in Marzocchi et al. (2004; 2006; 2008), and Newhall and Hoblitt (2002). Other references on similar Bayesian strategy and, in general, on probabilistic approach are Gelman et al. (1995), Aspinall et al. (2003), Jacquet et al. (2006). Here, we report only the main features of BET that can be summarized in few general points:

a. Despite the probabilistic nature of the method, BET merges all kinds of relevant information, coming from theoretical/empirical models, geological and historical data, and monitoring observations. In brief, BET is a probabilistic model that transforms all of the input volcanological information into probabilities; such probabilities represent an homogeneous and quantitative synthesis of the present knowledge about the volcano.
b. BET has the most important characteristic for a model to be "scientific", that is, it gives the possibility to "falsify" the results provided; this important feature gives also an opportunity to make scientifically testable any scientific belief/hypothesis.
c. In general, BET does not rule out any possibility, but it shapes the probability distribution of the event considered around the most likely outcome accounting for all the information reported above. This is accomplished by dealing with *aleatory* and *epistemic* uncertainties (see above) in a proper way (see Woo, 1999; Marzocchi et al., 2004; 2008).
d. BET estimates short- and long-term PVHA/EF, depending on the present state of the volcano, providing a useful tool in several contexts: i) to compare different types of risks, ii) to carry out cost/benefit analysis of risk mitigation actions, iii) to indicate appropriate land-use planning and location of settlements, and iv) to suggest immediate vulnerability (and risk) reduction actions, such as the evacuation of people from danger areas (Fournier d'Albe, 1979).

The Event Tree

BET is based on the concept of event tree; the event tree is a branching graph representation of events in which individual branches are alternative steps from a general prior event, state, or condition, and which evolve into increasingly specific subsequent events. Eventually the branches terminate in final outcomes representing specific hazardous phenomena that may turn out in the future. In this way, an event tree attempts to graphically display all relevant possible outcomes of volcanic unrest in progressively higher levels of detail. The points on the graph where new branches are created are referred to as *nodes* (Newhall and Hoblitt, 2002; Marzocchi et al., 2004; 2006; 2008). In Figure 1, we report a general event tree for a volcano.

Note that since the definition reported above is mainly driven by the practical utility of the event tree, the branches at each node point to the whole set of different possible events, regardless of their probabilistic features. In other words, the events at each node need not be mutually exclusive.

At each node we have the following states:
- Node 1: there is unrest, or not, in the time interval $(t_0, t_0+\tau]$, where t_0 is the present time, and τ is the time window considered.
- Node 2: the unrest is due to magma, or to other causes (e.g., hydrothermal, tectonics, etc.), given unrest is detected.

Fig. 1. Event Tree for a generic volcano. See text for the explanation of each single node. In red, a pattern of a selected event is reported (The thickness of an ash fall produced by a VEI 5+ eruption overcomes a specific threshold in area 2).
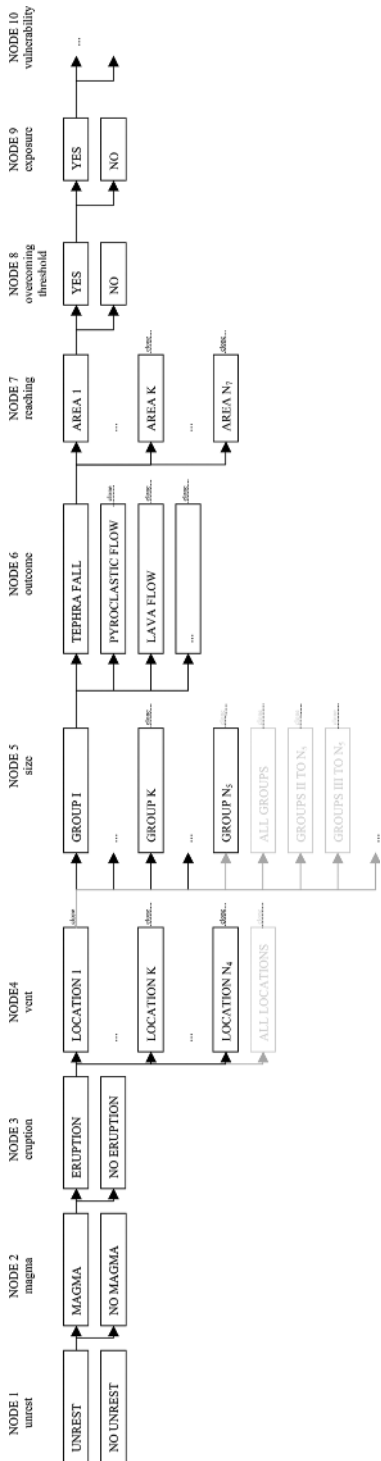
- Node 3: the magma will reach the surface (i.e., it will erupt), or not, in the time interval $(t_0, t_0+t]$, provided that the unrest has a magmatic origin.
- Node 4: the eruption will occur in a specific location, provided that there is an eruption.
- Node 5: the eruption will be of a certain size (i.e., VEI), provided that there is an eruption in a certain location.
- Node 6: the occurrence of a specific threatening event (i.e., pyroclastic flow, lahars, etc.), given an eruption of a certain size in a certain location.
- Node 7: the area reached by the threatening event, given that the threatening event is occurred.
- Node 8: the overcoming of a threshold related to a certain threatening event in a certain area, given the threatening event has reached this area.

At each one of these states we attribute a probability function. As described in the following, the use of these probability functions (characteristic of the Bayesian approach) allows BET to estimate aleatory and epistemic uncertainties. Let us define θ^E as the probability of the conditional event E (note that each event reported above is conditioned to the occurrence of other events at previous nodes); therefore, for each one of the nodes we define [$\theta_1^{(\text{unrest})}$], [$\theta_2^{(\text{magma})}$], [$\theta_3^{(\text{eruption})}$], [$\theta_4^{(\text{location})}$], [$\theta_5^{(\text{size})}$], [$\theta_6^{(\text{threat})}$], [$\theta_7^{(\text{area})}$], [$\theta_8^{(\text{threshold})}$], where the square brackets stand for a generic "probability density function (pdf)". Since the first three nodes have only two possible states that are mutually exclusive and exhaustive (for instance, unrest or not), we set, for the sake of simplicity, [$\theta_1^{(\text{unrest})}$]=[$\theta_1$], [$\theta_2^{(\text{magma})}$]=[$\theta_2$], and [$\theta_3^{(\text{eruption})}$]=[$\theta_3$]. In other words, BET considers the conditional probability at each node as a random variable, therefore it estimates each probability through a pdf, not as a single value.

PVHA and EF

Given all the pdfs at each node, BET combines them in order to obtain the absolute probability of each event at which we are interested in. For instance, the pdf of the probability to have an eruption of VEI 5+ in a the time interval $(t_0, t_0+t]$, at the *j*-th vent location, i.e, [Θ_1], is

$$[\Theta_1] = [\theta_1]\,[\theta_2]\,[\theta_3]\,[\theta_4^{(\text{loc } j)}]\,[\theta_5^{(\text{VEI 5+})}] \tag{1}$$

In other words, [Θ_1] is a quantitative measure of EF. The probability to have the same eruption at any location, i.e, [Θ_2], is

$$[\Theta_2] = \Sigma_j\,[\theta_1]\,[\theta_2]\,[\theta_3]\,[\theta_4^{(\text{loc } j)}]\,[\theta_5^{(\text{VEI 5+})}] \tag{2}$$

where the sum is on the number of all possible vent location considered. In this case we have assumed that the distribution of possible vents is a set of com-

pletely mutually exclusive events. The functional form of [Θ] is not determined analytically, but through a Monte Carlo simulation. In practice, we sample 1000 times each pdf, and we perform the calculation by using each sample. Therefore, we obtain 1000 values of [Θ] that are used to determine the functional form numerically. In this way, we propagate in a proper way both aleatory and epistemic uncertainties at all nodes, and we estimate best guess and errors of the absolute probability of any possible event in which we are interested.

In summary, BET provides quantitative estimations of PVHA through the evaluation of the pdfs of the nodes, by accounting for any kind of available information (i.e., *a priori* and theoretical beliefs, historical and geological data, and monitoring data). We remark that we do not estimate directly the probability of eruption, because in most of the cases it is much easier to estimate conditional probabilities. For the sake of clarity, in Figure 2 we report a scheme that describes the main logical steps of BET applied to EF. The generalization to the PVHA problem is straightforward.

Estimating the probability at each node: the volcanological input becomes probability

From what reported until now, it is easy to understand that the main technical problem in BET is to estimate the pdf for each node. This estimation is the core of the procedure because it translates volcanological input for each node into probability. Since each node deserves a careful discussion about how such a probability is estimated, here we report only the general features common for each node. A full and detailed description of the technical details can be found in Marzocchi et al. (2004, 2006, 2008).

Generally speaking, we have two broad classes of information that can be considered in EF/PVHA: measurements from monitoring (dataset M) and all the other kinds of data/information (dataset $\overline{M}$). This subdivision is mainly due to the fact that, usually, these two types of information have different weights in different states of a volcano. During an unrest, monitoring data may be the most relevant for EF/PVHA purposes, while the same data do not carry relevant information about EF/PVHA during a quiet period, apart from telling that the volcano is at rest. At the same time, it is obvious that monitoring data contain fundamental information that must be used to quantify mid- to short-term PVHA. For these reasons, we introduce these kinds of information through two different functions. At the generic k-th node, the pdf of the j-th event ($[\theta_\kappa^{(j)}]$, see notation used before) is

$$\left[\theta_k^{(j)}\right] = \gamma_k \left[\theta_k^{(j)\{M\}}\right] + (1-\gamma_k)\left[\theta_k^{(j)\{\overline{M}\}}\right] \tag{3}$$

where γ_k is a variable in the interval [0,1], $\left[\theta_k^{(j)\{M\}}\right]$ and $\left[\theta_k^{(j)\{M\}}\right]$ have the

BAYESIAN EVENT TREE (BET) MODEL
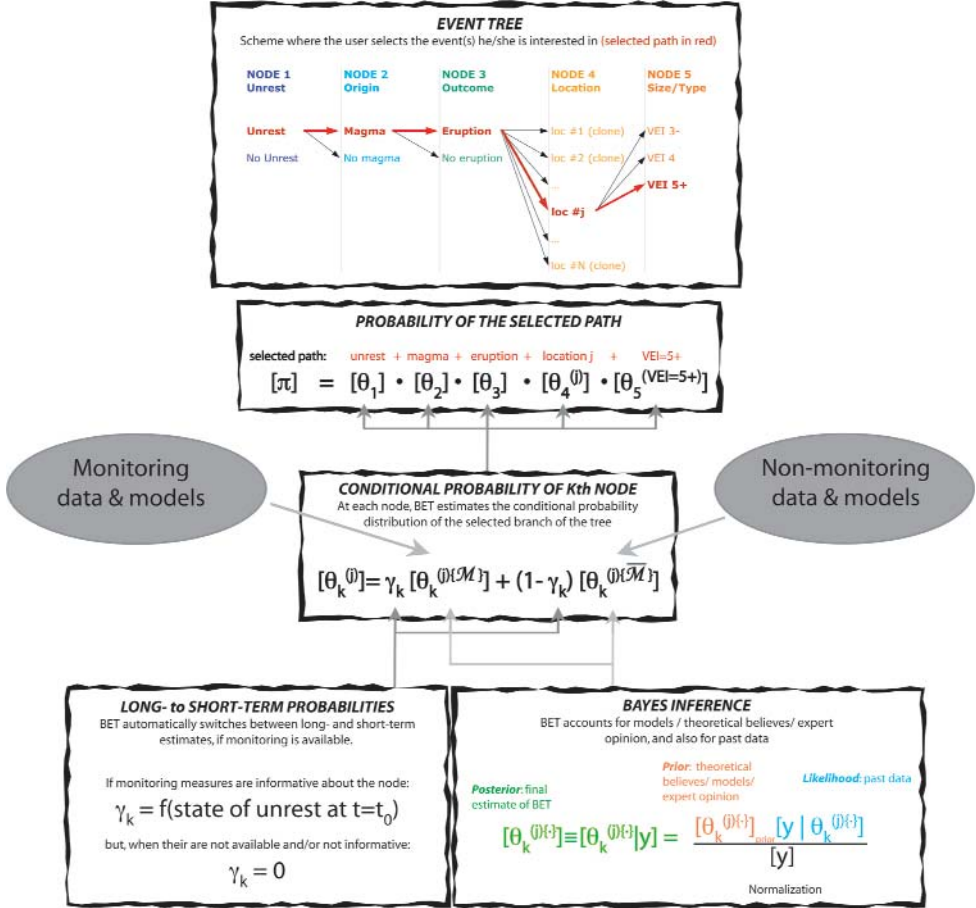
Fig. 2. General scheme of BET. Beginning at the top, there is (1) the selection of a path within the event tree; (2) the computation of the probability of the path; (3) the computation of each conditional probability from all of the monitoring and nonmonitoring information, (4) the computation of the weight of the monitoring part, and (5) the Bayesian inference core of BET.

same meaning as $[\theta_k^{(j)}]$, but they are defined by using only monitoring information and all the other kinds of information (non-monitoring, hereinafter), respectively. In other words, $[\theta_k^{(j)}]$ is a linear combination of the probabilities based on these two types of knowledge, weighted with γ_k and $(1-\gamma_k)$ respectively.

It follows that the unknowns of BET are the pdfs of the conditional probability of the selected events at the nodes. The evaluation of each one of these

probabilities passes through the estimation of the three unknowns in equation (3), i.e., γ_k, $\left[\theta_k^{(j)\{M\}}\right]$, and $\left[\theta_k^{(j)\{M\}}\right]$. In particular:

1. The parameter γ_k sets the degree at which monitoring data (useful for short-term EF) control the posterior probabilities with respect to the non-monitoring part (useful for long-term EF); for the nodes where monitoring parameters are informative, γ_k is a function of the "state of unrest" (see Marzocchi et al., 2008) which, in turn, is a *fuzzy* parameter (Zadeh, 1965) in the interval [0,1] that indicates the degree at which unrest is detected by the monitoring observations at $t=t_0$. In practice, through γ_k, BET switches dynamically from long-term (when the volcano is found to be at rest) to short-term (during unrest) probabilities.

2. $\left[\theta_k^{(j)\{M\}}\right]$ is the monitoring part in equation 3, i.e., the leading term in short-term probability evaluation. It is determined through Bayes' rule, which combines estimated probabilities from monitoring measures at time t_0 and monitoring measurements from past episodes of unrest (if any). Here, the present and past monitoring measurements are transformed into probabilities by means of a physical model that depends on the node considered.

3. $\left[\theta_k^{(j)\{M\}}\right]$ is the non-monitoring part in equation 3, i.e., the leading term in long-term probability evaluation. It is determined through Bayes' rule, which combines estimated probabilities from all our knowledge based on theoretical models and/or beliefs, and past data, i.e., past frequencies of occurrence.

The estimation of these three unknowns requires the use of two important technical concepts, namely the Bayesian inference and the fuzzy approach (Zadeh, 1965). The Bayesian inference is necessary to merge together theoretical models/beliefs with data, and to deal with aleatory and epistemic uncertainties. The *fuzzy* approach is used to manage monitoring measures into the probability calculations and to define the state of unrest. The state of unrest is used to detect unrest from monitoring measures, and then to define γ_k. The specific estimation of γ_k, $\left[\theta_k^{(j)\{M\}}\right]$, and $\left[\theta_k^{(j)\{M\}}\right]$ for each node of BET (equation 3), and all technical details are reported in Marzocchi et al. (2008).

FINAL REMARKS ON BET

To summarize, in this section we report some central features of BET

- BET is a tool to calculate and to visualize probabilities related to PVHA/EF. In particular, BET "dynamically" assesses long-term (useful for land use planning, and for comparing the volcanic hazard with other different kinds of hazard), and short-term (useful during emergency to help managing short-term actions aimed to reduce risk) eruption forecasting.
- BET estimates probabilities by using all of the available information such as models, state of the volcano, geologic/volcanologic/historic data, present and past monitoring observations, expert opinion, and theoretical beliefs.
- BET takes properly and explicitly into account the epistemic (data- or knowledge-limited) and aleatory (stochastic) uncertainties. This guarantees reliable outputs, given reliable input information.
- BET is a scientific tool because it provides probabilities that can be used to test any hypothesis/models contained in BET.
- BET is a quantitative and "transparent" tool that allows to move from subjective choices made, for example, during an emergencies, to more quantitative, objective, and clear rules that can assist decision-makers in handling at best emergencies and land-use planning.

References

Aspinall W.P., G. Woo, B. Voight, P.J. Baxter, 2003. Evidence-based volcanology: application to eruption crises. J. Volcanol. Geoth. Res., 128; 273-285.

Fournier d'Albe E.M., 1979. Objectives of volcanic monitoring and prediction. J. Geol. Soc. Lond., 136; 321-326.

Gelman A., J.B. Carlin, H.S. Stern, D.B. Rubin, 1995. Bayesian Data Analysis. Chapman and Hall/CRC.

Hill D.P., et al., 2001. Response plan for volcano hazards in the Long Valley Caldera and Mono craters region California. USGS Bulletin 2185.

Jaquet O., C. Connor, L. Connor, 2006. Probabilistic methodology for long term assessment of volcanic hazards. International High- Level Radioactive Waste Management Conference, Las Vegas, Nevada, 30 April-4 May 2006.

Kilburn C.R.J., 2003. Multiscale fracturing as a key to forecasting volcanic eruptions. J. Volcanol. Geoth. Res., 125; 271-289.

Marzocchi W., L. Sandri, P. Gasparini, C. Newhall, E. Boschi, 2004. Quantifying probabilities of volcanic events: the example of volcanic hazard at Mt. Vesuvius. J. Geophys. Res. 109; B11201. DOI 10.1029/2004JB003155.

Marzocchi W., L. Zaccarelli, 2006. A Quantitative Model for the Time-Size Distribution of Eruptions. J. Geophys. Res. 111; B04204. DOI 10.1029/2005JB003709.

Marzocchi W., L. Sandri, C. Furlan, 2006. A quantitative model for Volcanic Hazard Assessment. In: Mader HM, Coles SG, Connor CB, Connor LJ (eds) Statistics in Volcanology. IAVCEI Publications, ISBN 978-1-86239-208-3, pp 31-37.

Marzocchi W., A. Neri, C.G. Newhall, P. Papale, 2007. Probabilistic Volcanic Hazard and Risk Assessment, Eos Tran. AGU, 88(32), 318.

Marzocchi W., L. Sandri, J. Selva, 2008. BET_EF: a probabilistic tool for long- and short-term eruption forecasting. Bull. Volcanol., 70, 623-632, doi: 10.1007/s00445-007-0157-y.

Marzocchi W., G. Woo, 2007. Probabilistic eruption forecasting and the call for an eva-cuation. Geophys. Res. Lett., vol. 34, L22310, doi: 10.1029/2007GL031922.

Newhall C.G., R.P. Hoblitt, 2002. Constructing event trees for volcanic crises. Bull. Volcanol. 64; 3-20. DOI 10.1007/s004450100173.

Sparks R.S.J., 2003. Frontiers: Forecasting volcanic eruptions. Earth Planet. Sci. Lett., 210; 1-15.

Toffler A., 1990. Powershift, Bantam Books, New York.

Unesco, 1972. Report of consultative meeting of experts on statistical study of natural hazards and their consequences, Document SC/WS/500, United Nations Educational Scientific and Cultural Organization, pp 1-11.

Voight B., R.R. Cornelius, 1991. Prospects for eruption prediction in near real-time. Nature 350; 695-698.

Woo G., 1999. The Mathematics of Natural Catastrophes. Imperial College Press, London.

Monitoring the source evolution of volcanic seismic swarms through a Nonstationary ETAS modeling (NETAS)

J. Selva[1], W. Marzocchi[1], A.M. Lombardi[2]

[1] *Istituto Nazionale di Geofisica e Vulcanologia, Bologna, Italy*

[2] *Istituto Nazionale di Geofisica e Vulcanologia, Roma 1, Italy*

PURPOSE

The purpose of this report is to discuss the analysis of volcanic seismic swarms with a nonstationary Epidemic-Type Aftershocks Sequences (NETAS) modeling, and its possible practical uses during volcanic unrest episodes. NETAS models seem to have the intriguing capability of correctly tracking the origin (in terms of presence of magma) and the energetic evolution of volcanic seismic swarms [Hainzl and Ogata, 2005; Lombardi et al., 2006; Selva et al., 2007]. This capability may have an important impact in managing volcanic crises, providing important clues to be used in real-time Probabilistic Volcanic Hazard Assessment (PVHA) [see Marzocchi et al., 2007, 2008a, 2008b], in particular in calderas [Selva et al., 2007].
Here, we shortly describe the NETAS modeling, and we discuss its prerogatives, limitations, and the physical interpretation of the results. The latter is the basic ingredient to infer the nature of the source responsible for seismic swarms in volcanic areas, and to track its temporal evolution. In principle, this procedure can be used in real-time implementations; the application to future unrest episodes allows the capability of the NETAS model to be rigorously tested, and it provides a quantitative tool for scientists and Civil Protection to achieve a better understanding of the processes involved in a volcanic unrest, therefore reducing significantly the epistemic uncertainty of eruption forecasting.

NETAS MODELING

NETAS is a generalization of ETAS models [Ogata, 1988, 1998] that allows time variations of the parameters to be accounted for. Here, with the term stationary we mean a process/model whose parameters do not vary through time.
In order to include secondary aftershocks activity, ETAS stochastic model describes the short-time clustering features of earthquakes as superposition of

modified Omori functions [Utsu, 1961] shifted in time. The total occurrence rate at a time t is given by the sum of triggering rates of all preceding events and of a background rate λ_0 [e.g., Ogata, 1988, 1998]:

$$\lambda(t) = \lambda_0 + \sum_{t_i < t} \frac{K}{(t - t_i + c)^p} \; e^{\alpha(m_i - M_{\min})} \tag{1}$$

The background rate λ_0 accounts for the non interacting part of the sequence. The parameter K measures the productivity of the aftershocks activity, whereas α defines the relation between triggering capability and magnitude m_i of a triggering event. The parameter c measures the incompleteness of catalog in the earliest part of each cluster, caused by lowering in detectability of stations after a strong event [Kagan, 2004]. The parameter p controls the temporal decay of triggered events. M_{min} is the threshold of magnitude completeness of the catalog.

In many areas, in particular in volcanic areas, seismic activity is strongly controlled by fluid intrusions and shows mixed occurrence of mainshock-aftershocks sequences and magma/fluids-related swarms. As a consequence, background as well as inducted activity could be strongly characterized by time variation of the parameters (nonstationarity). One example of such a nonstationarity was provided by Matsu'ura [1983]; he shows that temporal evolution of triggered seismicity in volcanic areas cannot be always described by a single Omori law.

Not all the parameters of ETAS model can be directly linked to a physical process. For instance, the parameters c and M_{min} are related to properties of the recording network. Instead, the other parameters K, α, p and λ_0 are related to the properties that locally characterize the crust. While K and α are related to intrinsic properties of the crust/swarm [Utzu et al., 1995], λ_0 is related to the energy of active external sources for earthquakes (tectonic, dykes, fluid migrations, etc.) [Hainzl and Ogata, 2005] and the p-value is related to the answer of the fractures to a stress perturbation; for instance, p varies with temperature, presence of fluids, etc. [Mogi, 1967; Kisslinger and Jones, 1991]. Statistically significant changes of such parameters mean changes in the local properties of the seismogenic crust during the swarm. In volcanic seismic swarms, the variation of the parameters p and λ_0 are particularly important [Lombardi et al., 2006], because the processes associated to them can vary in time scales of hours/few days. On the other hand, it is very unlikely to have similar time scales for variations of the parameters K and α. This is the main reason for what NETAS consider only time variations of λ_0 and p ($\lambda_0(t)$ and $p(t)$, respectively). Estimation of the model parameters $\{\lambda_0, K, c, p, a\}$ is carried by the Maximum Likelihood Method [Dalay and Vere-Jones, 1988]. We use the Davidon-Fletcher-Powell optimization procedure [Fletcher and Powell, 1963], which provides also a numerical approximation of errors.

The scheme we have chosen to estimate λ_0(t) and p(t) is similar to the one used by Hainzl and Ogata [2005]. We fit the ETAS model in a moving non-overlapping time window with length τ. The choice of τ is a balance that accounts for two opposite requirements: the need to have a short time window to follow the details of the time evolution of the process, and the need to have a large time window including enough data for calculations. A rule of thumb may be to have at least 10 events per time window, but the stability of results can be checked using different choices of τ. In brief, we first estimate the constant parameters on the whole catalog. Then we bin the time series in non-overlapping time windows of length τ, and for each time interval we estimate the (joined) variation of the parameters that change with time (p and λ), setting all the other parameters to the previously found values. In computing *log*-likelihood, we take in account all past earthquakes occurrence, to include probability that an earthquake is triggered by an event occurred in a previous interval time.

EXPLORING THE ORIGIN OF VOLCANIC SEISMIC SWARMS

Most of volcanic unrest episodes are somehow related to magma, but only some of them are strictly related to episodes of magma migration (onset of dykes, seals, etc.), especially in calderas [e.g., Newhall and Dzurisin, 1988]. Such distinction is ultimately the key point to scientifically evaluate the probability of eruption during an ongoing unrest, and to reduce its epistemic uncertainty. NETAS modeling separates statistically the seismic events directly connected to the volcanic source and the seismicity triggered by previous earthquakes of the sequence. Basically, taking into account their physical meaning (see previous section), different volcanic sources have major effects on some of NETAS parameters, so that the discrimination between different volcanic sources is made possible.
The specific goal of the analysis of volcanic seismic swarms presented in this report is the detection of movement of magma bodies. The analysis consists of two steps. First, we describe the post-processing of NETAS results, that is, the statistical analysis of the NETAS time series λ_0(t) and p(t). Second, referring to a conceptual model, we describe a possible interpretation scheme that can be followed to detect episodes of magma migration.

Post-processing

The statistical post-processing of NETAS results essentially consists of searching for significant change points on both time series λ_0(t) and p(t). In a nutshell, the goal is to find whether common significant change points exist and interpret their physical origin.

The algorithm for change point hunting consists of multiple non parametrical statistical tests (Kolmogorov-Smirnov with a predefined significance level) between neighbor subsets of the time series [Mulargia and Tinti, 1985; Mulargia et al., 1987]. The great advantages of such method are that it can work properly also with few data, that it can find multiple change points [Mulargia and Tinti, 1985; Mulargia et al., 1987], and that it does not assume any a priori statistical distribution of the data, since it is based on a non parametric test [e.g., Gibbons, 1971].

The stability of results must be checked, since the presence of multiple tests leads to the unavoidable possibility of finding change points by chance, even though they are statistically significant in a single test. Therefore, we analyze the consistency of the results using different time windows length τ to find only real change points. The presence of "(almost) synchronous" change points in different time series corroborates their statistical significance and supports the existence of a common physical origin of such variations.

Interpretation scheme

To physically interpret the temporal variations of the time series, we refer to a conceptual model. Dyke propagation is normally characterized by high rates of induced seismicity, which strongly varies in short times with outbursts of activity, and high temperature in the seismogenic volumes of the crust. In terms of NETAS parameters, this behavior induces significantly high values of the background seismicity λ and of the *p*-value during the most significant episodes of activity [Lombardi et al., 2006]. Moreover, with high temperatures in the seismogenic crust, the parameter *p* assumes very high values, 2 or more times the "normal" value around 1 that *p* has in purely tectonic settings [Utsu et al, 1995, and references therein].

Following this conceptual model, when magma migration episodes occur, we should expect to observe the following behavior:

1. almost simultaneous significant change points in both $\lambda_0(t)$ and $p(t)$ time series at the beginning and at the end of migration episodes;
2. significantly higher value of λ_0 and p during the period of high activity of the volcanic source;
3. generally high value of p, in particular $p(t) >= 2.0$;
4. highly varying background activity $\lambda_0(t)$ with outbursts.

The key point is that all the changes listed above are equally important to detect magma. In particular, points 2 and 3 allow us to reasonably discriminate between magma and hydrothermal fluids [see Selva et al., 2007]. This distinction is a crucial issue and it will the main goal of future investigations, in which NETAS modeling will be used in both volcanic swarms and tectonic seismic sequences.

The rules previously defined have been tested in past well known unrest episodes [at Izu Islands, Japan, Campi Flegrei, Italy and Long Valley, USA; Lombardi et al., 2006; Selva et al., 2007]. As an example of NETAS modeling in real seismic sequences, we report in Figure 1 the results relative to the 2000 Izu Island seismic swarm driven by a clear magmatic intrusion. A complete discussion of this application of NETAS can be found in Lombardi et al [2006].
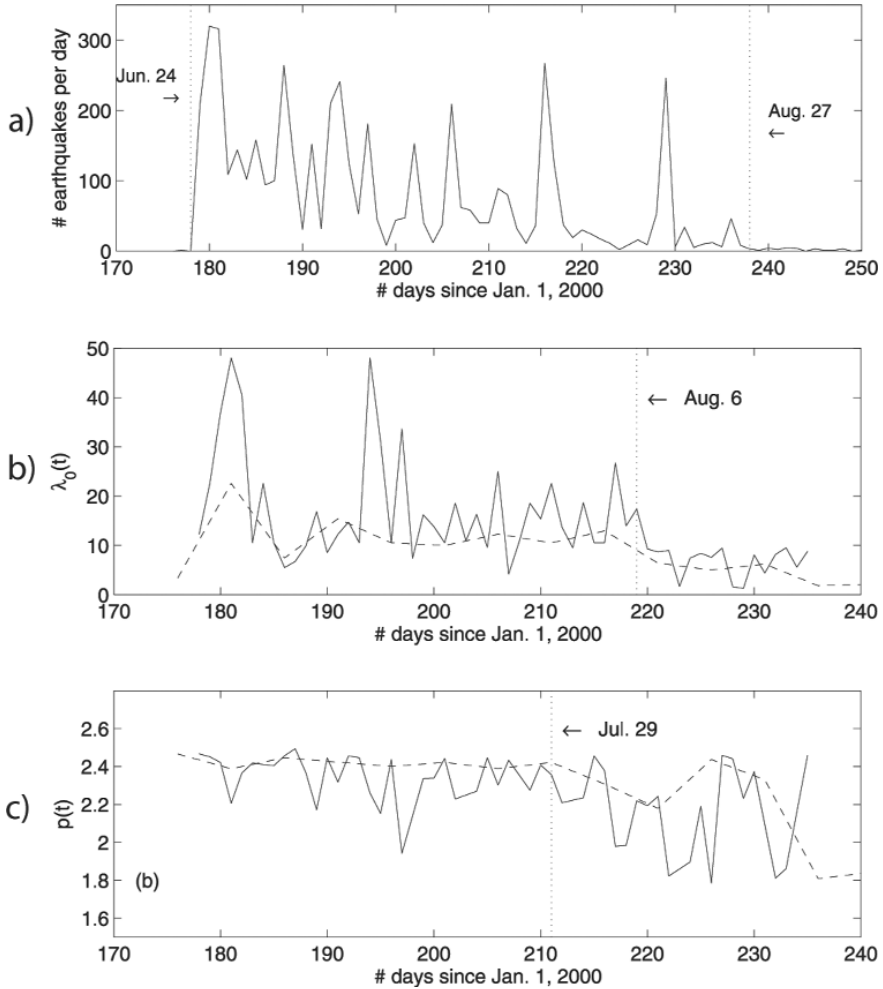
Fig. 1. Analysis of the 2000 Izu Islands swarm, from Lombardi et al [2006]. From top to bottom, we report the seismicity rate, the background activity $\lambda_0(t)$ and the p-value as obtained from a NETAS model with τ of 1 day (solid line) and 5 days (dashed line). Change points are reported with vertical dashed lines and dates.

Here, we want to stress only some key points of such analysis:

– The $\lambda_0(t)$ time series (Figure 1a) is not the proxy of the seismic rate (Figure 1b), but it adds substantial information. For instance, the last peak of activity (around days 230) reported in panel (a) was not connected with a comparable peak of the background activity in panel (b), supporting a driving process of typical aftershock sequences (short-term elastic interaction).

– The two episodes of magma migrations [see Ozawa et al, 2004] are evident at the beginning of the $\lambda_0(t)$ time series, but at the time of the crisis they were not recognizable from the seismic rate.

– Both $\lambda_0(t)$ and $p(t)$ values significantly decrease at the beginning of august, highlighting the decrease of the energy of the magma source; this information was not evident from the seismic rate (Figure 1, top panel)

FINAL REMARKS

NETAS modeling allows a statistical discrimination between seismically triggered events and earthquakes directly connected to the volcanic source. In particular, the analysis of the temporal variation of the NETAS parameters let us to track the evolution and nature of the volcanic source. This may give an important contribution to Eruption Forecasting, and, thus, to PVHA. In fact, one of most problematic issue in Eruption Forecasting during a crisis is the distinction (at least statistically speaking) between unrest episodes that lead, and the ones that do not lead, to an eruption [e.g., Marzocchi et al, 2008a]. This point is particularly critical in calderas, where most of unrest do not lead to eruptions [e.g., Newhall and Dzurisin, 1988].

NETAS modeling, in our opinion, may give important practical contribution to the scientific managing of future volcanic unrest episodes. In fact, it is worth noting that NETAS modeling can be set to work in almost real-time. This is possible because the input data are few and robust (only time and magnitude of the events) and the estimation procedure is quite stable and quick. In this report, we have described the basic features of the model, of the post-processing, and of the physical interpretation scheme of NETAS analysis. These issues represent the cornerstone of a possible future implementation for real-time applications.

REFERENCES

Dalay, D. J., and D. Vere-Jones, An Introduction to the Theory of Point Processes, 702 pp., Springer, New York, 1988.

Fletcher, R., and M. J. D. Powell, A rapidly convergent descent method for minimization, Comput. J., 6, 163-168, 1963.

Gibbons, J.D., Nonparametric Statistical Inference, McGraw- Hill, 1971.

Hainzl, S., and Y. Ogata, Detecting fluid signals in seismicity data through statistical earthquake modeling, J. Geophys. Res., 110, B05S07, doi:10.1029/2004JB003247, 2005.

Kagan, Y. Y., Short-term properties of earthquake catalogs and models of earthquake source, Bull. Seismol. Soc. Am., 94(4), 1207-1228, 2004.

Kisslinger, C., and L. M. Jones, Properties of aftershock sequences in southern California, J. Geophys. Res., 96, 11,947-11,958, 1991.

Lombardi, A. M., Marzocchi, W., and J. Selva, Exploring the evolution of a volcanic seismic swarm: The case of the 2000 Izu Islands swarm, Geophys. Res.Let., VOL. 33, L07310, doi:10.1029/2005GL025157, 2006.

Marzocchi, W., A. Neri, C. G. Newhall, and P. Papale, Probabilistic volcanic hazard and risk assessment, Eos Tran. AGU, 88(32), 318, 2008.

Marzocchi W., L. Sandri, J. Selva, BET_EF: a probabilistic tool for long- and short-term eruption forecasting, Bull. Volcanol., 70, 623-632, doi: 10.1007/s00445-007-0157-y, 2008 (a).

Marzocchi, W., Selva, J., and L. Sandri, Probabilistic Volcanic Hazard and Eruption Forecasting: the Bayesian Event Tree approach, V4 open file report (this issue), 2008 (b).

Matsu'ura, R. S., Detailed study of the earthquake sequence in 1980 off the east coast of the Izu peninsula, Japan, J. Phys. Earth, 31, 65-101, 1983.

Mogi, K., Earthquakes and fractures, Tectonophysics, 5, 35-55, 1967.

Mulargia, F., and S. Tinti, Seismic sample areas defined from incomplete catalogues: An application to the Italian territory, Phys. Earth Planet. Inter., 40, 273-300, 1985.

Mulargia, F., P. Gasperini, and S. Tinti, Identifying different regime ineruptive activity: An application to Etna volcano, J. Volcanol. Geotherm. Res., 34, 89-106, 1987.

Newhall, C.G., and D. Dzurisin, Historical unrest at large calderas of the world, U. S. Geological Survey bulletin 1855, United States Government Printing Office, 1988.

Ogata, Y., Statistical models for earthquake occurrences and residual analysis for point processes, J. Am. Stat. Assoc., 83, 9-2, 1988.

Ogata, Y., Space-time point-process models for earthquake occurrences, Ann. Inst. Stat. Math., 50(2), 379-402, 1998.

Ozawa , S. , Miyazaki, S., Nishimura, T., Murakami, M., Kaidzu, M., Imakiire, T., and X. Ji, Creep, dike intrusion, and magma chamber deflation model for the 2000 Miyake eruption and the Izu islands earthquakes, J. Geophys. Res., 109, B02410, doi:10.1029/2003JB002601, 2004.

Selva, J., Marzocchi, W. and A.M. Lombardi, Characterizing volcanic swarms source in calderas with NETAS modeling, in preparation, 2007.

Utsu, T., A statistical study on the occurrence of aftershocks, Geophys. Mag., 30, 521-605, 1961.

Utsu T., Ogata Y. and R.S. Matsu'ura, The Centenary of the Omori Formula for a Decay Law of Aftershock Activity, J. Phys. Earth, 43, 1-33, 1995.

Task 2

**High resolution seismic imaging
of volcanic structures**

Combining active and passive data for velocity reconstruction

J. Battaglia[1], D. Dello Iacono[2], A. Zollo[2], J. Virieux[3]

[1] *Laboratoire Magmas et Volcans, Université Blaise Pascal, CNRS, Clermont-Ferrand, France*

[2] *Dipartimento di Scienze Fisiche, Università degli Studi di Napoli Federico II, Napoli, Italy*

[3] *UMR Geosciences Azur, Sophia Antipolis, France*

INTRODUCTION

The Campi Flegrei caldera is situated west of the city of Naples in a highly populated area. It is assumed to be mostly the result of two explosive events: the Campanian Ignimbrite eruption (37 ka) and the Neapolitan Tuff eruption (12 ka) (Scandone et al., 1991; Orsi et al., 1996). The caldera is strongly affected by bradyseismic activity which is characterized by large scale vertical ground deformations. The two most recent episodes of large and rapid ground uplift, which occurred in 1970-72 and 1982-84, led to a cumulative maximum uplift of about 3.5 meters in the town of Pozzuoli (Orsi et al., 1999) and were accompanied by swarms of earthquakes and increased degassing.
The 1982-1984 bradyseismic crisis led to an uplift of about 1.8 meters (Barberi et al., 1984) and was accompanied by more than 15000 earthquakes. Part of this seismicity is used in the present tomographic study. The Campi Flegrei caldera has already been the target of several tomographic studies based on various sets of passive and active data. The different existing tomographic works provide various velocity models for Campi Flegrei depending on the data set and technique which was used. Our main goal in this paper is to provide a unique velocity model which satisfies both passive and active data sets: data from earthquakes recorded in 1984 as well as data from the more recent shots of the SERAPIS experiment. After presenting the different data sets which we use, we examine the effect of merging these sets which have very different characteristics and quantities. We then search for the optimal tomographic parameters and finally present the tomographic results and resolution tests.

DATA

To obtain P and S velocity models of the Campi Flegrei caldera structure we proceed with a tomographic inversion based on travel times recorded during two distinct experiments (Figure 1). The first data set is composed of 606

earthquakes recorded during the end of the last bradiseismic crisis which occurred in 1982-1984. The events were recorded by a temporary digital network composed of 13 3-component stations which were installed by the University of Wisconsin, USA (UW) and by the 25 analog stations operated by the Osservatorio Vesuviano (OV) and AGIP. From the available events we selected a subset of 606 well constrained earthquakes with a minimum of 4 P travel times and 3 S travel times and an azimuthal gap in station coverage of less than 180 degrees. This passive data set provides a total of 4472 P and 3268 S travel times. The second data set is composed of recordings for 1528 shots produced during the SERAPIS experiment in September 2001. During the experiment were fired more than 5000 air-gun shots (Figure 1). To provide a high density of data in the bay of Pozzuoli, about 2500 shots were fired in the bay along E-W and N-S parallel lines 250 m apart with shots repeated every 125 m along each line. The shots were recorded with 154 stations, inclu-
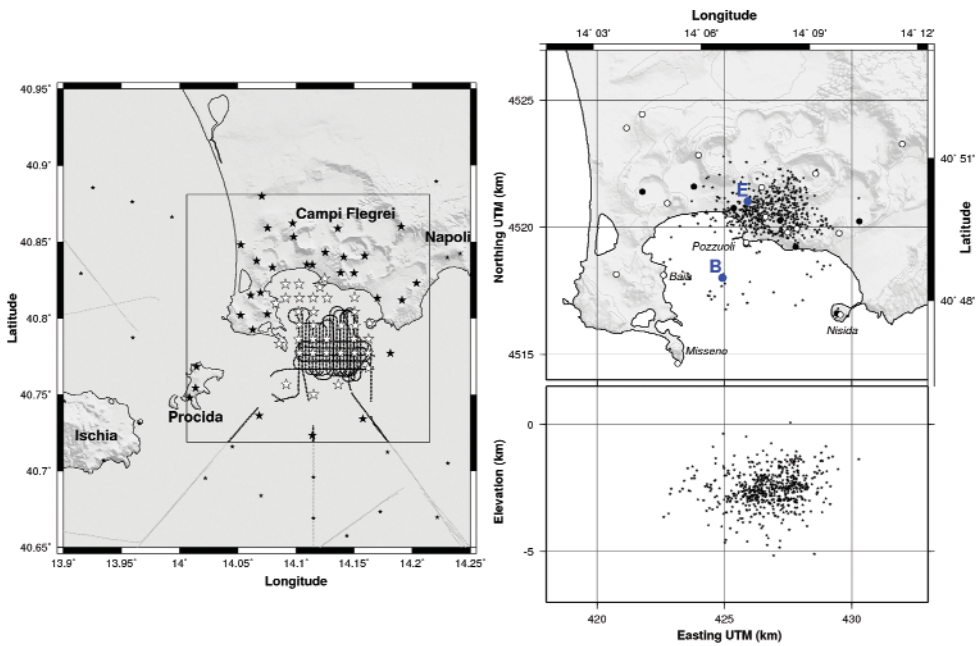
Fig. 1. Left: Shaded relief view of the Campi Flegrei caldera and Ischia and Procida islands with the tomography area in the center. The location of the shots used for tomography is indicated as black dots and the seismic stations are plotted as stars: empty stars for stations for which precisely re-picked arrival times are available and filled stars for stations for which only preliminary picks are available. The location of the shots outside the tomography area area and stations not used in the study is also indicated in lighter color. Right: hypocenters of 606 earthquakes recorded during the end of the 1982-1984 bradiseismic crisis and used in this study: map view and East-West cross-section below. The stations used for locating the events are shown as white circles for the stations of the temporary UW network and as black filled circles for the stations of the OV. Epicentral locations were spike tests have been performed to determined the effect of merging the data sets are indicated with blue dots.

ding 70 sea-bottom receivers (OBS three-component sensors) and 84 land stations (66 with 3-component sensors). The entire experiment produced a total of 700000 waveforms. In present work we only consider a subset of the entire available data set as we only use the shots and stations included in our tomographic area. Our active data set includes a total of 55123 travel times including 36195 re-picked (Dello Iacono et al. submitted) and 18928 picked travel times.

THE TOMOGRAPHIC INVERSION PROCEDURE

Three dimensional P and S velocity models are obtained by inverting P and S first arrival times simultaneously for both velocity models and earthquake locations (Thurber, 1992). The procedure is iterative and at each iteration a linearized inversion of delayed travel times is performed. The inversion is done with P and S velocity models parametrized as 3D grids of regularly spaced nodes. According to our station/source configuration, we consider a tomographic volume of 18*18*9 km starting 0.5 km above sea level (Figure 1) with a node spacing of 0.5 km in all directions. The forward problem of travel time computation is done by solving the Eikonal equation with a finite differences algorithm (Podvin and Lecomte, 1991). For this calculation we use fine P and S grids of constant slowness cells with a spacing of 0.1 km in all directions obtained by trilinear interpolation of the tomographic inversion grids. Travel time partial derivatives are computed simultaneously for P and S slowness fields, hypocenter locations and origin times of earthquakes (Le Meur et al., 1997). Normalization and scaling of the derivative matrix is performed to control the quality of the retrieved parameters. To ensure numerical stability and to control the degree of model roughness, the system is preconditioned and smoothed. The quality of the different observations is taken into account by weighting the different travel times. Finally, the inversion of the scaled and weighted linear system is done using the LSQR algorithm (Page and Saunders, 1982). The inversion is regularized using a damping factor.

MERGING OF THE TWO SETS OF DATA

The joint inversion problem is made difficult since the passive and active data sets are complementary: the first one provides both Vp and Vs velocity models, as well as earthquake locations but has a lower resolution and a limited spatial coverage, while the second has a higher resolution but only provides P velocity and samples mostly shallow layers. Moreover the ray coverages provided by the two sets overlap only over a limited area and amounts of rays are very different. To examine the effect of merging the two data sets we made some spike tests at different epicentral locations and depths. Each spike test is

done by (1) adding to a smooth 1D initial velocity model a 500 m/s anomaly with a width of 1 km at half the pick amplitude, (2) calculating synthetic travel times for the chosen event/station configuration and (3) inverting the synthetic travel times starting from the original velocity model and using the same inversion parameters as for tomography. The tests emphasize that in areas where earthquakes are dominant, the joint inversion leads to a loss in resolution since spike reconstitution is lower than the one obtained when using only earthquakes. In areas dominated by shots the resolution remains unchanged when merging as compared to shots only, even if the resolution of the earthquakes is low (Figure 2). An adequate solution to compensate for the loss of resolution is to increase the weight of the earthquakes. Figure 3 shows
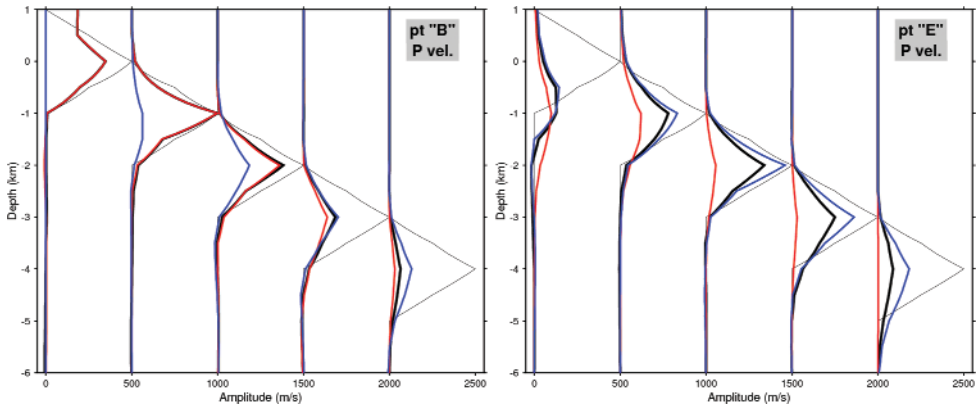
Fig. 2. Comparison between spike restitutions for P waves at points B and E when using shots only (red), earthquakes only (blue) and both (black).
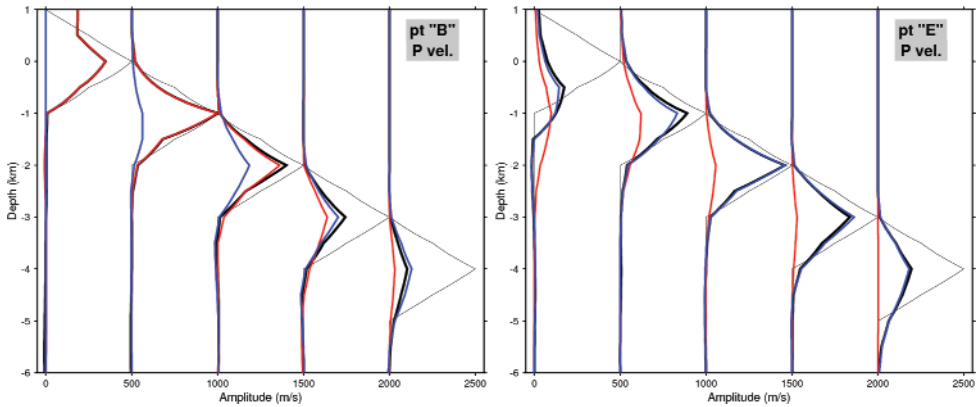
Fig. 3. Comparison between spike restitutions for P waves at points B and E when using shots only (red), earthquakes only (blue) and both with earthquakes weights multiplied by 2 (black).

a comparison of spike restitutions for three combinations of data: both shots and earthquakes alone and shots and earthquakes with the weight of earthquakes multiplied by a factor 2. However, we note that over-weighting the earthquakes using a factor higher than 2 has a negative effect on tomography as it can lead to unstable tomographic images. An alternate solution which allows to avoid the loss of resolution is to reduce the amounts of shots, but we note that it reduces the ability of reconstructing larger scale anomalies as shown later by doing larger scale "shape tests".

INVERSION SETTINGS

To determine the optimal parameters to use in the tomography we perform synthetic tests in which larger scale velocity anomalies with various shapes are introduced ("shape tests"). We present here results for 2 different tests:
– Test T01: an annular anomaly with a 100 m/s amplitude added at each depth in the periphery of the tomography grid to the P velocity model.
– Test T02: a 100 m/s anomaly shaped as a cross added in the center of the grid at each depth to both P and S velocity models.

Figure 4 shows results obtained for tests T01 and T02 for various values of the damping and for various multiplicative factors applied to the weight of the earthquakes. Results suggest that appropriate values for Damping are in the range between 0.3 and 0.5. For P waves a good compromise is found in multiplying the weight of earthquakes by 2. To choose the proper S-wave multiplicative factor, we need to take into account another criterion which is the simplicity of the obtained velocity models when doing the tomography. It is well known that in tomography it is generally possible to find a whole class of models, which fits equally well the observations (Monteiller et al., 2006). The choice of the best model in that class is done by choosing the result with the lower degree of freedom (Akaike, 1974; Tarantola and Valette, 1982). For this purpose we examine the variance of the P and S velocity models and Vp/Vs ratio obtained with various multiplicative factors and examine the corresponding residuals for P and S travel times. Results indicate that a good choice is found with P-weights multiplied by 2 as suggested by above synthetic tests and S-weights multiplied by 2 or 4. The results for shape tests, performed by reducing the amounts of shots, indicate that it leads to a significant reduction in the ability to reproduce anomalies in the peripheral area of the grid where the resolution comes mostly from the shots. Results also indicate that the weight increase is only allowed by the stabilizing effect brought by the large amount of shots travel times. Finally, to determine a proper value to use for the smoothing coefficients we proceed with visual inspections of the recomposed anomalies. The images indicate that appropriate values for LX are in the range 0.2 to 0.3.
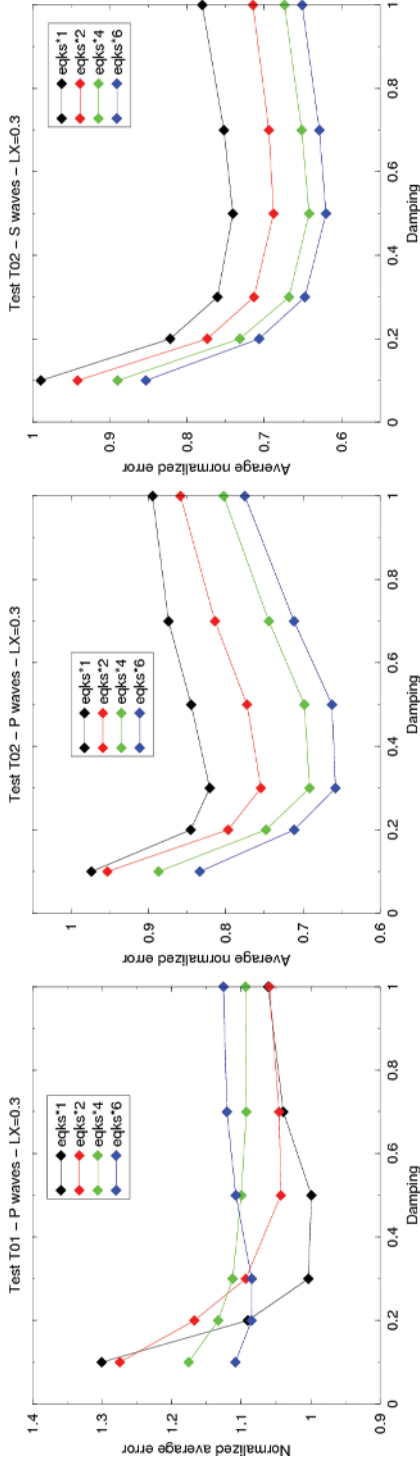
Fig. 4. Mean error rates for test T01 P waves and test T02 P and S waves as a function of the Damping. Each symbol represents the average of the absolute value of the difference between the introduced velocity anomaly and the one restored. This average is calculated over all nodes between 0 and 4 km b.s.l.

TOMOGRAPHY RESULTS

We present tomographic results obtained with DAMP=0.5, LX=0.3 and with the weight of earthquakes multiplied by 2 for both P and S waves. The tomography technique which we use is an iterative, linearized and perturbative technique. The choice of the initial 1D model was done in two steps. First, the 1D model chosen for Campi Flegrei caldera by Vanorio et al. (2005) was used as a starting model to process a first tomographic run. In a second time, the P and S resulting velocity models were used to calculate average vertical velocity profiles for both P and S waves. The obtained profiles are used as initial models. The iterative process is stopped after 15 iterations, while most of the rms residual reduction is achieved in the first five iterations. The process drops the rms from about 0.15 to 0.07.

The obtained 3D velocity models, as well as earthquakes locations are shown in Figures 5 and 6. The obtained high resolution tomographic images outline 3 major features: 1/ The P velocity model (Figure 5) confirms the presence of
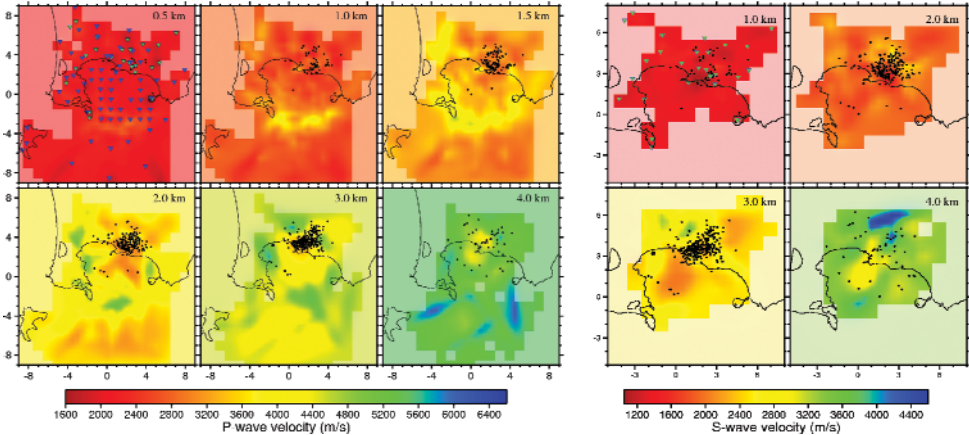
Fig. 5. Tomography results: (left) horizontal sections of the P velocity model. (right) horizontal sections of the S velocity model. Cells not sampled by any ray are shown in lighter colors.

a high P velocity ring in the southern part of the bay of Pozzuoli and extends its trace inland as compared to previous results. 2/ The Vp/Vs East-West cross section at y=2500 (Figure 6), which passes below the town of Pozzuoli, outlines the presence of a very high Vp/Vs anomaly located below the town of Pozzuoli. 3/ Horizontal cross-sections of the Vp/Vs ratio (Figure 6) confirm the presence of a low Vp/Vs body extending at about 4 km depth below a large part of the caldera
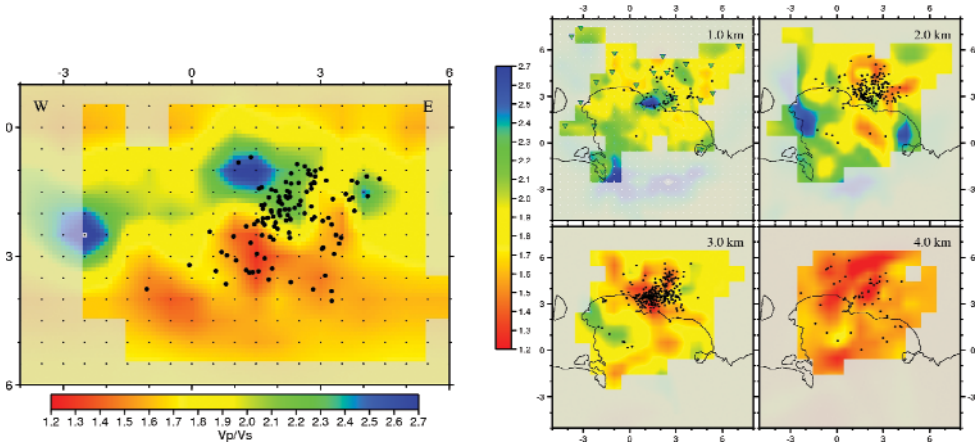
Fig. 6. Tomography results: (left) East-West cross-section at y=2500 of the Vp/Vs ratio; (right) horizontal cross-sections of the Vp/Vs ratio.

RESOLUTION TESTS

To identify the well resolved areas of the tomographic images, we made several synthetic tests including a checkerboard test with 2 km cells with a +/-100 m/s amplitude and several shape tests (Figures 7 and 8). Those are done in a similar way as the tests used to determine proper inversion parameters except that in the present case the position of the earthquake sources are fixed. The checkerboard test indicates an optimal resolution for P waves at 1.5 km b.s.l. below a large part of the tomography grid. For S waves a good resolution is obtained below and around the town of Pozzuoli from about 1.5 to 3.5 km b.s.l.. The shape test in Figure 8 indicates a good restitution of an annular anomaly added to the P velocity model in the periphery of the tomography grid down to 2-3 km b.s.l.. A good reproduction of Vp/Vs anomalies is also obtained below the Pozzuoli area.

CONCLUSION AND DISCUSSION

We show that by properly weighting the different data sets we are able to retrieve optimally the information provided individually by each set. The merging of the two types of data provides a single set of P and S velocity models which satisfy simultaneously all available data. Previous results obtained from gravimetric, seismic activity, and drilled-rock sampling analyses conducted in Pozzuoli Gulf and on land have been used for geological interpretation of Vp and Vp/Vs anomalies.
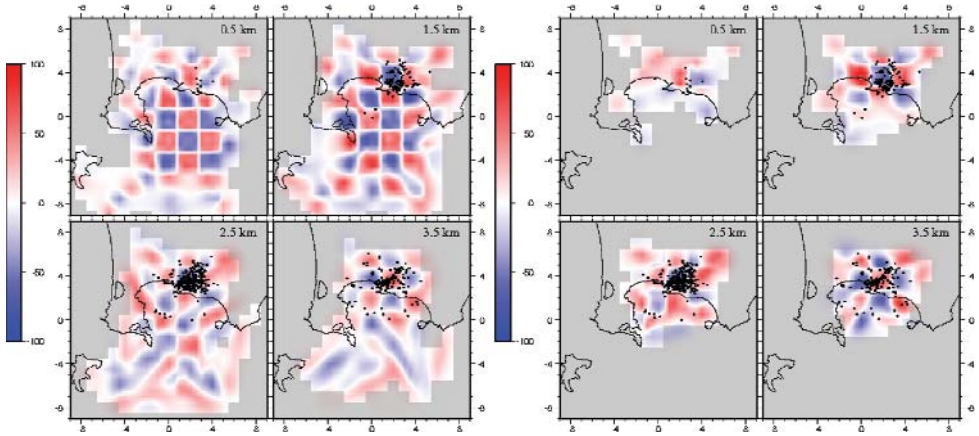
Fig. 7. Results for a checkerboard test with 2*2*2 km cells with +/- 50m/s anomalies added to P (left) and S (right) velocities.
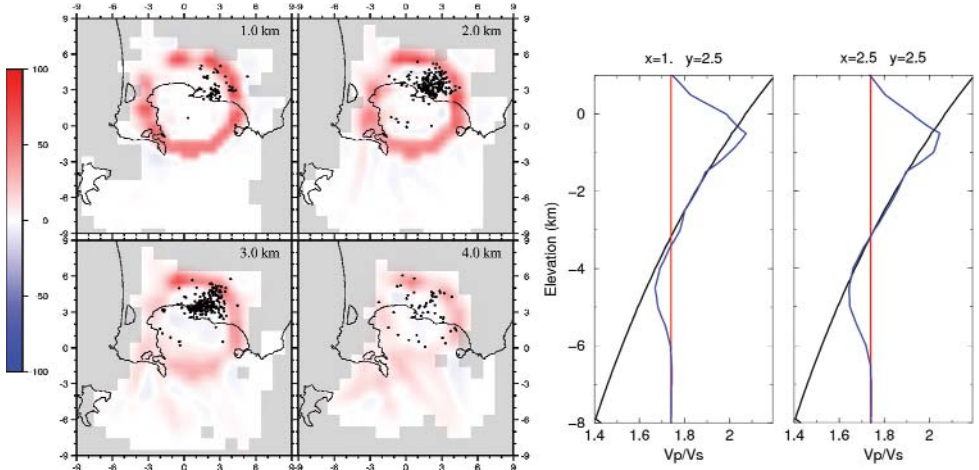
Fig. 8. Results for synthetic T01b showing the reconstruction of the P anomaly at different depths (left) and 2 vertical profiles showing the reconstruction (blue) of the Vp/Vs anomaly (black).

By analysing the horizontal sections of the P-velocity model (Figure 5) we observe at about 1.5 km depth an arc-like positive anomaly with a diameter of about 10 km and a width of about 1 km which is interpreted as the buried trace of the caldera rim (Zollo et al., 2003; Judenherc and Zollo, 2004). By comparing the tomographic image with Bouguer anomaly maps, based on data acquired in early eighties (Agip, 1987; Barberi et al., 1991, Florio et al., 1999; Capuano and Achauer, 2003) one can find a good correlation between the

geometry and position of the velocity anomaly and the positive gravity anomaly, which has been attributed to the presence of hydrothermalized lava formations. At approximately the same depth an anomalous high value of the Vp/Vs ratio is observed in the central area of the caldera on the vertical cross-section passing below the town of Pozzuoli (Figure 6). This anomaly may be the evidence for a thick brine rock sedimentary layer (Vanorio et al., 2005). Recently Dello Iacono et al. (submitted), by analysing the P-to-P and P-to-S reflected phases, extended the area of abnormally high Vp/Vs ratio observed in the first 500/700 m to the entire bay of Pozzuoli and interpreted this result as a consequence of the presence of incoherent, water saturated, volcanic and marine sediments.

Overall, The Campi Flegrei caldera appears as a sub-circular shape with a height of about 2 km. Because of the strong lateral heterogeneity, the caldera border acts like a strong scatterer for seismic waves (Tramelli et al., 2006). At about 4 km depth the annular Vp anomaly disappears. The tomographic Vp velocities of 5500 m/s found at that depth are compatible with those of carbonatic rocks which likely form the deep basement of the caldera (Judenherc and Zollo, 2004). At the same depth, the horizontal crosssections of the Vp/Vs ratio confirm the presence of a low Vp/Vs body extending below a large part of the caldera (Vanorio et al., 2005; Chiarabba and Moretti, 2007). Earthquakes are located at the top of this anomaly. According to the dependence of Vp and Vs velocities to fluid saturation and the interpretation of Vanorio et al. (2005), we believe that the low Vp/Vs value at 4 km depth excludes the presence of melted rocks and is due to the presence of overpressured gas-bearing fractured formations.

REFERENCES

Akaike, H., 1974. A new look at the statistical model identification. IEEE Trans. Autom. Contr., 19 (6), 716-723.

Barberi, F., Corrado, G., Innocenti, F., Luongo, G., 1984. Phlegrean Fields 1982-1984: Brief chronicle of a volcano emergency in a densely populated area. Bull. Volcanol., 47 (2), 175-185.

Barberi, F., Cassano, E., La Torre, P., Sbrana, A., 1991. Structural evolution of Campi Flegrei caldera in light of volcanological and geophysical data. J. Volcanol. Geotherm. Res. 48, 33-49.

Capuano P., Achauer U. 2003. Gravity field modeling in the Vesuvius and Campanian area. TomoVes Seismic Project: Looking Inside Mt. Vesuvius, edited by A. Zollo et al., Cuen, Napoli, 2003

Chiarabba C. and Moretti M. 2006. An insight into the unrest phenomena at the Campi Flegrei caldera from Vp and Vp/Vs tomography. Terra Nova, 18, 373-379.

Dello Iacono D., Zollo A., Vassallo M., Vanorio T., Judenherc S. 2007. Seismic images and rock properties of the very shallow structure of Campi Flegrei caldera (southern Italy). Submitted

Florio G., Fedi M., Cella F., Rapolla A., 1999. The Campanian Plain and Campi Flegrei: structural setting from potential field data. J. Volcanol. Geotherm. Res., 91, 361-379.

Judenherc S. and Zollo A. 2004. The Bay of Naples (Southern Italy): constraints on the volcanic structures inferred from a dense seismic survey. J. Geophys. Res. 109, B10312.

Le Meur, H., J. Virieux, and P. Podvin (1997), Seismic tomography of the Gulf of Corinth: A comparison of methods, Ann. Geophys, 40, 1-25.

Monteiller V. 2005. Tomographie à l'aide de décalages temporels d'ondes sismiques P: développements méthodologiques et applications, Thèse de Doctorat, Université de Savoie.

Orsi, G., de Vita, S., Di Vito, M., 1996. The restless, resurgent Campi Flegrei nested caldera (Italy): constraints on its evolution and configuration. J. Volcanol. Geotherm. Res., 74, 179-214.

Orsi, G., Civetta, L., Del Gaudio, C., de Vita, S., Di Vito, M.A., Isaia, R., Petrazzuoli, S.M., Ricciardi, G.P., Ricco, C., 1999. Short-term ground deformations and seismicity in the resurgent

Campi Flegrei caldera (Italy): An example of active block-resurgence in a densely populated area. J. Volcanol. Geotherm. Res., 91, 415-451.

Paige, C. C., and M. A. Saunders, 1982. LSQR: An algorithm for sparse linear equations and sparse least squares, Trans. Math. Software, 8, 43-71.

Podvin, P., and I. Lecomte, 1991. Finite difference computation of traveltimes in very contrasted velocity models: A massively parallel approach and its associated tools, Geophys. J. Int., 105, 271-284.

Scandone, R., Bellucci, F., Lirer, L., Rolandi, G., 1991. The structure of the Campanian plain and the activity of the Napolitan volcanoes. J. Volcanol. Geotherm. Res., 48, 1-31.

Tarantola, A., and B. Valette, 1982. Generalized nonlinear inverse problems solved using the least-squares criterion, Rev. Geophys., 20, 219-232.

Tramelli A., Del Pezzo E., Bianco F. and Boschi E., 2006. 3D scattering image of the Campi Flegrei caldera (Southern Italy). Phys. Earth Planet. Inter. 155, 3-4, 269-280.

Thurber, C. H., 1992. Hypocenter-velocity structure coupling in local earthquake tomography, Phys. Earth Planet. Inter., 75, 55-62.

Vanorio T., Virieux J., Capuano P. and Russo G., 2005. Three-dimensional seismic tomography from P wave and S wave microearthquake travel times and rock physics characterization of the Campi Flegrei Caldera. J. Geophys. Res. 110, B03201, doi:10.1029/2004GL003102.

Zollo, A., et al., 2003. Evidence for the buried rim of Campi Flegrei caldera from 3-d active seismic imaging, Geophys. Res. Lett., 30(19), 2002, doi:10.1029/2003GL018173.

A shear wave analysis system for semi-automatic measurements of shear wave splitting above volcanic earthquakes: descriptions and applications

L. Zaccarelli, F. Bianco

Istituto Nazionale di Geofisica e Vulcanologia, sezione di Napoli, Italy

Abstract: Our interest is the study of the seismograms with the purpose of monitoring and modeling volcanoes. In particular, since the shear waves bring information about the anisotropic system characterizing the shallow crust, they are also sensitive to all temporal variations caused by changes in the stress field acting on the area. Therefore we intend to realize an algorithm that can provide shear wave splitting estimates in quasi-real time and in a semi-automatic way. Finally we perform validation tests on both real and synthetic data, in order to define the accuracy and validity range of our program.

INTRODUCTION

A transverse wave that enters an anisotropic volume is split into two *quasi*-waves showing perpendicular polarizations and traveling with different velocities. This phenomenon, known as birefringence in optics, is called Shear Wave Splitting in seismology. It can be detected and well described directly from the seismograms, through the estimation of two parameters: the faster S-wave polarization direction ϕ, and the time delay T_d between the two S-waves. At crustal scale, the more common source of seismic anisotropy is the presence of preferentially oriented heterogeneities and (micro)cracks in the rock, whose orientation comes from the stress field acting on the area. In this framework, azimuth ϕ, expressed in degrees from the N, will be parallel to the maximum compressive stress. Time delays, instead, are related to the characteristics of the crack system inside the anisotropic volume, as well as its extension along the ray path. This dependency varies with the incidence angle at the seismic station, distinguishing 2 bands inside a solid angle that ensures no interference with the free surface. The cone of incidences, named Shear Wave Window (SWW), depends on v_p/v_s ratio, and extends until 35° from the vertical for crustal rocks. Between 0 and 15° T_d values are symptomatic of the microcrack

density -*Band2*-, from 15 to 35° T_d is affected by their aspect ratio -*Band1*- (Crampin and Chastin, 2003 and references therein). In this picture the two splitting parameters are more or less directly linked to the stress field and can be considered as an interesting tool for monitoring purpose describing not only the features of the stress field but even their temporal variations.

VOLCANIC STRESS MONITORING

When a volcanic area is interested by an impending eruption, some amount of magma rises from depth to the surface producing an increasing pressure on the surrounding rocks. This almost vertical stress change cause a variation in both crack density and aspect-ratio, if the upper crust is pervaded by fluid filled stress aligned microcracks. Indeed, cracks laying perpendicular to the stress variation tend to close while those parallel grow rounding their shape. The consequences in terms of time delays are that T_d values decrease in Band2, in opposition with those increasing in Band1. If the stress intensity is augmenting more and more, then it will join the system criticality. Such an overpressurized regime is visible through the 90°-flip of ϕ: the two *quasi*S-waves interchange their polarization directions. From this moment the system can fail for even a small perturbation and then the eruption may start. Its occurrence is accompanied by a stress relaxation in the area, that will produce an inversion in time delay temporal variations. All these phenomena are explained by the APE -Anisotropic Poro Elasticity- theoretical model (Zatsepin and Crampin, 1997; Crampin and Zatsepin, 1997) and have been observed in volcanic regions before eruptions such as Ruapehu (Gerst and Savage, 2004), Etna (Bianco et al. 2006), and before a major earthquake at Mt. Vesuvius (Del Pezzo et al., 2004).

This framework highlights the importance of developing the splitting parameter estimation in a (semi)automatic way and quasi-real time.

SPY: SPLITTING PARAMETER YIELD

Semi-automatic algorithm

Automation means any user can deal with a faster and easier tool, able to process a big amount of data at a time. We chosen a semi-automatic procedure in order to avoid as much as possible the fluctuations due to subjectivity with no reduction in terms of estimate accuracy. Actually, the picking phase loses in precision if not executed by an expert eye, especially when we are looking for shear wave arrival inside a volcanic event seismogram. The first step of our approach is therefore a manual resolution of P and S times, whose determination is usually made together with the event location process. Then it starts

the automation stage: a program written in Matlab, that is a versatile and user-friendly environment.

Command line >> SPY(*directory*)

Being *directory* the complete path where the data files are stored.

Input

The hypocenter locations of the events and the coordinates of all seismic stations both in km (UTM). The 2 file paths have to be set in advance directly in the code. Finally, the 3-component seismograms, and P and S arrival times organized in sub-directories per each earthquake or station inside the *directory* given in the command line.

Options

Data file format: *'SAC' / 'ASCII'* (To be set in the code)
Depending on the file format, the program will get the time information from the sac header or from a picking file, whose extension is ".pick" by default.
Plots: *'Y' / 'N'* (To be set in the code)
If the plot option has been set to 'Y', then during execution, the horizontal components of each event will be plotted either before and after rotation along the polarization direction found. This is a way to visually check the goodness of the results as well as the optional parameters, useful especially when the signal characteristics are unknown.
Shear Wave Window: *'y'* → *Band / 'n'* → $[i_1\ i_2]$ (Running the program request)
Here we can choose the incidence angles to be considered: Band can be 1 or 2, inside the shear wave window ($[0;\ 35]°$) or a different Band can be defined inserting $[i_1;i_2]$ in degrees.
Resampling: *'y' / 'n'* (Running the program request)
To be careful in manipulating the data, but if necessary the sampling rate can be doubled through the spline algorithm.
Filtering: *'y'* → $[f_1\ f_2]$ / *'n'* (Running the program request)
In case of very high noise, it is possible to clean the data through a filter, by default a Butterworth bandpass 1-pole, 0-phase with corner frequencies from input. This option is even more delicate and controversial than the previous one, therefore it would be appropriate to verify the stability of the results changing the interval $[f_1;f_2]$.
Cross-correlation threshold: *value* (Running the program request)

Setting a threshold value $\subset$ [0;1[for the similarity of the 2 components.

Algorithm

There exists many different techniques to calculate the splitting parameters and all of them present weakness as well as strength points (Crampin and Gao, 2006). Our choice was leaded by reducing to minimum the user intervention during the analysis.

ϕ **estimate.** The program takes a signal portion starting with the S picking, and ideally ending before the qS_2 arrival time. This time window is the only value that needs to be previously defined by the operator because strongly depends on the signal characteristics. Anyway, the delay between the 2 *quasi*-waves is not known yet, therefore it is convenient to run the program with a first guess, then to adjust the value of the window with the resulting T_d. This feed-back process has been functional even to study the variability of the outcomes versus the length of the sub-dataset under analysis. From this portion of seismogram it is calculated the covariance matrix, whose elements are indicators of the relationship between each component. The covariance diagonalization defines a new coordinate system where the horizontal E and N components would become qS_1 and qS_2. Hence, the fast polarization direction can be found through the azimuth defined by the eigenvector corresponding to the maximum eigenvalue. ϕ angle is estimated in degrees from the N and its value is positive and less then 180°.

T_d **estimate.** Firstly the 3 seismogram traces are rotated in the ϕ direction, obtaining the new decomposition in fast, slow, and everything else components. For the evaluation of the time delay we opted for the cross-correlation methodology: a comparison of the two split waves that measures their similarity versus a shift in time. Again, we need to extract a portion of signal starting from the S-wave arrival and lasting for no less than a period but not too much beyond it, in order to compare only the 2 *quasi*-waves without other seismic phases. This time we could automatically determine the length of the time window through the estimate of the predominant frequency inside 3 seconds of data from the P arrival time. The more energetic part of the spectrum, indeed, is due to the shear waves. Basically, the program operates a FFT algorithm on the data, and from that, it calculates the frequency at which the power spectrum reaches its maximum value. The period corresponding to the proper frequency found marks the end of the signal portion for the following step. The cross-correlation function of fast and slow components would join its maximum for a sample lag that, multiplied by the sampling rate gives the delay sought (in seconds). To refine the evaluation of this time lag, we resampled the function in the proximity of its maximum value, obtaining a more precise time resolution. This operation is not adding further uncertainties because of the smoothly property of the cross-correlation function (VanDecar and Crosson, 1990).

Statistics. In a further stage of the analysis, only those outcomes that meet all requirements defined in the options (acceptable incidence and cross-correlation) are considered for statistical manipulations. Moreover the events with a T_d=0 have to be discarded, because it can be symptom of no anisotropic volume or, more easily, of a mistaken value. The errors on polarization directions are estimated as standard deviation over more circular data (Mardia and Jupp, 2000), preferentially referring to the same station records. Errors associated to time delays, instead, come from the procedure used, and are equal to 1/2 sampling rate for all earthquakes, since the resolution of the refined cross-correlation function is half sample. We finally calculate the normalized time delays, dividing any T_d by its related hypocenter distance. These values are helpful for a comparison among events, under the assumption that all ray paths are sampling almost the same anisotropic volume. This hypothesis is not too strong, especially working on volcanic events that normally occur inside a small volume. In any case T_n is a helpful measure, even if not completely disconnected by location effects. Its error is defined by the propagation formula:

$$T_n = T_d / D \Rightarrow \delta Tn = \frac{\sqrt{\delta T_d^2 + T_n^2 \cdot \delta D^2}}{D} \tag{1}$$

Where D is the hypocenter distance to the seismic station, and with δ are indicated all error estimates. It is worthy to note the dependency of this value accuracy on the precisions of both time delays and locations.

Output

The program save two kinds of Matlab variables ("".mat"") for each subdirectory found in the input data path *directory*, i.e. for any station or event, established on how the data have been grouped and stored. Variable names are by default "swsSUB.mat" and "tdSUB.mat" where SUB stands for (and will be replaced by) subdirectory name.

swsSUB.mat. The first variable saves all rough results obtained by running the program. If loaded, it will appear as a matrix composed by a line for each 3-component record found in SUB, per 6 columns. The column meanings are, respectively: incidence angle (°); D (km); P time (s); ϕ (°N); cross-correlation maximum value; and T_d (s). When the event record is out of bound (out of allowed incidences, or cross-correlation threshold), it is assigned a fake value of 1000 or -9 to all cells.

tdSUB.mat. This second matrix is composed by as many lines as the selected events inside the incidence cone, with cross-correlation maximum greater than the similarity threshold, and whose time delay estimate is not zero. The 5 columns report time of the P wave (s); T_n (s/km); δT_n (s/km); ϕ (°N); Δ_ϕ (°).

APPLICATIONS

SPY program has been tested and calibrated through the analysis of both real and synthetic data.

Real data: Etna 2002

We had availability of seismograms recorded at Mt. Etna during the 2002-2003 fissure eruption. These events were not yet studied, but we could compare our results with those coming from previous works on Etna seismicity and its splitting parameter evaluations (Bianco et al., 2006). In general SPY outcomes are in agreement with those reported in literature, showing a roughly E-W mean polarization, 90(-flipped with respect to the regional stress direction (Musumeci at al, 2004); and small T_n values (of the order of few ms per km). Anyway a more detailed interpretation of the results is complicated by the great instability due to the ongoing eruption, and need further studies. In the present report we highlight the importance of the parameter set calibration phase through this practical example over real data. In particular, we tested the stability of the results in changing the covariance matrix time window length τ. As already described in the ϕ estimate paragraph, this window has to be ideally long as the time delay we are looking for. Starting from the qS_1 arrival time and lasting till the qS_2.

Figure 1 reports in dashed line the mean polarization directions over all events in the SWW at one station (ERCB, the closest to the hypocenter locations), while the straight segments outline the azimuthal difference between successive points. The lines draw the behavior of this 2 measures versus increasing τ from 0.026 s to 0.146 s, at constant steps of 10 ms. The window has a starting point fixed at the S picking time minus 2 samples (=0.016 s) to ensure the beginning of the shear wave begins inside the signal portion considered. For all trials we found time delays less than 0.092 s, marked with the vertical line, that hence become an upper limit for τ length. We are interested in points where the results are almost stable (Teanby et al., 2004), meaning that the covariance matrix is well defined, i.e. compound by enough data, before the slower wave arrival. In our case we can see big oscillations of ϕ in the first τ guesses, than a plateau is reached right before the boundary vertical line. Therefore we selected a window length of 0.076 s as the more plausible and accurate for these seismograms.

Synthetic data

The OGS group (Klin et al.) provided us with 3 synthetic events at Campi Flegrei, recorded by 13 seismic stations: ASE, ASO, BAC, DMP, NIS, O04,
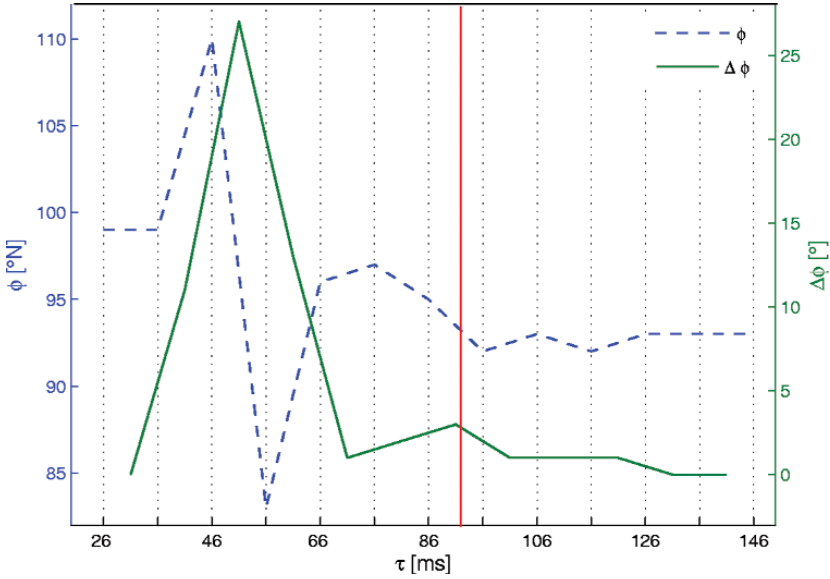
Fig. 1. φ measures (dashed line, y-axis on the left) and their variations Δφ calculated over subsequent values (straight segments, right y-axis), versus length of the time window used, τ. Beyond the vertical line the window is certainly taking some portion of qS$_2$ wave.

O14, O29, W03, W11, W12, W15, W20. The three simulations share the same epicenter coordinates but associate them three different depths, respectively: -1.7; -3.4; and -5.4 km. Each synthetic event is in form of a single sac file per component at any station. Figure 2a shows the horizontal projection of stations (blue triangles) and epicenter location (red asterisk) with the black curve marking the Campi Flegrei coast line, the inland on the upper part and the sea on the bottom. In Figure 2b is a vertical projection of stations and hypocenter locations together with a simplified sketch of the velocity model used for generating the simulations. The model is quite complex with only one isotropic layer, the shallower, from the surface down to -0.6 km with P velocity increasing linearly with depth from 2.5 to 3 km/s and v_p/v_s=2.5. The second layer extends from 0.6 till 1-1.5 km under the surface (the bottom floor being not planar), its v_p reaches the 3.9 km/s at depth, and v_p/v_s ratio is 2. Then it starts another layer that goes down until a variable depth between -4.5 and -5.5 km where v_p has its maximum value of 5.4 km/s, while v_p/v_s is constantly 1.8. Finally there is a half-space characterized by v_p=6.5 km/s and v_p/v_s=1.699. Below the first 600 m, all layers are thought as pervaded by a Shear Wave velocity Anisotropy swa=10% with symmetry axis parallel to the EW direction. From this velocity model we inferred a mean S-wave velocity averaging over all central v_s values weighted with the corresponding mean thickness of the ith layer:

$$\bar{v}_s = \sum_{i=1}^{3} \bar{v}_{s_i} \cdot \bar{h}_i / \bar{H} = 2.3 \ km/s \tag{2}$$

where $\bar{H} = \sum_i \bar{h}_i = 5 \ km$.

Following Savage et al., 1990, we combined this mean value with T_d estimated by SPY to obtain the shear wave anisotropy percentage (swa in equation 3), in order to make a comparison with the theoretical one.

$$swa = \left(\frac{\bar{T}_d}{\bar{D}} \cdot \bar{v}_s \right) \cdot 100 \tag{3}$$

$\bar{T}_d$, $\bar{D}$ averaged over all station records.
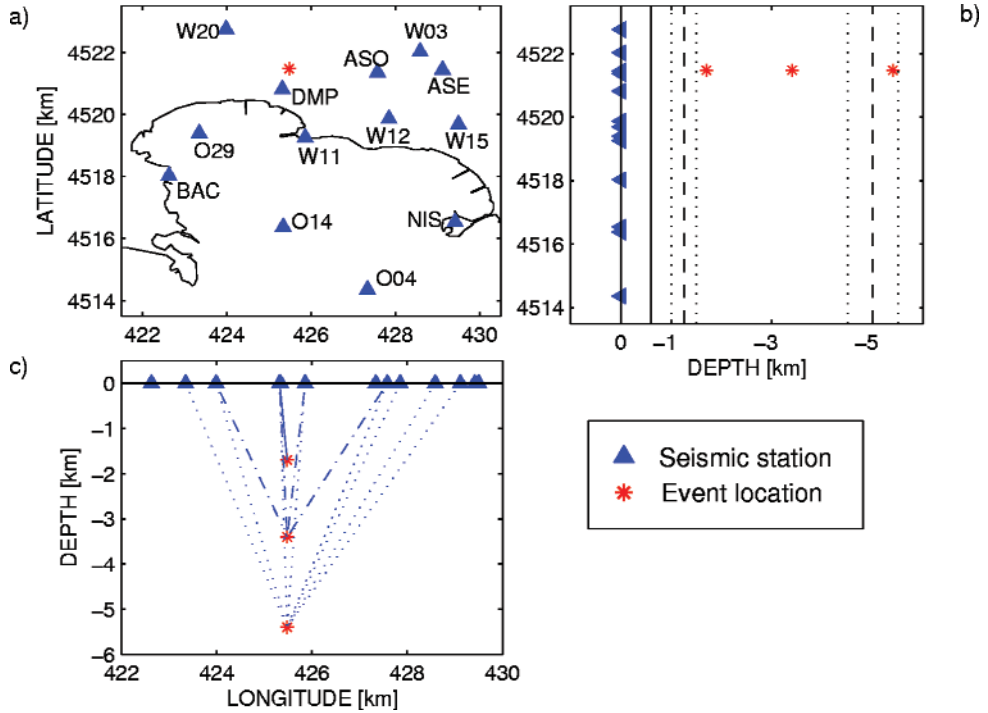
Fig. 2. Hypocenter and seismic station distributions, in UTM coordinates, for the synthetic experiments. a) Horizontal projection with Campi Flegrei coast line. b) Latitude versus depth where the vertical lines sketch the 4 layers compounding the velocity model: dotted lines evidence the depth range where the boundary can extend, with the dashed one in the middle for non planar separation mean depth. c) Depth versus longitude. The three events are linked to those stations laying inside their SWW (35° cone).

In Table 1 we report SPY measurements only for those seismic stations positioned in the shear wave window with respect to the simulated hypocenters (see also Figure 2c).

Tab. 1. Results for the three synthetic events recorded at stations where they had an incidence angle inside the shear wave window. The columns report: station name, incidence angle, hypocentral distance, fast polarization direction, time delay, anisotropy percentage.

station	i [°]	D [km]	ϕ [°N]	T_d [s]	swa [%]	
DMP	22	1.8	109	0.005	0.6	TEST 1
ASO	32	4.0	88	0.06	3	
DMP	11	3.5	1	0.15	10	
W11	34	4.1	2	0.12	7	TEST 2
W20	30	3.9	173	0.035	2	
ASE	34	6.5	86	0.06	2	
ASO	21	5.8	89	0.08	3	
DMP	7	5.4	106	0.035	1.5	
O29	29	6.2	92	0.21	8	
W03	30	6.3	159	0.065	2	TEST 3
W11	23	5.9	83	0.255	10	
W12	28	6.1	85	0.035	1	
W20	20	5.7	107	0.205	8	

Test 1 is the synthetic event with depth -1.7 km. Only DMP is inside the 35° cone of incidence. The qS_1 polarization direction is a little bit more than the theoretical 90° (Figure 3a) and swa calculated is almost 0.

The deeper source at -3.4 km (test 2) increases to 4 the number of stations inside SWW. The right ϕ direction has been detected only at ASO (see Figure 3b), whilst swa is 10% only for DMP. We are searching for possible reasonable explanations for the spurious ϕ measurements obtained in this second simulation at W11, DMP, and W20 stations; actually we are exploiting the possibility that qS_1 polarization may be corrupted by the presence of irregular interfaces near the source.

Last test hypocenter is located 5.4 km down from the surface. The stations viewed with an angle less than 35° are 8. All of them show a EW oriented ϕ, excepted W03 (Figure 3c), anyway only 3 (O29, W11, W20) time delays can produce a percentage anisotropy close to the 10%.
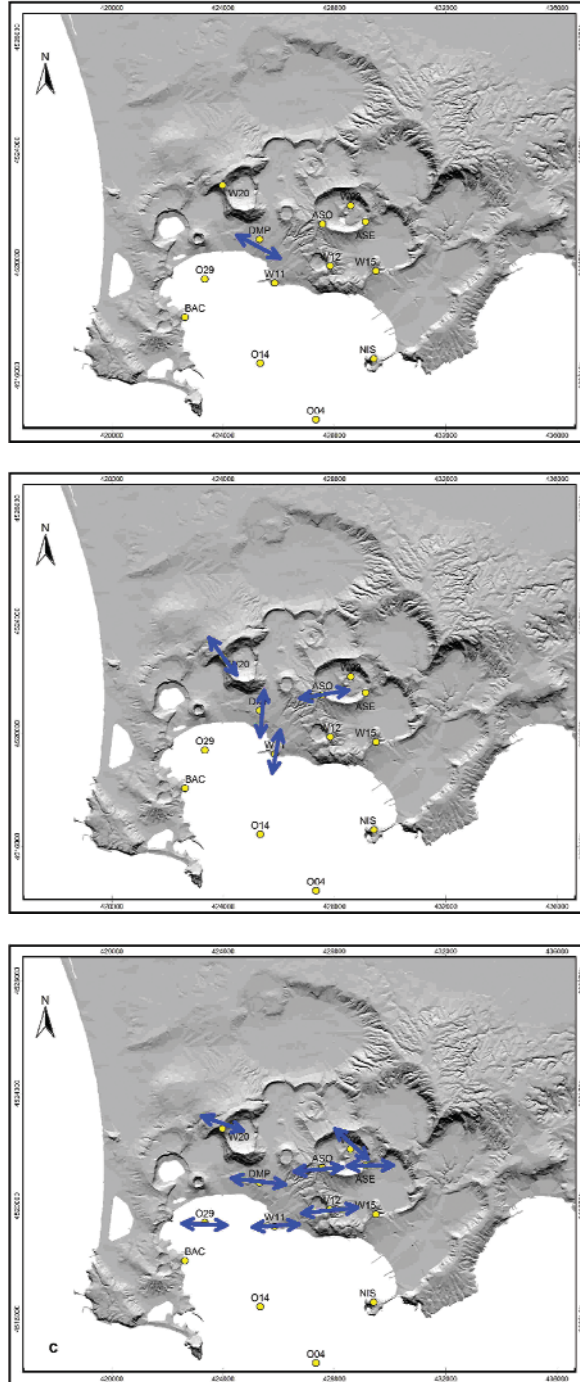
Fig. 3. Spatial distribution of ϕ directions retrieved for each synthetic test. **(a)** ϕ direction at the only station inside SWW for test 1; **(b)** the same for test 2; **(c)** test 3.

This disagreement can be ascribed to swa index we calculate that is not properly the same intended in the crustal model, since the splitting of the shear wave depends on both aspect ratio and density of microcracks, while the percentage used to build up the synthetic traces is a measure of the number of cracks inside the surrounding rock, independently from their volume. Moreover, equation 3 refers to averaged value over multiple records, meaning that we would need various simulated events to gain significance and accuracy in swa estimate. The interesting found is the right estimate of fast polarization direction. Even when we look at all records, independently from the incidence angle, the mean value is correctly around 90°.

Conclusions

We developed a semi-automatic algorithm able to yield shear wave splitting parameter estimates in quasi-real time. The final aim would be to exploit them as an additional and useful tool for monitoring temporal variations in the stress field acting on volcanic areas. The program has been tested through the analysis of both real and synthetic data. Results coming from 2002 eruption on Etna are completely in agreement with previous measurements. Furthermore the real data have been used to verify the capability in the feedback process to evaluate the correct parameter set or the validity range for the input choices (such as filtering and resampling operations). The analysis of synthetic data is an entirely unexplored field in terms of anisotropic system. We applied our algorithm to three simulated events with different depths, obtaining averaged values that can reproduce the underlying theoretical model, adding an independent validation of our program.

References

Bianco F., L. Scarfì, E. Del Pezzo, and D. Patanè (2006). Shear wave splitting changes associated with the 2001 volcanic eruption on Mt Etna. Geophys. J. Int. 167, 959-967.

Crampin S., and S. V. Zatsepin (1997). Modeling the compliance of crustal rock-II. Response to temporal changes before earthquakes. Geophys. J. Int. 129, 495-506.

Crampin, S. (1999). Calculable fluid-rock interactions. J. Geol. Soc. 156, 501-512.

Crampin S., and S. Chastin (2003). A review of shear wave splitting in the crack-critical crust. Geophys. J. Int. 155, 221-240.

Crampin S. and Y. Gao (2006). A review of techniques for measuring shear-wave splitting above small earthquakes. Phys. Earth Planet. Interiors 159, 1-14.

Del Pezzo E., F. Bianco, S. Petrosino, and G. Saccorotti (2004). Changes in coda decay rate and shear-wave splitting parameters associated with seismic swarms at Mt. Vesuvius, Italy. Bull. Seism. Soc. Am. 94, 2, 439-452.

Gerst A., and M. Savage (2004). Seismic Anisotropy Beneath Ruapehu Volcano: A Possible Eruption Forecasting Tool. Science 306, 1543-1547.

Mardia K.V., and P.E. Jupp (2000). Directional statistics. Ed.Wiley and Sons Ltd.

Musumeci C., O. Cocina, P. De Gori, D. Patanè (2004). Seismological evidence of stress induced by dike injection during the 2001 Mt. Etna eruption. Geophys. Res. Lett. 31, L07617, doi:10.1029/2003GL019367.

Savage M.K., W.A. Peppin, and U.R. Vetter (1990). Shear wave anisotropy and stress direction in and near the Long Valley caldera, California, 1979/1988. J. Geophys. Res. 95, 11,165-11,177.

Teanby N.A., J.M. Kendall, and M. van der Baan (2004). Automation of shear-wave splitting measurements using cluster analysis. Bull. Seism. Soc. Am. 94, 2, 453-463.

VanDecar J.C., and R.S. Crosson (1990). Determination of teleseismic relative phase arrival time using multi-channel cross-correlation and least squares. Bull. Seism. Soc. Am. 80, 1, 150-169.

Zatsepin S. V., and S. Crampin (1997). Modeling the compliance of crustal rock-I. Response of shear-wave splitting to differential stress. Geophys. J. Int. 129, 477-494.

Converted phases analysis of the Campi Flegrei caldera using active and passive seismic data

T.M. Blacic[1], D. Latorre[2], J. Virieux[1]

[1] *UMR Geosciences Azur, Sophia Antipolis, France*
[2] *Istituto Nazionale di Geofisica e Vulcanologia, CNT, Roma, Italy*

Abstract: We applied a type of depth migration for converted seismic phases to two data sets for the Campi Flegrei caldera: a synthetic 2-D active seismic experiment, and a portion of the SERAPIS 2001 active marine seismic experiment. The passive earthquake data set from the 1984 bradiseismic crisis, compiled as part of the SEARPIS project, was also investigated but was found to be not well suited to the converted phases analysis due to the acquisition geometry. The converted phases analysis is based on the diffraction summation migration technique. Travel times to grid points in a volume are calculated in smooth P and S-velocity models and trace energy near the calculated converted phase time is stacked over multiple sources at one receiver. Weighting factors based on Snell's Law at an arbitrarily oriented local interface can be applied to aid in focusing of trace energy. The non-smooth velocity models of the synthetic data set proved to make focusing trace energy very difficult with this method. However, when reflections from the underside of the local interface (resulting from rays turning at depth) are removed and first arrival energy is muted, a small part of the sloping carbonate basement can be imaged. An investigation of the effect of alterations to the velocity models used in the analysis emphasized the importance of the velocity model in the method but also showed that small changes to the velocity models yield little change in the resulting image. Better results were obtained for the SERAPIS active data set where we have smooth velocity models from seismic tomography. PP and PS reflection images show features near 2-2.5 km in depth, which may be associated with an over-pressured gas volume suggested by tomographic investigations. Possible deeper features near 3-4 km depth may be related to the presence of the carbonate basement.

INTRODUCTION

The Campi Flegrei caldera is an active volcanic system lying west of Vesuvius volcano and the city of Naples in a densely populated area of southern Italy. It last erupted in 1538 but seismic, fumerolic, and ground deformation conti-

nue to the present day. The threat of future eruptions and/or destructive ground deformation has prompted several active and passive seismic studies in the region. Seismic tomography (Judenherc and Zollo, 2004; Zollo et al., 2003) and a combined seismic tomography-rock physics study (Vanorio et al., 2005) have revealed remnants of the buried caldera rim both in the Bay of Pozzuoli as well as on the landward side of the caldera, plus evidence of over-pressured gas-bearing formations at a depth of about 4 km beneath the city of Pozzuoli.

In September of 2001, an active marine seismic experiment called SERAPIS (Seismic Reflection/Refraction Acquisition Project for Imaging complex volcanic Structures) was carried out in the Bay of Naples and Bay of Pozzuoli. During this experiment, ~5000 shots were produced by the vessel *Le Nadir* of Ifremer and recorded on an array of ocean bottom seismometers (OBS) and land stations. A subset of the SERAPIS active data set was combined with earthquake sources from the 1984 bradyseismic crisis that occurred in the Campi Flegrei caldera to produce high-resolution 3-D tomographic P- and S-velocity models of the caldera (Battaglia et al., 2006). These models confirm the presence of the caldera rim imaged as a high P-velocity anomaly at about 1.5 km depth in the southern part of the Bay of Pozzuoli. A low Vp/Vs anomaly was also imaged at about 4 km depth below much of the caldera.

This report summarizes work performed applying a type of depth migration for converted phases to synthetic and real data sets for the Campi Flegrei area. We first summarize the application of the migration imaging method to the synthetic active data set provided by P. Klin for the V4 project (Klin et al., 2007). The active and passive parts of the Battaglia et al. (2006) SERAPIS data set were analyzed separately. The active data set provided good coverage across the caldera for both PP and PS reflected phases. However, the acquisition geometry of the passive data set was not well suited to the converted phases analysis presented here. Most stations lay almost directly above the earthquake hypocenters resulting in short P-S time windows. Although some possible converted phases could be detected in the traces, the small P-S windows and energetic S-arrivals limited the coverage to small areas around each station resulting in a very poor image. Therefore, we will present only results from the active synthetic and active SERAPIS data sets here.

METHODS

The migration imaging technique is based on the diffraction summation method. The target volume is broken into a regular 3-D grid. Each grid point is considered to represent a local arbitrarily oriented interface where seismic reflection and transmission is assumed to occur. We then sum weighted trace energy along complex hyperbolic paths, whose shapes are determined by the velocity structure of the medium, and map the summed energy to the corre-

sponding grid points in space in order to build the image. Only kinematic and geometrical aspects of the migration procedure are considered; we do not take geometric spreading or wavelet-shaping factors into account.

The background velocity model is assumed to be smooth enough that ray theory can be applied throughout the volume resulting in travel times that are consistent with arrival times in the trace data. Into this smooth background we introduce sharp interfaces at grid points where we assume diffraction of waves occurs. The diffractions can be either reflections or transmissions and the grid points can be considered either as point scatterers or as oriented interfaces.

We analyze the data in receiver gathers. For each receiver, our migration procedure consists of three steps after data preparation: (1) Calculate travel times from each source and receiver to each image point, (2) Determine weighting coefficients based on Snell's Law, (3) Stack converted energy at each image point.

Travel time computation

Travel times are computed for each source-grid point-receiver ray-path in the smooth 3-D P- and S-wave velocity models. At each grid point, all incident and diffracted P- and S-waves are taken into account. First we use the finite difference solution of the eikonal equation in a fine grid to construct P and S travel time fields in the entire medium (Podvin and Lecomte, 1991). Then, we re-compute more accurate travel times along the rays by tracing backwards from each source and each receiver to each grid point and then integrating the slowness field along the rays (Latorre et al., 2004). The output from this step consists of: (1) tables of P and S travel times from each grid point to each receiver and from each grid point to each source, and (2) tables of ray-path vector coordinates at each grid point and at each source and receiver for both P- and S-waves.

Determine Snell's Law weights

We consider a local oriented interface at each grid point and examine the incident and diffracted rays hitting this surface. The interface orientation is arbitrary and is the same for all grid points. The Snell's Law weighting factor is calculated as the cosine of the angle θ between the normal to the local interface and the vector difference between the incident (source-grid point) and reflected or transmitted (grid point-receiver) rays. This weight is equal to one when Snell's Law is perfectly satisfied and decreases towards zero as the calculated rays move farther away from the condition predicted by Snell's Law. Only source-grid point-receiver paths with $\cos(\theta) \geq 0.5$ are considered. Applying these weights to the traces focuses energy and mitigates the limited folding by

smearing out "smiles" in the image. The output from this step consists of tables of $\cos(\theta)$ at each grid point for each source-receiver pair for each converted phase: PP reflections, PS reflections, PS transmissions, SP reflections, and SP transmissions.

Stack converted phase energy

For one receiver, we stack trace energy from all sources at each grid point. Traces are first muted (if desired), and then normalized. Single component or three-component normalization can be performed. The maximum trace amplitude is selected from within a narrow window around the calculated converted phase time and Snell's Law weight coefficients are applied (again, if desired). Note that if the Snell's law weights are not applied the image points are considered as point diffractors. Weighted seismic energy over multiple sources is stacked by summing the amplitude squared. The final image for one receiver is then normalized by the maximum stacked trace energy.

DATA

We investigated two data sets for the Campi Flegrei caldera: a synthetic active seismic experiment, and a part of the SERAPIS active marine seismic experiment.

Synthetic active seismic data set

The synthetic active data set was created by P. Klin as part of the V4 project (Klin et al., 2007). It is a 2-D (X-Z) experiment consisting of P- and S-wave velocity models, density models, and SAC-format trace files for 9 two-component receivers and 540 shots. The original velocity models have a grid point spacing of 25 m in X and Z. For application to the converted phases analysis, the velocity models were extended to 3-D such that the velocity does not vary in the Y-direction. The velocity models were also re-sampled to a grid spacing of 500 m in order to approximate the conditions of the real data set.

Active seismic data set

The active seismic data used here is a subset of the SERAPIS experiment performed in September of 2001. Approximately 5000 shots were produced by an array of 12 synchronized airguns offshore and 6 airguns in the Bay of Pozzuoli and near the shore. Receivers included 70 three-component OBS, 66

three-component land stations, and 18 vertical-component land stations. Within the Campi Flegrei area, shots were spaced 125 m apart in individual lines, but lines were sampled more than once on a staggered pattern making the effective shot spacing <65 m. The SERAPIS experiment thus resulted in a density of coverage that approaches commercial exploration surveys and allows us to stack seismic traces (Figure 1). This makes the data set well suited to investigations of geologic hazards in the Campi Flegrei area.

For the converted phases analysis, we selected data from a subset of the SERAPIS data used by Battaglia et al. (2006) in a recent 3-D seismic tomography study of Pozzuoli Bay. We chose stations that have at least 300 shots with P-wave first arrival picks. Thus, our active data set includes: 1528 shots, 33 OBS (41778 P-picks), and 13 3-component land stations (7484 P-picks). Selected stations and shots are shown in Figure 1.
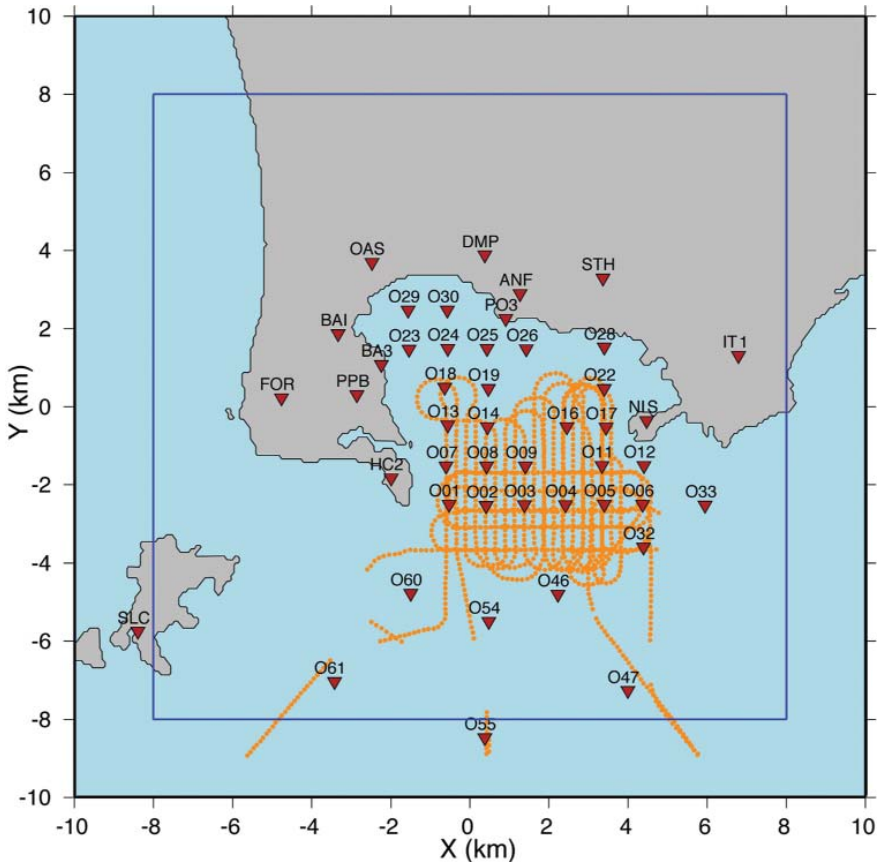
Fig. 1. Receiver (red triangles) and shot (orange dots) locations for SERAPIS active data set used in the converted phases analysis. Blue box outlines target area.

ANALYSIS OF CONVERTED PHASE FOCUSING

Our analysis consisted of two parts: investigation of the synthetic active data set including tests of the effect of changes in the velocity model on the energy focusing, and investigation of the "real" SERAPIS active data set.

Converted phases analysis of the synthetic active data set

The background velocity models used to generate the traces for the synthetic data set are not smooth models. They contain very sharp velocity contrasts where the carbonate basement is assumed to exist as well as more mild velocity contrasts where the caldera structure is modeled. This means that in our application of the converted phases migration to this data set we are working outside the original theoretical basis of the method. As a result, we find that while we were not able to reconstruct the complex structure of the model, we do see the imprint of the velocity model on our results when we apply the Snell's Law weighting factors.

We investigated primarily PP and PS reflected phases with a grid spaced 500 m in the X and Y directions, and 200 m in the Z direction. Due to the 2-D nature of the data set, only one X-Z profile was imaged at Y=0 where the sources and receivers are aligned. The re-sampled P-velocity model used in our analysis is shown in Figure 2a.

When we apply Snell's Law weight factors for a horizontal local interface and sum the images from all nine receivers we get the image shown in Figure 2b. The primary features are bright areas at either end of the model; these are artifacts resulting from the application of the ray tracing procedure to a complicated velocity model with abrupt changes in velocity. For many source-receiver pairs, these grid points have ray geometries that resemble "upside down" reflections. That is, the rays from the source turn at some depth below the grid point, reflect downward off of the underside of the local interface, and then turn back up to reach the receiver. Eliminating these upside down reflections by setting the Snell's Law weight to zero for rays with this type of geometry results in an image in which the brightest spots are just below the receivers where first arrival energy is stacked (Figure 2c). Applying a mute to the traces up to 0.2 seconds after the theoretical first P-arrival time (calculated in step 1 of our procedure) gives us an image in which we can see part of the sloping carbonate basement just below station R09 at X=22.5 km (Figure 2d).

Another interesting feature can be discerned in Figure 2b. The location of the carbonate basement appears to be defined by a region with near zero stacked energy (blue grid boxes). The blue image is even more pronounced in the PS reflection image (Figure 2e). This results from the application of the Snell's Law weight factors when we have an abrupt increase in velocity. Rays turn sharply at the top of the high-velocity carbonate basement resulting in geo-

metry that is far from satisfying Snell's Law for most source-receiver pairs. When individual receiver images are then summed, grid points at the top of the carbonate basement have very low values of stacked trace energy associated with them compared to surrounding grid points. Thus, in some way, we image the carbonate basement by not stacking energy in those grid points.

We ran several variations of the P- and S-velocity models in order to investigate the effect of the starting velocity model on the resulting image. These tests highlighted the dependence of the final image on the starting velocity model. When the variation in the model was small (e.g., blurred in the X or Z direction with a Gaussian averaging filter), the resulting image was very similar to the original image (Figure 2b). Re-sampling the velocity models to 250-m grid spacing likewise resulted in little change in the resulting image. In contrast to this, in one variation we removed the carbonate basement (Figure 3a). The resulting PP reflection image contained mostly artifacts, but the PS reflection image showed part of the bottom of the caldera structure near X=5 km, Z=3.5 km (Figure 3b). Increasing or decreasing the velocity everywhere in the models (by 10%) also had a marked effect on the resulting image (e.g., Figure 2f).
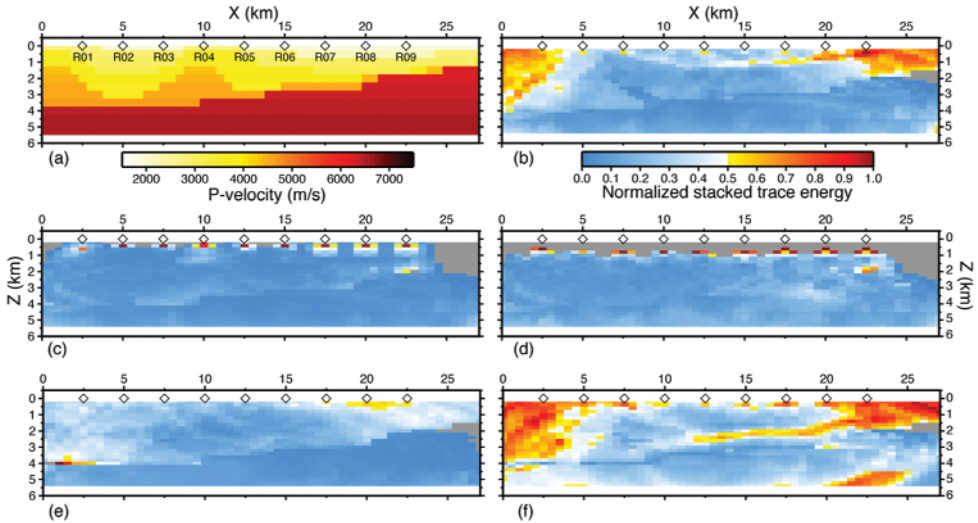
Fig. 2. X-Z cross-sections for synthetic active experiment. **(a)** P-velocity model re-sampled from the original 25-m to 500-m grid spacing. S-velocity model is similar in structure. **(b)-(e)** Summed, migrated images of normalized stacked trace energy computed using velocity model in (a). No filter was applied to the traces. Ground roll mute and single component trace normalization applied. Snell's Law weight factors for a horizontal local interface applied. **(b)** PP reflection image, vertical component. **(c)** PP reflection image, vertical component with upside down reflections removed. **(d)** PP reflection image, vertical component with upside down reflections removed and traces muted up to 0.2 sec after the theoretical first P-arrival. **(e)** PS reflection image, horizontal component. **(f)** Same as **(b)** but image computed using P-velocity model similar to that in **(a)** with velocity increased everywhere by 10%.
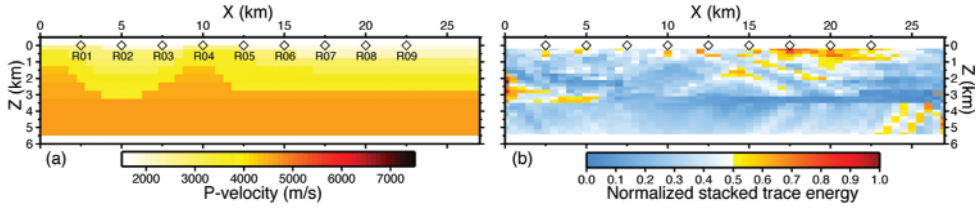
Fig. 3. (a) P-velocity model same as Figure 2a but with sloping carbonate basement removed. Corresponding S-velocity model is similar in structure. **(b)** Same as Figure 2e but PS reflection image computed using velocity models as described in **(a)**.

Converted phases analysis of the SERAPIS active data set

We investigated PP and PS reflected phases with a grid spaced 500 m in the X and Y directions, and 200 m in the Z direction. The grid extended to a depth of 7 km; the horizontal area of coverage is shown in Figure 1 by the blue box. Traces from many receivers showed a strong phase arriving shortly after the P-arrival picks (e.g., purple-highlighted phase in Figure 4). The phase was strongest in the vertical component and was often followed by one or two less energetic but coherent phases (yellow- and red-highlighted phases in Figure 4). This early phase was difficult to interpret, so we designed a mute to remove trace amplitude up to and including this phase (green line in Figure 3). Traces for all OBS were filtered by a Butterworth band filter with corner frequencies of 5 and 35 Hz. Some land stations were noisier than others, so band pass corner frequencies were chosen individually for each land station (range of lower corner: 1-10 Hz, range of upper corner: 20-40 Hz).

PP reflection images for individual stations showed features at a variety of depths, but most stations showed focused energy near 2.5 km and/or 4 km depth. Summing a large number of station images tended to blur out the image, therefore a selection of stations was made to produce the summed image in Figure 5. The shallow feature near 2.5 km depth is most clear in the northern part of the Bay of Pozzuoli at Y = 2 km. Further south at Y = 0 km, a shallow feature is visible farther to the east near X = 3 km. Near the mouth of the bay at Y = -1.5 km, two shallow features at the east and west sides of the bay can be discerned. The feature on the east side of the bay appears to extend farther to the south than the feature on the opposite side, but this may be due in part to the better station coverage on the eastern side. From approximately Y = -2 to -3 km we see energy just below the stations in the uppermost part of the grid. This appears to be an artifact of the acquisition geometry, thus we do not interpret it as representing any features in the subsurface. Below this artifact is an interval ~1 km thick where we stack very little energy, and below this we obtain focusing of trace energy around a depth of 2-3 km. Thus, we clearly image the top of the region of focusing. A possible
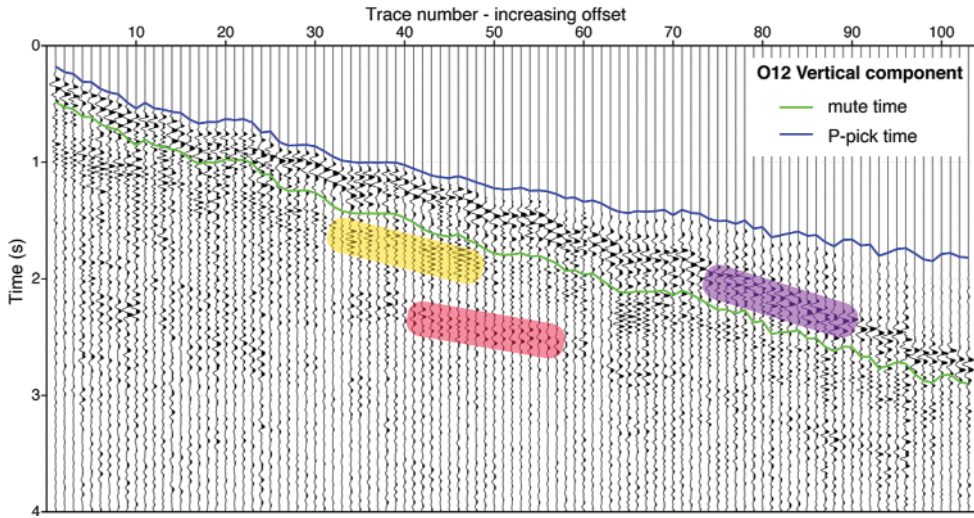
Fig. 4. Selected traces for station O12, vertical component. A strong early phase is highlighted in purple. Two later phases can be detected as the yellow and red highlighted phases. Green line shows time for a mute designed to remove the early phase. Traces are band pass filtered, 5-35 Hz, and normalized (single component).

deeper feature near a depth of 4 km is best seen in the northwest part of the bay (e.g., at Y = 1 km, X = ~0 to -2 km).

The summed image of PS reflections from a set of selected stations is shown in Figure 6. PS reflection images showed focusing of energy near 2 km depth in many individual station images. Some stations showed energy focused deeper, near 3.5 to 5 km depth. The summed image (Figure 6) primarily shows energy focused near 2 km depth across most of the caldera in the Bay of Pozzuoli.

There is some overlap between areas of focused energy in the PP and PS reflection images, although the brightest areas in the PS image tend to lie at slightly shallower depth compared to the PP image. It is possible that the same feature near 2-2.5 km is imaged by both phases. The same may be true for the possible deeper feature, but it is not as clear.

DISCUSSION AND CONCLUSIONS

The results of the application of the converted phases migration procedure to the synthetic active data set illustrates some of the problems that arise when the starting velocity model is not smooth. Turning rays become prominent when there is a very rapid increase in velocity with depth and it becomes difficult to focus trace energy. One way to mitigate this problem could be to
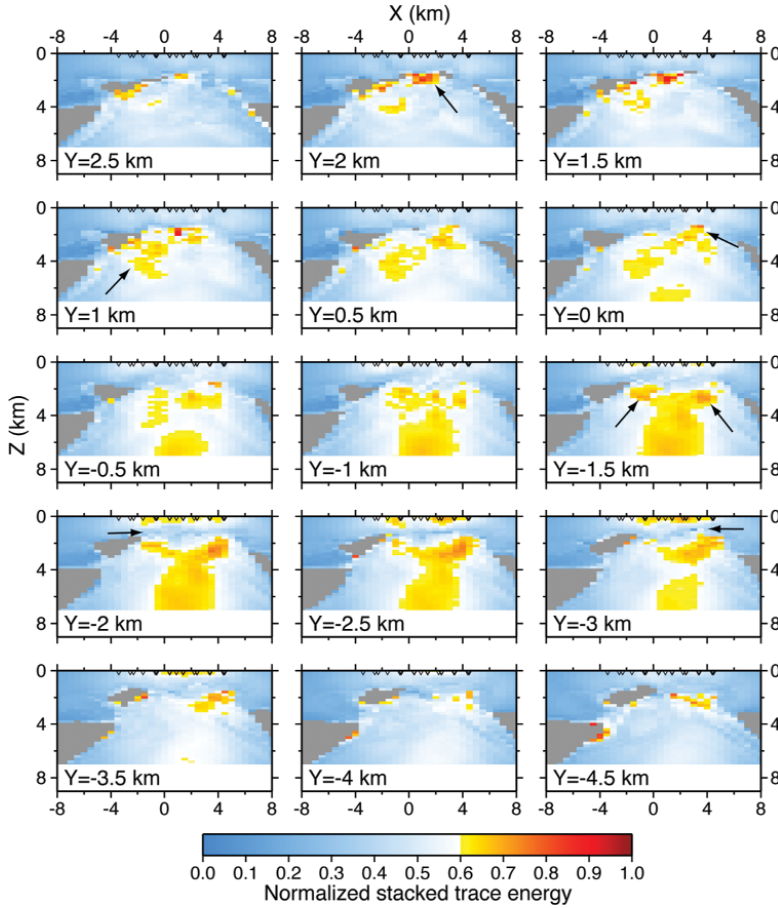
Fig. 5. X-Z cross-section slices of summed PP reflection receiver images for 23 selected stations (17 OBS and 6 land stations), vertical component. Band pass filter (see text for further explanation) and three-component trace normalization applied to traces before stacking. Traces were muted to remove a strong phase arriving shortly after the P-arrival picks. Snell's Law weight factors for a horizontal local interface applied. Selected stations: BA3, BAI, NIS, OAS, PO3, STH, O01, O02, O04, O06, O08, O09, O12, O13, O16, O18, O22, O23, O26, O29, O30, O32, O46. Black arrows point to features mentioned in the text.

apply tomography to the synthetic data set in order to obtain adequately smooth velocity models for use with the converted phases analysis. Altering the velocity model used in the converted phases analysis by removing the carbonate basement layer or changing the velocity everywhere in the model by ±10% had a strong effect on the image and illustrates the importance of the velocity model in the migration procedure. However, small alterations to the velocity model produced little effect on the resulting image implying there is some stability in the method even when applied to an unsuited data set.
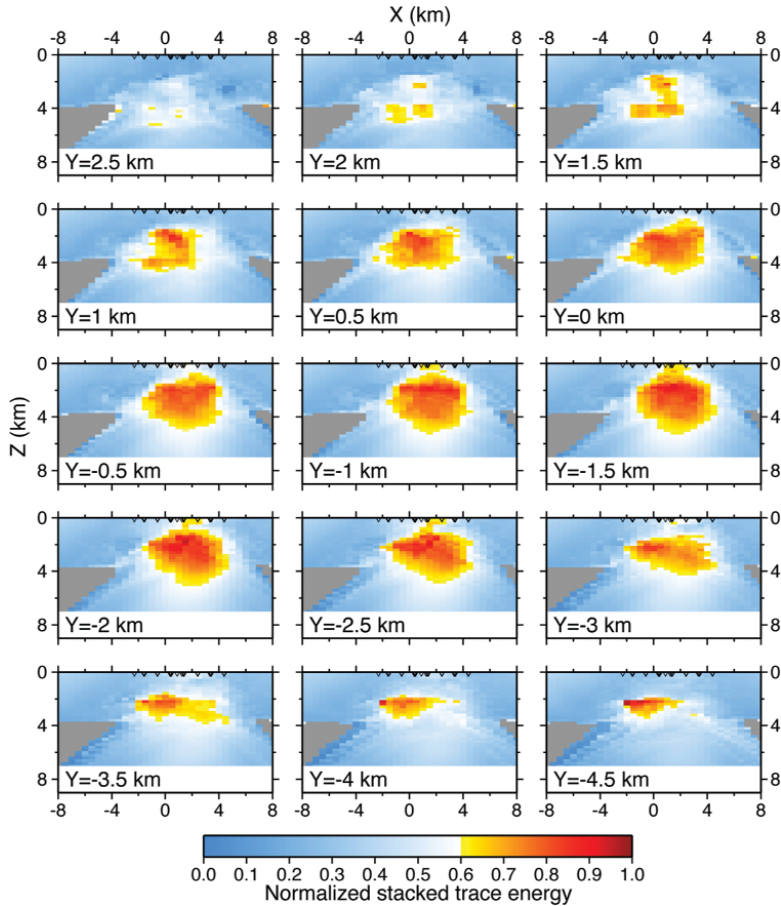
Fig. 6. X-Z cross-section slices of summed PS reflection receiver images for 25 selected stations (21 OBS and 4 land stations). The component sum of the two horizontal components is imaged. Band pass filter (see text for further explanation) and three-component trace normalization applied to traces before stacking. Traces were muted to remove a strong phase arriving shortly after the P-arrival picks. Snell's Law weight factors for a horizontal local interface applied. Selected stations: ANF, BA3, DMP, PO3, O01, O02, O03, O04, O05, O06, O08, O09, O11, O12, O16, O17, O19, O22, O24, O25, O26, O29, O32, O54, O60.

Imaging focused converted phase energy is more successful with the SERA-PIS data set because we have smooth velocity models from tomography performed by Battaglia et al. (2006). We detect features near 2-2.5 km depth in PS and PP reflection images. These shallow features may be associated with the presence of an over-pressured gas volume detected by Chiarabba et al. (2006) in a seismic tomography study as a low Vp/Vs anomaly from 2 to 4 km depth below the caldera. Deeper features can be tentatively identified in our PP and PS images lying near 3-4 km depth. These could be related to the carbonate

basement detected by tomography at approximately the same depth (Judenherc and Zollo, 2004).

REFERENCES

Battaglia, J., A. Zollo, J. Virieux, and T. Vanorio (2006) Merging Active and Passive Data Sets in Travel-Time Tomography: The Case Study of Campi Flegrei Caldera (Italy), Eos Trans. AGU, 87(52), Fall Meet. Suppl., Abstract S51C-1282.

Chiarabba, C., M. Moretti, and P. de Gori (2006), The Vp and Vp/Vs structure of the Campi Flegrei caldera, in Geophysical Exploration of the Campi Flegrei (Southern Italy) Caldera's Interior: Data, Methods and Results, A. Zollo et al. (eds.), GNV, 34-37.

Judenherc, S., and A. Zollo (2004), The Bay of Naples (southern Italy): Constraints on the volcanic structures inferred from a dense seismic array, J. Geophys. Res., 109, B10312, doi:10.1029/2003JB002876.

Klin, P. and E. Priolo, 2007, Numerical simulation of seismic experiments in volcanic areas: development of a technique based on the Pseudo-spectral Fourier method and its application to the build up of synthetic data sets for the Campi Flegrei area, V4-Task2 report.

Latorre, D., J. Virieux, T. Monfret, V. Monteiller, T. Vanorio, J.-L. Got, and H. Lyon-Caen (2004), A new seismic tomography of Aigion area (Gulf of Corinth, Greece) from the 1991 data set, Geophysical Journal International, 159, 1013-1031.

Podvin, P., and I. Lecomte (1991), Finite difference computation of travel times in very contrasted velocity models: A massively parallel approach and its associated tools, Geophys. J. Int., 105, 271-284.

Vanorio, T., J. Virieux, P. Capuano, and G. Russo (2005), Three-dimensional seismic tomography from P wave and S wave microearthquake travel times and rock physics characterization of the Campi Flegrei Caldera, J. Geophys. Res., 110, B03201, doi:10.1029/2004JB003102.

Zollo, A., S. Judenherc, E. Auger, L. D. Auria, J. Virieux, P. Capuano, C. Chiarabba, R. de Franco, J. Markis, A. Michelini, and G. Musacchio (2003), Evidence for the buried rim of Campi Flegrei caldera from 3-d active seismic imaging, Geophys. Res. Lett., 30(19), doi:10.1029/2003GL018173.

Seismic wave simulation in Campi Flegrei Caldera based upon Spectral Element Methods

E. Casarotti[1,2], A. Piersanti[2], J. Tromp[1]

[1] *Seismology and Tectonophysics Department, Istituto Nazionale di Geofisica e Vulcanologia, Rome, Italy*
[2] *Seismological Laboratory, California Institute of Technology, Pasadena, California, USA*

Introduction

Wave propagation phenomena can nowadays be studied thanks to many powerful numerical techniques. We have seen rapid advances in computational seismology at global, regional, and local scales thanks to various numerical schemes, such as the finite-difference method (FDM) [21], the finite-element method (FEM) [1, 2], the spectral-element method (SEM) [16, 18, 28], the integral boundary-element method (IBEM) [3], and the Arbitrary High-Order Discontinuous Galerkin method (ADER-DG) [11]. Spurred by the computational power made available by parallel computers, geoscientists and engineers can now accurately compute synthetic seismograms in realistic 3D Earth models. Among the methods previously listed, the SEM has convincingly demonstrated the ability to handle high-resolution simulations of seismic wave propagation in 3D domains. Nevertheless, a seismic wave simulation in volcanic structures still represents a challenge due to the high level of heterogeneity and topographic variations, and the presence of fractures, magmatic intrusions, and very low wave-speed regions. In order to study the applicability of the SEM to the complex caldera zone of Campi Flegrei, we adopted SPECFEM3D BASIN (geodynamics.org), the SEM implementation developed by [18]. The influence of topography, an accurate tomography, the presence of seawater, attenuation, and anisotropy are taken into account.

Methods

The SEM is as a generalization of the FEM based on the use of high-order piecewise polynomial functions. A crucial aspect of the method is its capability to provide an arbitrary increase in accuracy by simply increasing the algebraic degree of these functions (the spectral degree n). From a practical perspective, this operation is completely transparent to the users, who limit themselves in choosing the spectral degree at runtime, leaving to the software the task of building up suitable quadrature points and the relevant degrees of freedom. Obviously, one can also use mesh refinement to improve the accu-

racy of the numerical solution, thus following the traditional finite-element approach.

Referring to the literature for further details [9, 19, 4], we begin by briefly summarizing the key features of the SEM. We start from the general differential form of the equation of elastodynamics:

$$\rho\partial_t^2\mathbf{s} = \nabla \cdot \mathbf{T} + \mathbf{F} \tag{1}$$

where $\mathbf{s}(\mathbf{x}, t)$ denotes the displacement at position $\mathbf{x}$ and time t, $\rho(\mathbf{x})$ is the density distribution, and $\mathbf{F}(\mathbf{x}, t)$ the external body force. The stress tensor T is related to the strain tensor by the constitutive relation $\mathbf{T} = \mathbf{c} : \mathbf{s}$, where c denotes a fourth-order tensor. No particular assumptions are made regarding the structure of $\mathbf{c}$, which describes the (an)elastic properties of the medium (the formulation is general and can incorporate full anisotropy [14] or non-linear constitutive relationships [8]).

For seismological applications, a numerical technique needs to facilitate at least the following: (i) an attenuating medium, (ii) absorption of seismic energy on the fictitious boundaries of the domain in order to mimic a semi-infinite medium (the free-surface condition is a natural condition in the SEM), and finally (iii) seismic sources. In the SEM all these features are readily accommodated [19].

As in the FEM, the dynamic equilibrium problem for the medium can be written in a weak, or variational, form, and, through a suitable discretization procedure that depends on the numerical approach, can be cast as a system of ordinary differential equations with respect to time. Time-marching of this system of equations may be accomplished based upon an explicit second-order finite-difference scheme, which is conditionally stable and must satisfy the well known Courant condition [6].

The key features of the SEM discretization are as follows:

1. Like in the FEM, the model volume ? is subdivided into a number of non-overlapping elements Ω_e, $e = 1, \ldots, n_e$, such that $\Omega = \bigcup_{e=1}^{n_e} \Omega_e$.
2. The expansion of any function within the elements is accomplished based upon Lagrange polynomials of suitable degree n constructed from $n + 1$ interpolation nodes.
3. In each element, the interpolation nodes are chosen to be the Gauss-Lobatto-Legendre (GLL) points, i.e., the $n + 1$ roots of the first derivatives of the Legendre polynomial of degree n. On such nodes, the displacement, its spatial derivatives, and integrals encountered in the weak formulation are evaluated.
4. The spatial integration is performed based upon GLL quadrature (while most classical FEMs use Gauss quadrature).

Thanks to this numerical strategy, exponential accuracy of the method is ensured and the computational effort minimized, because the resulting mass matrix

is exactly diagonal. The latter feature does not occur in so-called hp FEMs, nor in SEMs based upon Chebychev polynomials [22].

Mesh design for Spectral-Element Methods

The first critical ingredient required for a spectral-element simulation is a high-quality mesh appropriate for the 3D model of interest. This process generally requires discouraging expertise in meshing and preprocessing, and is sub ject to several tough constraints: 1) the number of grid points per shortest desired wavelength, 2) the numerical stability condition, 3) an acceptable distortion of the elements, 4) balancing of numerical cost and available computing resources.

A poor-quality mesh can generate numerical problems that lead to an increase in the computational cost, poor (or lack of) convergence of the simulation, or inaccurate results. For example, a geological model often includes a layered volume, and a staircase sampling of the interfaces between the layers can produce fictitious diffractions. Therefore, a good mesh should honor at least the ma jor geological discontinuities of the model. As noted before, the SEM is similar to a high-degree FEM, and in fact these methods share the first part of the discretization process. The present paper is focused on this first meshing step, and thus the results are relevant to both FEMs and SEMs. In the SEM, the subsequent step is the evaluation of the model on the GLL integration points [19]. Here we only note that if we use Lagrange polynomials and GLL quadrature, the mass matrix is exactly diagonal, resulting in a dramatic improvement in numerical accuracy and efficiency. With this choice, each element of the mesh contains $(n + 1)^3$ GLL points. Unfortunately, this approach requires that the mesh elements are hexahedra [19]. It is worth mentioning that for 2D problems it is possible to develop a SEM with triangles keeping the diagonal mass matrix but with an higher numerical cost [15]. The fact that we are restricted to hexahedral elements complicates matters significantly. Whereas 3D unstructured tetrahedral meshes can be constructed relatively easily with commercial or non-commercial codes, the creation of 3D unstructured hexahedral meshes remains a challenging and unresolved problem.

For complex models, as in the case of realistic geological volumes, generating an all-hexahedral mesh based upon the available meshing algorithms can require weeks or months, even for an expert user [28]. A simpler approach could be to adapt the SEM to a non-comforming mesh, e.g. using an octree scheme. This is technically feasible by means of the so-called "mortar" matching method, but in this case the diagonal matrix is lost.

One of the features of the SEM that impacts the creation of the mesh is the polynomial degree n used to discretize the wave field. The following heuristic rule has emerged to select n for an unstructured mesh of a heterogeneous medium: if $n < 4$ the inaccuracies are similar to the standard FEM, while if n

> 10 the accuracy improves but the numerical cost of the simulation becomes prohibitive. The choice of n is related to the grid spacing Δh: in order to resolve the wave field down to a minimum period T_0, the number of points per wavelength λ should be equal or greater than 5, leading to the constraint expressed in Eq. 2. If $n = 4$, then Δh is roughly equal to λ. We note that, for the same accuracy, a classical low-degree FEM requires a higher number of elements. Since the material properties are stored for each GLL point and can vary inside an element, we are able to interpolate the geological interfaces that our mesh is not able to follow. Nevertheless, this is an undesirable staircase sampling of the model, which introduces non-physical diffractions. Therefore, it is necessary that the mesh honors the major seismological contrasts. Furthermore, when a discontinuity is honored, the elements across the interface share some nodes, which will have the properties of the material below the discontinuity in one case, and the proprieties of the material above the discontinuity in the other case. Thus, the actual behavior of the seismic waves at the geological interface is perfectly mimicked in a way that cannot be achieved by an interpolation solely based upon Lagrange polynomials and the GLL quadrature.

Another constraint on the design of the mesh is the stability condition imposed by the adoption of an explicit conditionally stable time scheme. For a given mesh, there is an upper limit on the time step above which the calculations are unstable. We define the Courant stability number of the time scheme as $C = \Delta t (v/\Delta h)_{max}$, where ?t is the time step and $(v/\Delta h)_{max}$ denotes the maximum ratio of the compressional-wave speed and the grid spacing. The Courant stability condition ensures that calculations are stable if the Courant number is not higher than an upper limit C_{max} [6], providing a condition that determines the time step Δt (Eq. 3). Again, an heuristic rule suggests that C_{max} is roughly equal to 0.3-0.4 for a deformed and heterogeneous mesh [19].

Like any technique based upon an unstructured deformed mesh, the SEM requires a smooth variation of the Jacobian and an acceptable distortion of the elements. Usually, to produce an acceptable accuracy the maximum equiangle skewness s [10] should not be greater than 0.5, although empirical tests show that $s < 0.8$ can sometimes be acceptable (Eq. 4) [13, 19].

To sum up, spectral-element simulations require an unstructured all-hexahedral conforming mesh subject to the following heuristic constraints:

$$\Delta h = v_{min} \, T_0 \, \frac{n+1}{f(n)} \tag{2}$$

$$\Delta t < C_{max} \, \frac{v_{min}}{v_{max}} \, T_0 \, \frac{n+1}{f(n)} \tag{3}$$

$$s < 0.8 \tag{4}$$

where v_{max} and v_{min} are the maximum and minimum seismic wave speeds in the element, C_{max} is the Courant constant discussed above, T_0 is the shortest period that we seek to resolve, and f(n) is an empirical function related to the number of points per wavelength and the polynomial degree n; for $n = 4$ f (n) = 5.

The mesh should have a similar number of grid points per wavelength throughout the entire model (i.e., the same numerical resolution everywhere), and since seismic wave speeds vary inside the volume, the mesh should have a variable element density, in agreement with Eq. 1. Wave speeds increase with depth in a typical geological model, so that the mesh should be denser near the surface and close to low wave-speed regions, such as an alluvial basin. In elements located at the top surface, v_{min} is the surface-wave speed, which controls the resolution of the mesh. Inside the volume, shear waves have the slowest speed and thus determine Δh. From Eq. 3, we note that the smaller the grid spacing, the smaller the time step needed to obtain numerical stability, at the expense of computational cost. Therefore, Δh should be carefully evaluated in order to optimize numerical efficiency and accurate geometrical representation of the model. In the current SEM implementation, the time step is constant for the whole model. It is evident that a mesh that coarsens with depth accommodates a larger time step than a mesh with a constant element size throughout the entire volume, leading to a significant saving in computational cost. Finally, one additional difficulty is the enormous number of elements that a typical seismic wave propagation simulation requires, ranging from hundreds of thousands of elements for local-scale simulations with low-frequency content, to tens of millions of elements for regional-scale simulations or for a high-frequency local-scale simulation. This implies that we need a parallel computational approach not only for the simulation of seismic wave propagation, but also for the mesh generation process.

The package of choice for our simulations is SPECFEM3D (geodynamics.org), which simulates global, regional (continental-scale) and local seismic wave propagation. Effects due to lateral variations in compressional-wave speed, shear-wave speed, density, a 3-D crustal model, ellipticity, topography and bathymetry, the oceans, rotation, and self-gravitation are all included, as well as full 21-parameter anisotropy and lateral variations in attenuation.

Mesh examples

In this section we present some examples of unstructured hexahedral meshes that have been developed for simulations with SPECFEM3D.

The SPECFEM3D_GLOBE software package has been created primarily to simulate 3D seismic wave propagation on a global scale. For this purpose, a unique optimized mesh has been generated based upon a cubed sphere decomposition [23]. The details are described in [19] Here we note that the

need to densify the mesh close to the surface has been resolved by introducing doubling layers. The mesh honors topography and bathymetry and the major internal discontinuities, but not the Moho (the bottom of the Earth's crust) and the intra-crustal interfaces, which are interpolated based upon the Lagrange interpolation. This approximation is justified since the shapes of the Moho and the intra-crustal interfaces are insufficiently known to support the increase in elements that a full description of these boundaries would require. The mesh adequately resolves broadband data with periods down to 3.5 seconds on modern computers [17]. As an example, for a simulation executed on the Japanese Earth Simulator (JAMSTEC), the mesh was composed of 206 million hexahedral elements, corresponding to 36.6 billion degrees of freedom.

More critical from the point of view of mesh creation is the application of the SEM to regional or local problems, especially if we are interested in wave propagation with periods below 1 second. The software package SPECFEM-3D_BASIN simulates seismic wave propagation in sedimentary basins, attempting to take into account the full complexity of these models. The solver is general and can be used to simulate seismic wave propagation on regional or local scales, but the mesh generator is currently specifically written for Southern California [18]. The mesh honors the Moho, surface topography, and the deeper parts of the basement of the Los Angeles and Ventura sedimentary basins. It is coarsened twice with depth: first below the low wavespeed layer, and then below the basement. The mechanical proprieties of the volume are stored at each GLL node, taking into account the 3D Southern California seismic model. The mesh contains approximately 700 thousand spectral elements (corresponding to 136 million degrees of freedom). The minimum resolved period of the seismic waves is roughly 2 seconds [18].

The mesh is used routinely to simulate earthquakes with a magnitude greater than 3.5 in Southern California. At periods of about 4 seconds and longer, the resulting simulated wave motion closely matches the data recorded at the stations of the Southern California Seismic Network. Animations of seismic wave propagation are posted in near real-time at shakemovie.caltech.edu.

If we want to analyze seismic wave propagation at shorter periods, we need to refine the mesh and constrain the mesh to honor the shape of the shallow parts of the basins, which is currently not done. Furthermore, the mesher is designed for this specific region. Unfortunately, generalizing the adopted meshing procedure to other geographical areas requires experience, internal modification of the code, and a significant amount of time.

For example, the SPECFEM3D_BASIN mesh generator was modified by [20] to produce a mesh for the Taipei basin (Taiwan). This work represents the state of the art for the SEM meshing process. The SPECFEM3D_BASIN mesher was modified to take into account the notable topography around Taipei city and the complex geometry of the underlying basin. Three new control surfaces were introduced at various depths and

one new doubling layer was added in order to honor the main geological features of the region. The top of the model is controlled by surface topography based upon a detailed Digital Elevation Model. Just below the surface, a buffer layer is used to accommodate mesh distortions induced by the steep topography. This is critical to ensure the accurate and stable accommodation of the free surface. This layer also defines the top of the first mesh doubling, needed to take into account the low seismic wave speeds inside the basin. The shallow sedimentary basin is introduced between the surface topography and the buffer layer. Seismic wave speeds in the basin are quite low, with a sharp contrast between the basin and the surrounding basement. Compared to the Los Angeles basin, the Taipei basin is relatively small and shallow. The meshing strategy of [18] would result in a basement layer honoring only a small portion of the deepest part of the basin, and most of the basin boundaries would be not constrained by the mesh. To overcome these limitations, the nodes were empirically adjusted close to the sedimentary basin to redefine the basin boundary mesh. Several additional empirical criteria were used to define how and where to move the nodes, leading to a stable and accurate mesh implementation. The resulting mesh is composed of 4.5 million spectral elements and 900 million degrees of freedom, and it is adequate for periods down to 1 second.

As in the Los Angeles basin example, we note that this meshing strategy is ad-hoc for this particular application. Furthermore, the size of the hexahedra on the surface is controlled by the speed of the surface waves inside the basin, leading to an oversampled mesh in the surrounding regions (i.e., an enormous number of unnecessary elements, with a serious impact on the computational cost of the simulation). Finally, empirical adjustment of the nodes close to the basin basement was an attainable solution for the Taipei basin, but this approach cannot be generalized.

Meshing in parallel

The meshes discussed in the previous section are simply too large to be built on a single processor or even on a large shared memory machine: they require clusters or other parallel computers with distributed memory. The approach in SPECFEM3D is to partition the model into one mesh slice for each available CPU. Mesh generation and the corresponding wave propagation simulation are accomplished in parallel, the latter requiring only one communication phase between shared slice interfaces at each simulation time step. Since the communication map is constant throughout the simulation, it is built once and for all at the end of the mesh generation phase. The challenge is to load-balance the mesh, i.e., to make sure that each mesh slice contains roughly the same number of spectral-elements as any other mesh slice. This further limits the flexibility of the mesher, and adds further complexity to the procedure.

New meshing strategies: CUBIT

In order to mesh the Campi Felgrei Caldera and with an ultimate goal of implementing a more general meshing design algorithm for SEM, we adopted a workflow that interfaces the current SPECFEM3D_BASIN mesher with CUBIT, a mesh generation tool kit from Sandia National Laboratories (cubit.sandia.gov).

From the overview in the previous paragraphs, it is clear that we are looking for software that has the following attributes: 1) the ability to accommodate general geological models, 2) minimal user intervention, 3) high resolution, 4) conforming, unstructured hexahedral elements, 5) a parallel, load-balanced implementation. The experience gained by the authors for various meshing problems [28] suggests that CUBIT comes very close to fulfilling these requirements. Although it currently lacks parallel capabilities, it incorporates a set of powerful and advanced meshing schemes developed to automatically handle the unstructured meshing problem. However, it is worth noting that meshing a large complex domain, such as any geological model, does not seem feasible with a desirable "single-button" procedure, due to the shape of the interfaces, the wide range of element sizes, and the broad range of possible geological models.

We adopted as our 3D model for Campi Flegrei the model proposed by [24] constituted of 3 layers with a P-wave speed ranging from 2.7 to 6.5 km/s. The top layer is composed of incoherent pyroclastic rocks and chaotic tuffs; the second of tuffites, tuffs and lava interbedded; the third of metamorphic rocks and limestone. The interfaces between the layers have a resolution of 250 m, while the topography is a based upon a 60 m Digital Elevation Model. The dimensions of the volume are 40x40x9 km.

The volume is split into rectangular slices of equal size, one slice for each processor following the original MPI map of SPECFEM3D_BASIN. We use a serial Fortran routine to build a journal file for each slice, creating and storing all the commands that drive the meshing process inside CUBIT. Schematically, we can summarize each journal file in five steps: 1) creation of the geological geometry by means of a bottom-up approach (i.e., vertices → splines → surfaces → volumes) and geometry healing, 2) definition of the meshing intervals along the curves based upon Eqs. 2 and 3, 3) definition of the meshing schemes and meshing, 4) refinement and smoothness, and 5) blocks and sidesets definition and export (Figure 1). One of the main advantages of using CUBIT is that the entire process can be fairly well automated both for mesh creation and quality checking. The user is only asked to provide the shape of the topographic and geological surfaces and a good choice of intervals based upon Eqs. 2 and 3. Unfortunately, some constraints on the meshing scheme are needed. As we will see later, due to the conformity requirements for the whole mesh and at the MPI interfaces (i.e., the surfaces that are shared by two adjacent slices), the vertical surfaces must be structu-

red, while the horizontal surfaces can be meshed with structured or unstructured schemes. The so-constructed volume has a 2.5D logical symmetry; therefore, the sweep algorithm [12,26] can be directly applied without any further decomposition. The profiles of seismic wave speeds demand a mesh coarsening with depth. Since the mesh resulting from the approach described above is structured along the vertical direction, the only way to produce a vertical densification of elements is the refinement algorithm included in CUBIT [7,25] which produces a transition between 1 to 27 hexahedra, tripling the elements along a linear direction in only one hex sheet (Figure 1b). It is more efficient than the refinement used in [18] (i.e., a transition from 1 element to 8 in 2 hex sheets) and it is perfect for a sharp high-contrast in seismic wave speeds. Nevertheless, where the variation of seismic wave speeds is smoother, the higher transition ratio in CUBIT's refinement produces a larger difference between the number of points per wavelength across the mesh (i.e., an unevenly sampled mesh). For this reason, the possibility of introducing a refinement with a lower transition ratio is under development. In this respect, let us mention that a refinement with linear ratio of 2, going from two elements to four in one sheet has successfully been implemented in SPECFEM3D_GLOBE V4.0. After the creation of the journal files, a second Fortran routine provides the MPI environment needed to build the mesh in parallel. CUBIT is executed on each processor (slice) and it plays back the related script file, meshing its portion of volume. A quality analysis of the skewness is then performed. Since each slice is meshed independently, we carefully check that each corresponding node in the surfaces shared by two adjacent independent slices has the same coordinates. The "refined-
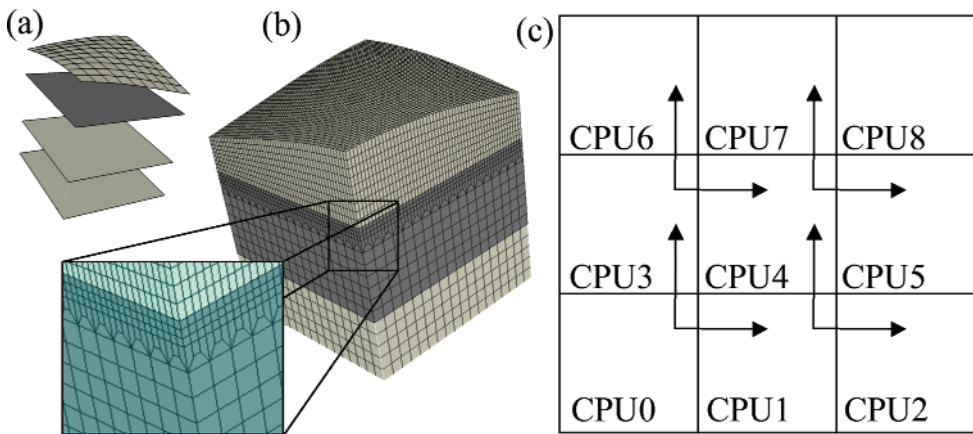
Fig. 1. Basic sketch for the mesh creation of a layer-cake geological model: **(a)** Step 1 of the strategy: creation of the geological geometry by means of a bottom-up approach. **(b)** Final result with a detailed zoom showing the tripling refinement layer in the upper part of the model. **(c)** The routine communicates the nodes to the adjacent MPI slices (up and right) following the map.

structured" scheme imposed in the vertical direction guarantees that the number of elements in each surface is the same; nevertheless, the possibility of a discrepancy in location between two corresponding nodes is not negligible, due to the applied smoothness algorithm and the influence of the background elements. The routine communicates the nodes to the adjacent MPI slice following the map in Figure 1c. If the nodes in the slices show a numerically significant location discrepancy compared to the corresponding neighboring nodes, they are adjusted accordingly. Then, the GLL points are evaluated for each element and the material proprieties are assigned. The GLL node numbering follows the same procedure as in [13,18] Consequently, the resulting GLL mesh can be written in order to follow the format required by the SPECFEM_BASIN solver, so that simulation can be performed directly. It is worth to note that this meshing strategy is valid for all the geological models that can be described by a layer-cake volume, consisting of a stack of non-degenerate heterogeneous quasi-parallel horizontal layers.

MODELLING

Both the mesh generation and simulation on Campi Flegrei are performed on 256 processors of CITERRA (a high-performance computing cluster in the Division of Geological & Planetary Sciences at Caltech [5]). The mesh contains 6.2 million hexahedral elements and 1.2 billion degrees of freedom. The resolution at the surface is 60 m and the mesh is numerically accurate beyond the maximum frequency content of the seismic source (6 Hz). Formally, the numerical accuracy is granted up to 15 Hz, far beyond the available geological information. The mesh is created in 5 min of user-time: 60% of this time is dedicated to geometry creation, and only 20% to evaluation at the GLL points and assignment of material properties. 1 sec of synthetics seismogram is evaluated in 1 hr CPU-time. Figure 2 shows the mesh and synthetic seismograms with a duration of 20 s for the main seismic event of the 1982-84 caldera unrest.

In the region the elevation ranges from -800 m to more than 800 m and it is dominated by the volcanic deposits and the caldera collapse. Although the topography is smooth with respect to the close Mt. Vesuvius, preliminary results highlight that it has a not negligible effect on wave propagation at the period that we are analyzing. Figure 3 shows the snapshots of the seismic wave propagation if we include (S1) or exclude (S2) the topography from our simulation. The third column is the difference S1-S2 that shows as the presence of topography can change the seismic wave propagation up to 30% than respect a simulation with a flat surface.

The result is confirmed in the seismograms plotted in Figures 4-12 with variations both in amplitude and in phase.
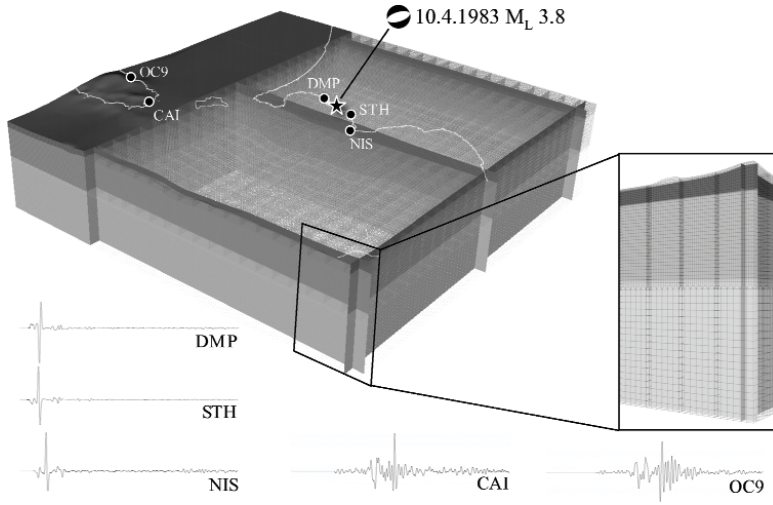
Fig. 2. CUBIT Mesh adopted for the simulation on Campi Flegrei caldera. The seismograms show 20 s of ground motion associated with the main event of the 1982--84 crisis. The mesh is composed of more than six million elements and is accurate for the propagation of seismic waves with frequencies up to 6 Hz. The close up highlights the single refinement layer.
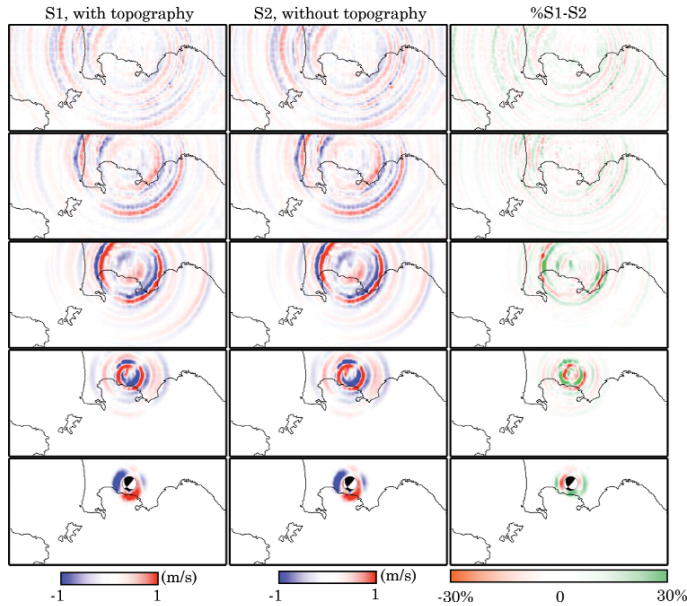
Fig. 3. Snapshot of the wave propagation in Campi Flegrei Caldera produced by a synthetic earthquake with seismic moment $M_0=9.9\cdot10^{13}$ N m, similar to some events that have been registered during the seismic crisis of 1982-1984. The first column (S1) shows the simulation with the topography incorporated in the model. The second one ($S2$) is the same simulation but with topography not included. The third column is the perceptual difference (S1-S2)/S1. The snapshots has been registered at 0.8 s, 1.6 s, 3.2 s, 4.8 s, 6.4 s after the event.
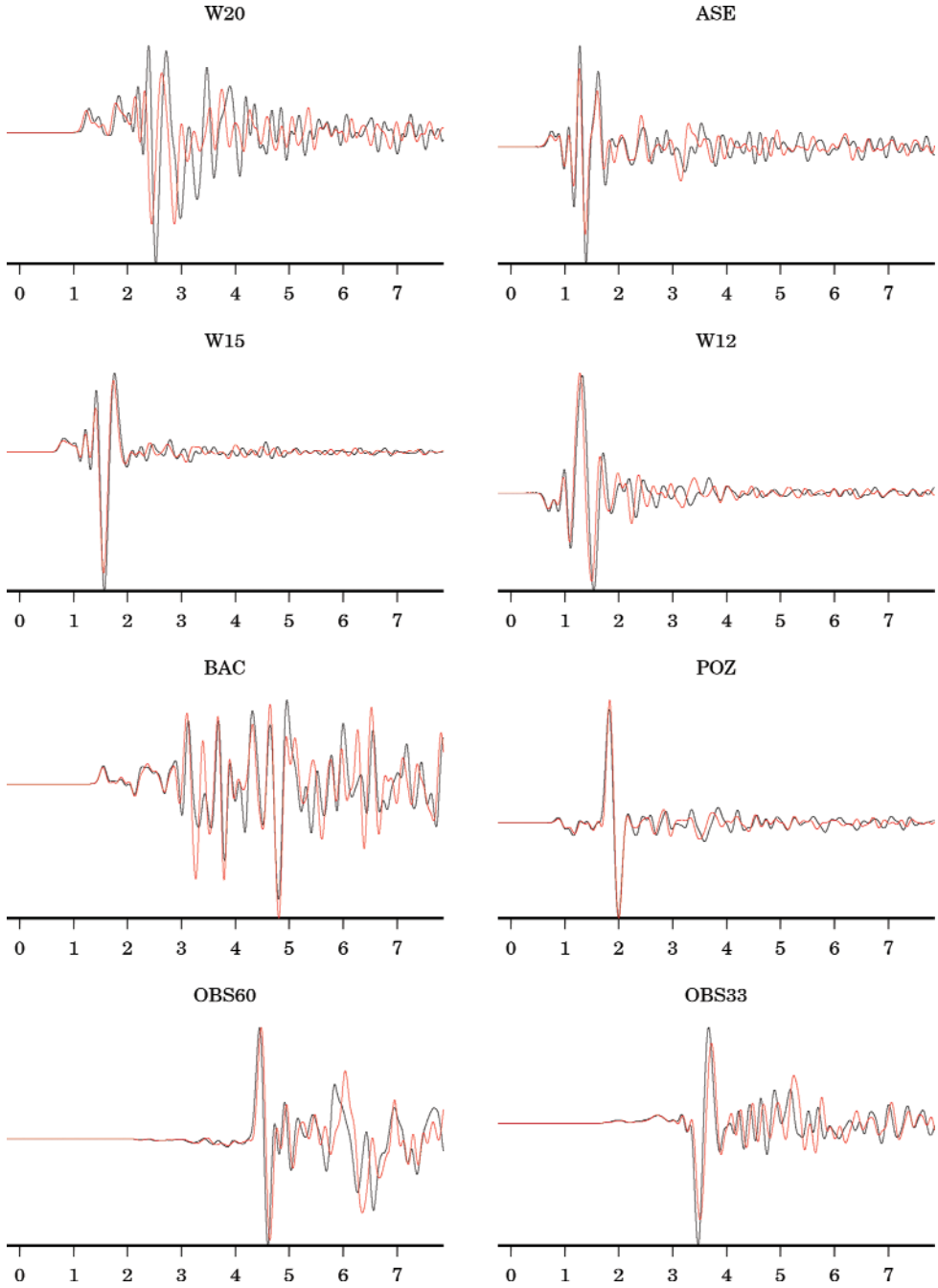
Fig. 4. East Velocity 8 s seismograms registered at the stations ASE, BAC, POZ, OBS33, OBS60, W12, W15, W20. Black: with topography; red: without topography (see [24]).
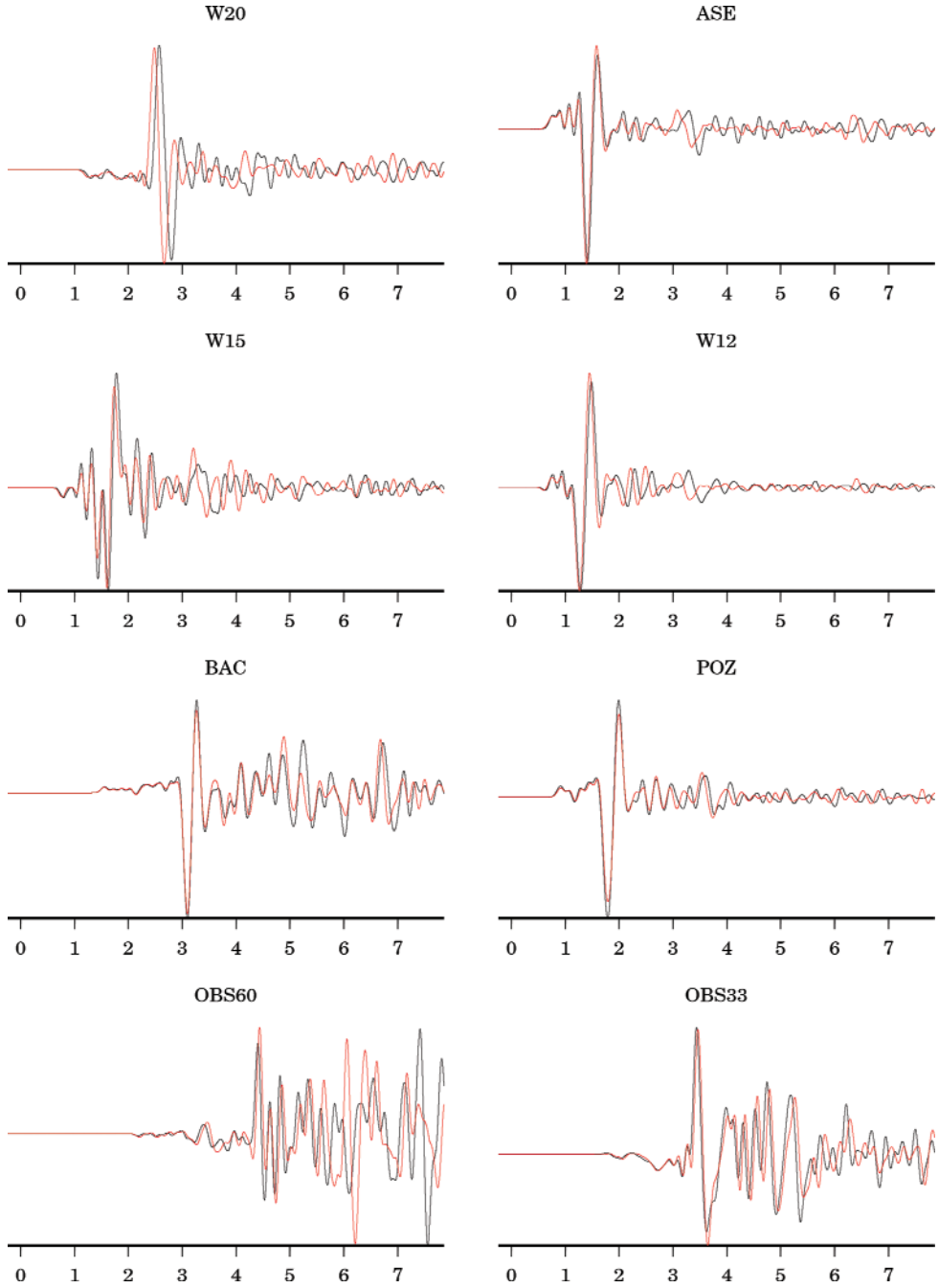
Fig. 5. North Velocity 8 s seismograms registered at the stations ASE, BAC, POZ, OBS33, OBS60, W12, W15, W20. Black: with topography; red: without topography (see [24]).
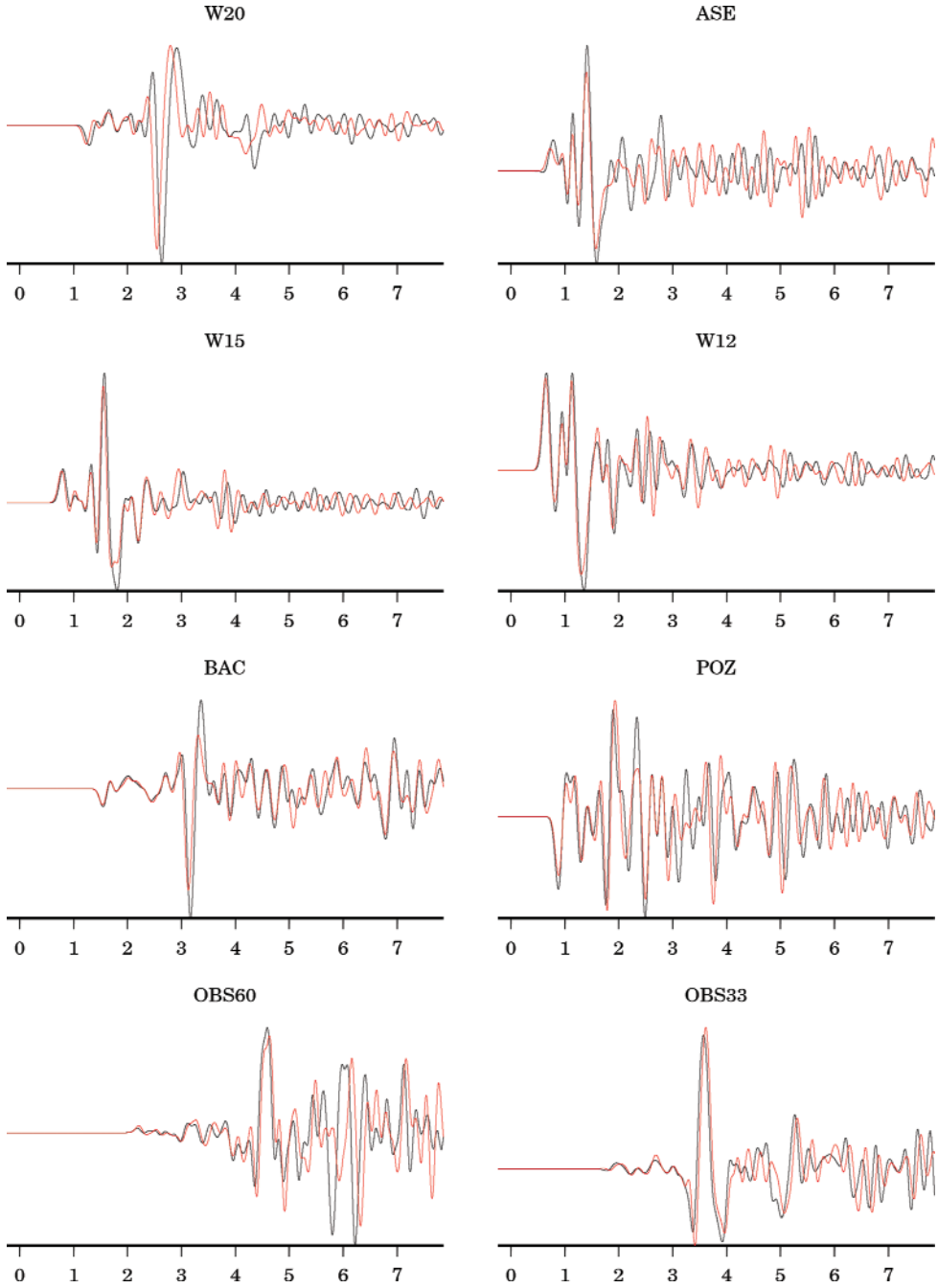
Fig. 6. Vertical Velocity 8 s seismograms registered at the stations ASE, BAC, POZ, OBS33, OBS60, W12, W15, W20. Black: with topography; red: without topography (see [24]).
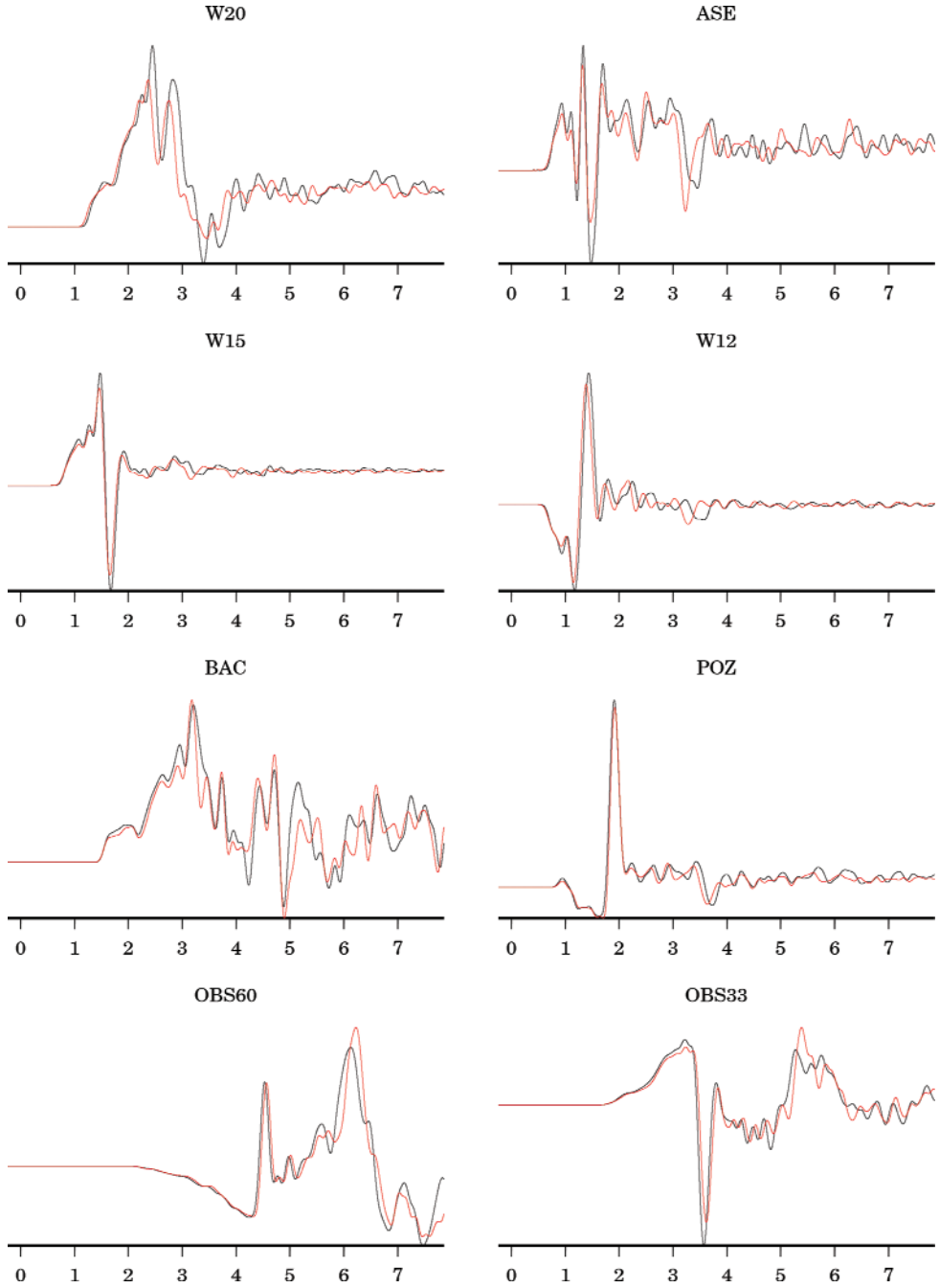
Fig. 7. East displacement 8 s seismograms registered at the stations ASE, BAC, POZ, OBS33, OBS60, W12, W15, W20. Black: with topography; red: without topography (see [24]).
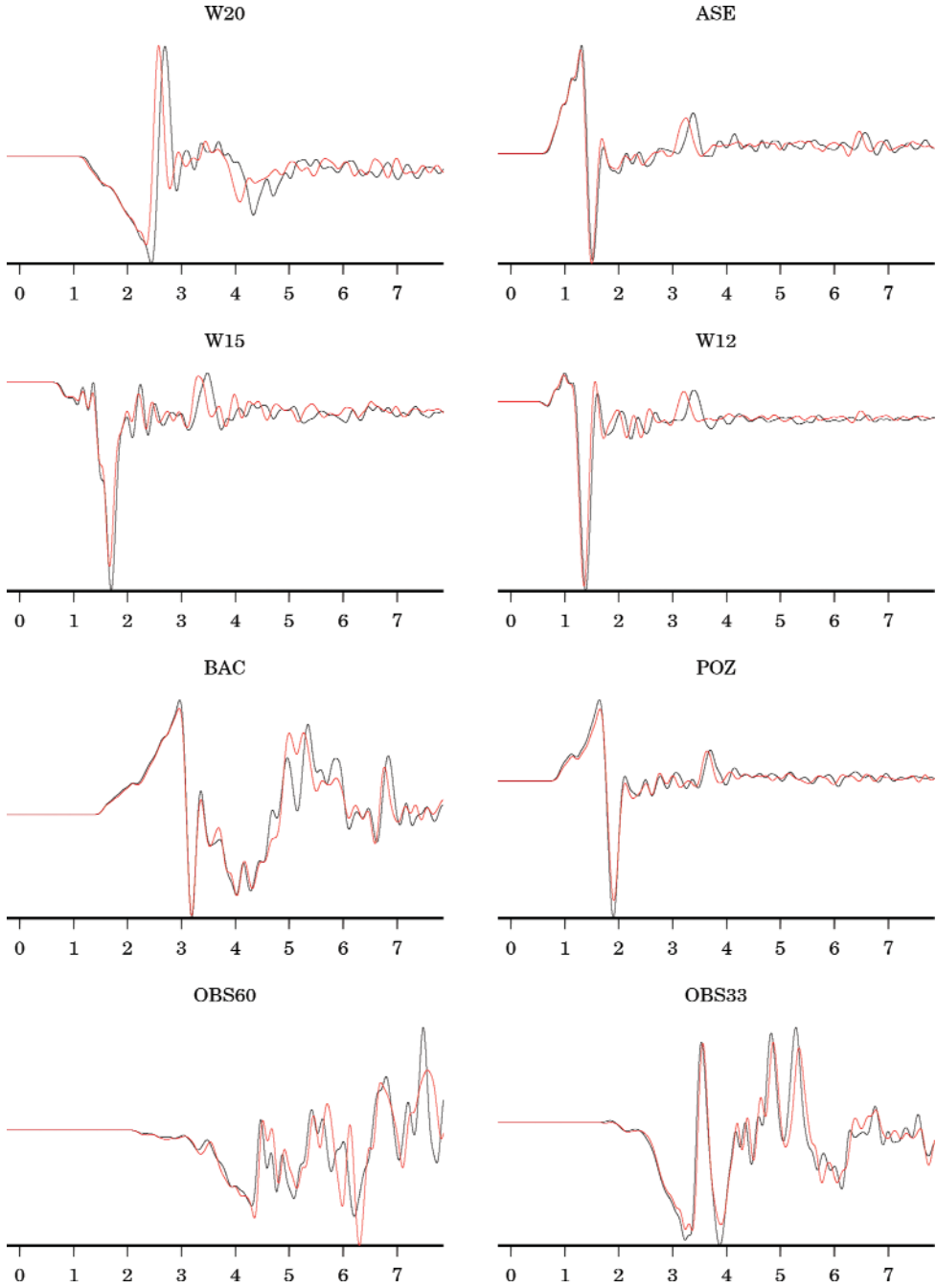
Fig. 8. North displacement 8 s seismograms registered at the stations ASE, BAC, POZ, OBS33, OBS60, W12, W15, W20. Black: with topography; red: without topography (see [24]).
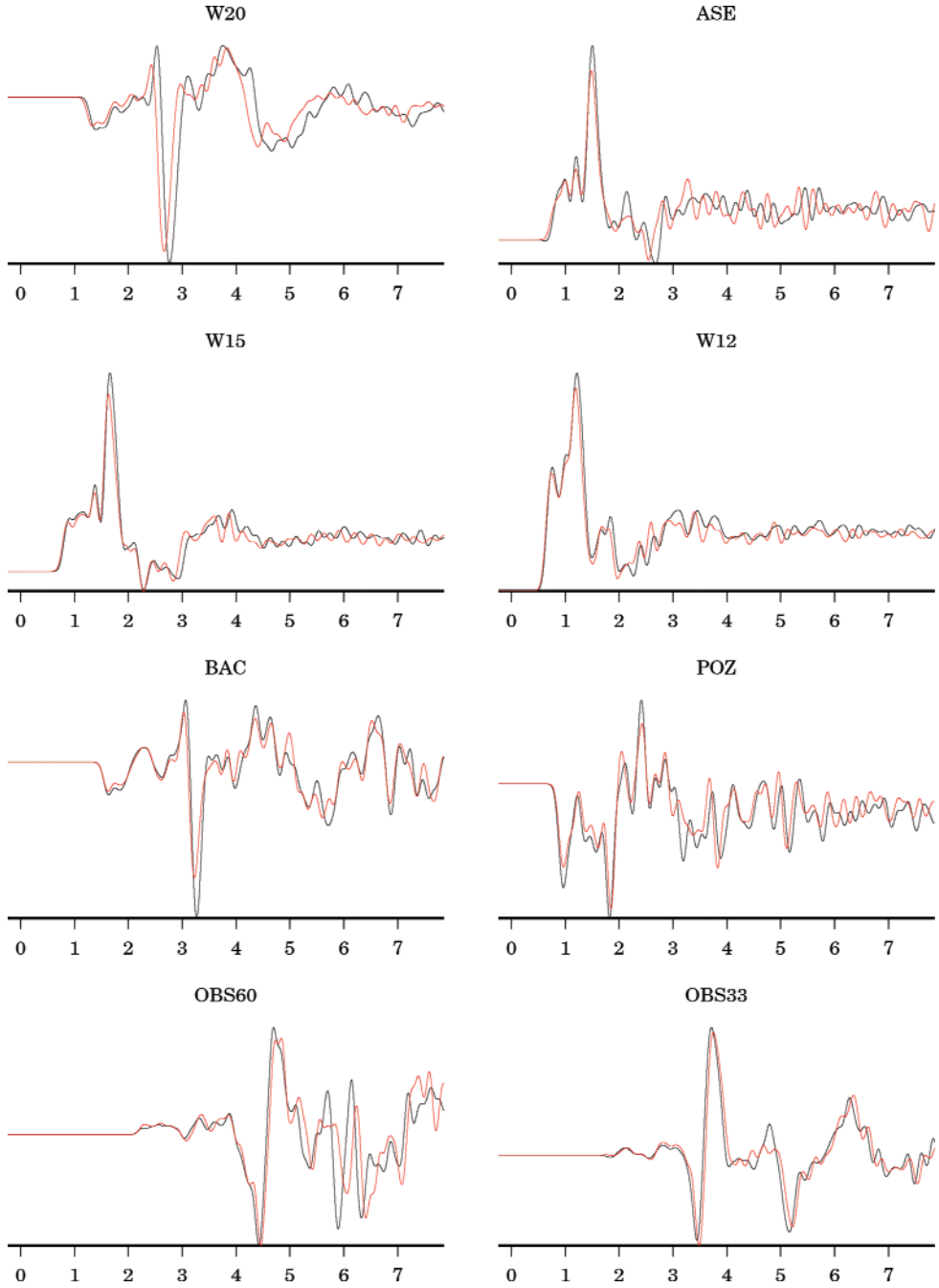
Fig. 9. Vertical displacement 8 s seismograms registered at the stations ASE, BAC, POZ, OBS33, OBS60, W12, W15, W20. Black: with topography; red: without topography (see [24]).
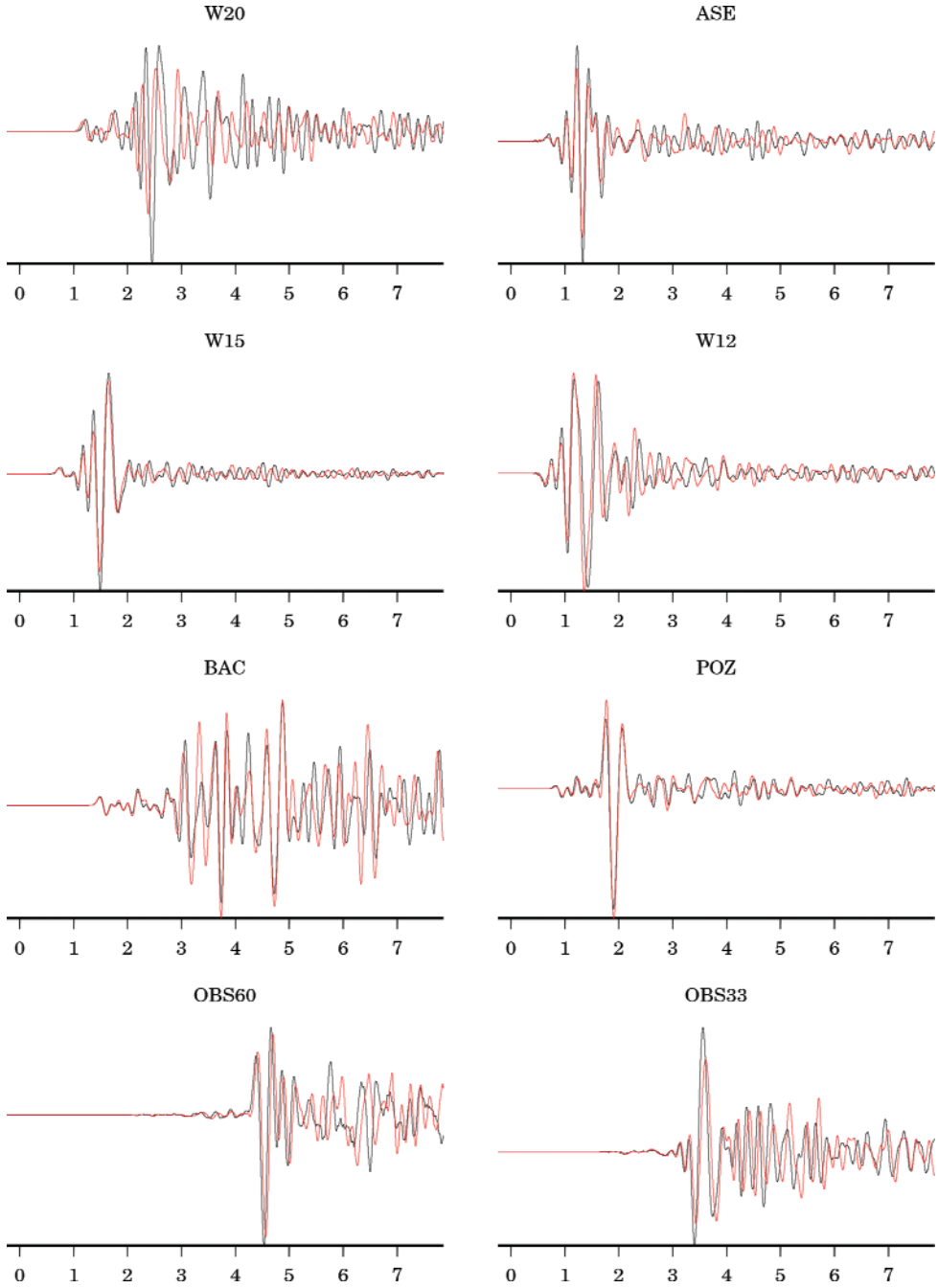
Fig. 10. East acceleration 8 s seismograms registered at the stations ASE, BAC, POZ, OBS33, OBS60, W12, W15, W20. Black: with topography; red: without topography (see [24]).
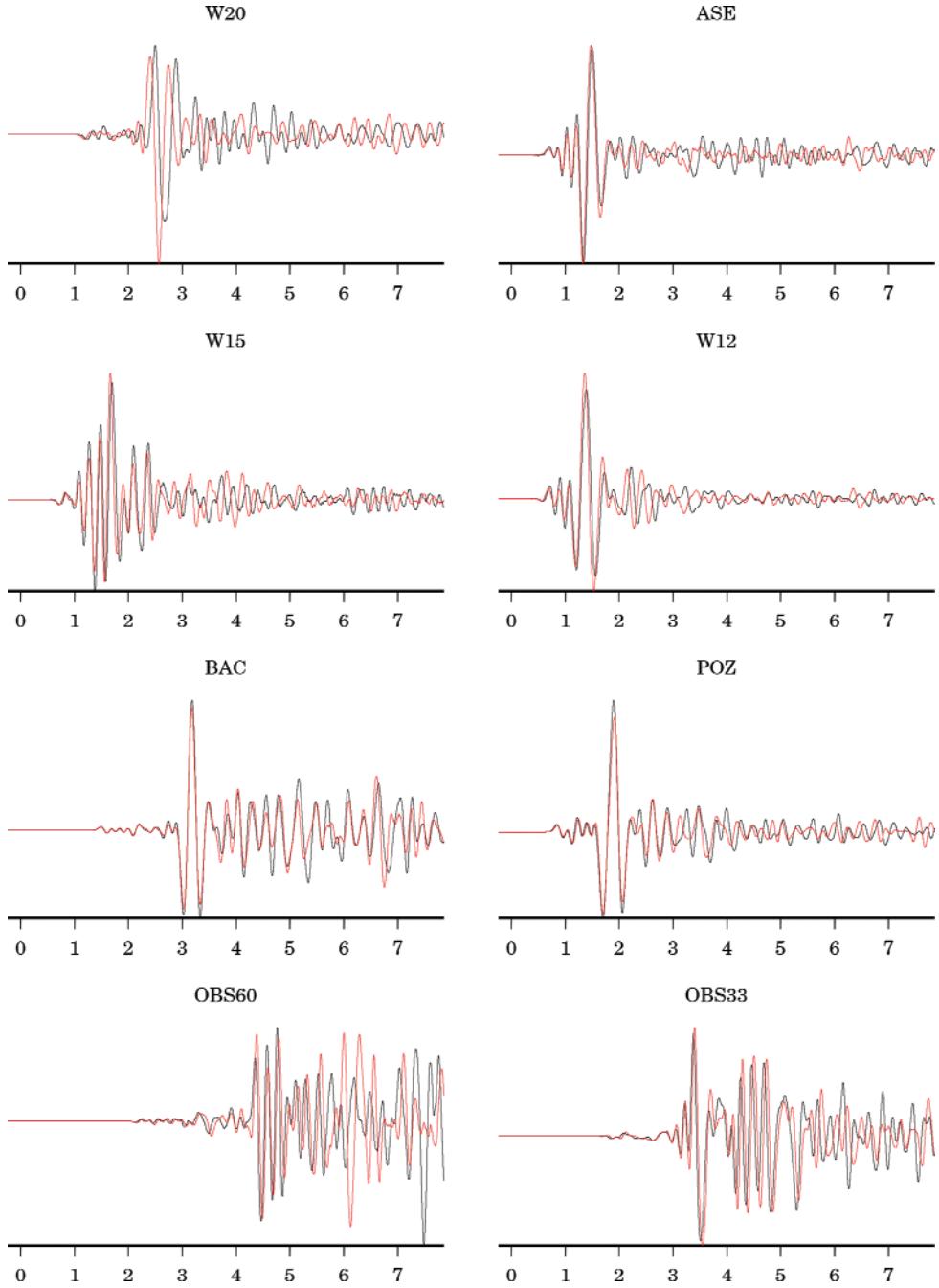
Fig. 11. North acceleration 8 s seismograms registered at the stations ASE, BAC, POZ, OBS33, OBS60, W12, W15, W20. Black: with topography; red: without topography (see [24]).
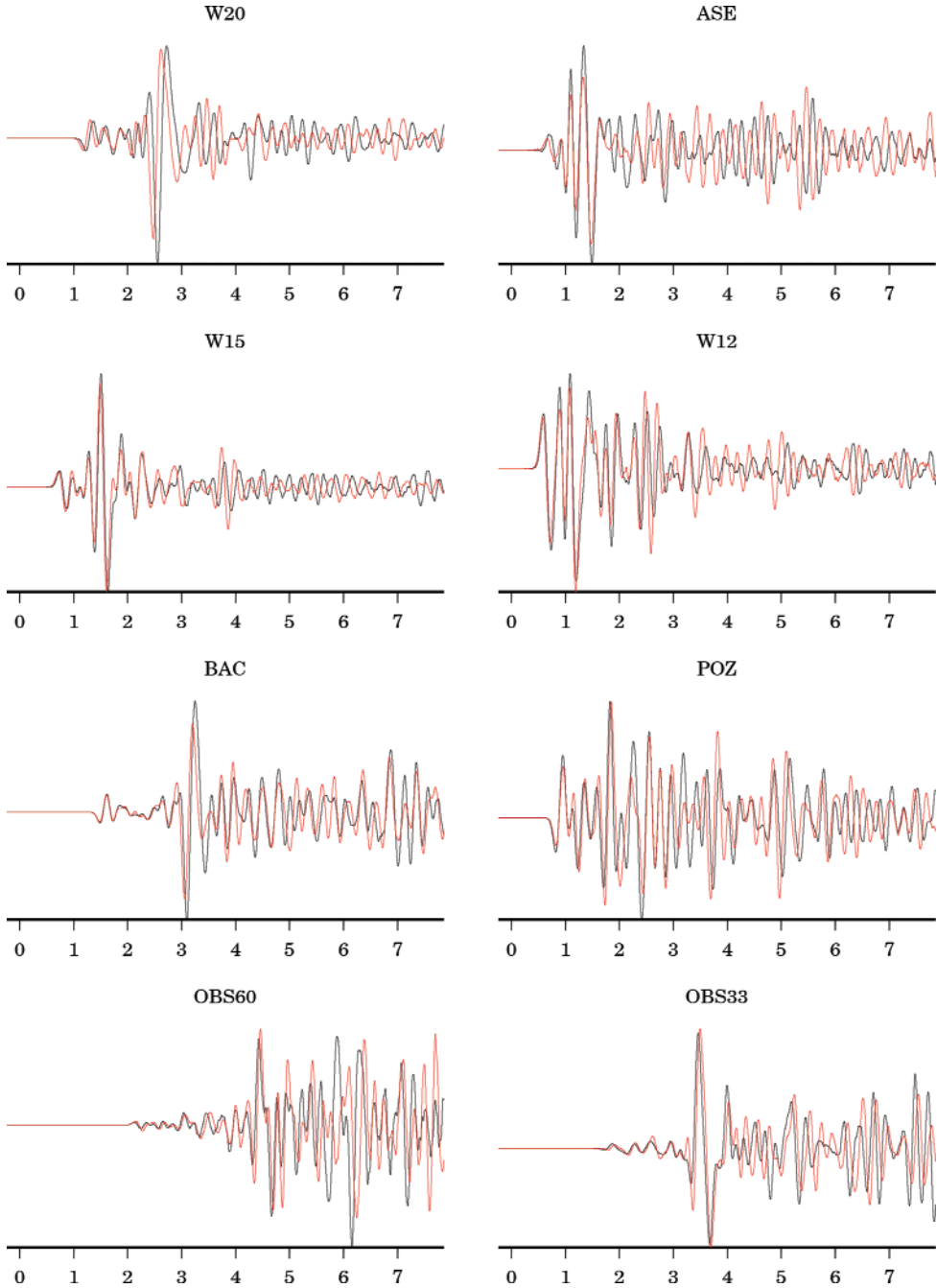
Fig. 12. Vertical acceleration 8 s seismograms registered at the stations ASE, BAC, POZ, OBS33, OBS60, W12, W15, W20. Black: with topography; red: without topography (see [24]).
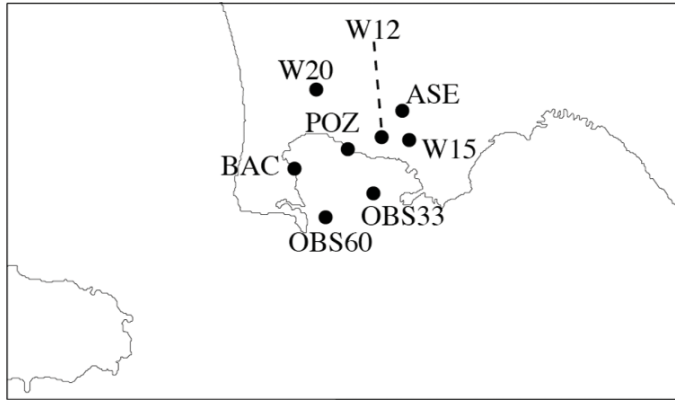
Fig. 13. Position of the stations ASE, BAC, POZ, OBS33, OBS60, W12, W15, W20.

DISCUSSION AND CONCLUSION

In summary, we have developed a parallel, semiautomatic mesher for a general geological layer-cake structure, capable of accommodating surface topography and the main internal discontinuities. The user provides only the shapes of the interfaces and the desired numerical resolution (balanced against the time step, i.e., against the numerical cost). The mesher includes some Fortran routines taken from the SPECFEM3D_BASIN solver and which allow the execution of CUBIT in an MPI environment.

The main limitation is due to the requirement that each slice has the exact same number of hexahedra. It is likely that in the next version of the solver this limitation will be overcome, opening new possibilities for simulating seismic wave propagation in complex geological volumes.

The meshing strategy has been applied to the Campi Flegrei Caldera and some simulations of the seismic wave propagation has been performed with results numerically accurate for period down to 0.16 s.

The preliminary results show that the topography has a not negligible effect on the wave propagation in region.

REFERENCES

[1] Bielak, J, Loukakis, K, Hisada, Y, and Yoshimura, C (2003) Domain reduction method for three-dimensional earthquake modeling in localized regions, part I: Theory. Bull Seism Soc Am, 93(2):817-824.
[2] Bielak, J, Ghattas, O, and Kim, E J (2005) Parallel octree-based finite element method for large-scale earthquake ground motion simulation. Computer Modeling in Engineering and Sciences, 10(2):99-112.

[3] Bouchon, M. and Sanchez-Sesma, F. (2007). Boundary integral equations and boundary elements methods in elastodynamics. In: Wu R-S and Maupin V (eds), Advances in Wave Propagation in Heterogeneous Media, Advances in Geophysics, 48 Elsevier-Academic Press.

[4] Chaljub, E, Komatitsch, D, Vilotte, J P, Capdeville, Y, Valette, B, and Festa, G (2007) Spectral element analysis in seismology. In: Wu R-S and Maupin V (eds), Advances in Wave Propagation in Heterogeneous Media, Advances in Geophysics, 48:365-419 Elsevier-Academic Press.

[5] citerra.gps.caltech.edu

[6] Courant, R, Friedrichs, K O, and Lewy, H (1928) ?Uber die partiellen differenzgleichungen der mathematischen physik (on the partial difference equations of mathematical physics). Mathematische Annalen, 100:32-74.

[7] cubit.sandia.gov

[8] Di Prisco C, Stupazzini M and Zambelli C (2007) Non-linear SEM numerical analyses of dry dense sand specimens under rapid and dynamic loading. International Journal for Numerical and Analytical Methods in Geomechanics, 31-6:757-788.

[9] Faccioli E, Maggio F, Paolucci R and Quarteroni A (1997) 2D and 3D elastic wave propagation by a pseudo-spectral domain decomposition method. Journal of Seismology, 1:237-251.

[10] GAMBIT (2004) User's Manual to GAMBIT 2. Fluent Inc, Centrera Resource Park, 10 Cavendish Court, Lebanon, USA.

[11] Käser M, Dumbser M, De la Puente J and Igel H (2007) An arbitrary high order discontinuous Galerkin method for elastic waves on unstructured meshes iii: Viscoelastic attenuation. Geophysical Journal International, 168:224-242

[12] Knupp, P M (1998) Next-generation sweep tool: A method for generating all-hex meshes on two-and- one-half dimensional geometries. In: Proceedings, 7th International Meshing Roundtable, pages 505-513 Sandia National Lab.

[13] Komatitsch, D and Tromp, J (1999) Introduction to the spectral-element method for 3-D seismic wave propagation. Geophysical Journal International, 139:806-822.

[14] Komatitsch, D, Barnes, C, and Tromp, J (2000) Simulation of anisotropic wave propagation based upon a spectral element method. 65(4):1251-1260.

[15] Komatitsch, D, Martin, R, Tromp, J, Taylor, M A, and Wingate, B A (2001) Wave propagation in 2-D elastic media using a spectral element method with triangles and quadrangles. Journal of Computational Acoustic, 9(2):703-718.

[16] Komatitsch, D and Tromp, J (2002) Spectral-element simulations of global seismic wave propagation-I validation. Geophysical Journal International, 149:390-412.

[17] Komatitsch, D, Tsuboi, S, Chen, J, and Tromp, J (2003) A 146 billion degrees of freedom, 5 teraflops, 25 terabyte earthquake simulation on the Earth Simulator. Proceedings of the ACM/IEEE Supercomputing SC'2003 conference.

[18] Komatitsch, D, Liu, Q, Tromp, J, S ?uss, P, Stidham, C, and Shaw, J H (2004) Simulations of ground motion in the Los Angeles basin based upon the Spectral-Element method. Bulletin Seismological Society American, 94:187-206.

[19] Komatitsch, D, Tsuboi, S, and Tromp, J (2005) The spectral-element method in seismology. In: Levander A. and Nolet G., (eds), Seismic Earth: Array Analysis of Broadband Seismograms, volume 157 of Geophysical Monograph, pages 205-228 American Geophysical Union, Washington DC, USA.

[20] Lee S J, Chen H W, Liu Q, Komatitsch D, Huang B S, and Tromp J (2007) Mesh generation and strong ground motion simulation in the taipei basin based upon the spectral-element method. submitted.

[21] Moczo P, Robertsson J O A, and Eisner L (2007) The finite-difference time-domain method for modeling of seismic wave propagation, in advances in wave propagation in heterogeneous Earth In: Wu R-S and Maupin V (eds), Advances in Wave Propagation in Heterogeneous Media, Advances in Geophysics, 48, Elsevier-Academic Press.

[22] Priolo E, Carcione J M and Seriani G (1994) Numerical simulation of interface waves by high-order spectral modeling techniques. J Acoust Soc Am, 95:681-693.

[23] Ronchi C, Ianoco R and Paolucci P S (1996) The "Cubed Sphere": a new method for the solution of partial differential equations in spherical geometry. J Comput Phys, 124:93-114.

[24] Satriano C, Zollo A, Capuano P, Russo G, Vanorio T, Caielli G, Lovisa L and Moretti M (2006) A 3D velociy model for earthquake location in Campi Flegrei area application to the 1982-84 uplift event. In: Zollo A, Capuano P and Corciulo M (eds.), Geophysical Exploration of the Campi Flegrei (Southern Italy) caldera interiors: Data, Methods and Results. DoppiaVoce ed, Naples.

[25] Schneiders R (1996) Refining quadrilateral and hexahedral element meshes. In: 5th International Conference on Numerical Grid Generation in Computational Field Simulations, pages 679-688 Mississippi State University.

[26] Scott M A, Earp M N, Benzley S E and Stephenson M B (2005) Adaptive sweeping techniques. In Proceedings of the 14th International Meshing Roundtable, pages 417-432 Springer.

[27] Staten M L and Canann S A (1997) Post refinement element shape improvement for quadrilateral meshes. In: Trends in Unstructured Mesh Generation, 220:9-16 AMD.

[28] Stupazzini M (2004) A spectral element approach for 3D dynamic soil-structure interaction problems. PhD thesis, Milan University of Technology, Milan, Italy.

[29] White D R and Kinney P (1997) Redesign of the paving algorithm: Robustness enhancements through element by element meshing. In: Proceedings, 6th International Meshing Roundtable, Sandia National Laboratories, pages 323-335.

Methodological advances in source and attenuation studies from the inversion of rise times of P pulses recorded at a local scale

S. de Lorenzo[1], E. Boschi[2], M. Filippucci[1], E. Giampiccolo[2], D. Patanè[2]

[1] *Università di Bari, Italy*

[2] *Istituto Nazionale Geofisica e Vulcanologia, Italy*

PREFACE

As outlined by many authors, the main problem in studying the seismic attenuation of the Earth from earthquake recordings is represented by the difficulty in removing the source effect from the waveforms. For this reason in this project we have substantially focused on the study of the joint effect of the seismic source and Q on seismograms. In particular we have made an attempt to develop a new methodology in separating source and Q from seismograms.

We report the result of a study aimed to infer source dimensions, fault plane orientation and Q from the inversion of rise times and pulse widths of a microearthquake recorded at local scale. It has been tested and applied to Etnean earthquakes. The paper describing the developed technique has been published on *Geophysical Journal International* (Filippucci et al., 2006). In that follows we summarize the technique and present a novel application to Mt. Etna.

INVERSION TECHNIQUE

In this section we present a technique aimed to infer the fault plane orientation, the source dimension of a small earthquake and the intrinsic quality factor Q of the ray-sampled volume. The technique is based on two steps. At the first step the possible focal mechanisms of the events are determined from the inversion of P polarities. At the second step the P rise times (Figure 1) are inverted to estimate L and Qp for each fault plane. The possible solutions are then compared to establish the most probable fault plane orientation.

We have assumed, as source model, a circular crack which ruptures with constant rupture velocity and instantaneously stops when the final perimeter of radius L is reached (Sato & Hirasawa, 1973). Under these assumptions and in the far-field range (Fraunhofer approximation), the source rise time τ_0 (i.e. the

rise time in an ideal elastic medium) is given by $\tau_0 = \dfrac{L}{V_r}\left(1 - \dfrac{V_r}{c}\sin\theta\right)$, where

V_r is the rupture velocity, c is the body wave velocity at the source and θ is the takeoff angle (the angle between the normal to the source plane and the tangent to the ray leaving the source). As an effect of the seismic absorption along the ray-path described by T/Q_p (where T is the travel time of the wave and Q_p the intrinsic quality factor of the P waves), an additional broadening of the first P pulse occurs. In de Lorenzo et al. (2004) the non linear equation relating the rise time to model parameters (L, δ, ϕ, Q_p) has been found. It is:

$$\tau = \tau_0 + \eta(L, c, \delta, \phi)\frac{T}{Q_p} + \lambda(L, c, \delta, \phi), \tag{1}$$

where $\eta(L, c, \delta, \phi)$ and $\lambda(L, c, \delta, \phi)$ are non linear function of source model parameters.

We propose an improvement of the inversion method of Zollo & de Lorenzo (2001) to account for "a priori" information on dip and strike. With respect to the previous study, the imposition of (δ,ϕ) allows us to reduce the number of unknown model parameters from four (L, δ, ϕ and Q_p) to only two (L and Q_p). The technique we developed consists of two steps: At the first step, focal mechanisms are computed from the inversion of P polarities using the FPFIT code, providing the values of (δ_i, ϕ_i) *(1≤i≤N$_p$)* for each of the N_p nodal planes. At the second step, by imposing $\delta=\delta_i$ and $\phi=\phi_i$ *(1≤i≤N$_p$)*, N_p inversions of rise times are carried out, providing N_p estimates of L and Q_p. The inversions are performed by using the Simplex Downhill method to search for the absolute minimum of the L^2-norm weighted misfit function between observed and estimated rise times, with weights equal to the inverse of the variance on data. The results of the N_p inversions are then compared to determine which of the N_p fault planes produces the best fit of the observed rise times. This plane will be considered the most probable true fault plane and it will be indicated with
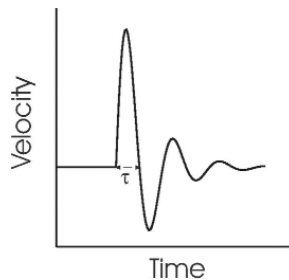
Fig. 1. The rise time of a first P-wave on a velocity seismogram.

the index 1. If FPFIT does not generate multiple solutions, the index 2 will indicate the conjugate plane. If multiple solutions are inferred from the inversion of P polarities, the index 2 will indicate the next most probable fault plane solution. We use the random deviates technique to evaluate how the errors on data map in the model parameter space. To this aim, we build N_{rand} different datasets adding to each datum a random quantity. This random quantity is selected inside the range of error affecting each datum. Our data are represented by rise times τ^{obs}, hypocenter locations, angles between rays and the vertical axis γ, azimuths α and takeoff angles θ. For a given event, the fault plane 1 will be considered really constrained by the rise times only when the standard deviation of the inversion σ_1^i for the fault plane 1 is systematically (i.e. for $1 \leq i \leq N_{rand}$) smaller than the standard deviation σ_2^i of the inversion for the fault plane 2. Considering the standard deviation reduction $\Delta\sigma^i$ of the *i-th* inversion, the fault plane 1 will be considered the most probable when

$$\Delta\sigma^i \geq 0 \quad \forall i: \ 1 \leq i \leq N_{rand} \tag{2}$$

For this event L and Q_p are estimated by averaging the results of the N_{rand} inversions using the fault plane 1.

DATA ANALYSIS

The data analysis consists firstly of testing the degree of complexity of a seismic rupture consists of integrating the P wave velocity waveform $v(t)$ to obtain the displacement field. In the case of a simple rupture process the displacement field would not significantly differ from a unipolar shape. Since the procedure of picking can be affected by a more or less pronounced degree of subjectivity, the comparison between $v(t)$ and $v^2(t)$ plots (Boatwright, 1980) can be useful to better determine the onset of the P phase. Following de Lorenzo & Zollo (2003), data affected by a clear multipathing effect during the first half-cycle of the wave have to be discarded. Rise time and its standard deviation have been measured taking into account the effect of the noise $N(t)$ on the vertical velocity seismogram $v(t)$. Three estimates of the rise time have been carried out. The first is based on the assumption that the onset of the P wave has been rightly picked at the time T_0, which corresponds to a first zero crossing at time T_1 and consequently a rise time equal to $T_1 - T_0$ (Figure 2). The other two measurements take into account the effect of the noise. To this end, we measured the average level of noise $<|N|>$ in L^1 norm in a time window $T_W = 0.5$ s which precedes the onset of the P wave (Figure 2). The intersections of the lines $v = \pm <|N|>$ with $v(t)$ allow us to determine a minimum $T_1^A - T_0^A$ and a maximum $T_1^B - T_0^B$ estimate of the rise time (Figure 2). These three estimates are then used to compute the average value of τ^{obs} and its standard deviation $\Delta\tau^{obs}$.
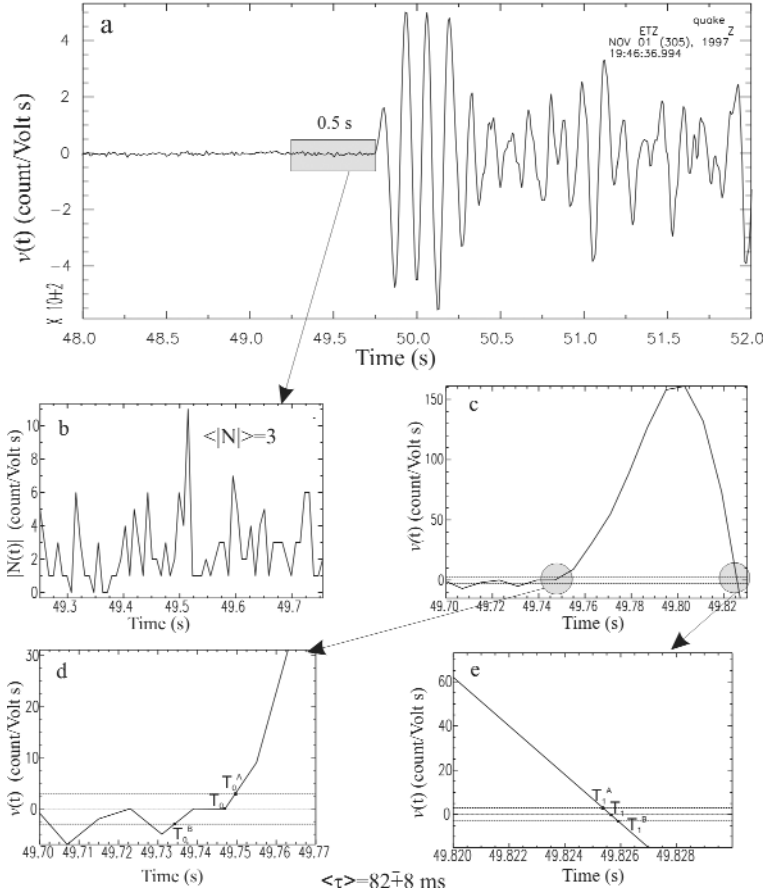
Fig. 2. Measurement of rise time on the first P-wave. **(a)** a velocity seismogram $v(t)$ recorded at station ETZ; the square encloses a time window of 0.5 sec of noise $N(t)$ before the estimated onset of the P-wave. **(b)** The absolute value $|N(t)|$ of $N(t)$ used to compute the average value $<|N|>$. **(c)** Intersections of the lines $v=\pm <|N|>$ with the first P wave. **(d)** Intersection points T_0^A and T_0^B of the rising part of P-wave with the lines $v = \pm<|N|>$. **(e)** Intersection points T_1^A and T_1^B of the descending part of P-wave with the lines $v=\pm<|N|>$.

DATA INVERSION

At the first step, the inversion of P polarities has been performed. According to the random deviates approach, for each studied event, $N_{rand}=100$ noisy datasets have been built, randomly varying either rise times and hypocenter locations. Rise time was let vary by adding to its average value a random quantity selected in the range of its standard deviation. Hypocenters were let vary inside a range (a cube of 1 km³) that is greater than the estimated error on coordinates, to take into account not only for the error on the localizations but

also for possible 3D effects. The consequence of varying the hypocenter locations is that γ, α and θ vary as well. As an example, in Figure 3 the inversion scheme is summarized for an event occurred in Sellano (Central Italy). For this event, first of all we select the fault plane 1 by observing that $\langle\sigma_1\rangle < \langle\sigma_2\rangle$ (Figures 3a, 3b). In addition, since the criterion (2) has been satisfied, the fault plane 1 can be considered the "true" fault plane, with an average standard deviation reduction $\langle\Delta\sigma\rangle$ of about 50% (Figure 3c). Once L and Q are determined, the source rise times (observed τ_0^{obs} and estimated τ_0^{teo}) can be computed from the rise times (observed τ_0^{obs} and estimated τ_0^{teo}). Observed and esti-
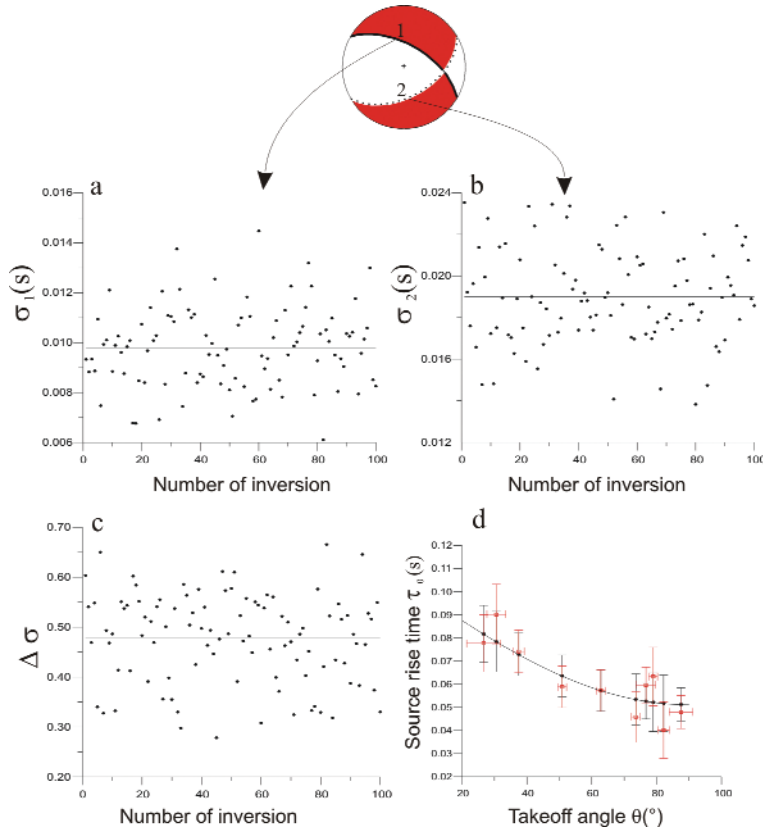
Fig. 3. The inversion of rise times for an event accurred in Central Italy. At the top, the focal mechanism of the event is shown. **(a)** the plot of the standard deviation vs. the number of inversion for the fault plane 1; the solid line represents $\langle\sigma_1\rangle$. **(b)** the plot of the standard deviation vs. the number of inversion for the fault plane 2; the solid line represents $\langle\sigma_2\rangle$. **(c)** plot of the standard deviation reduction between the two planes vs. the number of inversion. **(d)** Matching between theoretical and observed source rise times vs. the takeoff angle, for the fault plane 1; vertical red bar represents the error $\Delta\tau_\theta^{obs}$ on the observed source rise time; vertical black bar represents the range $\Delta\tau_0^{teo}$ of the theoretical source rise times explored in the N_{rand} inversions; horizontal red bar represents the range of the takeoff angles explored in the N_{rand} inversions; the solid line is the theoretical trend of τ_0 vs. θ.

mated source rise time can be plotted vs. the takeoff angle to visualize either the quality of the matching and the range of the takeoff angle which is covered by the data (Figure 3d).

The effect of adding a noise to both rise times and hypocenter locations is that the error on observed source rise time $\Delta\tau_0^{obs}$ (vertical red bar in Figure 3d) is greater than the error it would have considering only the standard deviation on rise time $\Delta\tau^{obs}$. In addition, the variation of hypocenter location gives rise to a variation of the takeoff angle (horizontal red bar in Figure 3d), for a given receiver, that depends on both the source to receiver position and the orientation of the fault plane. This is the reason why horizontal red bars (Figure 3d) vary from a station to another one.

FAULT PLANE RESOLUTION AND A POSTERIORI VALIDATION OF RESULTS

The degree of resolution R of the retrieved fault plane can be quantified taking into account that it depends on the exploration $\Delta\theta$ of the takeoff angle, on the number of rise times N available for the event, on the global quality of the observed source rise times $\left\langle \left| \dfrac{\Delta\tau_0^{obs}}{\tau_0^{obs}} \right| \right\rangle$, on the adherence of the rise times predicted by the model to data which is inversely proportional to the standard deviation $\langle\sigma_1\rangle$, and on the average standard deviation reduction $\langle\Delta\sigma\rangle$. We use the following relation to quantify R:

$$R = N \frac{\Delta\vartheta}{\pi/2} \log_{10} \frac{\langle\Delta\sigma\rangle}{\left\langle \left| \dfrac{\Delta\tau_0^{obs}}{\tau_0^{obs}} \right| \right\rangle \langle\sigma_1\rangle} \tag{3}$$

Let us consider the problem of quantifying the level of significance of the obtained solution. If we assume that the errors $\Delta\tau_i^{obs}$ on rise times are Gaussian distributed, the quantity $\displaystyle\sum_{i=1}^{N} \frac{\left(\tau_i^{obs} - \tau_i^{teo}\right)^2}{\left(\Delta\tau_i^{obs}\right)^2}$ will represent a χ^2 variable with a number of degrees of freedom equal to *N-k-1*, where *N* is the number of rise time data and *k=2* the number of parameters (*L* and Q_p) inferred from the inversion of rise times. Under this assumption, we can then perform, in the dip-strike plane, a χ^2 test for a given level of significance α_χ in order to accept or reject the following null hypothesis: H_0: the point (δ,ϕ) is the "true" fault plane orientation. In the dip-strike plane, a grid-search method with a grid step of 1°x1° has been implemented to find the points where H_0 can be accepted

for a given level of significance α_χ. Four levels of significance (α_χ = 25%, 10%, 5%, 1%) have been successively taken into account. The result for the event taken as an example in Figure 3 is in Figure 4 where grey areas represent regions of acceptance of H_0 and black dots are the FPFIT fault plane solutions.
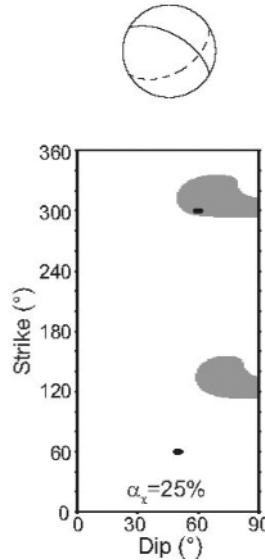
Fig. 4. Plot in the δ-ϕ plane of the (δ,ϕ) values which satisfy the H_0 hypothesis (grey-areas). Black dots represent the FPFIT fault plane solutions. On the top, the FPFIT fault plane solution is plotted in the focal sphere: solid line in the beach ball represents the "true" fault plane; hatched line the remaining plane.

APPLICATION TO MT. ETNA MICROEARTHQUAKES

The described technique has been applied to 171 seismic events occurred at Mt. Etna in the period October-December 2002. The events have been localized in the most recent 3D model of Mt. Etna. Seismic rays and consequently the takeoff angles have been computed with SIMULPS14. Only 109 of these events were selected using as criterion a minimum of 5 rise times available per event. After the analysis based on the criterion of standard deviation reduction we inferred 53 "true fault plane" which reduced to 46 after the χ^2 test. In Figure 5 we plotted the retrieved faults with different colours: a green lines represent the faults which are in good correspondence with the lineaments of faults observed at the surface (yellow lines); red lines represent the faults that do not show a correspondence with the surface faults. We estimated an average $<Q>$=42±24. This value is in agreement with the estimate of Q obtained with the classical rise time method (de Lorenzo et al.,2006).
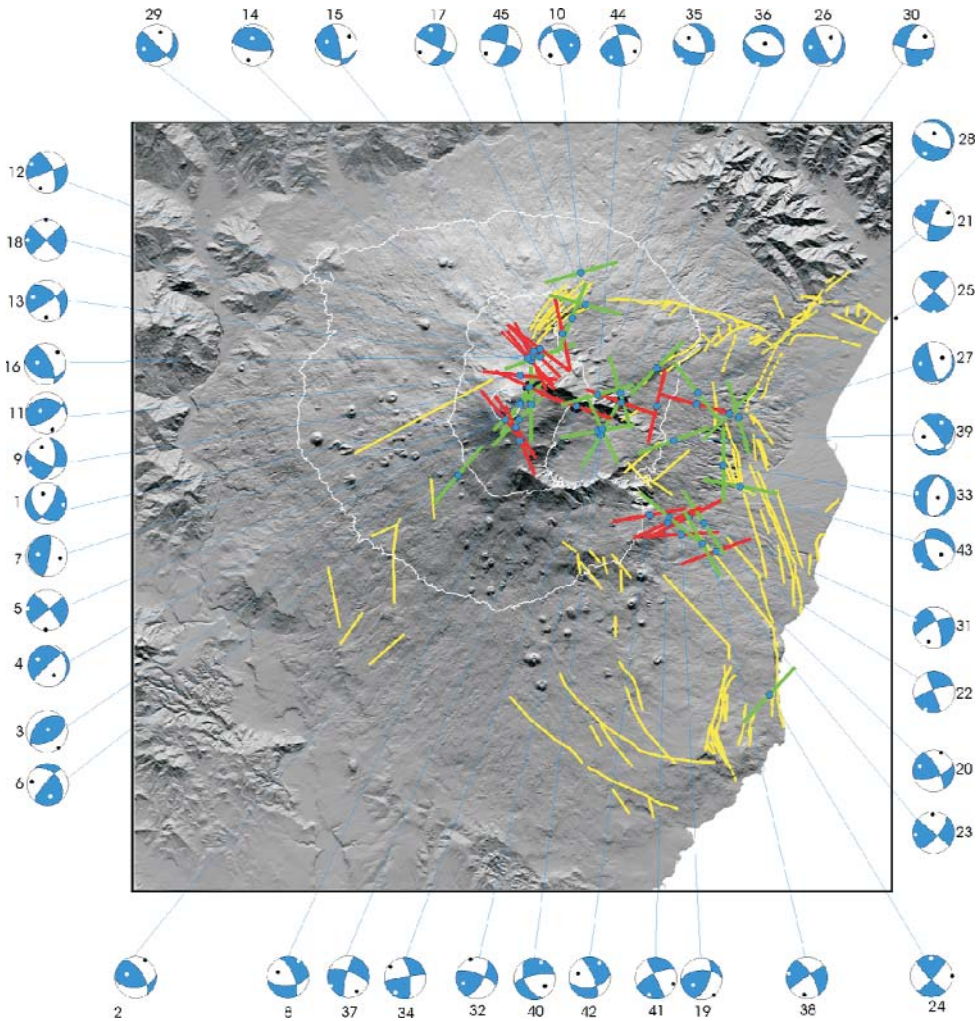
Fig. 5. Plot of strike faults. Yellow lines represente geological surface faults. Green and red lines represent the faults inferred inferred in this study.

REFERENCES

Boatwright, J., 1980. Bull. Seism. Soc. Am., 70, 1-28.

de Lorenzo, S. & Zollo, A., 2003, Geophys. J. Int., 155, 422-442.

de Lorenzo, et al 2004. J. Geophys. Res., 109, B07308, DOI:10.1029/2003JB002577.

Filippucci, M., de Lorenzo, S. and E. Boschi, 2006, Geoph. J. Int. 166, (1): 322-338. DOI: 10.1111/J.1365-246X.2006.02998.X

Sato, T., & Hirasawa, T., 1973. J. Phys. Earth., 21, 415-432.

Zollo, A. & S. de Lorenzo, 2001. J. Geophys. Res., 106 , 16287-16306.

QP and QS of Campi Flegrei from the inversion of rayleigh waves recorded during the SERAPIS project

S. de Lorenzo[1], A. Zollo[2], M. Trabace[1], M. Vassallo[2]

[1] Università di Bari, Italy

[2] Dipartimento di Scienze Fisiche, Università degli Studi di Napoli Federico II, Napoli, Italy

SUMMARY

Seismic shots recorded during the SERAPIS experiment were used to search a 1D elastic and inelastic model of the Gulf of Pozzuoli, south of the Campi Flegrei caldera. Waveforms were gaussian filtered in the range 5-8 Hz with a frequency step of 0.5 Hz and a half-width of the filter equal to 0.5 Hz. A clear dispersion of the most energetic propagation mode was revealed. This property of the surface wave in the gulf of Pozzuoli was theoretically reproduced using the classical wave-number technique. To infer the best fit propagation model, we developed a semi-automated procedure of fitting of filtered traces with progressive adjustment of the model. The quality of the fitting was estimated using the semblance among each couple of waveform (synthetic and observed). Our formulation allowed us also to estimate the error on model parameter by mapping the noise on seismograms on the semblance. The obtained 1D model confirms that in average intrinsic Qp at the Campi Flegrei caldera is of the order of 300-500 which is a background value higher than that of other volcanic areas.

This report is a summary of a part of the phd thesis in Earth Sciences at University of Bari of Maria Trabace.

DATA ANALYSIS

During the SERAPIS experiment, seismic signals produced by a battery of 12, 16-liters air-guns mounted on the oceanographic vessel NADIR (IFREMER) were recorded at a dense array of three-component, sea bottom (OBS) and on land seismographs installed in the bays of Naples and Pozzuoli (Zollo et al., 2003). The experiment was originally deployed to obtain 3D Vp and Vs images from the inversion of arrival times. The receiver array consisted of 70 ocean bottom receivers (OBS) and 84 land stations. In our study only OBS recordings were considered.

The OBS were equipped with 4.5 Hz three-component sensors and a continuous recording device (Judhenerc and Zollo, 2004). Before of the analysis all the waveforms were band-pass filtered between 5 and 15 Hz in order to work in the frequency range where the phase and amplitude response of the instruments deployed were the same.

In this report we discuss the results obtained by analyzing one of the seismic shots recorded during the experiment (Figure 1). We analyzed about 200 tra-
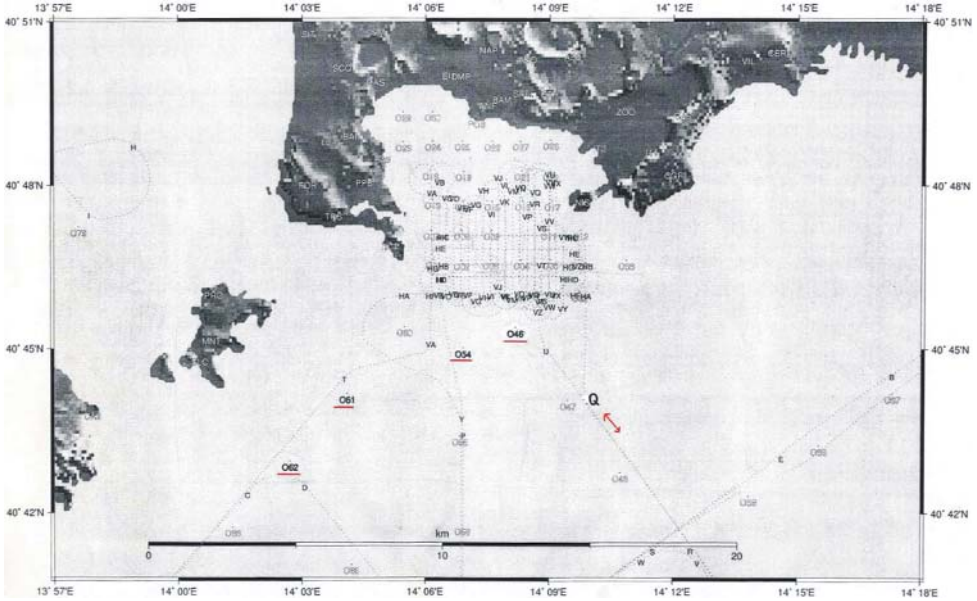
Fig. 1. Shot lines and position of OBs of the seismic experiment SERAPIS. The double arrow denotes the position of the seismic shot used in this study. The location of the four OBS used in this study are marked by a red line.

ces. At each trace we applied a Gaussian filter having a central frequency fc ranging from 5 to 10 Hz with a step of 0.5 Hz and a narrow bandwidth α=0.5 Hz (Dziewonski and Hales, 1972). The filter function is given by:

$$H(f) = \exp\left[-\pi^2 \frac{(f - f_c)^2}{\alpha^2}\right] \qquad (1)$$

The filter function (1) could introduce systematic errors when the medium is strongly dispersive (i.e. group velocity rapidly varies with frequency); in this case the error can be reduced by increasing α, with an increase in the degree

of uncertainty on the velocity estimate and the risk of the interference between adjacent modes (Dziewonski and Hales, 1972).An example of the filtering of traces is shown in Figure 2 for the OBS #61. Figure 2 indicates that there is a strong frequency dependence of the arrival time of the maximum energy, which is a clear dispersive effect. Many researchers (for instance Yao
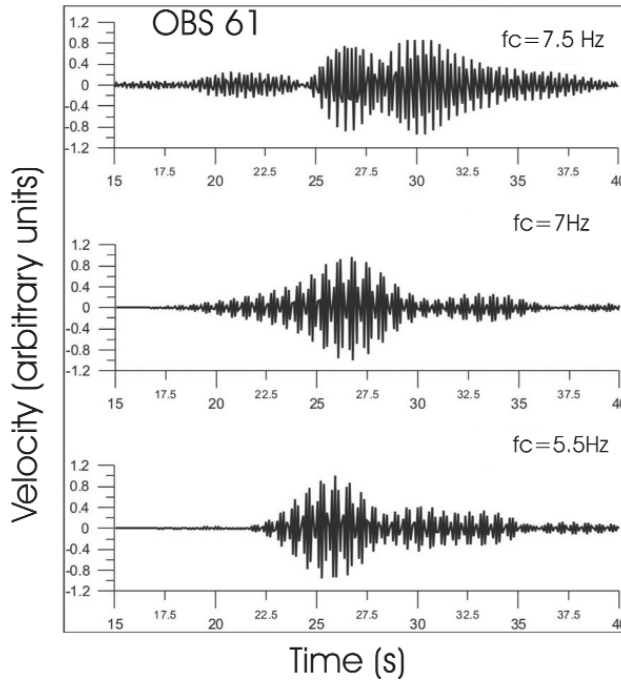
Fig. 2. Gaussian filtered recordings at the OBS 61 (α=0.5 Hz). The central frequency fc of the filter are reported on each seismogram.

and Dorman, 1992) have used the arrival time t* of the maximum of the wave packet to estimate group velocity U at each frequency through the relation:

$$U(f) = \frac{R}{t*} \qquad (2)$$

where R is the source to receiver distance. As discussed in Dziewonsky and Hales (1972) the previous equation furnishes unbiased estimates of group velocity only for an unimodal surface wave.

Since, as an effect of the filtering, several modes of propagation are inferred at the same central frequency, we strongly suspect that there is a bias in the arrival time of each group of each propagation mode and do not use, as preliminary information, the dispersion curve of group velocity. The existence of a clear dispersion of the most energetic propagation mode was also inferred by analyzing the arrival time of the most energetic mode vs. distance (Figure 3). We inferred the presence of a multiplicity of propagation modes at all the OBS. A summarizing plot of data is reported in Figure 4.

We discarded all the traces for which the filtered traces show unwanted arrivals preceding the first arrival on unfiltered traces and experienced a great difficult in separating the surface wave contribution. The main reason for this difficult is that the 4.5 Hz cutoff of the instruments does not allow us to study
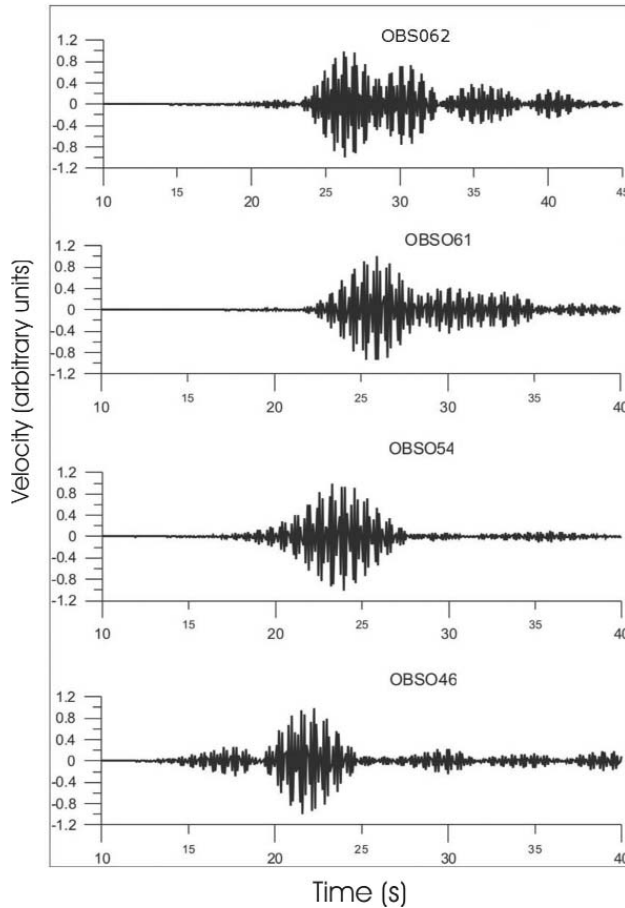
Fig. 3. Plot of Gaussian filtered traces (fc=5.5 Hz, α=0.5 HZ) at four OBS. This figure clearly shows the dispersion vs. distance of the most energetic propagation mode.
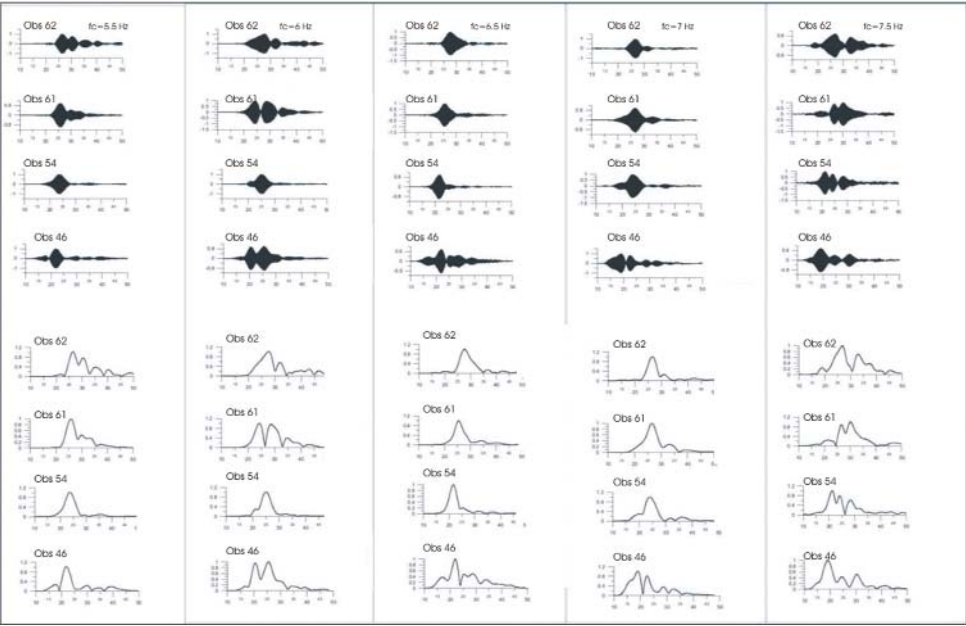
Fig. 4. Summary of filtered Gaussian traces and their absolute values.

the contribution of the Rayleigh waves below this frequency where it may be dominant. Moreover, we were unable to obtain filtered traces showing a clear contribution of the fundamental mode of propagation for frequencies of the gaussian filter greater than 7.5-8 Hz, owing to the superimposition of different modes of propagation. Another problem we experienced was the effect of high frequency noise (> 8Hz) on the filtered traces which tends to produce fictitious arrivals. The lower limit (5Hz) imposed by the instrument will limit our analysis only to a very thin layer below the sea bottom.

After the analysis of the waveforms we selected four stations which show a clearly readable and significant contribution of the Rayleigh waves and, from each trace, we extracted 5 gaussian filtered traces with fc= 5.5, 6, 6.5, 7 and 7.5 Hz and α=0.5 Hz. The source to receiver distance is reported in Table 1.

Tab. 1. Identification number of the Obs used in this study and their distance from the shot.

Obs #	Source to receiver distance (km)
46	9.5
54	10.3
61	12.8
62	14

Data inversion

The inversion technique used to model Vp, Vs, Qp and Qs is a refinement of the de Lorenzo et al. (2003) technique. It is based on the waveform fitting. The philosophy is to find the 1D elastic and anelastic model which best reproduces the entire waveform content in each frequency range where the Gaussian filter has been applied. This allows us to avoid the introduction of a subjective criterion of classification of the several propagation modes of surface waves which can be, at least partially, superimposed and then produce a bias in group velocity measurement. We use as data five Gaussian filtered waveforms (fc=5.5; 6; 6.5; 7; 7.5 Hz) with a bandpass width α=0.5 Hz at the four OBS. The time window considered is T=25 s for each seismogram. Since the time sampling of the four OBS is dt=4 ms, the number of data available for each filtered trace is N=6250. The total number of data is then Ntot=6250 x 20= 125000. Since we consider five layer with four unknown parameters the problem is clearly overdetermined.

The theoretical seismograms are computed using the discrete wave-number technique (Bouchon, 1981) considering a 1D layered anelastic medium and a point-like source whose frequency content is about equal to the inverse of the rise time τ of a ramp-like displacement source. In our calculation τ was fixed to 5 ms to simulate the sources of the SERAPIS experiment. Many studies on the inversion of Rayleigh waves (e.g. Nolet, 1990; and references therein) have pointed out the non-uniqueness of the solution. In the attempt to avoid the inference of a velocity and inelastic model which corresponds to a local minimum, we propose a forward modeling which uses as a priori information the 1D velocity model previously computed for the gulf of Pozzuoli (Judhenerc and Zollo, 2004). Considering the average frequency content of our data (f=6Hz) and a maximum value of phase velocity of 2 km/s (which is a typical maximum value for Vs of oceanic sediments) we can obtain a first order estimate of depth penetration of our signals of the order of 1 km. For this reason we have considered an initial model of two layers (a layer over an halfspace). The elastic and anelastic properties of the layers are reported in Table 2.

In the modeling we have subdivided the first layer in 4 layers of equal thickness (0.25 km). The procedure consists of evaluating the matching between theoretical and observed seismograms varying one of each model parameter (Vp, Vs, Qp and Qs) of each layer at a time.

Tab. 2. The initial model.

Layer id	Thickness (km)	Depth of the top (km)	Density (g/cm³)	Vp (km/s)	Vs (km/s)	Qp	Qs
1	1	0	1.9	2.86	1	300	100
2	∞	1	2.3	2.86	1.65	300	100

The quality of the fit is quantified by computing the value assumed by the semblance operator s (Telford et al.,1990). For a couple of signals s is defined as:

$$s_j = \frac{\sum\limits_{i=1}^{npt}\left[U_j^{est}(t_i)+U_j^{obs}(t_i)\right]^2}{2\sum\limits_{i=1}^{npt}\left(U_j^{est}(t_i)\right)^2+\left(U_j^{obs}(t_i)\right)^2} \tag{3}$$

where U_j^{est} and U_j^{obs} are respectively the theoretical and the observed seismogram at time ti; by considering N traces the semblance will be:

$$s = \sum\limits_{j=1}^{N} s_j \tag{4}$$

To quantify the error on model parameter we map the error on data in the model parameter space. The error on semblance due to the noise on data is:

$$\Delta s = \left|\frac{\partial s}{\partial U^{obs}}\right|\Delta U^{obs} \tag{5}$$

$$s_j = \frac{\sum\limits_{i=1}^{npt}\left[U_j^{est}(t_i)+U_j^{obs}(t_i)\right]^2}{2\sum\limits_{i=1}^{npt}\left(U_j^{est}(t_i)\right)^2+\left(U_j^{obs}(t_i)\right)^2} \tag{6}$$

$$\frac{\partial s}{\partial U^{obs}} = \frac{2s\left[U_j^{est}(t_i)+U_j^{obs}(t_i)\right]}{\sum\limits_{i=1}^{npt}\left[U_j^{est}(t_i)+U_j^{obs}(t_i)\right]^2} + \frac{2sU^{obs}(t_i)}{\sum\limits_{i=1}^{npt}\left[U_j^{est}(t_i)+U_j^{obs}(t_i)\right]^2} \tag{7}$$

The error on the observed seismogram is estimated in L1 norm by using the relationship:

$$\Delta U^{obs} = \frac{1}{T_1}\int_{0}^{T_1}\left|U^{obs}\right|dt$$

where T1=5 sec is the time duration of the signal, considered as the noise, which precedes the first arrival on each seismogram. The error on semblance

can then be mapped in the model parameter space to determine all the parameters which lie in the range [s-Δs;s]. This will allow us to estimate the average value of each parameter and the uncertainty affecting it.

Figure 5 shows the matching between observed and theoretical waveforms for the initial velocity model for a central frequency fc=7 Hz. Figure 6 shows the variations of the semblance with varying the model parameters during the inversion procedure.
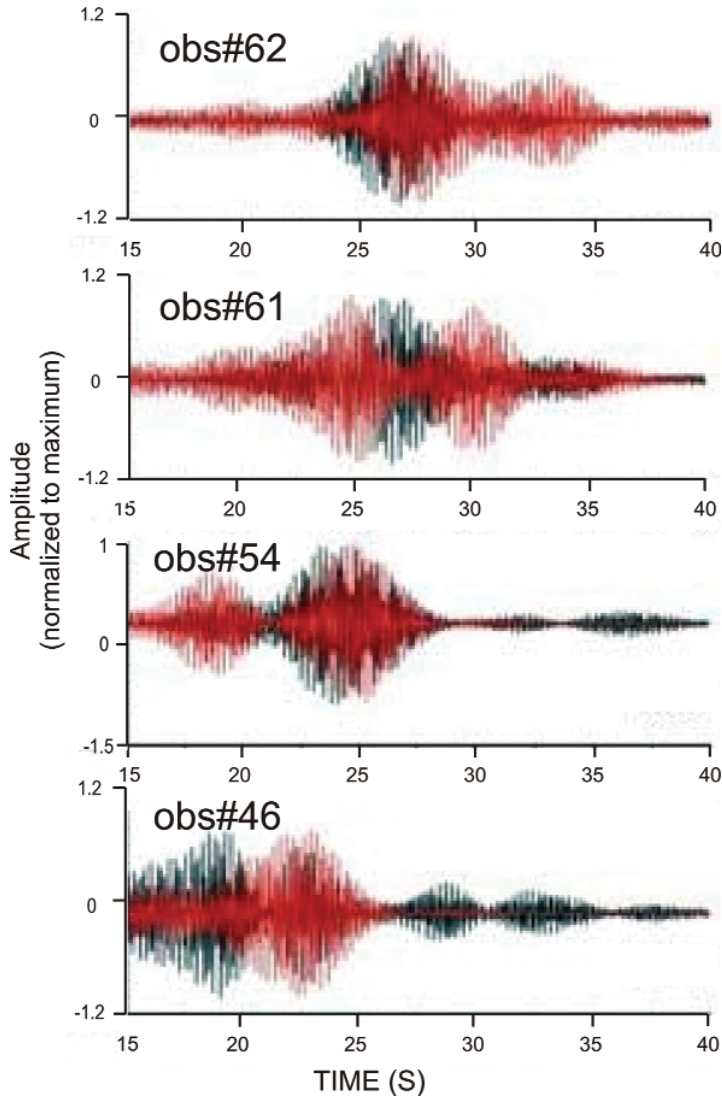
Fig. 5. Waveform fitting at fc= 6 Hz using the initial elastic and inelastic velocity model. The observed waveforms are plotted with a black line; the synthetic waveforms with a red line.
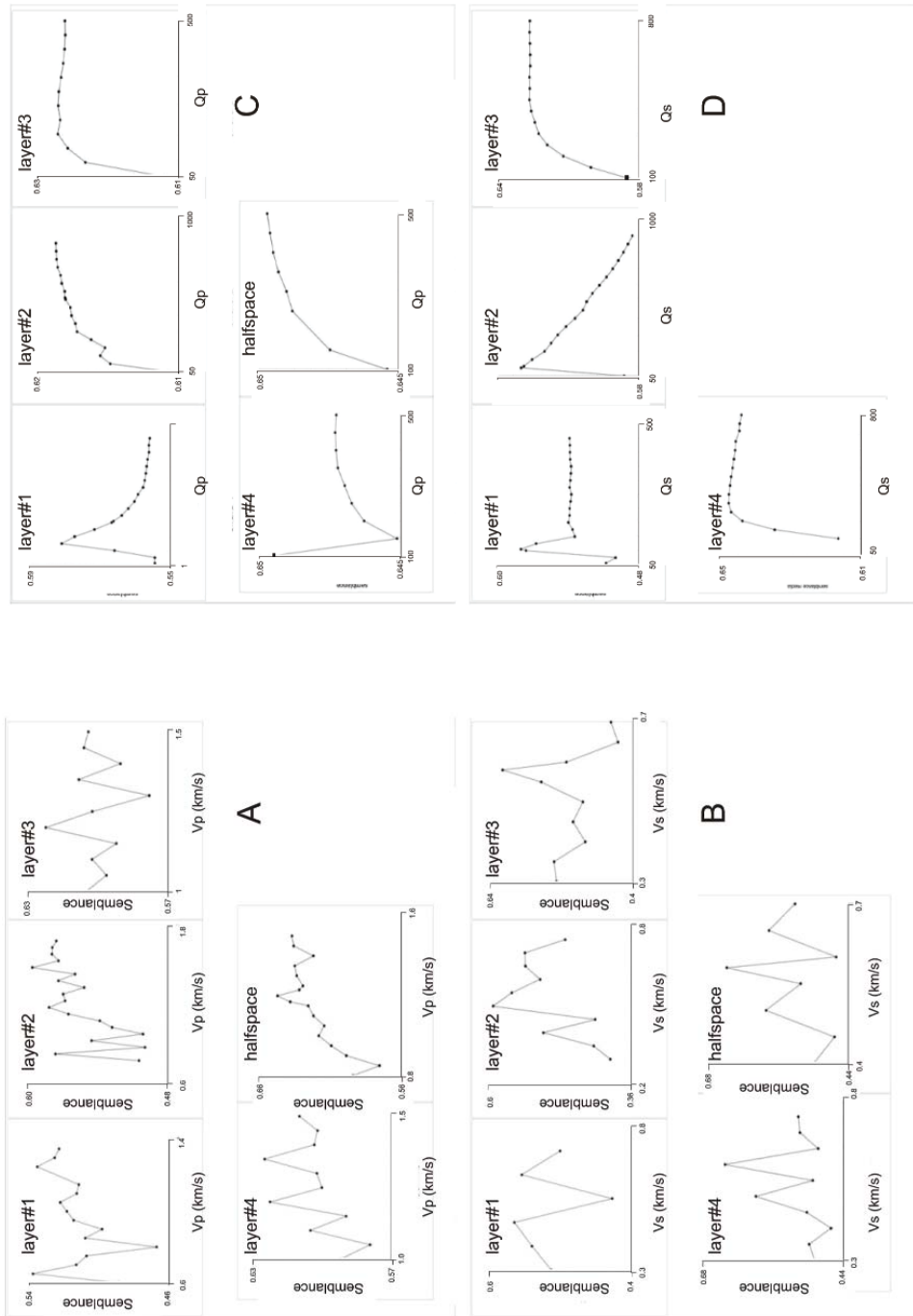
Fig. 6. Variation of the semblance with varying **(a)** Vp of each layer; **(b)** Vs of each layer; **(c)** Qp of each layer; **(d)** Qs of each layer.

The final velocity and inelastic model is reported in Table 3, together with the error on each parameter. The matching between observed and theoretical Gaussian filtered waveforms at fc=7Hz is shown in Figure 7. To better evaluate the quality of fitting we use the absolute value of the waveforms which allows us to enhance the energy content of the signals.

Tab. 3. Final velocity and inelasticity model.

Thickness (km)	Vp (km/s)	Vs (km/s)	Density (g/cm^3)	Qp	Qs
0.25	1.3± .05	0.4± 0.1	1.5± 0.1	150± 20	110± 20
0.25	1.3± .05	0.5± 0.1	1.2± 0.2	900±200	100± 10
0.25	1.2±0.05	0.58± .1	1.7± 0.2	200± 10	450±150
0.25	1.2± 0.1	0.58± .1	1.7± 0.1	200± 80	450±200
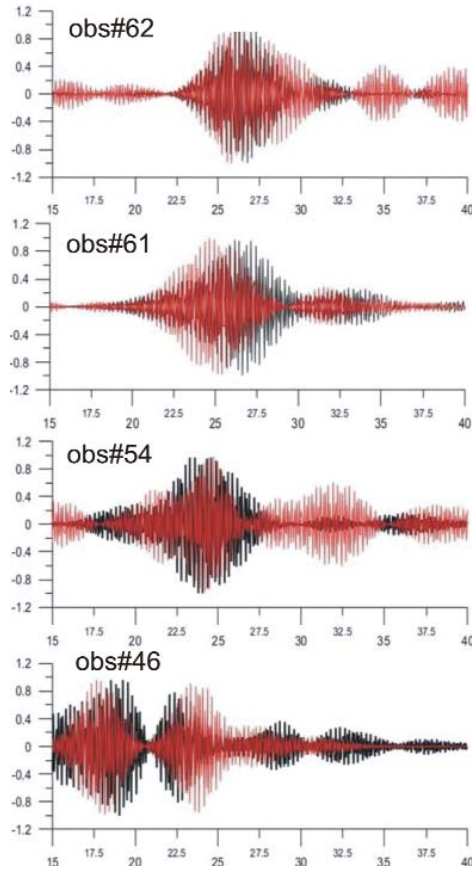
Fig. 7. Waveform fitting at fc=7 Hz using the final elastic and inelastic velocity model. The observed waveforms are plotted with a black line; the synthetic waveforms with a red line.

Figure 8 shows the comparison between the absolute values of filtered theoretical and observed waveforms for fc= 7 Hz. Since we did not perform the deconvolution for the instrumental response we compared the unit normalized traces.
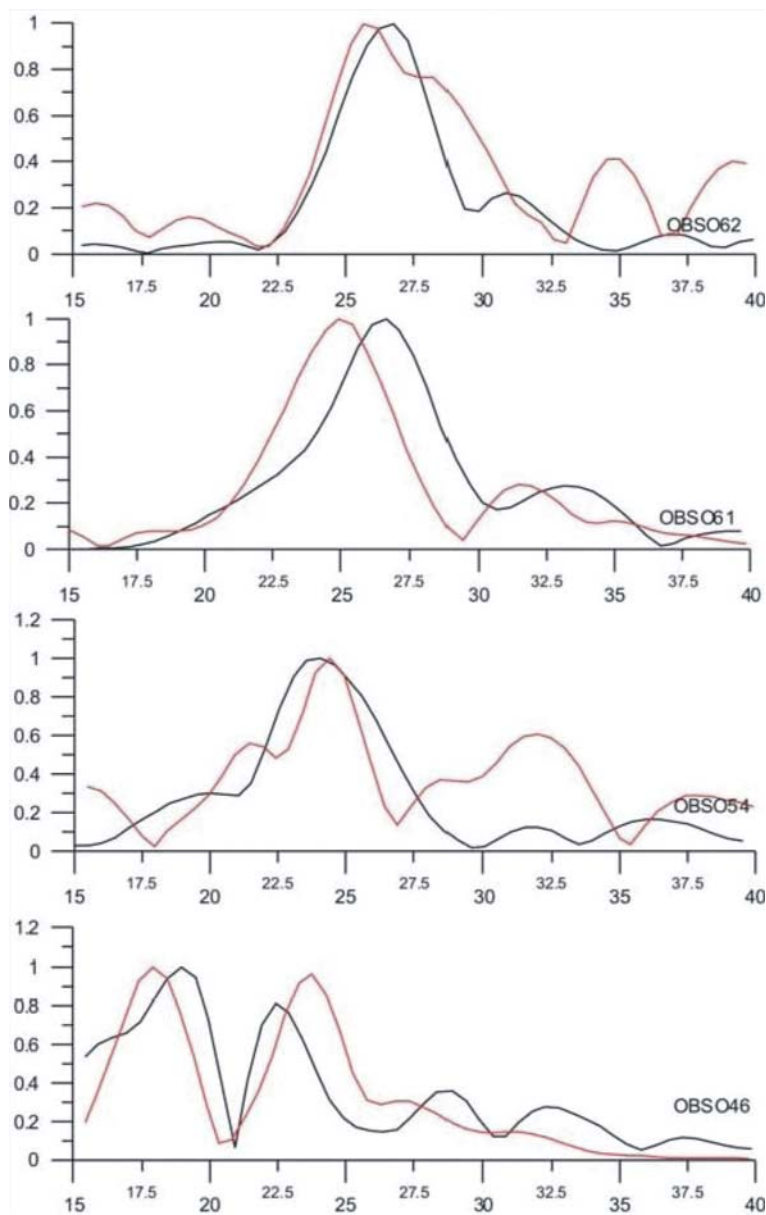
Fig. 8. Plot of the absolute values of synthetic filtered waveforms for fc=7 Hz. The observed waveforms are plotted with a black line; the synthetic waveforms with a red line.

Very interestingly the main energy content is very well reproduced by the model and, more interestingly, the repartition of the energy in at least two propagation modes, is also well reproduced, in particular at the OBS 46. The value of semblance increases of 28% from the initial model to the final one.

CONCLUSION

Qp values in the four thin layers is generally in the order of 100-200 which is roughly the same magnitude order of the average values previously inferred from a tomographic study of the Campi Flegrei caldera (de Lorenzo et al.,2001), whereas only a very high Qp (Qp=900) is inferred between 0.25 and 0.5 km. Vp values inferred for the first layer are slightly lower than those obtained by Judhenerc and Zollo (2004).

REFERENCES

Bouchon, M., 1981, Bull. Seism. Soc. Am. 71, 959-971.

de Lorenzo, S, Iannaccone, G, Zollo, A., Journal of Seismology 7: 49-64, 2003.

de Lorenzo, S., A. Zollo, and F. Mongelli (2001), J. Geophys. Res., 106, 16,265-16,286.

Dziewonski, A.M. and Hales, A.L., 1972, Numerical analysis of dispersed seismic waves, in: Bolt, B.A. (ed.), Methods of computational physics 11: Seismology: surface waves and earth oscillations, Academic Press, New York and London, 309 pp.

Judenherc and A. Zollo, J. Geoph. Res. Vol. 109, B10312, DOI:10.1029/2003JB002876, 2004.

Nolet, G., 1990, J. Geophys. Res. 95, 8499-8512.

Telford, W.M., Geldart, L.P., Sheriff, R.E. and Keys, D.A., 1990, Applied geophysics. 2nd edn. Cambridge University Press, Cambridge.

Yao, P.C. and Dorman, J., 1992, Bull. Seism. Soc. Am. 82, 962-979.

Zollo A., S. Judenherc, E. Auger, L. D'Auria, J. Virieux, P. Capuano, C. Chiarabba, R. De Franco, J. Makris, A. Michelini, and G. Musacchio, Geophysical Research Letters, Vol. 30, No. 19, 2002, DOI:10.1029/2003GL018173, 2003.

Multi-scale decomposition of velocity structure and application to first-arrival travel-time tomography

M. Delost, J. Virieux, S. Operto

Géosciences Azur, CNRS and UNSA, Sophia Antipolis, France

Abstract: Wavelet decomposition of the slowness model has been proposed as the possible decomposition of the velocity field which will enhance resolution performance of first-arrival time tomography. We have investigated effects of the so-called second generation wavelets which might be useful for describing complex structures as for volcanic zones. A linearized procedure for inverting delayed travel-times considering either slowness coefficients or wavelet coefficients has been developed. It relies on both an efficient ray tracing using an eikonal solver and an iterative solver as LSQR algorithm.

We develop wavelet decomposition over constant patches (Haar wavelet) or over linear patches (Battle-Lemarie wavelet) of coefficients at different scales and wavelet coefficients are considered as unknowns to be inverted. Synthetic examples show that the inversion behaves in a better way as wavelet decomposition seems to act as a preconditioner of the linear system. Applications to borehole-borehole geometry as well as surface-surface geometry illustrate that we may recover fine details nearby sources and receivers while preventing imprints of ray coverage as we move away from data acquisition systems. In spite of the increase demand of computer resources, the wavelet decomposition seems to be a rather promising alternative for controlling the resolution variation of seismic first-arrival tomography.

INTRODUCTION

First-arrival delayed travel-time tomography (FADTT) applied to wide aperture seismic data has proved to be an interesting tool to investigate the Earth structures (Aki & Lee, 1976; Spakman & Nolet, 1988; Hole, 1992; Zelt & Smith, 1992; Benz et al., 1996, Zhang et al., 1998). The resolution of FADTT is controlled both by the theoretical resolution imposed by the relation between velocity structure and first-arrival travel-times and by the data acquisition configuration as well as the structure itself, which may lead to uneven ray coverage. The theoretical resolution power of FADTT is limited by the size of the first Fresnel zone for each ray. There is an antinomy between the limited reso-

lution power of FADTT and the numerical sensitivity kernel of FADTT corresponding to rays. Rays have no thickness and, therefore, have an intrinsic infinite sensitivity although in practise discretization of the model space always smoothes out this feature (Dahlen, 2004). Indeed, one raypath induces high frequency information along the ray, even at locations where resolution of FADTT is expected to be low. Inversion can build up models which have a high degree of data fitting but which are far from the true model containing artefacts.

Accounting for the limited resolution of FADTT goes through regularized tomographic inversion (Farra & Madariaga, 1988; Delprat-Jannaud & Lailly, 1993; Zhang et al, 1998) often based on the Tikhonov regularization approach (Tikhonov & Arsenin, 1977). The introduction of the covariance matrix for the model as well as for the data (Tarantola & Valette, 1982; Tarantola, 1987) has given a precise theoretical background although estimation of those matrices is still a difficult task (Monteiller et al, 2005). Another alternative regularization is based on smoothing constraints easier to implement as the laplacian (Menke, 1984; Zhang et al., 1998). Whatever we choose, regularization strategies lack spatial adaptivity. Frequently, when the smoothing is tuned to remove the footprints of raypaths in poorly illuminated areas, short-scale features that could be resolved in other areas of the model according to the resolution of FADTT are smoothed simultaneously, leading to a loss of information in the well-resolved areas.

The resolution of FADTT generally varies locally. For example, considering surface acquisition geometries, the shallow structures will be sampled both by short- and long-offset rays running across the heterogeneities with different azimuths while the deeper structures will be sampled by long-offset rays only with a much narrower range of azimuths. The resolution of FADTT decreases quite significantly with respect to depth for this geometry. Two other factors creating non-uniform ray coverage are the presence of low velocity anomalies which induces shadow zones in the ray coverage and non-uniform source and/or receiver arrays especially in the case of passive tomography. For volcanic structures, these local variations of velocity might be quite common and prevent us recovering detailed structures at depth.

In order to consider this spatially varying resolution power, one could introduce adaptive parametrizations based on non-structured grids (Michelini, 1995; Spakman & Bijwaard, 1998; Spakman et al., 1998; Bohm et al., 2000; Trinks et al., 2005; Zhang & Thurber, 2005). The size of local cells is adapted to the local ray coverage such that the amount of control for each model parameter tends to be uniform. More promizing is the multigrid approach where the inversion procedure recovers values on different grids depending on the resolution power (Madych, 1999; Chiao & Kuo, 2001; Chiao & Liang, 2003; Zhou, 2003) based on wavelet tools (Mallat, 1999). In this article, we shall propose a further investigation of this multigrid approach using new wavelet transform named as second-generation wavelets (Sweldens, 1997).

WAVELET TRANSFORMATION

Over the last years, many constructions of wavelets have been proposed (Daubechie et al., 1986; Grossmann & Morlet,, 1984). An important step has been achieved with the construction of orthogonal, compactly supported wavelets by Daubechies (1988). For seismic tomography, wavelets can be used for the description of the model at various scales (Chiao & Kuo, 2001; Chiao & Liang, 2003; Zhou, 2003). The slowness model is expanded on a wavelet basis and the tomographic system is solved for the wavelet coefficients.

As Fourier driven transformation, wavelet decomposition encounters some relevant drawbacks: the number of samples has to be a power of two, samples have to be regularly spaced and one must deal with periodicity which makes complicated boundary conditions. For overcoming these difficulties, the concept of biorthogonal wavelets constructed by lifting scheme has been introduced (Sweldens, 1994; Sweldens & Schroder, 1995; Sweldens, 1997), leading to the so-called second generation wavelets. Such wavelets can be adapted to curved surfaces and can sample quite complex domains.

The lifting scheme leads to a faster, in-place calculation of the wavelet transform. As shown by Delost et al. (2007) for seismic tomography, this numerical strategy deals with the so-called *Lazy Wavelet* decomposition which does nothing but set aside odd and even indexed coefficients. A dual lifting operator is defined by predicting odd indexed coefficients using even indexed coefficients (by using the spatial correlation between neighbours and by considering that polynomials of degree up to N-1 should be exactly predicted). Then, we update the even indexed coefficients using new odd coefficients in such a way that N first moments are preserved. This flowchart has an inverse procedure which can be red in a reverse way and, because the transformation is linear, one may write it under the following expression:

$$\Delta c = W \ \Delta u \tag{1}$$

where wavelet coefficients perturbation are denoted by Δc and slowness coefficients perturbations are denoted by Δu The inverse transform is simply

$$\Delta u = W^t \ \Delta c \tag{2}$$

The Figure 1 shows the decomposition of V0 space with a positive anomaly in the centre of the medium. Please note that the V4 and V5 spaces spread out the anomaly over its extension.

TRAVEL-TIME TOMOGRAPHY

Once rays have been computed between each source and each receiver seeing the source through an eikonal solver (Podvin & Lecomte, 1991), the delayed

traveltime tomographic system relating slowness anomaly Δu to traveltime residuals Δt written as

$$\Delta t = A \ \Delta u \tag{3}$$

can be transformed into the new system

$$\Delta t = AW^t \ \Delta c \tag{4}$$

where the matrix **A** is the sensitivity or Fréchet matrix. The matrix product **AW^t** can be built by computing the 2D wavelet transform of each row of the original matrix **A**. A row of the sensitivity matrix has n_1 x n_2 number of model parameters in a 2D geometry where the number of horizontal grid points is n1 and the number of vertical grid points is n2: it contains the contribution of one ray to the Fréchet derivatives. After transformation, we have the same number of unknowns but they are in the wavelet domain and partial derivatives are for wavelet coefficients. Once the system equation (4) has been solved through an iterative procedure as the LSQR algorithm (Paige & Saunders, 1982), the perturbation model coefficients Δu in the slowness space are obtained by the inverse wavelet transform. We shall plot models from these slowness values.

Traveltime tomography in the wavelet domain has an interesting feature: as coefficients are associated to levels of the wavelet transform and, consequently, related to scales and local resolutions, adaptivity strategy is much easier to handle through scale hierarchy. The decomposition of a simple circular anomaly leads to cascades of grids V for each scale level *i* using square wavelet basis functions as shown in the Figure 1. Controlling incremental perturbations through wavelet coefficients between these different descriptions of the true model taken as the one in the V0 space is a hierarchical procedure.

As we estimate imprints of rays on different coarser grids through estimations of the Fréchet derivatives, we extend equivalently its area of sensitivity as shown in Figure 2. The sensitivity of a ray is related to the spatial discretisation of the slowness model at the given wavelet scale.

The adaptivity of the parameterization can be implemented by applying a mask to each row of the sensitivity matrix **AW^t**, zeroing coefficients in areas of the model where a poor resolution is expected et a given scale. This adaptivity selection can be implemented via a linear operator M applied to the Fréchet derivatives in the wavelet domain through the following extended linear system

$$\Delta t = AMW^t \ \Delta c \tag{5}$$

Designing this operator will depend on local resolution analysis. For surface acquisition, one could, for example, define an empirical rule relating the reso-
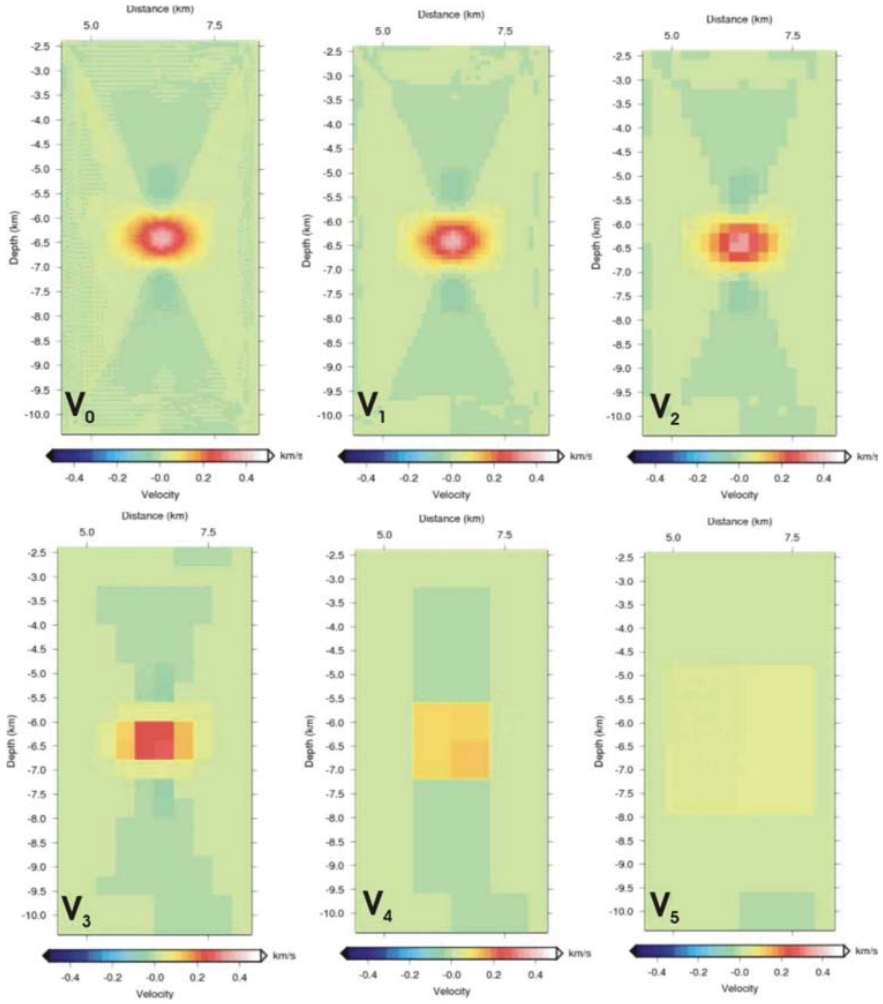
Fig. 1. Decomposition of a V_0 slowness model for a crosswell experiment into the V_i spaces using 5 levels of wavelet coefficients.
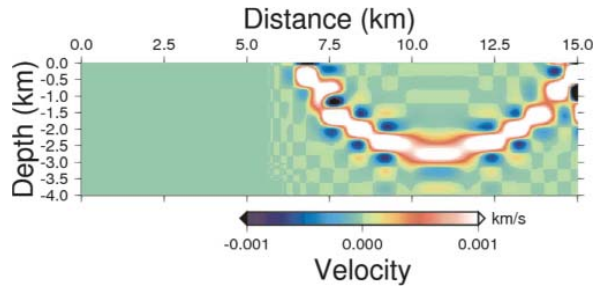
Fig. 2. Non-zero Fréchet derivative coefficients of a selected ray for the V4 grid. Please note the thickness at that scale of the derivatives associated to a ray wich has no thickness.

185

lution of the model at a given depth to the minimum source-receiver offset of the rays sampling this depth. The source-receiver offset would provide an estimate of the width of the first Fresnel zone at a given depth and, hence, of the expected resolution of the tomography varying with depth. According to the sampling theorem, only grids with mesh spacing twice smaller than the width of the first Fresnel zone would be locally involved in the inversion: a simple rule for construction the M operator.

We will discuss later how we can propose a more general strategy for building this operator. Let us remark that the wavelet transform has also the capacity to automatically adapt the parameterization to the resolution in the case where the real resolution is lower than the intrinsic one such as in the case of a shadow zone. In areas where no rays illuminate the medium, partial derivatives of the traveltime time with respect to the wavelet coefficients at the finest scales will be zero, thanks to the second generation property. On the contrary, the partial derivative of the traveltime time with respect to the wavelet coefficients of the coarsest scales will be non-zero due to the spatially extended sensitivity of the coarse grids representations of the rays. Hence, only the coarse-scale wavelet coefficients of the slowness model will be non-zero after inversion and will automatically lead to a smooth representation of the true model.

SYNTHETIC EXAMPLES

We present synthetic examples to illustrate how the wavelet decomposition enables us to reconstruct the P-wave velocity model. First, we focus our attention to the wavelet coefficients transformation. We shall show that similar results are found when compared with those of the standard tomography using slowness coefficients. Finally, we illustrate the efficiency of scales selection using the simple binary operator M. Designing an objective criterion for the spatial definition of this binary operator will be based on resolution matrix analysis.

A densely illuminated model with positive anomalies

As a first example, we design an acquisition system for a complete illumination of a simple circular positive velocity anomaly of 0.5 km/s that we want to reconstruct from a background model of constant velocity of 3 km/s. This background velocity model will be our starting model.

For each inversion, we estimate the lowest rms error from the misfit function as it flattens with linearized iterations. Moreover, we display horizontal and vertical sections for a better appreciation of the spatial frequency contents.

First, the model is reconstructed using slowness parameters in the inversion over a grid of 5 m step size. No damping is applied to the over-determined

system. The convergence is obtained after four iterations and the anomaly is accurately recovered although with high frequency artefacts (Figure 3). Other artefacts are related with uneven ray sampling in the center of the anomaly. How better will be a reconstruction in the wavelet domain?
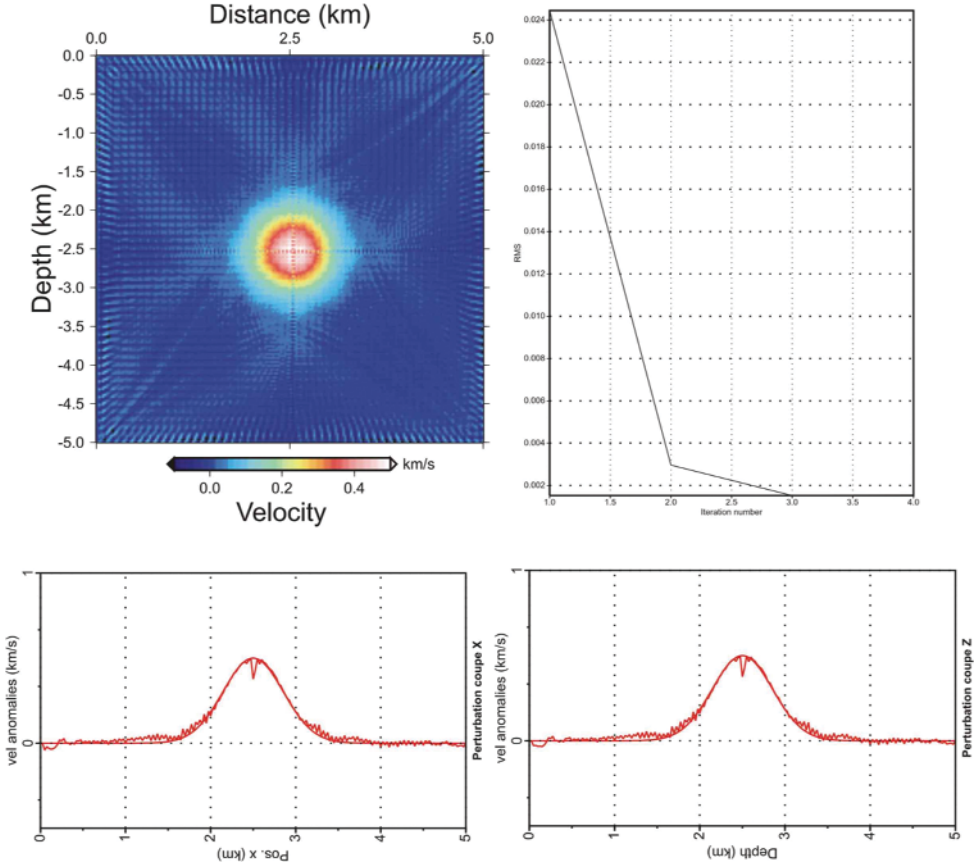
Fig. 3. Tomographic inversion without any regularization or daming. On the top left panel, the reconstruction anomaly, on the top right the misfit decrease to rms error of 1.52 ms. Please note high frequency noise and the glitch along vertical and horizontal profiles related to poor ray coverage.

When considering wavelet decomposition, we select wavelets with two vanishing moments. We consider four levels for the scale sampling. This means that the coarser grid size will have a 40m resolution. The anomaly is well recovered but the convergence to the flat level of the misfit function is slightly slower than before (Figure 4). We need thirteen iterations for reaching convergence. The high frequency artefacts are less noticeable providing a better fit of

the model. As we increase the number of levels, we can see the decrease of the amplitude of the high frequency artefacts. In other words, when coarser levels are introduced, the reconstruction is driven by a better spatial coherence, essentially for broad features. We may say that the parametrization into the wavelet domain provides a better conditioning of the system to be inverted, since it is less sensitive to high frequency perturbations.
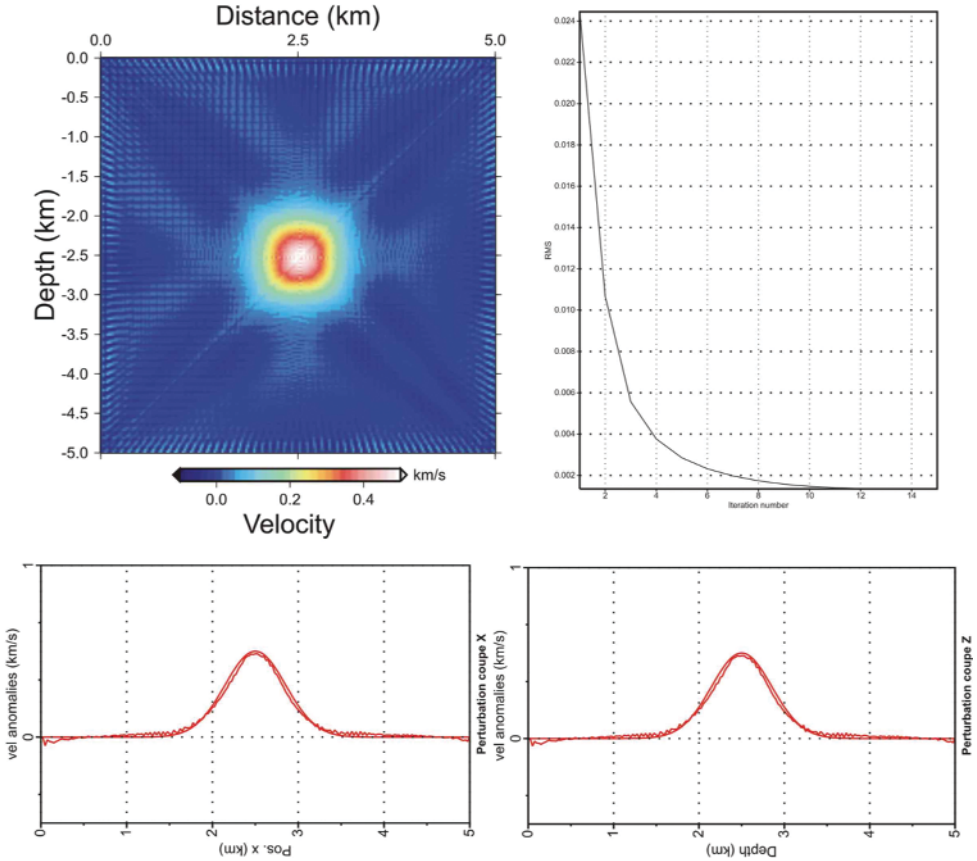
Fig. 4. Tomographic inversion using wavelet with two vanishing moments and four levels. The convergence is obtained with a a rms error of 1.35 ms after thirteen iterations. Please note the better reconstruction avoiding high frequency oscillations as for Figure 3.

RESOLUTION ANALYSIS FOR DEFINING THE BINARY M OPERATOR

For better focusing of the reconstruction through different scale levels, one has to proceed through a resolution analysis in order to overcome difficulties

coming from the linearized inversion. A more exhaustive exploration of the parameter space may be of great interest but it is beyond the scope of this paper. We assume that a model has been designed for which one can perform a resolution analysis. It could be the initial model or any model obtained through previous attempts of inversion. Starting with this model, we may want to have a rough estimation of the resolution matrix for better performance of the inversion (Nolet et al., 1999). Of course, once done, we may end up with another medium we shall use again for a new resolution analysis and so on. We cannot rule out this loop over adapted models.

For small systems, one can use a direct solver and computing the resolution matrix is quite fast. For important systems, we may rely on numerical iterative techniques as proposed by Latorre et al. (2004). We zero out Fréchet derivatives when less than 95 % of the wavelet amplitude is recovered at the central position of the spike. This decrease of the amplitude is related to the spreading of the reconstructed spike. Hence, we analyze only the amplitude right at the position where is the spike. Because the system is linear, positive or negative amplitudes give the same resolution matrix estimation.

APPLICATION TO A SYNTHETIC REAL DATE CONFIGURATION

Moreover, dealing with uneven ray coverage is a crucial issue in tomography: how the wavelet decomposition performs when illumination is far from an ideal one. The experimental data acquisition as well as the structure itself always creates areas of limited ray coverage. Hence parts of the model are expected to be known precisely, while other parts will suffer from low resolution. Wavelets deal with the multiscale nature of the information contained in the data but the inversion is not able to focus automatically anomalies on related scales. Working in the wavelet domain makes easy the selection scales of the parameter model by a simply predefined operator. Zeroing wavelet coefficients corresponding to scales finer than the expected local resolution will help spatial aliasing of the inversion procedure. By applying a mask operator to each row of the sensitivity matrix written in the wavelet domain, we may successfully distinguish well-resolved and poorly-resolved zones in our reconstruction.

Applying a mask does not increase the computational need as we perform a multiplication by zero or one for each term of the matrix. Defining the mask may be quite demanding although pre-tabulated masks should be designed for typical data acquisition configuration.

Wavelet decomposition allows different resolutions at different places in the model, as the traveltime tomography predicts. Once the Fréchet derivative is computed, we applied the M operator defined as follows. From the surface down to the depth of 800 m, wavelet coefficients are kept at all scales. From the depth of 800 m down to the bottom, only the fourth level of wavelet coef-
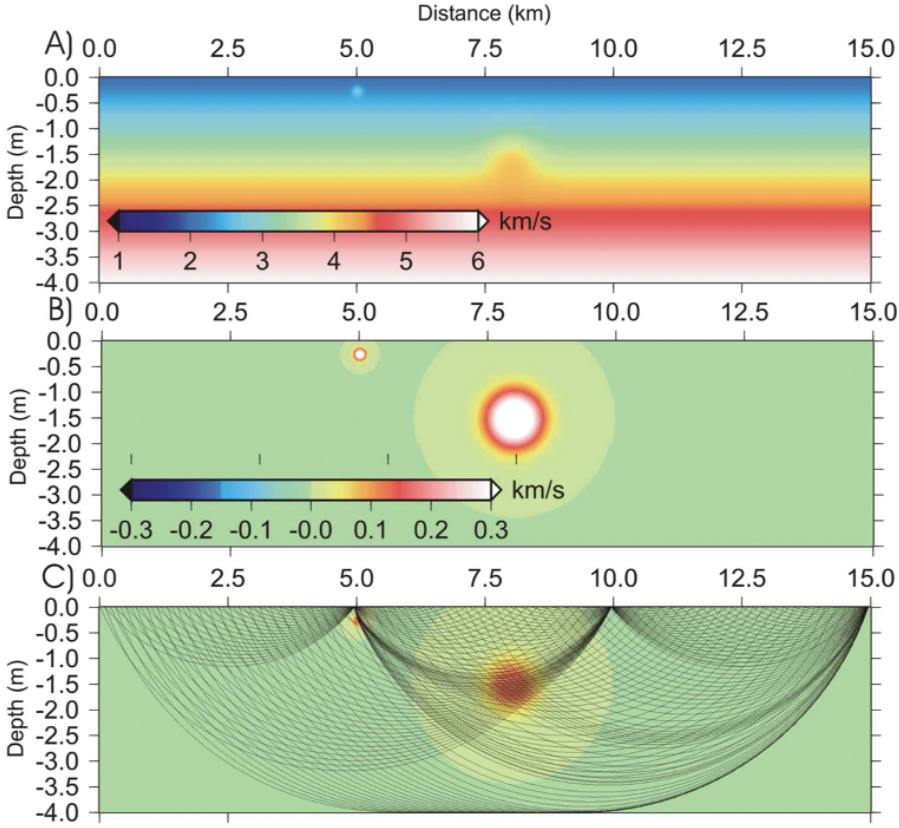
Fig. 5. The synthetic model with two circular anomalies of different sizes. Amplitude is 0.5 km/s in both cases.

ficients is kept, corresponding to a resolution of 400 m, coefficients of the finer other three scales are zeroed out. The inversion provides a reconstruction which varies in resolution as we move to deeper depths and the large heterogeneity is smoothly reconstructed while the small and shallow anomaly is well resolved (Figure 6). We have chosen the mask operator in order to separate zones of the two targets. This illustrates the local resolution with the wavelet decomposition: a high resolution in the shallow part and a broader resolution in depth.

We may conclude that wavelets enable us to adapt locally the resolution to the theoretical resolution of traveltime tomography. This adaptation is done with a multiplication between wavelet coefficients and the mask values, as the Fréchet derivative matrix is calculated in the wavelet domain. How to choose the mask operator is a problem we face? We have suggested a solution through the estimation of the resolution matrix and we have illustrated that we can apply a priori selection with depth, for example.
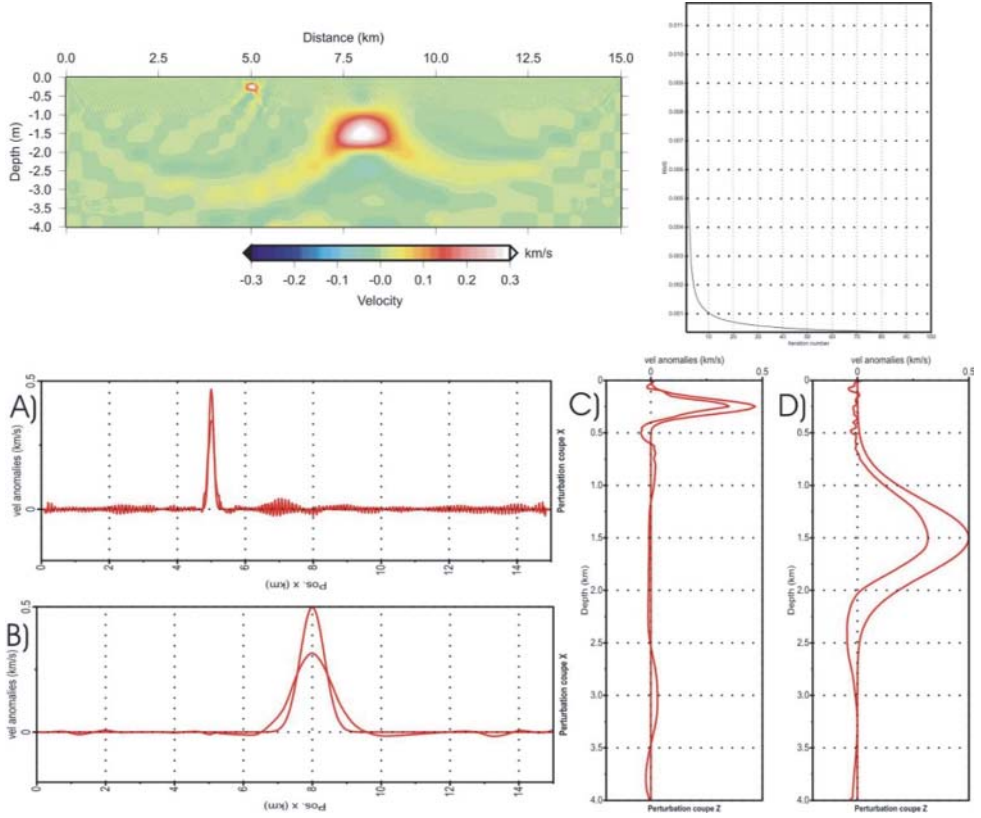
Fig. 6. Reconstruction using wavelets with four vanishing moments and four levels : a mask ensures that, under the depth of 800 m, the fourth level of wavelengths is the only one kept inside the inversion with an expected resolution of 400 m.

CONCLUSION

Seismic tomography of first-arrival delayed times could be performed using a wavelet decomposition of the model space. By doing so, one is able to control locally the expected resolution of the inversion. Using the linearized procedure does not automatically inject slowness anomalies at the appropriate scale as the resolution varies during the linearized iterations. Consequently, one must introduce an additional operator in order to prevent spatial aliasing which could lock the inversion procedure. The introduction of a binary operator over scale grids will forbid wavelet coefficients perturbation at a scale when we do not expect resolution. This operator M is a local operator: it will allow us reconstruction of various features as detailed ones nearby the free surface simultaneously with coarse ones at depth for surface-surface geometries. An illustration on a synthetic cross-well experiment should give similar features.

Improvement of data misfits is not significant and may be quite below the noise level which leaves us without clear quality control criterion. We are left with a strategy based on the model space representation and the wavelet decomposition leads to similar results as a local covariance analysis.

Extension to 3D configuration should be performed and combining this wavelet decomposition and the finite frequency tomography (Montelli et al., 2004) will certainly improve in the future local resolution of seismic imaging before tackling amplitude analysis of seismic traces (Pratt et al., 1998, Operto et al., 2006).

REFERENCES

Aki, K. & Lee, W., 1976. Determination of three-dimentional velocity anomalies under a seismic array using first P-arrival times from local earthquakes, J. Geophys. Res., 81, 4,381-4,399.

Benz, H. M., Chouet, S. A., Dawson, P. B., Lahr, J. C., Page, R. A., & Hole, J. A., 1996. Three-dimentional P and S wave velocity structure of Redoubt Volcano, Alaska, J. Geophys. Res., 101, 8111-8128.

Bohm, G., Galuppo, P., & Vesnaver, A., 2000. 3d adaptative tomography using delauney triangles and voronoï polygons, Geop. Prosp., 48, 723-744.

Chiao, L.-Y. & Kuo, B.-Y., 2001. Multiscale seismic tomography, Geophys. J. Int., 145, 517-527.

Chiao, L.-Y. & Liang, W.-T., 2003. Multiresolution parametrization for geophysical inverse problems, Geophysics, 68, 199-209.

Dahlen, F., 2004. Resolution limit of traveltime tomography, Geophys. J. Int., 157, 315-331.

Daubechie, I., Grossmann, A., & Meyer, Y., 1986. Painless nonorthogonal expansions, J. Math Phys., 27, 1271-1283.

Daubechies, I., 1988. Orthonormal bases of compactly supported wavelets, Comm. Pure Appl. Math., 41, 909-996.

Delprat-Jannaud, F. & Lailly, P., 1993. Ill posed and well posed formulation of the reflection traveltime tomography problem, J. Geophys. Res., 98, 6589-6605.

Delost, M., Virieux, J. and Operto, S., 2007. Multi-scale decomposition of velocity structure; application to first-arrival travel-time tomography, submitted to Geophysical Prospecting.

Farra, V. & Madariaga, R., 1988. Non-linear reflection tomography, Geophysical Journal , 95, 135-147.

Grossmann, A. & J.Morlet, 1984. Decomposition of hardy functions into square integrable wavelets of constant shape, SIAM, J. Math. Anal., 15, 723-736.

Hole, J. A., 1992. Nonlinear high-resolution three-dimensional seismic travel time tomography, J. Geophys. Res., 97, 6553-6562.

Latorre D., Virieux J., Monfret T., Monteiller V., Vanorio T., Got J.-L. and Lyon-Caen H. 2004b. A new seismic tomography of Aigion area (Gulf of Corinth, Greece) from the 1991 data set. Geophysical Journal International, 159, 1013-1031.

Madych, W., 1999. Tomography, approximate reconstruction, and continuous wavelet transforms, Applied and computational harmonic analysis, 7, 54-100.

Menke, W., 1984. Geophysical Data Analysis: Discrete Inverse Theory, Academic Press, Inc., Orlando, USA.

Michelini, A., 1995. An adaptative-grid formalism for traveltime tomography, Geophys. J. Int., 121, 489-510.

Monteiller V., Got J.-L., Virieux J. and Okubo P. 2005. An efficient algorithm for double-difference tomography and location in heterogeneous media, with an application to the Kilauea volcano. Journal of Geophysical Research 110, B12306, doi:10.1029/2004JB003466.

Montelli, R., Nolet, G., Masters, G., Dahlen, F. and Hung, S.-H., 2004, Global PP and PP traveltime tomography; rays versus waves, Geophys. J. Int., 158, 637-654.

Nolet, G. and Montelli, R. and Virieux, J., 1999. Explicite approximate expressions for the resolution and a posteriori covariance of massive tomographic systems, Geophys. J. Int., 138, 36-44.

Paige, C.C and Saunders, M.A., 1982. LSQR: an algorithm for sparse linear equations and sparse least squares. ACM Trans. Math. Software, 8, 43-71.

Podvin, P., and I. Lecomte (1991), Finite difference computation of traveltimes in very contrasted velocity models: A massively parallel approach and its associated tools, Geophys. J. Int., 105, 271- 284.

Operto, S., Virieux, J., Dessa, J. X., and Pascal, G. (2006). Crustal imaging from multifold ocean bottom seismometers data by frequency-domain full-waveform tomography: application to the eastern nankai trough. Journal of Geophysical Research, 111(B09306):doi:10.1029/2005JB003835.

Pratt, R. G., Shin, C., and Hicks, G. J. (1998). Gauss-newton and full newton methods in frequency-space seismic waveform inversion. Geophys. J. Int., 133:341-362.

Spakman, W. & Bijwaard, H., 1998. Irregular cell parametrization of tomographic problems, Ann. Geophys., 16, 28.

Spakman, W. & Nolet, G., 1988. Imaging algorithms, accuracy and resolution, in Mathematical geophysics, edited by N. Vlaar, pp. 155-187, D. Reidel Publ. Co., Dordrecht, Netherlands.

Spakman, W., Bijwaard, H., & Engdahl, E., 1998. Closing the gap between regional and global travel time tomography, J. Geophys. Res., 103, 30055-30078.

Sweldens, W., 1994. The lifting scheme, a custom design construction of biorthogonal wavelets, Tech. rep., Technical Report 1994:7, Indust. Math. Init., Dep. of Math., Univ. South Carol.

Sweldens, W., 1997. The lifting scheme, a construction of second generation wavelets, SIAM J. Math. Anal., 29, 511-546.

Sweldens, W. & Schröder, P., 1995. Buidling your own wavelets at home, Tech. rep., Technical Report 1995:5, Indust. Math. Init., Dep. of Math., Univ. South Carol.

Tarantola, A. & Valette, B., 1982. Generalized nonlinear inverse problems solved using the least square criterion, Reviews of Geophys. and Space Phys., 20, 219-232.

Tarantola, A., 2004. Inverse Problem Theory and Methods for Model Parameter Estimation, SIAM, Philadelphia.

Tikhonov, A. & Arsenin, V., 1977. Solution of ill-posed problems, Winston, Washington, DC.

Trinks, I., Singh, S., Chapman, C., Barton, P., Bosch, M., & Cherrett, A., 2005. Adaptative traveltime tomography of densely sampled seismic data, Geophys. J. Int., 160, 925-938.

Zelt, C. & Smith, R. B., 1992. Seismic traveltime inversion for 2-D crustal velocity structure, Geophys. J. Int., 108, 16-34.

Zhang, H. & Thurber, C., 2005. Adaptative mesh seismic tomography based on tetrahedral and voronoi diagrams: application to parkfield, california, J. Geophys. Res., 110, B04303,doi:10.1029/2004JB003186.

Zhang, J., ten Brink, U., & Toksöz, M., 1998. Nonlinear refraction and reflection travel time tomography, J. Geophys. Res., 103, 29743-29757.

Zhou, H., 2003. Multiscale traveltime tomography, Geophysics, 68, 1639-1649. 24.

An EGF technique to infer the rupture velocity history of a small earthquake: a possible solution to the tradeoff among Q and source parameters

M. Filippucci[1], S. de Lorenzo[1], E. Boschi[2]

[1] *Università di Bari, Italy*

[2] *Istituto Nazionale Geofisica e Vulcanologia, Italy*

INTRODUCTION

Classically, the Empirical Green's Function (*EGF*) technique consists of isolating the source-time function of a large event by dividing its spectrum by the spectrum of a smaller event, used as *EGF*. Both the events must have approximately the same location and the same focal mechanism. It is well known that the spectral deconvolution is an unstable process and, in the attempt to stabilize the solution, many methods have been developed (Clayton and Wiggins, 1976; Deichmann, 1999; Vallée 2004). In order to allow the positivity constraint of the source time function, Zollo et al. (1995) proposed a different approach to the *EGF* technique for the retrieval of the source function of the *MAIN*. The method allows the imposition of the physical constraint of positivity of the source. The inversion was performed by minimizing a misfit function between the observed and the computed seismograms in the frequency domain. Courboulex et al. (1996) proposed a time domain inversion technique to recover positive and stable source time function. These two methods are aimed to recover the slip distribution on the fault plane.

At the present, not a lot has been done yet in the attempt of inverting the rupture velocity with the aim of retrieving the rupture velocity history of a small earthquake. In this report, an *EGF* technique in the time domain method based on the first cycle *P* waveform data to infer the rupture velocity history is presented.

THE TECHNIQUE

Sato (1994) analyzed the wave field emanating from a circular crack growing at variable rupture velocity. He obtained the following expression of the the apparent moment-rate function (AMRF):

$$\dot{M}_c(\tau) = \frac{12}{7}\Delta\sigma_s\frac{c}{sen\theta}\Big[L_a^2(\tau) - L_b^2(\tau)\Big] \tag{1}$$

where c is the phase velocity of the observed wave, θ is the take-off angle, $L_a(\tau)$ is the distance between the centre of the fault and the point of the isochrone that is nearest to the observer and $L_b(\tau)$ is the distance between the centre of the fault and the point of the isochrone that is further from the observer. Deichmann (1997) rewrote the equation of the Sato (1994) *AMRF* considering a time dependent rupture velocity, which is expressed by a power law with an exponent q for the acceleration stage. He assumed that the rupture velocity history consists of three stages and introducing a power law with an exponent q for the acceleration stage:

$$Vr(t) = \begin{cases} p_1 t^q; & (0 \le t \le t_1) \\ Vr_{max}; & (t_1 \le t \le t_2) \\ Vr_{max} - p_2(t-t_2); & (t_2 \le t \le T) \end{cases} \qquad p_1 = \frac{Vr_{max}}{t_1^q}, \quad p_2 = \frac{Vr_{max}}{(T-t_2)} \tag{2}$$

where q specifies the rate of the rupture velocity increase with time. In the first stage (acceleration stage), the rupture accelerates until the rupture velocity reaches its maximum value Vr_{max} at the time t_1; in the second stage (the propagation stage), the rupture expands with constant velocity equal to the maximum from the time t_1 to t_2; in the third stage (the deceleration stage), it decelerates with a constant rate until it stops at a final circular perimeter having radius L at the time T (the total duration of the rupture process. To reduce the number of unknowns, we assumed a linear dependence of rupture velocity vs. time, $(q=1)$ (Figure 1).

To built the *AMRF*, we need to know seven source parameters: the final rupture dimension L, the average rupture velocity Vr_{ave}, the time duration of the
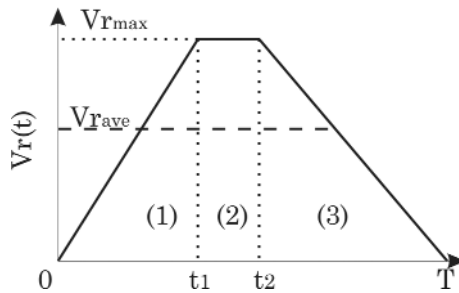
Fig. 1. The three stage rupture velocity history (see the text for explanation).

acceleration phase t_1, the time initiation of the deceleration phase t_2 the static stress drop $\Delta\sigma$, the take off angle θ and the body wave velocity at the source c. Since it is assumed that the velocity model and the fault plane orientation are known from other observations, senθ and c are assumed known and the number of unknowns reduces to five.

Let us consider two seismic events having different magnitudes, same focal mechanism and being recorded at the same seismic station. Let the greatest magnitude event be indicated with MAIN and its seismic recording be U^{obs} . Let us assume that the smaller event and the *MAIN* occur approximately in the same source region and that the source time function of the smaller event is a Dirac's delta function. Under these hypotheses, the smaller event can be treated as the Empirical Green's Function (*EGF*). Therefore, the seismogram of the *MAIN* can be written as the time convolution of the *EGF* with a true and unknown *AMRF*:

$$U^{obs} = AMRF(\vec{m}^{true}) * EGF \tag{3}$$

where $(\vec{m}^{true}) = (L, Vr_{ave}, t_1/T, t_2/T, \Delta\sigma)$ is the true and unknown source parameter vector. Equation (3) is non-linear in the model parameters. So, in order to estimate the model parameters, a non-linear inversion scheme has been used. The data in the inversion problem are θ and the points of the waveform of first cycle of the *P* wave of the *MAIN* (U^{obs}). In the inversion procedure, an estimate of the ground motion of the MAIN, U^{est}, can be computed by carrying out the time convolution of the *EGF* with the $AMRF(\vec{m}^{est})$:

$$U^{est} = AMRF(\vec{m}^{est}) * EGF \tag{4}$$

where $AMRF(\vec{m}^{est})$ is the *AMRF* evaluated in a given point $\vec{m}^{est}$ of the model parameter space and can be compared with the observed ground motion of the *MAIN* U^{obs}. The semblance operator s (Telford et al., 1990) was used to quantify the degree of similarity between the estimated and the observed ground motion. The purpose of the inversion is to find the point $\vec{m}^{best}$, in the model parameter space, which minimizes 1-s. To perform an exhaustive search of the best-fit model parameters, a numerical code based on the use of the Simplex Downhill method has been implemented. To overcome the problem of local minima, following Zollo and de Lorenzo (2001), the model parameter space has been subdivided in many different subspaces, each of them being characterized by fixed constraints on the source parameters. Twenty-seven local inversions are then performed (one in each subspace). The result of the inversion is the absolute minimum $(1-s)_{min}$ among the twenty-seven local minima. We computed the error on the semblance due to the noise on the seismograms and to the error on θ and mapped it in the model parameter space. The error due to the noise on the seismograms of the *MAIN* is calculated in L_1 norm by averaging the absolute amplitudes on a time interval T_1 before the

P wave arrival. The error on the estimated seismogram due to the error on the takeoff angle, $(\Delta U^{est})_\theta$, is computed in L_1 norm on the time interval T_s (i.e. the interval where the inversion is computed, that is the first cycle of the *P* wave) by averaging the amplitudes of the estimated seismogram of the *MAIN* obtained varying the takeoff angle θ into its error bar. The error on the take off angle θ is evaluated considering both the error on the localization of the event and the error on the fault plane orientation estimate (i.e. the fault dip and the fault strike estimates). Δs is computed in the point $\vec{m}^{best}$ of the model parameter space and it is then mapped in the model parameter space to estimate the error $\Delta\vec{m}^{best}$ on the best-fit model parameters. All the model parameter vectors, which satisfy the following criterion:

$$1-s \leq (1-s)_{min} + \Delta s$$

must be considered as acceptable solutions. This criterion will be referred to as the "*criterion of acceptability*".

TESTING THE EGF TECHNIQUE ON SYNTHETIC SEISMOGRAMS

In this section, we summarize the results of synthetic tests on synthetic data. The aim was to understand the reliability of the inversion in retrieving the source parameters. To this purpose the Green's function was computed for a 1D layered anelastic structure, using the DWN technique (Bouchon, 1979). The *EGF* is computed by the numerical convolution of the same Green's function with a ramp-like source time function with an assigned rise time at the source ($\tau_{0,EGF}$). First, we investigated the effect of the finite frequency content of the EGF. Theoretically, the *EGF* represents the ideal Green's function only if its source function coincides with a Dirac's delta function. In real cases, the source of the *EGF* differ from a Dirac's function either for non null time duration of the pulse at the source and for non infinite amplitude of the pulse itself. Several synthetic tests have been carried out to investigate this aspect. As an example, a synthetic test is in Figure 2 considering seven synthetic *EGF* varying the $\tau_{0,EGF}$ from 5 ms to 35 ms. The total pulse width of the EGF (the time interval between the onset of the P wave and its second zero crossing time, Zollo and de Lorenzo, 2001) ΔT_{EGF}, ranges from 70 ms to 110 ms while the pulse width of the *MAIN* is ΔT_{MAIN}~180 ms. The matching between observed and retrieved synthetic seismograms, indicate that the best fit result corresponds to the *EGF* having the lowest $\tau_{0,EGF}$, while the worst fit is obtained by using the *EGF* having the highest $\tau_{0,EGF}$. The different quality of the fit is recognizable looking at the initial rise of the *P* pulse (Figure 2d). It is worth to note that, increasing $\tau_{0,EGF}$, the fit of the rise part of the *P* pulse tends to be lost. Let us consider now the retrieved source parameters. Increasing $\tau_{0,EGF}$, all the parameters remain stable while the parameter t_1/T
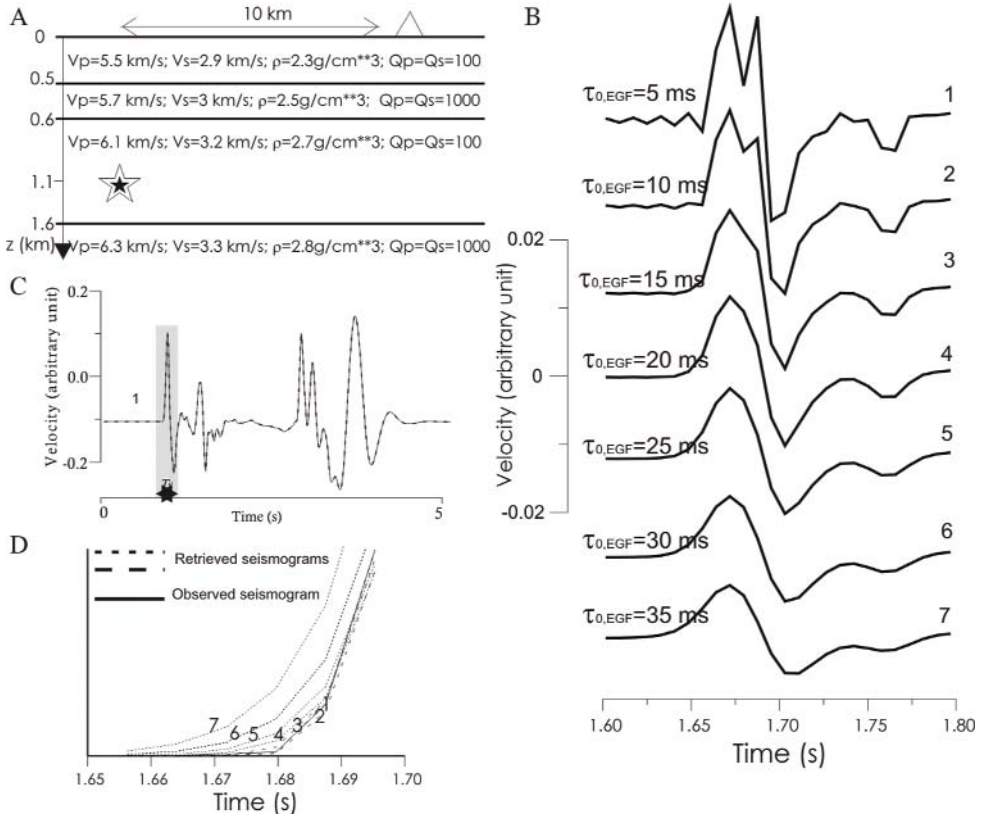
Fig. 2. Test on the frequency content of the EGF. **(a)** Crustal model used in the synthetic test; stars indicate the hypocenter of the MAIN (white) and of the EGF (black); the triangle represents the position of the recording station. **(b)** Vertical components of seven EGF with different $\tau_{0,EGF}$. **(c)** Matching between the observed vertical seismogram of the MAIN (solid line) and the retrieved one (dashed line). The last is computed by using the EGF with the shortest rise time ($\tau_{0,EGF}$ = 5 ms); Ts represents the time interval used in the inversion. **(d)** Comparison between the initial rise of the P wave on the observed and the retrieved seismograms, different numbers refer to different EGF used in the simulations and shown in **(b)**.

shows a great variation moving away from the true value. If we consider as acceptable only the solutions with a maximum error on the source parameters of 10%, we can deduce the following rule in selecting the *EGF*:

$$\left(\frac{\Delta T_{MAIN}}{\Delta T_{EGF}} \right)_{min} \cong 2$$

The second point we investigated was the intrinsic error due to the inversion procedure. To this aim we carried out about 200 inversions varying the earth model and the source parameters. The best resolved parameter is represented

by the source radius L (the average percentage absolute error is 0.5% and the maximum percentage absolute error is 5%) together with Vr_{ave}/Vs (the average percentage error is equal to 1.1 % and the maximum error is 10%). Since t_1/T and t_2/T are portions of the total duration of the rupture process T, errors on t_1/T and t_2/T are expressed as fractions of T. The inferred average error is $0.04 \cdot T$ on t_1/T and $0.01 \cdot T$ on t_2/T respectively, with a maximum expected error of $0.03 \cdot T$ on t_1/T and $0.1 \cdot T$ on t_2/T

To test the effect of noise, many synthetic tests were carried out for different signal S to noise N ratio. We estimated the model parameters using the random deviates. The major difficulty was to retrieve the parameter t_1/T. This parameter starts to move away from the true value with increasing the $(N/S)_{MAIN}$. We deduced that (N/S) ratio has to be less than 5% to obtain stable estimates of the source parameters.

Another kind of tests concerned the effect of a different localization and focal mechanism of the Main and the EGF. The two hypocenters could be slightly different, meaning that the radiation coming from the *EGF* source region does not exactly travel the same path to the receiver than the radiation coming
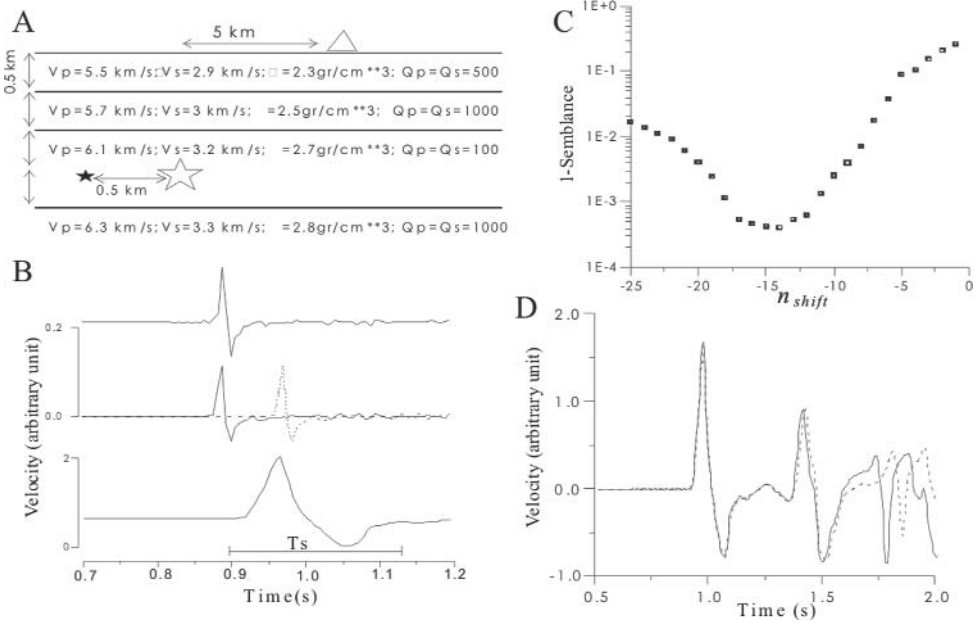
Fig. 3. Testing the effect of a different epicentre of the MAIN and of the EGF. **(a)** The crustal model used together with the positions of the MAIN (white star), of the EGF (black star) and the station (triangle). **(b)** Top: the seismogram of the ideal EGF, i.e. the EGF having the same hypocenter of the MAIN; middle: the true EGF before (solid line) and after (dashed line) the shift; bottom: the seismogram of the MAIN, with the indication of the time window *Ts* used to compute the semblance. **(c)** Plot of *1-s* vs. *n_{shift}*, i.e. the number of shifting points of the EGF. D: comparison between the vertical component of the observed (solid line) and of the best fit retrieved MAIN (dashed line).

from the source region of the *MAIN* (Courboulex et al., 1996). Under these conditions, not only the waveform of the *EGF* can be influenced by path effects, not included in the *MAIN*, but also the takeoff angle can be different for the *EGF* and the *MAIN*. Figure 3 summarizes this test for an horizontal difference in the hypocenters and for an epicenter distance from the receiver of 5 km. Since the inversion is carried out in the time domain, the problem consists in finding how much the EGF seismogram has to be shifted along the time axis to obtain the minimum value of 1-*s*. The procedure consists in running several inversions, by shifting the time window of the *EGF* relatively to the time window of the *MAIN*, step by step with a time step equal to the sampling time ΔT. It was found that, in correspondence of $(1-s)_{min}$ (Figure 3c), the best fit model parameters are the most reliable. Another test concerned the different vertical location of the Main and the EGF. We inferred that the parameters are usually well recovered for a model where the Vp velocity linearly increases with depth, whereas some difficulties occur for a layered media if one of the epicenters is located near a discontinuity. Another type of test concerned the effect of velocity model. We found that, independently on the complexity of the 1D velocity structure the parameters are always fully recovered (Figure 4).
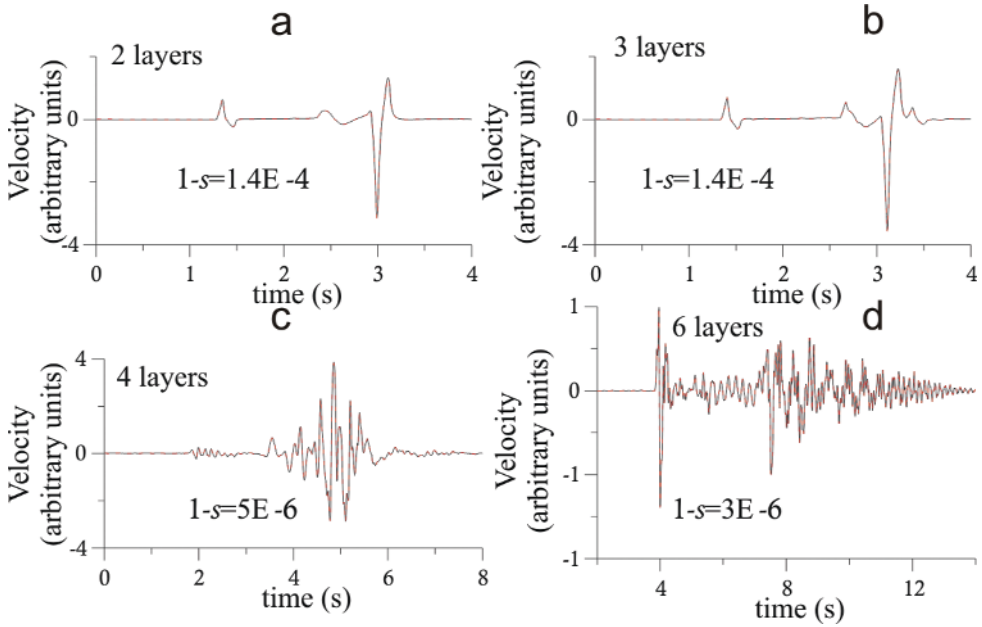
Fig. 4. Fit of synthetic "observed" and inverted seismograms for different Earth models. **(a)** Vertical component of the observed synthetic EGF with different noise to signal ratio (N/S)MAIN added. **(b)** **(c)** **(d)** Matching between the vertical component of the synthetic observed MAIN (solid line) and the MAIN (dashed line) retrieved from the inversion for different the noise to signal ratio (N/S)EGF and different values of t1/T. In the grey band there is the time window where the 1-s was computed.

TESTING THE EGF TECHNIQUE ON REAL SEISMOGRAMS

The most important point which needs to be investigated is the effect of using a real seismogram as EGF. To this end several trials have been made. Figure 5 summarizes an example. We used seismograms of an earthquake occurred in central Italy (Sellano, Umbria, 1997). To use real seismograms we have to account that the seismogram of the *EGF* will approximate a Green's function only for frequencies (below the corner frequency f_0) where the displacement amplitude spectrum is flat (e.g. Mueller, 1985). So once computed f_0, the seismograms of *EGF* and *MAIN* have been low-pass filtered with a cut-off frequency equal to the corner frequency f_0. The corner frequency of the EGF was estimated by fitting the *EGF* spectrum with a theoretical spectrum $S(\omega)$ computed by convolving a constant Q_p attenuation operator with a source model with a rate of decay at high frequency proportional to $\tilde{\omega}^2$ (Brune, 1970). We used Q_p=354 as inferred from Filippucci et al. (2006) for the Sellano area. We used the event 9711011946A as the Green's function of the Sellano crust (Figure 5). The synthetic *MAIN* (Figure 5) was built convolving this Green's function, recorded at three seismic stations (CANC, CMR and TREV), with a theoretical *AMRF*. In this synthetic test, to simulate the effect of a different location between the *MAIN* and the *EGF*, the waveforms of another event (9711012343A) were used in the inversion as *EGF* (Figure 6). Both the events have roughly the same fault plane orientation (Filippucci et al., 2006). The noise to signal ratio, $(N/S)_{EGF}$, of each component of the *EGF* at the three stations is computed in a time window of 0.5s before the onset of the *P* wave. The corner frequency of the *EGF* was estimated through the fitting of the EGF spectra to be $f_0 \sim 9$ Hz. The error on the take off angle was computed
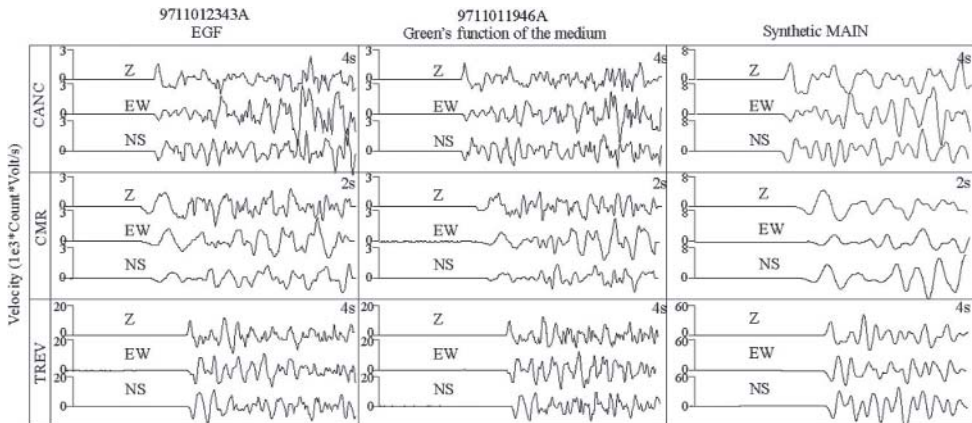
Fig. 5. Three component velocity seismograms of the events 9711011946A and 9711012343A recorded at the stations CANC, CMR and TREV. Left: three component velocity seismograms of the synthetic MAIN. On each rectangle the length of the time axis in seconds.
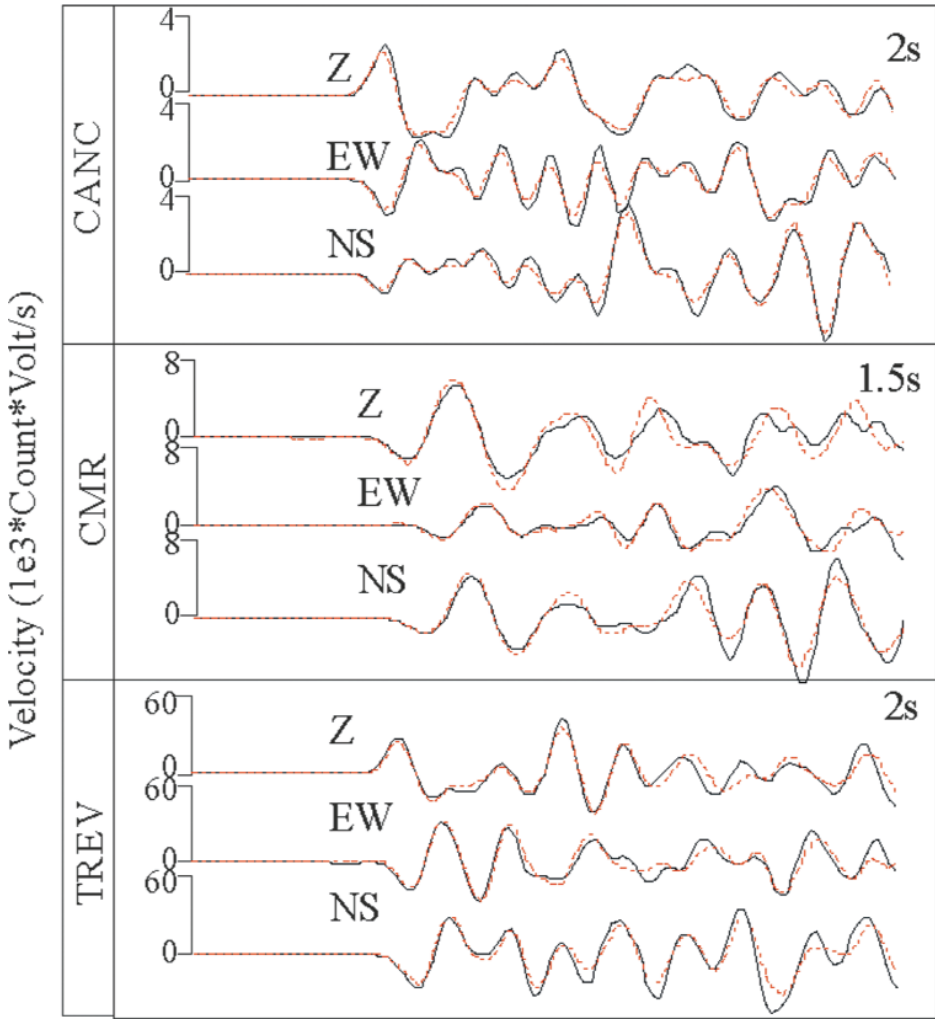
Fig. 6. Comparison between the three components of the synthetic observed waveforms of the MAIN (black solid line) with the waveform retrieved from the inversion in the best fit point (red dashed line) at the station CANC, CMR and TREV. On each rectangle the number represents the duration of the time window of the signal.

varying the hypocenter localization in a cube with side of 1 km, considered as the error on the localization of the event, and varying the fault dip δ and strike ϕ into their range of uncertainty ($\Delta\delta,\Delta\phi$) (Filippucci et al., 2006). We compared results of the inversions using single stations with the result of the joint inversion, using a corrected Akaike information criteria (Hurvich and Tsai 1995). Results are summarized in Table 1. The matching of the model to data is shown in Figure 6. The source parameters are fully recovered (Table 1).

Tab. 1. Selection of the best fit model for the test on real earthquakes.

	L(km)	t_1/T	t_2/T	Vr_{ave}/Vs	$\Delta\sigma$(bar)	$(1-s)_{min}\pm\Delta\sigma$	AICc	σ^2	N_{pti}
True	.35	.3	.7	.7	7				
CANC	0.29±0.1	0.50±0.49	0.92±0.07	0.61±0.01	19.7±16.5	6.5E-4±3E-5	-171.2	9.15E-3	39
CMR	0.36±0.06	0.42±0.31	0.73±0.15	0.74±0.10	6.9±5.4	6.1E-4±8E-5	-169.1	1.45E-1	93
TREV	0.48±0.08	0.40±0.23	0.51±0.23	0.92±0.05	3.8±1.8	1.4E-3±2E-4	-192.2	2.82E-2	57
JOINT	0.34±0.04	0.42±0.20	0.73±0.17	0.73±0.09	7.8±2.4	6.0E-3±1.1E-2	-316.6	1.77E-1	189

REFERENCES

Bouchon, M. (1979), J. Geophys. Res., 84(B7), 3609-3614.

Brune, J.N., (1970): J. Geophys. Res., 75, 4997-5009.

Clayton R. W. and R. A. Wiggins (1976), Geophys. J. R. Astron. Soc., 47, 151-177.

Corboulex, F., Virieux, J., Deschamps, A., Gibert, D., and A. Zollo (1996). Geophys. J. Int. 125, 768-780.

Deichmann, N. (1997) Bull. Seism. Soc. Am., 87, 1288-1296.

Filippucci, M., de Lorenzo, S. and E. boschi,2006, Geoph. J. Int. 166, (1): 322-338. DOI: 10.1111/J.1365-246X.2006.02998.X.

Hurvich, C. M. and C.-L. Tsai (1995), Biometrics, 51, 1077-1084.

Mueller, C. S. (1985), Geophys. Res. Lett., 12, 1, 33-36.

Sato, T. (1994), Bull. Seism. Soc. Am. 84, 4, 1199-1215.

Telford, W. M., Geldart, L. P., Sheriff, R. E., and D. A. Keys (1990), Applied Geophysics. 2nd Edn. Cambridge University Press, Cambridge.

Vallée, M. (2004), Bull. Seism. Soc. Am. 94, 2, 394-409.

Zollo, A. & S. de Lorenzo, 2001. J. Geophys. Res., 106 , 16287-16306.

Zollo, A., Capuano, P., and S. K. Sing (1995 Bull. Seism. Soc. Am., 85, 4, 1249-1256.

Fresnel or finite frequency approach

S. Gautier[1], G. Nolet[2], J. Virieux[3]

[1] *Géosciences Montpellier, Montpellier Cedex, France*

[2] *Department of Geosciences, University of Princeton, Princeton, NJ, USA*

[3] *Géosciences Azur, UMR 6526, Sophia Antipolis, Valbonne, France*

Abstract: In this paper we investigate finite-frequency effects in crustal tomography which might be useful for complex structures imaging as volcanoes or rifting zones. We developed a new inversion procedure based on an exact estimation of the sensitivity kernels. In this approach we compute the 3D travel-time sensitivity kernels by using (1) graph theory and an additional bending to estimate accurately both rays and travel-times between source/receiver and diffraction points and (2) paraxial ray theory to estimate the amplitude along theses rays. We invert both the velocity and the hypocenter parameters, using these so-called banana-doughnut kernels and the LSQR iterative solver. We compare the ray-theoretical and the finite-frequency tomography to image intermediate structures beneath the Gulf of Corinth (Greece), which has long been recognised as the most active continental rifting zone in the Mediterranean region. Our dataset consists of 451 local events with 9233 P- first-arrival times recorded in the western part of the Gulf (Aigion area) in the framework of the 3F-Corinth European project. Previous tomographic images showed a complex velocity crustal model and a low-dip surface that may accommodate the deformation. Accurate velocity models will help for better constraining the rifting process which is still a subject of debate. The main results of this study show that finite-frequency improve crustal tomographic images by providing better resolved images of the 3D complicated velocity structure. Because the kernels spread the information over a volume, finite-frequency tomography results in a sharpening of layer boundaries as we observed for the shallower part of the crust (down to 5 km depth) beneath the Gulf of Corinth.. Extensions to volcanic area will be possible in the future with dense passive seismic networks.

INTRODUCTION

Most seismic tomography experiments rely on the assumptions of classical ray theory. This approach is known to be an infinite-frequency approximation assuming that travel-time residuals are only influenced by velocity perturbations located along the ray path. Recent theoretical studies show that for realistic frequencies, seismic waves are in fact predominantly sensitive to structu-

re away from the ray path, within a volume known as the Fresnel zone, and that observed delay times are affected by wave front healing (Wielandt, 1987; Marquering et al., 1999; Hung et al., 2000; Zhao et al., 2000; Dahlen et al., 2000; Hung et al., 2001). These pioneering studies emphasize the limitations of the ray-based inversions, which break down whenever the size of heterogeneities becomes too small, and motivated the development of finite-frequency inversions (Montelli et al., 2004; Zhou et al., 2004). By accounting for the effects of scattered, off-path seismic wave propagation, the finite-frequency approach is a better forward theory, which may provide higher resolved tomographic images.

Several studies present comparisons of ray-theoretical and finite-frequency tomography in order to explore whether the sensitivity kernels provide a significant improvement of the images. Montelli et al. (2004) used the finite-frequency theory proposed by Dahlen et al. (2000) in global P and PP tomography. They report that, depending on depth and size, the amplitudes of the velocity perturbations in the finite-frequency tomographic images are 30-50% larger than in the corresponding geometric-ray images. Hung et al. (2004) show that finite-frequency tomography based on teleseismic data improves the resolution of the velocity models of the upper mantle beneath Iceland. Moreover Yang et al. (2006) find that, with a dense network, finite-frequency tomography provides 3D and high-resolved images of both the Azores hotspot and the nearby Mid-Atlantic Ridge. Despite these results, the beneficial effect of the sensitivity kernels on the tomographic mantle images, in particular for plumes identification, is currently strongly debated (De Hoop & Van der Hilst, 2005; Dahlen & Nolet, 2005; Van der Hilst & De Hoop, 2005). One objection raised by De Hoop and Van der Hilst is that finite-frequency kernels computed for simple, layered, background models have little validity once the model is three-dimensional, and ray trajectories exhibit caustics with infinities in seismic amplitudes. Since, in this paper, we trace rays directly in the 3D crustal model and repeat the computation of finite frequency kernels as the model evolves in subsequent iterations, we are in a direct position to verify the validity of this objection.

Sensitivity kernels for surface-wave travel-times at finite-frequency have been proposed by many authors (Spetzler et al., 2002; Yoshizawa & Kennett, 2002; Zhou et al., 2004; Tape et al., 2007). Results obtained both at global and regional scales do not enable us to assess the improvement of the finite-frequency images. Yoshizawa & Kennett (2004) and Zhou et al. (2005) report enhanced tomographic models whereas Sieminski et al. (2004), Levshin et al. (2005) and Trampert & Spetzler (2006) argue that ray theory can produce the same models with a good physically-based regularization, an appropriate damping parameter, a dense path ray coverage and in the presence of noise. While surfaces waves are dispersive, body waves are not and a specific investigation of how well the finite-frequency tomography will perform for body waves should be performed. This is the goal of this paper.

Here we investigate the finite-frequency effects in crustal compressional waves tomography by using the approach proposed by Dahlen et al. (2000). So far, the theory has only been considered for smooth global models. In this paper we present a new algorithm to compute accurate sensitivity kernels in a 3D complicated crustal environment. We compare the P-velocity models based on conventional ray theory with those resulting from a finite-frequency inversion and discuss the improvement of the tomographic images.

METHODOLOGY

We use a delayed travel-time tomography method to invert simultaneously the velocity distribution and the hypocenter parameters (Aki & Lee, 1976; Spakman & Nolet, 1988; Benz et al., 1996; Spencer and Gubbins, 1980; Thurber, 1992). A comprehensive description of the ray-theoretical approach and its linearized iterative scheme is given by Latorre et al. (2004) and Gautier et al. (2006). For finite-frequency inversion we introduce the estimation of the sensitivity kernels in the iterative scheme of this 3D tomography method. Contrary to finite-frequency procedures used at global scale (Dahlen et al., 2000; Montelli et al., 2004), no paraxial approximation of both travel-times and amplitudes between sources/receivers and diffracting points is used in the computation of the kernels. This significantly increases the computational effort, by at least a factor 10 for the CPU time, with respect to the ray method. In this formulation, we consider three different grids: the inversion grid, the intermediate grid and a fine grid. The inversion grid is where we want to update slowness quantities. The intermediate grid which we call ray grid is for storing raytracing results as travel-times or amplitudes. These quantities should behave smoothly at that grid scale. The fine grid, called kernel grid, will be employed for the computation and integration of sensitivity kernels. Informations on this fine grid are not stored at any time of the tomographic procedure.

Ray tracing is performed for each iteration of the linearized approach: we use graph theory (Moser, 1991) for computing rays from a source or a receiver to every node of the ray grid. This means that we simultaneously optimize the travel time from one source to all other nodes in the model. In a next step, the rays, which in the graph theoretical algorithm are force to follow straight paths between nodes, are bent to minimum travel-time. We apply paraxial theory (Virieux & Farra, 1991) along the bent ray for the estimation of the geometrical spreading and Maslov index. Since graph theory results in absolute first-arrival times, Maslov index is expected to be zero, unless the ray bending has moved it away from the absolute minimum travel time. Such excursions are rare as we have noticed in our computational experiments. Travel-time sensitivity kernels are computed by interpolating on the kernel grid the fields of travel-time and geometrical spreading estimated on nodes of the ray grid and by

combining them. As shown in Figure 1, in a 3D complex environment, the method provides a "banana-doughnut" shape with no sensitivity to velocity perturbation close to the geometrical ray. This picture also indicates that, in a 3D complicated structure, sensitivity is not uniformly distributed. In particular, we may notice a strong decrease of the sensitivity below 8 km depth where previous tomographic studies point out a high velocity gradient.

Partial derivatives, both for slowness field and for hypocenter parameters, are evaluated on nodes of the inversion grid. Partial derivatives for slowness field are computed by using the approach proposed by Dahlen et al. (2000). In order to eliminate problems in the estimation of the sensitivity kernels near singularities, we exclude a region with a specific radius R around the source and the receiver from the partial derivatives estimation. Here R is defined as R=0.5λ with λ the wavelength corresponding to the considered finite-frequency f and estimated respectively at the source and at the receiver location. Tests for different values of R, from R=0 to R=2λ, indicate that this limit is well-adapted to crustal tomography and has negligible impacts.
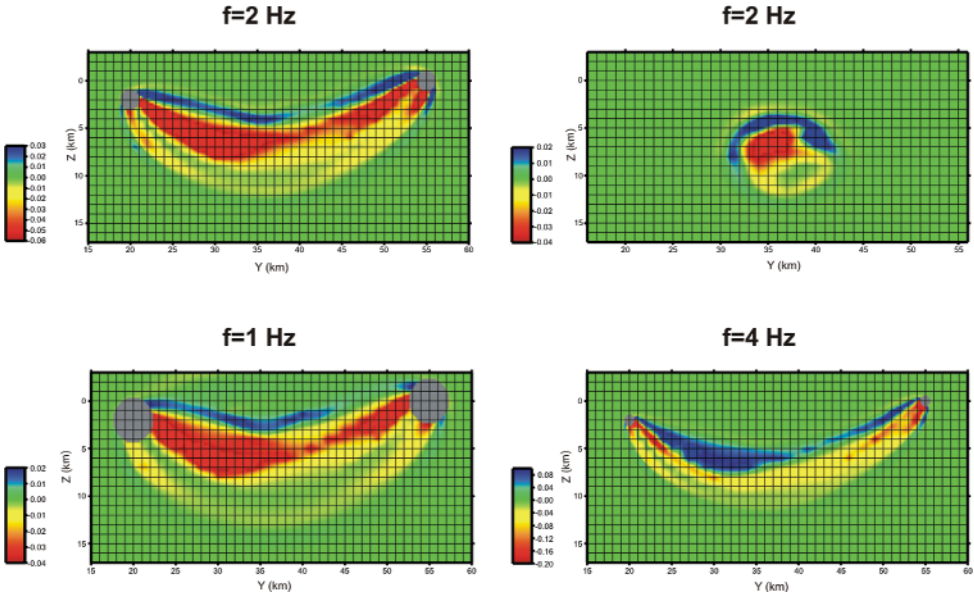
Fig. 1. One example of travel-time sensitivity kernel derived from a 3D complicated structure, the finite-frequency crustal velocity model beneath the western part of the Gulf of Corinth. Top: we find a S-N section (on the left) and a W-E section (on the right) of the travel-time sensitivity kernel computed using a Gaussian spectrum around 2 Hz. Bottom: S-N sections computed using Gaussian spectrum around 1 Hz (on the left) and 4 Hz (on the right). The grey circle represents the region with a specific radius R around the source and the receiver which is neglected in the estimation of the partial derivatives.

As proposed by some authors (Spakman & Nolet, 1988, Le Meur et al., 1997), normalization or scaling of the derivative matrix is performed for better reconstruction of the different parameters. This operation will remove influences of parameter units and also will take into account the sensitivity of the data to each class of parameters. Residual weighting of the dataset is also used in our tomography to eliminate the outliers. Finally, the scaled and weighted linear system is solved by means of the LSQR method (Paige & Saunders, 1982) and both the velocity models and the hypocenter parameters are updated.

APPLICATION TO THE WESTERN PART OF THE CORINTH RIFT

Study region

The study region is located in the Aegean area. In this paper, we focus on the western part of the Gulf of Corinth (Figure 2) which is the southernmost of a series of active grabens that discontinuously link the western part of the North Anatolian fault to the Hellenic subduction zone (Briole et al., 2000; Armijo et al., 1996; Tiberi et al., 2001). The Gulf of Corinth presents a 3D complicated crustal environment in a geological, tectonic and geodynamic point of view.

The Gulf of Corinth, which separates the Peloponnesus from the continental Greece, is a 110 km-long, N120°E oriented asymmetrical graben, bounded by quaternary E-W normal faults (Armijo et al., 1996). The current extension rate varies, decreasing from 16 mm.yr^{-1} in the West to 11 mm.yr^{-1} in the East (Avallone et al., 2004). Despite some variations, the direction of extension is on average approximately N-S. The most active faults crop out on the southern uplifted side of the gulf whereas some smaller antithetic faults can be found on the northern subsided coast.

The Corinth rift cuts obliquely across the NNW-SSE-trending fabric of the Hellenic mountain belt (Jacobshagen et al., 1978). Orogenic building leaves a complex lithologic structure resulting in heterogeneous stack of Mesozoic nappes (Aubouin et al., 1962; Doutsos & Poulimenos, 1992). In our area of study, the Pindos and the Gavrovo-Tripolitza series correspond to the shallowest units. They consist respectively of 3.5 km-thick deep-water carbonates and about 2.5 km-thick carbonate platform sediments. Below these nappes, a metamorphic unit called the Phyllite series, composed of an alternation of quartzites, phyllites and schists, is likely be encountered (Jacobshagen et al., 1978; Dornsiepen et al., 2001). Finally, field observations point out a 1 km-thick synrift sedimentary sequence in north Peloponnesus (Doutsos & Poulimenos, 1992; Flotté & Sorel, 2001) and at the east of the study region, the synrift sediment basin beneath the gulf reaches depth of 2.5 km (Sachpazi et al., 2003).

In the western part of the gulf, the microseismicity is mainly distributed along a sub-horizontal north-dipping trend, located at about 6-12 km depth (Rigo et

Ray theoretical
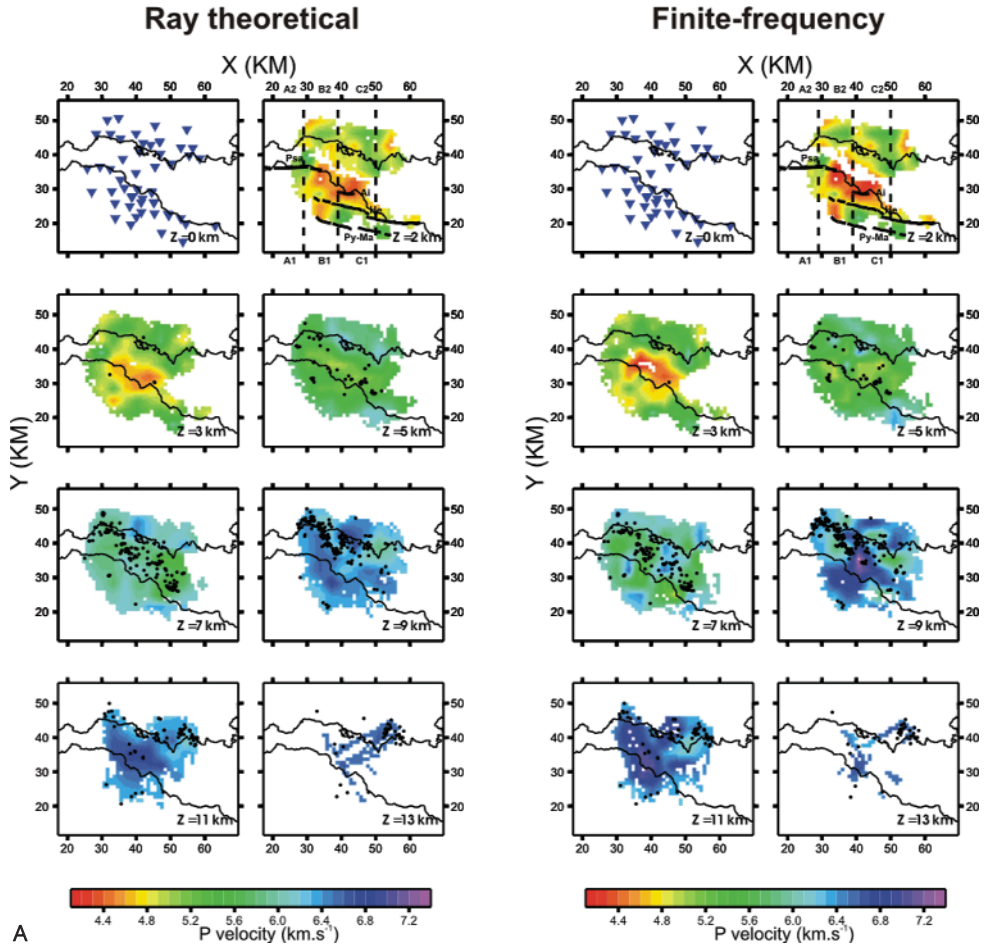
Finite-frequency

Fig. 2. (a) Presentation of the final tomographic results on map views at different depths ranging from 0 km to 13 km. The ray-theoretical images are represented on the left side and the finite frequency model on the right side. Distances are represented in the X-Y coordinate system derived from the Universal Transverse Mercator (UTM) projection (zone 34) and a local origin point (longitude=21.6°E and latitude=38°N) is used for plotting presentation. Events located in a range of 1 km around each layer are displayed (dark dots). Stations are plotted on the first section (blue triangle) whereas the major faults are drawn on the second map. Cells with no ray coverage have been masked. The colour scale indicates the absolute velocity from the lowest value in red to the highest value in blue. **(b)** Western Gulf of Corinth and the dense seismic network.
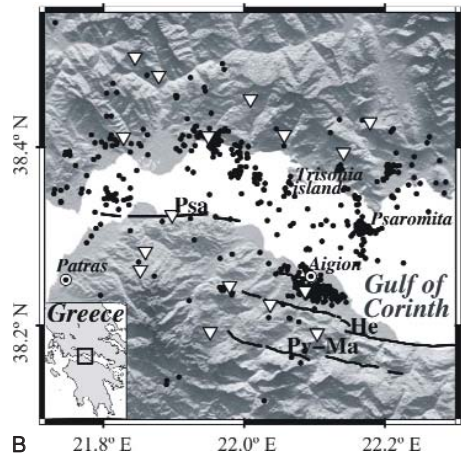
al., 1996; Latorre et al., 2004; Lyon-Caen et al., 2004). Rigo et al. (1996) interpret the seismogenic zone as a north-dipping detachment structure that could accommodate the deformation in this area. Fault plane solutions, indicating the presence of an active low-angle dipping structure at depth, are consistent with this tectonic model (Rietbrock et al., 1996; Bernard et al., 1997). Hatzfeld et al. (2000) proposed an alternative model suggesting the rise of the brittle-ductile transition up to 10 km depth. In their interpretation, microearthquake mechanisms with a dip steeper than 15° may be related to small faults located at the base of the brittle-crust.

Tomographic studies have revealed a two-layer vertical structure characterized by a sharp velocity gradient lying at 7-9 km depth and which may be interpreted as a lithological contrast between the Gavrovo-Tripolitza unit and the Phyllite series (Latorre et al., 2004; Gautier et al., 2006). The shallower part of the crust (down to 5 km depth) is controlled by the N-S extension and lacks seismicity. The deeper part (7-13 km depth) matches the seismogenic zone and is characterized by faster and more heterogeneous anomalies. In this zone the background seismicity reveals a low-angle active surface dipping about 20° toward the north and striking WNW-ESE (Gautier et al., 2006). The position of this active structure is consistent with both high Vp/Vs and low Vp. Vs anomalies identified at 8-12 km depth and suggesting a highly fractured and fluid-saturated zone.

Despite a large amount of recent tectonic, geodetic and seismic observations, there is considerable debate concerning the rifting process and the underlying mechanical mechanism. We apply finite-frequency tomography for better images of the intermediate structures beneath the Gulf of Corinth in order to provide additional constraints on the extension mechanisms.

Data and model parametrization

A dense passive seismological experiment took place from November 2001 to June 2002 in the western part of the Gulf in the framework of the European 3F-Corinth project. The experiment deployed 30 3C L22 2Hz digital and 19 3C CMG40 60s digital stations using GPS time (temporary stations and CRL permanent stations (Lyon-Caen et al., 2004)) on both sides of the Gulf during the year 2002. The distance between stations is around 5 km. During March-April, three 3C ocean-bottom seismometers were deployed in the centre of the gulf for a one-month period, allowing an increase of the ray coverage in the study area. The complete network is represented on Figure 2.

The dataset comprises direct P and S phases from regional earthquakes. On average, 400 events per month were recorded during this dense passive experiment. First-arrival times were hand-picked and an initial location was obtained using the 1D model proposed by Rigo et al. (1996). In order to obtain a more reliable and uniform tomographic dataset, we have performed a selec-

tion using different criteria (Gautier et al., 2006). A total of 451 local events with 9236 P- hand-picked first-arrival times are used to invert for velocity perturbations according to ray or 3D finite-frequency kernel formulations. In this paper, we shall concentrate only on the first-arrival P-wave times and we shall not consider here the S-wave times.

Our tomographic model is a 56 km x 56 km area with a local origin point located at (longitude=21.6°E and latitude=38°N) and extends to 19 km depth in order to include all the ray paths. This 3D model is discretized on a grid of 17 by 17 by 12 nodes. The distance between grid points is 3.5 km in the two horizontal X and Y directions and 2 km in the vertical Z direction. The finer grids used for the inversion are regular grids with a node spacing of 1 km in all directions for the ray grid and 250 m for the kernel grid. Some tests show that this discretization allows us to compute accurate sensitivity kernels in a reasonable computation time.

Here we choose to use the same parameterization for both ray-theoretical and finite-frequency inversion, i.e. the same 1D initial model (Rigo et al., 1996), the same regularization of the partial derivative matrix and the same damping parameter. All these different parameters are fixed through synthetic tests using the ray-based inversion and the real event-station geometry. A comprehensive description of these synthetic tests is presented in Gautier et al. (2006). We estimated that the optimal set of weightings for the 2002 tomographic study is 1 for P-waves, 5 for both the location and the origin time of earthquakes and finally 0.5 for the damping parameter.

RESULTS

We performed both ray theoretical and finite-frequency inversion on the same 2002 dataset and using the same parameterization as described in the previous paragraph. Here we present the results obtained for a finite-frequency of 2 Hz, since the dominant part of the seismic energy is around this frequency for the studied microseismicity. Moreover, it represents an upper bound to analyze the effect of the finite-frequency theory. Some tests performed for different frequencies in the range 1-5 Hz point indeed out that sensitivity kernels affect the tomographic images for frequencies lower than 2 Hz, whereas pictures are closed to ray theoretical predictions for higher frequencies.

We present the tomographic solution obtained after 5 iterations. There is no objective approach to compare models based on different theories. The difference between the weighted root mean square residuals is less than 2 ms suggesting that we compare models with equally good fit (Montelli et al., 2004; Hung et al., 2004). Therefore, we are using same inversion parameters for both ray and finite-frequency formulations with a damping of 0.5. Both the P-velocity models and the earthquake locations are shown on Figure 2. In addition to the map views, the results are also presented along three S-N vertical sec-

tions (Figure 3). This corresponds to different areas of the gulf region, from West to East. Their locations are indicated by dotted lines on the map views. At a regional scale the finite-frequency results are consistent with ray-theoretical images confirming a two-layer vertical structure of the mid-crust characterized by a sharp velocity gradient lying at 7-9 km depth. Both P-velocity models show a shallower low-velocity anomaly located beneath the Gulf down to 4 km depth and more heterogeneous anomalies in the deeper part (8-13 km depths). Moreover the S-N section C1-C2 reveals a low P-velocity anomaly located at 8-13 km depth beneath the northern side of the gulf, near the Psaromita peninsula.

Despite a same global structure, we notice some differences at small scales. The shallower low-velocity anomaly shows higher amplitudes in the finite-fre-
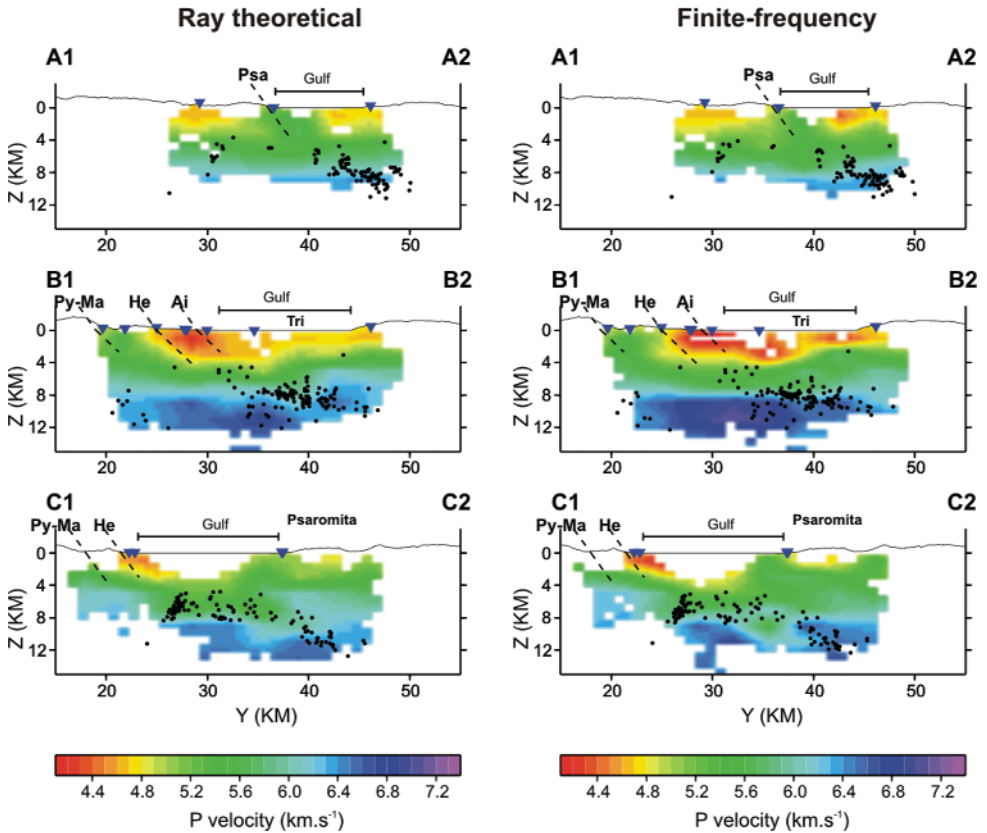
Fig. 3. S-N sections of the P- velocity tomographic results with respectively the ray-theoretical images on the left side and the finite-frequency model on the right side. The location of each S-N section is indicated on Figure 2. Earthquakes (dark dots) that are located in a 3.5 km wide area around each section are plotted. Major normal faults are displayed on the pictures. We used the same mask as for the map view.

quency images than in the ray-theoretical pictures. S-N sections seem to indicate that finite-frequency images provide a better resolved geometry of the shallow low-velocity anomaly boundary. In addition the finite-frequency model points out a sharper discontinuity at 7-9 km depth than the corresponding ray theoretical pictures, with a higher velocity contrast. Figure 3 confirms that both higher amplitudes of the velocity perturbations and a sharpening of layer boundaries are observed when finite-frequency effects are included in the inversion procedure.

Finally, in comparison with the ray-theoretical location, the finite-frequency approach produces a narrow picture of the microseismicity. Furthermore, S-N sections indicate differences in the event distribution at depth suggesting that a more flatten low-angle dipping surface is obtained with the finite-frequency procedure.

DISCUSSION AND CONCLUSION

In a methodological point of view, we have derived an exact estimation of the 3D sensitivity kernels. At each iteration of the tomography procedure, the sensitivity kernels are re-computed for the new 3D complex velocity structure. The steady convergence of these iterations clearly shows that the shape of the kernels is not critically altered by the ray bending or existence of small caustics in the 3D structure. In fact we find little or no evidence of the effect of small caustics, a fear raised by De Hoop and Van der Hilst (2005). We may conclude that the use of finite-frequency kernels is not subject to strong nonlinearities.

An other important result of this study is that the finite-frequency analysis affects crustal tomographic images. We find clear evidences of differences between the velocity models obtained by the ray theoretical and the finite-frequency methods. The finite-frequency model yields better reconstruction of the velocity perturbations, as observed at global scale (Montelli et al., 2004) or in the upper mantle (Hung et al., 2004; Yang et al., 2006). The finite-frequency tomography provides a better resolution of the geometry of the velocity anomalies, resulting in a sharpening of layer boundaries. These results demonstrate that the finite-frequency crustal effects are not negligible, especially in 3D complicated environment.

The increased sensitivity of the finite-frequency kernels in the shallower part seems to differ from results of some of the surface wave studies referred to in the introduction. In our opinion, this reflects two shortcomings of the surface wave studies. First, with the exception of Zhou et al. (2005), the resolution studies were performed on phase velocity maps, not on 3D tomographic models, and rely on the assumption that the surface wave travels with a velocity that is a localized property of the model. This assumption is fundamentally incompatible with a finite-frequency approach, in which the wave is influenced by scattered energy from different directions, hence its apparent

velocity is a function of the past history of the wavefront and cannot be properly localized. Secondly, a phase velocity imaging is for one frequency only and can never capture the influence of varying width of resolving kernels for different frequencies on the resolution of a 3D model.

Finally the finite-frequency velocity model confirms the two-layer vertical structure of the mid-crust beneath the Gulf of Corinth. Despite a same global structure, differences are observed at small scales. In particular, the finite-frequency interpretation allows us to increase the resolution of the shallow low-velocity anomaly located beneath the gulf, and related to the presence of thick synrift deposits and the existence of highly fractured carbonates in the first 3 km (Doustos & Poulimenos, 1992; Flotté & Sorel, 2001; Sachpazi et al., 2003; Pham et al., 2000). However the resulting model would not be interpreted any differently than the ray theory model. Earlier resolution studies by Latorre et al. (2004) and Gautier et al. (2006) show a reduced resolution for the ray theoretical model at larger depth. From the present study, it is clear that the finite-frequency does not improve on this. An exact resolution test for the finite-frequency inversion would require us to generate synthetic seismograms with a finite-difference technique in 3D, which is far beyond the scope of our investigation. The weak resolution of velocity structure below 8 km prevents us from providing additional constraints on the rifting process. Moreover, only the P velocity model is inverted here, suggesting a poor constrained location of events. Because of this limitation, we are not able to interpret differences between the event distributions obtained by the ray theoretical and the finite-frequency inversions as for the low dipping structure. The next step will be a simultaneous inversion of the P- and S- velocity distribution using the finite-frequency tomography method in order to better constrain both the structure and the dynamics of the mid-crust beneath the Gulf.

One must underline as well that the description of the model will be critical for better retrieving the velocity structure. The improved resolution of the finite-frequency approach will request more accurate and spatially varying description according to the expected resolution. Finite-Frequency approaches open new roads for better reconstructed images but still require careful analysis of the influence of the different parameters. This work is one step in this direction for the body-wave seismograms. The necessity of dense seismic networks is a crucial issue in such analysis and volcanic area as the Campi Flegrei area where one might want to implement this technique will need these dense networks.

REFERENCES

Aki K. and Lee W. 1976. Determination of three-dimensional velocity anomalies under a seismic array using first P-arrival times from local earthquakes. J. Geophys. Res. 81, 4381-4399.

Armijo R., Meyer B., King G., Rigo A. and Papanastassiou D. 1996. Quaternary evolution of the Corinth Rift and its implication for the late Cenozoic evolution of the Aegean. Geophys. J. Int. 126, 11-53.

Aubouin J., Brunn J., Celet P., Dercourt J., Godfriaux I., and Mercier J. 1962. Esquisse de la géologie de la Grèce. Mém. Hors Sér. Soc. Géol. France 2, 583-610.

Avallone A., Briole P., Agatza-Balodimiou A., BIrillis H., Charade O., Mitsakaki C., Nercessian A., Papazissi K., Paradissis D. and Veis G. 2004. Analysis of eleven years of deformation measured by GPS in the Corinth Rift laboratory area. C. R. Geoscience 336, 301-311.

Benz H.M., Chouet S.A., Dawson P.B., Lahr J.C., Page R.A., and Hole J.A. 1996. Three dimensional P and S wave velocity structure of Redoubt Volcano, Alaska. J. Geophys. Res., 101, 8111-8128.

Bernard P., Briole P., Meyer B., Lyon-Caen H., Gomez J.-M., Tiberi C., Berge C., Cattin R., Hatzfeld D., Lachet C., Lebrun B., Deschamps A., Courboulex F., Laroque C., Rigo A., Massonet D., Papadimitriou P., Kassaras J., Diagourtas D., Makropoulos K., Veis G., Papazisi E., Mitsakaki C., Karakostas V., Papadimitriou E., Papanastassiou D., Chouliaras M., Stavrakakis, G. 1997. A low angle normal fault earthquake: the Ms=3D6.2, June, 1995 Aigion earthquake (Greece). Journal of Seismology 1, 131-150.

Briole P., Rigo A., Lyon-Caen H., Ruegg J.-C., Papazissi K., Mistakaki C., Balodimou A.,

Veis G., Hatzfeld D. and Deschamps A. 2000. Active Deformation of the Gulf of Korinthos, Greece: Results from Repeated GPS Surveys between 1990 and 1995. J. Geophys. Res. 105, 25605-25625.

Dahlen F.A., Hung S.-H. and Nolet G. 2000. Fréchet kernels for finite-frequency travel-times – I. Theory. Geophys. J. Int., 141, 157-174.

Dahlen F.A. and Nolet G. 2005. Comment on the paper "On sensitivity kernels for wave equation transmission tomography" by de Hoop and Van der Hilst. Geophys. J. Int., 163, 949-951.

De Hoop M.V. and Van der Hilst R.D. 2005. Reply to comment by F.A. Dahlen and G. Nolet on "On sensitivity kernels for 'wave equation' transmission tomography". Geophys. J. Int., 163, 952-955, doi:10.1111/j.1365-246X.2005.02794.x.

Dornsiepen U.F., Manutsoglu E. and Mertmann D. 2001. Permian-Triassic paleogeography of the external Hellenides. Paleogeog. Paleoclimat. Paleoecol. 172, 327-338.

Doutsos T. and Poulimenos G. 1992. Geometry and kinematics of active faults and their seismotectonic significance in the western Corinth-Patras rift (Greece). J. Struct Geol. 14, 689-699.

Flotté N. and Sorel D. 2001. Structural cross sections through the Corinth-Patras detachment fault-system in Northern Peloponnesus (Aegean Arc, Greece). Bull. Geol. Soc. Greece XXXIV, 235-241.

Hatzfeld D., Karakostas V., Ziazia M., Kassaras I., Papadimitriou E., Makropoulos K., Voulgaris N. and PapaiOannou, C. 2000. Microseismicity and faulting geometry in the Gulf of Corinth (Greece). Geophys. J. Int. 141, 438-456.

Hung S.-H., Dahlen F.A. and Nolet G 2000. Fréchet kernels for finite-frequency traveltimes – II. Examples. Geophys. J. Int. 141, 175-203.

Hung S.-H., Dahlen F.A. and Nolet G. 2001. Wavefront healing: A banana-doughnut perspective, Geophys. J. Int. 146, 289-312.

Hung S.-H., Shen Y. and Chiao L.-Y. 2004. Imaging seismic velocity structure beneath the Iceland hotspot – A finite-frequency approach. J. Geophys. Res., 109, B08305, doi:10.1029/2003JB002889.

Gautier S., Latorre D., Virieux J., Deschamps A., Skarpelos C., Sotiriou A., Serpetsidaxi A. and Tselentis A. 2006. A new passive tomography of the Aigion area (Gulf of Corinth, Greece) from the 2002 dataset. Pageoph 163, 431-453, doi: 10.1007/500024-005-0033-7.

Jacobshagen V., Durr V., Kockel F., Kopp K.O., Kowalczyk G., Berckhemer H. and Buttner D. 1978. Structure and Geodynamic evolution of the Aegean Region. In Alpes Apennines Hellenides, ed. Closs H., Roeder D., Schmidt K., and Schweiz-Verlag, K., 537-564.

Latorre D., Virieux J., Monfret T., Monteiller V., Vanorio T., Got J.-L. and Lyon-Caen H. 2004. A new seismic tomography of Aigion area (Gulf of Corinth- Greece) from a 1991 data set. Geophys. J. Int. 159, 1013-1031.

Le Meur H., Virieux J. and Podvin P. 1997. Seismic tomography of the Gulf of Corinth: a comparison of methods. Ann. Geophy. XL, 1-25.

Levshin A.L., Barmin M.P., Ritzwoller M.H. and Trampert J. 2005. Minorarc and major-arc global surface wave diffraction tomography. Phys. Earth planet. Int. 149, 205-223.

Lyon-Caen H., Papadimitriou P., Deschamps A., Bernard P., Makropoulos K., Pacchiani F., and Patau G. 2004. First results of the CRLN seismic array in the western Corinth rift: evidence for old fault reactivation. C. R. Geoscience 336, 343-351.

Marquering H., Dahlen F.A. and Nolet, G. 1999. Three-dimensional sensitivity kernels for finite-frequency traveltimes: the banana-doughnut paradox. Geophys. J. Int. 137, 805-815.

Montelli R., Nolet G., Masters G., Dahlen F. and Hung, S.-H., 2004. Global P and PP traveltime tomography: rays versus waves. Geophys. J. Int., 158, 637-654.

Moser T.J. 1991. Shortest path calculation of seismic rays, Geophysics 56, 59-67.

Paige C.C. and Saunders M.A. 1982. LSQR : an algorithm for sparse linear equations and sparse least squares. ACM Trans. Math. Software 8, 43-71.

Pham V.N., Bernard P., Boyer D., Chouliaras G., Mouel J.L.L. and Stavrakakis G.N. 2000. Electrical conductivity and crustal structure beneath the Central Hellenides around the Gulf of Corinth (Greece) and their relationship with the seismotectonics. Geophys. J. Int. 142, 948-969.

Rietbrock A., Tiberi C., Scherbaum F. and Lyon-Caen H. 1996. Seismic slip on a low angle normal fault in the Gulf of Corinth: Evidence from high-resolution cluster analysis of microearthquakes. Geophys. Res. Lett. 23, 1817-1820.

Rigo A., Lyon-Caen H., Armijo R., Deschamps A., Hatzfeld D., Makropoulos K., Papadimitriou P. and Kassaras I. 1996. A microseismic study in the western part of the Golf of Corinth (Greece): implications for large-scale normal faulting mechanisms. Geophys. J. Int. 126, 663-688.

Sachapzi M., Clément C., Laigle M., Hirn A. and Roussos, N. 2003. Rift structure, evolution, and earthquakes in the Gulf of Corinth, from reflection seismic images. Earth Plant. Sc. Lett. 216, 243-257.

Sieminski A., Lévêque J.-J. and Debayle E. 2004. Can finite-frequency effects be accounted for in ray theory surfacewave tomography? Geophys. Res. Lett. 31, L24614, doi:10.1029/2004GL021402.

Sorel, D. 2000. A Pliocene and still active detachment fault and the origin of the Corinth-Patras rift, Greece. Geology 28, 83-86.

Spetzler J., Trampert J. and Snieder R., 2002. The effects of scattering in surface wave tomography. Geophys. J. Int. 149, 755-767.

Spakman W. and Nolet G. 1988. Imaging algorithms, accuracy and resolution. In Mathematical geophysics, ed. Vlaar N., D. Reidel Publ. Co., Dordrecht 1988, 155-187.

Spencer C.P. and Gubbins D. 1980. Travel-time inversion for simultaneous earthquake location and velocity structure determination in laterally varying media. Geophys. J. R. Astron. Soc. 63, 95-116.

Tape C., Liu Q. and Tromp J. 2007. Finite-frequency tomography using adjoint methods: Methodology and examples using membrane surface waves. Geophysical Journal International, on line, doi: 10.1111/j.1365-246X.2006.03191.x.

Tiberi C., Diament M., Lyon-Caen H. and King T. 2001. Moho topography beneath the Corinth Rift area (Greece) from Inversion of gravity data. Geophys. J. Int. 145, 797-808.

Trampert J. and Spetzler J. 2006. Surface wave tomography: finite frequency effects lost in the null space. Geophys. J. Int. 164, 394-400.

Thurber C.H. 1992. Hypocenter-velocity structure coupling in local earthquake tomography. Phys. Earth Planet. Inter. 75, 55-62.

Van der Hilst R.D. and De Hoop M.V. 2005. Banana-doughnut kernels and mantle tomography. Geophy. J. Int. 163, 956-961, doi:10.1111/j.1365-246X.2005.02817.x.

Virieux J. and Farra V. 1991. Ray tracing in 3-D complex isotropic media: An analysis of the problem. Geophysics 56, 2057-2069.

Wielandt E. 1987. On the validity of the ray approximation for interpreting delay times, in Seismic Tomography. ed. Nolet. G., D. Reidel Publishing Co., Dordrecht., 85-98.

Yang T., Shen Y., Van der Lee S., Solomon S.C., Hung S.-H. 2006. Upper mantle structure beneath the Azores hotspot from finite-frequency seismic tomography. Earth Planet. Sci. Lett. 250, 11-26.

Yoshizawa K. and Kennett B.L.N. 2002. Determination of the influence zone for surface wave paths. Geophys. J. Int. 149, 440-453.

Yoshizawa K. and Kennett B.L.N. 2004. Multimode surface wave tomography for the Australian region using a three-step approach incorporating finite frequency effects. J. Geophys. Res. 109, B02310,doi:10.1029/2002JB002254.

Zhao L., Jordan T.H. and Chapman C.H. 2000. Three-dimensional Fréchet kernels for seismic delay times. Geophys. J. Int. 141, 558-576.

Zhou Y., Dahlen F.A. and Nolet G. 2004. Three-dimensional sensitivity kernels for surface wave observables. Geophys. J. Int. 158, 142-168.

Zhou Y., Dahlen F.A., Nolet G. and Laske G. 2005. Finite-frequency effects in global surface-wave tomography. Geophys. J. Int. 163, 1087-1111.

Elastic full waveform inversion in the frequency domain

C. Gélis, J. Virieux, S. Operto

Géosciences Azur, CNRS and UNSA, Sophia Antipolis, France

Abstract: We have developed a full elastic waveform inversion in the frequency domain in a 2D geometry and we have investigated the feasibility of such procedure for complex volcanic structures as Campi Flegrei area. This method allows imaging of two physical seismic parameters, using vertical and horizontal field components. The forward problem is discretized using finite difference, allowing the simulation of the full elastic wavefield. Moreover, it is solved in the frequency domain, a fast approach for multisource and multireceiver acquisition. The non-linear inversion is based on a preconditionned gradient method. Non-linearity is taken into account by updating parameters at each iteration and proceeding from low to high frequencies. In spite of the multistep strategy, the selection of the initial model is quite important. On the Serapis experiment, we have analyzed the data and transformed it as a large-offset 2D line. We have analyzed both the orientation of sensors, frequency content of the source for fitting requirements of the inversion. We have investigated as well as possible initial models. Through the estimation of synthetic data, we have found that the initial model is too far from the real one and that makes unsuccessful the the linearized inversion. Moreover, in this complex structure, the 2D approximation seems to be a too strong hypothesis. Therefore, better initial models are necessary and moving to a true 3D full waveform inversion scheme is required for extracting information from real seismic data of Serapis experiment.

INTRODUCTION

Quantitative imaging using full wave equation has been achieved through the use of the adjoint formulation problem for seismic data in the last twenty years. Both formulations in time domain (Lailly, 1984; Tarantola, 1984; Gauthier et al, 1986) and in frequency domain (Pratt et al, 1996; Pratt, 1999; Ravaut et al., 2004) have been implemented and applied to various synthetic and real data examples with specific advantages on both sides. Easier seismic traces processing in time domain will allow progressive introduction of phases by increasing the time domain window in both observed and synthetic data (Kolb et al., 1986; Shipp and Singh, 2002; Sheng, 2004). Efficient ways of solving the forward problem in the frequency domain make the frequency formulation appealing (Stekl and Pratt, 1998). Moreover, the progressive introduction of higher frequencies

allows both to introduce and mitigate the non linearity and recover shorter and shorter heterogeneities (Pratt, 1999; Sirgue, 2003). Furthermore, for wide-angle data acquisitions, this frequency approach efficiently takes benefit of the wave-number redundancy by limiting the number of inverted frequencies (Pratt, 1990; Sirgue and Pratt, 2004). Furthermore, the attenuation may be introduced, which has been applied to real data examples (Hicks and Pratt, 2001).

In the report, we shortly present the full waveform inversion in the frequency domain and refer to the work of Gélis et al. (2007) for a more complete theo-retical formulation of the elastic approach. Then, we shall focus our attention towards the Serapis experiment which has been performed in the Naples Bay in September 2001. Dense OBS deployment has been performed although in a 3D geometry taking into account the quite complex structure of this zone. Therefore, we shall investigate how to extract a 2D line for application of the inversion which is still a method developed for 2D geometries. Because the active experiment has been performed with OBS, we shall focus on both hori-zontal and vertical components. Through synthetic simulations, we shall con-clude on the difficulties for constructing an accurate seismic image from fit-ting the full waveform.

FREQUENCY-DOMAIN FULL-WAVEFORM INVERSION

The inverse problem has been formulated as a weighted least-square gradient method where the misfit between synthetic seismograms *g(m)* computed from a model *m* and real seismograms d_{obs} has to be reduced. This misfit function is the following expression

$$E(m) = \frac{1}{2}(g(m) - d_{obs})^{\dagger} W(g(m) - d_{obs}) \tag{1}$$

The reduction of this misfit function is based on a classic local optimization approach through a steepest-descent algorithm (Tarantola, 1984).

Forward problem

The theory of frequency-domain waveform modelling and tomography has already been extensively presented (Jo et al., 1996; Stekl and Pratt, 1998; Hustedt et al., 2004; Pratt and Worthington, 1990; Pratt et al., 1998). Using the spatial finite difference stencil of Saenger et al. (2000), an accurate modelling of elastic waves have been proposed by Bohlen and Saenger (2003) including waves constructed by the free surface. An implementation has been proposed by Gelis et al. (2005).

Because of the spatial discretision and the fourier transform, the elastodynamic equations reduce to the following algebraic system,

$$A\,X = S \tag{2}$$

where the vector $X^\dagger = (V_x(x,\omega),(V_z(x,\omega))^\dagger$ is the particle velocity field at the frequency ω and the vector $S^\dagger = (S_x(x,\omega),(S_z(x,\omega))^\dagger$ is the source term while the impedance matrix A puts together influences of time and spatial operators into a discrete form

$$A(x,\omega) = \begin{bmatrix} A_{xx}(x,\omega) & A_{xz}(x,\omega) \\ A_{zx}(x,\omega) & A_{zz}(x,\omega) \end{bmatrix} \tag{3}$$

This impedance matrix may vary locally depending on the variation of medium properties described into a grid. Please note that the system (2) is not a linear system with respect to medium properties while it is linear for source excitation. Because the grid is finite, we must consider surrounding layers where waves must be efficiently absorbed. These PML zones have been introduced by Bérenger (1994) and applied in elastodynamic systems by Hastings et al. (1996) or Hustedt et al. (2004). In practice, we solve the system (2) by a direct solver where the matrix A is decomposed into an LU factorisation. We have selected the MUMPS software to do so (Amestoy et al., 2000, 2001) which helps handling the fill-in of the matrix through graph theory and parallel programming. Once this decomposition is performed which is the most CPU-demanding part (around 70 % of the total forward effort), computing the solution for different sources is simply a matter of substitution.

Inverse problem

Fréchet derivatives may be deduced from a local relation between medium parameter perturbations and particle velocity amplitudes perturbations. This relation requires only the first term of the Born series for the first derivative estimation. Because we fully solve the forward problem at each iteration, we do include multiple diffractions in our perturbation estimation. Spatial derivatives of data perturbations could be obtained through the discrete impedance matrix A (Pratt et al., 1996, 1998). The elastic adjoint operator (Pratt et al., 1998) could be written as

$$\Re\,(B_0^t\,\Delta d^*) = -S^t\,(A^{-1})^t\,\partial A/\partial m\,A^{-1}\Delta V^* \tag{4}$$

In this equation, we recognize the Born Kernel equal to $(A^{-1})^t\,\partial A/\partial m\,A^{-1}$ surround by two excitation terms: the real source S^t and a virtual source ΔV^*

composed of conjugate residuals located at receivers places. With another reading of this equation (4), we can distinguish three different terms, corresponding to physical phenomena: the forward propagation of the sources, the backpropagation of the residuals and the derivatives of the differencing operator. In order to obtain the model parameter perturbation, we must consider the Hessian for the stepping of the gradient of the equation (4), and mainly the diagonal of the approximate Hessian, which acts as a preconditioner of the gradient which properly scales the perturbation model (Shin et al., 2001). Of course we should iterate at each frequency and recomputed the impedance matrix each time. The Hessian or its approximation is computed once at the first iteration for a given frequency and it is kept through iterations. The number of forward problems is twice the number of shots for the gradient and the sum of the number of shots and the number of receivers for the Hessian.

SIMPLE CANONICAL EXAMPLE

Let us consider an infinite medium with a P-wave velocity of 1500 m/s and an S-wave velocity of 1200 m/s. Two finite-sized anomalous disks of radius 100 m are inserted with P-wave velocity of 1800m/s and an S-wave velocity of 1440 m/s. The numerical grid size is 201 by 201 points with a spatial step of 10 m. The vertical point force source is a Ricker signal centered on 5 Hz which represents a rather impulsive signal. Fifteen shots are defined per edge separated by 100 m (Figure 1). Each source is recorded by thirty-six geophones located on the opposite side along the bold line with a stepping of 40 m. This transmission acquisition geometry allows to densely sample the medium and illuminates anomalies with different diffracting angles. We choose to
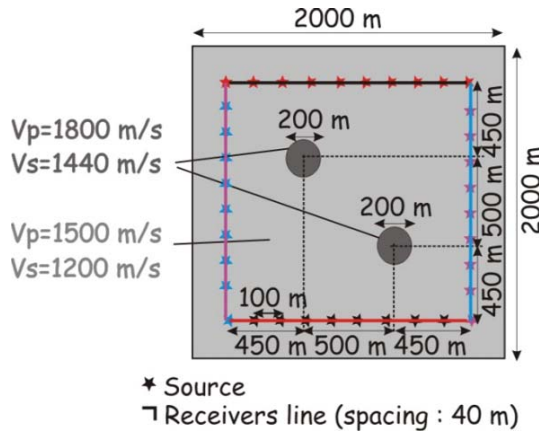

Fig. 1. Simple synthetic model for the illustration of the full waveform inversion.

image two anomalies because multiple scattering occurs. The forward problem should take care of that and ghost images, if any, should vanish.

The initial medium is the constant velocity medium without anomalies and we proceed from low frequencies towards high frequencies. This allows us to reconstruct long wavelength anomalies before going into details. This careful introduction of the frequency content will also prevent fast focusing of anomalies that may lead to some local minimum in the model space. One may hope we avoid somehow cycle-skipping which is often more dramatic at high frequency than at low frequency. For each frequency, the initial model comes from the inversion of the previously inverted frequency. Twenty iterations are performed at each frequency. We progressively introduce details in the reconstructed images. The inverted frequencies are 1.75 Hz, 3 Hz, 4.25 Hz and 10.25 Hz. Their choice depends on the acquisition geometry and on the anomaly position to be reconstructed as showed Sirgue & Pratt (2004) for a reflection acquisition geometry. We have used the relation proposed by Sirgue & Pratt (2004) for the selection of frequencies, such as to cover a continuous wavenumber spectrum in the target zone.

Figure 2 shows the progressive reconstruction of anomalies both in shape and in velocity amplitude for Vp parameter. Although the process is different for Vs parameter, we end up to a quite precise reconstruction of these anomalies. Although the local gradient formulation is strictly restricted to small perturbations, in this experiment the acquisition redundancy allows the use of a homogeneous starting model for an accurate reconstruction of the anomalies in shape, depth and amplitude. The size of reconstructed scatterers depends on the selected wavelength Λ. Details progressively appear when the inverted frequency increases, allowing to characterize scatterers more finely. The way anomalies are recovered is different when inverted parameters change, as already noticed by Mora (1987, 1988).

CONSTRUCTION OF A 2D PROFILE FROM THE 3D SERAPIS EXPERIMENT

In September of 2001, an active marine seismic experiment called SERAPIS (Seismic Reflection/Refraction Acquisition Project for Imaging complex volcanic Structures) was carried out in the Bay of Naples and Bay of Pozzuoli. During this experiment, ~5000 shots were produced by the vessel *Le Nadir* of Ifremer and recorded on an array of ocean bottom seismometers (OBS) and land stations. Although the experiment was designed to be 3D, by selecting launched OBS, we were able to select a nearly 2D wide-angle profile (Figure 3). The alignment of sensors along the shot line is always a difficult task and requires approximations. By rotating both receivers and shots, we were able to keep constant distances between receivers and shots for preserving the kinematic properties of common receiver gathers. Few OBS have been cancelled out like the OBS 07 which is too far away from the 2D shot line.
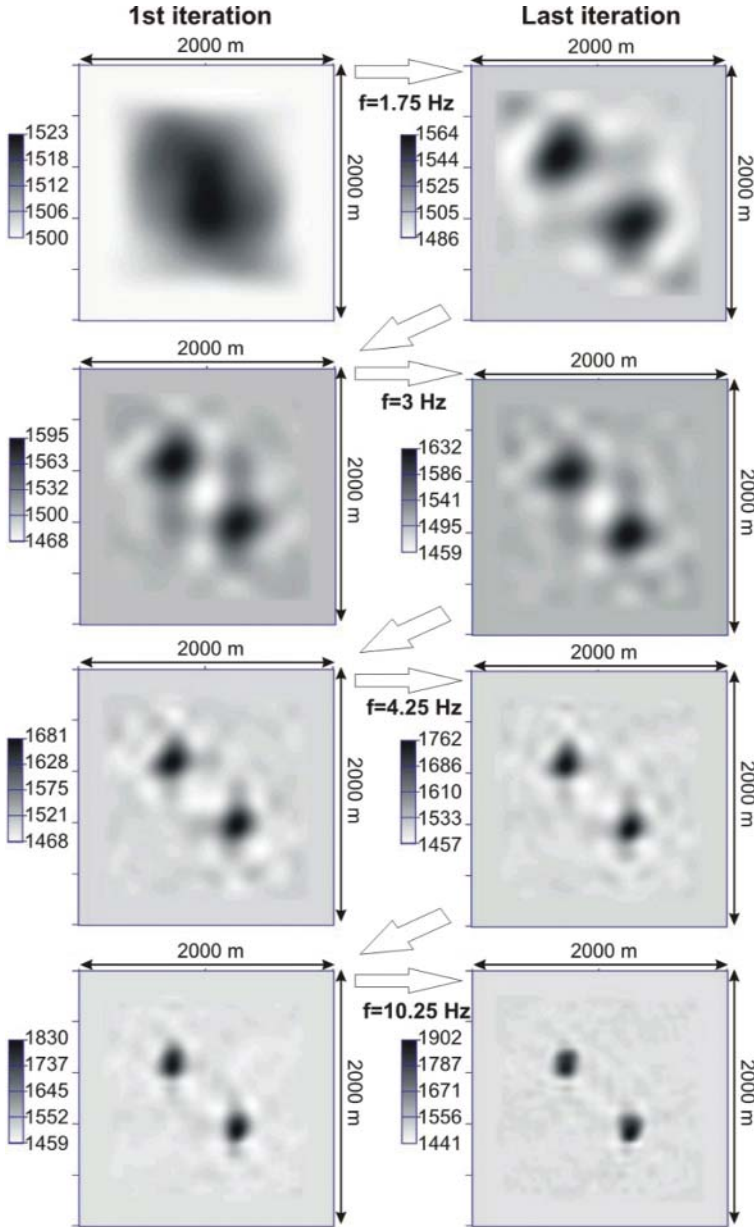
Fig. 2. Reconstruction of two circular anomalies for Vp velocity structure. Similar results have been obtained for Vs velocity structure.

The orientation of sensors is unknown as the OBS is launched from the sea surface and do only an automatic levelling. By considering direct waves inside the water layer, we may proceed to an a posteriori orientation and we are able
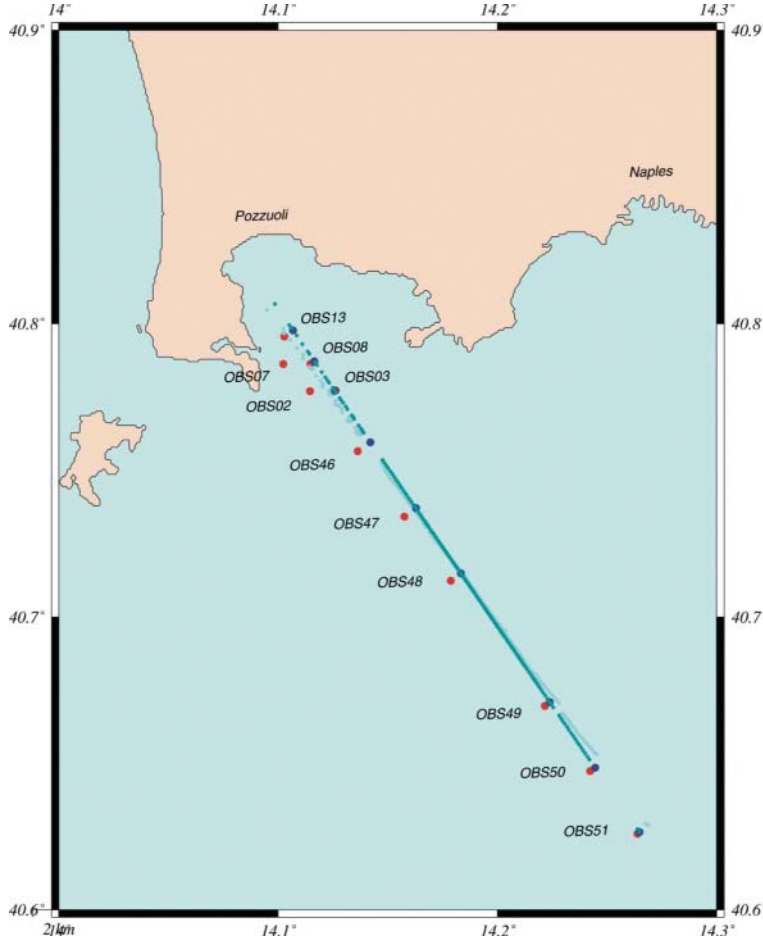
Fig. 3. Selection of a 2D profile crossing the Pozzuoli Bay for the Full Waveform Inversion. The blue line is the shot line.

to rotate the components into radial, vertical and transverse components. The amount of energy of the transverse components gives an indicator of the complexity of the propagation which is 3D. On the OBS 49, we have observed a transverse component of reduced amplitude but still significant compared to other components (Figure 4). This observation is true for any OBS we have examined.

The frequency content of the source signal is also an important parameter for better inversion convergence. If the low frequency part of the signal is significant, we may proceed first for low frequencies where the linearity has an extended domain of validity compared to the high frequency part. Figure 5 displays various source spectral content depending on the OBS position.

OBS 49: Three components station

Radial component   Vertical component   Transverse component
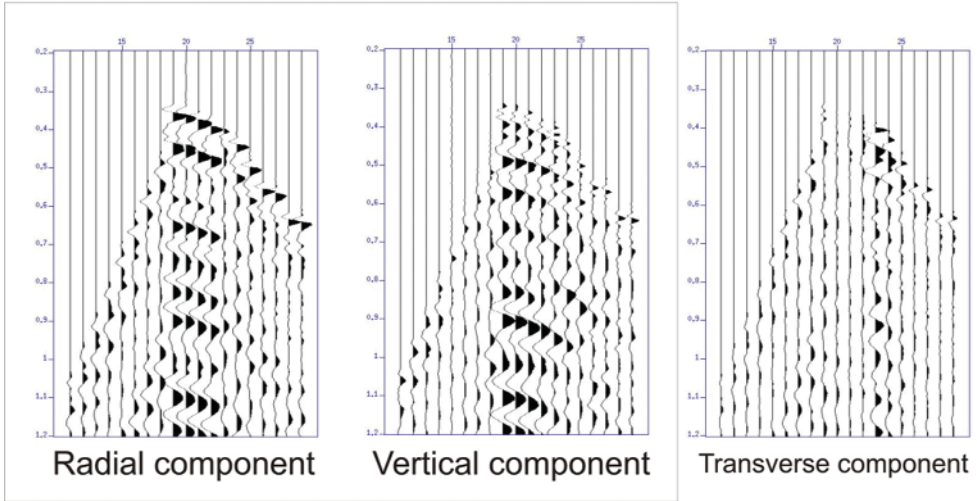
Fig. 4. Orientation of sensor components along radial and vertical directions using first-arrival waves inside the water layer. The transverse component should have a minimum energy if the propagation is mainly 2D.
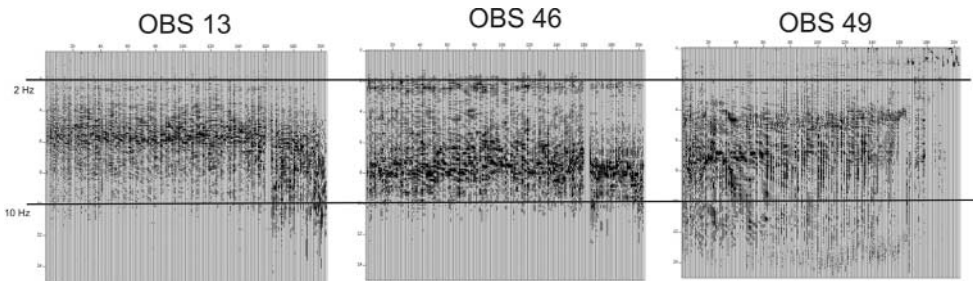
Fig. 5. Frequency content of the source on different sensors : 5Hz seems to be the most energetic frequency.

Therefore, the variability we observe on one station is essentially coming from the source time function. This will be taken into account in the inversion process by the adequate calibration of the source amplitude at each freaquency. In order to perform the inversion, we need to select an initial velocity model which has been extracted from two travel-time tomographies (Zollo et al., 2003; Vanorio et al., 2005). Although better tomographic models are now available (Battaglia et al., 2007), we have taken the one existing at the beginning of 2006. Two different interpolations have been performed for the reconstruction of the initial Vp velocity model (Figure 6). They produce dif-
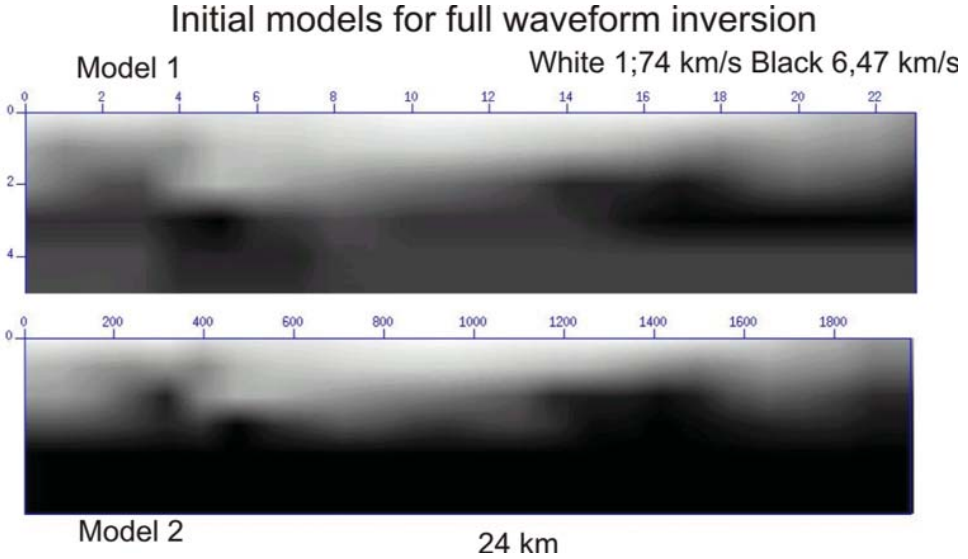
Fig. 6. Two initial models extracted from Zollo et al. (2003) and Vanorio et al. (2005).

ferent sharpness inside the medium. The Vs model is deduced as for a Poison medium.

Simple synthetic common receiver gathers may be constructed for assessing the good kinematic behaviour of these initial velocity models. Figure 7 shows that the kinematic structure of the CRG is quite similar between the synthetic data and the real data but still displays differences preventing a convergence of the inversion procedure.

Many different attempts have been performed by changing damping parameters for avoiding singularities but real seismograms present features that the elastic wave propagation could not model and, therefore, the inversion procedure could not transform into pertinent model parameters values.

PERSPECTIVE AND CONCLUSIONS

In this paper, we have applied the elastic full waveform inversion following a gradient optimization method to a 2D line of seismic data recorded during the SERAPIS campaign in 2001. The forward problem allows to model any kind of waves in complex media and to properly simulate the free surface. We highlight that the reconstruction of several parameters is possible as long as data allow the extraction of medium information. This means that we need to know the background medium and that this inverse scheme works for backscattering as long as the macromodel is accurate enough.
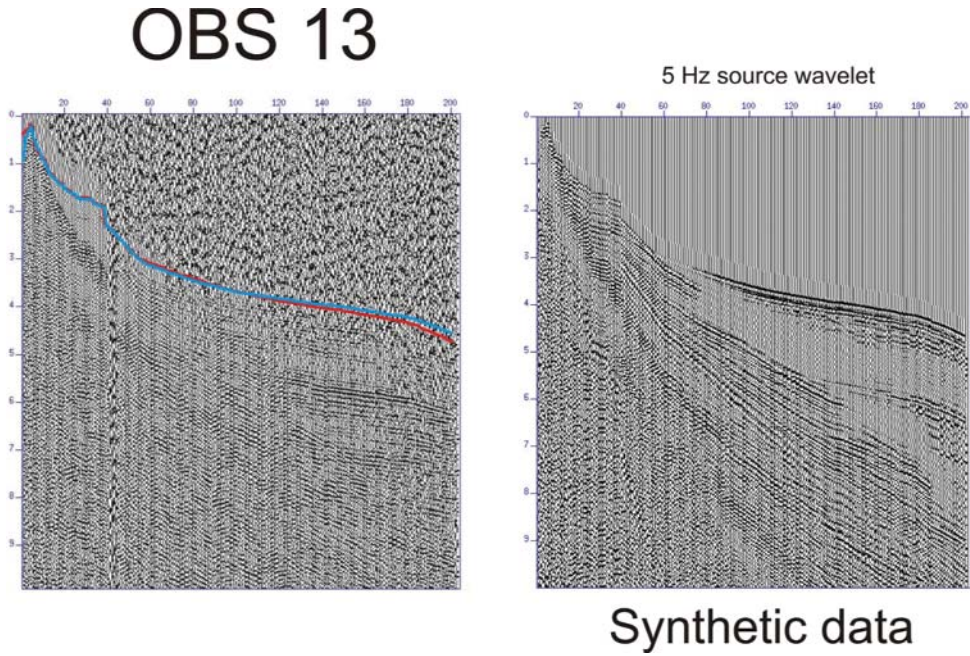
Fig. 7. On the left, real vertical particle velocity. The blue and red lines are first-arrival picking times for the two models of the Figure 6. Refracted waves have been modelled but different coherent wave packets are missing on the synthetic data on the right.

In spite of our difficulty in the reconstruction of the high resolution medium velocity structure, the potentiality of the full waveform inversion is important and this work may serve as a guideline for future data analysis protocol for a better reconstruction. Because of the intrinsic 3D configuration of the SERA-PIS experiment, we may face the need for a tool handling the 3D inversion allowing focusing of velocity anomalies at the right place in a 3D space. We may hope that, as our understanding of the area increases, the velocity structure will be better known and that we may successfully apply the inversion method we propose in the future to the Campi Flegrei area.

ACKNOWLEDGMENTS

REFERENCES

Amestoy, P. R., Duff, I. S., & L'Excellent, J.-Y., 2000.Multifrontal parallel distributed symmetric and unsymmetric solvers, Comput. Methods in Appl. Mech. Eng., 184, 501-520.

Amestoy, P. R., Duff, I. S., Koster, J., & L'Excellent, J.-Y., 2001. A fully asynchronous multifrontal solver using distributed dynamic scheduling, SIAM Journal of Matrix Analysis and Applications, 23(1), 15-41.

Bérenger, J., 1994. A perfectly matched layer for the absorption of electromagnetic waves, Journal of Computational Geophysics, 114, 185-200.

Bohlen, T. & Saenger, E., 2003. 3D visco elastic finite difference modeling using the rotated staggered grid-tests of numerical accuracy, in EAGE 65th conference and Exhibition, Stavanger, Norway.

Dessa, J., Operto, S., Kodaira, S., Nakanishi, A., Pascal, G., Virieux, J., & Kaneda, Y., 2004.Multiscale seismic imaging of the eastern nankai trough by full waveform inversion, Geophysical Research Letters, 31, L18606.

Gauthier, O., Virieux, J., & Tarantola, A., 1986. Two-dimensional non-linear inversion of seismic waveforms : numerical results, Geophysics, 51, 1387-1403.

Gélis, C., Leparoux, D., Virieux, J., Bitri, A., Operto, S., & Grandjean, G., 2005. Numerical modeling of surface waves over shallow cavities, Journal of Environmental and Engineering Geophysics, 10, 49-59.

Gélis, C., J. Virieux and G. Grandjean, 2007. Two-dimensional elastic full waveform inversion using Born and Rytov formulations in the frequency domain, Geophys. J. Int., 168, 605-633.

Hastings, F., Scheider, J., & Broschat, S., 1996. Application of the perfectly matched layer (PML) absorbing boundary condition to elastic wave propagation, Journal of Acoustic Society of America, 100, 3061-3069.

Hicks, G. & Pratt, R., 2001. Reflection waveform inversion using local descent methods: estimating attenuation and velocity over a gas sand deposit, Geophysics, 66, 598-612.

Hustedt, B., Operto, S., & Virieux, J., 2004.Mixed-grid and staggered-grid finite difference methods for frequency domain acoustic wave modelling, Geophysical Journal International, 157, 1269-1296.

Kolb, P., Collino, F., & Lailly, P., 1986. Prestack inversion of 1d medium, Proceedings of IEEE, 74, 498-508.

Lailly, P., 1984. The seismic inverse problem as a sequence of before stack migrations. In inverse scattering theory and applications, SIAM, Philadelphia.

Lambaré, G., Virieux, J., Madariaga, R., & Jin, S., 1992. Iterative asymptotic inversion in the acoustic approximation, Geophysics, 57, 1138-1154.

Mora, P., 1987. Nonlinear two-dimensional elastic inversion of multid´eport seismic data, Geophysics, 52, 1211-1228.

Mora, P., 1988. Elastic wavefield inversion of reflection and transmission data, Geophysics, 53, 750-759.

Operto, S., Ravaut, C., Improta, L., Virieux, J., Herrero, A., & Dell'Aversana, P., 2004. Quantitative imaging of complex structures from multi-fold wide aperture seismic data, Geophysical Prospecting, 52, 625-651.

Pratt, R., 1990. Inverse theory applied to multi-source cross-hole tomography. part II : elastic wave-equation method, Geophysical Prospecting, 38, 311-330.

Pratt, R., 1999. Seismic waveform inversion in the frequency domain, part I : theory and verification in a physic scale model, Geophysical Journal International, 64, 888-901.

Pratt, R., Song, Z., Williamson, P., & Warner, M., 1996. Two-dimensional velocity model from wide-angle seismic data by wavefield inversion, Geophysical Journal International, 124, 323-340.

Ravaut, C., Operto, S., Improta, L., Virieux, J., Herrero, A., & Dell'Aversana, P., 2004. Quantitative imaging of complex structures from multifold wide angle seismic data by frequency domain full waveform inversion : application to a thrust belt, Geophysical Journal International, 159,1032-1056.

Saenger, E. & Bohlen, T., 2004. Finite difference modeling of viscoelastic and anisotropic wave propagation using the rotated staggered grid, Geophysics, 69(2), 583-591.

Saenger, E., Gold, N., & Shapiro, S., 2000. Modeling the propagation of elastic waves using a modified finite-difference grid, Wave motion, 31, 77-92.

Sheng, J., 2004. High Resolution Seismic Tomography With the Generalized Radon Transform and Early Arrival Waveform Inversion, Ph.D. thesis, University of Utah.

Shin, C., Jang, S., & Min, D., 2001. Improved amplitude preservation for prestack depth migration by inverse scattering theory, Geophysical prospecting, 49, 592-606.

Shin, C., Yoon, K.,Marfurt, K., Park, K., Yang, D., Lim, H., Chung, S., & Shin, S., 2001. Efficient calculation of a partial-derivative wavefield using reciprocity for seismic imaging and inversion, Geophysics, 66(6), 1856-1863.

Shipp, R. & Singh, S., 2002. Two-dimensional full waveform inversion of wide-aperture marine streamer data, Geophysical Journal International, 151, 325-344.

Sirgue, L., 2003. Inversion de la forme d'onde dans le domaine fréquentiel de données sismiques grands déports. Thèse de doctorat. Sciences de la Terre, Ph.D. thesis, Laboratoire de géologie de l'Ecole Normale Supérieure. Université Paris XI.

Sirgue, L. & Pratt, R., 2004. Efficient waveform inversion and imaging: a strategy for selecting temporal frequencies, Geophysics, 69(1), 231-248.

Stekl, I. & Pratt, R., 1998. Accurate viscoelastic modeling by frequency-domain finite difference using rotated operators, Geophysics, 63, 1779-1794.

Tarantola, A., 1984. Inversion of seismic reflection data in the acoustic approximation, Geophysics, 49(8), 1259-1266.

Tarantola, A., 1987. Inverse Problem Theory, Elsevier Sci, New York.

Numerical simulation of seismic experiments in volcanic areas: development of a technique based on the Pseudo-spectral Fourier method and its application to the build up of synthetic data sets for the Campi Flegrei area

P. Klin, E. Priolo

Istituto Nazionale Oceanografia e Geofisica Sperimentale, Trieste, Italy

Abstract: This report summarizes the development of a computer code for the simulation of seismic waves propagation in volcanic areas. The code is based on the Fourier pseudospectral approach and was implemented in order to take into account properly some of the features which typically characterize the volcanic environments, in particular: three-dimensional (3D) heterogeneity in the elastic properties distribution, irregular topography, viscoelastic attenuation of seismic waves and seismic velocity anisotropy. The report also illustrates the application of the code to the build up of a synthetic data set aimed at providing a testing tool for innovative seismic imaging techniques and for seismic anisotropy measurement techniques. The synthetic dataset is a result of three numerical simulations: a passive seismic experiment in isotropic environment, consisting in the record of a swarm of 316 microearthquakes in 16 stations; an active seismic experiment with 540 shots along a 27 km long seismic line with 9 receivers; and a passive seismic experiment in anisotropic environment with 3 double couple sources at different depths.

INTRODUCTION

The modeling of the full seismic wave field in 3D heterogeneous structures is a key factor in studies concerning the translation of the seismic observations into quantitative information about the dynamics of the volcanoes. Seismic waves observed in volcanic environments are usually affected not only by the heterogeneity of the elastic properties of the medium but also by the viscous attenuation of the seismic waves (Jousset et al., 2004), the anisotropy of seismic waves velocity (Gerst and Savage, 2004) and the strong topography of volcanic edifices (Chouet, 2003).

The advances of computational environments and the use of massive parallel computing have allowed, in the recent years, for the successful applications of a certain number of numerical algorithms for the simulation of the seismic wave field propagation in 3D heterogeneous velocity structures. In order to implement our own code for the numerical simulation of seismic waves in volcanic areas we have chosen the Fourier pseudo-spectral method on staggered grids (FPSM), based on the explicit time-domain stress-velocity marching scheme. The choice of the Fourier method is motivated by both the low spatial sampling rate – a critical factor for performing of large scale 3D simulations – and the simplicity of the structured mesh for which no sophisticated mesh generators are needed.

Since the direct application of numerical modeling of seismic waves in 3D to the interpretation of observed seismic signals was beyond the scopes of our task, we performed a set of numerical experiments in order to provide synthetic databases to be used for the testing of seismic imaging techniques. The experiments were based on realistic structural models mainly based on recent tomographic studies of the Campi Flegrei volcanic area (Judenherc and Zollo, 2004). We performed 3 numerical experiments:

A) a swarm of 316 microearthquakes recorded in 16 stations which mimics the University of Wisconsin experiment performed in the Campi Flegrei area during the 1984 uplift episode.

B) an active seismic experiment with 9 receivers and 540 shots along a 27 km long line which mimics one of the Serapis experiment lines across the Pozzuoli Bay.

C) a passive seismic experiment in anisotropic environment with 3 double couple sources at different depths.

Our FPSM simulation tool resulted unable to model accurately the propagation of seismic wave through liquid layers, therefore simplified models with sea water layer removed were adopted for the simulations.

METHOD

General features

Memory requirements represent the foremost challenge in the computer implementation of the seismic wavefield numerical simulation in 3D complex geomodels. The advance of computer technology has allowed 3D seismic modeling applications only in the last decade and they are still regarded as matter for supercomputers. For this reason we have pondered with great attention the efficiency questions during the design of our numerical method for 3D seismic modeling. The numerical approach we have chosen is the Fourier pseudospectral method (FPSM), (Kosloff and Baysal, 1982), which is based on the evaluation of the

spatial derivatives by means of the Fourier differential operator. The computer implementation of this operator exploits the low computational cost of the fast Fourier transform (FFT) algorithm. If we denote with x the spatial variable, k the wavenumber, i the imaginary unit and u a suitable function of x, we can express the spatial derivative of u as:

$$\partial_x u(x) = FFT^{-1}\big[ik\,FFT\,[u(x)]\big]$$

The accuracy of FPSM is highly improved by evaluating the spatial derivatives on staggered grids shifted in space by half grid step (Özdenvar and McMechan, 1996). In order to account for the half grid step shift the Fourier differential operator is coupled with a shift in space operator. The solution of the wave equation in our code is therefore based on the following expression:

$$\partial_x u\Big(x \pm \frac{\Delta x}{2}\Big) = FFT^{-1}\Big[ik\,e^{\pm ik\frac{\Delta x}{2}}\,FFT\,[u(x)]\Big]$$

The FPSM requires that the spatial domain is sampled by a rectangular structured grid in the same way as the finite difference method (FD) and therefore it needs no sophisticated 3D mesh generators in the input preparation stage. Nevertheless, the FPSM overall computer memory demand results much lower than that of the FD: since the FPSM requires to sample at least two points per minimum wavelength whereas 4-th order FD requires at least eight (Fornberg, 1987), the same volume can be modelled by the FPSM using 64 times less nodes than the 4-th order FD. A parallel implementation of the code is however appropriate, and we set up it by means of the data decomposition approach as follows. The computational domain is evenly split into subdomains with the shape of horizontal slices, which are assigned to single processors. Each processor perform all the computations on the subdomain that has been allocated to it except for the differentiation in the vertical direction. In order to apply a vertical derivative the computational domain is temporarily re-organized in vertical slices. This step is easily achieved in a Message Passing Interface (MPI) framework using the apposite MPI subroutine. Since a significant amount of communication between processors is required and the efficiency of the scheme may be affected by the multiprocessor device characteristic latencies, tuning tests are required to exploit at the best the computing power of the available multiprocessor device.

The computation of time evolution of the seismic wave field is based on the time domain stress-velocity marching scheme (Virieux, 1986). The marching scheme consists in the explicit solution of the linearised form of a couple of

first-order hyperbolic equations which describes the momentum conservation and the stress-strain relation respectively:

$$v_i(t+\Delta t)=v_i(t)+\frac{\Delta t}{\rho}\left(\sigma_{ij,j}(t+\frac{\Delta t}{2})+f_i(t+\frac{\Delta t}{2})\right)$$

$$\sigma_{ij}(t+\frac{\Delta t}{2})=\sigma_{ij}(t-\frac{\Delta t}{2})+\Delta t\left(\dot{\psi}_{ijkl}*\dot{\epsilon}_{kl}(t)\right)$$

where v_i are the particle velocity components, σ_{ij} are the stress tensor components, f_i are the external force components, ρ is the mass density, Δt is the time step, the comma denotes spatial derivative and the sum on repeated indexes is intended. ψ_{ijkl} are the components of the relaxation tensor and ε_{kl} are the components of the strain velocity tensor. The convolution operation is not suitable for a time domain computational scheme, but it can be re-casted by introducing memory variables as shown in a following chapter, whereas in the ideal elastic case the convolution is reduced to a multiplication.

In the Fourier PSM the wave field propagates through the model borders and comes back in the computational domain from the opposite side (wrap-around effect). In order to prevent it, the model must be surrounded by apposite absorbing layers. In 3D problems the increase of the overall dimensions of the computational domain due to the application of classical absorbing layers may be meaningful, so we implemented the perfectly matched layer (PML) absorbing belts (Chew and Liu, 1996; Collino and Tsogka, 2000; Festa and Nielsen, 2003) in our FPSM mode.

Our FPSM simulation tool demonstrated an instable behavior in propagating the seismic wave through liquid layers. We found that the present formulation of the computational kernel in our code admits unphysical modes of propagation in the liquid, since the condition $\nabla\times v=0$ can not be imposed. We have not found yet an efficient way to work around the problem without drastic changes of the code.

Implementation of anisotropy

We focused on the implementation of a tool capable to simulate the crack-induced stress-aligned shear wave splitting which can be assimilated to the transverse isotropy with horizontal axis (TIH) (Crampin and Peacock, 2005). Transverse isotropy requires 5 independent parameters in order to fully define the elastic properties of the materials. If we adopt the Voigt notation and express the stresses and strains as six components vectors, the elastic stress-strain relation for a TIH medium with symmetry axis aligned with the x_1 direction writes as:

$$
\begin{pmatrix} \sigma_{11} \\ \sigma_{22} \\ \sigma_{33} \\ \sigma_{23} \\ \sigma_{13} \\ \sigma_{12} \end{pmatrix} = \begin{pmatrix} C_{11} & C_{13} & C_{13} & 0 & 0 & 0 \\ C_{13} & C_{33} & C_{23} & 0 & 0 & 0 \\ C_{13} & C_{23} & C_{33} & 0 & 0 & 0 \\ 0 & 0 & 0 & C_{44} & 0 & 0 \\ 0 & 0 & 0 & 0 & C_{66} & 0 \\ 0 & 0 & 0 & 0 & 0 & C_{66} \end{pmatrix} \begin{pmatrix} \varepsilon_{11} \\ \varepsilon_{22} \\ \varepsilon_{33} \\ \varepsilon_{23} \\ \varepsilon_{13} \\ \varepsilon_{12} \end{pmatrix}
$$

where $C_{23}=C_{33}-2C_{44}$, while the other components of the stiffness matrix are independent. We adopted the Thomsen (1986) approach for the description of the "weak" anisotropy of the materials, i.e. through the velocities of the body waves along the symmetry axis and three parameters ε, γ and δ defined as follows:

$$
\varepsilon = \frac{C_{33}-C_{11}}{2C_{11}} \quad , \quad \gamma = \frac{C_{44}-C_{66}}{2C_{66}} \quad \text{and} \quad \delta = \frac{(C_{13}+C_{66})^2-(C_{11}-C_{66})^2}{2C_{11}(C_{11}-C_{66})} \quad .
$$

We can found these definitions correspond, in sequence, to:

$$
\varepsilon = \frac{V_p(\pi/2)-V_p(0)}{V_p(0)} \quad , \quad \gamma = \frac{V_s^\perp(\pi/2)-V_s^\perp(0)}{V_s^\perp(0)} \quad \text{and} \quad \delta = 4\left(\frac{V_p(\pi/4)}{V_p(0)}-1\right)-\left(\frac{V_p(\pi/2)}{V_p(0)}-1\right)
$$

where Vp is the compressional wave velocity, $Vs^\perp$ is velocity of the shear wave with polarization plane perpendicular to the symmetry axis, and the value in the brackets denotes the angle between the direction of propagation and the symmetry axis. Therefore ε describes the P waves anisotropy, γ describes the S waves anisotropy and δ controls the shape of the P wavefront (it results elliptic only when $\varepsilon=\delta$).
The numerical scheme and the implemented code have been validated through a number of tests. As an example, in Figure 1 the splitting of the S wave into two different phases with different polarization directions is clearly seen.

Implementation of attenuation

The viscoelastic stress-strain relation was implemented in the time domain scheme by means of the "memory variables" technique (Carcione, 1995), which is resumed in the following.
The stress-velocity strain relation for an (isothermal), anisotropic viscoelastic medium can be written as (Boltzmann superposition principle):
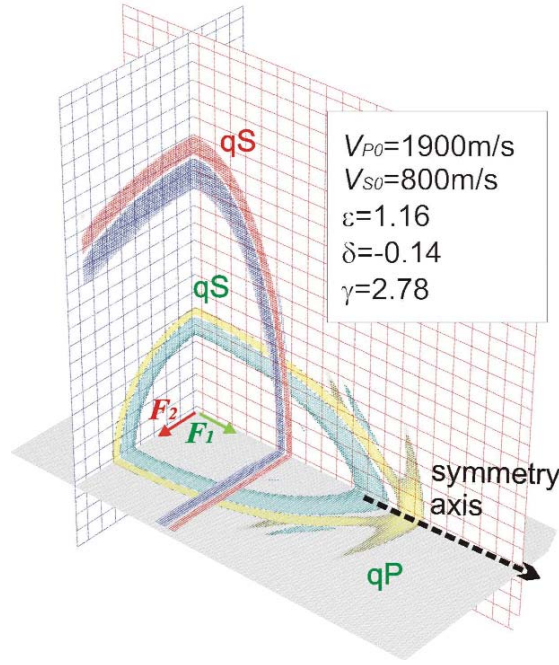
Fig. 1. Snapshot of the seismic wave-field simulated in a hexagonally anisotropic medium and gene-rated by two point forces (F1 and F2) parallel to the medium symmetry axis and perpendicular to it, respectively. In red/blue and yellow/cyan scale are shown the respective waves after 2 seconds of propagation. Only the component parallel to the force that has generated the wave is shown. The anisotropy is described by means of parameters whose meaning is defined in the text.

$$\dot{\sigma}_{ij} = \dot{\psi}_{ijkl} * \dot{\epsilon}_{kl}$$

where ψ_{ijkl} is the time domain symmetric relaxation tensor, whose compo-nents are of the form:

$$\psi_{ijkl}(t) = \tilde{\psi}_{ijkl}(t) H(t)$$

where $H(t)$ is the Heavyside function and the tilde denotes a "regular" real function defined on the whole time axis. Known theorems (Boltzmann ope-ration) allow rewriting the strain stress relation as:

$$\dot{\sigma}_{ij}(t) = \tilde{\psi}_{ijkl}(0) \dot{\epsilon}_{kl}(t) + \phi_{ijkl}(t) * \dot{\epsilon}_{kl}(t)$$

where $\phi_{ijkl} = \dot{\tilde{\psi}}_{ijkl}(t) H(t)$

Thus, we can express the stress time derivative as a sum of two terms:

$$\dot{\sigma}_{ij}(t) = c_{ijkl} \dot{\epsilon}_{kl}(t) + R_{ij}(t)$$

The first term corresponds to the instantaneous elastic response of the medium (described by the unrelaxed elasticity matrix c_{ijkl}, while the term $R_{ij}(t)$ called "memory variable" accounts for the contribution to the stress of past deformation states. The evolution of $R_{ij}(t)$ depends on the chosen relaxation mechanism and on the attenuation properties assigned to each propagation mode.

We have chosen to simulate the intrinsic attenuation by means of the Generalized Standard Linear Solid (GSLS) mechanical model, which is considered adequate to describe the viscoelastic behaviour of the volcanic media (Jousset et al., 2004). The GSLS is composed of several Standard Linear Solid (SLS) elements. Each SLS element accounts for the dissipation in a narrow frequency band and with an adequate superposition of SLS elements into a GSLS we can model a general frequency dependence of the dissipation (Carcione, 2001).

We implement the GSLS attenuation model for the anisotropic medium by following the approach described by Carcione (1995). We focused on the simulation of a nearly frequency independent intrinsic attenuation, considering separately the quasi-dilatational and quasi-shear propagating modes. Thus
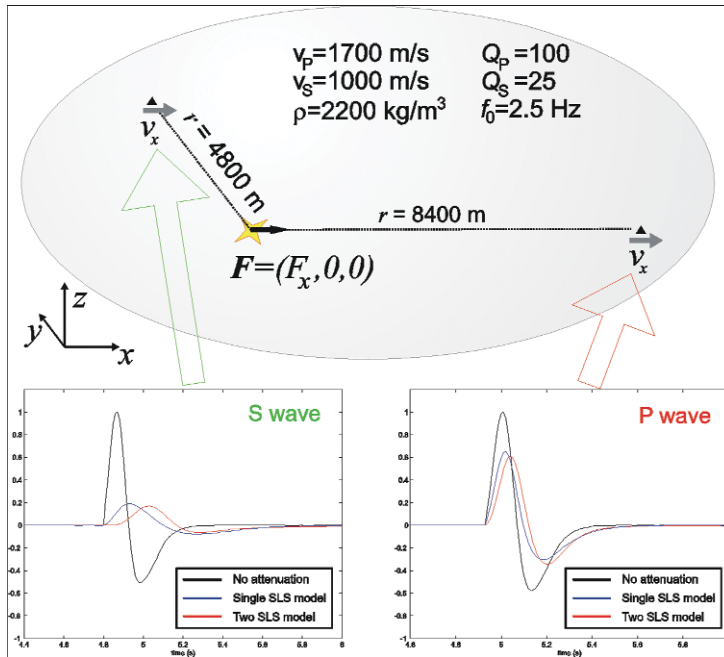
Fig. 2. Example illustrating the effectiveness of the attenuation modeling with one SLS and with two SLS elements. The latter results in a less peaked dependence of Q from the frequency. Note that different attenuation properties for the compressional and the shear modes of propagation can be assigned to the medium.

we consider the attenuation property of the material as described by two parameters, i.e. the frequency independent quality factors Q_P and Q_S. The GSLS parameters needed to reproduce a given quality factor $Q(\omega)$ which is approximately constant in a limited frequency band can be obtained by means of the "T-method" (Blanch et al., 1995). Since each additional SLS element requires a new memory variable to be defined over the spatial domain, the technique is avid of computer RAM. In order to avoid an excessive requirement of memory, we limited the description of the attenuation by means of the superposition of only two SLS elements, which guarantees a nearly frequency independent Q over a decade of frequency units.

Implementation of topographic surface

The implementation of topography represents the most significant improvement we made to the FPSM. The Fourier differential operator performs best on periodic functions, whereas seismic waves modelling imply derivatives of functions which are defined on limited intervals. An accurate application of FPSM to seismic modeling is therefore far from being trivial even for simple models with flat topography and we were not surprised to find the implementation of topography the most demanding feature to be included in the FPSM code.

In our approach we introduce the irregular 3D topography by discretizing it in a staircase of cubic cells centred in the nodes of the nominal grid, thus following a method very similar to that implemented by Ohminato and Chouet (1997) in their FD scheme. Alternative approaches, which imply the mapping of the rectangular grid onto a curved grid which follows the topograhic surface, were discarded because they turned out to be incompatible with the used staggered grids scheme and would require a drastic modification of the code with significant increase of the computational resources demand.

Flat topography models with 3D rectangular shaped domains requires differential operators acting on maximum three different lengths, and the execution of the code could be speed up if we choose these lengths as powers of two, allowing to exploit at maximum the potential of FFT. This is not the case for the application of FPSM to staircase shaped domains corresponding to models with included topography, when we need to define Fourier differential operators on a wide choice of lengths, many of which are not compatible with classical FFT. However the availability of new fast algorithms for the computation of discrete Fourier transforms of arbitrary length, such as the FFTW3 library (Frigo and Johnson, 2005), makes the application of FPSM to staircase shaped domains an attractive option, too.

The main point in the implementation of accurate modeling of free surface in our code consists in the distinction between the spatial differentiation of the stress and the velocity variables. The free surface condition implies that the

differentiated stress components simply vanish on the definition interval extremes and we can design the Fourier differential operators to take implicitly into account this property by using sine transforms instead of Fourier transforms. On the other hand the velocity variables are not constrained on the definition intervals and therefore can not be handled with accuracy by a Fourier differential operator. To solve this, we apply a procedure consisting in the detrending of the velocity spatial sequences along the direction of differentiation before the application of the Fourier differential operator and in the subsequent addition to the obtained derivative of the constant trend rate.

Some test were performed to evaluate the efficiency of the method. Figure 3 shows a snapshot of the simulation of the seismic wave propagation in a
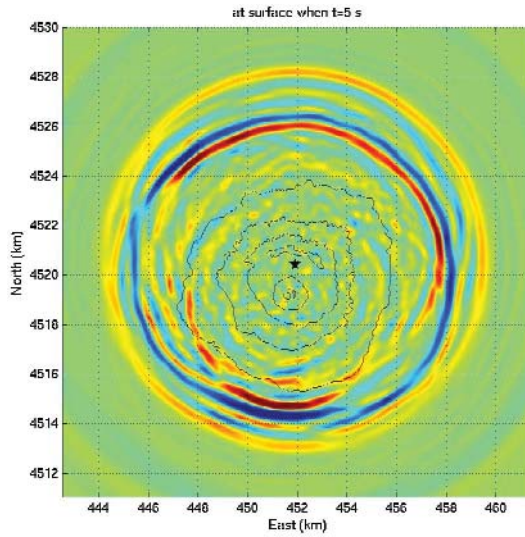
Fig. 3. Snapshot of the seismic wavefied at surface of a homogeneous medium (Vp=3000 m/s; Vp/Vs=1.8), with top surface shaped as the Vesuvius topography (black contour lines with 250-m interval). Black star denotes the epicenter location. The alteration of the wavefield (f_{max}=5 Hz) is remarkable, considering the symmetry of the source (vertical dipole at depth 700 m below sea level).

homogeneous medium with Vesuvius topography shaped surface using a vertical dipole point source buried below the volcano. The simulation was performed using a discretization of the volume in a 500 x 500 x 64 rectangular grid with 40 m spacing. The effect of the topography of the volcano on the wavefront shape (surface waves) is clearly observable. 6 seconds of wavefield propagation were computed in 12 hours of wall-clock time using 10 AMD-Opteron processors of a Sun Fire X4600 server.

MODELLING

Experiment A
Passive seismic experiment: swarm episode in Campi Flegrei

Local earthquakes represent the most common source of seismic data for the 3D imaging of a volcanic edifice structure. In order to provide a testing tool for seismic imaging techniques which rely on waveforms of local earthquakes we performed a synthetic seismic experiment which mimics the swarm episode recorded by a portable network at Campi Flegrei in the years 1983-84, (the University of Wisconsin – UW experiment). A reference 3D structural block model characterized by interfaces with given impedance contrast, thereafter called CF block model (Figure 5), has been constructed by Claudio Satriano (UniNa Research Unit) on the basis of the current knowledge of the Campi Flegrei structure. We painted the properties defined in the structural model onto a orthogonal grid oriented with the geographical directions with horizontal sampling step length of 100 m and vertical sampling step length of 20 m. The grid was taken 128 nodes long in the horizontal directions and 320 nodes deep and represents the structure below the area shown on the map in Figure 4 up to a depth of 6.4 km. For the sake of simplicity we neglected the
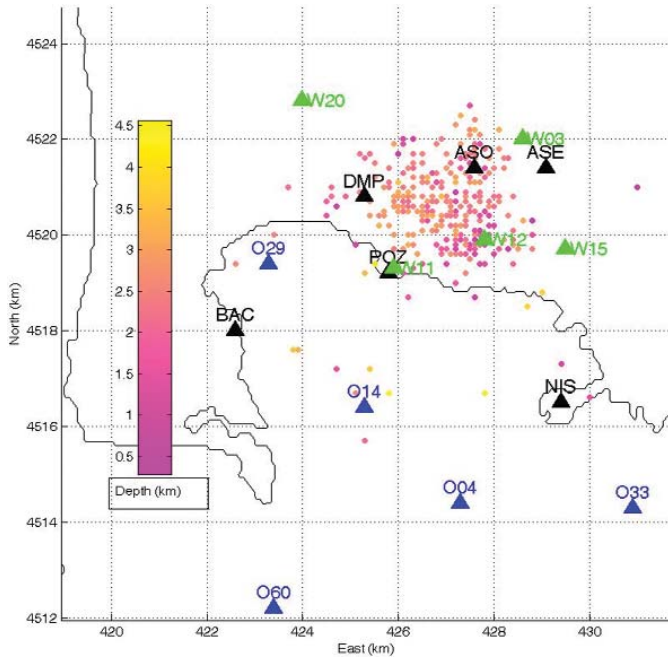
Fig. 4. Position of the 316 hypocenters (coloured dots) and of the 16 stations for the synthetic passive seismic experiment which simulates a swarm of microearthquakes.

sea water layer and the topography. The maximum frequency of the modelled waveforms is 5 Hz and their duration is 16 sec.

The result of the experiment consists in 316 three component velocigrams corresponding to microearthquakes with hypocentres marked by dots in the map in Figure 4 for each of the 16 stations located at the positions marked by triangles in the same figure. The locations of the stations correspond to 5 of those of the UW experiment (green triangles), 6 of the present Osservatorio vesuviano (OV) network and 5 OBS locations of the Serapis active seismic survey. The location, focal mechanism and seismic moment for each microearthquake has been randomly chosen among the known parameters of the 1983-84 events.

Since the experiment implies a number of receivers which is an order of magnitude lower than the number of seismic sources, we actually computed the waveforms by exploiting the reciprocity principle (Eisner and Clayton, 2001): only 48 simulations (3 component times 16 stations) instead of 316 were therefore sufficient to compute the whole dataset. Each simulation required 5 hours of wall-clock time on 44 Intel Xeon processors of the IBM-Linux Cluster at CINECA (Bologna, Italy).
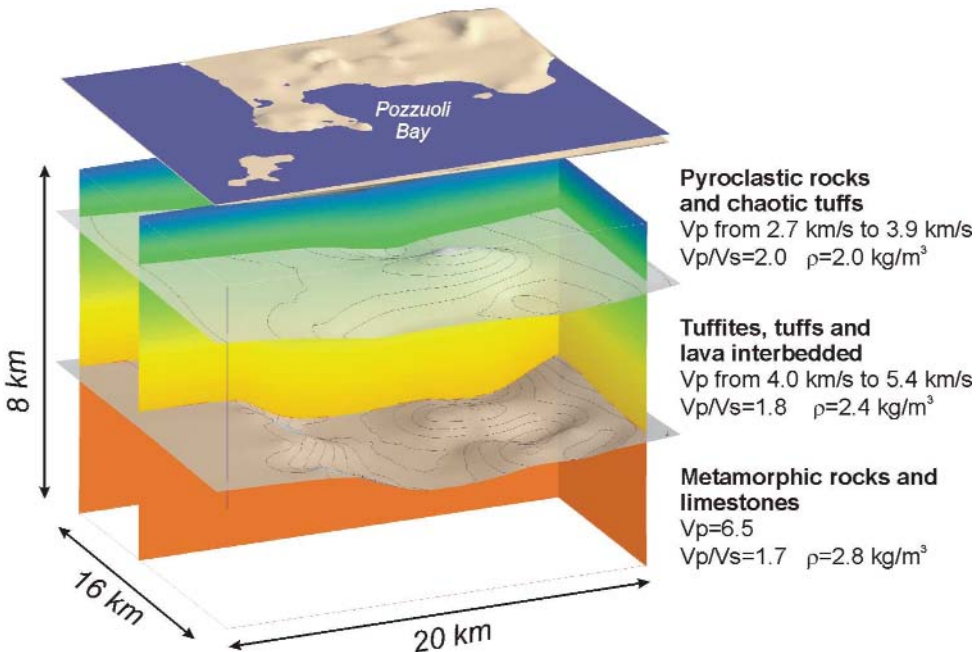
Fig. 5. Three dimensional view of the digital model prepared for the numerical simulations of the Campi Flegrei area. The vertical dimension is 2x-exaggerated. The topographic map is shown at the top only for the sake of clearness. Vp varies smoothly inside each of the three layers, whereas it features a discontinuity at the interfaces. The Vp/Vs ratio and density are constant inside each layer. A Q=280 value is assumed for the whole model.

Experiment B
Active seismic experiment: seismic line in Pozzuoli Bay (Campi Flegrei)

Many imaging techniques are designed to be applied specifically to active seismic data. In order to provide a testing database for these techniques, we produced a synthetic active experiment consisting in a 27 km long seismic line which mimics one of the seismic lines of the "Serapis" active seismic survey performed in the Pozzuoli bay in September, 2001 (Judenherc and Zollo, 2004). The considered line crosses the Pozzuoli bay with NW-SE orientation and a 2D structural model along that line has been interpreted by researchers of Naples University from the velocity depth section obtained from "Serapis" data. The
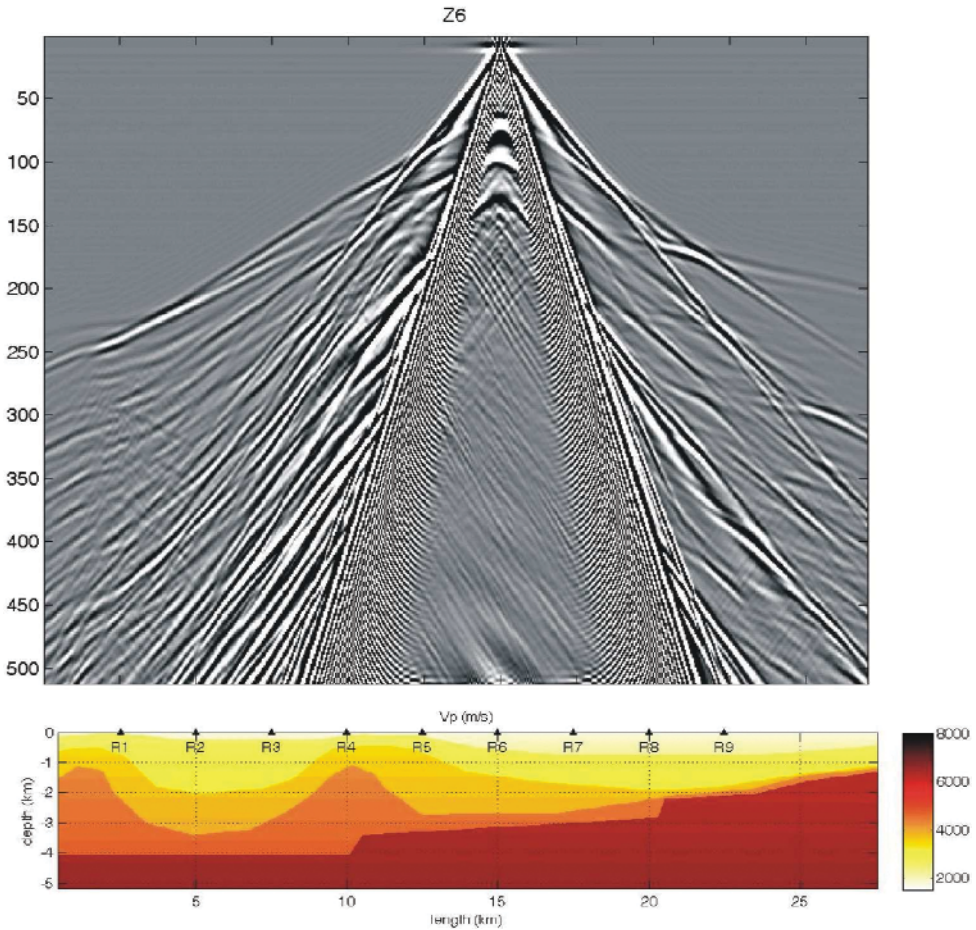
Fig. 6. Example of one of the 9 common receiver seismic sections along the input structural model (bottom). Vertical component. Timesteps in the ordinate, with time sampling step of 0.02.

structural model consists of 5 structural units with seismic velocities characterized by a vertical gradient of increase with the depth, plus the sea water layer. Since our method resulted inapplicable to models with sea layer, we performed the simulations using a "dry" version of the model, which was obtained from the provided one by removing the upper 500 m (Figure 6, bottom).

Since the wave propagation is solved through a 3D method (avoiding the well known limitations of 2D wave propagation simulations), the 2D model was extruded in the transversal direction to obtain an equivalent 3D model. The 3D model was then discretized in a rectangular grid with spacing 25 m, 1088 nodes long, 32 nodes wide and 208 nodes high.

About 10 second long synthetic vertical and radial component velocigrams with frequency content up to 10 Hz have been computed for 540 shots (regularly distributed on the surface with 50 m spacing) and 9 receivers (regularly distributed on the surface with spacing 2500 m). As in the experiment A we exploited the reciprocity principle to compute the waveforms, since the number of receivers is much lower than the number of shots.

The resulting common receiver gathers evidences strong ground roll due to the absence of the water layer. The produced synthetic database could therefore be of interest for imaging techniques which rely on large offset signals only.

Experiment C
Passive seismic experiment: anisotropy

Stress changes in the medium due to volcanic activity produces changes in anisotropy of seismic waves velocity (Gerst and Savage, 2004). Anisotropy changes can be detected by shear wave splitting (Crampin and Peacok, 2005). In order to provide a testing platform for shear wave splitting measurement and
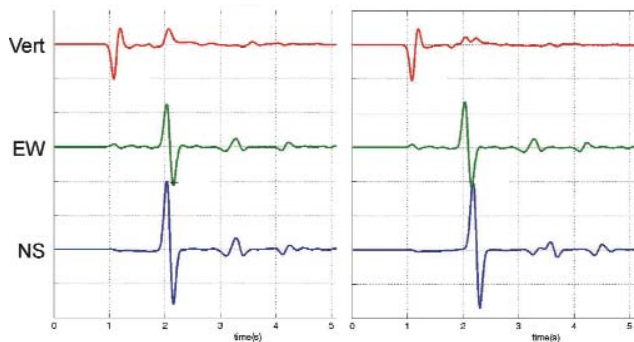
Fig. 7. Example of the synthetic seismograms obtained in Experiment C for the station DMP. Left: no anisotropy. Right: 10% SWVA in layers below 600m. Source depth 3.4 km. Epicentral distance 700m.

analysis techniques we synthesized a passive seismic experiment consisting in the simulation of 3 micoearthquakes. The used velocity model is CF block model (Figure 5) with an additional 600 m thick surface horizontal layer in which Vp ranges from 2500.0 m/s at surface to 3000.0 m/s at 600m with Vp/Vs=2.5. Below that layer TIH anisotropy with SWVA=10% is considered with symmetry axis parallel to the EW direction. Topography and sea layer were neglected.

The seismograms of 3 microearthquakes with epicenter at UTM coordinates 425480m East and 4521480m North and depths of 1700 m, 3400 m and 5400 m, respectively, were computed for the same 16 stations considered in the experiment A, but with an upper frequency limit of 10 Hz.

DISCUSSION AND CONCLUSION

We developed a versatile computer code (FPSM3D) for full wave seismic modeling in 3D heterogeneous anelastic medium with TIH anisotropy, bounded at top by a free surface with irregular topography. We applied it to the construction of synthetic datasets for the validation of techniques for seismic imaging and shear wave anisotropy analysis in volcanic environments. The application of the code to the reproduction of seismic experiments of different kind (passive and active ones) put in evidence some advantages of using FPSM3D as well as its drawbacks. The most appreciable advantages are the simplicity of the input preparation (the 3D model is described by a rectangular grid) and the relatively low computer memory requests (common applications run easily on less expensive multi core servers such as the Sun Fire X4600). The most evident disadvantage of the current version of FPSM3D resulted in the impossibility to model the seismic wave propagation in liquid media. We foresee to heal this weakness in a future improvement of the code.

REFERENCES

Blanch J.O., Robertsson J.O.A. And Symes, W.W., 1995. Modeling of a constant Q: Methodology and algorithm for an efficient and optimally inexpensive viscoelastic technique. Geophysics 60, 1, 176-184.

Carcione J. M., 1995. Constitutive model and wave equations for linear, viscoelastic, anisotropic media. Geophysics, 60, 2, 537-548.

Carcione J. M.., 2001. Wave Fields in real media: wave propagation in anisotropic, anelastic and porous media. Handbook of geophysical exploration – Klaus Helbig and Sven Treitel, Editors, Vol. 31. Pergamon.

Chouet, B., 2003. Volcano Seismology. Pure appl. Geophys. 160, 739-788.

Chew W, Liu QH. 1996. Perfectly matched layer for the elastodynamics: a new absorbing boundary condition. J. Comp. Acoust. 4, 341-359.

Collino F and Tsogka C. 2001. Application of the perfectly matched absorbing layer model to the linear elastodynamic problem in anisotropic heterogeneous media. Geophysics 1, 294-307.

Crampin S. and Peacock S., 2005. A review of shear-wave splitting in the compliant crack-critical anisotropic Earth. Wave motion 41, 59-77.

Eisner L. and Clayton R., W., A reciprocity Method for Multiple-Source Simulations. Bull. Seismol. Soc. Am.; 91: 553-561.

Festa G and Nielsen S. 2003. PML Absorbing Boundaries. Bull. Seismol. Soc. Am.; 93: 891-903.

Fornberg, B., 1987. The pseudospectral method: Comparisons with finite differences for the elastic wave equation. Geophysics, 52, 4, 483-501.

Gerst A. and Savage M. K., 2004. Seismic Anisotropy Beneath Ruapehu Volcano: A Possible Eruption Forecasting Tool. Science 306, 1543-1547.

Jousset, P., Neuberg, J., Jolly, A., 2004. Modelling low -frequency volcanic earthquakes in a viscoelastic medium with topography. Geophys. J. Int., 159, 776-802.

Judenherc S. and Zollo A., 2004. The Bay of Naples (southern Italy): Constraints on the volcanic structures inferred from a dense seismic survey. J. Geophys. Res. Vol. 109, B10312.

Kosloff D. D. and Baysal, E., 1982. Forward modeling by a Fourier method. Geophysics, 42, 10, 1402-1412.

Matteo Frigo and Steven G. Johnson, 2005. The Design and Implementation of FFTW3, Invited paper, Special Issue on Program Generation, Optimization, and Platform Adaptation. Proceedings of the IEEE 93 (2), 216-231 .

Ohminato, T., and Chouet, B.,A., 1997. A Free Surface Boundary Condition for Including 3D Topography in the Finite Difference Method. Bull.Seism.Soc.Am., 87, 2, 494-515.

Őzdenvar T and McMechan GA. 1996. Causes and reduction of numerical artifacts in pseudo-spectral wavefield extrapolation. Geophys. J. Int.; 126: 819-828.

Thomsen L., 1986. Weak elastic anisotropy. Geophysics, 51, 10, 1954-1966.

Vireux, J., 1986. P-SV wave propagation in heterogeneous media: Velocity-stress finite-difference method. Geophysics, 51, 4, 889-901.

Converted phases analysis
for passive/active seismic data

D. Latorre[1], T. Blacic[2], J. Virieux[2], T. Monfret[2]

[1] *Istituto Nazionale di Geofisica e Vulcanologia, CNT, Roma, Italy*

[2] *UMR Geosciences Azur, Sophia-Antipolis, France*

Abstract: Migration techniques, currently used in seismic exploration field, are still scarcely applied in earthquake seismology due to the poor source knowledge and to the sparse, irregular acquisition geometries. At crustal scale, classical seismological studies often perform inversions based on the arrival time of primary phases (P- and S-waves), but seldom exploit other information included in seismic records. Here we show how migration techniques can be adapted to earthquake seismology for converted wave analysis. Local earthquake tomography has provided earthquake hypocenter locations and three-dimensional models of P and S velocity fields. Strong secondary signals between first-arrivals of direct P- and S-waves may be interpreted as converted (transmitted and/or reflected) waves. Because amplitude can be weak, we must proceed to a summation over sources and receivers in a way similar to a prestack depth migration scheme based on the Kirchhoff summation technique. Since source parameters are either poorly constrained or unknown as radiation patterns, we must rely only on kinematic aspects of the migration process. Amplitudes will be used only for assessing the coherence of the summation procedure. Converted wave travel-times are calculated in the three-dimensional tomographic models by using a finite-difference eikonal solver and an accurate back ray-tracing. In the migrated images, the area of dominant energy conversion may be related to seismic horizons of complex shape. Validation of the identification of these converted phases leads to geodynamic interpretation.

INTRODUCTION

One of the aims of earthquake seismology is the study of physical phenomena related to the earthquakes and their effect on the Earth's surface. The achievement of these goals requires detailed knowledge of the subsurface structure, especially in seismogenic areas. At the crustal scale, a common tool for subsurface imaging is the Local Earthquake Tomography (LET), in which parameters of earthquake hypocenters and velocities of P- and S-waves are simultaneously inverted by using first-arrival delay-times (e.g., Thurber, 1983;

Michelini and McEvilly, 1991; Hole 1992; Le Meur et al., 1997; Monteiller et al., 2005, among others).

Beside the analysis of travel-times of some phases (mainly direct and surface waves), common tools of earthquake seismology seldom exploit other information included in seismic records. Nevertheless, recent studies demonstrate that microearthquakes (hereafter called passive sources) can be used as controlled sources for crustal-scale imaging with reflected, transmitted and mode-converted waves (James et al., 1987; Chavez-Perez S. and Louie, 1998; Stroujkova and Malin, 2000; Chavarria et al., 2003; Latorre et al., 2004a, Nisii et al., 2004).

One of the major problems in using passive data for seismic reflection/transmission imaging concerns the sparse and irregular distribution of sources and receivers, and the poor knowledge of the source, which includes magnitude, focal mechanism, earthquake hypocenter location and origin time. Moreover, in most passive seismic surveys, receiver coverage is sparse and irregular because seismic networks are mainly designed for earthquake monitoring rather than for seismic imaging. Nevertheless, Louie et al. (2002) showed, through synthetic tests, that passive-source migration approaches are able to image main features of the subsurface structure, despite artifacts due to the poor geometrical coverage. As the cost of one seismic station is reducing, we may expect that the increase of the number of receivers will make the analysis of converted phases more attractive for seismic crustal imaging and, more specifically, for volcanic area.

Hypocentral parameters (earthquake location and origin time) represent one of the main causes of error in focusing and positioning reflected/transmitted energies. Uncertainty in earthquake location is strictly correlated to our knowledge of both the P- and S-wave velocity structures. Moreover, earthquake location in seismogenic areas requires taking into account lateral variations of the velocity structure. In local-scale passive imaging approaches, the coupled hypocenter-velocity model problem is solved by inverting simultaneously velocity and hypocentral parameters (Thurber, 1993). In this context, reflection/transmission imaging with passive sources should involve previous estimation of background velocities and hypocenter parameters by using three-dimensional tomographic algorithms. The radiation pattern is another issue when analyzing amplitudes. Although we shall not attempt to handle this problem in this report, we may underline that it is possible de determine the double-couple radiation when enough polarities are extracted from seismograms.

Identification of phases as PP, SS, PS and SP phases is a crucial problem which leads to rather different geodynamical interpretations. Whatever will be our phase interpretation, we may rely on the three components at the receiver station to perform a partial discrimination aside the selection from the travel-time windows.

After discussing the method for depth projection of recorded converted phases, we shall investigate what are key parameters for better energy focusing

before concluding on the methodological approach. Applications have been performed for different areas as Corinth Gulf (Latorre et al, 2004a), Molise aftershock sequence in 2002 (Latorre et al, 2007). The application to the Campi Flegrei is presented in a complementary report of this project V4 (Blacic et al, 2007).

METHOD

Our migration scheme is based on the Kirchhoff summation technique. The migrated image is reconstructed in the space domain by summing weighted trace energies along complex hyperbolic trajectories in the time domain, whose shape is governed by the velocity distribution of the medium (e.g., Yilmaz, 2000).

In order to do so, we need information related to time delays performed by wave propagation and, equivalently, how to shift seismograms in time in order to take into account the position and the origin time of earthquakes will be the key ingredient of our energy projection inside the crustal structure. This is the kinematic step of the procedure.

In that attempt of focusing the energy, we shall cautiously consider amplitudes as quite sensitive although uncertain quantities. Therefore, strategies for preserving robust information by comparing, normalizing amplitudes will qualify the different focusing imaging procedures we may think about. This will correspond to the dynamic step of the procedure.

Kinematic parameters estimations

The target volume is divided into a three-dimensional regular grid of image points. Each point of the grid is associated with a local oriented interface where we assume that seismic diffraction (or reflections/transmissions when considering a local interface) may occur (Figure 1). Computation of kinematic parameters can be achieved quite efficiently when considering a smooth medium on top of which a diffractor is inserted. An interface might be viewed as a set of dense oriented diffractors points. Because we shall proceed through rays, these interface pieces do not interact and, therefore, the decomposition of an interface in independent oriented points is equivalent to consider the interface as a whole. First of all, we may proceed by computing fastest travel times for couples (source, diffractor) and (receiver, diffractor) by using an eikonal solver (Podvin & Lecomte, 1991). It allows in a single run for each (source/receiver) to perform the back raytracing towards each diffracting point. We re-compute more accurate travel times along ray-paths (Latorre et al., 2004b).

This 3D sampling of the medium by rays is efficiently performed as long as the medium does not have sharp contrasts. This means that each diffractor is
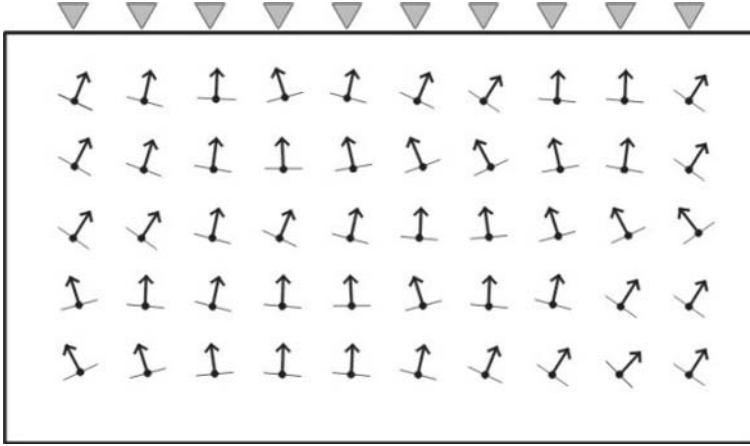
Fig. 1. Discretisation of the medium through regularly space diffraction points with a local orientation. A single interface could be considered as a selected sum of these oriented diffraction points as shown by the red line.

seen by both the source and the receiver. If not, the focusing at the image point will not be performed at that point.

Collecting information at diffraction points is crucial for efficient focusing procedure. We must compute slowness vectors for each ray: one for the source and one for the receiver. We must as well estimate geometrical spreading through paraxial ray tracing performed on top of the back-ray tracing module (Virieux and Farra, 1991). With the local normal information, this will give us 11 quantities to be stored at each grid point for each P and S wave. More complex reference media with reference interfaces could be considered by using more complete ray tracing tools (Virieux and Lambaré, 2007 for a review) but this will make the focusing analysis more delicate. We cannot rule out these interference waves although we do expect their amplitude to be weak enough for negligible contributions to the imaging point. From these kinematic informations, one may estimate travel-time curves for both direct waves and converted waves at the receiver considering single scattering points.

For a simple presentation, we consider a flat interface providing us a single line of diffracting points at a specific depth of 12 km for a top layer of P wave velocity of 5 km/s and a S wave velocity of 3 km/s. At each point, a vertical normal is considered which is the local translation of the flat interface geometry. A spherical anomaly is added in the center of this top layer below the fifteen receivers we consider as shown in the bottom panel of Figure 2. The velocity structure does not need to be considered below the reference depth although we let the wavefront estimation to be performed there. We may avoid possible fast rays going below the depth of 12 km before arriving to the diffractor. Consequently, velocity below the selected depth should be modified
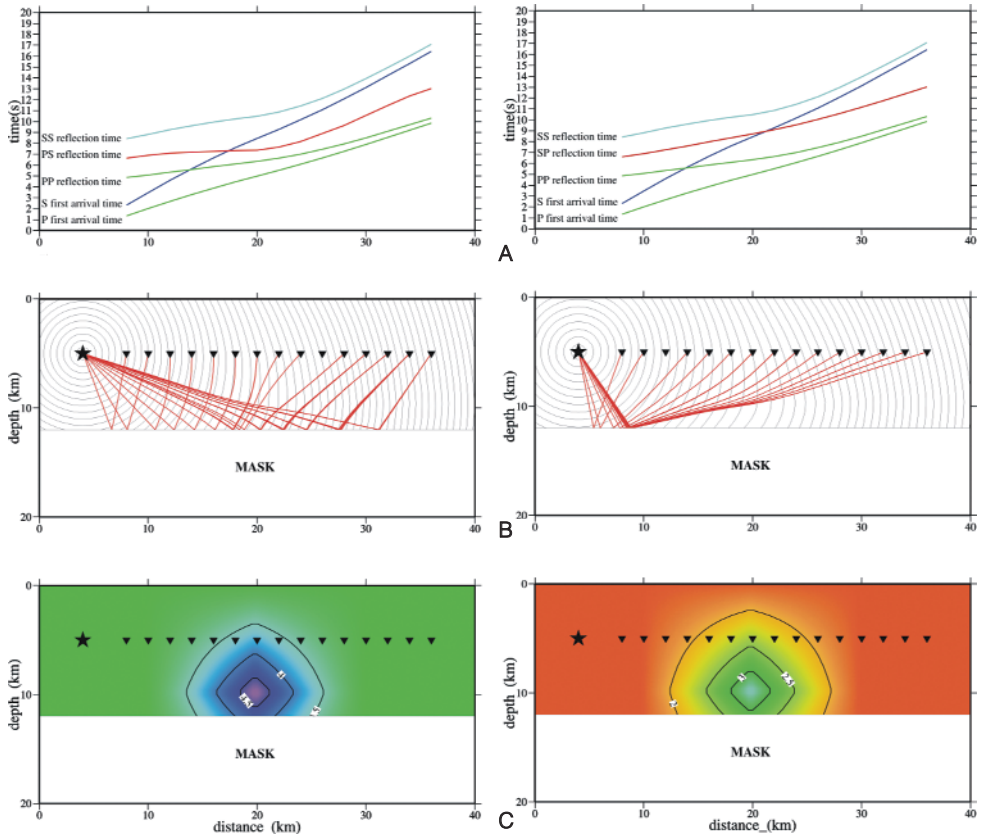
Fig. 2. Arrival time of a SP phase reflected at an horizontal interface in an heterogeneous 3D velocity model; **(a)** travel time curves of P and S first arrivals and PP, SP and SS reflected phases, **(b)** wave fronts of the direct S first arrival times and reflected ray tracing, **(c)** 2D S velocity model and the interface.

for preventing such configuration. Another way will be to cancel out the contribution of such rays in the focusing analysis. Wavefronts are computed from the source as well as from the fifteen receivers. By ray-tracing from each diffracting point of the selected depth back to the source or the fifteen receivers, we may have rays connecting the source and the receiver going through the diffraction point. Of course, only one ray will verify the Snell's law associated to a reflection as shown in the middle panel of Figure 2. Using this total ray from the source to the receiver, we may estimate travel-times and we shall discriminate converted phases from direct waves. In the top panel of Figure 2, the P and S waves are crossed by the PP, PS reflections at an other offset around 12 km while the SS reflection will always arrive later than the S direct wave.

The Figure 3 shows identical computation for a curved interface. This figure will illustrate the balanced effects between a top layer velocity anomaly and the deeper position of the interface in terms of kinematic parameters. Effects of the highest velocity structure in the center of the model are nearly cancelled out by the curved shape of the interface for travel-time estimations. Only the spatial sampling of the model space will go dramatic differences we shall expect to show up when stacking energy.

The computational effort although noticeable remains quite tractable, as the eikonal solver is an efficient tool for sampling 3D media. Storing informations at the diffraction points is done once before performing the summation procedure which requires tuning parameters.
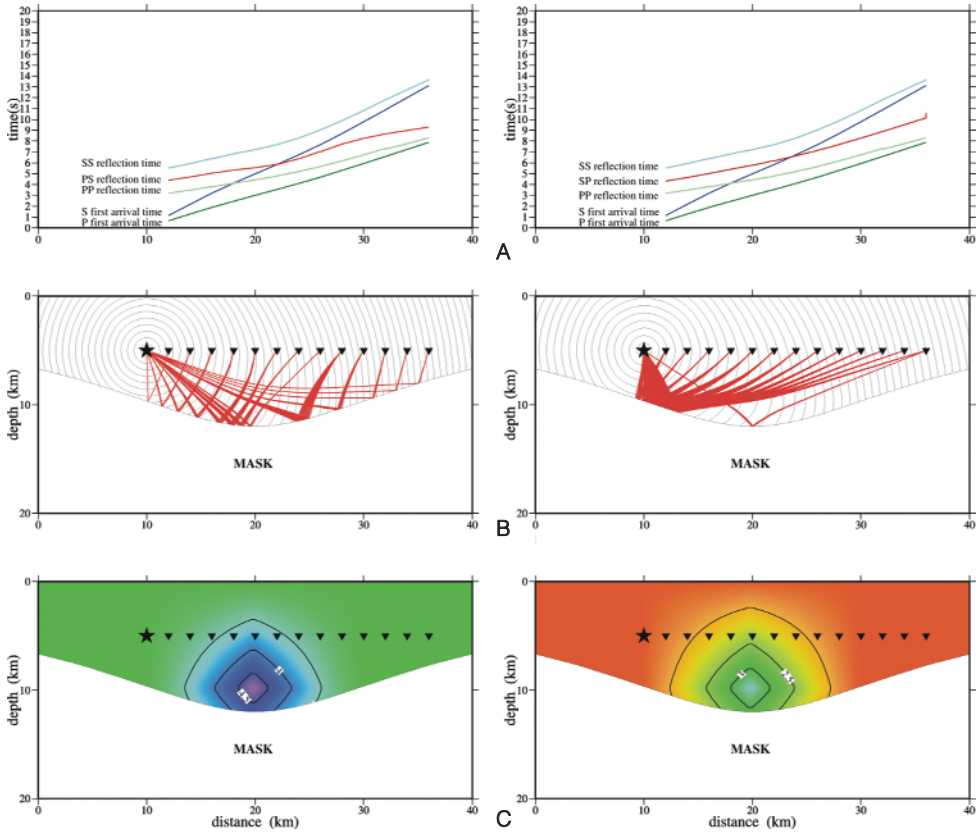

Fig. 3. Arrival time of a SP phase reflected at an interface with a complex geometry in an heterogeneous 3D velocity model; **(a)** travel time curves of P and S first arrivals and PP, SP and SS reflected phases, **(b)** wave fronts of the direct S first arrival times and reflected ray tracing, **(c)** 2D S velocity model and the interface definition.

Dynamic summation as the focusing procedure

At a given image point, the migrated image is obtained by summing the seismic amplitude of windowed trace segments corrected by the total travel-time computed along each source-image point-receiver path. The stacking procedure is the difficult task of the imaging procedure because we must take into account different factors that modulate the seismogram amplitude.

The first feature one has to be worried about is the difference between a diffraction wave and a reflection/transmission wave. While summing numerous diffractions will lead to a reflection for example as done in standard finite-difference solvers of the wave equation, we must consider a priori reflection directions in order to avoid this intensive diffraction summation which is impossible to achieve with the data we collect at receivers. This is the reason why we have introduced oriented diffracting points. Therefore, a weight factor based on the Snell's law may help the focusing: at each image point, we assume an oriented interface and we consider rays hitting this interface (incident and diffracted rays). The Snell's weighting factor is defined as the cosine of the angle between the computed image point-receiver ray direction and the predicted specular ray at the interface, i.e., the ray satisfying the Snell's law (Figure 4). Thus, the weight value decreases as the ray direction goes away
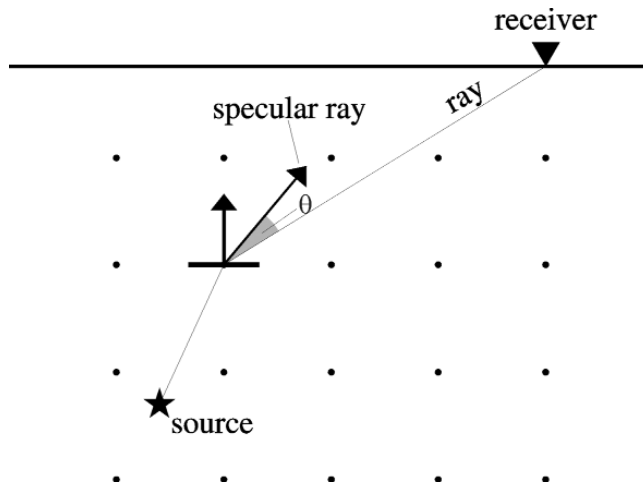
Fig. 4. Simplified sketch showing the migration scheme applied in this work. The target volume is divided into a regular grid of image points (black dots). Each of them is associated to an oriented local interface identified by its normal vector. The gray line represents the ray-path from the source to the image point and from the image point to the receiver. By assuming a given incident wave at the local interface, we can compute its predicted specular rays (transmitted and reflected), i.e., the rays satisfying the Snell's law at the interface, regardless of reflection/transmission coefficients. Thus, the angle θ represents the distance of the computed ray direction to the specular expected brightest direction for the converted phase.

from the specular ray. This Snell's factor focuses trace amplitudes and smears out "smiles" generated in migrated images because of our limited folding. As folding increases thanks to accumulation of data, we may accordingly reduce the influence of the Snell's factor.

When we deal with microearthquake records for seismic imaging, we do not know the source time function. Therefore, trace equalization becomes necessary to compare records of different source magnitudes and mitigate the lack of source corrections. Moreover, because we sum trace energies (i.e., squared trace amplitudes) we can neglect the problem of the sign correction, which is necessary when sources have different focal mechanisms. In some way, we loose the concept of true amplitude by this equalization procedure but we may argue that we preserve energy balance between adjacent time windows of traces. Correcting for amplitude decrease related to geometrical spreading is also needed as contributions of farthest couples (source, receiver) may be too weak with respect to nearest couples with this decrease is not taken into account.

We may introduce in the future reflection/transmission coefficients in order to increase the influence of velocity discontinuities. We have preferred upto-now this modulation of the amplitude as the velocity discontinuity is not constrained in our reference model essentially based on first-arrival time tomographic tools. Therefore, in this work, only kinematic and geometrical spreading aspects of the migration procedure are considered, while other weighting factors related to amplitude coefficients are neglected.

The duration of the trace segment is an important parameter as well when focusing energy inside the medium. When constructing an image point, we stack energies corresponding to the selected trace segment centered on the total travel-time. The choice of this segment length (here called twin) can influence the final migrated image. As we reduce it, we may have a better localization as long as the stack is working efficiently. As we increase it, we may blur the image but we are more tolerant to any uncertainty in velocity model and source positions. The estimation of this time length is still performed by trial and error while one may see that coherence analysis of images may help a more automate way of getting the optimal time window for good focusing with the highest possible spatial resolution. When considering the dispersion of the time estimation of converted phases (Figure 5) as well as the small amplitude of converted phases (Figure 5), we may need an efficient summation and, therefore, we may allow a significant time window well above the sampling rate of seismograms. We may compare this request to the one needed for full waveform inversion where the accuracy of time is few sampling rates for making the technique working (Pratt et al, 1998 or Operto et al, 2004).

Another important parameter to set up is the spatial stepping between diffractors. Although images are constructed independently in each individual point, improved spatial coherence may be achieved by performing the focusing operation in a quite enough dense number of points. By doing so, the continuity of any contrast of velocity could be easily detected.
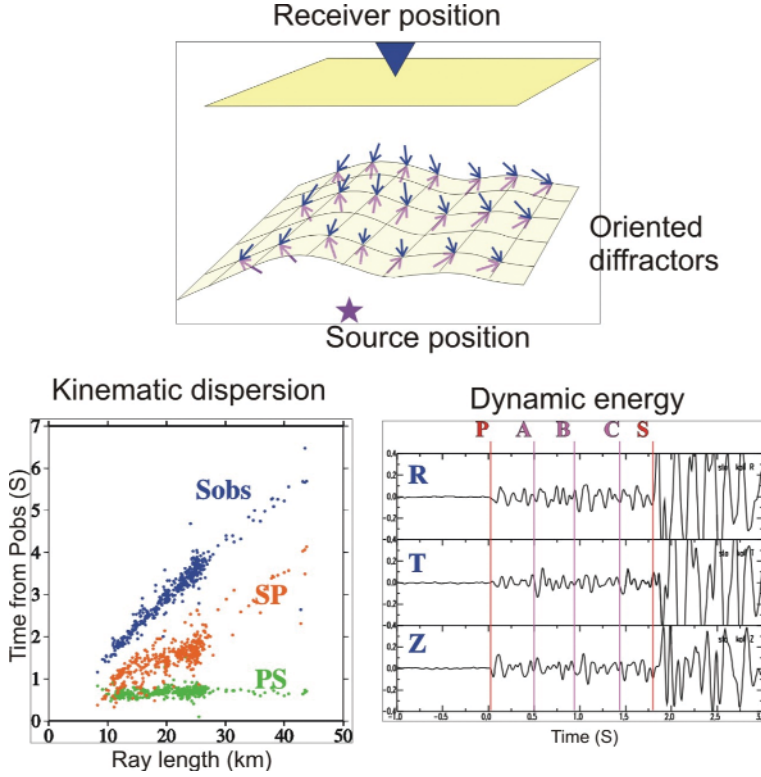
Fig. 5. Two difficulties on focusing energy: **(a)** the dispersion of travel times as shown in the bottom left panel when considering diffractors of the top panel, **(b)** the small amplitude of converted phases (A, B, C) with respect to other direct waves amplitudes as the S amplitude as shown in the bottom right panel.

DISCUSSION AND CONCLUSION

In this study, we show and demonstrate the efficacy of migration techniques applied to passive/active source data for realistic imaging of the subsurface structure. In our presentation, we point out that reasonable precautions should be taken into account for adequately focus energy at the right place. We outline the importance of using both background three-dimensional velocity models and source parameters estimated through first-arrival time tomographic inversion. Moreover, we introduce few key features for well focusing seismogram energies and for reducing image artifacts. Any one willing to use these techniques of converted phases imaging should be aware of these parameters.

On the opposite side, once these parameters are set, we may find the technique quite robust as it is driven mainly by kinematic parameters and that

dynamic ones as the observed amplitude is only moderately used inside the efficient of the energy focusing and not for the spatial position of this focusing.

REFERENCES

Chavarria, J. A., Malin P. E., Catchings R. D., and Shalev E. 2003. A look inside the San Andreas Fault at Parkfield through vertical seismic profiling, Science, 302, 1746-1748.

Chavez-Perez, S. and J. N. Louie, 1998, Crustal imaging in southern California using earthquake sequences: Tectonophysics, 286, (March 15), 223-236.

Hole J. A. 1992. Nonlinear high-resolution three-dimensional seismic travel-time tomography. Journal of Geophysical Research 97, 6553-6562.

Latorre D., Virieux J., Monfret T. and Lyon-Caen H. 2004a. Converted seismic wave investigation in the Gulf of Corinth from local earthquakes. Comptes Rendus Geosciences, 336, 259-267.

Latorre D., Virieux J., Monfret T., Monteiller V., Vanorio T., Got J.-L. and Lyon-Caen H. 2004b. A new seismic tomography of Aigion area (Gulf of Corinth, Greece) from the 1991 data set. Geophysical Journal International, 159, 1013-1031.

Latorre D. 2004c. Imagerie sismique du milieu de propagation à partir des ondes directes et converties : application à la région d'Aigion (Golfe de Corinthe, Grèce). Phd thesis, Université de Nice-Sophia Antipolis, France.

Le Meur, H., J. Virieux and P. Podvin, 1997, Seismic tomography of the Gulf of Corinth: a comparison of methods, Ann. Geophys., XL, 1-25.

Louie J. N., Chávez-Pérez S., Henrys S. and Bannister S. 2002. Multimode migration of scattered and converted waves for the structure of the Hikurangi slab interface, New Zealand. Tectonophysics 355, 227-246.

Michelini A. and McEvilly T. V. 1991. Seismological studies at Parkfield, I, Simultaneous inversion for velocity structure and hypocentres using cubic b-splines parameterization, Bullettin Seismological of Society of America, 81, 524-552.

Monteiller V., Got J.-L., Virieux J. and Okubo P. 2005. An efficient algorithm for double-difference tomography and location in heterogeneous media, with an application to the Kilauea volcano. Journal of Geophysical Research 110, B12306, doi:10.1029/2004JB003466.

Nisii V., Zollo A and Iannaccone G. 2004. Depth of a midcrustal discontinuity beneath Mt. Vesuvius from the stacking of reflected and converted waves on local earthquake records. Bulletin of Seismological Society of America 94, 1842-1849.

Operto, S., Ravaut, C., Improta, L., Virieux, J., Herrero, A. and P. Dell'Aversana, 2004. Quantitative imaging of complex structures from dense wide-aperture seismic data by multiscale traveltime and waveform inversions: a case study, Geophysical Prospecting, 52, 625-651.

Podvin, P., and I. Lecomte (1991), Finite difference computation of traveltimes in very contrasted velocity models: A massively parallel approach and its associated tools, Geophys. J. Int., 105, 271- 284.

Pratt, R. G., Z.-M. Song, P. R. Williamson, and M. Warner (1996), Two-dimensional velocity models from wide-angle seismic data by wavefield inversion, Geophys. J. Int., 124, 323-340.

Stroujkova A. F. and Malin P. E., 2000. A magma mass beneath Casa Diablo? Further evidence from reflected seismic waves. Bulletin of Seismological Society of America 90, 500-511.

Thurber C. H. 1983. Earthquake locations and three-dimensional crustal structure in the Coyote Lake area, Central California. Journal of Geophysical Research 88, 8226-8236.

Thurber C. H. 1993. Local earthquake tomography: velocity and Vp/Vs-theory. In Seismic Tomography: Theory and pratice. H. M. Iyer and K. Hirahara, CRC Press, Boca Raton, Fla.

Virieux, J. and V. Farra, 1991, Ray tracing in 3-D complex isotropic media: an analysis of the problem, Geophysics, 56, 2057-2069.

Virieux, J. and G. Lambaré, 2007. Theory and observations-body waves: ray methods and finite frequency effects, Editors B. Romanovitz and A. Diewonski in Treatise of Geophysics, volume 1: Seismology and structure of the Earth, Elsevier, in press.

Yilmaz O.. 2001. Seismic Data Analysis: Processing, Inversion and Interpretation of Seismic Data. Society of Exploration Geophysicists, Tulsa Oklahoma.

Seismic scatterer imaging using shot array beamforming: method and application to the Campi Flegrei caldera

N. Maercklin

Dipartimento di Scienze Fisiche, Università degli Studi di Napoli Federico II , Italy

Abstract: The shallow crustal structure of the Campi Flegrei caldera, southern Italy, is imaged with P-to-P scattered seismic waves. The imaging (migration) method is based on array beamforming and coherence analysis of the scattered phase. Airgun shots from a controlled-source seismic experiment are grouped into arrays, and a 1-D background velocity model is used to calculate travel times for potential scatterer locations on a regular grid in the image volume. A high coherence measured on aligned traces indicates the presence of a scatterer at the corresponding location. A stack of the individual images from several pairs of a shot array and a single receiver provides the final image. First results show a prominent region of seismic scattering that coincides with the buried caldera rim.

INTRODUCTION

Seismic waves are subject to scattering at small inhomogeneities. The superposition of scattered seismic energy generated by statistical perturbation of elastic parameters is often used to model the seismic coda. A complementary approach is to model the subsurface as a layered medium, which is the basis of many seismic processing and migration techniques. Models based on single scattering from spatially localised, omnidirectional scatterers fill the range between these two end members (e.g. Rietbrock and Scherbaum, 1999; Maercklin et al., 2004, and references therein) and form the basis of diffraction-stack or pre-stack Kirchhoff depth migration.

Krüger et al. (1995) applied source and receiver array beamforming simultaneously to image inhomogeneities at the core-mantle boundary. Rietbrock and Scherbaum (1999) extended this technique to spherical wavefronts to locate sources of scattering, and Maercklin et al. (2004) stacked the imaging results from several pairs of a shot and a receiver array to enhance the image quality. Steeply dipping fault planes can act as reflectors, and small-scale structures such as volcanic vents or magmatic intrusions can be the sources of seismic

scattering. In general, these structures are not easily detected by conventional near-vertical seismic reflection surveys, and methods employing small arrays with a good azimuthal resolution may be more appropriate. This report introduces an imaging method based on array beamforming, and first results of an application to the Campi Flegrei caldera are shown.

IMAGING METHOD

Seismometer arrays are often used in earthquake seismology, because the different arrival times of an incoming wave at each receiver provide information on the azimuth to the seismic source and on the wave slowness. With an array, the signal-to noise ratio of a seismic signal can be improved by stacking the coherent signals from the single seismometer sites after correcting for the delay times, which depend on the azimuth and slowness of the incoming plane wave (e.g. Schweitzer et al., 2002). This stack trace is called a beam, and it is commonly used in event location procedures or to detect secondary, for example scattered arrivals.

If the seismic scatterers are located close to the sources or receivers, a curved wave front has to be considered and the standard plane-wave approach typically applied in earthquake array seismology cannot be used (Rietbrock and Scherbaum, 1999). The travel times of the scattered arrivals are therefore calculated from a local velocity model.

Figure 1a illustrates the basic idea behind the imaging concept. Considering the first sketch, seismic energy excited by a single shot or an earthquake is recorded by an array of receivers. The first arrival is the direct P-wave, and a second arrival denoted as PxP is related to scattering at a subsurface inhomogeneity. For each trace the travel time of the PxP phase is given by the sum of the travel times from the source to the scatterer and from the scatterer to the corresponding receiver. Applying the calculated times as static shifts to the initial recordings aligns the PxP phase (Figure 1b). A stack of these aligned traces forms a PxP beam and enhances this phase relative to the direct P-wave and other possible phases. Due to the travel time reciprocity, a group of shots or earthquakes can be considered as a shot array (Figure 1a, bottom), and the same beamforming approach can be applied. A combination of a shot array and a receiver array leads to a double beamforming method (Krüger et al., 1995).

Generally, real data are contaminated with noise, and the scattered PxP phase may have rather small amplitudes. Compared to a simple stack of the traces, coherence measures are superior for the detection of such weak but coherent phases. Here, the semblance NE (normalised energy) is used to measure the coherence, and it is calculated in a time window around the aligned PxP phase (see Figure 1b). The assumption of a coherent PxP phase is typically justified, when the direct P-wave is coherent across a receiver array or when the diffe-
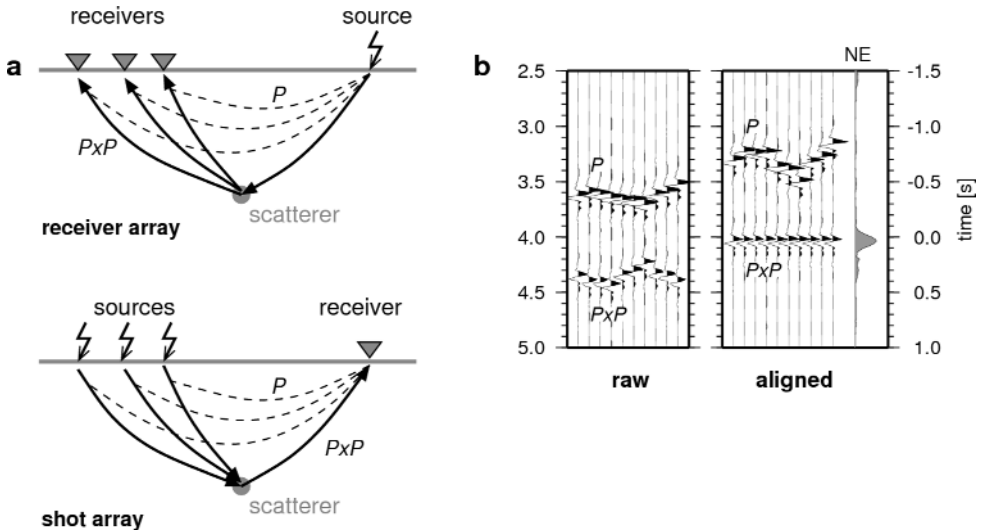
Fig. 1. (a) Sketch of a receiver array and of a shot array with ray paths for the direct P-wave (dashed lines) and the scattered PxP phase (solid lines). (b) Synthetic example seismogram for an array of ten traces showing the direct P phase and the scattered PxP phase (taken from Maercklin et al., 2004). The section on the right shows the aligned PxP phase and the semblance trace labelled NE.

rent source signals of a shot array are coherent. A high semblance value observed for PxP indicates the presence of a scatterer at the corresponding subsurface location. Thus, a discrete scan through a subsurface volume yields an image of regions, where sources of seismic scattering are located. A stack of the individual semblance images obtained from several shot-receiver array or receiver-shot array combinations can improve the final image.

The size of an array and its geometry (spatial distribution of receivers or shots) are a matter of economy and purpose (see e.g. Schweitzer et al., 2002). For all azimuths of interest the distances between receivers or shots shall be small to avoid spatial aliasing. To exclude significant phase variations of PxP, only a limited number of scattering angles shall be involved in the beamforming process, implying a small array aperture. On the other hand, azimuthal resolution of a point scatterer is inversely proportional to the array aperture, because energy is dispersed away from the true location of the scatterer to locations having the same PxP traveltime (isochrone). Such migration artefacts are reduced in a stack of the images from different arrays. Stacking also suppresses the influence of spatially correlated noise, which might be mapped into an apparent scatterer near the array (Hedlin et al., 1994). Recovery tests using synthetic data and an analysis of energy dispersion at scatterer locations help to evaluate the final image resolution (Maercklin et al., 2004).

APPLICATION TO THE CAMPI FLEGREI CALDERA

Campi Flegrei is a resurgent caldera that is partly covered by a shallow water layer in the Bay of Pozzuoli, southern Italy. During the SERAPIS controlled-source seismic experiment in 2001 (e.g. Zollo et al., 2003) a large number of airgun shots was recorded by a grid of three-component ocean bottom seismometers (OBS) deployed at an average water depth of about 100 m (Figure 2a). The aim of this study is to image small-scale structures using P-to-P scattered waves (PxP). Since the airgun shots are very coherent and more densely spaced than the OBS, a shot array approach is applied here. The shots are grouped into 18 shot arrays with an average aperture of about 1000 m, and each array contains between 42 and 108 individual shots. The corresponding array centroids are plotted as diamonds in Figure 2. To assess the influence of the array geometry on the final image, I assigned the same individual shots also to an alternative set of 46 shot arrays with an average aperture of 500 m. From the entire dataset I selected the vertical component seismograms of 22 OBS that cover the same region as the shots used here. All traces are bandpass filtered between 3 Hz and 18 Hz.

The image volume covers a region of 11x11 km in horizontal directions and extends from 0.2 km down to 3.0 km depth (Figure 2a). The spatial sampling
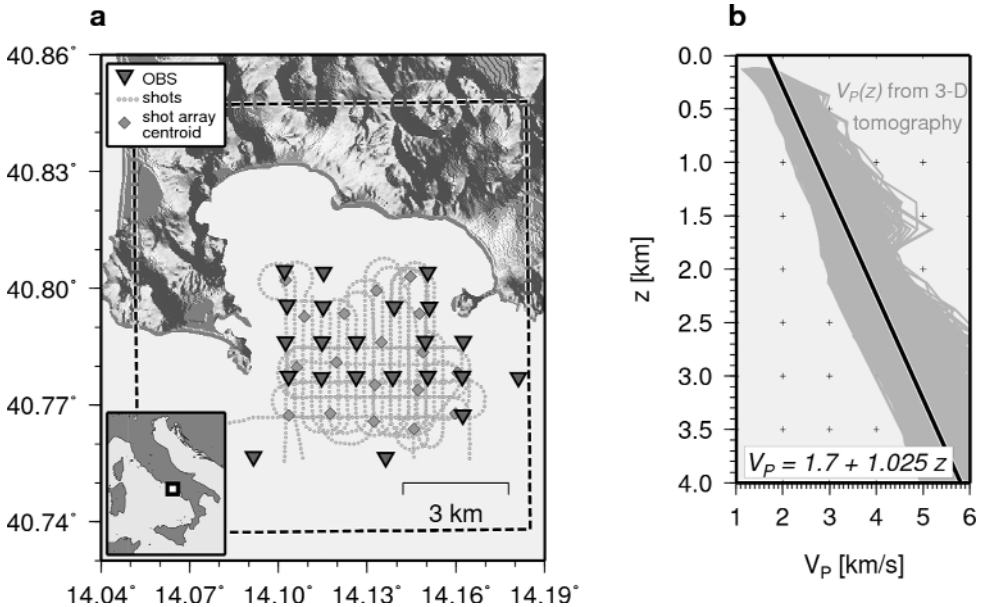

Fig. 2. (a) Map of the Bay of Pozzuoli (Campi Flegrei) and the seismic acquisition geometry used in this study. The dashed line marks the boundary of the image volume. **(b)** Velocity-depth profiles from 3-D P-velocity tomography (Zollo et al., 2003) overlain with the 1-D linear velocity model used for the scatterer imaging.

of possible scatterer locations is 0.2 km in each direction (47040 grid nodes). The 1-D P-velocity model used here (Figure 2b) is a linear gradient that approximates the velocity-depth profiles from a 3-D P-velocity model in the study region (Zollo et al., 2003). In this 1-D model, travel times are computed efficiently via analytical ray tracing.

The semblance value is determined in a 0.25 s Hanning-tapered time window around the calculated PxP traveltime for a given grid node. This process is first repeated for all remaining nodes and second for all individual pairs of a shot array and a single receiver (OBS). The final image is a stack of all these individual images. The two sets of shot arrays are processed in the same fashion, and Figure 3 compares the results for a horizontal slice at 1 km depth through the image volume. Dark colours indicate regions where seismic scattering occurs.

The image from the set of 46 small-aperture shot arrays (Figure 3, left) shows a west-east trending zone of scattering between 4 km and 6 km y-distance. Additional prominent scatterers appear to be located in the southeast of the image volume and in the northwestern part of the Bay of Pozzuoli. Some circular features visible near the boundaries of the image volume are (migration) artefacts caused by the smearing of energy along isochrones. These features are absent in the central part of the volume, i.e. in the region close to the sources and receivers (see Figure 2). Figure 3, right, shows the imaging result obtained from the set of 18 shot arrays with a larger aperture. The general appearence of this image is similar to that from the smaller arrays but less smooth.
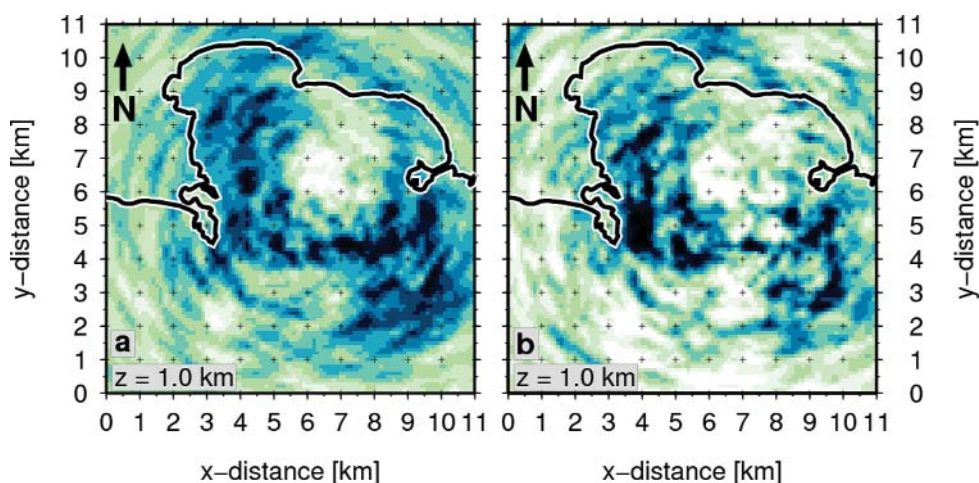
Fig. 3. Comparison of imaging results at 1 km depth for two different shot array geometries. Dark colours indicate regions of seismic scattering. The image obtained using 46 shot arrays with an aperture of about 500 m is shown on the left, and the image from 18 shot arrays with an aperture of about 1000 m is shown on the right.

Individual zones of scattering are more isolated and exhibit a stronger contrast. Furthermore, migration artefacts in the outer regions of the image volume are reduced due to the larger array aperture.

Figure 4 shows six horizontal depth slices through the image obtained with the set of 18 shot arrays. This image is a stack of the contributions from 374 pairs of a shot array and a single receiver. Prominent regions of scattering are found in the west-east trending zone mentioned above, down to about 1.2 km depth. With increasing depth the larger-scale structures disappear, and at 2.4 km depth only a few sources of scattering are imaged.

DISCUSSION AND CONCLUSIONS

An imaging method based on array beamforming for P-to-P scattered seismic phases has been introduced. The method utilises either arrays of seismometers, arrays of shots or earthquakes, or a combination of these two. The extension of the method for P-to-S or other scattered phases is straightforward. An important aspect to consider beforehand is the choice of the array geometry (e.g. Schweitzer et al., 2002). If the spatial distribution of shots or receivers is already given, different groupings into arrays can be analysed as in the Campi Flegrei case study. A comprehensive discussion on the imaging method and its resolution is given in Maercklin et al. (2004) and Maercklin (2004), chapter 6. First results for the Campi Flegrei caldera are promising. Resolution tests and a detailed interpretation of the imaging results are part of this ongoing study. Among other structures, seismic scatterers in the upper 2 km of the crust are imaged in a west-east stretching zone between 4 km and 6 km y-distance (Figure 4). This observation is in agreement with a coarser scattering image obtained from coda wave envelopes of local microearthquakes (Tramelli et al., 2006). The seismic scattering in this region and a coinciding high P-velocity anomaly has been interpreted as related to the buried rim of the caldera (Tramelli et al., 2006; Zollo et al., 2003).

REFERENCES

Hedlin, M. A. H., Minster, J. B., and Orcutt, J. A. (1994). Resolution of prominent crustal scatterers near the NORESS small-aperture array. Geophysical Journal International, 119(1), 101-115.

Krüger, F., Weber, M., Scherbaum, F., and Schlittenhardt, J. (1995). Evidence for normal and inhomogeneous lowermost mantle and core-mantle boundary structure under the Arctic and northern Canada. Geophysical Journal International, 122(2), 637-657.

Maercklin, N. (2004). Seismic structure of the Arava Fault, Dead Sea Transform. Doctoral thesis, University of Potsdam, Germany. http://opus.kobv.de/ubp/volltexte/2005/103/.
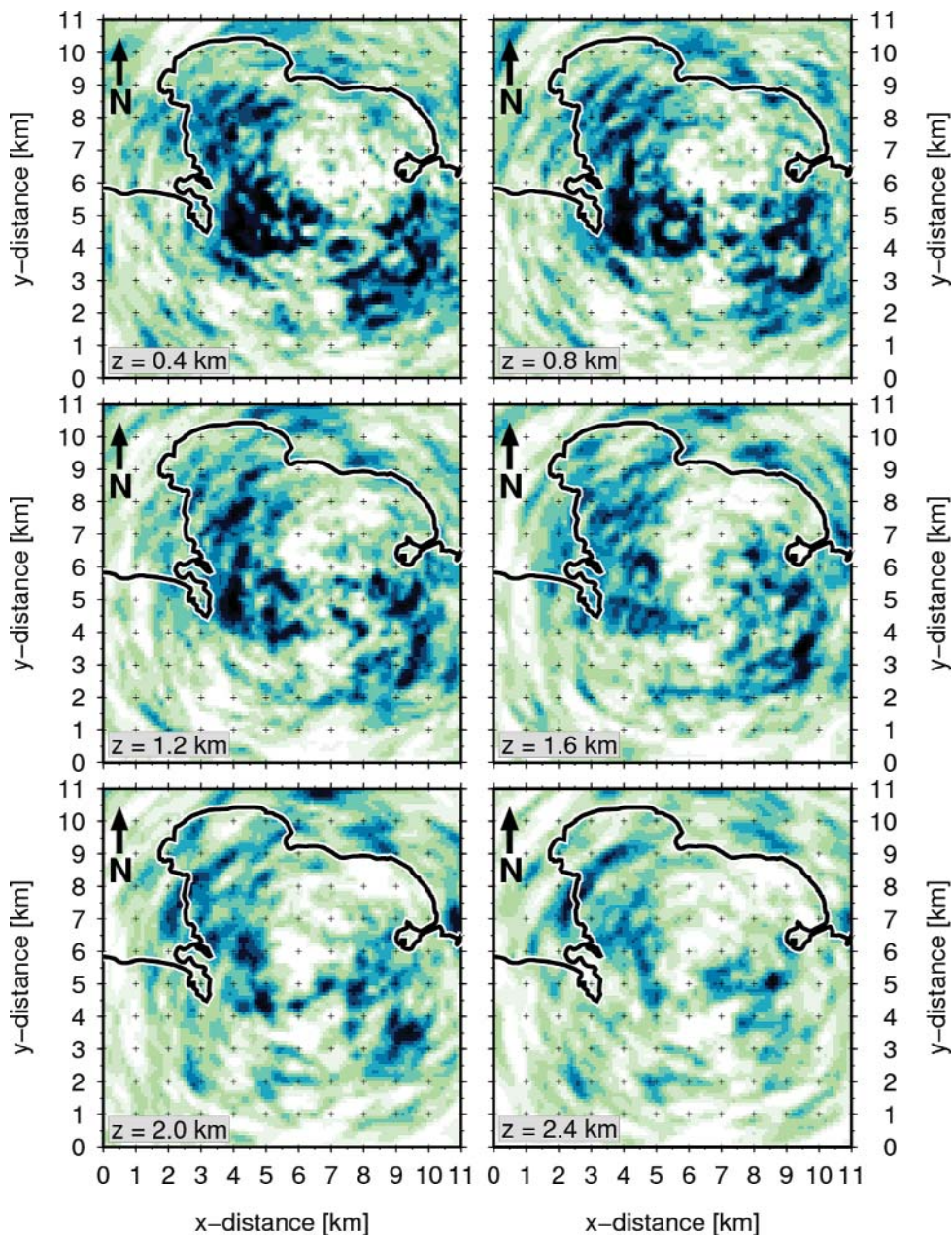
Fig. 4. Imaging result at six different depth using 18 shot arrays with an aperture of about 1000 m each. Dark colours indicate regions of seismic scattering. An additional slice at 1 km depth is shown in Figure 3, right. The coordinate origin is at Easting 420000 m, Northing 4510000 m (UTM zone 33, WGS-84).

Maercklin, N., Haberland, C., Ryberg, T., Weber, M., Bartov, Y., and DESERT Group (2004). Imaging the Dead Sea Transform with scattered seismic waves. Geophysical Journal International, 158(1), 179-186.

Rietbrock, A. and Scherbaum, F. (1999). Crustal scattering at the KTB from combined microearthquake and receiver analysis. Geophysical Journal International, 136(1), 57-67.

Schweitzer, J., Fyen, J., Mykkeltveit, S., and Kværna, T. (2002). Seismic arrays. In P. Bormann, editor, IASPEI New Manual of Seismological Observatory Practice, chapter 9. GeoForschungsZentrum Potsdam, Germany.

Tramelli, A., Del Prezzo, E., Bianco, F., and Boschi, E. (2006). 3D scattering image of the Campi Flegrei caldera (Southern Italy): New hints on the position of the old caldera rim. Physics of the Earth and Planetary Interiors, 155(3-4), 269-280.

Zollo, A., Judenerc, S., Auger, E., D'Auria, L., Virieux, J., Capuano, P., Chiarabba, C., de Franco, R., Makris, J., Michelini, A., and Musaccio, G. (2003). Evidence for the buried rim of Campi Flegrei caldera from 3-d active seismic imaging. Geophysical Research Letters, 30(19), 2002, doi:10.1029/2003GL018173.

Analysis of PS-to-PP amplitude ratios for seismic reflector characterisation: method and application

N. Maercklin, A. Zollo

Dipartimento di Scienze Fisiche, Università degli Studi di Napoli Federico II, Italy

Abstract: Elastic parameters derived from seismic reflection data provide information on the lithological contrast at an interface and support the geological interpretation. We present a method to estimate elastic parameter contrasts at a given interface in a 1-D layered medium from PS-to-PP amplitude ratios. The method is applied to synthetic data to demonstrate its possibilities and limitations. First results for real data acquired in the Campi Flegrei caldera (southern Italy) reveal a gas-bearing layer at around 3 km depth and indicate a strong negative velocity contrast at 7.5 km depth, possibly related to the presence of partial melt.

INTRODUCTION

Elastic parameters derived from seismic data can be related to the rock type, porosity, and fluid or gas content through empirical relationships and rock physics modelling (e.g. Avseth et al., 2005). Seismic first-arrival travel time tomography leads to a smooth image of the subsurface velocity structure, and ray modelling, reflection tomography, or depth migration can provide depths of reflectors and their topography. Seismic reflection amplitudes carry information on the elastic parameter contrasts at the reflectors itself. Amplitude variation with offset (AVO) or incident angle (AVA) analyses are standard tools in exploration seismics to estimate these contrasts. Typically, these methods are applied to PP reflection amplitudes and employ approximations to the Zoeppritz (1919) equations controlling the reflection amplitude variation with incidence angle. The relationships between physical rock properties and P-wave seismic data are highly non-unique, but an additional analysis of S-wave data may increase the ability to extract lithology and fluid effects from seismic data, because S-waves do not propagate through fluids (e.g. Veire and Landrø, 2006).

Standard AVO or AVA methods are applied to reflection coefficients, and therefore source, receiver, and propagation effects must be removed from the sei-

smic data before the analysis. Furthermore, the approximations made for the Zoeppritz equations are often valid for small incidence angles (small source-receiver offsets) and weak elastic contrasts only. For a given source-receiver offset, amplitude ratios between PS and PP reflected waves depend mostly just the elastic parameters at the reflector of interest, and total ray theoretic amplitudes can overcome the limitations of the approximate equations. This report presents a technique to analyse PS-to-PP amplitude ratios for arbitrary elastic contrasts using a wide range of source-receiver offsets. The method is introduced along with synthetic examples and applied to two major reflectors observed in the Campi Flegrei caldera, southern Italy.

ANALYSIS METHOD

A 1-D layered subsurface model is assumed, in which a constant P-velocity Vp, a P-to-S velocity ratio Vp/Vs, and a density ρ is assigned to each layer (Figure 1a). Six elastic parameters (Vp, Vp/Vs, ρ above and below a reflector) or three parameter contrasts characterise a given reflector. Ignoring anelastic attenuation and anisotropy, the amplitudes of primary PP and PS reflected phases (Figure 1b) depend on the source amplitudes and receiver site effects, on the geometrical spreading, and on the reflection coefficients at the reflector of interest. The reflection coefficients are a function of the elastic parameter contrasts and the incidence angles at the reflecting interface (Zoeppritz, 1919). We model the PP and PS amplitudes using ray theory, thereby including not only the effect of the elastic parameter contrast at the reflector but also the propagation effects in the overburden.

PS-to-PP amplitude ratios

The solid ray paths shown in Figure 1b for PP and PS connect the same source and receiver. Considering the ratio between the PS and PP amplitude for this acquisition geometry, the effects of source and receiver on the observed amplitudes are cancelled. Also the effect of geometrical spreading is reduced, and the exact dependency is accounted for in the ray theoretical forward modelling. Thus, measured PS-to-PP amplitude ratios provide a means to estimate the elastic parameters at the reflector without the need for additional amplitude correction factors.

Whereas PP is reflected at the midpoint (CMP) between source and receiver, the corresponding PS reflection lies closer to the receiver (Figure 1b). The asymmetry of the PS ray path depends on the Vp/Vs ratios in the layers above the reflector, and the distance between CMP and PS reflection point increases with increasing source-receiver offset and decreasing reflector depth. If the elastic parameter contrast at the reflector is varying laterally, the ratio
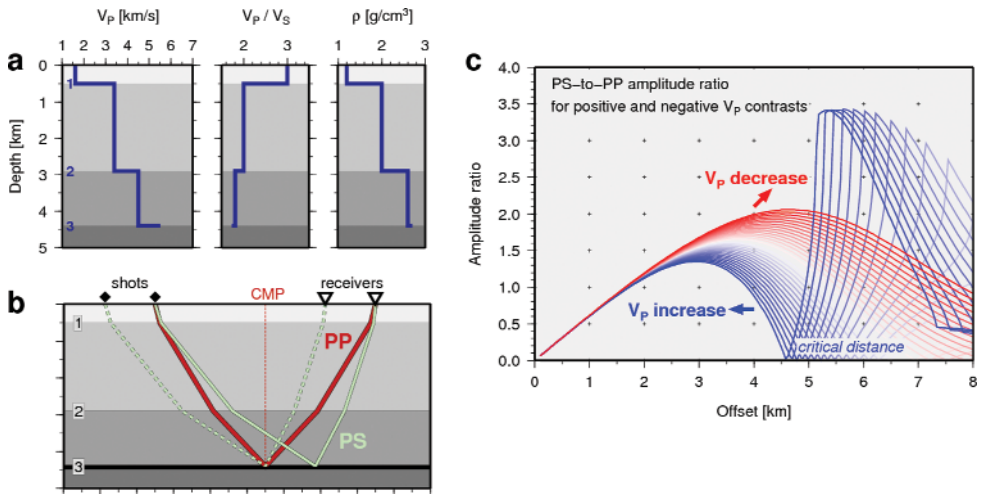
Fig. 1. (a) A layered 1-D velocity and density model. **(b)** Ray paths for primary PP and PS reflections from interface 3, recorded at the same source-receiver offset. **(c)** PS-to-PP amplitude ratios as a function of source receiver offset for positive P-velocity contrasts (blue) and negative contrasts (red) at interface 3. Successive lines correspond to a 2% velocity increase or decrease relative to the P-velocity in the layer above the interface.

between PS and PP reflected at the same subsurface location must be considered instead of the ratio calculated for the same source and receiver. An additional, laterally shifted source and receiver pair can provide the required PS observation (dashed PS ray path in Figure 1b). However, in this case the source amplitudes and possible receiver site effects have to be normalised before the calculation of the PS-to-PP ratio.

Figure 1c shows example PS-to-PP amplitude ratio curves as a function of offset for interface 3 of the model shown in Figure 1a. The ratios are calculated for a common offset of PS and PP. The blue lines are for models with a positive P-velocity contrast at that interface (Vp increase in the layer below the reflector), and the red curves are related to models with a negative contrast (Vp decrease). The maximum P-velocity contrast is 30% relative to Vp in the layer above the reflector. The general shape of the amplitude ratio variation with offset is dominated by the amplitude behaviour of the PS reflection. Due to a vanishing PS amplitude at zero offset, also the PS-to-PP ratio is always zero for coinciding source and receiver locations. The curves for the positive Vp contrast approach zero again at the distance of critical reflection, followed by a rapid increase of the amplitude ratio at post-critical distances. In case of a negative velocity contrast a critical reflection does not exist, resulting in smooth amplitude ratio curves with one single peak.

The six elastic parameters above and below a reflector are not independent. Generally, a higher value for a parameter in the layer above the reflector requi-

res also a corresponding higher one in the layer below to fit a given PS-to-PP amplitude ratio curve. This means that PS-to-PP ratio analysis essentially provides elastic parameter contrasts at a reflector, and some parameters must be constrained or fixed during an inversion. Furthermore, there is a trade-off between P-velocity and density, where the product of velocity and density, i.e. the seismic impedance, is constant. However, for a positive impedance contrast this trade-off can be resolved, if the critical distance depending only on the *Vp* contrast is observed.

Generic processing sequence

The observational basis for the analysis are travel times and amplitudes of PP and PS reflected at the same interface. The amplitudes must be extracted from seismograms at several source-receiver offsets covering a distance range large enough for a significant PS-to-PP amplitude ratio variation with offset, e.g. about 5 km for the example shown in Figure 1. We constrain the velocity structure above the reflecting interface by travel time modelling and assign initial values for the densities. Then we calculate PS-to-PP amplitude ratios at common offsets of PP and PS using seismic ray theory. Finally, we vary the unconstrained model parameters to minimise the RMS misfit between observed and theoretical amplitude ratio curves. The minimisation process is a grid search through the model parameter space, possibly combined with simplex optimisation to find a local minimum of the misfit function. Slices through the parameter space showing the misfit value as a function of selected model parameters provide an estimate of the uncertainty of the solution.

Synthetic case study

A dipping reflector and a laterally varying overburden violates the assumption of a 1-D model. To illustrate these effects on the analysis of PS-to-PP amplitude ratios, we apply our method to amplitude ratios extracted from synthetic data for a hypothetical volcanic caldera structure (Figure 2a). The target of this case study is a segment of the deepest reflector in the 2-D model. The subsurface structure above the target shows lateral variation, and the target reflector itself is dipping toward the left side of the profile (Figure 2a). The data to be analysed are vertical and horizontal component seismograms calculated for a line of shots in a shallow water layer and recorded at a single receiver at the sea bottom (common receiver gather). Primary PP and PS reflections from all model interfaces are included in the synthetics. The use of this acquisition geometry is justified, because the shot amplitudes are all the same and the elastic parameter contrasts at the reflector are nearly homogeneous.

First, we construct an approximate 1-D velocity model from the PP and PS travel times of the target reflector and of the three reflectors above (see Figure 2b, top). The densities for each layer are taken from the 2-D model. Second, we measure the PP amplitudes for the target reflector from the vertical component seismograms and the corresponding PS amplitudes from the horizontal sections, excluding those parts of the reflection signal that is contaminated by other phases. Third, theoretical PS-to-PP amplitude ratios for this model are fit to the measured curve by varying Vp, Vp/Vs, and the den-
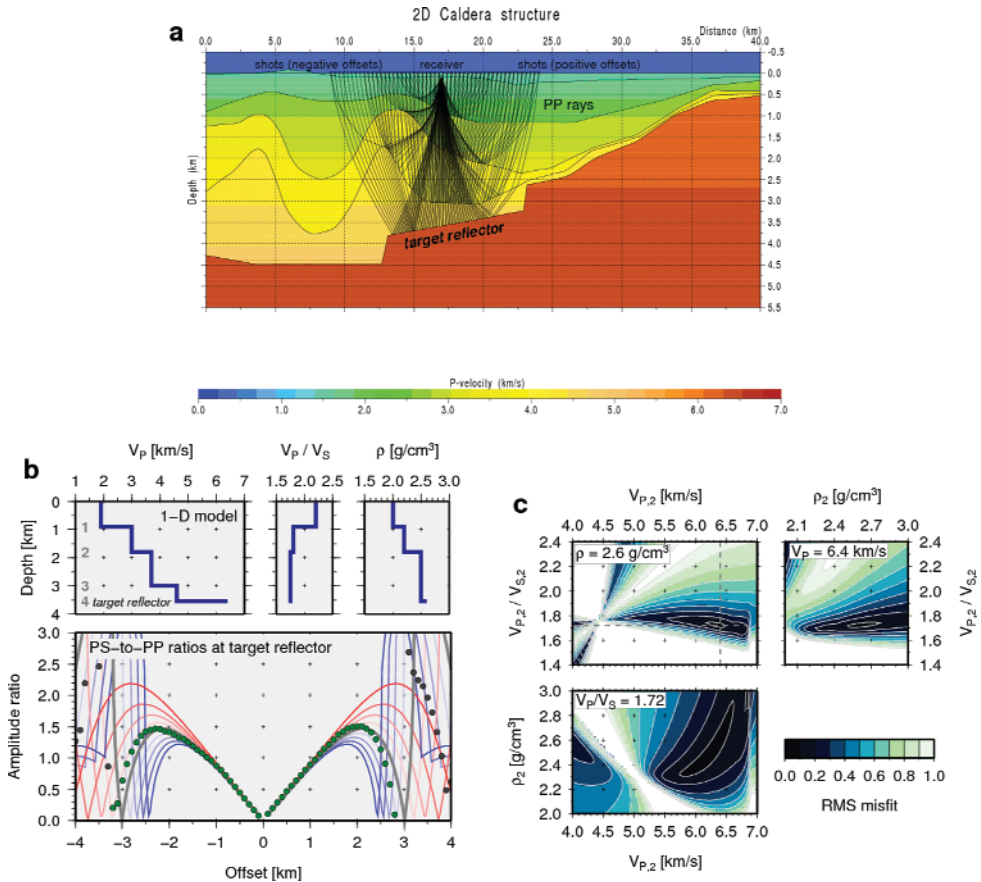
Fig. 2. (a) P-velocity profile through a hypothetical caldera structure and PP ray paths for a common receiver gather. **(b)** Approximate 1-D model based on travel times for the common receiver gather. The *Vp/Vs* ratios and densities are the same as in the 2-D model. The bottom panel shows synthetic PS-to-PP amplitude ratio curves (lines) overlain with pre- (green dots) and post-critical (grey dots) amplitude ratios. The grey line is the theoretical curve for the model shown above, and blue and red lines correspond to models with higher and lower P-velocity in the layer below the target reflector (maximum variation of 20%). **(c)** Slices through the parameter space for the model parameters in the layer below the target reflector.

sity in the layer below the reflector. Here, the PS-to-PP ratio curve is an average of that for negative offsets (shots on the left of the receiver) and that for positive offsets (shots on the right).

Figures 2b and 2c summarise the results of the PS-to-PP amplitude ratio analysis outlined above. Figure 2b is an overlay plot of the measured amplitude ratios (dots) and a theoretical curve for the best fitting model obtained with the density contrast fixed to the known value (grey line). The additional blue and red curves are for alternative models with higher and lower Vp contrasts, respectively. The critical distance for the estimated (and true) P-velocity contrast ΔVp=1.8 km/s (39% increase) is reached at an offset of about 3 km. Measured pre-critical amplitude ratios (green dots in Figure 2b) are fit well by the theoretical values. For the positive offset branch the measured amplitude ratios approach zero at a smaller offset than the theoretical curve, which suggests a higher Vp contrast than that of the optimum 1-D average model. The opposite observation is made for the negative offset branch. Post-critical amplitude ratios are much more sensitive to small changes of elastic parameters and incidence angles. Measured post-critical amplitude ratios and the theoretical values for the approximate 1-D model do not match because of the reflector dip and the lateral velocity variation in the overburden. Here, a reasonable fit is only obtained for the large post-critical PS-to-PP amplitude ratios at offsets up to about 3.4 km, i.e. at offsets exceeding the critical distance only slightly.

Figure 2c illustrates the resolution of the estimated elastic parameters below the target reflector. Each of the three panels shows the RMS misfit between the measured pre-critical PS-to-PP amplitude ratios and the theoretical values as a function of two elastic parameters for the layer below the reflector. The third parameter for the layer below and the three parameters of the layer above are kept constant at the value of the best model (Figure 2b, top). The dark regions in these slices through the model parameter space outline elastic parameter combinations that yield a good fit, i.e. a narrow dark region indicates a better resolution of the related parameter than a wide region of possible values. In the panel for Vp and ρ (bottom left) the trade-off between these two parameters is clearly visible as a large region of probable Vp-ρ pairs. A similar but less pronounced parameter correlation can be seen in the other two panels (Vp/Vs versus Vp and ρ versus Vp/Vs). An uncertainty of 10-15% for each estimated elastic parameter may be assigned here.

## APPLICATION TO THE CAMPI FLEGREI CALDERA

During the SERAPIS controlled-source seismic experiment in 2001 (e.g. Zollo et al., 2003) a large number of airgun shots was recorded by a grid of three-component ocean bottom seismometers (OBS) deployed in the Bay of Pozzuoli (Figure 3a), which covers a part of the Campi Flegrei caldera. The average water depth at the OBS locations is about 100 m, and the orientation

of their horizontal components have been determined by polarisation analysis of the direct wave travelling in the water layer.

We identified three major reflectors on several common midpoint (CMP) gathers from this dataset, and the travel times of PP and PS arrivals from each reflector were picked. The association of the PP phase and the PS phase from the same interface is based on travel time modelling for a layered 1-D average velocity model (Vp and Vp/Vs) and on reflection move-out analysis. The PP and PS travel time picks used here are shown in Figure 3b together with theoretical travel times of PP (solid lines) and PS (dashed lines) for the preliminary 1-D model derived from travel time modelling and the amplitude ratio analyses described below (see Figure 5). The maximum offsets considered here are 2 km for the shallowest reflector and up to 8 km for the deeper ones.

As in the synthetic case study, we extracted the PP amplitudes from vertical component seismograms and corresponding PS amplitudes from radial sections constructed from the two horizontal OBS components. We applied a 5-15 Hz bandpass filter and measured the amplitudes in a time window of 0.2 s around the maximum of the respective arrival. Since the measured amplitudes exhibit a large variation, we smoothed the amplitude variation with offset for each phase by taking the median value in 0.25 km wide offset bins. Then we calculated the PS-to-PP amplitude ratios at common offsets for PP and PS for two interfaces (Figure 3c).
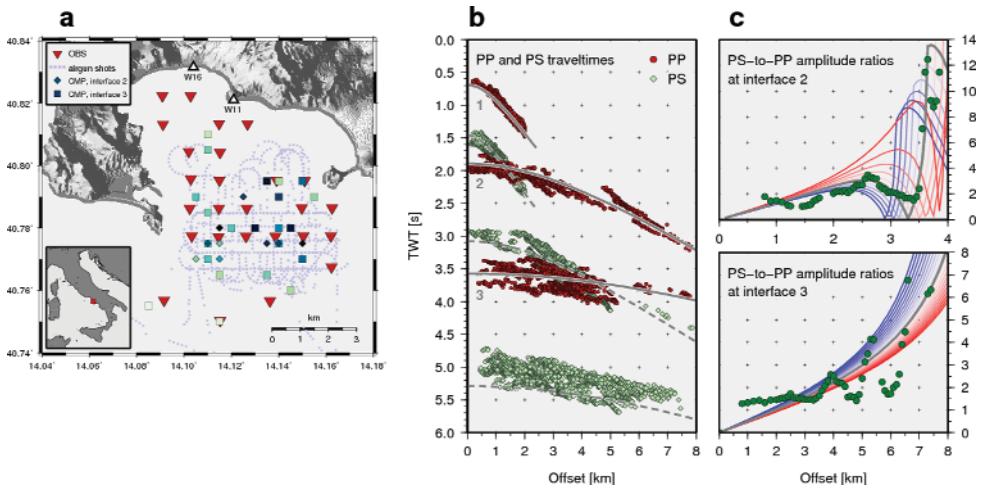
Fig. 3. **(a)** Map of the seismic acquisition geometry used. A higher number of available PP amplitude measurements is indicated by darker colours of the CMP symbols. **(b)** PP and PS travel time picks (dots) for three major reflectors overlain with theoretical times (grey lines) from a 1-D average model. **(c)** Average of the observed amplitude ratio variation with offset (dots) for two reflectors (interfaces). Theoretical curves for the 1-D model (Figure 5) are shown as grey lines. The blue and red curves are for models with higher and lower *Vp* in the layer below the respective interface (2% interval).

The PS-to-PP amplitude ratios (dots) plotted in Figure 3c are the average of all measured PS-to-PP amplitude ratios available for the respective interface. A decrease of PS-to-PP ratios is observed for interface 2 at around 3.3 km offset, followed by a rapid increase toward greater offsets. This behaviour suggests a well-constrained positive Vp contrast at that interface. The PS-to-PP ratio variation with offset for interface 3 is undulating, but it shows a tendency for an increase of PS-to-PP ratios with offset.

Grey lines in Figure 3c are the theoretical PS-to-PP amplitude ratio curves that fit the general trend of the observed ratios. The used 1-D velocity model is based on travel time modelling and on Vp and Vp/Vs below the respective interface estimated from the amplitude ratios. Density contrasts are not included in the modelling (ρ=2.6 g/cm^3 within each layer). Slices through the model parameter space illustrate the resolution of the obtained 1-D model. Figure 4 shows the colour-coded RMS misfit between observed and theoretical amplitude ratios as a function of two elastic parameters in the layer below the reflector while keeping the remaining parameter constant at the value printed in each panel.

The misfit function for interface 2 at 2.7 km depth shows a narrow minimum in the plane of Vp/Vs versus Vp (Figure 4a, top left). Thus, the measured PS-to-PP amplitude ratios provide a good estimate of the P-velocity contrast at this interface. A variation of ρ does not have a significant influence on Vp (bottom left), and also Vp/Vs depends only slightly on the value of (top right). A different pattern is found for interface 3 at 7.5 km depth (Figure 4b). Several combinations of Vp and Vp/Vs for the layer below yield the same RMS misfit between measured and theoretical curves (top left panel), and also several density values are possible. Since the layer above interface 3 has a P-
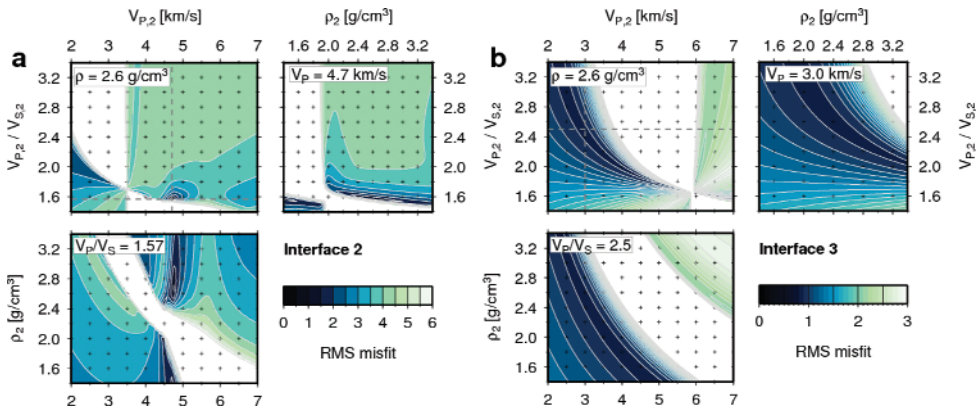
Fig. 4. Slices through the model parameter space for two interfaces showing the colour-coded RMS misfit as a function of two model parameters for the layer below the interface while keeping the remaining parameter constant at the value given in each panel. See Figure 5 for the velocities above the interfaces.

velocity of Vp=5.9 km/s, a good fit typically requires a negative velocity contrast at this interface.

Figure 5 summarises the preliminary 1-D velocity model obtained from the combined travel time and PS-to-PP amplitude ratio analyses assuming a constant density. The shallowest layer is characterised by a low P-velocity and a high Vp/Vs ratio (Vp=1.6 km/s, Vp/Vs=3.4). Large amplitudes of PP and PS reflections from interface 1 suggest a strong Vp and Vp/Vs contrast at this interface (0.6 km depth), but their actual values may be smaller than shown here due to a probably velocity gradient in the first layer. At interface 2 the P-velocity increases from 3.5 km/s to 4.7 km/s, accompanied with a Vp/Vs decrease from 1.7 to 1.57. Another model discontinuity introduced at 3.3 km depth is not observed in the reflection data, but a further, most likely gradual Vp increase to about 5.9 km/s is required to fit the travel times from the deepest reflector (interface 3). The results of the PS-to-PP amplitude ratio modelling indicate a strong negative Vp contrast and an even higher Vs contrast (Vp/Vs increase) at interface 3 in 7.5 km depth. The 1-D P-velocity and Vp/Vs model presented here is consistent with the 1-D average from a 3-D P-velocity model for the study region (Zollo et al., 2003), and Vanorio et al. (2005) derived similar Vp/Vs ratios at stations located near our study region.
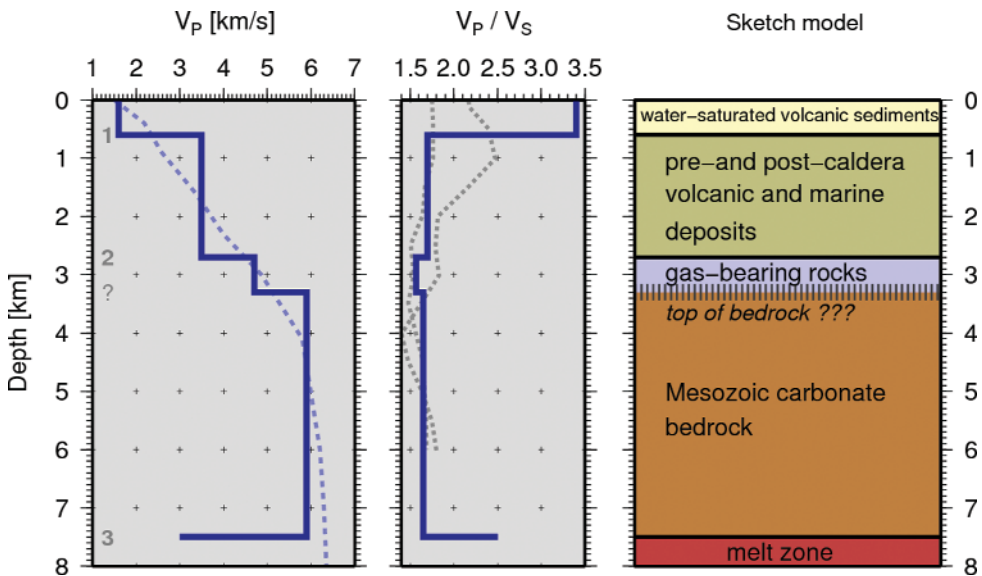
Fig. 5. Average 1-D P-velocity and *Vp/Vs* model for the Campi Flegrei caldera, based on PP and PS travel times, and on PS-to-PP amplitude ratios. The dashed line is the average of a 3-D P-velocity model in the study area (Zollo et al., 2003), and the dotted lines are *Vp/Vs* profiles derived by Vanorio et al. (2005) at the stations W16 and W11 (Figure 3a).

DISCUSSION AND CONCLUSIONS

The PS-to-PP amplitude ratio analysis described above yields elastic parameter contrasts at reflectors using wide-angle reflection data, and the method does not require additional amplitude correction factors as needed for standard AVO techniques. However, at small offsets the PS-to-PP amplitude ratios do not change significantly with the Vp contrast at the reflector (Figures 1c and 2b). Additionally, noise in real data has a stronger influence on the small PS amplitudes at short offsets and may introduce a systematic bias toward higher PS-to-PP ratios. Therefore, amplitude ratio measurements are needed for sufficiently large offsets. In this case, the method is applicable also to subsurface structures that violate the 1-D assumption by a slightly dipping reflector or a laterally varying overburden (Figure 2). If the critical distance is observed, the positive Vp contrast is well-resolved, and also a good estimate for Vp/Vs can be expected. Generally, the recovery of density contrasts may require additional constraints e.g. from empirical velocity-density relations.

As for all AVO/AVA methods using PP and PS simultaneously, these two phases must be identified for the same reflector. The most reliable association between the two phases can be made from well log data. Due to the lack of such information for the deeper layers in the Campi Flegrei caldera, we guided the search for corresponding PP and PS phases by travel time modelling. In an alternative approach that does not require PP and PS from the same interface, Auger et al. (2003) used amplitude ratios between PS reflections and the first-arrival P-wave.

We successfully applied the PS-to-PP amplitude ratio analysis to two reflectors in the Campi Flegrei caldera. Main features of the observed amplitude ratio curves are reproduced by our preliminary 1-D model assuming a vanishing density contrast (Figure 5). The 1-D velocity structure is consistent with the PP and PS travel times for three interfaces and with a 3-D P-velocity model from first-arrival tomography (Zollo et al., 2003). The sketch model in Figure 5 summarises our tentative interpretation of the model. A layer of water-saturated volcanic sediments from the recent activity covers a succession of pre-and post-caldera deposits. Vanorio et al. (2005) interpreted regions with low Vp/Vs ratios in the study region as gas-bearing rocks, and the observed amplitude ratios provide evidence for such a layer at around 3 km depth. The thickness of this layer and the transition to the Mesozoic carbonate basement remains unresolved. Following an interpretation by Auger et al. (2003) for a similar observation beneath Vesuvius volcano, a strong negative velocity contrast at 7.5 km depth may be related to partially molten rock in the layer below.

REFERENCES

Auger, E., Virieux, J., and Zollo, A. (2003). Locating and quantifying the seismic discontinuities in a complex medium through the migration and AVA analysis of reflected and converted waves: an application to the Mt. Vesuvius volcano. Geophysical Journal International, 152(2), 486-496.

Avseth, P., Mukerji, T., and Mavko, G. (2005). Quantitative seismic interpretation: Applying rock physics tools to reduce interpretation risk. Cambridge University Press, Cambridge, UK.

Vanorio, T., Virieux, J., Capuano, P., and Russo, G. (2005). Three-dimensional seismic tomography from P wave and S wave microearthquake travel times and rock physics characterization of the Campi Flegrei Caldera. Journal of Geophysical Research, 110, B03201, doi:10.1029/2004JB003102.

Veire, H. H. and Landrø, M. (2006). Simultaneous inversion of PP and PS seismic data. Geophysics, 71(3), R1-R10.

Zoeppritz, K. (1919). Erdbebenwellen VII b: über Reflexion und Durchgang seismischer Wellen durch Unstetigkeitsflächen. Nachrichten von der Gesellschaft der Wissenschaften zu Göttingen, Mathematisch-Physikalische Klasse, 1919, 66-84.

Zollo, A., Judenerc, S., Auger, E., D'Auria, L., Virieux, J., Capuano, P., Chiarabba, C., de Franco, R., Makris, J., Michelini, A., and Musaccio, G. (2003). Evidence for the buried rim of Campi Flegrei caldera from 3-d active seismic imaging. Geophysical Research Letters, 30(19), 2002, doi:10.1029/2003GL018173.

Iterative tomographic analysis based on automatic refined picking

C. Satriano[1], A. Zollo[2], C. Rowe[3]

[1] *RISSC-Lab, AMRA scarl, Napoli, Italy*

[2] *Dipartimento di Scienze Fisiche, Università degli Studi di Napoli Federico II, Napoli, Italy*

[3] *Los Alamos National Laboratory, USA*

Abstract: We developed a new, iterative scheme for 3D seismic tomography built on semi-automatic phase picking of first arrivals.

Based on the original work of Rowe et al. (2002), the technique uses cross-correlation to examine waveform similarity and to perform picking adjustment. Starting from a preliminary set of picks as reference, we cross-correlate each pair of traces, following a station-by-station approach. The maximum correlation time is an estimate of the relative time-lag between traces, while the maximum correlation amplitude quantifies waveform similarity and is used as a weighting function in the process of pick adjustment using a smaller correlation window. Additionally, maximum correlation values can be used to build clusters of similar records. Adopting a clustering process can be advantageous in cases where "a priori" assumptions regarding the waveform similarity (such as the distance between sources and receivers) may be inappropriate.

Automatic picks, obtained from the first step of the process, are used to build an initial 3D tomographic model through a standard inversion code (here we use Benz et al., 1996). Travel times calculated from the resulting model are then taken as reference picks for the next step of automatic pick adjustment. The result is a tomographic image, refined at each step of the procedure.

We tested this procedure on the waveform data set recorded during the 2001 SERAPIS active seismic survey in the gulfs of Naples and Pozzuoli, Italy. We show that the technique can be effectively employed for fast analysis of large data-sets to support rapid decisions such as re-orienting a seismic survey or setting-up automatic 4D tomographic investigations.

INTRODUCTION

Modern seismological studies are more and more frequently associated with very large data sets produced by dense seismic networks or by large experiments such as active seismic surveys.

The development and the use of automatic, reliable procedures to analyze massive data sets is a primary requirement, especially in those cases for which

rapid analysis is to facilitate time-critical decision making, i.e., phases during volcanic crises, modifying the configuration of active seismic survey or continuous updating of 4D monitoring an oil/gas/geothermal reservoir.

One of the crucial problems in analyzing seismic waveforms is the correct identification of the different phases and their arrival (phase picking). Both earthquake location and earthquake tomography are critically based on the quality of phase arrival time measurements. These applications historically have depended on the ability of human analysts to estimate arrival times. Standard operations generally involve the manual measuring of P-wave and S-wave arrivals or, more recently, computer identification of these phases using software autopickers (see for example Allen, 1982; Baer and Kradolfer, 1987; Sleeman and Van Eck, 1999; Zhang et al., 2003). In both cases, the most common approach is to pick one event at a time, with or without considering consistency among picks. These methods, although adequate for real-time or near-real-time operations of seismic networks, can lead to erroneous interpretation in the presence of inconsistencies due to path effects, signal-to-noise ratios, and source radiation pattern differences.

Significant improvements in the quality of hypocenter location have been achieved through the use of quantitative cross-correlation for relative doublet and multiplet location (Fremont and Malone, 1987; Got et al., 1994; Waldhauser and Ellsworth, 2000; Moriya et al., 2003) and correlation-based phase repicking (Dodge et al., 1995; Shearer, 1997; Rowe et al., 2002, 2004). These methods have produced some impressive resolution of seismogenic structures within families of similar events. We will apply the technique of Rowe et al. (2002) for refining phase picks in large data sets, based on cross-correlation and clustering of similar waveforms. This approach not only provides robust similarity classification and event discrimination, without making a priori assumptions regarding waveform similarity, but also facilitates high-resolution relocation of seismic sources.

The problem of seismic tomography is linked to earthquake location, since it is based on the same observed quantity (body wave arrival times), but the velocity model is unknown and must be determined. Fast tomographic imaging tools are available, based on iterative, linearized techniques and approximate ray-tracing or finite difference solution of the eikonal equation (Thurber, 1992; Benz et al., 1996; Monteiller et al., 2005). Such techniques are strongly dependent on the quality of the data set (first arrival times) and therefore require care in correctly determining phase arrivals on seismograms. This is typically a time-consuming process, relying on the skill and the experience of the human analyst. This makes it difficult to rapidly obtain tomographic images.

The idea behind this work is to couple the tomographic process with the phase picking measurement trough iterative reconstruction of the 3D seismic velocity model. Starting from a quick preliminary pick (hand made, or theoretically computed from a reference 1D model) a first, low-definition 3D model can be obtained very rapidly. Theoretical travel times obtained from this 3D

velocity model, can then be used as a new reference pick, and the process is iterated, through a bootstrap procedure which, at each step, provides an improved model.

PICKING REFINEMENT BASED ON CROSS-CORRELATION

Travel time tomography associates arrival times of seismic phases (generated by active or passive sources) to velocity anomalies in the Earth through an inverse theory (Lay and Wallace, 1995). Phase arrival identification for seismic imaging is seldom performed on a trace-by-trace basis: the lateral consistency of seismic phases has to be carefully verified, since an abrupt change in arrival time can turn into spurious anomalies in the retrieved model. In active seismic data analysis, a typical approach is to group traces in common receiver gathers (CRG) or common source gathers (CSG), ordered by horizontal distance (offset) between source and receiver, and try to follow a certain arrival by evaluating its lateral coherence.

An effective phase identification algorithm for seismic imaging, must take into account and try to preserve lateral consistency. We try to accomplish this task by using a picking refinement algorithm based on cross-correlation and clustering of similar waveforms. The technique is based on the automatic, adaptive repicker by Rowe et al. (2002) which will be only briefly outlined here. For a deeper insight, reader should refer to the original article.

In this paper we will show an application to P-wave tomography. To retrieve a Vp image of the subsurface, the most common approach is to pick the first phase onset on each recorded trace. Typically, as the offset increases, this arrival is related to a seismic ray which samples a layer or a structure at increasing depth. To identify the first arrival on waveforms we begin by selecting a correlation window from a reference time. At the first step of the procedure, a relatively large window can be used, so as to capture the first arrival at every offset. For example, considering offsets between 0 and 6 km and travel times computed for a mean, uniform velocity model, the order of magnitude of arrival time differences will typically be about 0.5 s for each trace at increasing offset (see next section); therefore a 1 s correlation window around the reference pick is appropriate.

Following a station-by-station approach, we cross-correlate each pair of traces within a CRG. The cross-correlation maximum, which is an estimation of waveform similarity, is used as a weight for the corresponding time-lag. If N is the number of traces we are correlating, at the end of the process, N(N-1)/2 weighted lags will be computed.

Corrections for preliminary picks are obtained through the solution of the system of lag equations, which can be written in a matrix form as:

$$\mathbf{Gb = 1} \tag{1}$$

where **l** is the $M = N(N-1)/2$ vector of weighted lags, **b** is the N-vector of pick adjustments and **G** is a $M \times N$ first-difference operator of the form:

$$\mathbf{G} = \begin{bmatrix} -1/w_{21} & 1/w_{21} & 0 & 0 & 0 & 0 & ... \\ -1/w_{31} & 0 & 1/w_{31} & 0 & 0 & 0 & ... \\ -1/w_{41} & 0 & 0 & 1/w_{41} & 0 & 0 & ... \\ 0 & -1/w_{32} & 1/w_{32} & 0 & 0 & 0 & ... \\ 0 & -1/w_{42} & 0 & 1/w_{42} & 0 & 0 & ... \\ 0 & -1/w_{52} & 0 & 0 & 1/w_{52} & 0 & ... \\ 0 & 0 & -1/w_{43} & 1/w_{43} & 0 & 0 & ... \\ 0 & 0 & -1/w_{53} & 0 & 1/w_{53} & 0 & ... \\ ... & ... & ... & ... & ... & ... & ... \end{bmatrix} \quad (2)$$

where w_{ij} is the weight for the pair (i,j). The system is solved following a conjugate gradient L1 norm minimization technique, taking advantage from the sparseness of **G** (Polak, 1971). This system has at least one degree of freedom since we are only considering lags between traces, without any absolute reference time. In order to obtain an absolute time, the correlation windows are realigned according to the pick adjustments and stacked. The first arrival on the stacked trace can be picked either manually or by an autopicker, since the signal to noise ratio is highly improved by the stack; then, it is used as reference time to shift all the adjusted picks (e.g., Rowe et al., 2004).

The seismic phase associated with the first arrival is a function of the offset. For small distances it is generally related to the direct wave traveling from the source to the receiver; as the offset increases, the first arrival corresponds to head-waves generated by strong velocity discontinuities at increasing depth.

The identification of these phases can be improved by introducing a clustering strategy based on waveform similarity measurements. This can be a convenient approach because it does not require a-priori assumptions on the nature of the first arrival and it can reduce the complexity of the problem, since arrival times are adjusted within each cluster.

Given N traces, the clustering procedure starts defining an event distance matrix as:

$$\mathbf{K}_{i,j} = 1.001 - \mathbf{M}_{i,j} \quad (3)$$

where M is the $N \times N$ matrix of cross-correlation maximums (using 1.001 rather than 1.0 eliminates divide-by-zero errors).

At the first step of the clustering process, the two traces with the smallest **K** value are joined. A vector **k¹**, representing the distance of the pair from all the other traces, is constructed:

$$\mathbf{k^1}_m = \alpha_1 \mathbf{K}_{i,m} + \alpha_2 \mathbf{K}_{j,m} + \beta \mathbf{K}_{i,j} \quad m = 1, ..., N \quad (4)$$

where α_1, α_2 and β are coefficients whose value controls the clustering process (Lance and Williams, 1967). The vector $\mathbf{k}_1$ is added as a new row and a new column to the matrix $\mathbf{K}$; then the two rows and two columns corresponding to traces i and j are removed, obtaining a matrix $\mathbf{K}^1$ with N-1 values. This new matrix is again searched for minimum distance.

At each step g, a new matrix $\mathbf{K}^g$ with N-g values is generated. The process is terminated at the step $g = N$-1, when all the traces have been joined in one single cluster. The result is then backward reviewed to find the optimal step at which to stop the aggregation; the cutoff point corresponds to the biggest drop in the distance between elements in the matrix $\mathbf{K}^g$, measured by cophenetic correlation (Sneath and Sokal, 1973).

The system of equations (2) is solved to obtain picking adjustments within each cluster.

ITERATIVE TOMOGRAPHIC IMAGING

We embedded the pick refinement technique described above into an iterative scheme for tomographic imaging (Figure 1). The method can be outlined as follows:

1. Using a preliminary pick as reference, a correlation window is selected for all the traces. This window must be large enough to include the first arrival
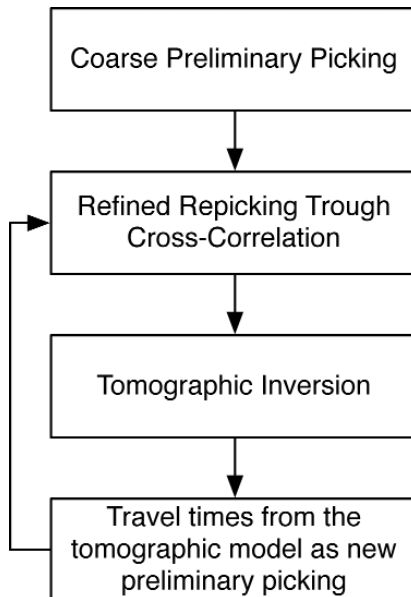

Fig. 1. Iterative tomography (ITAAP) schema.

along the whole range of offsets. For each common receiver gather, we perform waveform cross-correlation, clustering and picking adjustment.

2. Refined travel times obtained from this first step are used to compute an initial velocity model. We use the linearized tomographic inversion procedure based on finite difference solution of the eikonal equation proposed by Benz et al. (1996), but other approaches can be employed as well.

3. The resulting velocity model is used to compute theoretical travel times, which provide a new set of reference picks. A new correlation window, generally smaller than the previous one, is selected and picking refinement is again performed.

4. Resulting travel times are used for a new tomographic inversion and the process is iterated.

We named this procedure Iterative Tomographic Analysis based on Automatic Picking (ITAAP).

## APPLICATION TO THE ACTIVE SEISMIC DATA OF THE SERAPIS EXPERIMENT

As a test study for the ITAAP procedure, we have applied it to the SERAPIS (SEismic Reflection/Refraction Acquisition Project for Imaging complex volcanic Structures) seismic survey, carried out in September 2001, in the gulfs of Naples and Pozzuoli. A dense array of 60 three-component on-land stations and 72 three-component ocean bottom seismographs (OBS) were deployed (Figure 2), recording more than 92,000 traces from <5000 air gun shots having a source spacing of about 125m (Zollo et al., 2003). The survey has given a new insight into the structure of the volcanic areas of Mt. Vesuvius and Campi Flegrei, illuminating several structures, including the buried rim of the Campi Flegrei caldera (Zollo et al., 2003; Judenherc and Zollo, 2004).

Recently, Dello Iacono et al. (2007) obtained a very high resolution tomographic image of the Campi Flegrei caldera by carefully picking first arrivals on <45,000 traces recorded in the Pozzuoli Bay area. Phase detection and picking was manually performed following trace by trace the first arrival on seismic gathers and performing visual correlations between different sections. Although slow, this system has allowed a considerable reduction in the residual distribution with offset, leading to a high-definition P-velocity image (Figure 3). Choosing a model parameterization with cells of $250m \times 250m \times 100m$ (X, Y and Z, respectively), Dello Iacono et al. performed a tomographic inversion using the technique described by Benz et al. (1996). The resulting image shows an arc-shaped, high-velocity anomaly already revealed by Zollo et al. (2003) and interpreted as the buried rim of the Campi Flegrei caldera. In their study Dello Iacono et al. show an extremely complex vertical development of the structure: it appears as a double arch (starting at $400m$ depth), becoming then
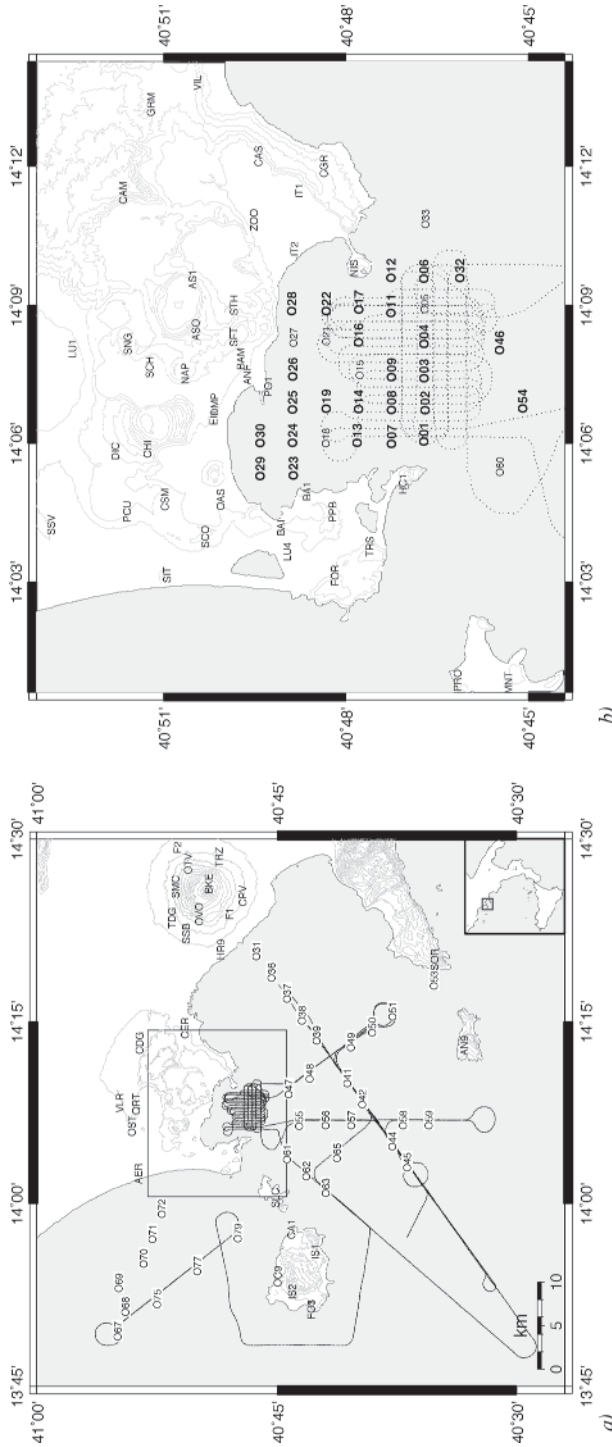
Fig. 2. The SERAPIS experiment, conducted in the Gulfs of Naples and Pozzuoli in September, 2001. **(a)** Labels show the names and positions of 72 OBS and 60 on-land recording stations. Dotted lines show the ship's path; each point corresponds to one of over 5000 shot positions, spaced at 125 m intervals. **(b)** Close-up of the Pozzuoli Bay area. OBS used for this study are indicated in bold
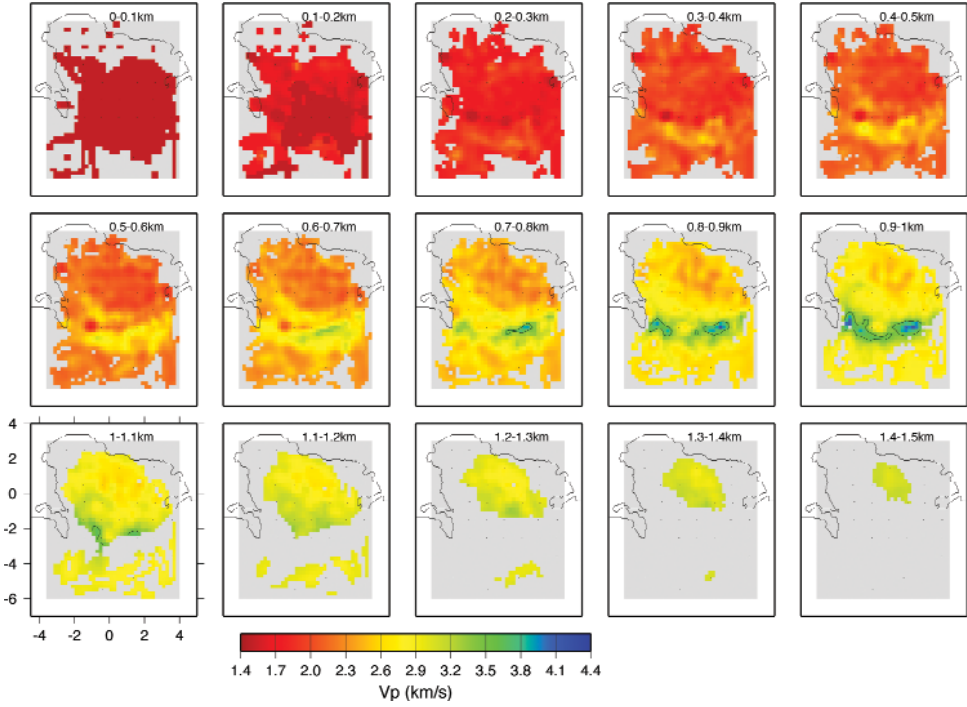
Fig. 3. Very high resolution tomography of the Gulf of Pozzuoli by Dello Iacono et al. (2007). The model is parameterized as cells of 250m × 250m × 100m (X, Y, and Z). This image was obtained using manually picked travel times on the full Pozzuoli Bay data set; we show it here as a reference model against which to compare our results.

a single arch (at 700-800*m*). The authors correlated this double-arch structure with the presence of dikes and fumaroles in the Bay of Pozzuoli, which imply the existence of a highly fractured area through which the magma and gases may have been able to rise.

Using manually picked travel times and the resulting tomographic model from Dello Iacono et al. as a reference, we tested ITAAP on a sub-set of the SERA-PIS data: 26 OBS in Pozzuoli Bay for a total of <42,000 traces. The selected stations are shown in bold on Figure 2b.

Correlation windows for the first run have been selected using a reducing velocity of 2 km/s for each of the common receiver gathers (CRGs), using a 1 s correlation window about the reduced zero time (Figure 4). This includes both the small-offset first arrival (which aligns at a reduction velocity of 1.5 km/s) and the large-offset first arrival (aligning at 3 km/s) in the correlation window.

We compared the results of the first run of refined repicking with the reference manual picking (Figure 5): 80% of picking differences are between -0.1 and 0.1 s; RMS is 0.098s. Travel times derived from repicked arrivals are used
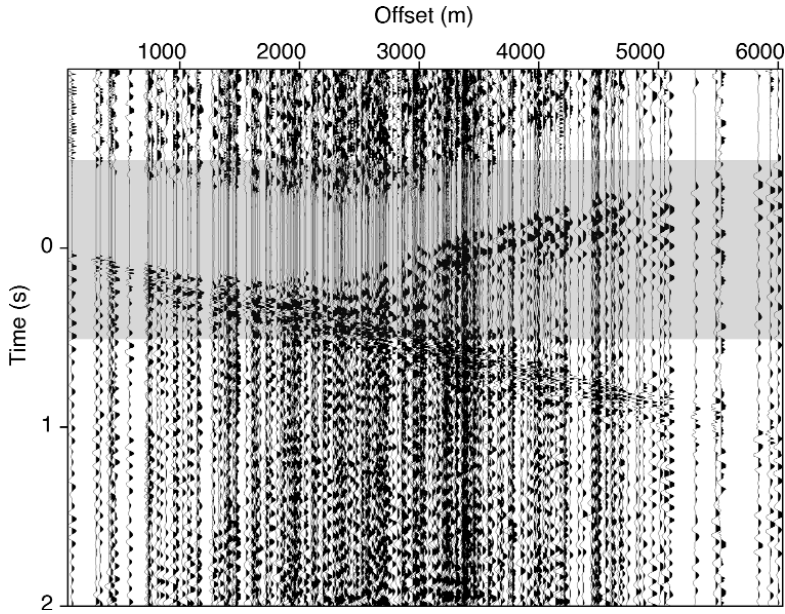
Fig. 4. To define the initial correlation window, we applied a reducing velocity of 2 km/s to each common receiver gather (CRG) and selected a 1 s window centered about the resulting zero time. The first arrival, related to two main phases that align at 1.5 km/s and 3 km/s, respectively, is always within the correlation window (gray band). Here the CRG for OBS O14 is shown as an example.
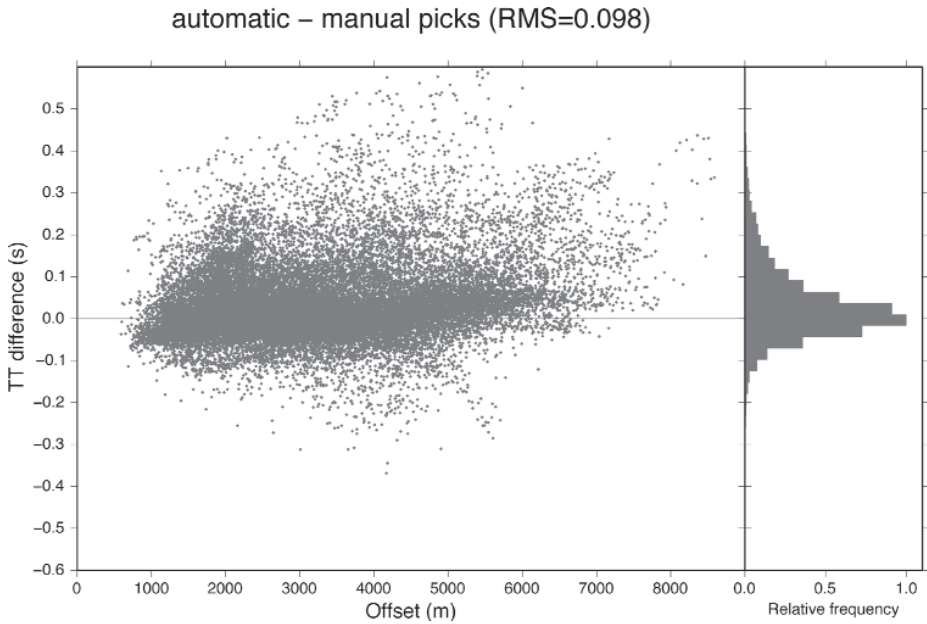
Fig. 5. Automatic vs. manual travel time (TT) differences as a function of offset after the first run.

to build the first tomographic image. We used the same model parameterization as Dello Iacono et al. The resulting velocity image is shown in Figure 8a: cell color is associated to the Vp value obtained by the tomographic inversion; gray cells are those for which no information is available since no seismic ray crosses the cell. The model is largely 1D, with the exception of a high-velocity anomaly at southern Pozzuoli Bay emerging at 0.4 to 0.5 km of depth. This anomaly is related to the arc-like velocity contrast found in previous studies.

The velocity model obtained from the first run is used to compute theoretical travel times at each station, which are set as the new starting pick for the second iteration of the process (Figure 6). Picking adjustments for the second run, obtained using a correlation time window of 0.2 s, are again compared with the reference pick in Figure 7; now 84% of picking difference is between -0.1 and 0.1 s and the RMS is 0.082 s. The new velocity image is shown in Figure 8b. As the quality of the picking improves, more details appear on the tomographic image. The model resolution increases at deeper layers (1.2 to 1.5 km), since arrivals at greater offsets become useable as a result of the repicking. Now the arc-shaped anomaly clearly emerges, showing a double-arch substructure (starting at 0.5 km depth) and a higher velocity anomaly (starting at 0.8 km) which was also delineated by Dello Iacono et al.
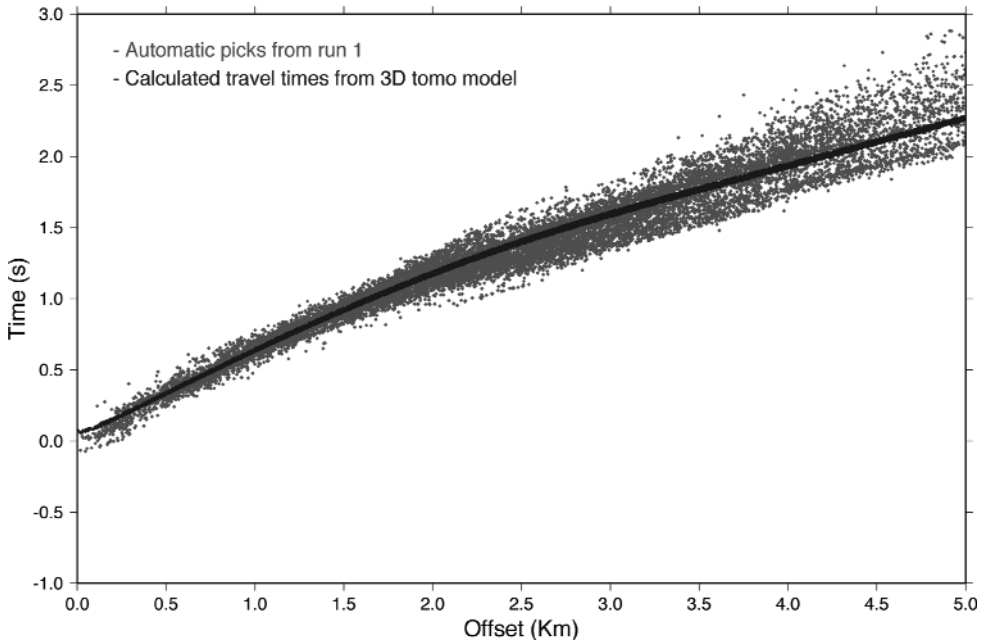
Fig. 6. Travel times (gray dots) calculated from the tomographic 3D inversion of automatic picks from first run (black dots). Tomographic travel times are used as preliminary picks for the second run of picking adjustment which was performed using a shorter, 0.2 s correlation window.

automatic – manual picks (RMS=0.082)
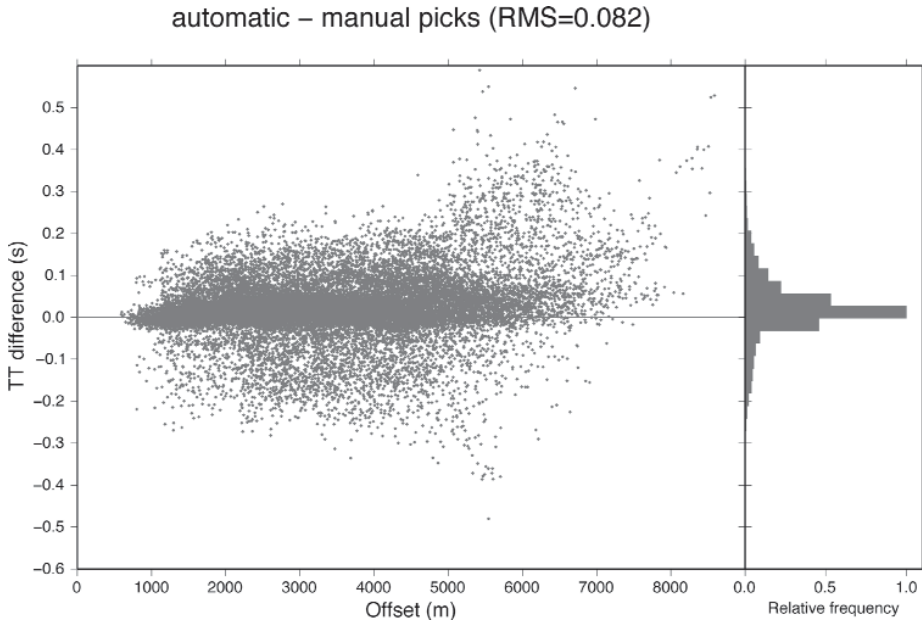
Fig. 7. Automatic vs. manual travel time (TT) differences as a function of offset after the second run.

After two iterations of picking refinement, the tomographic image exhibits several structures observed in the high-resolution image obtained through manual picking. In an ideal scenario, the technique could have been applied to a preliminary data-set while the SERAPIS survey was still in progress making it possible to focus the investigation on particular features, by re-arranging, the shot geometry, for instance.

DISCUSSION AND CONCLUSIONS

This work shows the feasibility of applying refined repicking techniques, commonly used for the problem of earthquake location, to seismic imaging, through an iterative tomographic approach.

The input of the ITAAP procedure is a coarse reference pick which, at each step, is improved by a) the use of a picking refinement technique and b) the computation of new theoretical travel-times for a velocity model obtained through tomographic inversion. The use of cross-correlation to estimate waveform similarity, and the application of a clustering approach ensure that the picking consistency among traces on the seismic section is verified and preserved. The output of the procedure is a tomographic velocity model which, at each new step, provides a better definition of the structures.
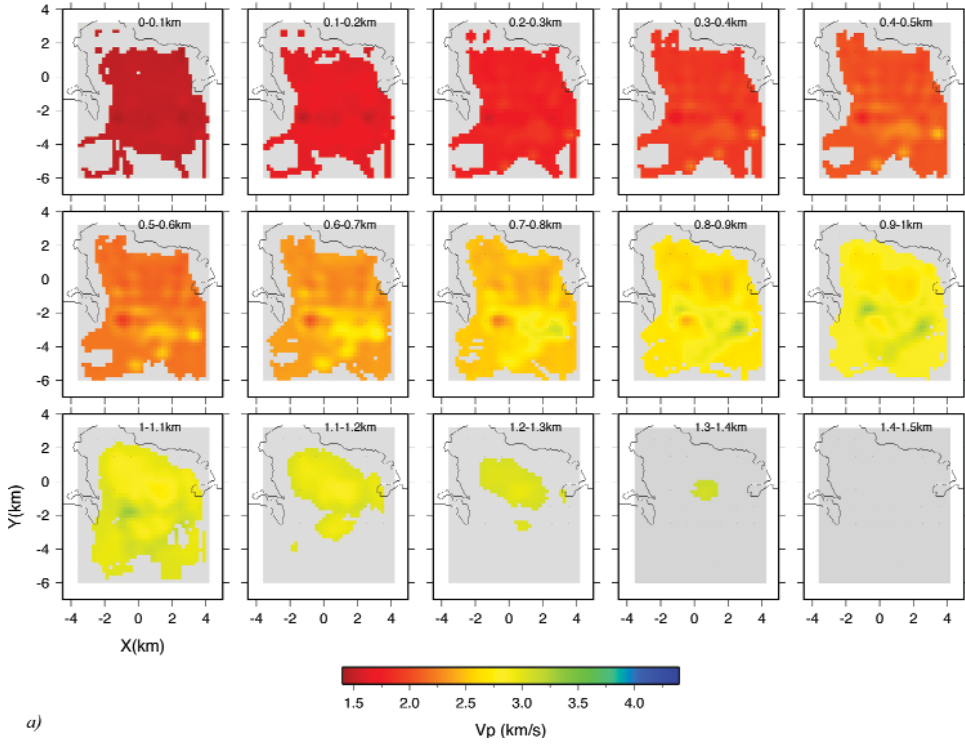
Fig. 8. (a) Velocity image for the Gulf of Pozzuoli after the first run of refined re-picking and tomographic inversion. The model is parameterized as in Figure 7. The image definition is low; nevertheless it is possible to see, starting at 0.4 - 0.5 km of depth, a high velocity anomaly at the center of the model delineating the southern border of the Gulf. This anomaly was interpreted by Zollo et al. (2003) as the buried rim of the Campi Flegrei caldera.

The case-study of Campi Flegrei caldera illustrates how the ITAAP technique can be used to rapidly analyze a large active seismic data set (<42,000 traces), obtaining a tomographic image which, after two runs of the procedure, already shows the main features of the model.

The availability of such a tool can be of great advantage when a reference image is required in to support critical decisions such as re-orienting an ongoing seismic survey or rapidly analyzing data coming from permanent or temporary networks during a crisis in a volcanic or a tectonic area.

We propose that this technique may be included easily into standard operations at permanent seismic networks. A reference model can be continuously updated via automated routines as new earthquake data are available. Based on this method, procedures for 4D monitoring of critical structures can be established for targets such as active fault systems, volcanic areas and oil and gas reservoirs (e.g. Patanè et al., 2006).

b)
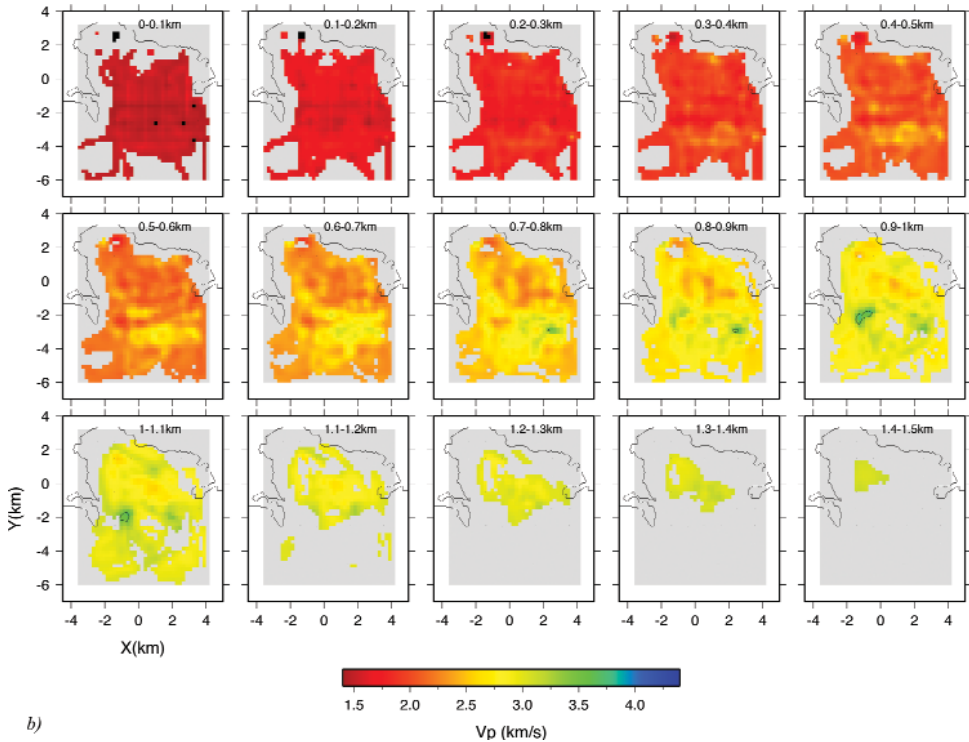
Fig. 8. (b) Velocity model after the second run. Image definition is improved and more details emerge, such as a double-arch structure and a high velocity anomaly starting at about 0.7 km depth.

These procedures might be coupled with a 4D seismic monitoring system in which events are relocated in the updated model to analyze seismicity during a volcanic crisis, or spatial and temporal evolution of induced seismicity at geothermal fields.

REFERENCES

R. Allen. Automatic phase pickers: their present use and future prospects. Bull. Seismol. Soc. Am., 72(6):S225-S242, 1982.

M. Baer and U. Kradolfer. An automatic phase picker for local and teleseismic events. Bull. Seismol. Soc. Am., 77(4):1437-1445, 1987.

H. M. Benz, B. A. Chouet, P. B. Dawson, J. C. Lahr, R. A. Page, and J. A. Hole. Three-dimensional P and S wave velocity structure of Redoubt Volcano, Alaska. J. Geophys. Res., 101:8111-8128, 1996.

D. Dello Iacono, A. Zollo, M. Vassallo, T. Vanorio, and S. Judenherc. Seismic images and rock properties of the very shallow structure of Campi Flegrei caldera (southern Italy). Bull. Volcanol., 2007 (submitted).

D.A. Dodge, G.C. Beroza, and W.L. Ellsworth. Foreshock sequence of the 1992 Landers, California earthquake and its implications for earthquake nucleation. J. Geophys. Res., 100:9865-9880, 1995.

M. J. Fremont and S. D. Malone. High precision relative locations of earthquakes at Mount St. Helens, Washington. J. Geophys. Res., 92:10223-10236, 1987.

J. L. Got, J. Fréchet, and F. W. Klein. Deep fault plane geometry inferred from multiplet relative relocation beneath the south flank of Kilauea. J. Geophys. Res., 99:15375-15386, 1994.

S. Judenherc and A. Zollo. The Bay of Naples (southern Italy): Constraints on the volcanic structures inferred from a dense seismic survey. Bull. Volcanol., 109:B10312, 2004.

G. N. Lance and W. T. Williams. A general theory for classificatory sorting strategies. 1. hierarchical systems. Comput. J., 10:271-276, 1967.

T. Lay and T. C. Wallace. Modern Global Seismology. Academic Press, San Diego, 1995.

V. Monteiller, J.-L. Got, J. Virieux, and P. Okubo. An efficient algorithm for double-difference tomography and location in heterogeneous media, with an application to Kilauea volcano. J. Geophys. Res., 110:B12306, 2005.

H. Moriya, H. Niitsuma, and R. Baria. Multiplet-clustering analysis reveals structural details within the seismic cloud at the Soultz geothermal field, France. Bull. Seismol. Soc. Am., 93:1606-1620, 2003.

D. Patanè, G. Barberi, O. Cocina, P. De Gori, and C. Chiarabba. Time-Resolved Seismic Tomography Detects Magma Intrusions at Mount Etna. Science, 313:821-823, 2006.

E. Polak. Computational Methods in Optimization. Academic Press, New York, 1971.

C. A. Rowe, R. C. Aster, B. Borchers, and C. J. Young. An Automatic, Adaptive Algorithm for Refining Phase Picks in Large Seismic Data Sets. Bull. Seismol. Soc. Am., 92(5):1660-1674, June 2002.

C. A. Rowe, Thurber C. H., and R. A. White. Dome growth behavior at Soufriere Hills Volcano, Montserrat, revealed by relocation of volcanic event swarms. Jour. Volc. Geotherm. Res., 134:199-221, 2004.

P. M. Shearer. Improving local earthquake locations using the L1 norm and waveform cross correlation: application to the Whittier Narrows, California, aftershock sequence. J. Geophys. Res., 102:8269-8283, 1997.

R. Sleeman and T. Van Eck. Robust automatic P-phase picking: an on-line implementation of broadband seismogram recordings. Physics of the Earth and Planetary Interiors, 113(1-4):265-275, 1999.

P. H. A. Sneath and R. R. Sokal. Numerical Taxonomy. W. H. Freeman & Company, San Francisco, 1973.

C. H. Thurber. Hypocenter-velocity structure coupling in local earthquake tomography. Phys. Earth Planet. Inter., 75:55-62, 1992.

F. Waldhauser and W. L. Ellsworth. A double-difference earthquake location algorithm: method and application to the northern Hayward Fault, California. Bull. Seismol. Soc. Am., 90:1353-1368, 2000.

H. Zhang, C. Thurber, and C. Rowe. Automatic P-wave arrival detection and picking with multiscale wavelet analysis for single-component recordings. Bull. Seismol. Soc. Am., 93:1904-1912, 2003.

A. Zollo, S. Judenherc, E. Auger, et al. Evidence for the buried rim of Campi Flegrei caldera from 3-D active seismic imaging. Geophys. Research Letters, 30(19):SDE 10-1, 2003.

Acoustic full waveform inversion in the frequency domain

F. Sourbier, S. Operto, J. Virieux

Géosciences Azur, CNRS and UNSA, Sophia Antipolis, France

Abstract: We present a massively parallel algorithm for distributed-memory platform to perform 2D visco-acoustic frequency-domain Full-Waveform Inversion (FWI) of wide-aperture seismic data. This algorithm is designed for extracting information when complex structures mask informations contained in the seismic signal as for foothill structures, salt dome area and volcanic structures. This dramatic change in resolution requires a quite accurate initial structure at the specified frequency we start with for the considered acquisition geometry. These three ingredients (initial velocity structure, starting frequency and data acquisition geometry) are essential for the success of the FWI. Our code is written in Fortran 90 and uses Message Passing Interface (MPI) for parallelism. Given a model of a physical system (and a physical theory), the problem of predicting the result of some observations is the forward problem. The inverse problem consists in using observations in order to infer the values of the parameters representing the subsurface of the Earth. The linearized inverse problem is solved by a classical gradient method which consists in finding a model perturbation which minimizes in the least-square sense the misfit function of amplitude perturbations of seismic waves. The forward problem is the acoustic wave equation: it is discretized by a compact finite-difference stencil using the so-called mixed-grid stencil. The related sparse linear system with an unsymmetrical matrix with complex coefficients is decomposed into an LU structure which partially fills the matrix leading to huge memory requirements, thanks to the MUlti frontal Massively Parallel direct Solver (MUMPS) for distributed-memory computer. It allows efficient computations of numerous pressure solutions for multiple Right Hand Side (RHS) source terms. As an illustration, we have applied this algorithm to a simple 2D profile of 105 km long over 25 km in depth. More than 1000 shots and 93 stations have provided a realistic configuration of acquisition. With dedicated cluster configuration, roughly 30 Gbytes of RAM memory and less than 4 days were required to perform this application. The geometry of acquisition has been found a key issue with well localized stations along the 2D line. Frequency content at frequencies below 4 Hz is necessary for a coherent imaging.

INTRODUCTION

Among geophysical approaches used in crustal investigations, active seismic methods are theoretically those which best characterize and resolve structures.

They are thus expected to provide key information on deformation mechanisms and feeding systems as volcanoes at depth. However, some serious limitations remain with that respect. The crust is classically investigated by wide-aperture seismic experiments using either networks of ocean bottom seismometers or on-lance seismometers in order to record refracted waves. Often collected data are exploited through travel time inversion methods. Whether first arrivals are used alone or with later reflections, these techniques essentially return information on the large-scale velocity distribution. Alternatively, using the full wavefield does not require phase identification and allows significant improvement in resolution. Hence, waveform inversion based on an accurate resolution of the full wave equation should allow a breakthrough in our knowledge and understanding of crustal processes as subduction zones, foothills structures or volcanic areas.

Of course, there is a drawback related to this high resolution performance: the estimation of the initial model we must start with. In order to overcome this limitation, we rely on two acquisition features: the full aperture range spanned by global offset geometries imaging a broad and continuous range of wavelengths in the medium including large to middle wavelengths and the sequential sweep procedure from the low to the high frequencies making a multi resolution imaging strategy which helps to fulfil assumptions associated with linearized inverse methods which may be trapped in local minima of the function to be optimized.

The inverse problem is solved by an iterative local linearized approach using a gradient method. For each iteration, the residual wavefield is minimized in the least-square sense. This process is iterated in a non-linear sense which means that the final model of the current iteration is used as the starting model for the subsequent iteration at a given frequency. The final model at a previous frequency will be also used as the starting model for the next chosen higher frequency. Therefore, the full-waveform modelling is performed at each iteration step. In the frequency-domain, solving the wave equation requires the resolution of a large system of linear equations. We use MUMPS (MUMPS-team, 2006) for distributed-memory computer to solve this system. The MUMPS algorithm is subdivided in three main steps. First a symbolic analysis step that performs re-ordering of the matrix coefficients to minimize the fill-in of the matrix during the subsequent factorization and an estimation of the assembly tree of the matrix. Second, the factorization is computed which provides LU factors distributed over all the processors. Third, the resolution is performed in parallel for multiple sources (i.e. multiple RHS vectors). After resolution, the multiple solutions are distributed over processors and each processor stores a sub-domain of all the solutions.

For the computation of the gradient of the cost function, two simulations per shot are required (one for the computation of the forward wavefield and one for the back-projection of residuals). In other words, the calculation of the gradient requires solving a huge sparse system of linear equations with twice

the number of shots as RHS vectors. These multi-sources distributed solutions can be exploited to compute in parallel the gradient of the misfit function because the gradient of the misfit function is a weighted stack of the solutions of MUMPS associated with the shots and the back propagated residuals. After summation, sub-domains of the gradient are distributed over the processors. At the end, the gradient is centralized on the master processor using collective communication. The gradient is scaled by the diagonal elements of the Hessian matrix. This could be achieved at each iteration in the inversion procedure but this scaling could be computed only once per frequency before the first iteration of the inversion if one wants to save computer resources. The estimation of the diagonal terms of the Hessian requires performing one simulation per non-redundant shot and receiver position. The same strategy that the one used for the gradient is used to compute the gradient scaling through the Hessian matrix in parallel.

This algorithm could be applied to dense wide-angle 2D data set and around thirteen frequencies ranging from 3 and 15 Hz could be inverted. Twenty iterations per frequency is a standard number of iterations leading to 260 updated velocity models of increasing resolution. A finite-difference grid of 4201x 1001 with a 25-m grid interval will span a model of 105 km x 25 km dimensions. Thousands of shots could be envisioned with a number of sensors of the order of one hundred. The time required to perform such inversion is around 4 days using 10 dual-core bi-processor nodes (40 cores) with 8 Gbytes of memory each.

FREQUENCY-DOMAIN FINITE-DIFFERENCE WAVEFORM MODELLING

The theory of frequency-domain waveform modelling and tomography has already been extensively presented (Jo et al., 1996; Stekl and Pratt, 1998; Hustedt et al., 2004; Pratt and Worthington, 1990; Pratt et al., 1998; Dessa and Pascal, 2003). Only a brief introduction to the method is given here. The 2-D visco-acoustic wave equation is written in the frequency domain as

$$
\frac{\omega^2}{\kappa(x,z)}P(x,z,\omega) + \frac{\partial}{\partial x}\left(\frac{1}{\rho(x,z)}\frac{\partial P(x,z,\omega)}{\partial x}\right) + \frac{\partial}{\partial z}\left(\frac{1}{\rho(x,z)}\frac{\partial P(x,z,\omega)}{\partial z}\right) =
$$
$$
= -S(x,z,\omega) \tag{1}
$$

where the density is denoted by $\rho(x,z)$, the bulk modulus by $\kappa(x,z)$, the frequency by ρ with the pressure field by $P(x,z,\omega)$ and the source term by $S(x,z,\omega)$. Since the relationship between the pressure wavefield and the source is linear, the discrete acoustic wave equation (equation 1) can be recast into a matrix form as the following linear system

$$A\,P = S \tag{2}$$

where the complex-valued impedance matrix A depends on the frequency and the medium properties. The 2-D pressure P and source S fields at one frequency ω are stored as vectors of dimension $nx \times nz$ where nx and nz denote the dimensions of the regular finite-difference grid with a grid interval h. The wave equation is discretized in a finite-difference sense using the so-called mixed-grid stencil (Jo et al., 1996; Hustedt et al., 2004). The wave equation formulated as a first-order hyperbolic system in pressure-particle velocity is discretized using two second-order staggered-grid stencils. The first one is defined in the classic Cartesian coordinates system (Virieux, 1984) while the second one is defined on a 45° rotated one (Saenger et al., 2000). Parsimonious elimination of the particle velocity fields leads to discrete second-order wave equation in pressure which embeds implicitly the staggered-grid structure. Discretizations of the spatial partial derivative operators on two coordinate systems are combined linearly to minimize phase velocity dispersion. Moreover, the mass term is averaged over the 9 surrounding points following an anti-lumped mass approach (Jo et al., 1996). With this quite compact spatial stencil, a discretisation of at least 4 nodes for the smallest wavelength will produce accurate propagating fields. The pressure field is obtained by solving the system of linear equations. If a direct method can be used to solve the equation (2), solutions for multiple sources (i.e. multiple RHS terms) can be obtained efficiently by forward and backward substitutions once the matrix A has been factorized using the LU factorisation:

$$LU\,[P_1 P_2 ....P_n] = [S_1 S_2 ....S_n] \tag{3}$$

We may consider that half of the time is devoted to the LU factorisation while the other part is devoted to deduce solutions of few thousands of sources. Practically, the multi-source resolution is performed in parallel with the MUMPS solver.

FREQUENCY-DOMAIN FULL-WAVEFORM INVERSION

Theoretical aspects

The inverse problem is solved with a weighted least-square gradient method, based on a classic local optimization approach based on a steepest-descent algorithm. The weighted least-square norm of the misfit function is given by

$$\mathcal{L}(m) = \Delta d^t W_d \Delta d \tag{4}$$

where $\mathcal{L}(m)$ is the misfit function (the difference between the observed data and the data computed in model m). The superscript t indicates the adjoint (trans-

pose conjugate). The weighting operator W_d is applied to the data which scales the relative contribution of each component of the vector Δd in the inversion. Minimization of the cost function leads to the following solution for the model perturbation Δm after scaling and smoothing of the gradient [see (Pratt et al., 1998; Ravaut et al., 2004; Operto et al., 2006) for more details].

$$\Delta m = -\alpha (diag H_\alpha + \varepsilon I)^{-1} \mathsf{G}_m \Re \left\{ p^t \left[\frac{\partial A^t}{\partial m_i} \right] A^{-1} W_d \Delta d^* \right\} \tag{5}$$

where $diag H_\alpha = diag(\Re\{J^t W_d J^*\})$ denotes the diagonal elements of the weighted approximate Hessian H_α and the Jacobian matrix is denoted by J. The diagonal of the approximate Hessian provides a preconditioner of the gradient which properly scales the perturbation model (Shin et al., 2001). The damping parameter ε is used to avoid numerical instability (i.e. division by zero). The matrix G_m is a smoothing regularization operator, implemented with the shape of a 2-D Gaussian spatial filter. The correlation lengths are adapted to the inverted frequency component (Ravaut et al., 2004). The Gaussian filter applied at a point of coordinates $(x0, z0)$ is given by

$$\mathsf{G}_{x_0, z_0}(x, z) = \exp\left[-\frac{(x-x_0)^2}{\tau_x^2} - \frac{(z-z_0)^2}{\tau_z^2} \right] \tag{6}$$

where τ_x, τ_z are the horizontal and vertical correlation lengths respectively. An amplitude gain with offset applied to each seismic trace has been used for the operator W_d with the following expression:

$$W_d(O_{sr}) = \exp(g \, Log|O_{sr}|) \tag{7}$$

where the scalar g g controls the amplitude of the gain with respect to the source-receiver offset O_{sr}. The inversion code can be applied to vertical geophone data or to hydrophone data generated by explosive sources. Vertical geophone data can be handled thanks to the reciprocity principle using the pressure wave equation (Operto et al., 2006). The inversion is applied sequentially to discrete frequencies of increasing values. The final model obtained for one frequency step is used as a starting model for the next frequency step. For each frequency, several iterations can be computed.

Least-square solution of the FWI

Equation 5 describes the imaging principle of FWI based on generalized diffraction tomography (Lailly, 1984; Tarantola, 1984): the model perturbation is

computed by zero-lag correlation between the forward wavefields p with residuals backpropagated in time $A^{-1}\Delta d^*$. Contribution of several shots is taken into account by simple summation. It requires two forward problems per shot, one to compute the forward wavefield and one to compute backpropagated residuals. The scaling of the gradient in equation 5 requires the explicit estimation of the jacobian and therefore one forward simulation per shot and receiver position. In our algorithm, the scaling of the gradient could be estimated once per frequency during the first iteration and kept constant over iterations or re-computed at each iteration. The term $\partial A/\partial m_i$ is the radiation pattern of the diffraction by the model parameter m_i. In the case of the P-wave velocity, this radiation pattern is for an explosion. In other words, this matrix reduces to one scalar. In the case of density, the radiation pattern is for a vertical force for a shot located at the vertices of the model parameter.

## Advanced use of MUMPS: multifrontal massive parallel Solver

MUMPS, a multifrontal massively parallel sparse direct solver package, developed by CERFACS, ENSEEIHTIRIT and INRIA, is use here to solve systems of linear equations of the form $A\ P = S$ for sparse multiple RHS, where A is a square complex unsymmetric matrix with symmetric pattern. Like other direct methods, the multifrontal technique uses in MUMPS is based on an elimination tree, which is a sensitive reduction of the graph of L, where L is the Cholesky factor of the matrix $(A+A^t)$, and is the smallest data structure representing dependencies between operations. The multi frontal algorithm is an approach to organize right-looking sparse matrix factorization in which the factorization of the matrix is done by performing a succession of partial factorizations of small dense matrices called frontal matrices. The factorization process is given by the assembly tree where a frontal matrix is associated to each node. Reordering (i.e. renumbering the unknowns of a sparse linear system) is a well known technique to reduce fill in the final factors, and this has a strong impact on the memory size. The software MUMPS offers several ordering algorithms, particularly the METIS package from University of Minnesota (Karypis and Kumar, 1998) who gives the large well-balanced trees for huge sparse matrix. Our interest in using direct solver is related to the fact we need to perform a large number of simulations in the frame of full-waveform inversion. Since the LU factorization is independent of the number of shots, direct methods should be superior to iterative ones as the number of shots increases.

The algorithm provided in Figure 1 summarizes the main steps of our algorithm. In the mixed parallel sequential algorithm, only the factorization is performed in parallel. The solution and the dense RHS vector are centralized on the host processor. In addition, solutions for each RHS must be temporally stored on disk to compute the gradient of the cost function. On some cluster

with low-level disk access and low bandwidth, centralizing the solution on the host processor and stored solutions on disk might be a costly and critical operation. A first improvement is to store solutions not on the frontal disk but on the local disk of the master node. The fully-parallelized algorithm performs in parallel the multiple shot resolutions, the calculation of the diagonal terms of the Hessian and the gradient of the cost function.

With the objective of full parallelization of our calculation to be more efficient in memory and CPU time, an advanced use of MUMPS and parallel programming using MPI are required. The inversion code can be applied to vertical geophone data or to hydrophone data generated by explosive sources.
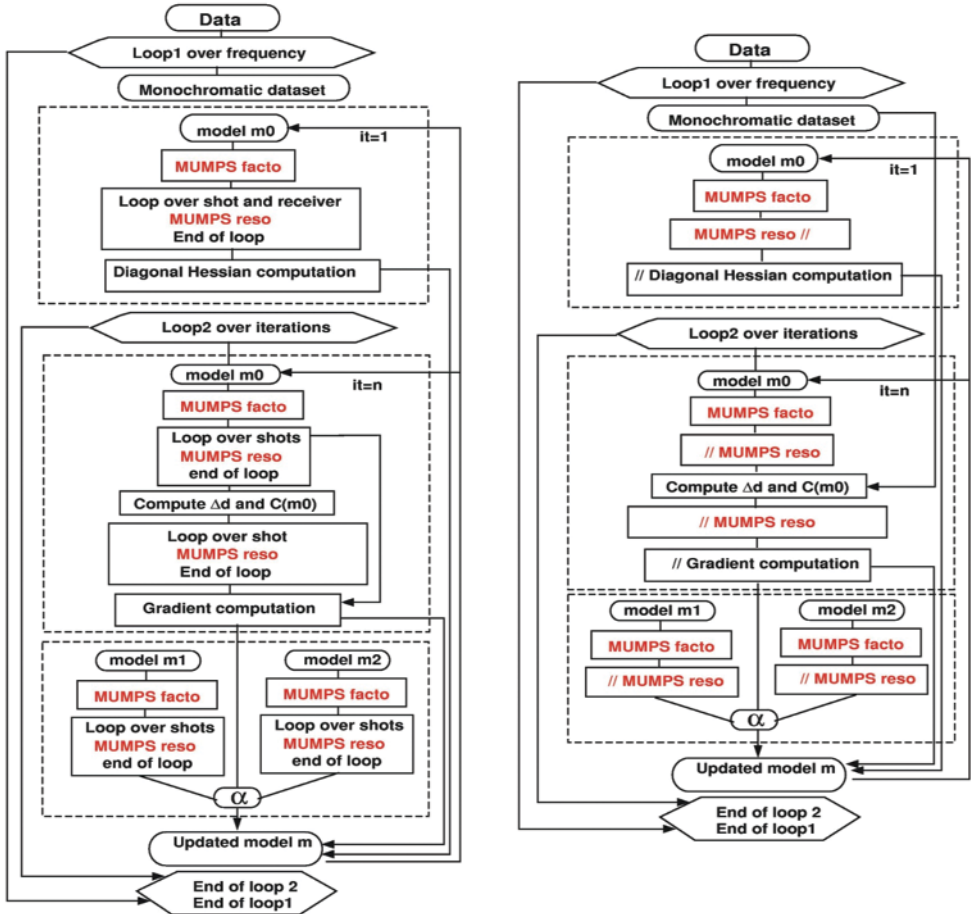
Fig. 1. Mixed parallel-sequential algorithm (left) and fully-parallelized algorithm (right) implemented in a 2D acoustic frequency-domain tomography full parallel program. We note Δd the difference between the observed and the computed data in the model, $\mathbb{C}$ the cost function and α the step length. In both algorithms, the gradient scaling must be also re-computed at each iteration of one frequency inversion.

It means that only few grid points near from the source have non-zeros values. Taking into account the great number of RHS and their huge sparse structure, the multiple RHS vectors are stored with sparse method. When storing sparse array, non-zero entries should be saved. A classical data structure for the storage of a sparse array is used. Moreover, we exploited the solution in its distributed form to compute in parallel the subsequent inverse problem (which is implemented as a weighted summation over the system solutions). It means that each processor contains a part of the LU factors and the RHS vectors associated after the MUMPS factorization and solve steps. It implies that many parameters like the observed data, the Green function's, the cost function, etc. are distributed like those determined by the MUMPS domain decomposition. Figure 2 shows, in the physical model and for each core, the area of the grid corresponding to all grid points stored in memory. Some difficulties appear using the solutions in its distributed form. First, the distribution can change from one model per frequency to the next due to pivoting. Therefore, the table relating a given position in the model to a processor index and vector index needs to be determined at each iteration. Second, we need to identify solutions outside the Perfectly Matched Layer (PML, sponge boundaries conditions) below a given topography and at receiver positions. Finally, in the case of multi-parameter full-waveform inversion, we need to identify adjacent grid points within the distributed solutions. For a better efficiency of the solve phase for multiple RHS, MUMPS allocates workspace memory of size proportional to the blocking factor for multiple right-hand side (a specific parameter of MUMPS software). For a constant number of RHS vectors, the elapsed time to solve the linear system is a critical value of this blocking parameter. Note that there is potential problem of swap when this parameter is too high. The difference of CPU time implies by this parameter is not negligible because running a full simulation (for example 20 iterations over 13 frequencies) may require more than 1000 multiple RHS resolutions.

Numerical behaviour

We performed series of numerical tests to assess the memory and time scalability (behaviour of the algorithm when the problem size increases) of the MUMPS. We consider square grids with increasing numbers of grid points N (the total number of points in the grid is $N2$). The numerical simulation is computed for a homogeneous medium where a pressure wavefield velocity is 4 km/s and the density is 2 $kg/m3$. The frequency is 15 Hz. The grid interval is 50 m and the PML is discretized with forty grid points. The number of cores is 20 for N ranging from 500 to 3500 and 40 for $N = 4000$. We use also two popular orderings, the Approximate Minimum Degree (AMD) and the hybrid approach based on multilevel nested dissection and multiple minimum
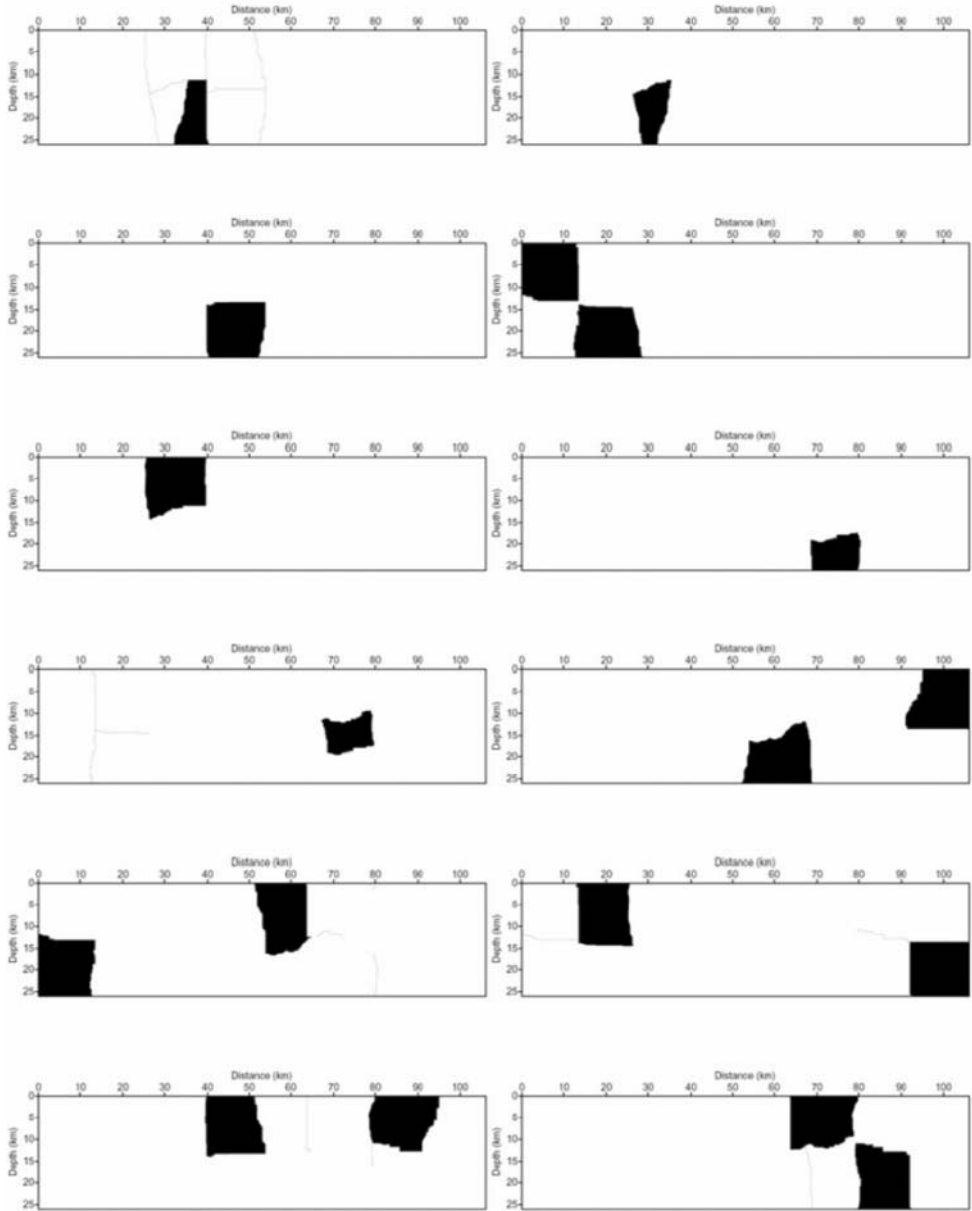
Fig. 2. illustration of the MUMPS domain decomposition after a solve phase of a linear system of size 1041 x 4241 (ie. 25 km x 105 km) with a 25 m grid step. Each core stores in memory a sub-domain of all the solutions (ie. for all the RHS), so we represent for each core the area of the grid corresponding. The number of cores is twelve.

degree (METIS). The theoretical memory complexity of the LU factorization is $O(N^2 Log_2 N)$ (George and Liu, 1981) if nested dissection ordering is used. The number of LU factors for METIS and AMD ordering as a function of the grid size is shown in Figure 3. These two curves are compared with different curves to some power of N. This suggests that the memory complexity is of the order of N^{26}. The number of cores has been set to 40 cores for simulations with 4000 grid points in order to avoid possible swapping.

In parallel computing, speedup refers to how much a parallel algorithm is faster than a corresponding sequential algorithm. It is defined by the ratio between the effective time used by a sequential and parallel execution. In our application and for 40 cores, parallel factorization was 14 times faster than the sequential one. Another important performance metric is the efficiency, defined by the ratio between the speed up and the number of core. The efficiency estimates how well is used processors (cores) for the problem at hand and compares how much effort is wasted in communication and synchronization.
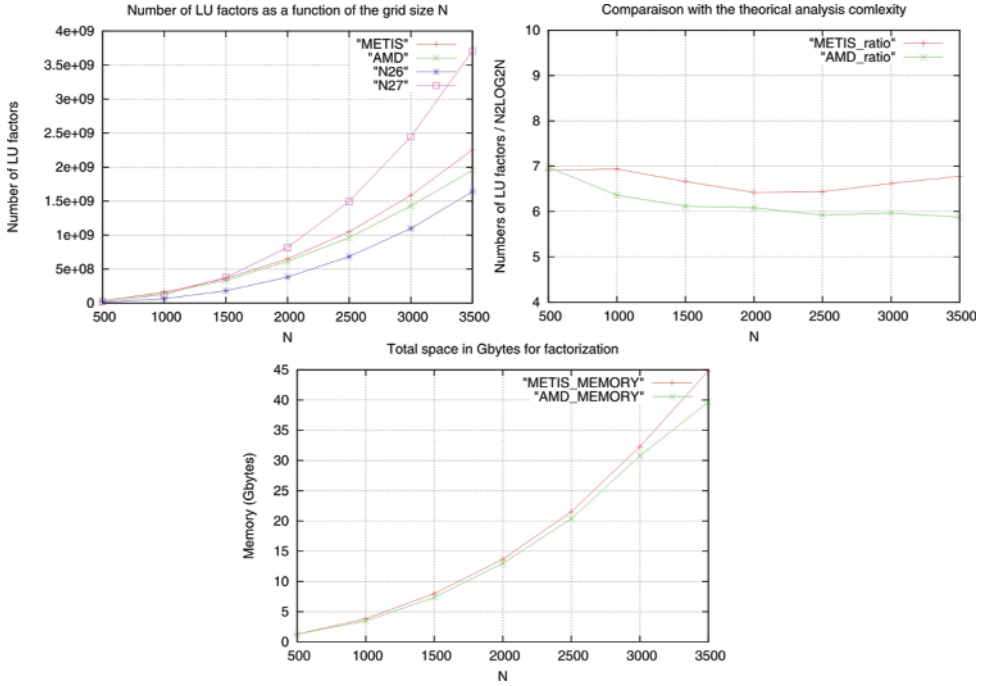
Fig. 3. Evolution of the memory complexity (number of LU factors) as a function of the grid size N with two orderings (AMD and METIS). On the left, comparison between the curve $N_{LU}=f(N)$ and some power of N (2.6 & 2.7). On the right, the ratio $N_{LU}/N^2 Log_2 N$ is shown. The bottom panel displays the total memory allocated during factorization as a function of the grid dimension N. The number of cores is 20.

Numerical aspects

The mixed parallel-sequential and the fully-parallelized algorithm have both been performed on two clusters to assess their numerical behaviour. Increasing by two the number of nodes decreases only by 1.2 the elapsed time for the mixed parallel-sequential algorithm versus by 2.0 for the fully-parallelized algorithm. The behaviour of those algorithms strongly depends on the architecture of the cluster, especially on the storage architecture and the interconnect network. Because of the number of writing and reading phases on disk, the mixed parallel-sequential algorithm is more sensitive to the storage architecture than the interconnect hardware. Due to the increase of MPI communication in the fully-parallelized algorithm, an efficient interconnection is required for a CPU time improvement.

A first test of scalability consists in performing series of simulations by increasing the number of cores to evaluate the behaviour of CPU time and memory. The total CPU time for completing one iteration after inverting 3 Hz frequency component as a function of cores has been estimated. Fourteen simulations were made between 12 and 64 cores with a uniform interval equal to 4. This is a classical curve in parallel computing, the CPU time decreases extremely rapidly at the beginning until it reaches a minimum for 40 cores. Over 40 cores, significant MPI communication will be required and the curve tends toward an asymptote. The optimal number of cores for this application is 40 which is expected for direct solvers. The re-ordering is performed by METIS and 19 Gbytes of RAM is necessary for the factorisation of the impedance matrix with the MUMPS solver. The number of LU factors is about 645.10^6 corresponding to 5.16 Gbytes. For factorization and solve phases, the elapsed time is divided by 2 (50% of reduction) when the number of cores is increased from 12 to 24. The decrease of the curve is quasi linear at the beginning. For 40 cores, the elapsed time reduction is about only 40%. An important saving of time appears when increasing the number of cores for the calculation of the Hessian and the Gradient (more than 90% of reduction), because these calculations contain only loops without MPI communication.

We have found that the number of RHS has a stronger impact on the CPU time than the number of non-zeros in all the RHS vectors. The functionality of MUMPS for performing multiple RHS resolution improves considerably the elapsed time for the solve phase. On average, for one RHS, the multiple RHS resolution requires 1.16 seconds compared to 3.96 sec for the sequential RHS resolution.

Another critical point is also the memory required during the factorization of the matrix. Increasing the number of cores improves CPU time but increases the memory required to perform the factorization. The memory allocated during the factorization is a linear function as the number of cores. The amount of memory increases with the number of cores because of increasing overheads. On average, each node uses the same RAM memory, except the

master node. Table 1 resumes the computational complexity of this application. The total memory to store one solution (complex value in single precision) is about 32 Mbytes. It appears clearly that, for a great number of sources, the memory requirement to store in core the solutions could be far greater than those to perform the LU factorization.

The speed up of our code is about 15 for 40 allocated cores. The trend is nearly linear and reaches a flat plateau over 40 cores. A key issue to have good numerical results is the power of the computer systems and the efficiency of the network. One may consider alternatives with respect to direct solvers for possible extensions in 3D geometries.

Tab. 1. Computational complexity of the fully-parallelized algorithm for an example of seismic imaging procedure.

Optimal number of cores	40
Number of LU factors (complex)	645.10^6
Total memory to store LU factors	5 Gb
Total memory to store one solution	32 Mb
Total memory for factorization	19 Gb
Real time for factorization (one frequency)	30 sec
Real time for 354 resolutions (diagonal Hessian)	404 sec
Real time for 93x2 resolutions (gradient estimation)	2x 110 sec
Real time for one iteration of one frequency inversion	1306 sec
Total time of inversion for 20 iterations over 13 frequencies	4 days

PERSPECTIVE AND CONCLUSIONS

We have presented a fully-parallelized algorithm for 2D visco-acoustic full-waveform inversion using the MUMPS software. The main concern of this article is the implementation of a fully-parallelized algorithm optimized for High Performance Cluster which facilitates the study of dense data acquisition system as required for complex structures (volcanoes, subductions, foothills). Moreover it allows more complete sensitive studies. The elapsed time of our algorithm has been divided by ten when compared to the mixed parallel sequential algorithm on a beowulf cluster. Future works will concern the implementation of parallelism in the 3D acoustic and the 2D elastic full-waveform inversion algorithm.

Potential applications to real data should be performed on areas where we have already a good knowledge of the velocity structure whatever is its complexity and where dense seismic records are available. The Campi Flegrei zone will be a target for such improved imaging technique, once detailed structures have been constructed.

The free software developing the Full Waveform Inversion could be recovered at the web page http://seiscope.unice.fr/opendownload.php with an available user manual.

REFERENCES

Dessa, J. X. and Pascal, G. (2003). Combined traveltime and frequency-domain seismic waveform inversion: a case study on multi-offset ultrasonic data. Geophysical Journal International, 154(1):117-133.

George, A. and Liu, J. W. (1981). Computer solution of large sparse positive definite systems. Prentice-Hall, Inc.

Hustedt, B., Operto, S., and Virieux, J. (2004). Mixed-grid and staggered-grid finite difference methods for frequency-domain acoustic wave modelling. Geophysical Journal International, 157:1269-1296.

Jo, C.-H., Shin, C., and Suh, J. H. (1996). An optimal 9-point, finite-difference, frequency-space, 2-d scalar wave extrapolator. Geophysics, 61(2):529-537.

Karypis, G. and Kumar, V. (1998). METIS – A software package for partitioning unstructured graphs, partitioning meshes and computing fill-reducing orderings of sparse matrices – Version 4.0. University of Minnesota.

Lailly, P. (1984). The seismic inverse problem as a sequence of before stack migrations. In inverse scattering theory and applications, SIAM Philadelphia.

MUMPS-team (2006). MUMPS – MUltifrontal Massively Parallel Solver users' guide – version 4.6.3 (February 2006). ENSEEIHT-ENS Lyon, http://www.enseeiht.fr/apo/MUMPS/ or http://graal.enslyon.fr/MUMPS.

Operto, S., Virieux, J., Dessa, J. X., and Pascal, G. (2006). Crustal imaging from multifold ocean bottom seismometers data by frequency-domain full-waveform tomography: application to the eastern nankai trough. Journal of Geophysical Research, 111(B09306):doi:10.1029/2005JB003835.

Pratt, R. G., Shin, C., and Hicks, G. J. (1998). Gauss-newton and full newton methods in frequency-space seismic waveform inversion. Geophys. J. Int., 133:341-362.

Pratt, R. G. and Worthington, M. H. (1990). Inverse theory applied to multi-source cross-hole tomography. Part 1: acoustic wave-equation method. Geophysical Prospecting, 38:287-310.

Ravaut, C., Operto, S., Improta, L., Virieux, J., Herrero, A., and dell'Aversana, P. (2004). Multi-scale imaging of complex structures from multi-fold wide- aperture seismic data by frequency-domain fullwavefield inversions: application to a thrust belt. Geophysical Journal International, 159:1032-1056.

Saenger, E. H., Gold, N., and Shapiro, A. (2000). Modeling the propagation of elastic waves using a modified finite-difference grid. Wave motion, 31:77-92.

Shin, C., Yoon, K., Marfurt, K. J., Park, K., Yang, D., Lim, H. Y., Chung, S., and Shin, S. (2001). Efficient calculation of a partial derivative wavefield using reciprocity for seismic imaging and inversion. Geophysics, 66(6):1856-1863.

Stekl, I. and Pratt, R. G. (1998). Accurate viscoelastic modeling by frequency-domain finite differences using rotated operators. Geophysics, 63(5):1779-1794.

Tarantola, A. (1984). Inversion of seismic reflexion data in the acoustic approximation. Geophysics, 49(8):1259-1266.

Virieux, J. (1984). SH wave propagation in heterogeneous media, velocity-stress finite difference method. Geophysics, 49:1259-1266.

Development of a multi-phase dynamic ray-tracing code

T.A. Stabile[1], R. De Matteis[2], A. Zollo[1]

[1] *Dipartimento di Scienze Fisiche, Università degli Studi di Napoli Federico II (RISSC-Lab), Napoli, Italy*

[2] *Dipartimento di Studi Geologici ed Ambientali, Università degli Studi del Sannio, Benevento, Italy*

Abstract: We here propose a method for rapid, high-frequency seismogram generation that makes use of an algorithm to automatically generate an exhaustive set of seismic phases that produce an appreciable amplitude on the seismogram. The method uses a hierarchical order of rays and seismic phases generation, taking into account some existence constraints for a ray-path and some physical constraints. To compute synthetic seismograms, the COMRAD code (from the Italian: "COdice Multifase per il RAy-tracing Dinamico") uses as its core a dynamic ray-tracing code. To validate the code, we have computed in a layered medium synthetic seismograms using both COMRAD and a code which computes the complete wavefield by the discrete wavenumber method. The seismograms are compared according to a time-frequency misfit criteria based on the continuous wavelet transform of the signals. The comparison shows that the ray-theory seismogram is enough complete and moreover, the time for the computing of the synthetics using the COMRAD code (truncating the ray series at the 10th generation) is 3-4-fold less than that needed for the Axitra code (to a frequency of 25 Hz).

INTRODUCTION

Over the last decades, the calculation of synthetic seismograms has become a useful tool in seismological research, and a wide variety of techniques have been developed. Forward modelling, which is the generation of synthetic seismograms, represent an important part of many seismological studies, such as seismic tomography or the kinematic inversion of source parameters. The solution of an inverse problem requires the repeated solving of the forward problem, so that speed is the most stringent condition that the method must supply.

It is possible to obtain the solution of the wave equation in a short time by using approximate high-frequency methods (Cerveny, 2001). The final solution of the elastodynamic equation is composed of elementary body waves that correspond to the various rays connecting the source to the receiver. Although the computation of ray synthetic seismograms are only approxima-

te and the ray method can fail in certain situations, the high-frequency methods are preferable to direct numerical methods for many applications, both for the shorter computing times and for the full interpretability of the seismograms. The problems arise when we want to use a synthetic seismogram as similar to the real one as possible in the high-frequency approximation, such that the seismogram should be relatively complete, although it is not necessary that it contains every feature of the full elastic wave field. It is becoming necessary to select from all of the rays connecting the source to the receiver only those that produce an appreciable amplitude on the seismogram. The problem of generating a comprehensive set of rays was approached for the first time by Hron (Hron, 1971, 1972, Hron et al., 1986) for layered media, by grouping individual rays into families of kinematic equivalents. Afterwards, Clarke (1993 a, b) developed a technique for computing synthetic seismograms based on a ray-generation algorithm that involved the symbolic manipulation of complete wavefield expressions from reflectivity theory, which were truncated to produce a finite ray series.

In this study, we propose a new technique for the rapid definition of an exhaustive set of rays that is based on the hierarchic generation of strings that describe the ray paths and the phase types. The string generation is subjected to physical constraints that are related to the propagation medium and the source-receiver geometry. The ray sets will represent the input of a kinematic or dynamic ray-tracing algorithm (i.e. Cerveny and Hron, 1980; Farra and Madariaga, 1987; Virieux, 1991; Snieder and Spencer, 1993). In particular, the technique developed has been implemented in the multiphase dynamic ray-tracing code (COMRAD) that uses as its core the dynamic ray-tracing code provided by Farra (1987).

METHOD

Our goal is to carry out an algorithm that rapidly generates an exhaustive number of seismic-phases to calculate an high frequency seismogram as complete as possible. The amplitudes, the raypaths and the travel times of the seismic-phases are computed by the dynamic ray-tracing code provided by Farra and Madariaga (1987). In this section we describe our method and the discretization of the propagation model.

It is possible to use an arbitrary medium as long as it is discretized by M ordered elements between a free surface and an half space. Each element should have an arbitrary shape and it is characterized by the following properties:

- Vp_i: compressive wave velocity (P wave);
- Vs_i: shear wave velocity (S wave);
- ρ_i: density;
- Qp_i: P-wave quality factor (optional);
- Qs_i: S-wave quality factor (optional);

- T$_i$:   top surface of the element;
- B$_i$:   bottom surface of the element (= T$_{i+1}$: top surface of the next element);
- i=1,...,M: index of the element.

where the elastic wave velocities, densities and quality factors should be functions of spatial coordinates.

Both the source and the receivers take the index i of the element in which they are included. Each ray goes from the source to the receiver and is divided into L curves if it passes through L elements. The numerical string of a ray is composed of L numbers, and each one is the index of the element crossed by the ray. For a ray there are also 2^L phase numerical strings, because in each element crossed by the ray the wave can have two different polarization (P wave or S wave). A numerical string for a phase is composed of L numbers and each one can be 1 (to indicate a P wave) or 2 (to indicate an S wave).

An example of how the numerical strings for the direct ray should be and for all of its possible phases is shown in Figure 1. Here, the elements of the medium are horizontal, parallel layers, while the source and the receiver are inside the third and first layers (elements), respectively.
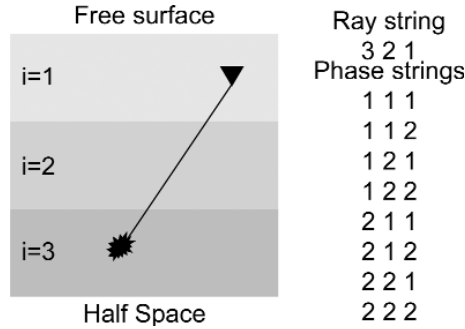
Fig. 1. Example of the ray and phase strings for a medium with three elements, where the source is in the third element and the receiver is in the first element.

Once the length L of the numerical ray strings is fixed there are M^L ray strings of the same length if the medium is discretized by M elements. However, not all of the ray strings describe a real ray, because there are some existence constraints for a ray path:

a) The ray starts at the source;
b) The ray arrives at the receiver;
c) The ray path is bordered by the free surface and the half space;
d) If a ray crosses the top surface of the ith elements, it must go to the (i-1)th element;

e) If a ray crosses the bottom surface of the ith elements, it must go to the $(i+1)^{th}$ element;

f) If the receiver is on the free surface, the ray must come from below;

g) If the source is on the free surface, the starting direction of each ray cannot be up.

To generate only the ray strings that describe real ray paths, we use a hierarchic order of ray generation, where the root is the index of the element that contains the source, and the number of the generations is the length of the numerical strings of the rays. The hierarchic order of ray generation satisfies itself for the a, b, c, d and e constraints. Using the additional f and g constraints, we discard some branches inside the numerical string tree. An example of hierarchic ray generation taken to the fourth generation for the same case as Figure 1, although putting the receiver on the free surface, is shown in Figure 2. In this case, we have two ray strings (3-2-1 and 3-3-2-1) to the fourth generation. If we put the receiver inside the first element instead of on the free surface, we will have the additional ray string 3-2-1-1 because there is no f constraint yet, and consequently the ray can arrive at the receiver also from above.
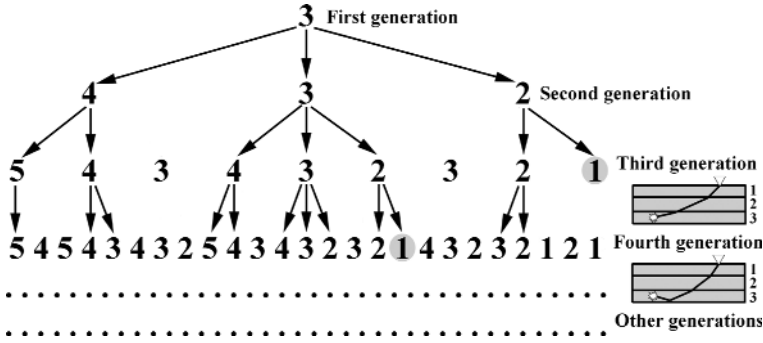
Fig. 2. Hierarchical ray strings generation using all of the a to g constraints. There are only two ray strings until the fourth generation because the receiver is on the free surface. If the receiver is inside the first element, there will also be the string 3-2-1-1.

Since the number of phase strings becomes greater and greater if the number of generations grows up, and consequently the computing time rises, it is possible to introduce some propagation constraints in order to reduce the number of phases. For this reason, we created two additional constraints: the first is on the maximum number of reflections in each element (selected by the RIFMULT parameter), and the second is a phase selection based on their expected amplitude values (selected by the PHS parameter).

METHOD VALIDATION

The higher the number of generations we consider, the higher the number of phases the core must calculate. To make the best choice on the number of generations, we have to compare the calculation time with the complexity we need for the synthetics. We compute synthetic seismograms for two receivers respectively at 1 km and 30 km distance from the epicentre of an explosive source. We use a crustal velocity model (Bernard and Zollo, 1989), where the elements are considered as horizontal parallel layers. The model is described in Table 1, while the results of the simulations are given in Table 2.

Tab. 1. The crustal velocity model used for our simulations.

Interfaces	Depth (km)	Vp (km/s)	Vs (km/s)	ρ (g/cm^3)
1	0	2.30	1.33	2.2
2	3	5.30	3.06	2.3
3	7	6.00	3.46	2.4
4	10	6.28	3.63	2.6
5	20	6.54	3.78	2.8

The source depth is 4 km, and both of the receivers are at 1 m in depth. For this source-receiver geometry, the source is in the second layer, the receivers are in the first layer and the first real phases start at the second generation. In Table 2, for each generation, the time needed by both the COMRAD and core programmes for the calculations can be seen, along with the total number of phases and the RMS. This has been calculated between the synthetic seismogram S_{REF} obtained at the previous generation and the seismogram S obtained for that generation, for both of the receivers and for both of the X and Z components. The amplitudes are normalized with respect to their maximum amplitudes. The RMS is defined as follows:

$$RMS = \sqrt{\frac{\sum_{t}\left|S(t) - S_{REF}(t)\right|^2}{\sum_{t}\left|S_{REF}(t)\right|^2}} \tag{1}$$

where t is the time.
From Table 2, it is clear that the RMS is lower and lower as a function of the number of generations. Moreover, starting from the RMS calculated between the 9th and 10th generations, the RMS decrease rate at 30 km distance becomes

Tab. 2. Results obtained for when the source is in the second layer and the receivers are in the first layer. The RMS is calculated between the seismograms calculated at the i-1th and i[th] generation.

N. GEN.	COMRAD TIME	CORE TIME	N. PHASES	RMS CompX 1 km	RMS CompZ 1 km	RMS CompX 30 km	RMS CompZ 30 km
2	0m 00.05s	0m 00.06s	2	-	-	-	-
3	0m 00.05s	0m 00.15s	10	1.037	0.992	4.628	4.789
4	0m 00.05s	0m 00.29s	34	0.108	0.104	0.980	0.932
5	0m 00.05s	0m 01.13s	114	0.107	0.103	0.262	0.340
6	0m 00.05s	0m 04.42s	370	0.027	0.144	0.440	0.494
7	0m 00.05s	0m 16.84s	1266	0.026	0.028	0.398	0.399
8	0m 00.05s	1m 07.45s	4210	0.008	0.010	0.186	0.252
9	0m 00.11s	4m 18.82s	14706	0.008	0.010	0.131	0.220
10	0m 00.27s	16m 18.15s	49522	0.002	0.004	0.087	0.109
11	0m 01.18s	1h 00m 23.47s	174450	0.002	0.004	0.077	0.092
12	0m 03.39s	3h 40m 56.38s	590194	0.001	0.002	0.037	0.058

stable for both the X and Z components. This means that if we want both complete body wave seismograms and short computing times, we can truncate the ray series at the 9th or almost at the 10th generation for this study. We can also reduce the number of phases using the RIFMULT and the PHS parameters discussed in the previous paragraph.

To better understand if our choice is appropriate, we can calculate the complete wavefield for the case under study by the Axitra programme, which uses the discrete wavenumber method developed by Bouchon (Bouchon, 1981; Coutant, 1989). Afterwards, we can compare the Axitra results with those obtained using the COMRAD programme stopped at the 10th generation, where the amplitudes of the synthetics are expressed in velocity and are normalized with respect to their maximum amplitudes. The computation is carried out using a PC with an AMD-3GHz processor and 2Mb SD-RAM memory. The Axitra computation time (up to the frequency of 25 Hz) is 53 minutes and 41.6 seconds, 3-4-fold longer than the COMRAD+core computation time (see Table 2). For a quantitative comparison between the synthetics, we use the misfit criteria in time and frequency that was developed by Kristekova et al. (2006), calculating both the time frequency envelope misfit (TFEM) and the time frequency phase misfit (TFPM). The TFEM is calculated according to the following equation:

$$TFEM(t,f) = \frac{\Delta E(t,f)}{\max_{t,f}(|W_{REF}(t,f)|)}$$
(2)

while the TFPM is calculated according to equation (3):

$$TFPM(t,f) = \frac{\Delta P(t,f)}{\max_{t,f}(|W_{REF}(t,f)|)}$$ (3)

where t is the time, f is the frequency, $\Delta E(t,f)$ is the local time-frequency enve-
lope difference, $\Delta P(t,f)$ is the local time-frequency phase difference, and
$W_{REF}(t,f)$ is the time-frequency representation of the reference signal $S_{REF}(t)$
based on the continuous wavelet transform.
In Figure 3, the TFEM and the TFPM for the Z component of the receiver
at 30 km distance (as worst case scenario) are shown. Red colour in the TFEM
and the TFPM images indicates a greater amplitude and a positive phase shift
in the COMRAD seismogram respect to AXITRA seismogram. Blue colour
represent the opposite case. We also overlap the two synthetic seismograms in
Figure 4, cutting the synthetics from six to 20 seconds (with respect to the ori-
gin time).
From the TFEM plot in Figure 3, and looking also at Figure 4, we can see that
there are differences in the amplitudes for some of the seismic phases, but
only for two of them (7.5 s, 11 s) there is an envelope misfit of about 20%.
Moreover, from the TFPM plot in Figure 3, and again looking also at Figure
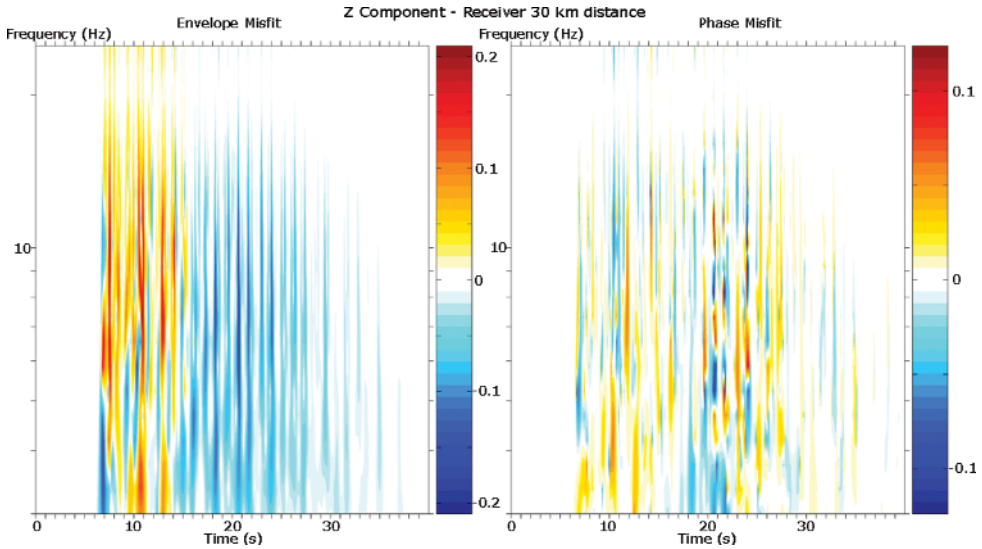
Fig. 3. The TFEM (left) and TFPM (right) plots for the vertical components of a receiver at 30 km dis-
tance from the source.
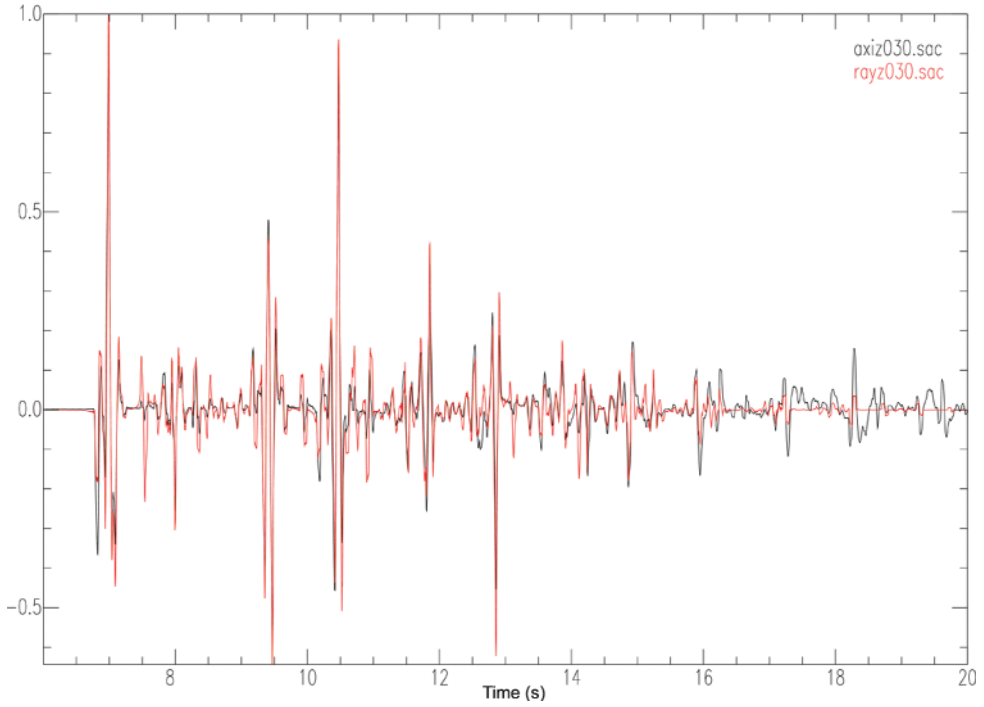
Fig. 4. The two synthetic seismograms for velocity computed by Axitra (in black) and COMRAD (in red). The amplitudes are normalized with respect to the maximum amplitude of each seismogram.

4, we can see that the phase misfit is less than 7% until 6 s, after which time it increases to about 10% because of the absence of the surface waves calculated by Axitra and not by COMRAD; moreover not all body waves are calculated by COMRAD due to the truncation of the ray-series.

STRUCTURE OF THE COMRAD.F CODE

The Comrad.f code is the Fortran77 version of multiphase code that uses as its core the dynamic ray-tracing code developed by Farra (Farra and Madariaga, 1987) to compute synthetic seismograms, travel times and ray paths. It is accompanied by the bash script multiphase.sh, which optimizes the whole calculation process and runs both the COMRAD and core programmes.
The structure of the code is represented in Figure 5, where we outline its most important features. The code requires the following input data:
– a file (creation.inp) which contains the medium information;
– a file (xxxx.dis, where xxxx represents a four characters word) which contains the source-receiver geometry;
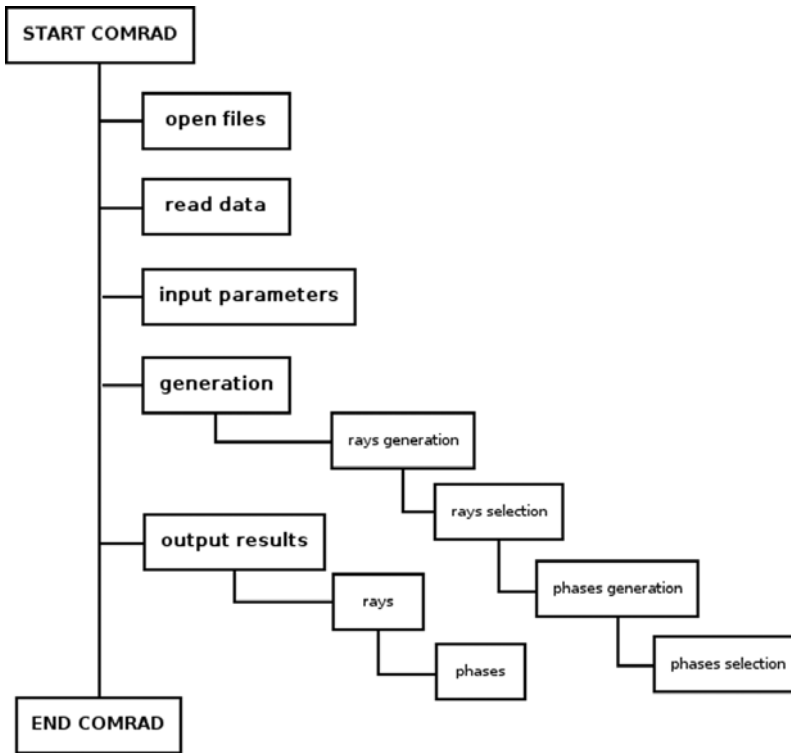
Fig. 5. Block scheme of the comrad.f computer code.

– the maximum number of generations (Lmax), which truncates the ray series. The user can choose to use the default value (Lmax=Lmin+2*m);
– the multiple reflections parameter (RIFM), which allows the ray to have a finite number of reflections in each element. The user can choose to use the default value (RIFM=8);
– the phase selection parameter (PHS), which discards phases with negligible amplitudes. The user can choose to use the default value (calculated on the approximated amplitude value of the direct P wave and fixed at $1*10^{-4}$% of this value);
– the initial polarization of the phases (P), which allows the user to use an explosive source (only P waves from the source) or a non-explosive source (both P and S waves from the source).

Using the hierarchical generation method with the constraints described previously, the code generates the ray and phase strings and creates the following output data:
– a file (kernel.inp) which contains the input parameters for the core;

– two files (xxx1.dis and xxx2.dis, where xxx represents a three character word) inside which the comrad.f code will write all of the ray and phase strings to be used by the core programme for the computation of the synthetics. The first file describes rays where their starting direction is up, and the second, where it is down.

The existence of the two xxx1.dis and xxx2.dis files assures that the calculations of both the P/P\ and P\P/ phases (and similar) are described by the same ray and phase strings if the source and the receiver are both in the same element (i.e. the ray string is 1-1 both for P/P\ and P\P/ phases if the source and the receiver are in the first element of the medium). Moreover, if the source is on the free surface, the xxx1.dis does not exist because of the g constraint.

CONCLUSIONS

We have developed a method for rapid high frequency seismogram generation. The method is used in a code (Comrad.f) to compute high frequency synthetic seismograms, which uses as its core the dynamic ray-tracing code developed by Farra and Madariaga (1987).
We have numerically tested the results in two steps. First, generation by generation, we evaluated both the computing time and the RMS between the COMRAD synthetics obtained in each generation and those obtained in the previous generation, to understand what the best choice is to have both an exhaustive seismogram and a short computing time. Using the crustal velocity model described in Table 1 and an explosive source at 4 km in depth, we found that the best choice is to stop the ray series at the 10th generation. After fixing the number of generations, we compared the COMRAD-derived synthetic seismograms with Axitra-derived synthetic seismograms, the latter being a programme that calculates the complete wavefield. We computed the seismograms in velocity and we normalized the amplitudes with respect to the maximum amplitudes. The numerical tests were carried out by the quantitative misfit criteria developed by Kristekova (2006).
The comparison of seismograms computed by the COMRAD and Axitra programmes is good, in particular if the source-receiver distance is short. In this study we have shown the misfits for a receiver 30 km distant from the source, where we have more differences. We demonstrate that the envelope misfit is about 20% only for the 8 s and 11 s seismic phases, due to the differences in amplitudes. Although there are also amplitude differences for some other phases, the envelope misfit is less than 10%-15%. Moreover, for the receiver at 30 km distance, the phase misfit between COMRAD and Axitra seismograms is about 10% due to the truncation of the ray-series and the absence of surface waves in COMRAD synthetic seismogram. However the higher the

frequency is, the lower the misfit is between the two seismograms. Finally, we compared the computation times for both of the programmes, and we can be sure that COMRAD (with 10 generations) is 3-4-fold faster than Axitra (up to a frequency of 25 Hz). If we want to compute the synthetics at higher frequencies, the Axitra code needs more time, while the computation time of the COMRAD code remains the same.

REFERENCES

Bernard, P. and Zollo A., 1989. The Irpinia (Italy) 1980 Earthquake: detailed analysis of a Complex Normal Faulting. J. Geophys. Res., 94, No. B2, 1631-1647.

Bouchon, M., 1981. A simple method to calculate Green's functions for elastic layered media. Bull. Seism. Soc. Am., 67, 259-277.

Cerveny, V., 2001. Seismic Ray Theory, Cambridge University Press, Cambridge.

Cerveny, V., and Hron, F., 1980. The ray series method and dynamic ray-tracing system for three-dimensional inhomogeneous media. Bull. Seis. Soc. Am., 70, 47-77.

Clarke, T.J., 1993. The complete ordered ray expansion -I. Calculation of synthetic seismograms. Geophys. J. Int., 115, 421-434.

Clarke, T.J., 1993. The complete ordered ray expansion -II.Multiphase body wave tomography. Geophys. J. Int., 115, 435-444.

Coutant, O., 1989. Program of Numerical Simulation AXITRA. Res. Report LGIT, Grenoble, in French.

Farra, V. and R. Madariaga, 1987. Seismic waveform modeling in heterogeneous media by ray perturbation Theory. J. Geophys. Res., 92, No. B3, 2697-2712

Hron, F., 1971. Criteria for selection of phases in synthetic seismograms for layered media. Bull. Seism. Soc. Am., 61, No.3, 765-779

Hron, F., May B.T., Covey J.D. and Daley P.F., 1986. Synthetic seismic section for acoustic, elastic, anisotropic inhomogeneous layered media, Geophysics, 51, 710-735

Hron, F., 1972. Numerical methods of ray generation in multilayered media, in Methods in Computational Physics, 12, Academic Press, New York.

Kristekova, M., Kristek J., Moczo P. and Day S.M., 2006. Misfit criteria for quantitative comparison of seismograms. Bull. Seism. Soc. Am., 96, No. 5,1836-1850

Snieder, R., and Spencer, C., 1993. A unified approach to ray bending, ray perturbation, paraxial ray theories. Geophys. J. Internat., 115, 456-470.

Virieux, J., 1991. A fast and accurate ray tracing by Hamiltonian perturbation, J. Geophys. Res., 96, 579-594.

Pore pressure prediction based on passive seismic and rock physics modeling

T. Vanorio[1], J. Virieux[2], D. Latorre[3]

[1] *Rock Physics Laboratory, Stanford University, USA*
[2] *Géosciences Azur, CNRS and UNSA, Sophia Antipolis, France*
[3] *INGV, Roma, Italy*

Abstract: This study presents a methodology for mapping pore fluid pressure from P-wave and S-wave velocities from passive seismic data. The method is applied to a geothermal reservoir that is experiencing notable ground deformations, seismic swarms and increases in the degassing activity related to natural fluid injection. As the first step, the passive seismic data were modeled using a tomographic method based on an accurate finite-difference travel-time computation. The P-wave and S-wave first-arrival times from micro-earthquakes were simultaneously inverted for both the velocity model parameters and the hypocenter locations. We then used rock physics modeling to transform P- and S-velocity parameters into rock properties at depth. The modeling was calibrated by using laboratory measurements, where the bulk and elastic properties of site-relevant rocks were measured under pressure conditions. The rock-property images were finally determined by minimizing the differences between the tomographic and the modeled velocities through the use of local and semi-global inversion schemes. Pore fluid pressure images show earthquakes distributed within the high pore pressure anomaly. This anomaly is located at 3 km in depth beneath the area of maximum uplift (~2 m). The existence of a localized, over-pressurized gas source at depth satisfies the presence of an anomalous low Vp/Vs ratio determined by the P-wave and S-wave reversal-velocity trends.

INTRODUCTION

It is widely recognized that the World demand for energy is continuously increasing. This has prompted oil and gas industries to develop reservoirs where production is more difficult, such as in hard-rock (e.g. carbonates, volcanic rock) or tight-gas reservoirs. Moreover, in areas where the mapping of fluid migration/ fluid flood is problematic due to difficulties of detection (e.g. with small impedance changes), there is also the need to find new technologies aimed at supplementing conventional time-lapse seismic methodologies. Stress changes are inherent in reservoirs undergoing production and stimula-

tion programs, such as those caused by pressure changes associated with fluid injection (e.g. Rutledge and Phillips, 2003; Jones et al., 1995), thermal changes due to steam injection (Maxwell et al., 2003), or strain changes associated with depletion (e.g. Segall, 1989; Maury et al., 1992). Whatever the source, stresses are released by movements at fractures or zones of weakness through micro-seismic events. Such events show both tensile-opening (Sneddon, 1946) and shear-slip mechanisms (Pearson, 1981) as a function of the distance from the injection point (Evans et al., 1999, and references therein). As supported by several studies (Zoback and Harjes, 1997; Cornet and Yin, 1995; Fehler, 1989), shear slip can be triggered by relatively low pressures, in comparison to crack-opening pressures, and hence shear stress may be released through the seismic cloud on the surrounding/ optimally oriented fractures, and beyond the *near-field* zone where the hydraulic fracture has opened.

Micro-seismicity can be localized in space and monitored over time to delineate fluid-flow pathways. Similarly, it can be used for local earthquake tomography to image P-wave and S-wave velocity variations at depth. In soft/ high porosity sands, laboratory measurements under pore fluid pressure and temperature conditions (Agar et al., 1986; 1987), as well as passive seismic monitoring of hydrofractures caused by steam injection (Gendzwill, 1992), have shown that: (1) shear failure is mainly controlled by intergranular friction; and (2) shear resistance is lost under low effective pressure (e.g. high pore pressure conditions). Thus, low seismicity rate and/or aseismic behavior is detected in comparison with brittle rocks, such as granites (Baria et al., 1989). Therefore, passive imaging can be used as a tool in older, more compacted rocks or in hard-rock reservoirs undergoing stimulation. This thereby offers both a complementary description of the geometries in areas where active time-lapse seismic methods are more challenging, and short-term information on reservoir dynamics that arise from abrupt changes in stress. The latter is useful for intervention during the stimulation, as it provides an updated image of the fracture growth that can be used to calibrate numerical flow models.

The present study offers an exploratory example of the use of passive seismic methods and rock physics in a volcanic geothermal reservoir experiencing natural fluid injection. Rock physics is used to link the P-wave and S-wave velocity models from micro-earthquake travel-time inversion to rock properties. Here, we show a model-based prediction of pore fluid pressure at depth and its comparison with the earthquake locations.

GEOPHYSICAL OUTLINE OF THE AREA

The Phlegrean Fields is one of the active volcanic systems in Southern Italy (Figure 1). The numerous hydrothermal manifestations that occur in the area are the surface expressions of a deep geothermal system, the existence of

which has long been known from deep exploration wells (Agip, 1987). The area experiences notable unrest episodes periodically, which include ground deformations, seismic swarms and increases in the degassing activity (Barberi et al., 1984). Several unrest episodes have occurred since the early 1970s, briefly interrupting the secular subsidence of this field. During the 1982-1984 crisis, more than 15,000 micro-earthquakes occurred and there was an uplift rate of 3 mm/day (Aster and Meyer, 1988). This uplift resulted in a total vertical displacement of 1.8 m (Barberi et al., 1984), which stopped by January 1985, along with the seismic activity. A slow subsidence then began, which to date has removed about 70 cm of the total uplift.

Based on published data, Chiodini et al. (2001, 2003) have shown that a time correlation exits between ground displacement, variations in gas emissions, and seismic activity. Numerical modeling of fluid flow has shown that these variations are consistent with periods of enhanced fluid injection at the base of the hydrothermal system. On the basis of the degassing rate measured in the Solfatara area, the order of magnitude of the corresponding injection rates was estimated to be 1,000 ton/day for CO_2 and 2,400 ton/day for H_2O (Chiodini et al., 2003).

As well as affecting the state of stress of the flooded region, fluid injection may also change the rock properties, and hence the P-wave and S-wave seismic
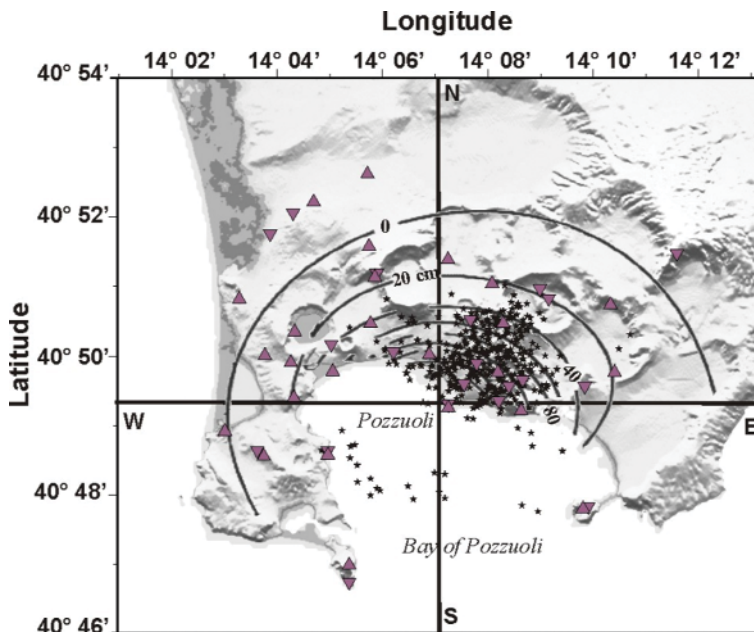
Fig. 1. Map of the Campi Flegrei Caldera showing the seismometer stations (inverted triangles, WS network; triangles, VO and AG networks) and the final earthquake locations (black stars). The map also shows the elevation contours (black lines) for the 1982-1984 uplift.

velocities. We have used the natural seismic activity occurring in this area to image the P-wave and S-wave velocities of the structure at depth. Rock physics modeling was then applied to translate the velocity changes into rock properties that can describe the stress variations.

METHODS

Local Micro-Earthquake Tomography

Local earthquake tomography constituted the basic tool that was used to assess the 3-D velocity structure of this area (Vanorio et al., 2005). Although this method provides '*smooth*' velocity models (i.e. long wavelength features) compared to those from active seismic methods, passive imaging has the advantage of revealing the structures at depth while changes in the stress field occur. Also, the inversion from micro-earthquake travel-time data allows a straightforward assessment of the S-wave velocity structure, which is crucial to overcome the ambiguities that derive from the interpretation of the P-wave velocity field alone. We outline here the most salient steps of the tomographic procedure, while Vanorio et al. (2005) is recommended for further details concerning the tests of resolution and the uncertainties associated with velocity images.

Network, Dataset, and Data Selection

To monitor the seismic activity that occurred in 1982-1984, the University of Wisconsin began a field experiment that deployed a temporary network consisting of 21 three-component digital short-period seismometers (WS) (Aster and Meyer, 1988). This network complemented those maintained by the Vesuvian Observatory (VO) and Agip (Azienda Generale Italiana Petroli, AG), which consisted of 25 analog vertical seismic stations (Figure 1).
We used a sub-dataset consisting of 1,209 micro-earthquakes that occurred from January to April in 1984, which provided 7,264 P-wave and 3,121 S-wave arrival-time readings. The arrival times picked from the digitized seismograms were estimated to have an accuracy in the range of 0.02-0.05 s for the P-waves, and 0.02-0.10 s for the S-waves. A preliminary hypocenter location was determined by using the 1-D P-wave velocity model that resulted from an active seismic experiment performed in the area (Zollo et al., 2003). The earthquakes that had at least six P-wave and four S-phase readings, an azimuth gap smaller than 180°, and RMS time residuals smaller than 0.5 s were selected from the initial dataset. This selection provided a database that consisted of 462 high-quality earthquakes, with a final number of P-wave and S-wave readings of 3,447 and 2,289, respectively.

The Tomographic Approach

A linearized, iterative tomographic approach was taken using the TLR3 (Tomography-Localization-Relocalization v.3) computer code, which is based on an accurate finite-difference travel-time computation (Latorre et al., 2004; Monteiller et al., 2005). Travel-time partial derivatives were computed for the P-wave and S-wave slowness fields, the hypocenter location, and the origin time, and then they were inverted simultaneously without any parameter separation technique by using the LSQR algorithm (Paige and Saunders, 1982). Here, we should underline the importance of coupling the inversion of micro-earthquake hypocenter parameters (location and origin time) on the one hand, and velocities on the other, to provide mutually consistent parameters and to avoid bias in the deduced models (Thurber, 1992).

Selection of the Initial 1-D Velocity Model

In a perturbative tomographic approach, the final solution depends strongly on the choice of the 1-D reference model (Kissling et al., 1994). As a first step, we used the 1-D P-wave velocity model that resulted from the inversion of 77,000 P-wave first-arrival times that were recorded during an active seismic experiment by a dense array of 60 three-component, sea-bottom seismographs (OBS) and 72 three-component seismographs installed on land (Zollo et al., 2003). We then verified the consistency between the initial 1-D velocity model (Zollo et al., 2003) and the passive dataset, because of both the different geometry of the passive and active networks and the elapsed time between the acquisitions. A statistical study of the final 3-D solution was inferred from 400 initial 1-D models that were randomly generated within two extreme 1-D velocity bounds (see Figure 2a, upper panel, gray solid lines). The upper and lower velocity bounds were chosen so as to have the 1-D reference model of Zollo et al. [2003] as the average (see Figure 2a, upper panel, cyano dashed line). The statistical approach showed (see Vanorio et al., 2005, for details) that even though the data misfit of all of the final solutions reached roughly similar values (0.08 s on average), the 400 initial models provided substantially different RMS time residuals that fell into two ranges. The first of these included the values smaller than 0.2 s, and the second, those greater than 0.2 s. The reference 1-D velocity model fell in the range of the values greater than 0.2 s (see Figure 2a, middle panel, cyano star). In addition, the distribution of the initial time residuals associated with the P-wave and S-wave reference models and the earthquake locations (Figure 2a, lower panel, gray histogram) was shifted towards positive values (i.e. t $_{observed}$ > t $_{theoretical}$), as compared to the distribution associated with the final solution (Figure 2a, lower panel, black histogram). Such a shift implies an overestimation of the reference 1-D velocity model, which could affect the velocity estimates in the final models. Due to these con-
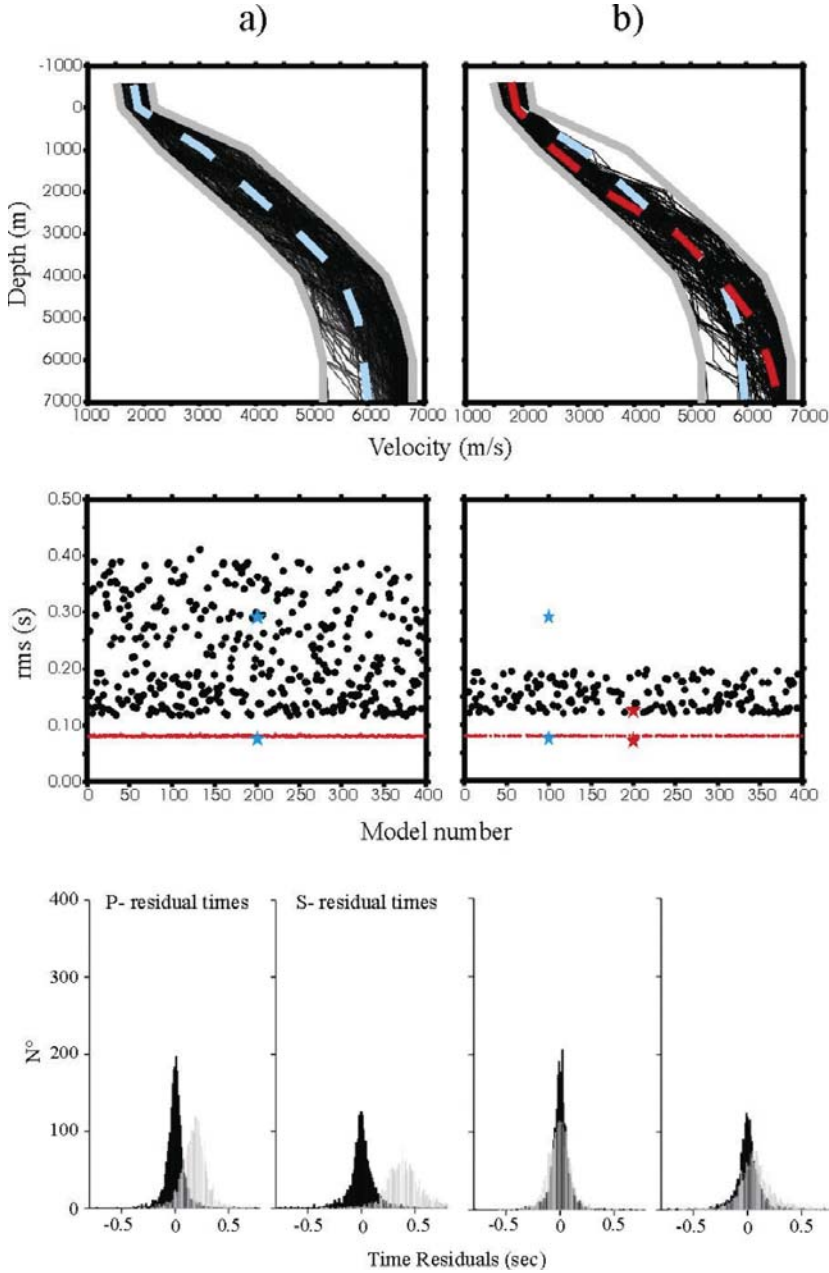
Fig. 2. (a) left upper panel: randomly generated initial 1-D velocity models. The upper and lower velocity bounds (solid gray lines) and the 1-D velocity model from Zollo et al. (2003) (dashed cyano line) are also shown; left middle panel: initial (black points) and final misfit values (red points) obtained from the inversions. Cyano stars indicate the initial and final misfit values for the 1-D velocity model of Zollo et al. (2003); left bottom panel: initial (gray) and final (black) distribution of travel-time residuals for the P-wave and S-wave velocity models using the 1-D velocity model from Zollo et al. (2003). (b) Same as (a), but after the restrictive selection described in the text.

siderations, we made a more restrictive selection for the 1-D reference model. The reference model was thus chosen by averaging all of the velocity models showing RMS residuals <0.2 s (see Figure 2b, upper panel, red dashed line). This selection provided a lower RMS of the final 3-D solution (~0.07 s) (see Figure 2b, middle panel, lower red star), and a zero-centered distribution of initial travel-time residuals (see Figure 2b, lower panel, gray histogram).

The Vp/Vs Images

A heterogeneous distribution of source and receivers requires a careful assessment of the solution quality in seismic tomography (i.e. defining of the areas of reliable solution and detecting the possible artifacts). In general, the solution quality of a specific model parameter depends mainly on the geometric distribution and density of rays (ray coverage, see Figure 3). Through plotting resolution estimates such as the hit count, the diagonal elements of the resolution matrix are a common way of assessing ray coverage. Also, bootstrap statistics can provide a possible approach to assess the most representative distribution of the model parameters, and thus to evaluate the uncertainties in the velocity values in the final solutions (Aoike et al., 1998).

Our augmented database allowed an improved resolution of the inferred 3-D models at depths between 4 km and 5 km, as compared to the database used in the Aster and Meyer study (1988). The resolution of velocity images was determined by synthetic tests on a global scale (e.g., standard checkerboard tests) as well as on a local scale (e.g., spike tests, which provide a numerical method for estimating the resolution matrix). The tests results demonstrated
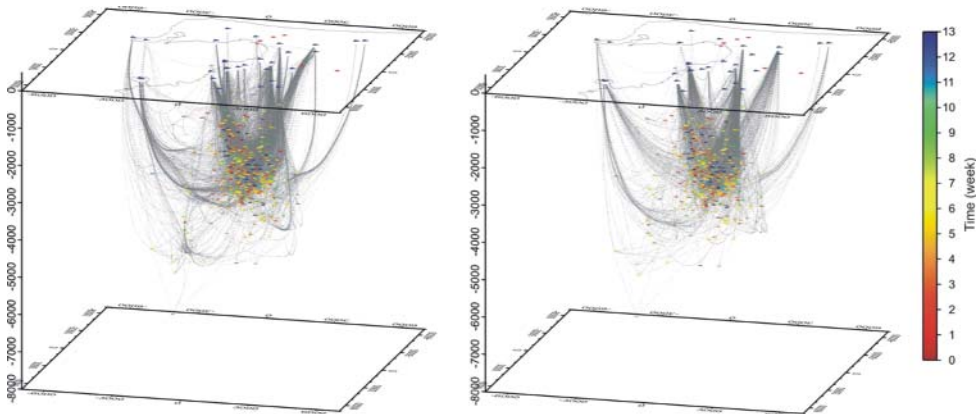

Fig. 3. Three-dimensional ray path for the P- waves and S- waves between the stations (blue triangles) and the earthquakes, color coded as a function of time.

that the size and amplitude of both positive and negative anomalies with a minimum wavelength of 1 km, and placed at 4-5 km in depth, are fairly well resolved. Also, the uncertainty assessed by bootstrap statistics showed a δV of the velocity values of 400 m/s (see Vanorio et al., 2005).

The Vp/Vs images were deduced from the final solution of the 3-D P- wave and S- wave velocity field. Figure 4 shows the Vp/Vs vertical cross-sections along the E-W and N-S directions. The Vp/Vs images show a centered high Vp/Vs anomaly that is located at ~1.5 km in depth, which is surrounded by a low Vp/Vs anomaly that shows a flat feature at 4 km in depth beneath the area of maximum uplift.

Vertical velocity profiles were extracted from the final 3-D velocity models (Vp, Vs, and Vp/Vs) for several sites. Figure 5 shows the variations in Vp, Vs,
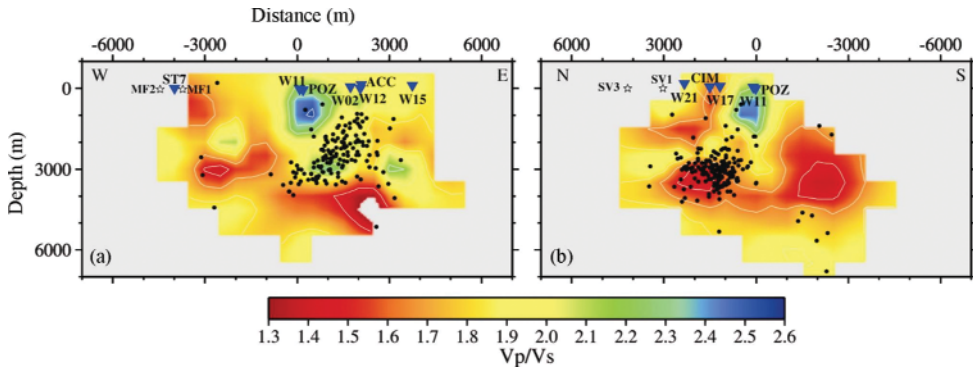
Fig. 4. Vertical cross-sections illustrating the variations in the Vp/Vs ratio and the earthquake distribution (black points) along the **(a)** E-W and **(b)** N-S directions reported in Figure 1. The black stars and triangles indicate the well and station locations.
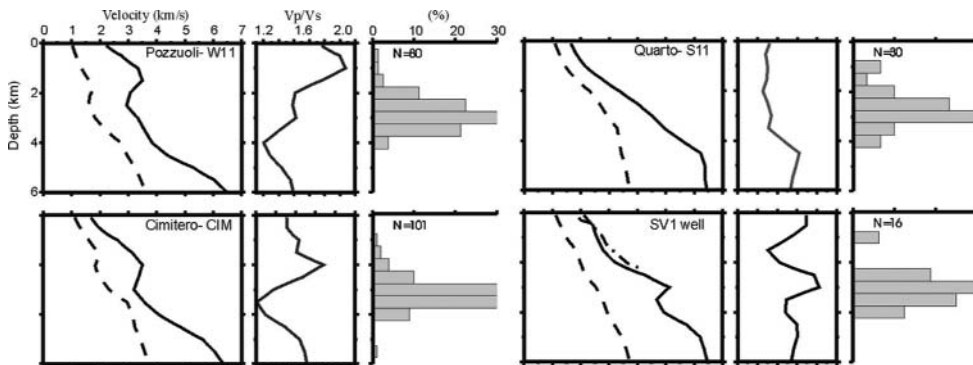
Fig. 5. The vertical velocity profiles, showing Vp (solid line), Vs (dashed line), and the Vp/Vs ratio (solid line) extracted from the final 3-D velocity models. The earthquake distribution was computed along the vertical profiles by using a radius of 0.5 km. The dot/dash line for the SV1 site shows the result obtained by averaging well log data.

Vp/Vs and the earthquake distribution as functions of depth. Several P-wave and S-wave velocity profiles show reversal trends that tend to disappear when moving radially away from the center of the caldera (e.g. the Pozzuoli-Solfatara zone, where the maximum uplift occurs) towards the more external sites. The P-wave velocity shows a stronger reversal when compared to the S-wave velocity, which, in turn, is ultimately responsible for the decrease in the Vp/Vs ratio. Also, the histograms mapping the earthquake occurrence at depth (Figure 5) show that the earthquakes mainly occur both at the top of the reversal trends and within the low Vp/Vs.

From Delay-Time Tomography to Rock Physics Properties

Selection of Rock Physics Model and Minimization Algorithm

To translate the P-wave and S-wave velocity images into images that describe the lithology, porosity, pore-filling phase and *in situ* pressure conditions, quantitative relations that relate the elastic properties and the bulk properties of the rock are required.

The procedure for estimating rock properties from P-wave and S-wave velocity models is illustrated in Figure 6. The input data are the P-wave and S-wave velocity models, the δV uncertainty of the velocity models, and the temperature and density. The temperature and density data were estimated from well logs (Agip, 1987), and they are the inputs for the computation of the elastic moduli of the fluid phases (Batzle and Wang, 1992) as functions of depth, and the lithostatic pressure at each node of the grid, respectively. For a more robust computation of the lithostatic pressure, the starting density model is replaced through an iterative procedure, by the final density solution computed at each step.

The skeleton moduli of a given rock are implicitly dependent on the rock texture and the degree of lithification, and explicitly dependent on lithology and porosity. The first step of the procedure consisted of the setting of the vector $\mathbf{X}$ of dry constituent mineral volume fractions (X_i) by using the mineralogical composition of site-relevant rocks from Rosi and Sbrana (1987). For each lithology, we used the Voigt-Reuss-Hill estimate to compute the mixed grain incompressibility. The next step was to calculate the elastic properties of the dry skeleton as a function of porosity and effective pressure. Pore fluid pressure was assumed to vary from zero to the lithostatic pressure corresponding to each grid node. The elastic properties of the dry frame were then computed using the Herz-Mindlin contact theory and the modified Hashin-Shtrikman bounds (Dvorkin et al. 1999) to model the tuff lithology. Self-consistent theory (Berryman, 1995) was instead used to model cracked media, like carbonates and solidified lava. We verified our rock models by using laboratory data from Vanorio et al. (2002) for dry site-relevant rocks (tuffs and lava

samples), and data from Anselmetti and Eberli (1997) for limestone (Figure 7). Once the elastic properties of the dry rock had been computed, the effects on P-wave and S-wave velocities of varying the fluid saturation were estimated by combining the Gassmann equations, the mass balance for a composite rock density, and the Wood equation. The last of these is applied to estimate the incompressibility of the homogeneously mixed fluid.
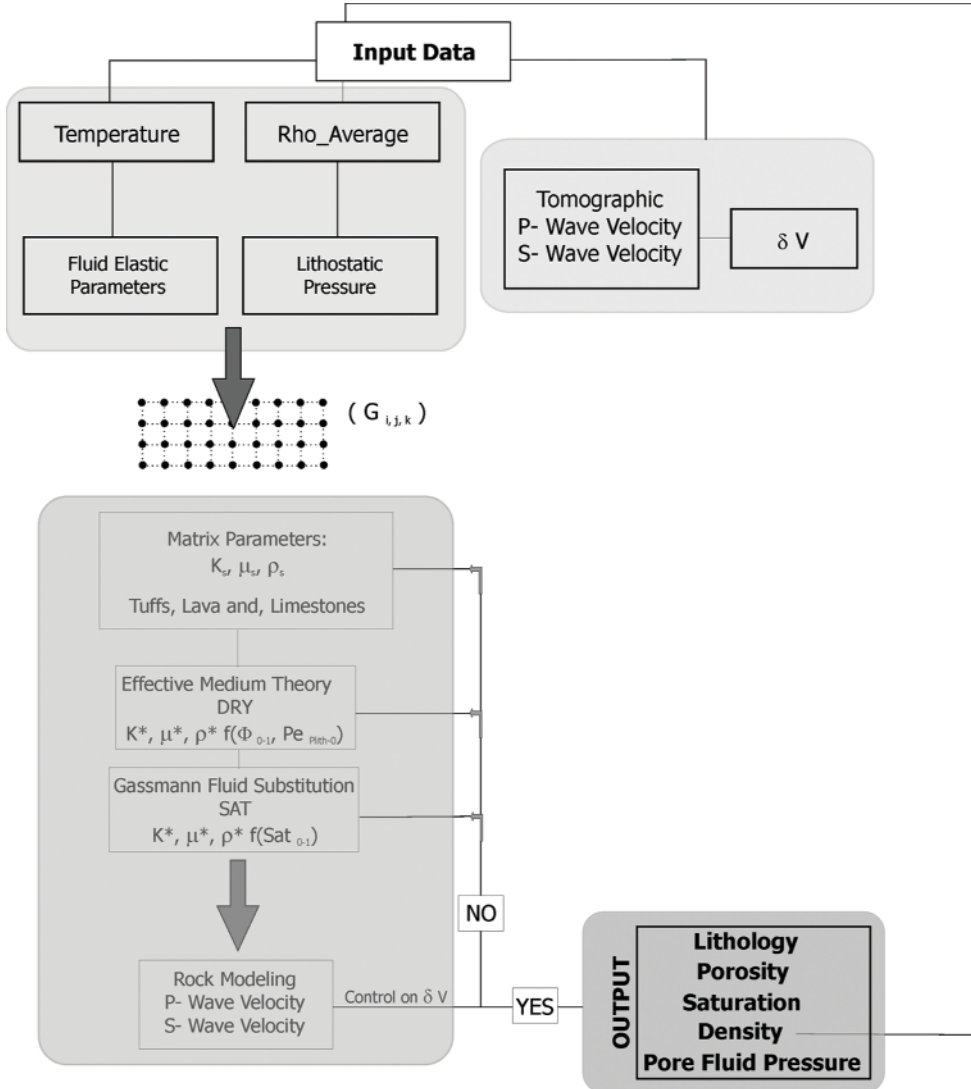

Fig. 6. Procedure for the estimation of the rock properties, starting from the measurements of the P-wave and S-wave velocities, and the temperature and density.

We used a simple global optimization scheme that performs a systematic 3-D grid-search of the global solutions of the constrained rock model. The merit function, *M* (e.g. P-wave and S-wave velocity residuals), was evaluated at each point of the regular grid used in the tomographic inversion, through comparison to the variable δV. The solution with the lowest value of residuals (Velocity$_{Tomography}$-Velocity$_{Rock\ Physics}$) was then taken as an estimate of the global minimum.

RESULTS

The results of the tomographic inversion show an anomalously low Vp/Vs ratio at depths between 3 km and 4 km (Figure 4). The vertical velocity profiles extracted from the final 3-D velocity models show that the decrease in the Vp/Vs ratio is caused by both P-wave and S-wave velocity-reversal trends. The onset of the reversals at 2.5 km marks departures of the effective stress from normal compaction trends at that depth. The earthquakes mostly distribute on the top of the velocity reversals and within the low Vp/Vs anomaly.
By following the rock physics modeling described above, we performed a joint translation of the P-wave and S-wave velocity models into the rock properties.
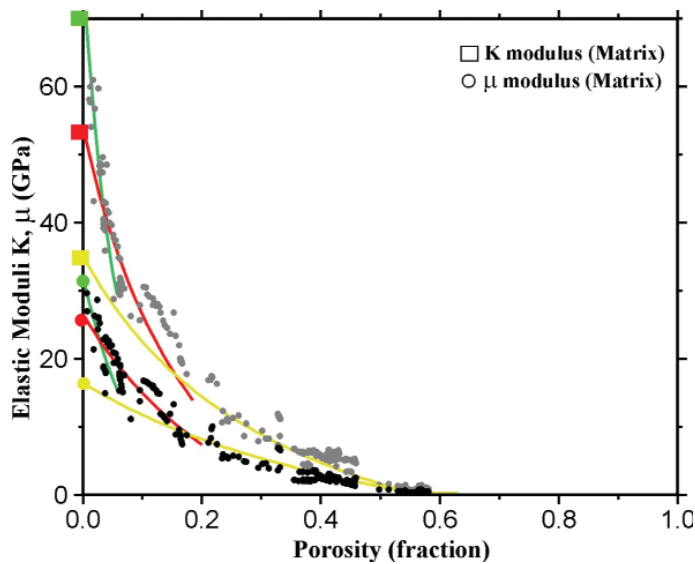

Fig. 7. Modeling of the elastic moduli versus the total porosity for the Campi Flegrei lithologies (green: limestone; red: solidified and metamorphosed lava; yellow: tuff. The modeling refers to dry and ambient pressure conditions. Laboratory data for the site-relevant rock are given for comparison. Symbols at 0% porosity define the elastic properties of the matrix phase, computed by the Voigt-Reuss-Hill estimate.

Here, we show the images of pore fluid pressure as a function of depth (Figure 8), with earthquake locations superimposed for comparison. The earthquakes mainly distribute within the high pore pressure anomaly, which appears to be located at 3 km in depth and centered beneath the area where the maximum uplift occurs (see uplift contour in Figure 1).

Both the earthquake locations and the results of the rock physics modeling lead us to interpret the low Vp/Vs anomaly at 3 km in depth as being due to a localized over-pressurized gas formation.

CONCLUSION AND PERSPECTIVES

We show here a methodology for the mapping of pore fluid pressure from passive seismic data. This method offers complementary and short-term information on reservoir dynamics.

The formation properties were estimated by selecting site-specific rock physics transforms. Dry laboratory measurements on core samples were used to provide the basis for the validation of the theoretical framework. For each modeled lithology, Gassmann fluid substitution was applied to compute the effects of fluid saturation on the P-wave and S-wave velocities.
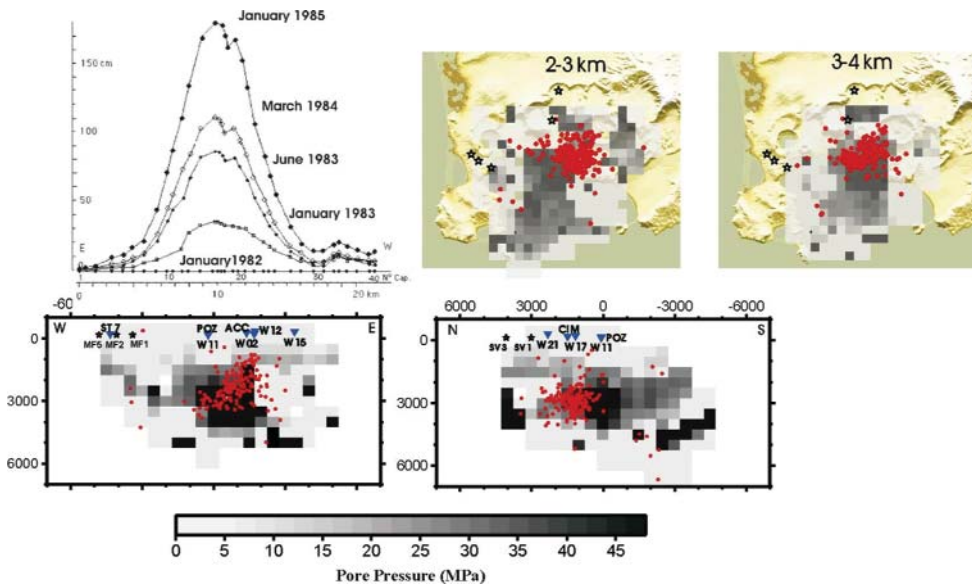
Fig. 8. Horizontal and vertical cross-sections showing the pore fluid pressure variation as a function of depth. The pore pressure anomaly shows a fairly good spatial agreement with the earthquake locations. Upper-left- Uplift (m) as a function of time, recorded along the W-E direction. The pore pressure anomaly is centered beneath the area of maximum uplift.

The results show a fairly good spatial correlation between the seismicity, uplift and location of a pore pressure anomaly, the modeling of which satisfies, within the uncertainties inherent in the velocities, both the P-wave and S-wave velocity values obtained through delay-time tomography.

Error estimates in the formation properties have not yet been performed in this study. Based on the methodology presented here, errors can arise from several sources, ranging from the choice of the rock model to the resolution of the velocity images.

The retrieved formation properties can be deemed correct as long as the rock physics model used to retrieve them is reliable. Uncertainties in the mineralogical composition and/or in the elastic moduli of the pure minerals are all factors that affect the rock physics transforms that are used to translate velocities into rock properties. Also, earthquake mislocation may represent an added source of error that affects the final velocity solutions obtained through the passive tomography. One way to improve the location accuracy is by performing tomographic inversions based on double-difference (DD) earthquake localization. This method assumes that the waves generated by two close sources (i.e. those for which the hypocentral distance is small, as compared both to the source/ station distance and to the wavelength of heterogeneities) that propagate towards a common station along similar ray paths will show similar waveforms. As a consequence, the travel-time differences between several pairs of earthquakes observed at a given station will only be due to the spatial offset of the sources. Therefore, the use of the DD localization in passive tomography would allow a more constrained estimation of the earthquake locations, enhancing the resolution of the rock volumes in which seismicity is induced.

Finally, passive tomography inherently produces smooth P-wave and S-wave velocity images. However, multimode migration of reflected and transmitted converted waves (Latorre, 2004, 2005) may provide complementary information about geometries and the position of geobodies at depth. One future goal from this study is to adapt classical seismic exploration tools to the analysis of micro-earthquake recording, so that migrated images of crustal structures can be obtained. The advantages inherent in this study arise from: 1) the availability of both 3-D P-wave and S-wave velocity models that can be used as background velocities in the migration procedure; and 2) the possibility of imaging seismic structures at depths where active data are usually not available. Also, the coupled use of passive seismic and rock physics modeling through the provision of physical properties parameters, such as density and P-wave and S-wave velocities, may further constrain the migration procedure of converted waves.

REFERENCES

Agar, A.G., Mongenstern, N.R. and Scott J.D., 1986, Thermal expansion and pore pressure generation in oil sands: Can. Geotech. J., 23, 327-333.

Agar, A.G., Mongenstern, N.R. and Scott J.D., 1987, Shear Strength and Stress-strain behavior of Athabasca oil sands at elevated temperatures and pressures, Can. Geotech. J., 24, 1-10.

Agip, 1987, Geologia e geofisica del sistema geotermico dei Campi Flegrei, internal Report, 17 pp., Milan, Italy.

Anselmetti, F.S. and Eberli, G.P., 1997, Sonic velocity in carbonate sediments and rocks, in Palaz, I. and Marfurt K.J. (eds.), Carbonate Seismology, SEG Geophysical Developments Series, 6, 53-74.

Aoike, K., O. Nishizawa, and T. Sato, 1998, Application of the Extended Information Criterion to Seismic Tomography using Local earthquakes, paper presented at 4th SEGJ International Symposium, Soc. of Explor. Geophys. of Jpn., Tokyo.

Aster, R. C., and R. P. Meyer, 1988, Three-dimensional velocity structure and hypocenter distribution in the Campi Flegrei caldera, Italy, Tectonophysics, 149, 195-218.

Barberi, F., G. Corrado, F. Innocenti, and G. Luongo, 1984, Phlegreaen Fields 1982- 1984: Brief chronicle of a volcano emergency in a densely populated area, Bull. Volcanol., 47, 175- 185.

Baria, R., Hearn, K., and Batchelor, A.S., 1989. Induced seismicity during the Hydraulic Stimulation of the potential hot dry rock geothermal reservoir, in Hardy, HR Jr Ed. Fourth conferences on acoustic emission/microseismic activity in geological structures and materials: Trans. Tech. Pub. 127-352.

Batzle, M. L., and Z. W. Wang, 1992, Seismic properties of pore fluids, Geophysics, 57, 1396-1408.

Berryman, J. G., 1995, Mixture theories for rock properties: in Rock Physics and Phase Relations: American Geophysical Union Handbook of Physical Constants, T. J. Ahrens (ed.), AGU, New York, 205-228.

Chiodini, G., F. Frondini, C. Cardellini, D. Granieri, L. Marini, and G. Ventura, 2001, CO_2 degassing and energy release at Solfatara Volcano, Campi Flegrei, Italy, J. Geophys. Res., 106, 16,213-16,221.

Chiodini, G., M. Todesco, S. Caliro, C. Del Gaudio, G. Macedonio, and M. Russo, 2003, Magma degassing as a trigger of bradyseismic events: The case of Phlegrean Fields (Italy), Geophys. Res. Lett., 30 (8), 1434.

Cornet, F. H., and Yin, J., 1995, Analysis of induced seismicity for stress field determination and pore pressure mapping: Pure Appl. Geophys., 145, 677-700.

Dvorkin, J., M. Prasad, A. Sakai, and D. Lavoie, 1999, Elasticity of marine sediments: Rock physics modelling, Geophys. Res. Lett., 26, 1781-1784.

Fehler,M. C., 1989, Stress control of seismicity patterns observed during hydraulic fracturing experiments at the Fenton Hill Hot Dry Rock geothermal site, New Mexico: Internat. J. Rock Mech. Min Sci. Geomech. Abstr., 26, 211-219.

Gendzwill, 1992 Passive Seismic Monitoring of Hydrofracture and Steam Injection in Heavy Oil Sands Near Fort Mcmurray, Alberta, Canadian Journal of Exploration Geophysics, 28, 117-127.

Jones, R. H., Beauce, A., Jupe, A., Fabriol, H., and Dyer, B. C., 1995, Imaging induced microseismicity during the 1993 injection test at Soultz-sous-Forêts, France: Proc. World Geotherm. Cong., 2665-2669.

Kissling, E., W. L. Ellsworth, D. Eberhart-Phillips, and U. Kradolfer, 1994, Initial reference models in local earthquake tomography, J. Geophys. Res., 99, 19,635-19,646.

Latorre, D., J. Virieux, T. Monfret, V. Monteiller, T. Vanorio, J.-L. Got, and H. Lyon-Caen, 2004, A new seismic tomography of Aigion area (Gulf of Corinth-Greece) from a 1991 dataset: Geophys. J. Int., 159, 1013-1031.

Latorre, D., Jean Virieux, Tony Monfret, Hélène Lyon-Caen, 2004, Converted seismic wave investigation in the Gulf of Corinth from local earthquakes: Compte Rendu Géosciences 336, 4-5, 259-267.

Latorre Diana, 2005, Imagerie sismique du milieu de propagation à partir des ondes directes et converties: application à la région d'Aigion : Ph.D thesis Université de Nice Sophia Antipolis, Nice.

Maury, V. M. R., Grasso, J. R., and Wittlinger, G., 1992, Monitoring of Subsidence and Induced Seismicity in the Larq Gas Field (France): The Consequences on Gas Production and Field Operation: Engineering Geology, 32, 123.

Maxwell, S.C., Urbancic, T.I., Prince, M., and Demerling, C., 2003, Passive imaging of seismic deformation associated with steam injection in Western Canada: Society of Petroleum Engineers Annual Technical Conference and Exhibition, Denver, SPE 84572. 8 p.

Monteiller, V., Got, J.L., Virieux J., and Okubo P., 2005, An efficient algorithm for double difference tomography and location in heterogeneous media, with an application to Kilauea volcano, submitted to J. Geoph. Res.

Paige, C. C., and M. A. Saunders 1982, LSQR: An algorithm for sparse linear equations and sparse least squares: Trans. Math. Software, 8, 43-71.

Pearson, C., 1981, The relation between microseismicity and high pore pressure during hydraulic simulation experiments in low permeability granitic rocks: J. Geophys. Res., 86, 7855-7864.

Rutledge J.T., and W. S. Phillips, 2003, Hydraulic stimulation of natural fractures as revealed by induced microearthquakes, Carthage Cotton Valley gas field, east Texas: Geophysics, 68, 2, 441-452.

Segall, P., 1989, Earthquakes triggered by fluid extraction: Geology, 17, 942-946.

Sneddon, I. N., 1946, The distribution of stress in the neighbourhood of a crack in an elastic solid: Proc. Roy. Soc., 187, 229-260.

Thurber, C. H., 1992, Hypocenter-velocity structure coupling in local earthquake tomography: Phys. Earth Planet. Inter., 75, 55-62.

Vanorio, T., Virieux, J., Capuano, P., and Russo, G., 2005, Three-dimensional seismic tomography from P- and S- wave microearthquake travel times and rock physics characterization of the Campi Flegrei Caldera, J. Geophys. Res.: 110, B03201, 10.1029/2004JB003102.

Vanorio, T., M. Prasad, A. Nur, and D. Patella, 2002, Ultrasonic velocity measurements in volcanic rocks: Correlation with microtexture: Geophys. J. Int., 149, 22-36.

Zoback, M.D. and HP Harjes, 1997, Injection induced earthquakes and crustal stress at 9 km depth at the KTP deep drilling site, Germany: J. Geophys. Res., 102, 18,477-18,491.

Zollo, A., et al., 2003, Evidence for the buried rim of Campi Flegrei caldera from 3-D active seismic imaging, Geophys. Res. Lett.: 30(19), doi:10.1029/2003GL018173.

Depth and morphology of reflectors from the 2-D non-linear inversion of arrival-time and waveform semblance data: method and applications to synthetic data

M. Vassallo[1,2], A. Zollo[1]

[1] *Dipartimento di Scienze Fisiche, Università di Napoli Federico II (RISSC-Lab), Italy*
[2] *AMRA Scarl, Napoli, Italy*

Abstract: We propose a two-dimensional, non-linear method for the inversion of reflected/converted traveltimes and waveform semblance designed to obtain the location and morphology of seismic reflectors in a lateral heterogeneous medium and in any source-to-receiver acquisition lay-out. This method uses a scheme of non-linear optimisation for the determination of the interface parameters where the calculation of the traveltimes is carried out using a finite-difference solver of the Eikonal equation, assuming an a priori known background velocity model. For the search of the optimal interface model, we have used a multiscale approach and the Genetic Algorithm global optimization technique. During the initial stages of inversion, we used the arrival times of the reflection phase to retrieve the interface model that is defined by a small number of parameters. In the successive steps, the inversion is based on the optimization of the semblance value determined along the calculated traveltime curves. Errors in the final model parameters and the criteria for the choice of the bestfit model are also estimated from the shape of the semblance function in the model parameter space. The method is tested and validated on a synthetic dataset that simulates the acquisition of reflection data in a complex volcanic structure.

INTRODUCTION

The reconstruction of geological discontinuities from active seismic data is usually carried out by migration techniques that generally demand an a priori known background velocity model in order to place a reflection event at a particular subsurface location. The success of these migration methods strongly depends on the data quality and the accuracy of the adopted background velocity model. In complex geologic structures, the presence of unmodelled multiples, very energetic principal phases, and diffraction and scattering phenomena can often produce poor quality reflected signals. In these complex envi-

ronments, the estimation of a reliable velocity distribution in the subsurface is extremely difficult when significant lateral velocity variations are present.

Recently, Improta et al. (2002) [7] used a two-step procedure for the joint 2-D inversion of the first-P and reflected P-to-P traveltimes. In the first step, a background P-velocity model was determined by the first-arrival, non-linear, traveltime tomography. Then this model was used as a reference model to perform an inversion of reflected traveltimes for retrieve the interface parameters. Both of these inversion methods used techniques for solving the forward problem solution based on the finite difference solver of the Eikonal equation combined with a multiscale approach [2] and a non-linear optimization scheme for model-space exploration. The method proposed in the present study follows a similar approach to that of Improta et al. (2002) [7] but, regarding this last one, the inversion is based on a combined optimization of traveltimes and waveforms semblance data. The location and reconstruction of a two-dimensional (2-D) seismic interface geometry is performed in an a priori known background velocity model using a non-linear optimization scheme. The reference medium is obtained by the first-arrival tomography or the integrated tomography-velocity analysis procedures.

Thus we propose a method for parameter estimation of multiple irregular interfaces embedded in the subsurface medium. This is based on an iterative, non-linear, inversion scheme that follows a two-step procedure to combine with this the information from picked traveltimes and waveform semblance data. No data reduction is performed before the inversion (i.e. normal move-out and/or stack), while the effects of lateral heterogeneities are taken into account by the 2-D background velocity medium. The inversion problem is solved by the use of the Genetic Algorithm (GA) optimisation technique [5] [4], through searching in the global parameter space for the minimum of a cost function that depends on the theoretical and observed data. The theoretical arrival times of the P-to-P arrivals are calculated using the Podvin and Lecomte (1991) [11] solver of the 2-D finite difference equation, and a multiscale strategy of inversion is adopted, as used by Improta et al. (2002) [7]. Moving from the shallowest interface, we follow a layer-stripping approach [9] to determine the location and morphology of the deeper interfaces, by accurate re-picking of the deep-reflection traveltimes on zero-time move-out (ZTMO). This method is specifically designed for geophysical investigations in complex geological environments, in order to obtain the morphology and positions of embedded discontinuities.

METHOD

Forward modelling

The reflection interface is described by a 2-D cubic-spline function, where the control points are equally spaced in the horizontal direction at fixed horizon-

tal positions, and they can move vertically with continuity within an assigned depth range. The vertical coordinates of the nodes of the spline-function are the parameters of the interface model. For a given interface model, the reflection traveltimes are calculated following a four-step procedure:

1. The medium is discretized as a fine grid, with nodes equally spaced along the vertical and horizontal directions. The grid dimension depends on the accuracy required for the traveltime calculations (see step 2).
2. The first-arrival times from each source and receiver at the nodes of the-grid are calculated using the 2-D Eikonal equation and the finite difference solver of Podvin and Lecomte (1991) [11].
3. The one-way traveltimes for a source/ receiver to each point of the discretized interface are calculated by performing an interpolation among the nearest four grid nodes.
4. For a given source-receiver pair, the reflection location point and the total traveltime are calculated according to the Fermat principle: the reflection point will be the one providing the minimum total traveltime.

Data inversion

For a given reflection event identified on seismic sections, the data space is subdivided into two subsets: one containing the arrival-time pickings, and the other the complete waveform of the reflection phase considered. The data inversion proceeds first with the modelling of the traveltime data, to retrieve a smooth, low-frequency model of the interface; then the waveforms are used to obain a more refined model. The non-linear inversion of the traveltime data is based on the search for the minimum of the RMS function computed using computed and the observed raveltimes of reflection events.

According to the multiscale inversion approach [2] we adopt an optimization strategy whereby several optimization runs are performed by progressively increasing the density of cubic-spline nodes describing the interface reflector. At the very early stages (where the interface is described by a very small number of parameters) the optimization is performed over a quite wide range of possible depth values for the interface nodes. Furthermore, for runs where the interface is parametrized by a large number of nodes, the search is performed with smaller allowed depth variations around the model estimated in the previous run. The search for the model parameter vector that minimizes the RMS cost function is performed by GA optimization technique [5] [4] [13].

In our inversion scheme, the picked arrival times of the reflection phase are initially used to retrieve a smooth interface model, i.e the interface is defined by a small number of cubic-spline nodes. In the successive steps a more refined interface model is obtained using the reflection waveform information. In this case, the optimal interface model is determined through a global search for the maximum of the semblance objective function [10] computed using

the amplitudes of waveforms in a time window chooses to bracket the calculated reflection arrival time for a given source and receiver couple. The window length is arbitrarily defined based on the dominant period of the reflection events considered. The semblance function is therefore calculated in the selected time windows for all of the records along the whole Common Receiver or Common Shot seismic gathers. Since the semblance is a measure of the waveform similarity and coherence, the main advantage of using the semblance [10] objective function is that at this stage, the inversion does not require phase picking, thus improving the time performance of the whole procedure and removing the effects which might be introduced by the subjectiveness of the picking.

The reliability of the retrieved model can be verified a posteriori by the construction of the seismic panel offset-two-way-time (TWT), where each seismogram is shifted back in time according to the theoretical reflection traveltime calculated for the optimal interface model retrieved by the time-picks and waveform semblance inversion. Following on form Improta et al. (2002) [7], these panels are designated as zero-time move-out (ZTMO) sections.

The inversion procedure described above is iteratively applied to a sequence of reflection events identified on seismic sections. Starting from the shallowest interface, an approach similar to layer-stripping [9] is used to determine the location and morphology of the deeper interfaces, by accurate re-picking of deep reflection traveltimes.

The uncertainty in the depth values of each node describing the interface is estimated by local exploration of the semblance function in the neighbourhood of the model which maximizes the semblance value. We use the second-order Akaike Information Criterion (AICc) [1] [6] for determines when the multistep process should be stopped.

SYNTHETIC DATA MODELLING

To validate the proposed methodology we have applied it to a synthetic dataset calculated on a complex velocity model (Figure 1a) constructed based on the images of the Campi Flegrei (Southern Italy) caldera structure that were recently obtained through high resolution tomographic inversion of the first P-arrival times from active seismic experiments [15] [8]. Inside each layer below the water the P-wave velocity is assumed to increase linearly with depth while the Vp/Vs ratio and the density are constant is constant. Using this model we simulated a seismic experiment with an acquisition lay-out consisting of 55 seismic stations with a horizontal spacing of 500 m (at an equal depth of 270 m). Each receiver records the seismic signals generated by 21 shots spread around the receiver, with an offset of between -200 m and 200 m, and a horizontal spacing of 10 m. The synthetic seismograms were computed using a 2-D, elastic, velocity-stress finite-differences algorithm [3]. The
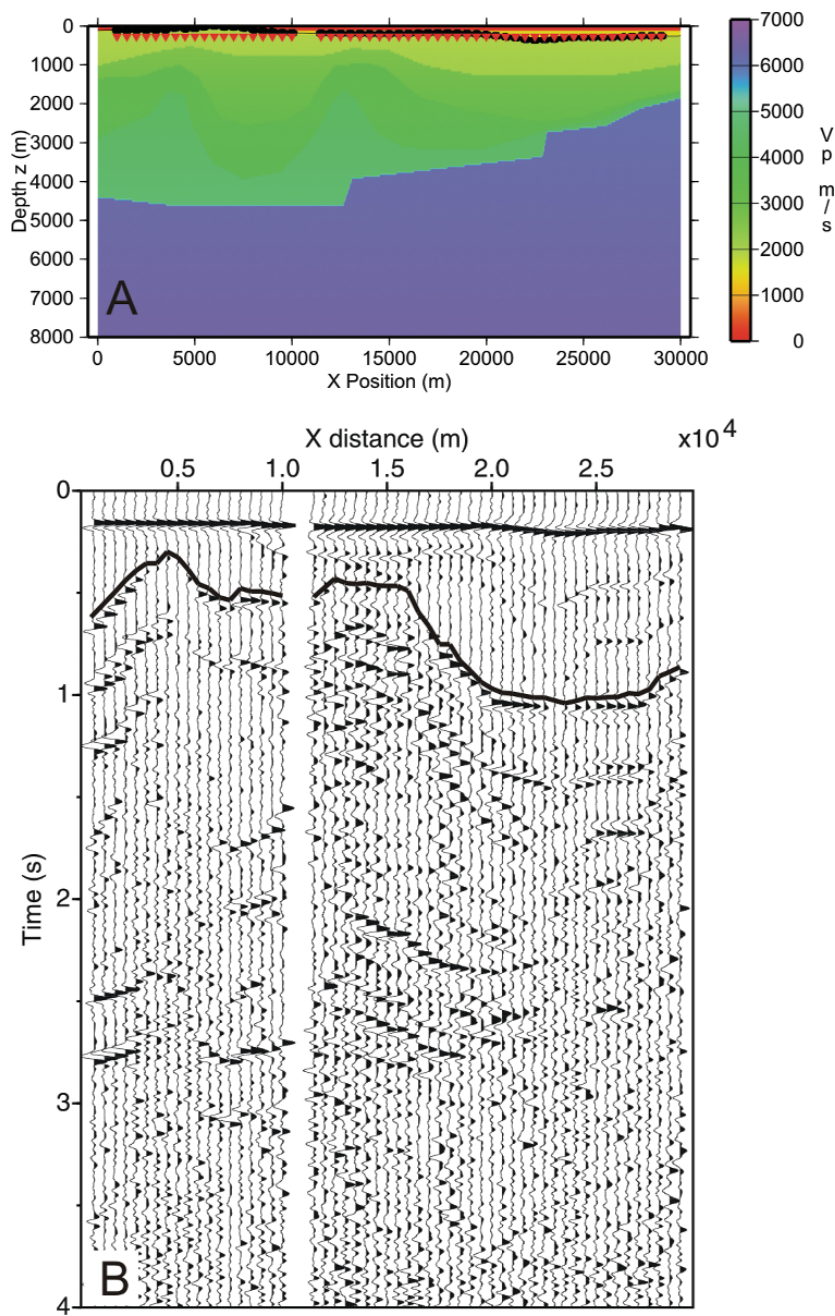
Fig. 1. Model adopted for the generation of synthetic seismograms **(a)** and synthetic zero offset section **(b)**. The red triangles in upper part of the model show the positions of the receivers, and the black stars show the positions of the sources on the topographic surface. The traces in the section are normalized for the maximum trace value and are filtered with an AGC filter with a window of 1 s. No filters were applied to the traces during the inversion. The black line in the section shows the picking of a reflected phases.

synthetic seismograms were normal-move-out corrected [14] and stacked to obtain the final section used for the inversion. Gaussian noise was added to each trace to have a mean signal-to-noise ratio of 5. The resulting traces were band-pass filtered in the frequency range of 6-30 Hz. These stacked, noised and filtered traces are displayed as a function of distance in Figure 1b, after an amplitude equalization had been applied using an automatic gain control with a window of 1 s.
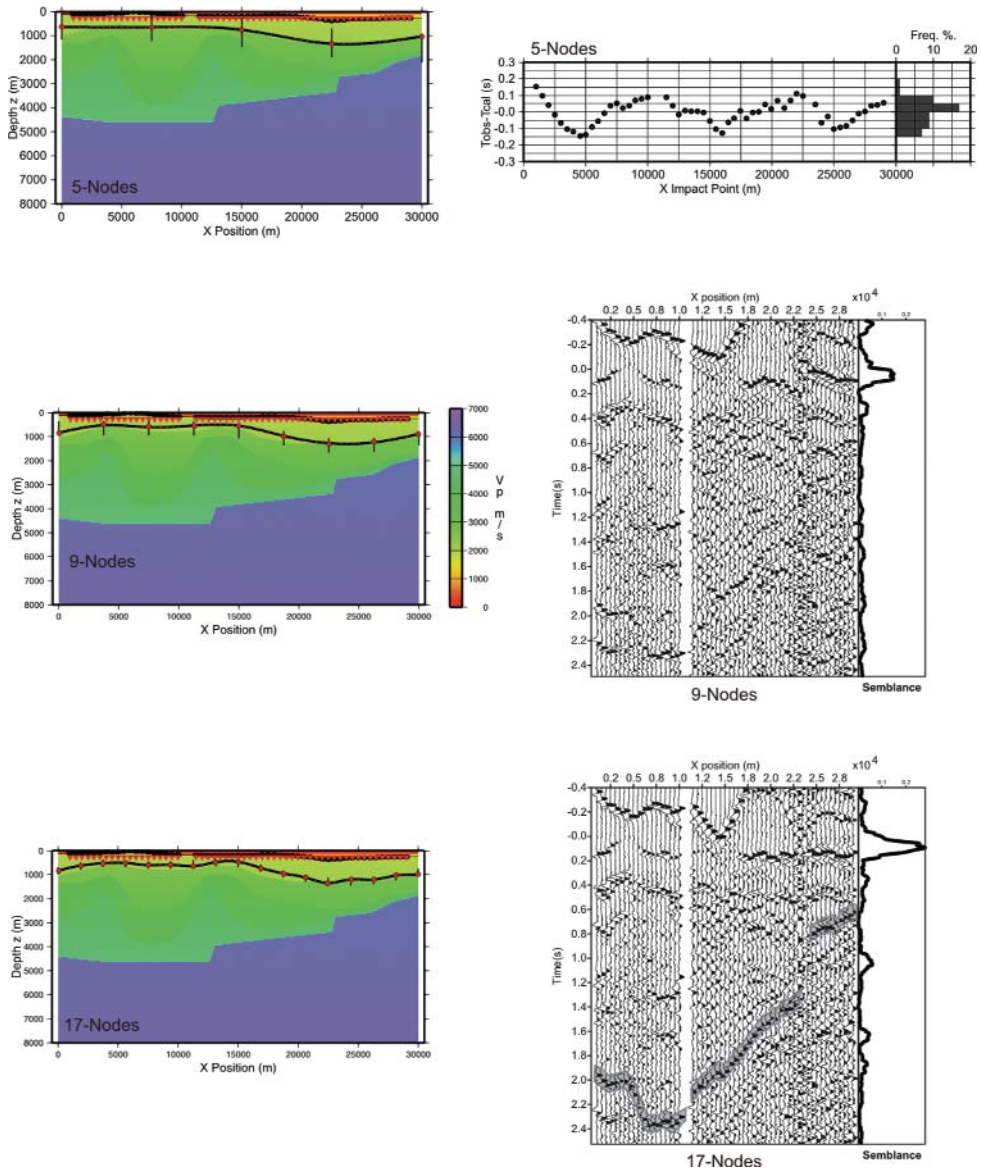
Data inversion

The normalised and filtered section (Figure 1b) was used to measure the arrival times of the first reflected phase. These times (Figure 1b) were taken from all of the seismograms and were inverted using the eflected traveltimes RMS as the cost function, as described above. The theoretical arrival times were calculated using a square grid with 50 m sides. In each cell, the velocity was calculated through averaging the values of the model used for the synthetic calculations in a 1000 m×1000 m surrounding the centre of the cell. We used a smooth background model, as in this way we closely approach the models provided with tomography techniques (through the inversion of the first-arrival times) that have been used as starting models for interface inversions [7]. Following the multiscale approach [2], three interface models were inverted, with parameterisations of two, three and five nodes. Increasing the number of nodes a reduction in the RMS function is seen, which goes from 0.13 s for the model defined by two nodes, to 0.07 s for that defined by five nodes.

Starting from the model defined by five nodes (Figure 2), a succession of two models parameterised by 9 and 17 nodes is progressively determined while optimising the semblance function [10]. For these inversions, the waveforms represent the data and the code searches for the interface models on the basis of the likeness of the waveforms around the arrival times calculated. The interfaces determined are shown in Figure 2 with the ZTMO sections relative to each model. In these sections, the alignment of the waveforms near 0 s becomes evident. The semblance goes from 0.18 for the model with nine nodes, to 2.9 for that defined by 17 nodes (Figure 2).

The ZTMO sections (Figure 2) show a very clear deep phase. We used this sections for the individuation and picking of the very clear secondary phase (17-nodedes ZTMO section in the Figure 2). The times from the ZTMO sections were again corrected, adding the time shifts relative to the modelled reflected phase, and the values obtained were inverted. Also for the inversion of this deeper phase, we started with an optimisation of the reflected traveltimes RMS function for three successive inversions searching the model parameterisation of two, three and five nodes. Starting from the interface parameterised by five nodes, two new models with 9 and 17 nodes were calculated using the semblance [10] optimization. The models obtained relative to five,

Fig. 2. Results of the inversion method for the reflected phase shown in the section of Figure 1b. The three images on the lefthand side show the interface models used to calculate the distribution of the residuals and the ZTMO panels on the right. The three interface models were obtained by performing a succession of inversion runs with an increasing number of interface nodes (large dots). The five-node model (top) was obtained by performing the inversions based on the optimization of reflected traveltimes. The nine-node and 17-node models (middle and bottom) were obtained using the semblance optimization starting with the five-node model. The vertical bars are the search intervals of each of the spline nodes. The semblance trace shown on the right of the ZTMO panels as a heavy dark line allows us to quantify the coherence of the aligned phases. A semblance maximum trace is seen at zero-time, confirming the phase alignment modelled.

nine and 17 nodes are shown in (Figure 3), which also shows the trend of the residuals and the ZTMO sections relative to the models with five, nine and 17 nodes. The final semblance obtained for the model defined by nine nodes is 0.13, while that for the model defined by 17 nodes is 0.19.

DISCUSSION AND CONCLUSION

We have presented a method for the non-linear inversion of arrival times and waveforms of reflected seismic phases that is aimed at the reconstruction of the depth and morphology of seismic reflectors. With respect to existing non-linear 2-D interface inversion methods [7] [12] we introduce a new approach based on the combined optimization of traveltime (global search) and waveform semblance data (local search). Moreover, we adopt a criterion (the Akaike Information Criteria [1]) based on the the principle of parsimony, for determining when the multi-scale iterative process should be stopped. The method is based on the search for the interface model that optimises at successive steps an objective function defined either through a comparison between the arrival times calculated and those observed, or through the similarities of the waveforms (waveform semblance) around the calculated arrival times. The general principle used here is that reflected travel times provide long wavelength information about the interface morphology while more refined models can be retrieved by the waveform semblance optimization, using as a starting model the one obtained from traveltime misfit. The direct forward problem is solved by a modified version of the method of Podvin and Lecomte (1991) [11], which allows for obtaining accurate and fast estimates of the reflection arrival times even in strongly heterogeneous velocity models. The global search for the optimal model in the parameter multidimensional space is carried out using the Genetic Algorithm (GA) [5] [4], a search technique well adapted for the determination of the solution of non-linear problems. The parameter uncertainty is evaluated by the local exploration of the semblance around the best-fit model along orthogonal directions of the parameter space.

The method has been applied to synthetic data generated in a heterogeneous velocity structure that simulates a complex volcanic structure. The choice of a non-linear approach for the reconstruction of the reflector morphology is motivated by the high level of non-linearity that exists between the reflected arrival times and waveforms particularly in the presence of strong heterogeneity of the propagation medium. The use of an non-linear optimisation scheme coupled to a multiscale inversion strategy results in more stable and robust estimates of the model parameters, and reduces the risk of convergence towards local minima.

The inversion based on the optimization of the semblance is advantageous since it limits the human and manual intervention in the final definition of the
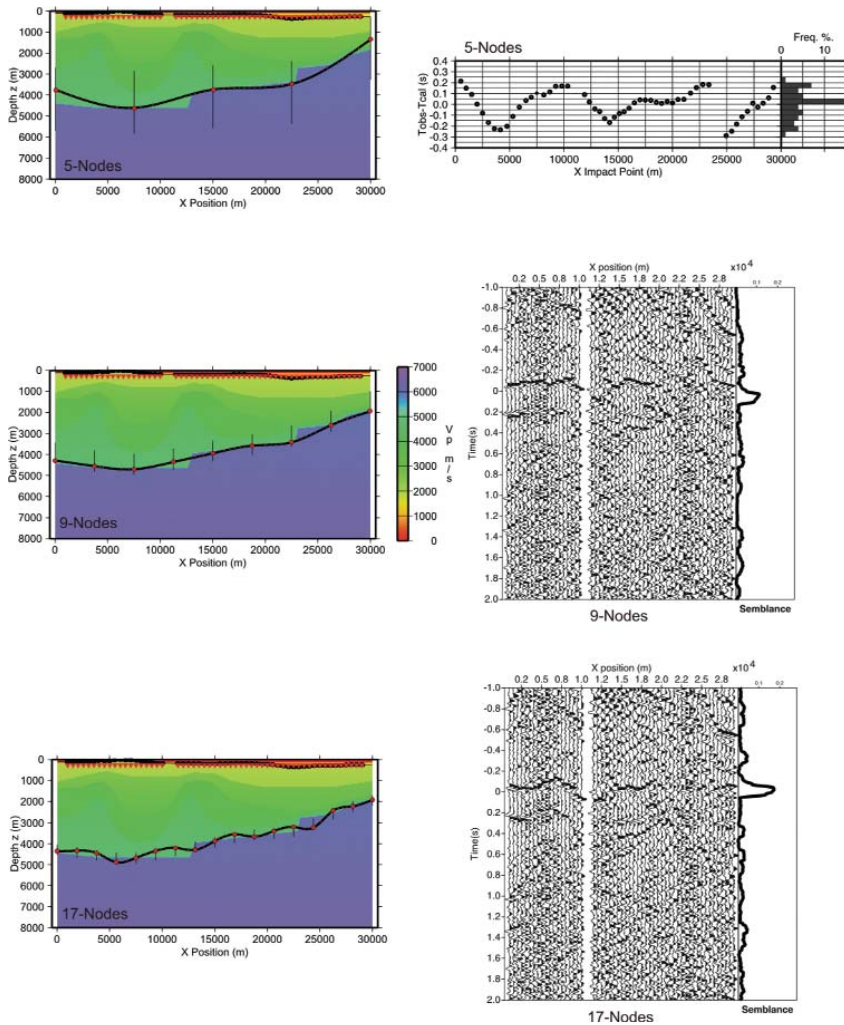
Fig. 3. Results of the inversion method for a reflected phase shown in the 17-nodes ZTMO of Figure 2. The three images on the lefthand side show the interface models used to calculate the distribution of the residuals and the ZTMO panels on the right. The three interface models were obtained by performing a succession of inversion runs with an increasing number of interface nodes (large dots). The five-node model (top) was obtained by performing the inversions based on the optimization of reflected traveltimes. The nine-node and 17-node models (middle and bottom) were obtained using the semblance optimization starting with the five-node model. The vertical bars are the search intervals of each of the spline nodes. The semblance trace shown on the right of the ZTMO panels as a heavy dark line allows us to quantify the coherence of the aligned phases. A semblance maximum trace is seen at zero-time, confirming the phase alignment modelled. We used the Akaike criteria for the choice of the optimal parametrization for both the interfaces (shallow interface and deep interface). Computing the AIC for all the retrieved models we obtained that for both the interfaces the 9-nodes models minimize the AICc values so they were chosen as best model. The uncertainties in depth for the nodes of minimum AIC interfaces are evaluated by the local exploration of the semblance around the best-fit model along orthogonal directions of the parameter space. Figure 4 shows the final interfaces retrieved and the corresponding errors. Geometry and depth of the retrieved interfaces are in good agreement with the interfaces used to compute synthetic data.
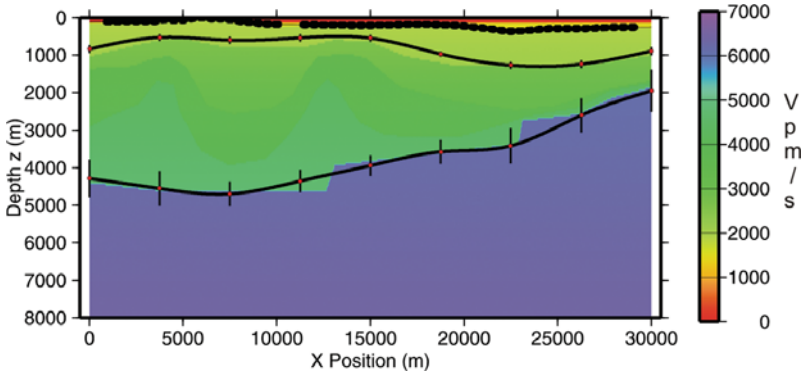
Fig. 4. Final interface models and parameter uncertainty. Uncertainty in depth of the interface nodes are estimated by locally exploring the variation of the cost function around the best-fit interface nodes.

reflector model. Moreover, the use of the zero-time move-out sections (ZTMO) can help in to identify more clearly than on original sections the seismic phases generated by deeper discontinuities. Indeed, particularly for strongly heterogeneous propagation media, the shallow interfaces can destroy the lateral coherence of the reflected seismic phases generated at the deep interfaces. However the inversion procedure is not fully independent of the manual intervention that is needed for the initial arrival time picking of the reflected seismic phases. Indeed, several preliminary tests indicated that this two-step inversion strategy is preferred to the direct inversion of semblance waveforms, which generally leads to unreliable solutions associated with relative minima of the objective function and reflection events not necessarily generated by the same reflector.

The proposed method suffers of some limitations. It allows to reconstruct a single interface at a time, and for each of them, different models are obtained according to the multi-scale strategy. In this way, the computing time can be relatively high when compared with the one needed for the reconstruction of the interfaces with the pre-stack migration techniques that are usually used to solve similar problems [14].

A future development could be represented by the 3D extension of the inversion procedure. This will allows to define seismic discontinuities as surface rather than curves. This is particularly relevant for combining active and passive (earthquakes) dataset. The latter would represent an important advancement allowing through earthquake records to use the complete information carried out by primary P and S reflections in addition to the converted arrivals for constraining the shape and depth of seismic discontinuities.

REFERENCES

[1] H Akaike. A new look at the statistical model identification. IEEE Trans. Autom. Control,6:716723, 1974.

[2] C. Bunks, F. M. Salick, S. Zaleski, and G. Chavent. Multiscale seismic waveform inversion. Geophysics, 60:1457-1473, 1995.

[3] G. Festa and S. Nielsen. PML absorbing boundaries. Bull.Seism.Soc.Am., 93(2):891-903, 2003.

[4] D. Goldberg. Genetic Algorithms in Search, Optimisation and Machine Learning. Addison-Wesley Professional, 1989.

[5] J. Holland. Adaptation in natural and artificial systems. The University of Michigan Press, 1975.

[6] C. M. Hurvich and C. Tsai. Regression and Time Series Model Selection in Small Samples. Biometrika, 76:297-307, 1989.

[7] L. Improta, A. Zollo, A. Herrero, R. Frattini, J. Virieux, and P. Dell'Aversana. Seismic imaging of complex structures by non linear traveltime inversion of dense wide-angle data: application to a thrust belt. Geophys. J. Int., 151(1):264-278, 2002.

[8] S. Judenherc and A. Zollo. The Bay of Naples (Southern Italy): constraints on the volcanic structures inferred from a dense seismic survey. J. Geophys. Res., 109:doi:10.1029/2004GL019432, 2004.

[9] T. Krey. Seismic stripping helps unravel deep reflections. Geophysics, 43(5):899-911, 1978.

[10] N. S. Neidell and M. T. Taner. Semblance and other coherency measures for multicannel data. Geophysics, 36(3):482-497, 1971.

[11] P. Podvin and I. Lecomte. Finite difference computation of traveltimes in very contrasted velocity models: a massively parallel approach and its associated tools. Geophys. J. I., 105:271-284, 1991.

[12] S. K. Pullammanappallil and J. N. Louie. Inversion of seismic reflection traveltimes using a non linear optimization scheme. Geophysics, 58(11):1607-1620, 1993.

[13] D. Whitley. A Genetic Algorithm Tutorial. Samizdat Press (http://samizdat.mines.edu/ga tutorial), 1994.

[14] O. Yilmaz and R. Chambers. Migration velocity analysis by wave-field extrapolation. Geophysics, 49(10):1664-1974, 1984.

[15] A. Zollo, S. Judenherc, E. Auger, J. Virieux, R. Capuano, C. Chiarabba, R. De Franco, J. Makris, A. Michelini, and Musacchio G. Evidence for the buried rim of Campi Flegrei caldera from 3-d active seismic imaging. Geophys. Res. Lett., 30(19):doi:10.1029/2003GL018173, 2003.

Converted phase identification and retrieval of Vp/Vs ratios from move-out reflection analysis: application to the Campi Flegrei caldera

M. Vassallo[1,2], A. Zollo[1], D. Dello Iacono[1], N. Maercklin[1], J. Virieux[3]

[1] *Dipartimento di Scienze Fisiche, Università di Napoli Federico II (RISSC-Lab), Italy*

[2] *AMRA Scarl, Napoli, Italy*

[3] *Institute Geosciences Azur, CNRS, Nice, France*

Abstract: Here, we propose a method for the determination of Vp/Vs ratios in a horizontally layered propagation media using maximization of a coherency function along theoretical travel-times of PS reflected phases. The theoretical travel-times are computed using the information about the propagation media that is extracted by velocity analysis or by topographic analysis performed on the first arrivals. The method is also a valid tool for the identification of the PS phases associated with a fixed seismic reflector, and it is particularly suitable for data that is stored in common mid-point and common conversion point binning; for this kind of data the hypothesis of horizontally and layered media can usually be verified.

We applied the method to both simulated and real datasets. The use of the real data that was acquired in the Campi Flegrei caldera (southern Italy) allowed us to estimate a relatively high Vp/Vs ratio (3.5 ± 0.6) for a very shallow layer (maximum depth, 600 m). This hypothesis has been tested by theoretical rock physical modeling of the Vp/Vs ratios as a function of porosity, suggesting that the shallow layer appears to be formed of unconsolidated, water-saturated, volcanic and marine sediments that filled Pozzuoli Bay during the post-caldera activity.

INTRODUCTION

Tomography is one of the most popular techniques for geophysics investigations. The tomographic models inferred from inversions of first-arrival times do not have sufficient resolution to accurately define the morphology and location of the main crustal reflectors at depth. Reconstruction of buried seismic discontinuities is usually performed by seismic reflection analysis, which in the cases of very complex media and non-conventional seismic data acquisition, cannot be processed using standard seismic exploration tools. This is

M. Vassallo, A. Zollo, D. Dello Iacono, N. Maercklin, J. Virieux

especially true in the case of near-shore active seismic surveys in densely populated coastal areas, where mixed and sparse acquisition lay-outs (shots at sea and recordings on land and/or on the sea bottom) can only be used. Therefore, it is necessary to develop new techniques of data processing and analysis to be able to understand unconventional data-acquisition geometries (sparse or irregular distribution of source/ receivers) and complex waveforms in the complete incidence angle range (from near vertical, to wide angle). Once the interfaces have been found, new methods are also necessary for the characterization of rock layers in terms of lithological and rheological features. The Vp/Vs ratio provides a very good lithology discriminator. This elastic parameter can improve predictions of mineralogy, porosity, and reservoir fluid types (Pickett, 1963; Tatham, 1982; Rafavich et al., 1984; Miller and Stewart, 1990). Compressional seismic velocity alone is not a good lithology indicator because of the overlap in Vp for various rock types. The additional information provided by Vs can reduce the ambiguity involved in the interpretation. Pickett (1963) demonstrated the potential of the Vp/Vs ratio as a lithology indicator through laboratory research. We propose a method for the determination of the Vp/Vs ratio through an analysis of multi-component seismic data. The vertical components of the data are used for the determination of interface depth and the Vp values for normal move-out (NMO) analysis and/or tomographic studies of first arrivals. These values are used to search for the Vp/Vs ratio that maximizes a coherency function that is computed using the horizontal component of the data along theoretical travel-times of PS reflected phases.

METHOD

In a horizontally layered media, the travel-times of reflected/ converted PS phases depend on the P velocity Vp, according to the depth h of interfaces for the Vp/Vs ratio of layers and for the source-receiver offsets and depths. With active seismic data, the shot and receiver positions are well know, and the information relating to the velocity Vp of the propagation media are generally retrieved using the tomographic inversion of first arrivals or using velocity analysis based on NMO corrections of the PP reflected phases (Yilmaz, 1987). Using this information, the Vp/Vs ratio can be estimated by move-out analysis of the PS phases on the radial component, i.e. the horizontal component oriented in the source-to-receiver direction.
Fixing the interface depth and the layer P-velocity, the theoretical travel-time of a PS phase can be computed for a given value of the Vp/Vs ratio. Then a narrow window can be selected on the radial component of the section, beginning at the estimated arrival time of the PS phase. For each Vp/Vs value limited in a defined range, we can evaluate the STACKPS function, which is defined by:

$$STACKPS(V_p/V_s) = \sum_{t=T_{Theo}^{PS}}^{T_1^{PS}} \left(\sum_{i=1}^{N_{sis}} A_i(t) \right)^2 \tag{1}$$

where T_{Theo}^{PS} is the theoretical PS travel-time for a given Vp/Vs value, and $T_1^{PS} = T_{Theo}^{PS} + 0.3s$; $A_i(t)$ is the amplitude at time t for the i-th seismogram, and N_{sis} is the number of seismograms contained in a given seismic section.

The STACKPS function estimates the presence of a PS phase in the seismic section near to the T_{Theo}^{PS} theoretical travel-time. If there is a clear PS phase present in the section that associates with the considered reflection interface, the shape of the STACKPS function will show a clear peak that corresponds to the Vp/Vs ratio of the layer.

APPLICATION TO A SYNTHETIC DATASET

To validate the proposed methodology, we have applied it to a synthetic dataset that was calculated for a horizontally layered medium. Using the model shown in Figure 1a, we simulated a seismic experiment with an acquisition layout of one receiver located at position x = 50 m that recorded the signals produced by 80 seismic shots with a horizontal spacing of 100 m, disposed across the topographic surface. The seismograms were obtained by Norsar2d ray-theory code (Cerveny, 2001) and they are shown in the common receiver gathers (Yilmaz, 1987) sections of Figures 1a, 1c. The seismograms contain only the six primary PP and PS phases that were reflected on the three interfaces of the propagation model (Figure 1a).

Using the CVS (Constant Velocity Stack) velocity analysis (Yilmaz, 1987), we obtained information about the Vp velocity model and the depth of discontinuity h. For each PP phase individuated, we computed the STACKPS function for Vp/Vs values in the range [1.5;4] and with a window of 0.2 s. The retrieved shapes of the STACKPS function are shown in Figure 2, as the stack function *versus* the Vp/Vs ratio for each of the phases/ interfaces analyzed. The curves show a peaked shape, where the width depends on the length of the window used for the PS phase extraction and the errors in the propagation model.

For the phase reflected to the first interface, the peak is centred on $Vp/Vs = 3$ (Figure 2a), which corresponds to the ratio used in the first layer of the model (Figure 1a). For the phase reflected to the second interface, the peak is centred on $Vp/Vs = 2.5$ (Figure 2b), while for the phase reflected to the third interface, it is centred on $Vp/Vs = 2.2$ (Figure 2c). For these phases, the Vp/Vs values do not correspond to the values in the 2-th and 3-th layers of the model, but they are values obtained by averaging the Vp/Vs values of the layers above the interface under consideration. Using the formula proposed by
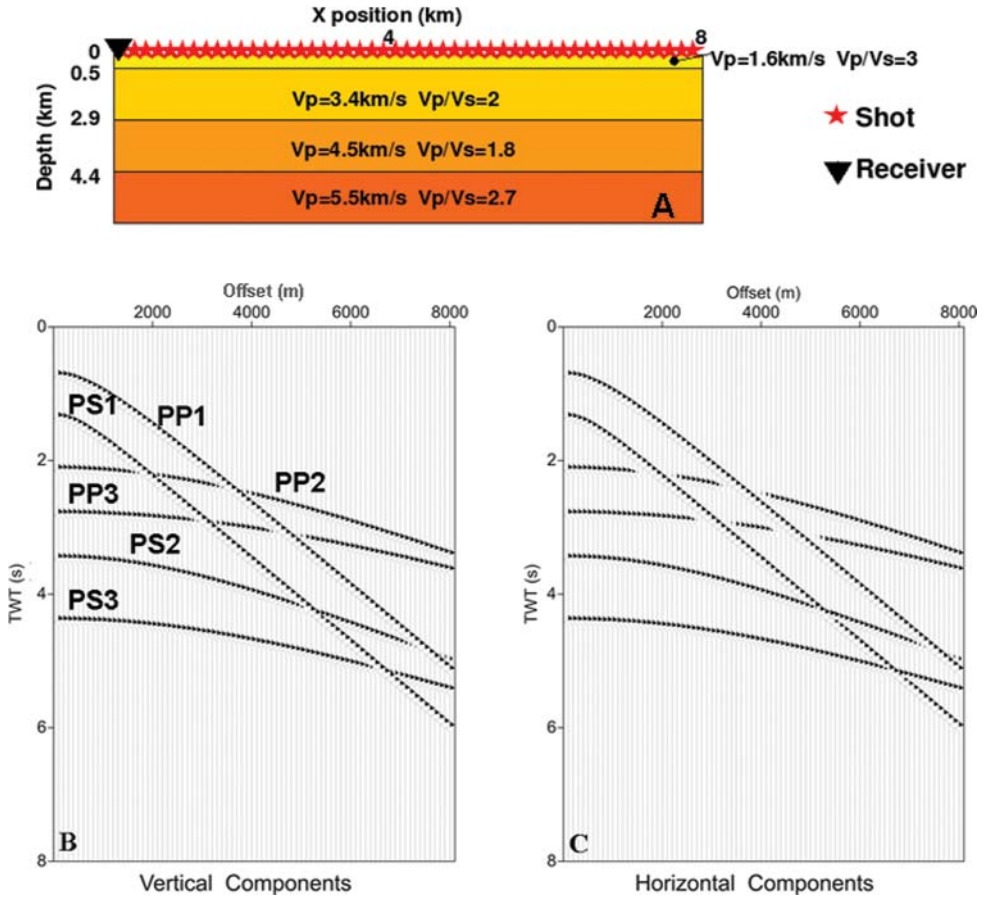
Fig. 1. Model adopted for the generation of synthetic seismograms **(a)** and synthetic zero offset section **(b)**, **(c)**. The traces in the section were normalized for the maximum trace value and were filtered with an AGC filter.

Stewart et al. (1997), it is possible to estimate the Vp/Vs ratio of a medium composed of several horizontal and flat layers with different Vp/Vs ratios. Appling the Stewart formula to our model, we obtain for the second interface a Vp/Vs of 2.3, and for the third interface, 2.2; these are close to the values obtained performing our analysis. The reliability of the retrieved values can be verified *a posteriori* by the construction of an NMO-corrected section, where the seismograms are corrected by the NMO for the PS phase using the Vp/Vs ratios found for each interface. We expect a PS-aligned phase at the theoretical travel-time. The sections corrected by the NMO are shown in Figures 2a-c. For the different layers, a clear aligned phase is seen in correspondence with the theoretical travel-time (red arrow).
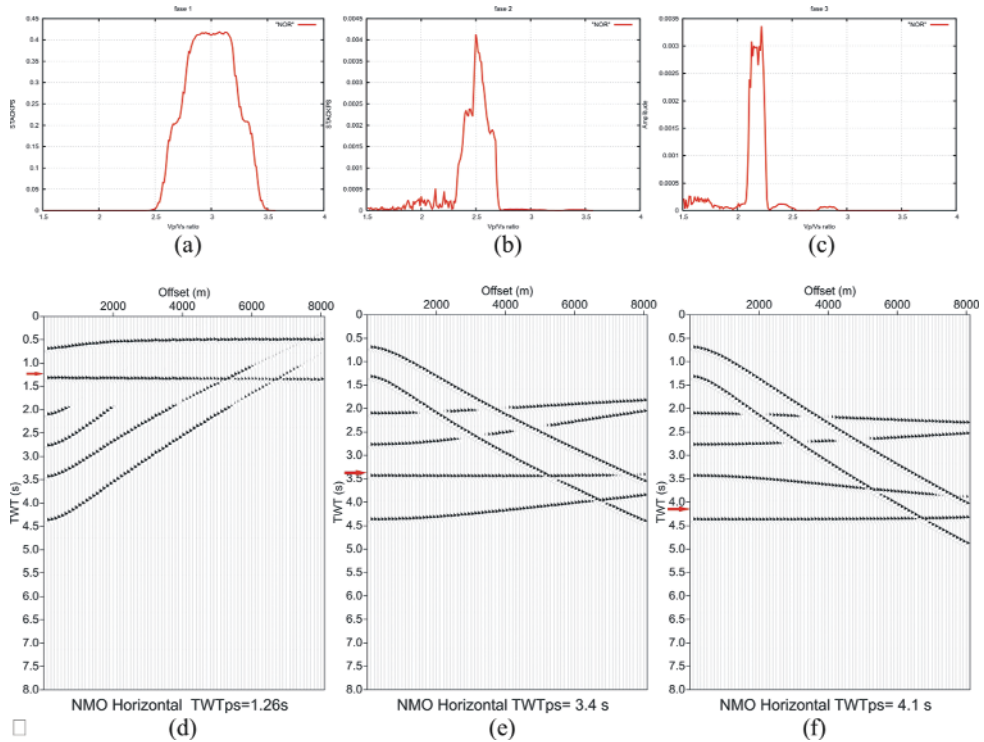
Fig. 2. Results of the method for the first interface **(a)**, **(d)**; the 2nd interface **(b)**, **(e)**, and the 3rd interface **(c)**, **(f)**. Panels **(a)**, **(b)** and **(c)** show the shapes of the STACKPS function, while the sections **(d)**, **(e)** and **(f)** are PS move-out corrected sections. The NMO was applied using the value of *Vp/Vs* which maximized the relative STACKPS function. The red arrow on the left side of the panels indicates the theoretical PS travel-time.

APPLICATION TO THE **SERAPIS** DATA

We applied this method to a dataset acquired during SERAPIS (Zollo et al, 2003), which was carried out in the gulfs of Naples and Pozzuoli (Southern Italy) in September 2001 (Figure 3). The aim of SERAPIS was to reconstruct the structure of the Campi Flegrei caldera, to individuate the presence and the forms of potential superficial magma reservoirs, and to define the geometric relationships between the volcanic structures and the carbonatic bedrock. Several important features about the caldera and the regional geology were revealed by these tomographic studies (Zollo et al., 2003; Judenherc & Zollo 2004), although the tomographic models provided give us a smooth velocity model that does not have sufficient resolution to accurately define the morphology and depth of seismic reflectors present in the area under investigation. For these reasons, we have here performed a seismic reflection analysis
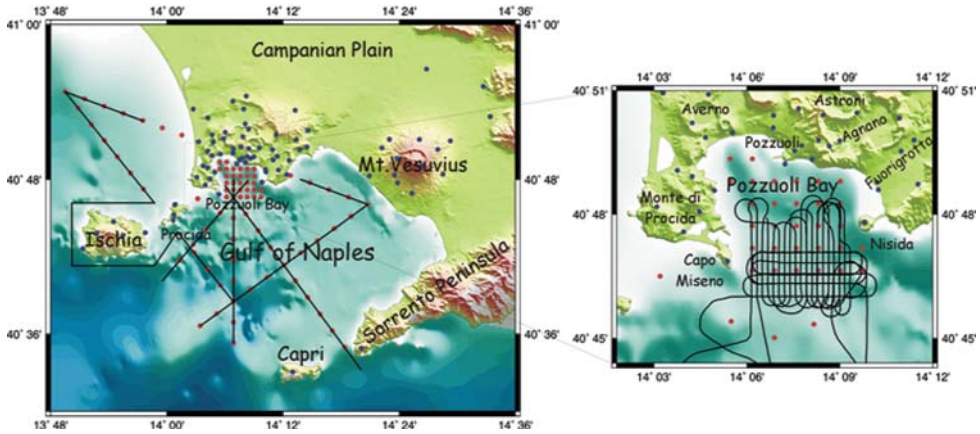
Fig. 3. Map of the area investigated during the SERAPIS experiment (left side), and zoom in on Pozzuoli Gulf (right side). The black lines trace the path of the vessel during the survey. The red circles show the positions of OBS, and the green ones the positions of land-stations deployed during the experiment.

on the acquired data, with the aim of reconstructing the reflector discontinuities and studying the seismic properties of the volcano-clastic layers.

We used the data acquired in the Pozzuoli Gulf for our analysis. The recorded seismic traces were arranged in common mid-point gathers: the Pozzuoli Bay area was subdivided into square cells, and the mid-point positions between the corresponding sources and receivers were calculated for each trace considered, taking a distance of 2,000 m as the maximum offset. All of the records where the mid-point fell into a given cell have been grouped in the same CMP (Common Mid Point), independent of the source-receiver azimuth. This kind of data storage reduces the influence of interface morphology irregularities on the reflected phases. Given the distribution of the sources and receivers during the SERAPIS experiment, the cells with most records are those in the central part of the Bay, between Capo Miseno and the island of Nisida. After several trials, a cell size of 500 m² was chosen, based on the criteria of having a sufficiently high number of traces in each CMP gather (>30) and having a dense coverage of the area under investigation.

The two-way times of a PP reflected arrival have been picked on the vertical component sections that were corrected for a move-out velocity of 1,600 m/s. We have chosen 10 CMPs that show relatively high signal-to-noise ratios for the PP phase and good lateral coherency. Examples of processed CMPs are shown in Figure 4. A total of 1,108 readings of the PP arrival times have been performed, providing a eman value of 0.64 s for the two-way travel-time (TWT), with a standard deviation of 0.06 s (Figure 5). Assuming the mean two-way time of the PP phase as the zero-offset time for the identified reflector, and using the mean P-velocity profile inferred from the seismic tomo-

Fig. 4. Example of the CMP gather section (745) after filtering, AGC and normalization **(a)**. Note the reflection hyperbola with its apex at about 0.7 s TWT. **(b)** NMO correction of the previous section, with Vnmo = 1,600 m/s. Note the aligned reflection phase at about 0.7 s TWT. **(c)** Static phase correction at 0.7 s TWT. **(d)** Example of the presence and coherency of superficially reflected phases on adjacent CMPg sections (vertical component). In the righthand map, the positions of CMPs are shown.

355
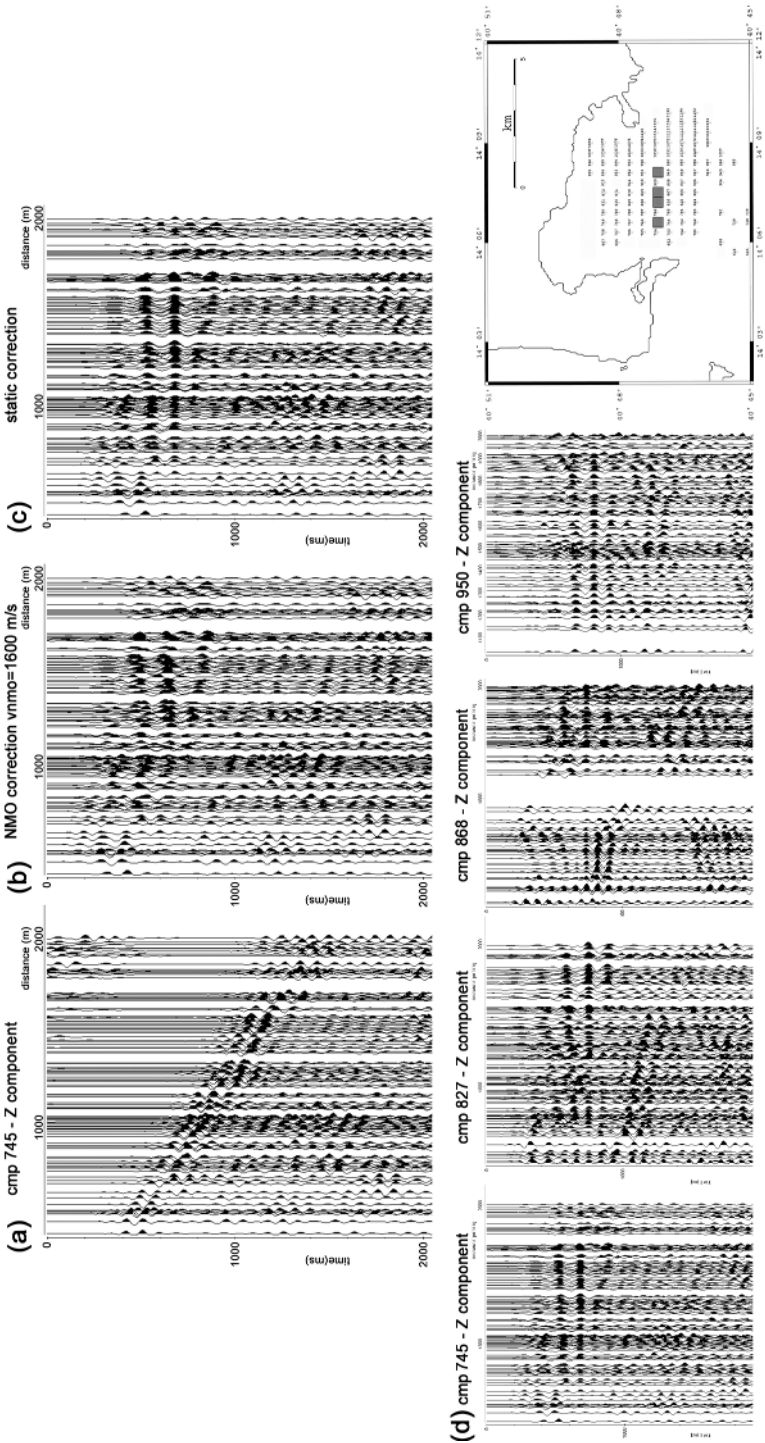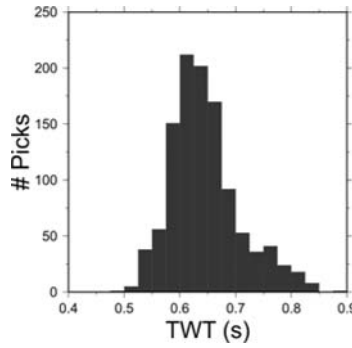
Fig. 5. Distribution of the 1,108 PP pickings.

graphy in the Pozzuoli bay area, an interface depth of 600 m ±120 m is obtained. The depth uncertainty is determined by propagating the errors on time picks (0.06 s) and on P-velocity (0.2 km/s) through the formula $h=(T_0 V_p)/2$. The Vp/Vs ratio has been estimated for each CMP using the move-out analysis of the PS phases described above, applied at radial components, i.e. the horizontal component oriented in the source-to-receiver direction (Jurkevics 1988). We used the radial components for PS identification because in the absence of azimuthal anisotropy, the energy of S waves will be recorded primarily on the radial (inline horizontal) component of the receiver.

Given the mean interface depth and P-velocity layer, the theoretical travel-time of a PS phase can be computed for a given value of the Vp/Vs ratio. Then a narrow window (0.3 s) was selected on the radial component CMP section, beginning at the estimated arrival time of the PS phase. For each Vp/Vs value limited to the range [1.5;5.5], we evaluated the STACKPS function (1). The STACKPS function versus Vp/Vs was computed for 27 CMPs using a step of 0.01 in the Vp/Vs quantity. We selected the CMP sections for which a relatively high number of traces was available (>60) and where there was a good offset coverage (at least 750 m to 1,950 m). Several examples of STACKPS functions are shown in Figure 6, where the functions have been normalized to their maximum values. For the selected CMPs, the shapes of the STACKPS functions generally show a single, broad peak centred at Vp/Vs values ranging between 3.0 and 4.0.

An estimate of the Vp/Vs ratio at each CMP is obtained by the value corresponding to the maximum of the STACKPS function. Figure 7 shows two examples of the PS move-out corrected radial section at CMP 908 and CMP 951, using the value of Vp/Vs that maximized the relative STACKPS function. This example shows good agreement between the aligned PS phase and the theoretical travel-time estimated.

To obtain a weighted mean value of Vp/Vs in the considered shallow layer, along with its relative uncertainty, we defined the uncertainty of each Vp/Vs
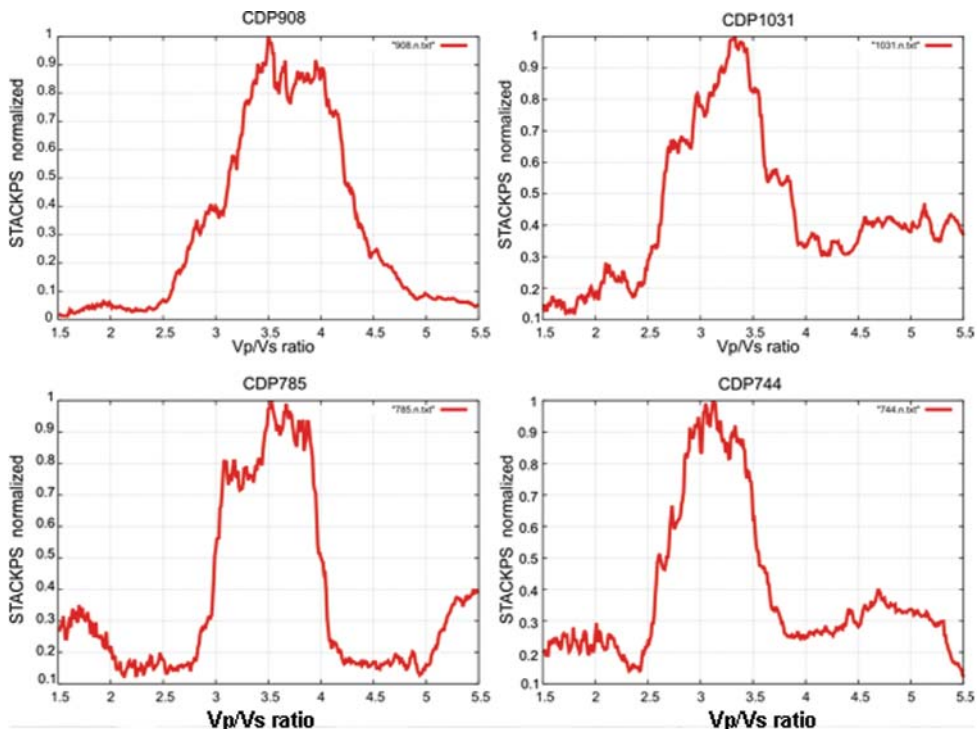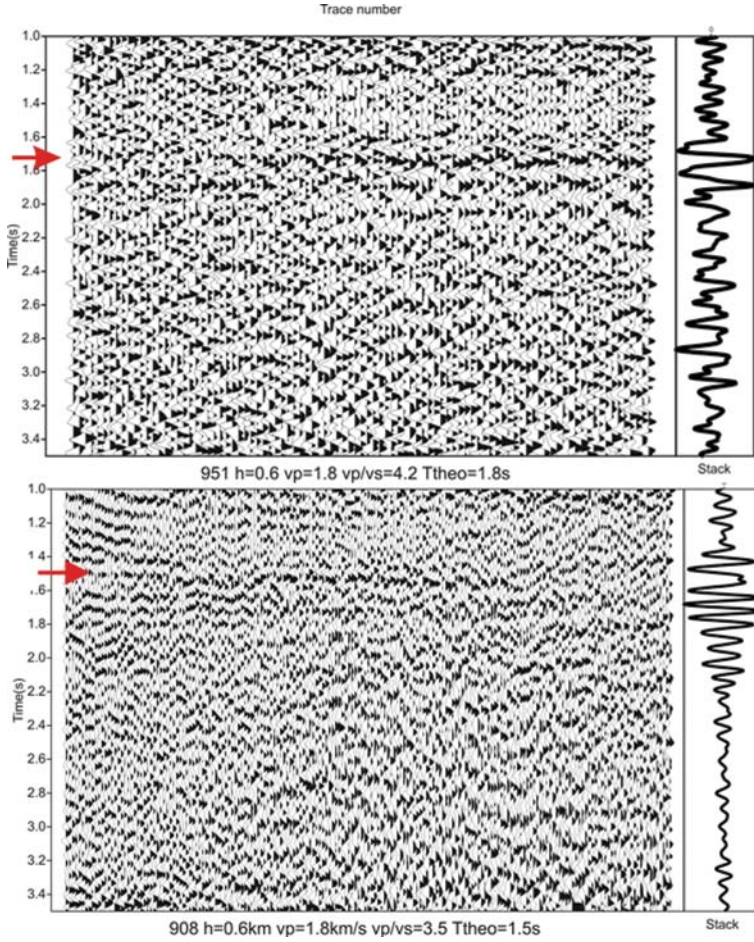
Fig. 6. Examples of the STACKPS functions normalized to the maximum values. The function generally shows a single, broad peak centred at *Vp/Vs* ratios ranging from 3.0 and 4.0.

estimate as the half-width of the STACKPS function at a level equal to half of the maximum amplitude (Tab. 1). The weighted means and standard errors were therefore computed using the inverse of the uncertainties of the Vp/Vs estimates as weighting factors. This procedure provided a value for the whole layer of $Vp/Vs = 3.5 \pm 0.6$.

CONCLUSION

We have here proposed a method for the individuation of PS phases in seismic sections and for the determination of the Vp/Vs ratio of layers present into the propagation model. The method is based on optimizing the STACKPS function (1), computed using the data along the analytic travel-times of PS reflected converted phases. The method is applicable for the hypothesis of the propagation media being horizontally layered, and for this reason, it is more simply applicable to data stored in a common mid-point gather or a common conversion point gather. The theoretical PS travel-times

Fig. 7. Examples of the PS move-out corrected radial section for CMP 908 (top) and CMP 951 (bottom). The NMO was applied using the value of *Vp/Vs* that maximizes the relative STACKPS function. The red arrow at left side of panels indicate the theoretical PS traveltime. The thick traces on the right sides of the panels show the stack trace computed using the traces stored in the section.

are computing using the information on the propagation media (depth of interface and Vp of layer above the interface) that are obtained performing the CVS (Yilmaz, 1987) analysis on the PP reflected phases or using the tomographic models obtained by inversion of first arrivals.

Initially, to validate the code, we applied it to a synthetic CRG dataset that was calculated for a horizontally layered velocity model. The subsequent application to real radial component CMP gathers acquired in the Pozzuoli Gulf allowed the constraining of the mean Vp/Vs ratio in the shallow sediment to 3.5 ±0.6. Together with the estimated P-wave velocities, this mean value provided shear-

Tab. 1. *Vp/Vs* ratios and errors estimate for several of the CMP using the proposed method.

CMP	Vp/Vs	Σ
703	3.2	0.6
704	3	0.5
707	3.3	0.75
744	3.1	0.45
745	2.2	0.6
747	4	0.5
748	3.7	0.55
784	3	0.95
785	3.5	0.5
825	4.2	1
866	3.3	0.6
868	3.2	0.8
907	4	0.75
908	3.5	0.55
910	4.3	0.5
948	3.2	0.8
951	4.2	0.55
989	3.9	0.7
1032	3.9	0.55
1035	2.6	0.5
1072	2.7	0.5
1073	3.8	0.7
1075	3.9	0.55
1112	2.9	0.83
1113	4.6	0.6
1114	3.9	0.5
1152	3	0.45

wave velocities of 450-515 m/s. The robustness of this result is confirmed by the clear alignment of the PS arrivals at the theoretical arrival times on moved-out radial sections obtained by using $Vp = 1600\text{-}1800$ m/s and Vp/Vs ratios that maximize the STACKPS function (1) defined above. It is worth noting that the high Vp/Vs ratio represents a mean estimate of the whole shallow layer, and thus such a value can be strongly influenced by the saturation conditions of the rocks in the first hundreds of meters (Zimmer, 2004).

REFERENCES

V. Cerveny. Seismic Ray Theory. Cambridge, 2001.

S. Judenherc and A. Zollo. The Bay of Naples (Southern Italy): constraints on the volcanic structures inferred from a dense seismic survey. J. Geophys. Res., 109:doi:10.1029/2004GL019432, 2004.

Jurkevics, A. (1988). Polarization analysis of three-component array data. Bulletin of the Seismological Society of America, 78(5), 1725--1743.

Miller, S.L.M. and Stewart, R.R., 1990, The effect of lithology, porosity and shaliness on P and S wave velocities from sonic logs: Can J. Expl. Geophys., 26, 94-103.

Picket,, G.R., ,963, Acoustic character logs and their applications in formation evaluation: 1. Can. Petr. Tech. 15, 659-667.

Rafavich, F., Kendall, C.H.St.C., and Todd, T.P., 1984, The relationship between acoustic properties and the petrographic character of carbonate rocks: Geophysics, 49, 1622-1636.

Tatham, R.H. and Stoffa, P.L., 1976. Vp/Vs a potential hydrocarbon indicator. Geophysics 41, pp. 837-849.

Stewart, R. R., Qi Zhang Bland, H. C. and Guthoff, F. Average versus interval vp/vs. CREWES Research Report, Volume 9, 1997.

Yilmaz, O. Seismic data Processing. Investigation in Geophysics. Society of Exploration Geophysicists, 1987.

Zimmer, M. Controls on the seismic velocities of unconsolidated sands: Measurements of pressure, porosity and compaction effects. PhD thesis, Stanford University, Stanford, CA, 2004.

Zollo A., S. Judenherc, E. Auger, L. D'Auria, J. Virieux, P. Capuano, C. Chiarabba, R. de Franco, J. Makris, A. Michelini, and G. Musacchio 2003. Evidence for the buried rim of Campi Flegrei caldera from 3-D active seismic imaging. Geophysical Research Letters, VOL. 30, NO. 19, 2003.

Task 3

Real time observations and measurements

PLINIO: an interactive web interface for seismic monitoring of Neapolitan volcanoes

L. D'Auria, R. Curciotti, M. Martini, G. Borriello, W. De Cesare,
F. Giudicepietro, P. Ricciolino, G. Scarpato

Istituto Nazionale di Geofisica e Vulcanologia, Osservatorio Vesuviano, Italy

INTRODUCTION

Seismic monitoring of active volcanoes has different and sometimes contrasting requirements. The peculiar features of volcanic seismicity makes an interactive system more complex than required for typical seismic monitoring.
Intense seismic swarms of small magnitude earthquakes need a rapid but consistent processing for tracking in real time the evolution of an ongoing volcanic unrest. At the same time a comparison with the past record for detecting patterns still observed or anomalous behaviours is needed. Furthermore a correlation between different parameters as event magnitude and depth, event occurrence rate and volcanic tremor amplitude may be required. Finally, a rapid exchange of information among scientists located worldwide can be important for drawing conclusions about the evolution of a crisis.
The first task can be fullfilled by an automatic seismic processing system, followed by a manual revision from expert seismologists. The second and the third can be simply accomplished storing the results of the processing in relational databases, that very well suited for such applications. The last task can be simply achieved by making the dataset accessible on-line thour a web server, in a friendly and interactive way.
On the basis of the experience matured on the automatic seismic monitoring system of Stromboli ([2]) the research team of Monitoring Centre of I.N.G.V. "Osservatorio Vesuviano" started developing a similar software infrastructure for the monitoring of Neapolitan volcanoes.
The existing databases: GeoVes, with supervised analysis, and Web Based Seismological Monitoring (WBSM) system, with automatic location, have been joined into a single friendly graphical interface aimed at improving the data accesibility and efficiency of the monitoring system.

GENERAL OVERVIEW OF PLINIO

The core of PLINIO is a PHP engine that queries two relational databases and gives a graphical output to the users. Actually we have used a PHP engi-

ne (release 5.1.2) embedded in a Apache (2.0) web server. The PHP engine uses JpGraph libraries (release 1.2) by Aditus Consulting. All these software are freely available on common Linux platforms.

The PHP core queries a Microsoft SQL database, containing results of manual processing of seismic data and a MySQL database containing results of real-time automatic analysis. The automatic analysis are performed by an Earthworm installation. The general scheme is depicted in Figure 1.
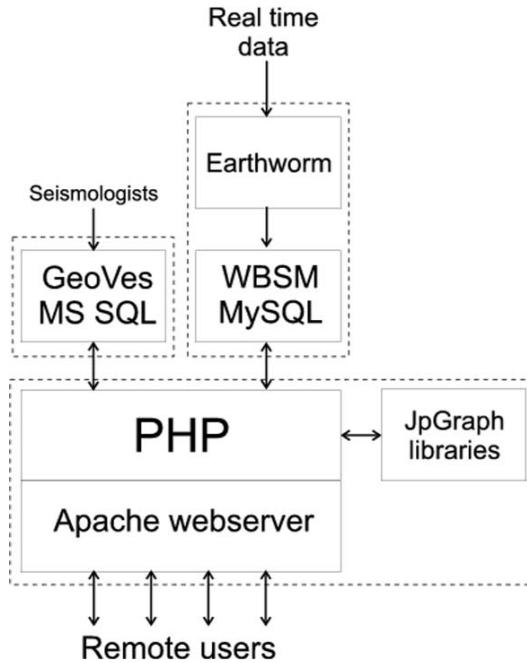
Fig. 1. General scheme of PLINIO. Dashed lines defines separated computers.

REAL-TIME EARTHWORM PROCESSING AND WBSM DATABASE

Earthworm (EW) is one of the most used software package devoted to seismic monitoring [1]. It consist of a set of software packages and libraries aimed at real time seismic data acquisition, transmission and processing. One of the key point of EW is its modularity. Different EW installation can run simultaneously on different remote machines and can interact each other through the Internet Protocol (using either TCP and UDP connections).

The core of each installation is a set of shared memory buffers (RINGS) that can hosts incoming data (waveforms, pickings, hypocenter locations and control

messages) and share them among processes attached to the RING. A typical EW installation own 3 rings: a *WAVE_RING* (for waveforms), a *PICK_RING* (for automatic pickings) and an *HYPO_RING* (for automatic locations).

The scheme of the EW installation used by WBSM is shown in Figure 2. The module *coaxtoring* collects incoming data using the UDP/IP protocol and put them into a *WAVE_RING*. Here they are continuously analysed by the *pick_ew* module that performs an STA/LTA based automatic picking and puts them into the *PICK_RING*. The *binder* module, clusters the pickings supposed to be related to the same seismic event. Once clustered pickings are processed by a pipe of modules (*eqproc*, *eqbuff*, *eqcoda*, *eqverify* and *hypo_mgr*). The last module, interacts with *HypoInverse* routines that performs the actual location. Resulting hypocenters are delivered to the *HYPO_RING*, where they are collected by the *OV_report* module and inserted into the WBSM database. *OV_report* does not belong to the EW software distribution but it has been developed by the INGV-OV "Centro di Monitoraggio" team. Other ausiliary modules (*copystatus* and *statmgr*) are needed for verifying the status of the modules and for notifying system malfunctioning to the administrators.
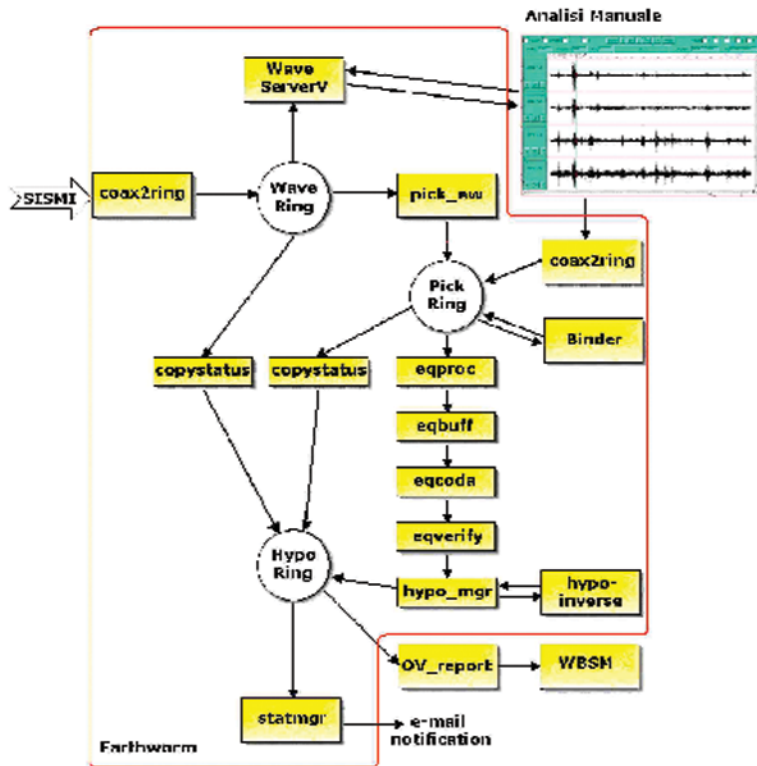

Fig. 2. Scheme of the Earthworm installation used by WBSM. (from [6]).

Tab. 1. Structure of the table *evento* in WBSM database.

Name	Description	Type	Size (bytes)
id	Event id	integer	10
subId	Secondary id	char	50
tipoSisma	Type of event	char	50
tempo	Origin time	date	8
frazioneSec	Decimal part of the O.T.	real	7
area	Geographic area	char	50
lat	Latitude	real	15
long	Longitude	real	15
prof	Depth	real	7
magnitudoTipo	Type of magnitude	char	50
magnitudoValore	Magnitude	real	7
stationNumber	Numer of stations	integer	5
gap	Azimuthal gap	integer	5
minDistanza	Distance between epicenter and closest station	real	7
rms	Final RMS	real	7
errH	Epicentral uncertainty	real	7
errV	Depth uncertainty	real	7
qualityIndex	Hypo71 quality index	char	10
autore	Location author	char	100
NomeSum	Summary file mane	char	100
NomeArc	ARC file name	char	100
NomeDMX	DMX file associates	char	100
Sumbin	Hypo71 summary file	blob	

MANUAL PROCESSING AND GEOVES DATABASE

Routine seismic data analysis at INGV-OV are performed by seismologists belonging to the "Seismic Laboratory". They perform daily a visual inspection of digital seismograms searching for natural and artificial seismic events. Earthquakes are manually picked and locates using the WinPick software code (developed at INGV-OV). Results are inserted into a relational database GeoVes, containing information about all the detected seismic events (earthquakes, artificial explosion, thunders, landslides and other events with a doubtful classification). The database contains also information about the seismic network (sensors, data loggers etc...) and raw waveforms for each event.
GeoVes is intented for internal usage only. It is equipped with an ASP web interface for low level queries and download of picking, hypocenters and waveforms.

PHP INTERFACE AND JPGRAPH LIBRARIES

PHP is one of the most powerful tools for the management of dynamic web pages [5]. One of the aims of PLINIO is to provide a friendly output in real

Tab. 2. The structure of the table *Sismi* in GeoVes.

Name	Description	Type	Size (bytes)
Id	Event id	integer	4
Data	Event Date	date	8
OraHH	Origin time hour	byte	1
OraMM	Origin time minutes	byte	1
OraSS	Origin time seconds	real	4
Tipo_Sisma	Event type	integer	4
Intensita	Intensity	byte	1
Lat_Epicentro	Latitude	real	4
Long_Epicentro	Longitude	real	4
Magnitudo_Ml	Local magnitude	real	4
Magnitudo_Mb	Body wave magnitude	real	4
Profondita	Event depth	real	4
Area	Geographic area	integer	4
Num_Dati	Number of phases	integer	4
Gap	Azimuthal gap	real	4
Rms	Final RMS	real	4
Errh	Epicentral uncertainty	real	4
Errz	Depth uncertainty	real	4
Qualita	Hypo71 quality index	char	2
Processing	Type of processing	integer	4
Nome_File	Location file name	char	50
Tipo_File	Type of file	integer	4
Stato_File	Current state of the file	integer	4
Label_CD	Label of the backup CD	char	50
Descr	Description	char	255

time. We have accomplished this task using PHP libraries for querying both the Microsoft SQL server (GeoVes) and the MySQL (WBSM) databases. We have used JpGraph libraries for plotting the results [4].

The main page of PLINIO has a lateral menu (Figure 3) allowing the selection of pages within 3 submenus:

1. **Latest events:** a list and a map of the most recent events recorded by the INGV-OV network, last events in Italy recorded by the Italian Seismic Network managed by INGV-CNT, latest events in the Euro-Mediterranean region (from EMSC web site *http://www.emsc-csem.org*) and latest events worldwide (from NEIC website *http://wwwneic.cr.usgs.gov*).
2. **Station maps:** an interactive detailed map of the seismic networks with reference to each station (Figure 4)
3. **Queries:** a set of queries on the databases. They are described in sec.6.

Queries are managed by selecting a time interval, a geographic area and a minimum quality index. This selection is perfomed in a frame positioned in the top of the main PLINIO web page (Figure 3). It is based on JavaScript functions,
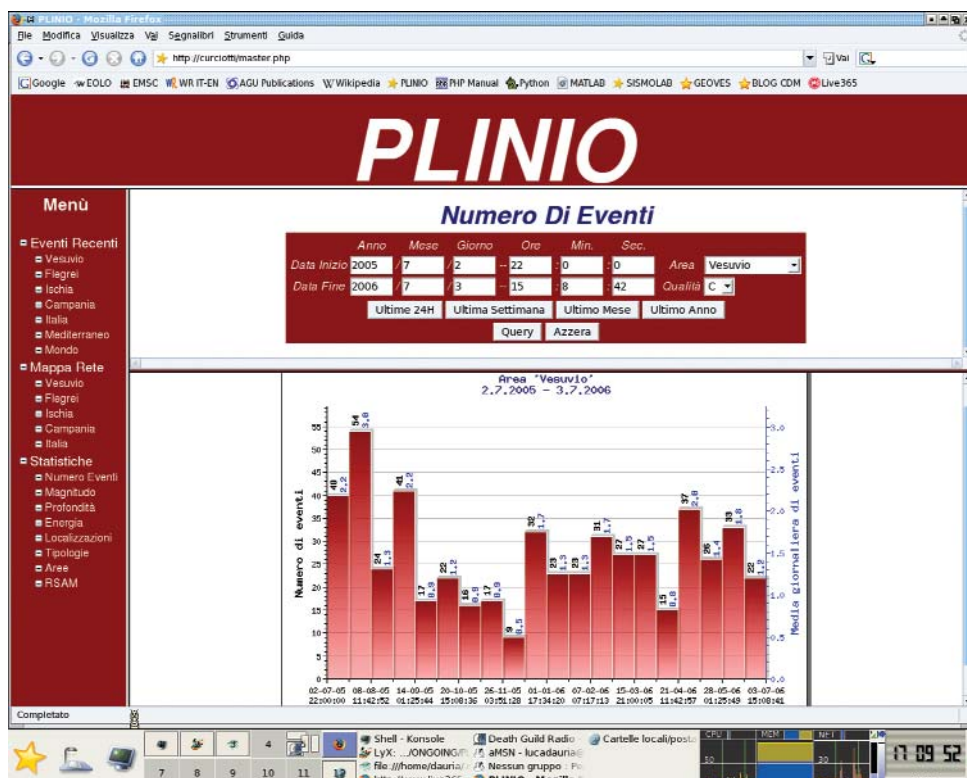
Fig. 3. Screenshot of the main page of PLINIO. On the left the menu, on the top the interval and area selection form.
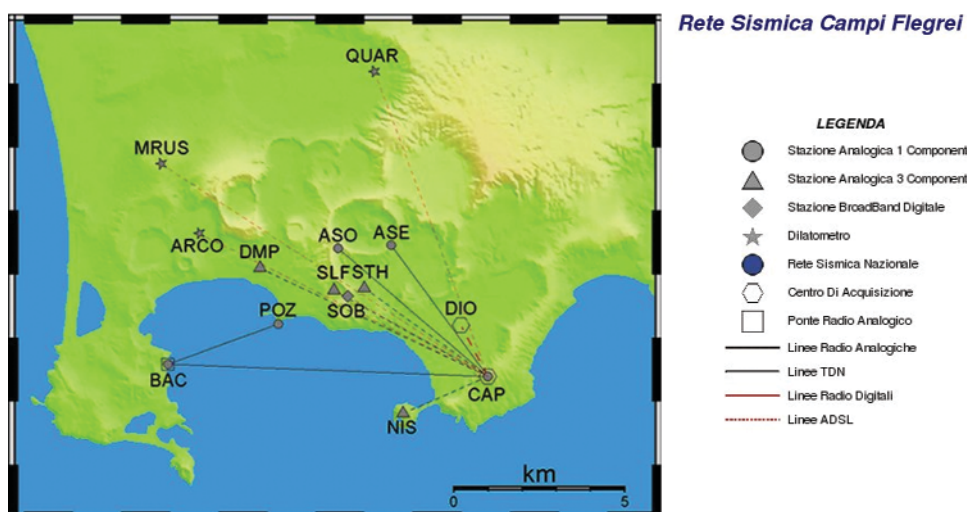

Fig. 4. Example map of a seismic network: Campi Flegrei.

triggered by buttons, that allows a rapid selection of predefined intervals (Last 24h, Last week, Last month, Last year). Once the selection has been done, it is kept using the SESSION mechanism of PHP (Table 3). So also changing the type of query (locations, magnitudes etc..) the selected interval, area and quality are kept constant if not explicitly changed.

Tab. 3. PHP SESSION variables used by PLINIO.

Variable	Type	Description
sYY, sMM, sDD, sHH, sMI, sSS	integer	Begin of the interval
eYY, eMM, eDD, eHH, eMI, eSS	integer	End of the interval
area	char	Geographic ares
qualità	char	Hypo71 quality index

EXAMPLE QUERIES

The submenu *Statistiche* allows the following queries:
– **Number of events:** this query gives an histogram showing the time varia-tion in the occurrence rate of seismic events in the selected area. The num-ber of bar of the histogram is selected automatically (i.e. 20). Each bar height is proportional to the event occurrence rate (events/day). This allows a comparison of occurrence rate even using different time intervals (years, months, days). On the top of each bar also the total number of events for the interval spanned by the bar is shown (Figure 5).
– **Magnitude:** this query shows a plot where magnitudes of single events are shows as function of time. It may allows the detection of pattern of increasing magnitudes (Figure 6). Together with the time-varying plot also an histogram showing the relative percentage of events for a magnitude interval is shown.
– **Depth:** using this query time variations in the depth of hypocenters are plotted (Figure 10). Also an histogram showing the statistical distribution of hypocenters over the depth range is generated.
– **Energy:** this query plots the cumulative energy released by earthquakes in the selected time interval and area, using the magnitude-energy relation E=109.9+1.9M (Figure 7).
– **Location:** this query shows an interactive map using the GoogleMap JavaScript API [3]. First a Keyhole Markup Language (KML) file is created, then using a GGeoXML object of the API two map overlays (one for the events and one for the stations) are created (Figure 8). Together with the KML file, also another file is written using the Hypo71 format. This file can
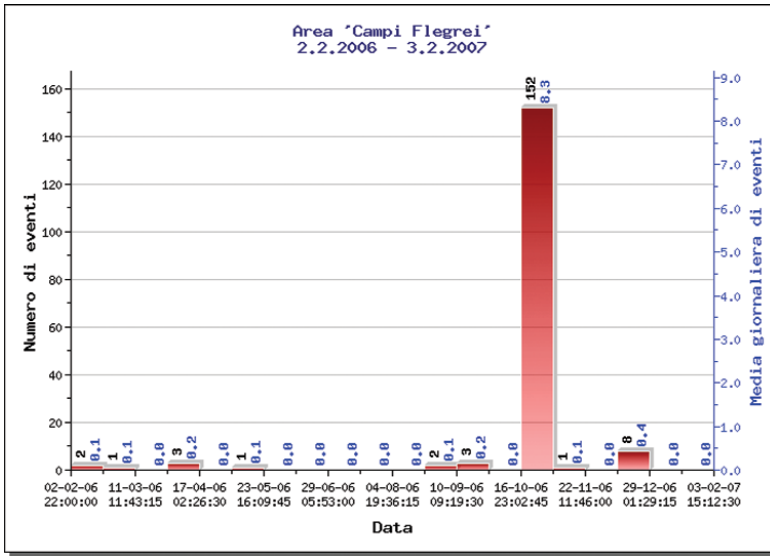
Fig. 5. Frequency occurrence rate in the Campi Flegrei area between February 2006 and February 2007. Blue numbers are the occurrence rates (events/day) while the black ones are the absolute number of events.
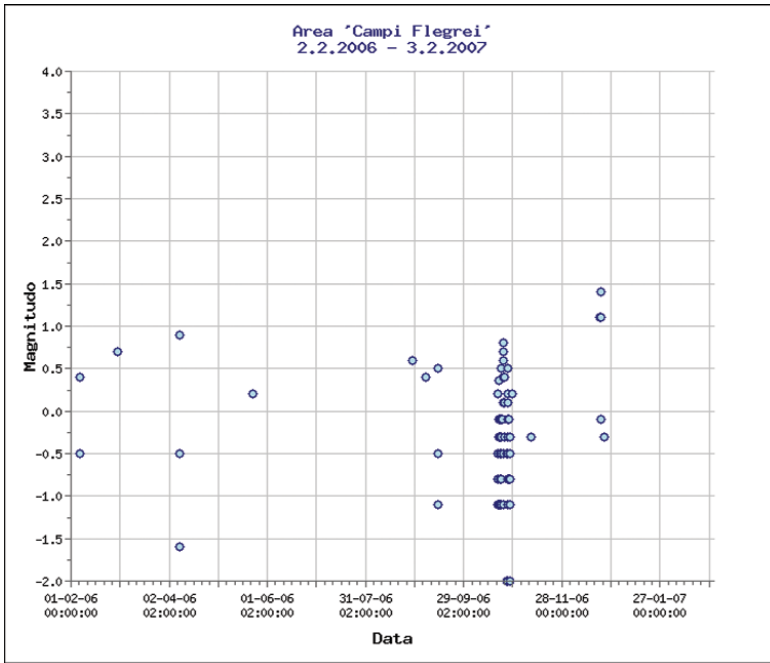
Fig. 6. Magnitude distribution in the Campi Flegrei area between February 2006 and February 2007. Notice the swarm in October 2006.
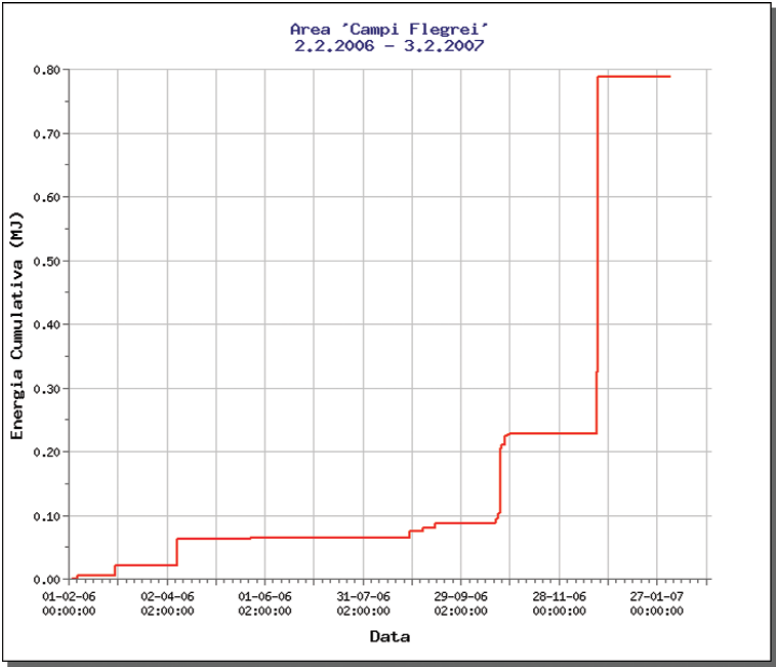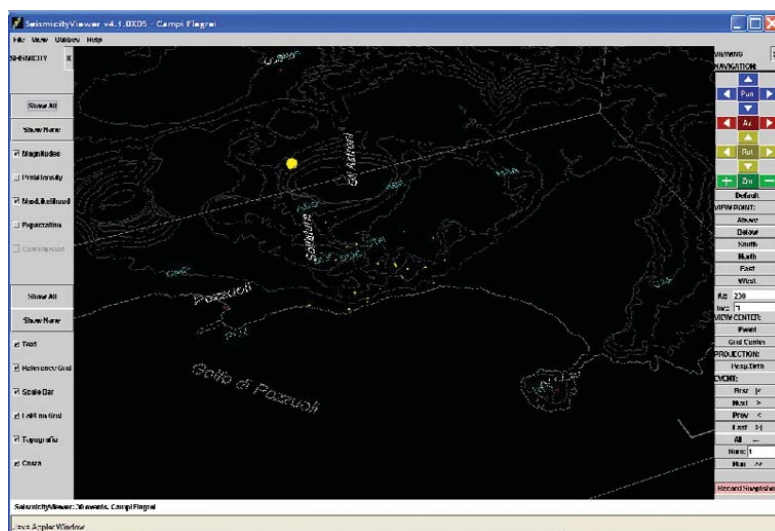
370

Fig. 7. Cumulative energy trend in the Campi Flegrei area between February 2006 and February 2007. The energy-magnitude relation used is 109.9+1.9M.

Fig. 8. GoogleMaps view of epicenters in the Campi Flegrei area between February 2006 and February 2007 (blue crosses. Seismic stations are indicated by red symbols.

Fig. 9. 3D view of hypocenters in the Campi Flegrei area between February 2006 and February 2007 using the SeismicityViewer applet.
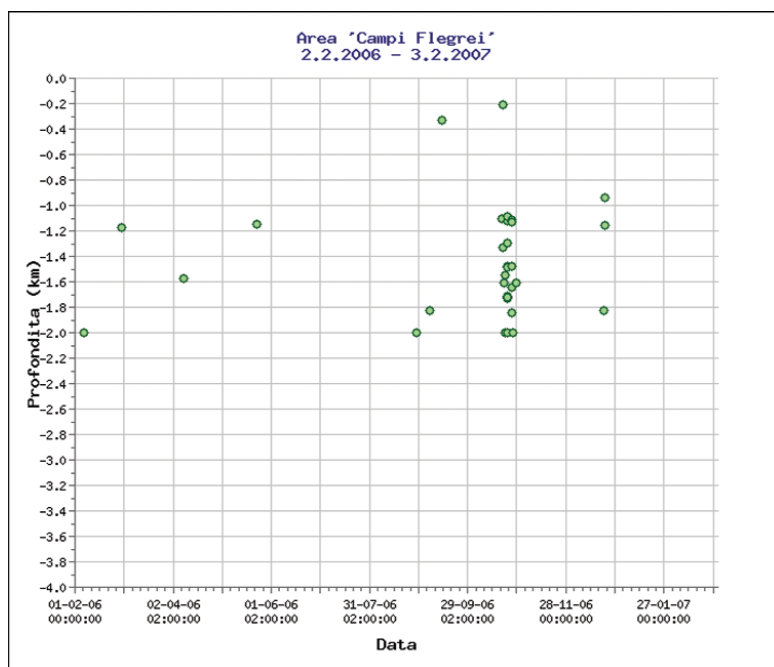
Fig. 10. Depth variation of hypocenters in the Campi Flegrei area between February 2006 and February 2007.

be used for a 3D interactive visualization using the SeismicityViewer applet [7] (Figure 9).

– **Typology:** a pie diagram showing the distribution of seismic events in the selected time interval and area by typologies (earthquakes, long-period, landslides, other) is plotted (Figure 11).

– **Area:** this query gives a pie diagram showing the distribution of earthquakes in the selected time interval by areas (Figure 12).
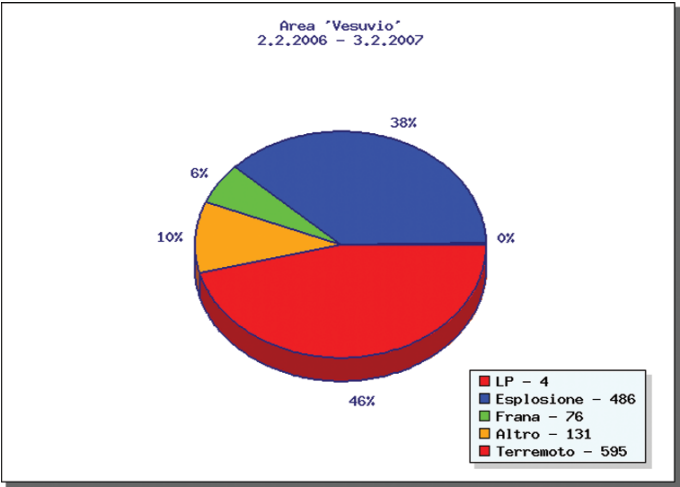
Fig. 11. Distribution of event typologies in the Vesuvius area between February 2006 and February 2007.
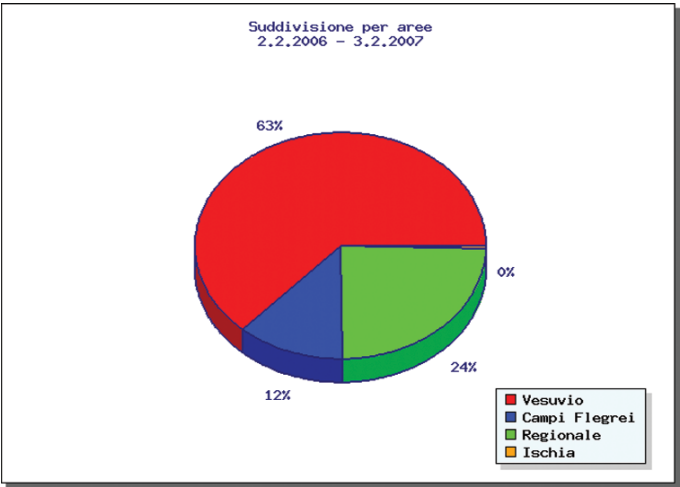
Fig. 12. Areal distribution of earthquakes between February 2006 and February 2007.

REFERENCES

[1] U.S.G.S., Reston, Virginia and C.E.R.I. Memphis, Tennessee, Earthworm documentation 7.1. http://folkworm.ceri.memphis.edu/ew-doc.

[2] L. D'Auria EOLO: Automatic Seismic Monitoring of Stromboli, http://eolo.ov.ingv.it.

[3] GoogleMaps Javascript API Documentation, http://www.google.com/apis/maps.

[4] JpGraph library Documentation, Aditus Consulting, http://www.aditus.nu/jpgraph.

[5] PHP Documentation, http://www.php.net/manual/en.

[6] Scarpato, G., Giudicepietro, F., Romano, S., Martini, M., Ventre, G., and De Cesare, W. (2004). Dispositivo virtuale per l'analisi da remoto degli eventi sismici DiVARES. Technical report, INGV "Osservatorio Vesuviano".

[7] SeismicityViewer Documentation, Anthony Lomax Scientific Software, http://alomax.free.fr/seismicity.

A unified 3D velocity model
for the Neapolitan volcanic areas

L. D'Auria, M. Martini, A. Esposito, P. Ricciolino, F. Giudicepietro

Istituto Nazionale di Geofisica e Vulcanologia, Osservatorio Vesuviano, Italy

INTRODUCTION

One of the main issues in seismic monitoring of active volcanic areas is the accurate location of earthquake hypocenters. Volcano-tectonic seismicity is often characterized by small magnitude swarms, recorded by few seismic stations with a high picking uncertainty. Sometimes events lacks clear S-wave arrivals, due to the nature of some volcanic sources. All these features, together with the complex crustal structure of volcanoes, makes the earthquake location problem critical in such areas.

One of the most important effort for improving the quality of hypocenter location is the use of realistic 3D velocity models. In the last 10 years, several scientific papers proposed 2D and 3D velocity models for Mt. Vesuvius, Campi Flegrei and the Gulf of Naples. They comes from both active seismic data (VESUVIO 94, TOMOVES 96, MAREVES 97 and SERAPIS 2001 experiments) and from local earthquake tomography.

In this report we propose a global unified velocity model spanning from Ischia island to Appennine Mts. that allows us to locate earthquakes in the Neapolitan volcanic areas and in the Gulf of Naples. This model comes from a weighted averaging of 5 tomographic velocity models and a background regional model. Most of the model provides only P-wave velocities, only 2 models, obtained through local earthquake tomography at Mt. Vesuvius and Campi Flegrei also gives a S-wave velocity estimate.

We show the difference between this new model and the previous 1D models adopted for routine locations at INGV-Osservatorio Vesuviano. We also relocate some events, using non-linear techniques showing differences in hypocenter position from previous locations and the improvement in final traveltime residuals and location uncertainties.

STARTING VELOCITY MODELS

We selected 5 velocity model, from existing literature, choosing among the most recent papers the ones using the highest number of data. Numerical data have been kindly provided us by the authors. In the following we describe the

characteristics of each model, ordered by date of publication.

The regional background (Improta et al., 2000)

The Neapolitan volcanic region lies close to the Appennine chain. This region is characterized by complex crustal structures due to the tectonic evolution of the area [Improta2000]. For this region a simple 1D model for the whole area is unrealistic. [Improta2000] proposed simplified 1D velocity models for the Sannio region (North of Naples) and the Irpinia region (South of Naples) (Figure 1). We interpolated these two models for obtaining a pseudo-2D velocity model for the eastern side of the considered area. No such detailed models exists for the western side of the Neapolitan region.
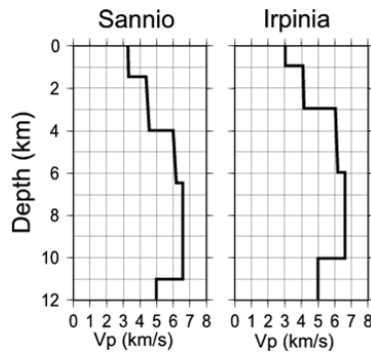
Fig. 1. 1D P-wave velocity models for Sannio and Irpinia regions. Redrawn from Improta et al., 2000.

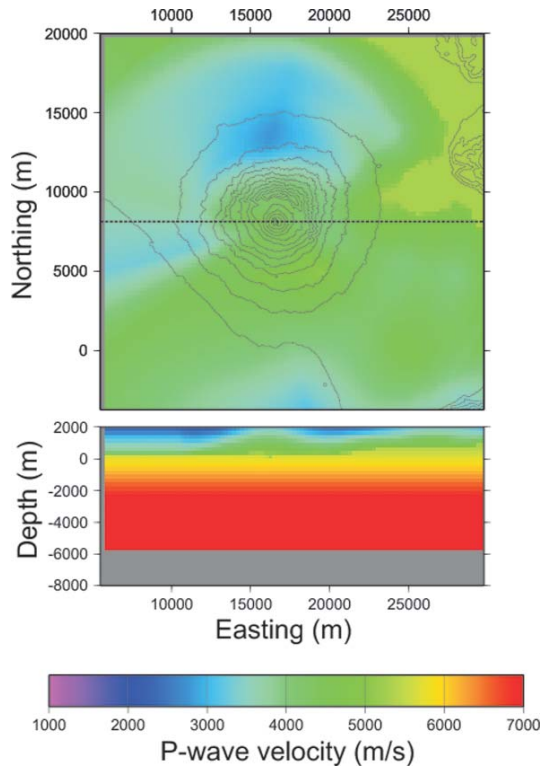## The TOMOVES model (Lomax et al., 2001)

This model comes from the interpolation of 5 2D tomographic velocity models [Lomax2001] obtained through non-linear traveltime inversion of active seismic data [Zollo2002].
A first preliminary dataset was recorded in the "Vesuvio 94" experiment, when 3 shots where recorded by 80 seismographic stations deployed along a 30 km long profile. In 1996 a wider experiment: "TOMOVES 96" was performed. It consisted of 14 on-land shots recorded by 140 seismographic stations deployed along 4 profiles from 25 to 40 km long.
The 2D velocity models were obtained from the inversion of traveltimes observed along each profile, generated by shots located along the profile itself. P-wave velocity models have a spatial resolution of about 1 km and the maximum depth of the model is 5 km [Zollo2002]. [Lomax2001] performed a

radial interpolation of the 5 2D models of [Zollo2002]. The velocity model proposed in that paper consists of a grid having a volume of 24x24x10 km³ and a spacing of 250 m. The model considers only P-wave velocities. The authors propose an average value of 1.9 for the Vp/Vs ratio.

The isosurface of about 5500 m/s velocity marks the depth of the carbonatic "basement" in the Vesuvius area. It shows a global decreasing trends toward the Gulf of Naples and a depression North of Vesuvius (Acerra depression). The central area of Vesuvius shows a high P-wave anomaly (Figure 2), interpreted by [Zollo2002] as a solified magma body.

Fig. 2. P-wave velocity model of Lomax et al., 2001. The top map represents the velocity at a depth of 1 km. The dashed line is the projection of the EW cross section shown below.

The LET model of Mt. Vesuvius (Scarpa et al., 2002)

This model has been obtained though a linearized traveltime inversion of data from a set of 2139 earthquakes recorded at Vesuvius from 1987 to 2001 by at least 8 stations. The total number of phases used is 8600 P and 1900 S

[Scarpa2002]. The average resolution in the central part of the model is about 0.5 km.

A high-Vp anomaly at about the sea-level altitude, marks the separation between two clusters of hypocenters,located above and below it [Scarpa2002] (Figure 3). The Vp/Vs ratio shows anomalously high values at shallow depths.
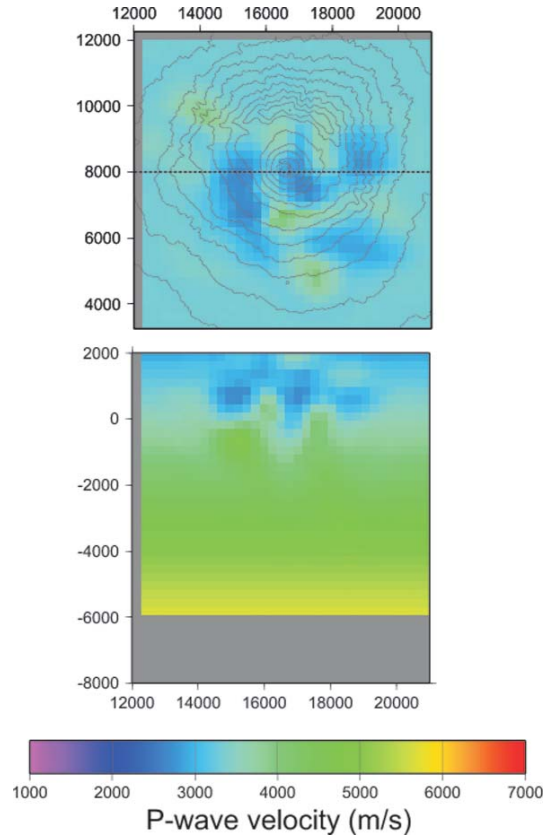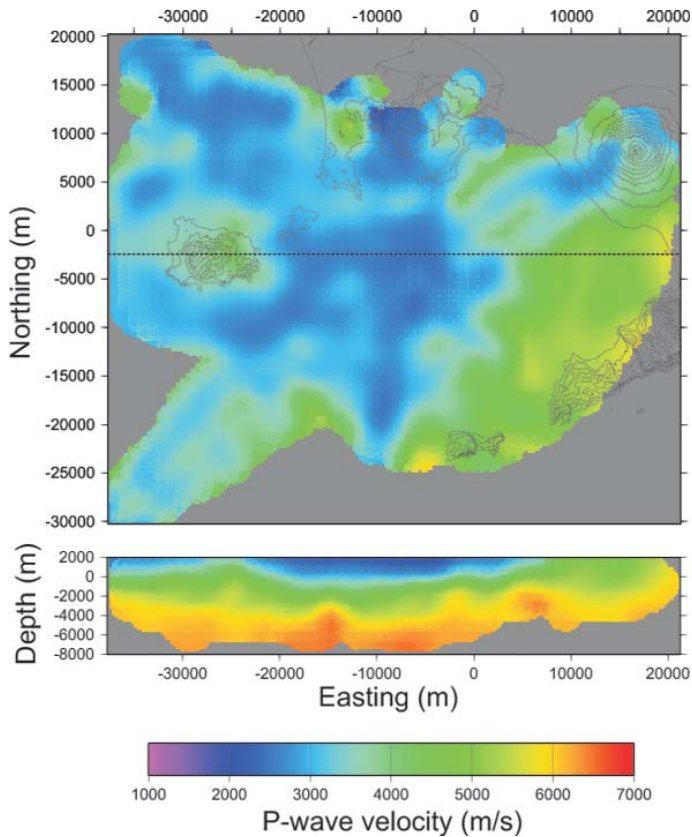

Fig. 3. P-wave velocity model of Scarpa et al., 2002. The top map represents the velocity at a depth of 1 km. The dashed line is the projection of the EW cross section shown below.

The SERAPIS models (Zollo et al., 2003) and (Judenherc and Zollo, 2004)

Following the results obtained with the TOMOVES experiment, a new active seismic survey was performed in September 2001. The aim of the experiment was to investigate the crustal structures of Campi Flegrei, Ischia and the Gulf

of Naples [Zollo2003]. The survey consisted of about 5000 airgun shots recorded by 62 OBS and 72 on-land stations [Zollo2003]. Two velocity models were obtained from the dataset using a linerized tomographic inversion technique [Judenherc2004]. The first model (NB) spans the whole Gulf of Naples, with a volume of 55x50x8 km³ and spacing of 1 km. The second one (PB), with a higher resolution of 250 m, covers the Bay of Pozzuoli and the Campi Flegrei area with a volume of 20x15x5 km³.

The NB model shows the main structural features of the Gulf of Naples, evidencing the depth of the carbonatic basement and a NE-SW fault system that dislocate it (Figure 4). The PB model shows details of the structure of the

Fig. 4. P-wave velocity model (NB) of Judenherc and Zollo, 2004. The top map represents the velocity at a depth of 1 km. The dashed line is the projection of the EW cross section shown below.

Campi Flegrei caldera in the Pozzuoli Bay (Figure 5). An high velocity ring marks the caldera rim.
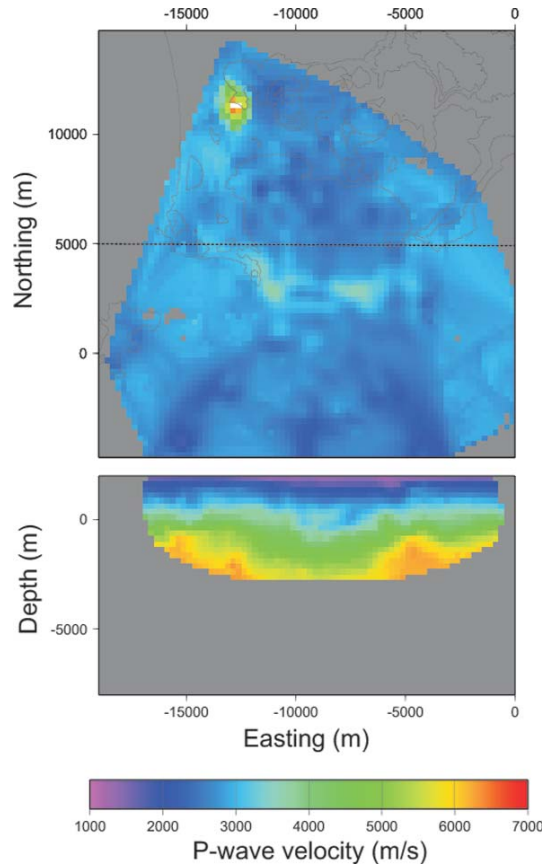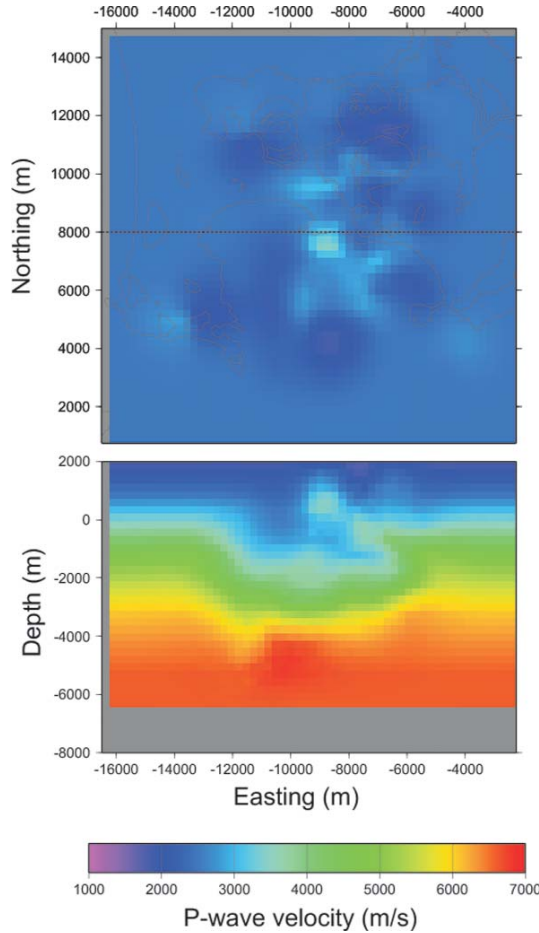
Fig. 5. P-wave velocity model (PB) of Judenherc and Zollo, 2004. The top map represents the velocity at a depth of 1 km. The dashed line is the projection of the EW cross section shown below.

The LET model of Campi Flegrei (Vanorio et al., 2005)

This tomographic model has been obtained from the inversion of traveltime data recorded by a digital network of 21 seismic stations. The dataset consists of 3447 P and 2289 S travel times from 462 local earthquakes at Campi Flegrei [Vanorio2005]. The events were recorded during the period from January 1st to April 15th 1984, when an unrest crisis was ongoing at Campi Flegrei. The main results of the tomographic inversion were a P and a S-wave velocity models. These models spans a volume of 14x14x5 km^3. The average resolution in the central part of the model is about 1 km.

This model gives a clear insight into the structure of the Campi Flegrei caldera (Figure 6). A huge low velocity anomaly marks the central depressed volume of the caldera. Small localized high Vp/Vs anomalies, below the town of Pozzuoli, probably marks a pressurized geothermal reservoir [Vanorio2005].

Fig. 6. P-wave velocity model of Vanorio et al., 2005. The top map represents the velocity at a depth of 1 km. The dashed line is the projection of the EW cross section shown below.

UNIFICATION OF VELOCITY MODELS

Each velocity model spans a limited area of the considered region. Furthermore each model has a different spatial grid dimension and a variable resolution. For this reasons the unification of the models followed 6 steps. First individual models have been interpolated on the same spatial grid (250 m spacing) using a triangulation technique. Then for each model a spatial weighting function has been defined on the basis of its resolution. This function *w* has a range from 0 to 1. Usually tomographic models have a higher resolution in the central part, where there is a higher ray density and a good azimutal coverage of ray directions. An example of weight function for the SERAPIS NB and the Vanorio models is shown in Figure 7.
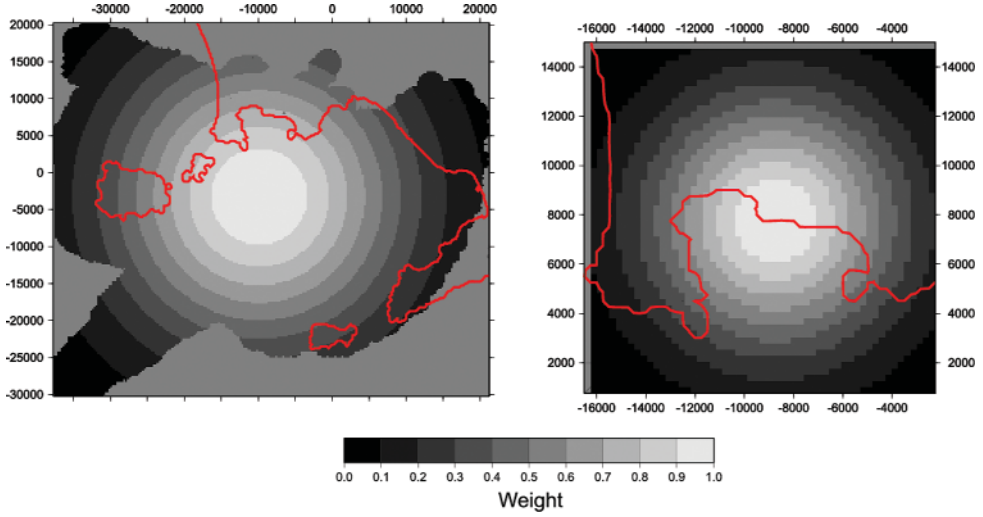
Fig. 7. Example of weighting scheme for the Serapis NB model (left) and for the Campi Flegrei model of Vanorio et al., 2005.

Then individual P wave models have been joined into a single one, using a weighter averaging as:

$$v\left(x_i, y_j, z_k\right) = \frac{\displaystyle\sum_{m=1}^{M} v_m\left(x_i, y_j, z_k\right) w_m\left(x_i, y_j, z_k\right)}{\displaystyle\sum_{m=1}^{M} w_m\left(x_i, y_j, z_k\right)} \tag{1}$$

where M is the number of models available at the point (x_i, y_j, z_k), $v_m(x_i, y_j, z_k)$ is the velocity (P or S) and $w_m(x_i, y_j, z_k)$ is the weight of the m-th model. Some portions of the model volume where not covered by any of the available tomographic models (Figure 8a). They were obtained by interpolation using a nerest-neighbour algorithm. The eastern border of the model has been defined following the two models of [Improta2000], while the western has been obtained by averaging the westernmost part of the Serapis PB model (Figure 8b). Then the resulting model has been smoothed with a gaussian filter with λ=1 km (Figure 8b).

The S wave model has been obtained in a similar way. Available tomographic models were only Scarpa et al., 2002 for Vesuvius and Vanorio et al, 2005 for Campi Flegrei. For the Lomax et al., 2001 model of Vesuvius it has been assumed V_P/V_S=1.9, while for the SERAPIS models it has been assumed V_P/V_S=1.8.

The resulting P and S models are shown in Figures 9 and 10.
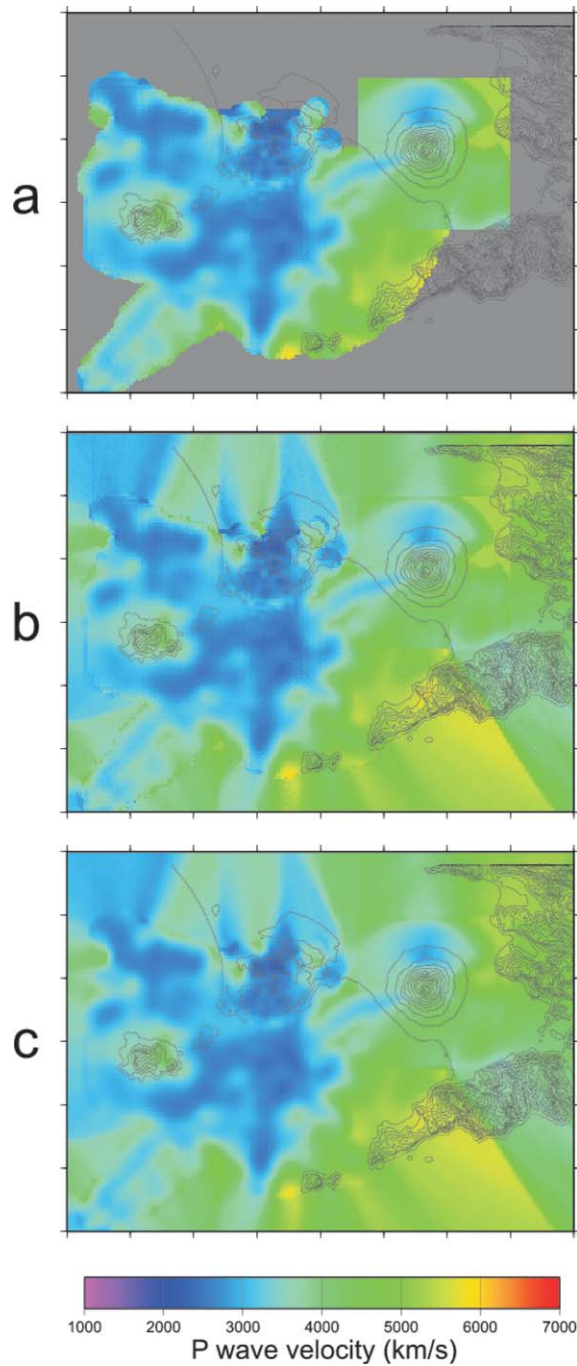
Fig. 8. Steps in the building of the global model. **(a)** represents the model after the weighted averaging of single models. **(b)** is the model after the extrapolation to undefined zones (gray areas in **(a)**). **(c)** is the final model after the smoothing. Each image represents the velocity model at 1:Km depth.
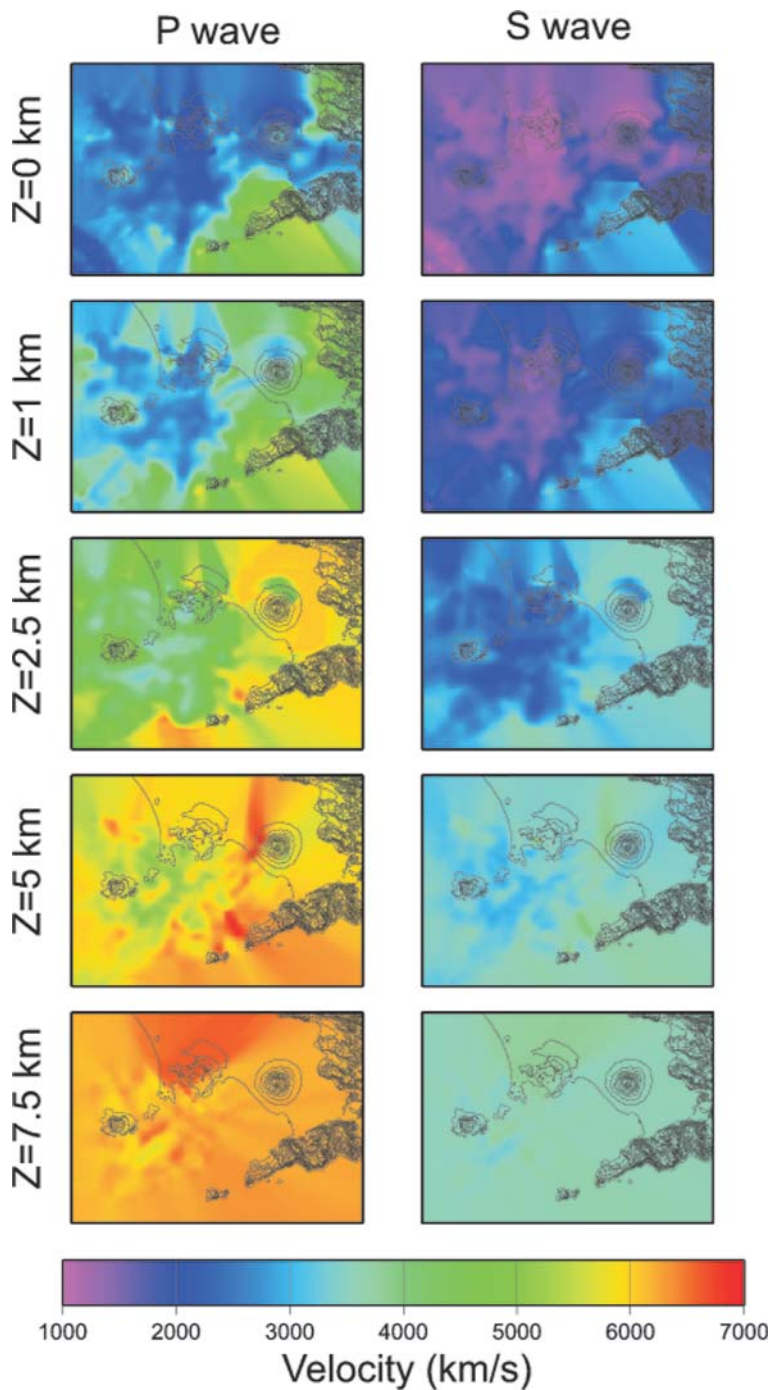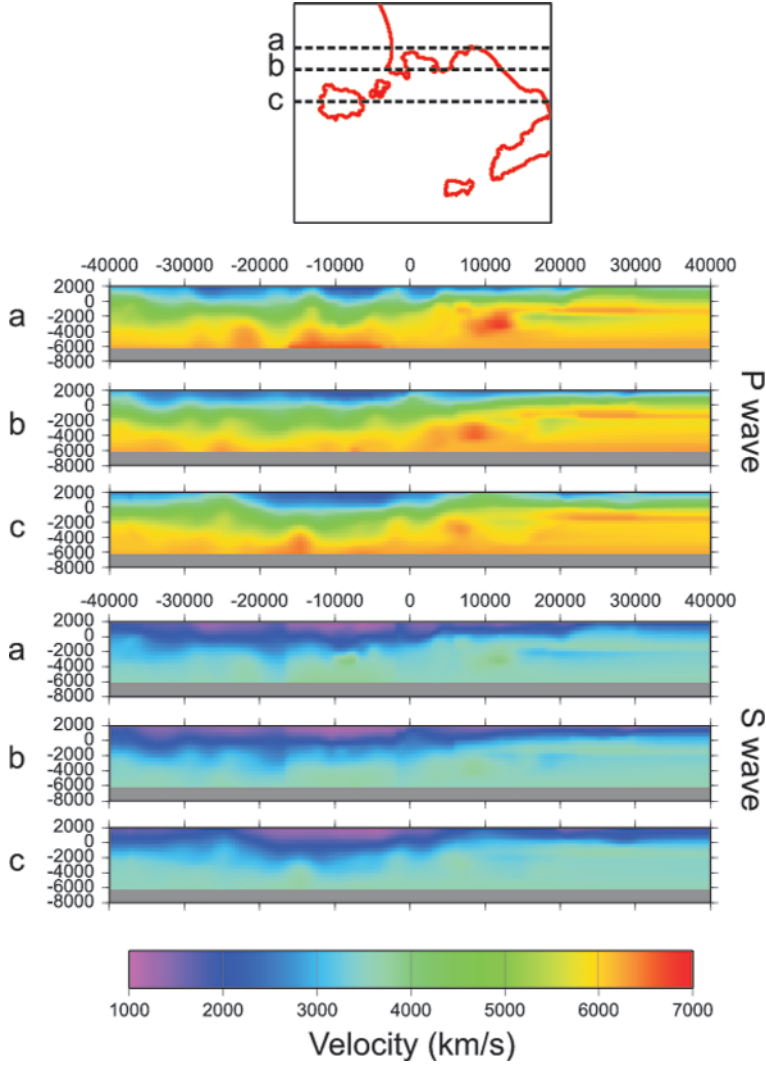
**Fig. 9.** P and S wave velocities at different depths.

Fig. 10. EW cross-sections of the velocity model. Section traces are depicted in the top panel.

RELOCATION OF SEISMIC EVENTS

The routine location procedures at INGV "Osservatorio Vesuviano" are based on Hypo71-like 1D layered velocity models (Figures 11 and 12). We have relocated, part of the available dataset for checking changes in the hypocenters between the 1D and 3D locations. For 1D models the locations have been perfomed using HYPO71 software, while for the 3D model the software used is NonLinLoc (by Anthony Lomax).

Relocating events at Mt. Vesuvius

The current 1D velocity model of Vesuvius consists of only 2 layers (Figure 11). In Figure 12 we show the comparison of locations in the 1D and in the 3D model of about 800 events (with at least 6 pickings) recorded from 1999 to 2004 by the seismic monitoring network of INGV-OV. The most striking feature is the higher depth of hypocenters in the 3D model. While in 1D locations they are mostly located above 4 km depth, in 3D locations they are distributed until a depth of 6 km. The reason of this discrepancy can be understood from Figure 11. The 1D velocity model strongly underestimates the velocity above 2 km depth, making the hypocenters shallower than the 3D
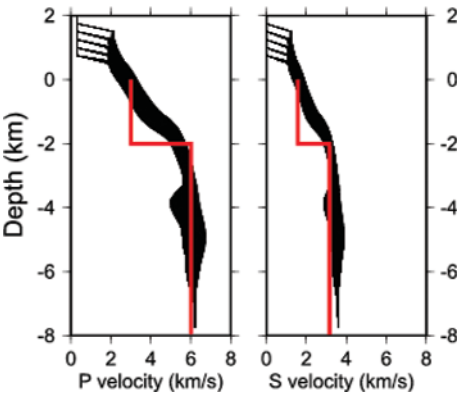

Fig. 11. Comparison between 1D velocity model (red line) and the velocity range of the 3D model (black area) in the Vesuvius area.
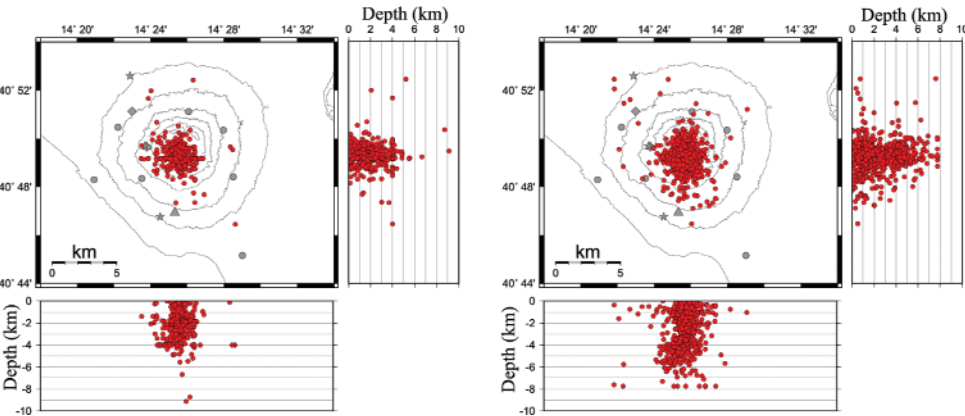
Fig. 12. Comparison between hypocenters located in the 1D (left) and the 3D model (right).

ones. From Figure 13 it is evident the improvement in the final RMS, that is known to be related to the quality of the velocity model [Klimes1996], but also in the location uncertainties (ERH and ERZ parameters).
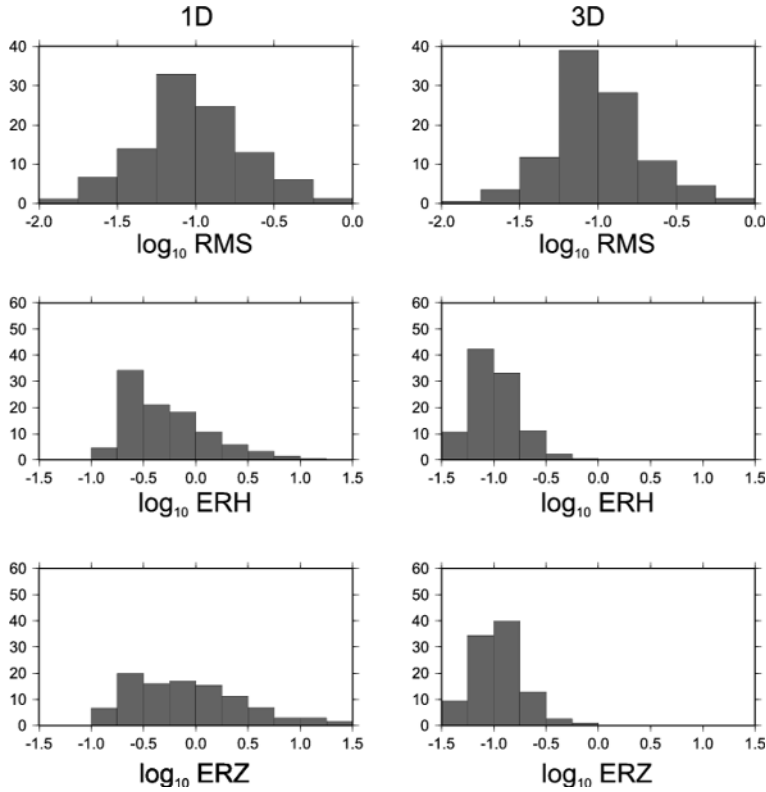
Fig. 13. Comparison between final residuals and location uncertainties in the 1D and 3D location for Vesuvius.

Relocating events at Campi Flegrei

The dataset of Campi Flegrei consists of about 100 events (with at least 6 pickings) recorded from 2000 to 2007. The comparison of 1D and 3D velocity models (Figure 14) shows a general underestimation of 1D model velocities but a rough agreements of the trend above 3 km depth. Also in this case, as for Vesuvius, hypocenters are slightly deeper in the 3D locations (Figure 15). Furthermore in the 3D model they shows a greater clustering of the epicenters. The improvement both in the RMS and on the location uncertainties is shown in Figure 16.
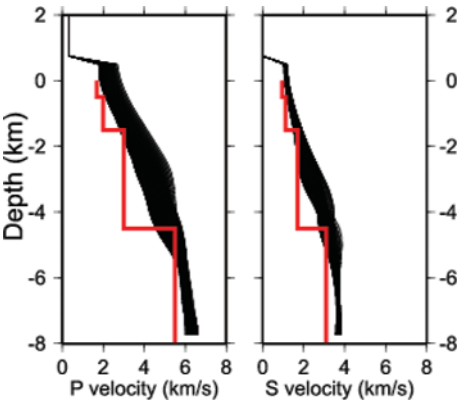
Fig. 14. Comparison between 1D velocity model (red line) and the velocity range of the 3D model (black area) in the Campi Flegrei area.
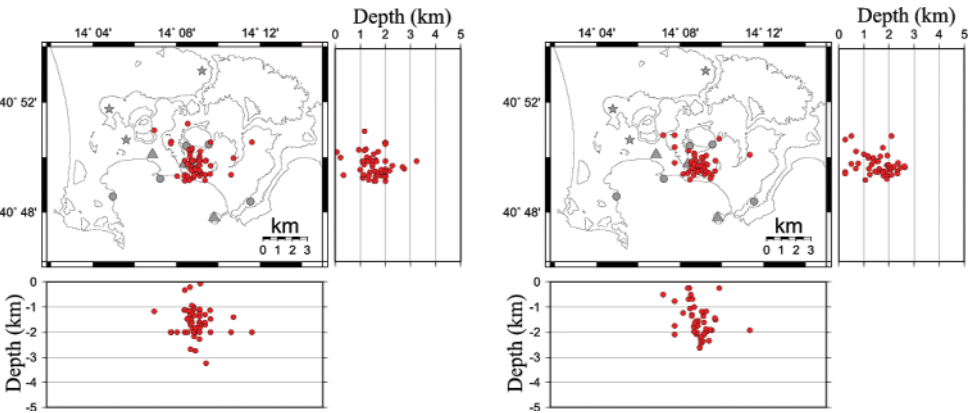
Fig. 15. Comparison between hypocenters located in the 1D (left) and the 3D model (right).

CONCLUSIONS

This new global 3D velocity model for the Neapolitan volcanic region, has shown to improve the quality of the locations both in Vesuvius and Campi Flegrei. The general shift in the hypocenter depths is significant and is due to the general underestimate of velocities in previous 1D models. The improvement in location quality will be useful both for monitoring as well as for scientific purposes.
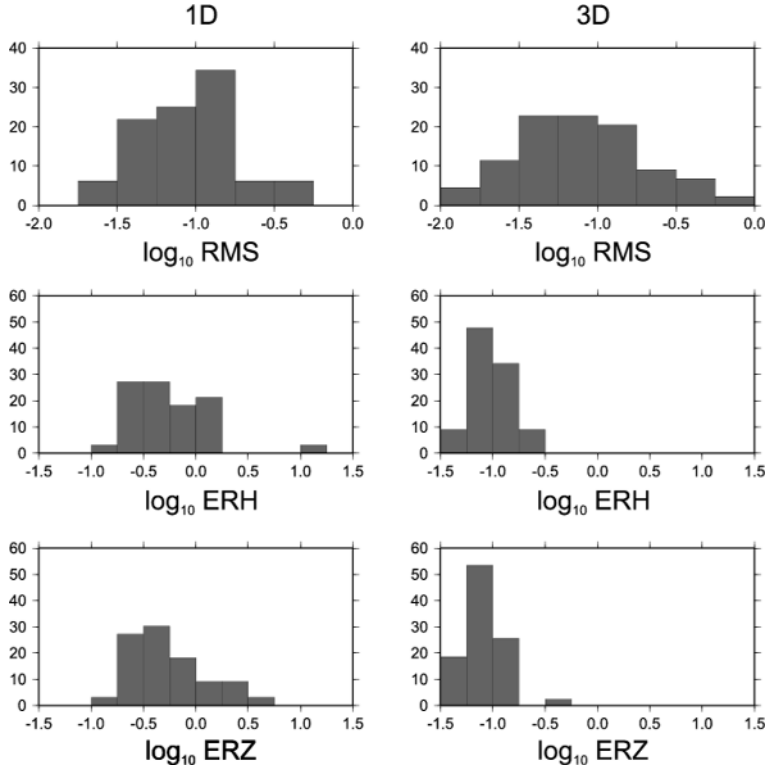
Fig. 16. Comparison between final residuals and location uncertainties in the 1D and 3D location for Campi Flegrei.

ACKNOWLEDGEMENTS

REFERENCES

[Improta et al., 2000]Improta, L., Iannaccone, G., Capuano, P., Zollo, A., and Scandone, P. (2000). Inferences on the upper crustal structure of southern Apennines (Italy) from seismic refraction investigations and subsurface data. Tectonophysics, 317(3-4):273-298.

[Judenherc and Zollo, 2004]Judenherc, S. and Zollo, A. (2004). The bay of Naples (southern Italy): Constraints on the volcanic structures inferred from a dense seismic survey. J. Geophys. Res., 109.

[Klimes, 1996]Klimes, L. (1996). Arrival-time residuals and hypocentre mislocation. PAGEOPH, 148(1-2):337-342.

[Lomax et al., 2001]Lomax, A., Zollo, A., Capuano, P., and Virieux, J. (2001). Precise, absolute earthquake location under Somma-Vesuvius volcano using a new three-dimensional velocity model. Geophys. J. Int., 146(2):313-331.

[Scarpa et al., 2002]Scarpa, R., Tronca, F., Bianco, F., and Pezzo, E. D. (2002). High resolution velocity structure beneath Mount Vesuvius from seismic array data. Geophys. Res. Lett., 29(21).

[Vanorio et al., 2005]Vanorio, T., Virieux, J., Capuano, P., and Russo, G. (2005). Three-dimensional seismic tomography from p wave and s wave microearthquake travel times and rock physics characterization of the Campi Flegrei caldera. J. Geophys. Res., 110.

[Zollo et al., 2002]Zollo, A., D'Auria, L., Matteis, R. D., Andr? Herrero, Virieux, J., and Gasparini, P. (2002). Bayesian estimation of 2-d p-velocity models from active seismic arrival time data: imaging the shallow structure of Mt Vesuvius (southern Italy). Geophys. J. Int., 151:566-582.

[Zollo et al., 2003]Zollo, A., Judenherc, S., Auger, E., D'Auria, L., Virieux, J., Capuano, P., Chiarabba, C., de Franco, R., Makris, J., Michelini, A., and Musacchio, G. (2003). Evidence for the buried rim of Campi Flegrei caldera from 3-d active seismic imaging. Geophys. Res. Lett., 30(19).

RS-485 interface for external use of the GPS receiver of the Kinemetrics® dataloggers

S. Guardato, G. Iannaccone

Istituto Nazionale di Geofisica e Vulcanologia, Osservatorio Vesuviano, Naples, Italy

SUMMARY

In this technical report, we present an electronic interface that we designed and produced as part of a new system that allows the remote acquisition of data provided by the GPS receiver for the *Quanterra* Q330 and Q330HR dataloggers, and for the whole range of the *Altus* series of systems produced by Kinemetrics, using an RS-485 bus via a serial cable that can be of kilometres in length. This function is not normally available for any of the equipment reported and it is needed when the installation of the GPS receiver antenna needs to be more than some tens of metres from the datalogger. This can be necessary, for example, for installations in tunnels, in large buildings, or for seafloor systems with a cable connection to the surface.

This document describes the functioning and the hardware of the interface boards, particularly considering the *Quanterra* Q330 datalogger. The system designed in this way is introduced as an element that maintains all of the functions of the apparatus in a fully transparent mode without the need to modify the communication-software procedures for the exchange of data between the datalogger and the integrated GPS receiver, therefore leaving untouched the various functional modalities normally associated with the GPS receiver.

FUNCTIONING PRINCIPLES

The Quanterra Q330 is equipped with a GPS receiver module (M12 Motorola®) for the correct time marking of the data acquired. The operating manuals specify that the GPS receiver inside the Q330 can be used in various modes: continuous functioning, or for a predefined time, or only when the tracking of the phases is lost. In this last case, the quality of the GPS signal drops to 60% (still a good level of GPS signal) and decreases by a further 1% about every 10 minutes. This means that under these conditions after a time of about 8 hours the level drops to 10% (equivalent to an absence of GPS signal).

In such cases, a new time base is used, provided by a TCXO (high-stability quartz with temperature compensation) usually coupled via the use of a phase-locked loop (PLL) circuit, with the timing signal from the GPS receiver.

The quartz oscillates with a clock at 15,360 MHz and has a thermal stability of 10 ppm/°C. This results in a time drift of the datalogger clock of a few seconds about every 30 days of use in the absence of a GPS signal, with the datalogger continuously functioning.

The technical specifications supplied by Kinemetrics describe the possibility of using an external GPS receiver through the use of some lines of the connector labelled as "Ext. GPS" on the front panel of the Q330. In this case, it is possible to export the data in NMEA format directly from the GPS receiver through a serial interface made available physically via this connector (supported by two serial standards: RS-232 and RS-422).

For our needs for the running of a data acquisition experiment from the seafloor, there was the need to use an external GPS receiver to be connected to the Q330 datalogger via a serial cable of a length of about 400 m . Initially, we thought to use the active GPS antenna, provided with the equipment for the Q330 datalogger with an appropriate RF cable of the required length. This, however, meant that there was the need for a line-amplifier for the GPS signal due to the high loss along the cable (about 0.3 dB m^{-1} for a very good quality cable), without knowing if it would be possible to continue to use the GPS receiver inside the Q330 on the seafloor, at about 100 m feet in depth.

Therefore, it was preferable to modify the Q330 datalogger by taking out the integrated GPS receiver and designing two electronic modules that would at the same time provide for further functions. Importantly, these would act as RS-485 interfaces between the GPS receiver (once removed from the Q330) and the datalogger, allowing the digital GPS signals to be passed over long distances (up to 3,000 metres of cable with a baud-rate of 9,600 bps, or over with appropriate digital line amplifiers that are commercially available at low-cost). The bidirectional interface conversion system from the serial RS-232 standard (TTL with active low voltage levels of +3 V) to the RS-485 bus standard, here referred to as GPS-485, comprises two electronic modules that need to be installed as described below.

Specifically, the system allows the reception of the data by the Q330 from the above-mentioned GPS receiver connected to the antenna, through a serial cable provided of four differential twisted pairs. This allows the exchange of control data and the receiving of information from the GPS, with the receiving of the 1PPS signal and the turning on (and turning off) of part of the electronics of the two interfaces, and consequently, of the GPS receiver.

The system comprises:

– Antenna for receiving the GPS signal;
– Interface board (referred to as the GPS-485 receiver side) with which, as indicated below, the GPS receiver module from the Q330 will be connected. It also contains the RS-232/RS-485 interface with the line-driver/receiver circuits, the power supply circuits, and all the electronics necessary for the monitoring of the charge condition of a specific back-up battery for the GPS module;

– Serial connection cable (1:1) for the two boards;
– Interface board (referred to as the GPS-485 datalogger side) containing, as will be shown later, the RS-485/RS-232 interface with the line-driver/receiver circuits, and the power supply circuits.

Figure 1 illustrates the complete connection scheme of the two interface boards with the GPS antenna and the Q330 datalogger.
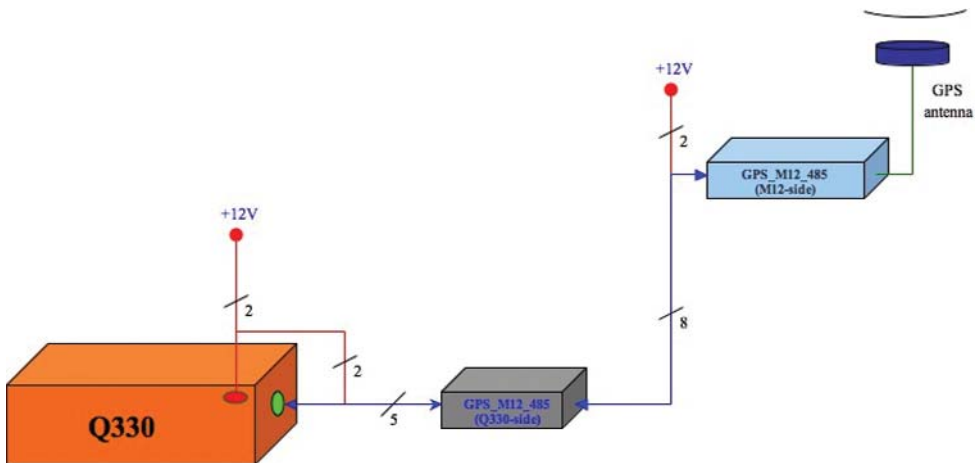
Fig. 1. The final connection scheme.

INTERFACE DESCRIPTION

The system includes two interface boards. One of these (on the GPS receiver side) contains all of the electronics necessary for the power supply to the GPS receiver, the active antenna, and the interface circuits necessary for the control of the GPS data to be transmitted through the RS-485 bus with a serial cable over long distances. This board can also receive configuration commands from the GPS receiver that are sent from the datalogger; in particular, this board is used to interface this information from electrical levels that conform to the RS-485 standard, to TLL at +3 V logic levels.

The other board (on the datalogger side) will carry out the same functions as the board above but in an opposite sense, except regarding the GPS receiver and the antenna, which, obviously, are not a part of this side.

The exchange of information between these two interface boards is through the above-mentioned cable containing four twisted pairs (with a characteristic impedence of 120 Ω). The cable can be up to 3 km in length.

The interface boards are completely active only when the GPS is turned on via the Willard© management software of the datalogger. Once this is done, the controlling digital differential line reaches the high-logic state and activates all the rest of the electronics that had remained in standby mode. The introduction of the two interface boards allows the use of the GPS receiver for the datalogger in an fully transparent mode.

No software modifications are needed for the system, which will therefore continue to function as before. The two boards can be installed inside their own containers to protect them from external atmospheric agents, or they can be mounted in the same box that normally contains the instrumentation.

THE DATALOGGER-SIDE BOARD

The Figure 2 shows the interface circuit that manages the data acquired by the GPS receiver and that is directly connected to the datalogger (modified). Table 1 provides a summary of the technical specifications of this circuit board.
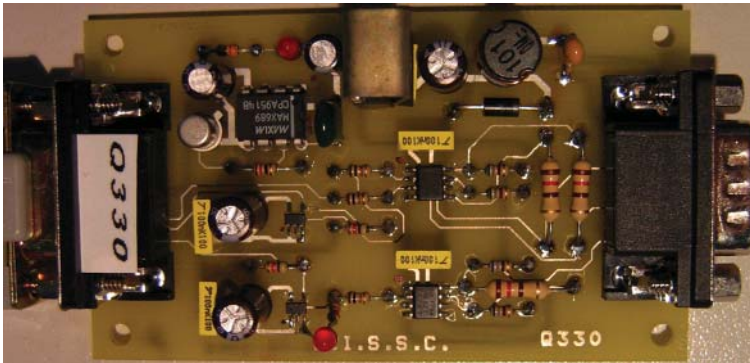
Fig. 2. GPS-485 (datalogger side).

The power supply to the board is external and can be provided by a normal 12 V battery. The power supply input circuit is protected by a self-resetting fuse to protect against possible short circuits or other anomalies; moreover, there is also diode protection against possible accidental inversions of the polarity of the power supply.

There are also two switching-type voltage regulators. One of these provides the power supply at +5 V for the line-driver/receiver circuits for the RS-485 bus. The other voltage regulator, at +3 V output, provides the power supply

Tab. 1. Technical specifications of the board on the datalogger side.

Power supply	8 ÷ 14 V DC
Current	30 mA @ 12 V DC
Data Rate	Up to 100 kbps for a cable length less than 1200 m
Connectors	DB9 male (RS-485 cable side) DB9 female (datalogger side)
Monitor LEDs	GPS power, 1PPS
Container	Plastic box
Weight	40 g
Dimensions	100 x 50 x 20 mm

for the step-down DC/DC converter from +5 V to +3 V for the signals received from the GPS receiver module[1].

The line driver/receiver interface circuits on the RS-485 bus in this board are used to be able to correctly carry out dialogue with the remote GPS receiver. In particular, this involves adapting the differential signals received (RX+, RX-, 1PPS+ and 1PPS-) to a TLL logic level standard and then to adapt them to a TLL logic level at +3 V, as described below. As a similar concept, but in the opposite sense, this is done to adapt the differential signals to be transmitted to the GPS receiver (TX+, TX-, ON+ and ON-) and to the activation circuit of the power supply, from a TLL logic level at +3 V to differential levels compatible with the characteristics of the RS-485 bus.

An equivalent circuit was planned for the differential input signal pair (1PPS+ and 1PPS-) coming from the GPS receiver, and for the differential output signal pair (ON+ and ON-) needed for the remote turning on of the GPS receiver (which under normal running conditions the current absorption is about 100 mA).

Downstream of the 1PPS signal received, there is a LED that flashes at a frequency of 1 Hz to indicate the correct functioning of the external GPS receiver. As indicated above, the interface line-receiver circuits on the RS-485 bus installed on this board have output signals at the TLL logic level standard.

---

[1] In this case, for the power supply to the interface board on the side of the K2 datalogger, no power supply circuits are needed at present. Indeed, here the need is only for a voltage of +5 V for the power supply to the line driver/receiver circuits on the RS-485 bus that is taken from the connector of the datalogger itself that is normally used as the power supply of the internal GPS receiver. Moreover, the +3 V voltage is not needed because the GPS receiver (ACEIII, Trimble®) has a serial communication interface with the TTL standard of +5 V.

Since it is planned that the interface to the GPS receiver of the Q330 will carry out dialogue with the Q330 via a serial port with a TLL of +3 V, instead of the standard, the signals received (RX and 1PPS) need to be adapted to this voltage logic level.

An equivalent circuit was planned for the RX input signal coming from the GPS receiver[2].

THE GPS RECEIVER-SIDE BOARD

The Figure 3 shows the interface circuit that manages the data acquired by the GPS receiver removed from the Q330 (and the commands directed to it) to be transmitted to (received by) the Q330 datalogger (modified) via the serial connection cable on the RS-485 bus, and Table 2 provides a summary of the technical specifications of this board.
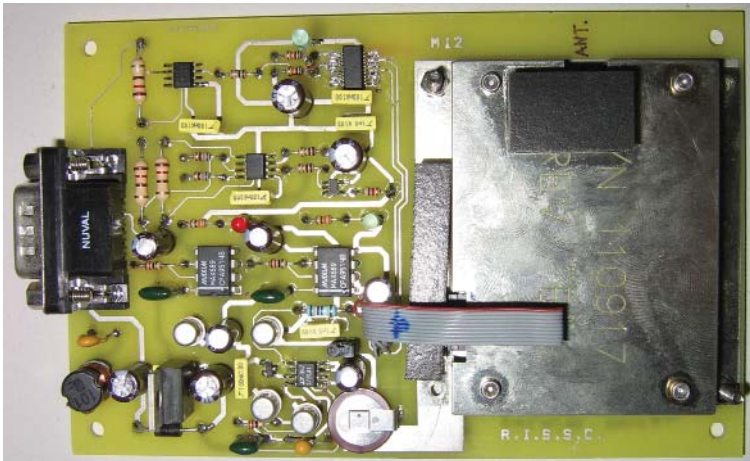
Fig. 3. GPS-485 (GPS receiver side).

The power supply is also external for this board and can be provided by a normal 12 V battery. The power supply input circuit is protected by a self-resetting fuse to protect against possible short circuits or other anomalies; moreover, it is also protected by a diode against possible accidental inversions of the

---

[2] In this case, there are no DC/DC step-down converter circuits. Indeed, here the need is only for a single pair of line-driver/receiver circuits on the RS-485 bus, because the GPS receiver (ACEIII) has a serial communication interface with the TTL standard of +5 V.

Tab. 2. Technical specifications of the board on the GPS receiver side.

Power supply	8 ÷ 14 V DC
Current	40 mA @12 V DC (GPS receiver off)
Data Rate	Up to 100 kbps for a cable length less than 1200 m
Connectors	DB9 male (cable side) MMCX plug (GPS antenna)
Monitor LEDs	GPS Power, 1PPS
Container	Plasic box
Weight	80 g (GPS receiver not included)
Dimensions	150 x 80 x 20 mm

polarity of the power supply. There are also three switching-type voltage regulators that are the same as those for the interface board on the datalogger side. One of these provides the power supply at +5 V for the line-driver/receiver circuits for the RS-485 bus. The other two voltage regulators at +3 V provide the power supplies for the step-down DC/DC converter from +5 V to +3 V for the signals transmitted by the GPS module towards the datalogger, and for the power supply to the GPS antenna.

The electronics scheme adopted for the power supply section is the same as that for the interface board on the datalogger side, with the particular considerations already discussed.

In addition, there is a monitoring circuit for the recharging of the 3 V lithium back-up battery for the retain of the data received by the GPS module in the case of loss of external power.

In the same way, the line-driver/receiver interface circuits on the RS-485 bus on this board are also used to allow dialogue between the GPS receiver and the remote datalogger. In particular, this involves the adapting of the differential signals transmitted to the datalogger (TX+, TX-, 1PPS+ and 1PPS-) to a TTL logic level standard and then their adapting to a TLL logic level of +3 V. The same procedure, but from the opposite side, is followed to adapt the differential command signals transmitted from the datalogger to the GPS receiver (RX+, RX-, ON+ and ON-) and to the power supply activation circuit, from TLL logic levels at +3 V to differential levels on the RS-485 bus.

The pair of integrated devices used is the same as that for the interface board on the RS-485 bus for the datalogger side with the relevant changes in the input/output signals.

Also in this case, the signals needed for the dialogue with the GPS receiver must be converted to +3 V. Therefore, a pair of voltage step-down DC/DC converters are used, identical to those designed for the interface board on the

datalogger side, with the exception that the signals to be treated are RX and POWER_ENABLE (ON)[3].

ELECTRICAL INTERCONNECTIONS

The interface board for the RS-485 bus on the GPS receiver side has a DB9 male connector mounted on the printed circuit, which makes available the differential signals for the transmission of the GPS data (TX+ and TX-), the transmission of the 1PPS logic signal (1PPS+ and 1PPS-) and the reception of commands directed to the GPS receiver module (RX+ and RX-) coming from the datalogger, as well as a pair of activation signals (ON+ and ON-) that allow the remote turning on and partial turning off of the boards through the Willard software.

The GPS receiver side board also has a connector (*SamTech*®, FTSH-105-D2-L-DH header) mounted on the printed circuit on which the logic signals (TTL +3 V, negative logic) are available for transmission of the GPS data (TX) and of the 1PPS logic signal from the GPS receiver module, and for the reception of commands directed for the GPS receiver module (RX) coming from the Q330 datalogger after the voltage conversion from the RS-485 level. This connector also has an activation line that provides remote control for the turning on and the partial turning off of the board.

The interface board for the RS-485 bus on the datalogger side has two DB9 connectors (male and female) mounted on the printed circuit. These make available the differential signals for the transmission of commands destined for the GPS receiver (TX+ and TX-), the reception of the 1PPS timing signals (1PPS+ and 1PPS-), and the reception of the GPS data for the datalogger (RX+ and RX-) coming from the GPS receiver, as well as a pair of transmission signals (ON+ and ON-) that provide remote control for the turning on and the partial turning off of the board.

REFERENCES

Guardato S., Iannaccone G., 2006: Protocollo di comunicazione del sistema di acquisizione dati Quanterra Q330, Technical Report I (in italian) RT01-V4/UR11.

M12 Oncore – Engineering Note – Motorola Corp. – Rev. 1.0, Marh, 31, 1999.

Q330 Quick Start Guide – Kinemetrics Inc. – Doc. 304808 – Rev. A, June, 2004.

Q330HR Initial Operation and Overview of Support Tools – Kinemetrics Inc. – March, 14, 2006.

ACE III GPS – System Designer Reference Manual – Trimble Inc. – P/N 41265-00 – Rev. A – June, 2000.

---

[3] In this case, there is the need for a single switching voltage regulator at +5 V and there are no step-down DC/DC converter circuits, in agreement with the considerations indicated above.

Automatic analysis of seismic data by using Neural Networks: applications to Italian volcanoes

F. Giudicepietro[1], A. Esposito[1], L. D'Auria[1], M. Martini[1], S. Scarpetta[2]

[1] *Istituto Nazionale di Geofisica e Vulcanologia, Sezione di Napoli (Osservatorio Vesuviano), Italy*

[2] *Dipartimento di Fisica "E.R. Caianiello", Università di Salerno, Italy*

Abstract: The availability of the new computing techniques allows to perform advanced analysis in near real time, improving the seismological monitoring systems, which can extract more significant information from the raw data in a really short time. However, the correct identification of the events remains a critical aspect for the reliability of near real time automatic analysis. We approach this problem by using Neural Networks (NN) for discriminating among the seismic signals recorded in the Neapolitan volcanic area (Vesuvius, Phlegraean Fields). The proposed neural techniques have been also applied to other sets of seismic data recorded in Stromboli volcano. The obtained results are very encouraging, giving 100% of correct classification for some transient signals recorded at Vesuvius and allowing the clustering of the large dataset of VLP events recorded at Stromboli volcano.

INTRODUCTION

Active volcanoes produce a wide variety of seismic events related to different physical processes. A systematic and efficient monitoring of the volcanic activity helps in eruption forecasting and provides the scientific data to understand the structure and dynamics of the volcanoes.

A key contribute to the monitoring improvement is the automation of many functions, which can enhance the capability to analyze several types of data in short time and to determine the significant parameters for volcano status description. Thus, an effective automatic strategy for the detection and discrimination of seismic signals integrated into an analysis system in real time could considerably reduce the heavy and time-consuming work of the experts without affect the monitoring system reliability.

Several methods exist in literature for the detection and discrimination of different typologies of seismic signals (Hartse et al., 1995; Gitterman et al., 1999; Joswig 1990; Rowe et al., 2004). However, encouraging results have been rea-

ched also with the neural networks (Dowla et al., 1990; Cercone and Martin, 1994; Dowla, 1995; Tiira, 1999; Del Pezzo et al., 2003; Scarpetta et al., 2005). Our application mainly regards the Neapolitan volcanic area (Vesuvius, Phlegraean Fields). The aim is to apply the neural automatic system for discriminating the Volcano-Tectonic (VT) events from false signals, i.e. those generated by external sources (quarry o undersea artificial explosions) or natural events (thunders).

Moreover also the seismicity of the Stromboli volcano is taken into account. In this case, the neural system is able to classify other typologies of seismic signals, i.e. the explosion-quakes, the landslides, the volcanic microtremor and the Very Long Period (VLP) signals associated with the explosions.

A crucial aspect for a correct classification of the seismic signals by using a neural strategy is the data preprocessing or feature extraction step. Thus, it is important to describe appropriately the seismic signal through some characteristics or *features* which represent it in a compact and significant way allowing its analysis and the comparison with other data. In particular, we have considered the *Linear Predictive Coding* (LPC) (Makhoul, 1975) and a *Waveform Parameterization* which characterize adequately the seismic signal in the frequency and time domain respectively.

Finally, the coded signal obtained shows good discrimination using neural algorithms. In particular, for the classification task is applied a supervised neural network, the Multi-Layer Perceptron (MLP) (Bishop, 1995), while an unsupervised analysis of the seismic signals is performed using the Kohonen Self-Organizing Map (SOM) (Kohonen et al., 1996; Kohonen, 1997), in order to validate the neural automatic strategy as well as to cluster huge high-dimensional datasets with no a-priori information.

NEURAL NETWORKS

The Neural Networks (Haykin, 1999) are computational models inspired to human brain behavior. Figure 1 shows a biological neuron and its mathematical abstraction. The first model consists of several dendrites (input connections), which are connected via synapses to other neurons, and one axon (output connection). If the sum of the input signals exceeds a certain threshold value, then the neuron fires and an output signal is transmitted down the axon. The artificial neuron is an abstraction of biological neuron and represents the basic unit in an artificial neural network. It receives one or more inputs (representing the one or more dendrites), shown as $x_1, x_2, \dots x_N$ in the Figure 1, and sum them to produce an output. To each input is associated a weight, denoted as $w_1, w_2, \dots, w_N$, which correspond to the synaptic connections in the biological neuron. The weighted sum of each node is passed through a non-linear function known as an activation or transfer function, whose typical form is the sigmoid, but other kinds can be considered.
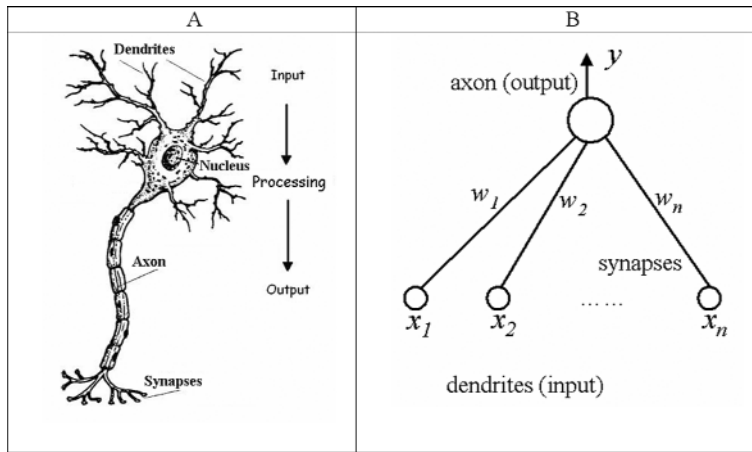
Fig. 1. The biological **(a)** and the artificial neuron **(b)**.

A neural network acquires the knowledge through a learning process and store it within inter-neuron connection (synaptic weights). Basically, learning is a process by which the network adapts itself to the external stimulus so that it can produce the correct output.

The general structure of a neural network is composed of:

– a set of processing units (input – hidden – output);
– an activation state $a_i(t)$ for each unit u_i at time t and an activation function $f_i(a_i(t))$ determining the network output;
– a connection scheme among the states or network architecture or topology (single or multi-layers);
– a learning algorithm which controls the network adaptation process to the external stimulus. An error function is defined on the net output characterizing the quality of the learning.

The NN implement the *learning by examples*, realized modifying the weights on the connections in order to minimizing the error function. In relation to the learning process, the neural networks can be *supervised* or *unsupervised*.

In a supervised neural network the learning process requires a pre-classified subset of data (i.e., a certain number of input/output examples) to train the net. Thus, the dataset will be divided into a training and testing set, containing different data from the training set, that will allow to test the network generalization capability. The model of supervised network used for our classification task is the Multi-Layer Perceptron (MLP).

In an unsupervised neural net the network output is unknown, meaning that the learning process does not need a previous data classification. The network uses neurobiological principles, such as Hebbian learning and competitive

approaches, to discover the similarity in the data structure. These networks allow to process huge datasets with high-dimensional input vectors. Thus, they are extensively used in data mining applications and large datasets clustering. The model of unsupervised network applied for our clustering task is the Self-Organizing Map (SOM).

Supervised Neural Network: MLP

For the classification of the seismic data we have used a feed-forward MLP (Figure 2). The network structure is organized in layers: an input layer, one or more hidden layers and an output layer.
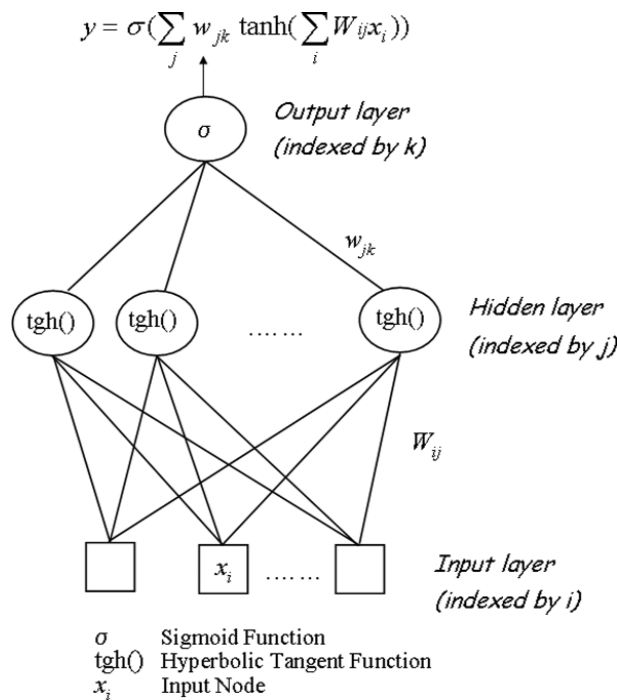

$$y = \sigma(\sum_j w_{jk} \tanh(\sum_i W_{ij} x_i))$$

Output layer
(indexed by k)

w_{jk}

Hidden layer
(indexed by j)

W_{ij}

Input layer
(indexed by i)

σ	Sigmoid Function
tgh()	Hyperbolic Tangent Function
x_i	Input Node

Fig. 2. The structure of a MLP network.

No intra-state connections are present in the network neither feed-back connections (i.e. feed-forward). The activation functions are the sigmoid (σ) for the hidden units and the Hyperbolic tangent (tgh) for the output units. The network output is calculated as:

$$y = \sigma(\sum_j w_{jk} \tanh(\sum_i W_{ij} x_i))$$

where W_{ij} are the weights on the connections from the input to the hidden layer and w_{jk} the weights on the connections from the hidden to the output layer. The network output has a probabilistic interpretation, i.e. it represents the probability of the net input to belong to a specific class of events.

If the discrimination is between two sets of signals the output layer has a single unit while for the three-class discrimination there will be three output units (Esposito et al, 2006 c).
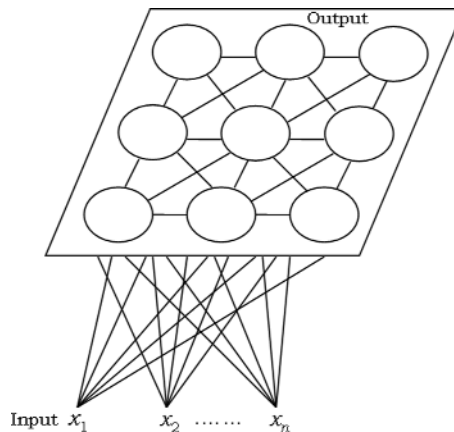
This kind of network is mainly applied when the data are not-linearly separable (Figure 3).

Linear separability Non-linear separability

Fig. 3. Linear and non-linear separability of the data.

Unsupervised Neural Network: SOM

For the unsupervised analysis and clustering of the seismic data we have exploited the Self-Organizing Map (SOM) (Figure 4).

Fig. 4. A schematic architecture of the SOM.

The SOM network presents an input layer and an output layer: each input is connected to all output neurons organized on a bi-dimensional grid. To each node is associated a prototype vector or weight vector and adjacent nodes are connected by a neighborhood function defining the map topology. The basic SOM algorithm (*winner take all*) is iterative and sequential. Formally, at each iteration *t*:

– an input vector x(t) is randomly extracted;
– the winning node *c* (Best Matching Unit) is found by comparing the input and prototype vector $\mathbf{m}_i(t)$ of all nodes (competitive aspect) by using the Euclidean distance metrics ($\| \cdot \|$). Explicitly, the BMU is identified by the condition:

$$\forall_i, \| \mathbf{x}(t) \text{-} \mathbf{m}_c(t) \| \leq \| \mathbf{x}(t) \text{-} \mathbf{m}_i(t) \|$$

– the winning node's prototype and its topological neighbors (cooperative aspect) are then updated according to the rule:

$$\mathbf{m}_i(t+1) = \mathbf{m}_i(t) + h_{c,i}(t)(\mathbf{x}(t) \text{-} \mathbf{m}_i(t))$$

where $h_{c,i}(t)$ is the Gaussian decreasing neighborhood function of distance between the *i*-th and *c*-th node on the map grid.

The SOM algorithm carries out a non-linear mapping of input data onto a two-dimensional grid preserving the most important topological and metric data relationships.
The SOM (Kohonen et al., 1996) has proven to be an efficient tool for data exploration tasks in various applications.

FEATURE EXTRACTION STAGE

An important phase of the data classification or clustering by using the neural networks is the pre-processing or feature extraction stage. The aim is to perform a transformation from data space into a feature space in order to remove redundancy from data, extract robust information and represent them in a compact form. The critical point is to identify the appropriate features which are significant for the specific application.
Usually, to characterize univocally the seismic signal we codify it in the frequency and time domain through spectral content and waveform features. The joint exploration of these two features is due to the fact that this information is the same used by the analysts in the visual classification of the events.
The procedures employ for extract this information from the signal are the Liner Predictive Coding (LPC), which gives the spectral features, and a Waveform Parameterization, which returns the temporal characteristics.

The LPC is a technique mostly used in audio signal processing and speech analysis for representing the spectral envelope of a speech signal in a compressed form, using the information of a linear predictive model. The basic idea of the LPC algorithm is to model each signal sample s_n at time n as a linear combination of a certain number p of its past values as shown below:

$$s_n^* = \sum_{k=1}^{p} c_k s_{n-k} + G$$

where c_k are the *prediction coefficients*, G is the *gain* and p represents the *model order*. The choice of p is problem dependent. The c_k estimation is obtained by an optimization procedure which minimizes the error between the real value of the signal sample and its LPC estimate. The coefficients c_k efficiently encode the signal frequency features.

For waveform feature extraction we use a function computed as the difference, properly normalized, between the maximum and minimum signal amplitudes within a 1-sec sliding window.

APPLICATION AREAS AND RESULTS

The seismic zones under examination are the Neapolitan volcanic area (Phlegraean Fields, Vesuvius) and the Stromboli volcano (Figure 5) (Giudice-pietro et al, 2007).
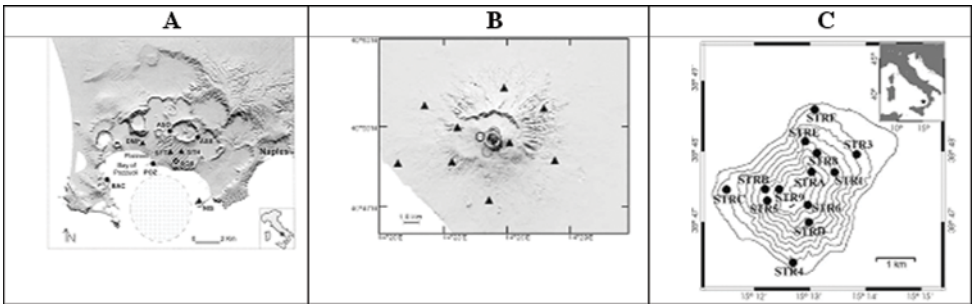
Fig. 5. The seismic areas under examination: the Phlegraean Fields **(a)**, the Vesuvius **(b)** and the Stromboli volcano **(c)**.

Phlegraean Fields

For the Phlegraean Fields (Del Pezzo et al, 2003) the intend is to distinguish between the artificial events, i.e. the undersea explosions generated by fisher-

men in Pozzuoli bay, and the volcano-tectonic earthquakes. In this case, for the feature extraction stage, we apply the LPC method and so we encoded the seismic signals using only their spectral features. For the classification we use a MLP-based discriminator. On the test set the neural net gave a classification performance of 92%, demonstrating a good generalization capability.

Vesuvius

For the Vesuvius (Scarpetta et al, 2005) the aim is to discriminate between the local seismic signals, which can cause false event detection, and volcano-tectonic earthquakes. In particular, we want to distinguish between couples of signal types recorded at the same seismic station. The classes of signals (Figure 6) under examination are:
– earthquakes
– quarry blasts – limestone
– underwater explosions
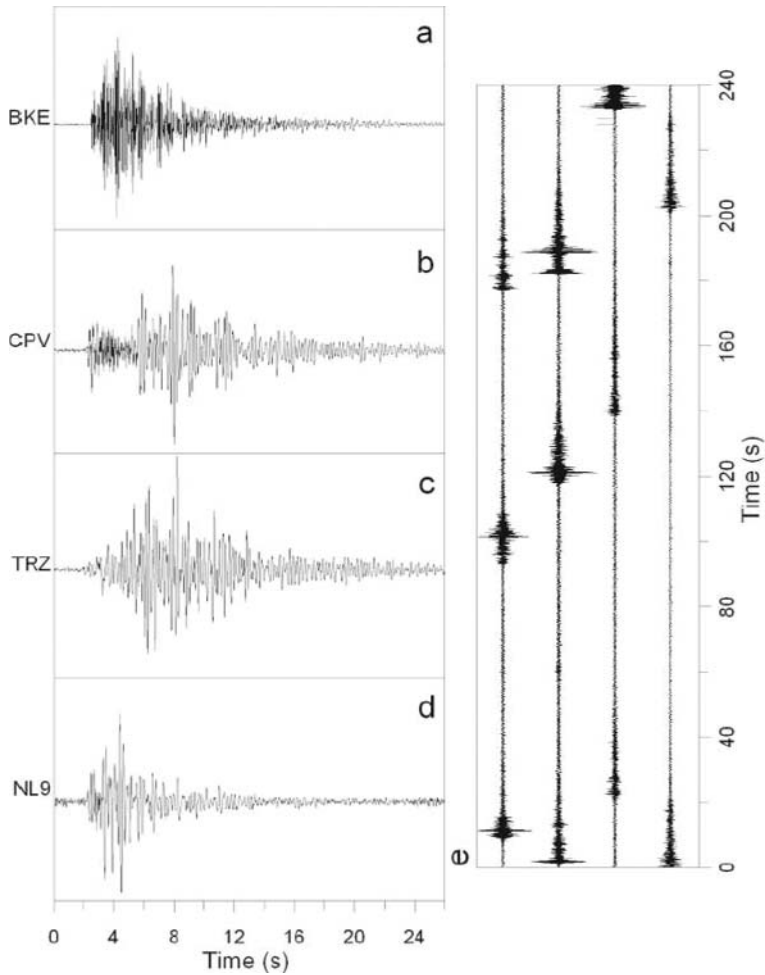– quarry blasts – pyroclastics
– thunders

In the preprocessing phase we use the LPC technique and a waveform parameterization representing the signals through their spectral and waveform features. For the classification task, we implement a specialized supervised two-class MPL-based automatic classifier for each couple of signal typologies.

Table 1 reports the MLP network Performance (percentage of correct classification on test sets) for each classification task.

It is possible to observe that the joint use of spectral and temporal features improves the net performance with respect to the previous work (Del Pezzo et al, 2003). This means that both features provide a significant contribution to the discrimination, and play a critical role in obtaining a reliable system.

On the Vesuvius dataset it has been realized also an unsupervised analysis (Masiello et al, 2005) using the SOM algorithm. In this case the task is more complex because the aim is not the two-class discrimination but the clustering of all the five typologies of events. Still the signals are preprocessed and so encoded by their frequency content, extracted by the LPC technique, and time-domain information, obtained by using the waveform parameterization. The SOM works without assumption about the data distribution and no external information, like previously expert classification, is provided to obtain the final output. Thus, the class labels have been used afterwards to aid in the interpretation of the results, without affecting the structures that have been found.

The results (Figure 7) show that the SOM gives a good representation of the cluster structure and a good separation of the five classes of signals identified by the experts.

Fig. 6. Typical waveforms of Vesuvius events: **(a)** VT earthquake (at BKE station), **(b)** undersea explosion (CPV), **(c)** quarry blast in pyroclastic caves (TRZ), **(d)** quarry blast in limestone caves (NL9), **(e)** a sequence of thunders (BKE).

Tab. 1. Net classification performance for the Vesuvius dataset.

| Classification Task	Performance
earthquakes/quarry blasts – limestone (NL9)	100%
earthquakes/underwater explosions (CPV)	99%
earthquakes/thunders (BKE)	98%
earthquakes/quarry blasts – pyroclastic (TRZ)	95%
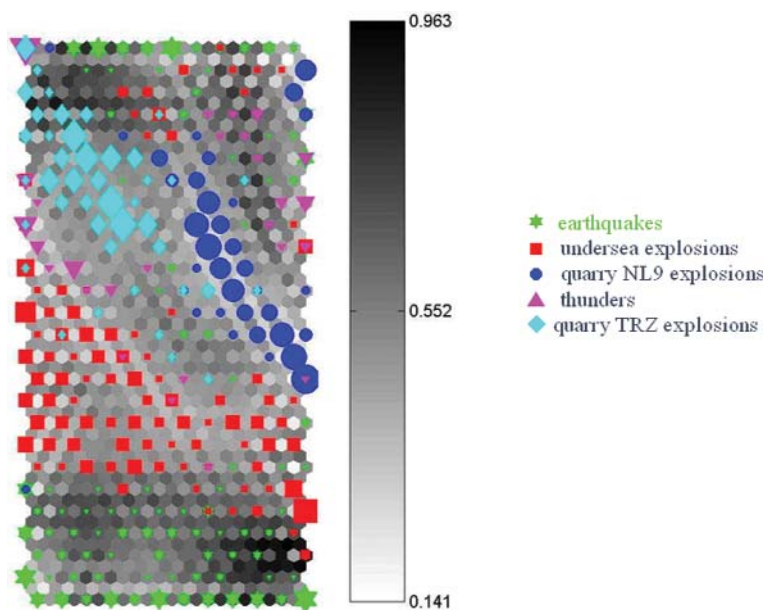
Fig. 7. The SOM map (with 312=26x12 nodes) for the Vesuvius data. The node's size represents the number of signals clustered in that node (data density). The gray hexagons separating the nodes indicates the Euclidean distances between the prototypes. Thus, high distance values correspond to dark gray hexagons.

Stromboli

For Stromboli (Esposito et al, 2006 c) the aim is to distinguish the seismic signals due to landslides from explosion-quakes produced by the volcano. In order to implement the method on a continuous data stream we also considered to separate these events from the volcanic microtremor that is the background of seismic wave-field of Stromboli volcano. The dataset is composed of:
– explosion-quakes
– landslides
– microtremor signals

Figure 8 shows the typical waveforms and the spectrograms of these signals. From the figure it is possible to note that while the explosion-quake (A) and the microtremor signal (C) exhibit limited frequency content (1-6 Hz), the landslide (B) has a broader spectrum. The explosion-quakes are characterized by a signal exhibiting no distinct seismic phases. Landslide signals are higher in frequency than the explosion-quakes and their typical waveform has an emergent onset. The microtremor is a continuous signal having frequencies between 1 and 3 Hz.
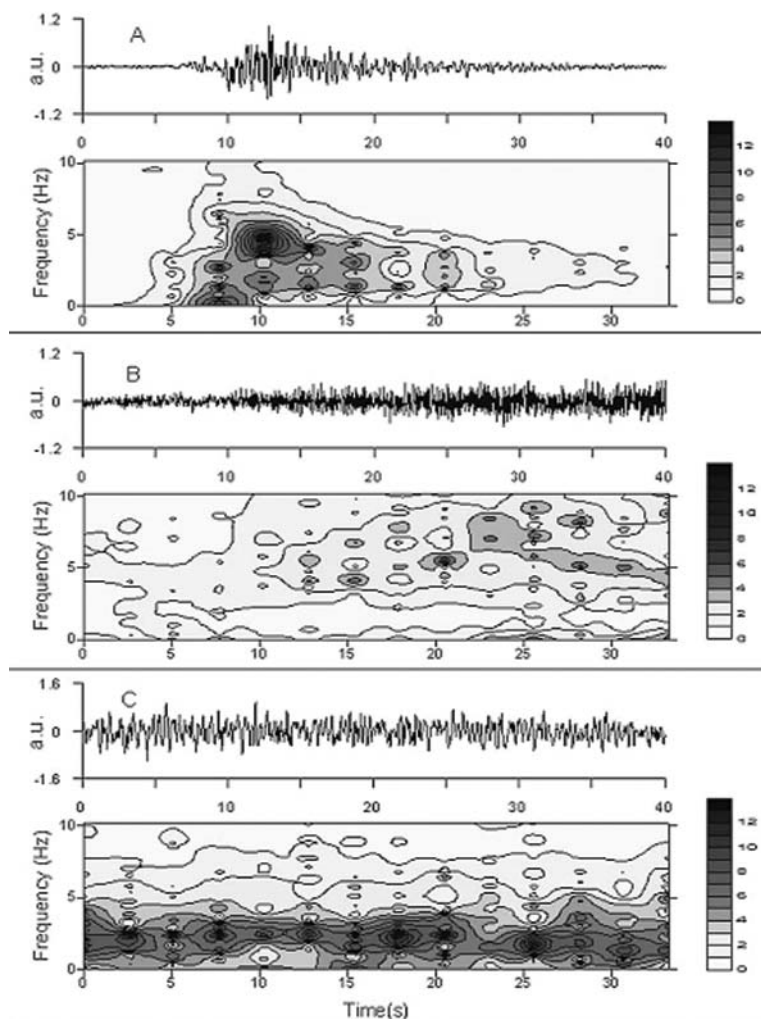
Fig. 8. Seismogram and spectrogram of Stromboli typical signals: explosion-quake **(a)**, landslide **(b)** and volcanic microtremor **(c)**.

After the feature extraction step, the signals are represented as feature vectors obtained using the LPC and the waveform parameterization. For the classification we implement a MLP-based classifier for the two and three-class discrimination tasks to distinguish between couples of events (explosion-quakes/landslides, landslides/microtremor and explosion-quakes/microtremor) and among landslides, explosion-quakes and microtremor signals. The obtained results are reported in Table 2.

Tab. 2. Net classification performance for the Stromboli dataset.

Classification Task	Performance
Explosion-quakes/Landslides	99.7%
Landslides/Microtremor signals	96.5%
Explosion-quakes/Microtremor signals	99.6%
Landslides/Explosion-quakes/Microtremor signals	97.2%

To determine the intrinsic structure of the data and to validate the parameterization strategy used for the MLP-based classifier, we analyzed the whole dataset of explosion-quakes, landslides and volcanic microtremor signals by employing the SOM algorithm (Esposito et al, 2006 b; Giudicepietro et al, 2006). The results (Figure 9) confirm that the unsupervised method is able to
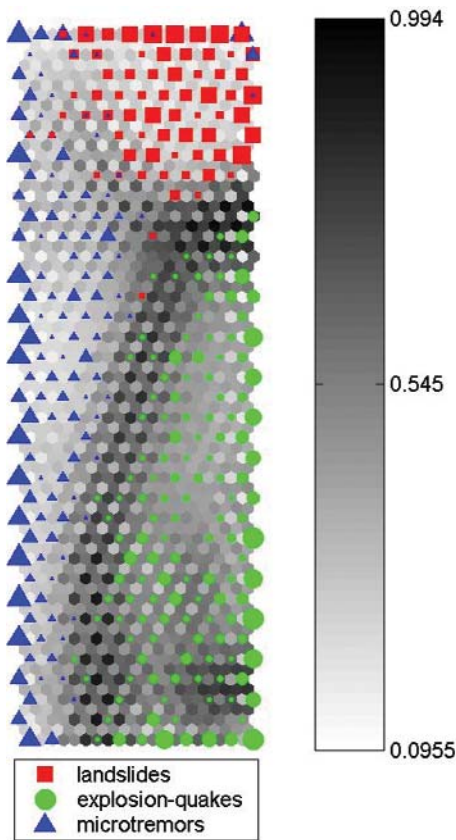

Fig. 9. The SOM map (with 396=36x11 nodes) for the Stromboli data. The node's size represents the number of the input samples in each node (the data density), while the gray coloring scale between colored symbols indicates the distances between the prototype vectors.

distinguish three clusters corresponding to the three classes of signals classified by the analysts, proving at the same time that the adopted parameterization strategy characterize appropriately the data.

Moreover, thanks to the installation at Stromboli of the broadband seismometers it has been possible to observe and record *Very Long Period* events (VLP), considered an interesting phenomenon for volcano monitoring. As first approach, we have realized an unsupervised analysis and clustering of these signals through the SOM network (Esposito et al, 2006 a), in order to cluster the events on the basis of their waveform similarity, that can be useful for improving the classification task. As consecutive step we investigated the relationships between the different classes of events and the associated physical processes. Therefore, in our analysis we have considered two large datasets: the first one contains about 4000 VLP events, recorded in about one-week period, while the second one is composed of about 100000 VLP signals, recorded in a two-year period (2003-2004).

As preprocessing step, all signals have been filtered in the VLP-band (0.05-0.5 Hz) and resampled at 2Hz and normalized allowing to represent the data in a compact and meaningful way. By using this feature extraction technique input vectors correspond to seismograms and the prototypes obtained from the analysis are similar to seismograms too. This facilitates the results comprehension and aids the estimation of the neural system performance.

The SOM map and the associate prototype plot obtained for the first and the second dataset are shown in the Figures 10 and 11 respectively. Observing them, we could conclude that the analysis of the VLP events in a short temporal interval, as a week, allows us to detect particular waveforms and to cluster them (Figure 10). In a large temporal range, the analysis can be not easy due to the complexity of the volcano behavior and the resulting variety of VLP waveforms which can be much different among them (Figure 11).

Finally, showing Stromboli an average of 200-300 explosions per day from different vents in the summit area of the cone and being the VLP events related to the explosions, it has been noted that different waveforms are often associated with different vents. Thus, we have applied the SOM algorithm to a set of 147 VLP events in order to explore the relationship between the vent producing the explosion and the associated VLP waveform (Esposito et al, 2007). These events have been recorded at Stromboli in a period between November and December 2005, when also digital infrared camera recordings were available. Therefore, from a visual inspection of the infrared camera images we have classified the VLPs on the basis of the vent producing the explosion, obtaining six vent-classes. The location of the vents is shown in a frame of the infra-red camera (Figure 12), where the label S stay for South, N for North and C for center.

For the feature extraction stage, the signals have been filtered in the VLP-frequency band (0.05-0.5 Hz), resampled at 2 samples/s and normalized obtaining a compact data representation.
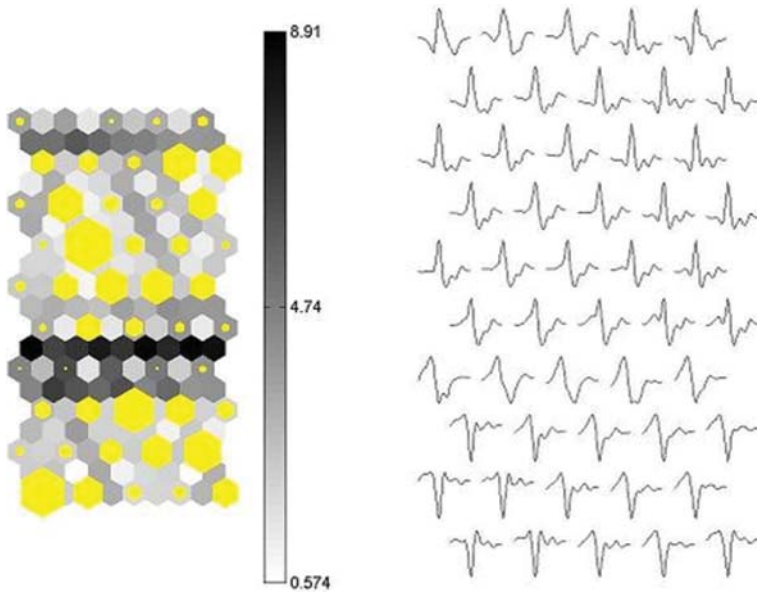
Fig. 10. The SOM map (with 50=10x5 nodes) and the associate prototypes' plot for the dataset of about 4000 VLP events.
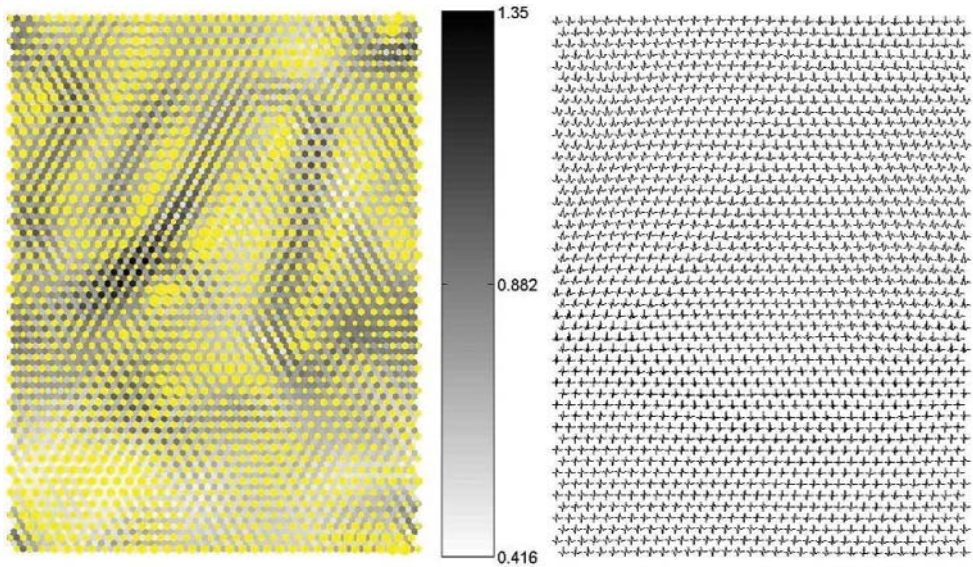

Fig. 11. The SOM map (with 48x33=1584 nodes) and the associate prototype plot for the dataset of about 100000 VLP events.
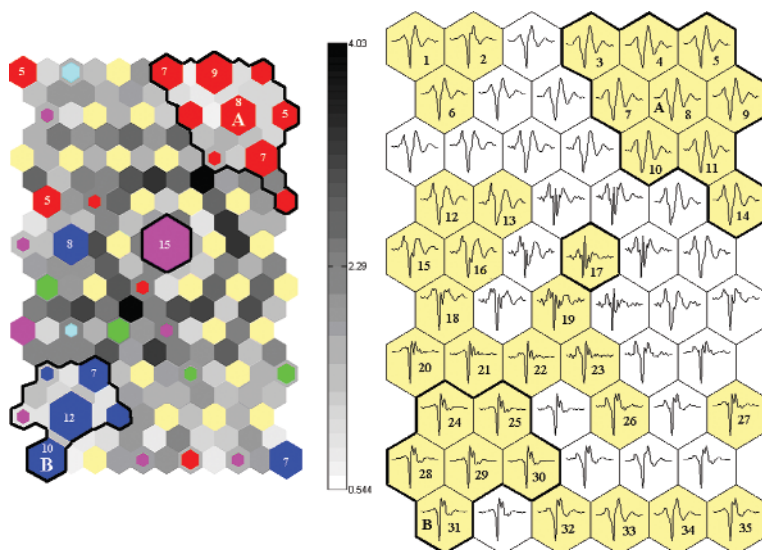
Then, we clustered the VLPs applying the SOM algorithm and obtaining the map shown in Figure 13.

In our analysis, three main clusters have been individuated on the map, evidenced by a thick black line in Figure 13. They roughly correspond to the three main active vents in the summit area of the volcano: S2; N1; N2b. The not
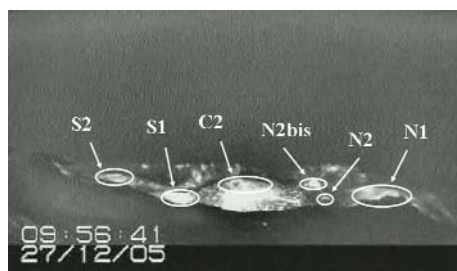
Fig. 12. The six vent-classes and their location.

Fig. 13. The SOM map (with 10x6=60 nodes) for the dataset of about 147 VLP events. The light yellow hexagons on the map indicate the empty nodes (zero data density). The size of the other colored hexagons represents the data density, indicated with the numerical labels for the nodes having more than 4 VLP waveforms. The gray hexagons represent the Euclidian distances between the prototypes. The different colors depict the predominant vent-class in each node: red for the S2 vent-class, blue for the N1, magenta for the N2b, green for the S1, light cyan for the N2. The prototypes corresponding to each node are shown in the right side of the plot. The white hexagons identify the nodes with zero data density (empty nodes), while the yellow hexagons show the prototypes of the nodes with one or more input signals. The thick black line on both images of the plot evidences the three main clusters identified on the map by the SOM algorithm.

perfect matching between the clusters discovered by the SOM and the activity of the principal vents is due to the not systematic correspondence between the vent producing the explosion and the seismic signature of the VLP.

Actually, the most of the VLP signals associated with a given vent shows a specific waveform type, however some of them have different shapes, sometimes similar to those usually associated with an other vent.

In conclusion the SOM method correctly clustered the VLP events on the basis of their waveform similarity. Thus, as future approach, we are planning to apply this method, able to process large datasets, for the analysis and classification of the whole dataset of more than 300000 events recorded at Stromboli volcano in the last 4 years. Actually, the analysis of such a dataset can be only approached by automatic unsupervised techniques.

REFERENCES

Bishop C. (1995) – Neural Networks for pattern recognition, Oxford University Press. 500 pp.

Cercone J.M. and Martin J.R. (1994) – An application of neural networks to seismic signal discrimination, Phillips Laboratory, report no. 3, PL-TR-94-2178, Hanscon, AFB, Massachusetts.

Del Pezzo E., Esposito A., Giudicepietro F., Marinaro M., Martini M. and Scarpetta S. (2003) – Discrimination of earthquakes and underwater explosions using neural networks, Bull. Seism. Soc. of Amer., BSSA Vol. 93, n.1, pp.215-223, 2003.

Dowla F.U., Taylor S.R. and Anderson R.W. (1990) – Seismic discrimination with artificial neural networks: preliminary results with regional spectral data, Bull. Seism. Soc. Am. 80, 1346-1373.

Dowla F.U. (1995) – Neural networks in seismic discrimination, in Monitoring a Comprehensive Test Ban Treaty, E.S. Husebye and A.M. Dainty (Editors), NATO ASI, Series E, Vol. 303, Kluwer, Dordrecht, The Netherlands, 777-789.

A. M. Esposito, F. Giudicepietro, L. D'Auria, S. Scarpetta, M. Martini, C. Rowe, M. Marinaro (2006 a) – Unsupervised Neural Classification of Seismic Events for Volcano Monitoring. Poster Sessions in Cities on Volcanoes 4 Conference (COV4) – SYMPOSIUM IV, SESSION B: VOLCANO MONITORING – January 23-27 2006, Quito.

A. M. Esposito, S. Scarpetta, F. Giudicepietro, S. Masiello, L. Pugliese, A. Esposito (200 b) – Nonlinear Exploratory Data Analysis Applied to Seismic Signals. B. Apolloni et al. (Eds.): WIRN/NAIS 2005, LNCS 3931, pp. 70-77, 2006, Springer-Verlag Berlin Heidelberg 2006.

A. M. Esposito, F. Giudicepietro, S. Scarpetta, L. D'Auria, M. Marinaro, M. Martini (2006 c) – Automatic discrimination among landslide, explosion-quake and microtremor seismic signals at Stromboli volcano using Neural Networks. Bull Seismol. Soc. Am. (BSSA) Vol. 96, No. 4A, pp. 1230-1240, August 2006, doi: 10.1785/0120050097.

A. M. Esposito, F. Giudicepietro, L. D'Auria, S. Scarpetta, M. Martini, M. Marinaro, M. Coltelli (2007) – Automatic Analysis of VLP Seismic Signals by using Unsupervised Neural Network. Poster in the Session "New Developments in Semi-automatic and Fully-automatic Tools in Seismic Data Analysis" of the 2007 SSA Annual Meeting, 11-13 April 2007, Big Island, Hawaii.

F. Giudicepietro, A. M. Esposito, S. Scarpetta, L. D'Auria, M. Marinaro, M. Martini (2006) – Discrimination among Landslide, Explosion-Quake and Volcanic Microtremor Seismic Signals at Stromboli Volcano. Poster Sessions in Cities on Volcanoes 4 Conference (COV4) – SYMPOSIUM IV, SESSION B: VOLCANO MONITORING – January 23-27 2006, Quito.

F. Giudicepietro, A. M. Esposito, L. D'Auria, M. Martini, S. Scarpetta, M. Marinaro (2007) – Neural Analysis for Automatic Classification of Seismic Data: Applications to the Seismicity of Italian Volcanoes. Abstract in the Session "New Developments in Semi-automatic and Fully-automatic Tools in Seismic Data Analysis" of the 2007 SSA Annual Meeting, 11-13 April 2007, Big Island, Hawaii.

Gitterman Y., Pinky V. and Shapira A. (1999) – Spectral discrimination analysis of Eurasian nuclear tests and earthquakes recorded by the Israel seismic network and the NORESS array, Phys. Earth. Planet. Interiors 113, 111-129.

Hartse H.E., Phillips W.S., Fehler M.C. and House L.S. (1995) – Single-station spectral discrimination using coda waves, Bull. Seism. Soc. Am. 85, 1464-1474.

Haykin, S. (1999) – Neural Networks: A Comprehensive Foundation, 2nd ed. (Englewood Cliffs, NJ: Prentice-Hall).

Joswig, M. (1990) – Pattern recognition for earthquake detection, Bull. Seism. Soc. Am. 80, 170-186.

Kohonen T., Hynninen J., Kangas J., Laaksonen J. (1996) – SOM_PAK: The self-organizing map program package. Report A31. Helsinki University of Technology, Laboratory of Computer and Information Science, Espoo, Finland. Also available in the Internet at the address http://www.cis.hut.fi/research/som_lvq_pak.shtml.

Kohonen T. (1997) – Self-Organizing Maps, Series in Information Sciences, Vol. 30. Springer, Heidelberg. Second ed. 1997.

Makhoul J. (1975) – Linear prediction: a tutorial review, Proc. IEEE 63, 561-580.

S. Masiello, A. M. Esposito, S. Scarpetta, F. Giudicepietro, A. Esposito, M. Marinaro (2005) – Application of Self Organized Maps and Curvilinear Component Analysis to the Discrimination of The Vesuvius Seismic Signals. In Proceedings of the International Workshop on Self Organizing Maps WSOM2005, Paris, France, pp. 387-396, 5-8 September 2005.

Rowe C.A., Thurber C.H. and White R.A. (2004) – Dome growth behavior at Soufriere Hills volcano, Montserrat, revealed by relocation of volcanic event swarms, 1995-1996, Jour. Volc. Geotherm. Res. 134, 199-221.

Scarpetta S., Giudicepietro F., Ezin E.C., Petrosino S., Del Pezzo E., Martini M. and Marinaro M. (2005) – Automatic Classification of seismic signals at Mt. Vesuvius Volcano, Italy using Neural Networks, Bull. Seism. Soc. Am. 95, 185-196.

Tiira T. (1999) – Detecting teleseismic events using artificial neural networks, Comp. Geosci. 25, 929-939.

CUMAS (Cabled Underwater Module for Acquisition of Seismological data): a new seafloor module for geohazard monitoring of the Campi Flegrei volcanic area

G. Iannaccone[1], S. Guardato[1], M. Vassallo[2], L. Beranzoli[1]

[1] *Istituto Nazionale di Geofisica e Vulcanologia, Napoli, Italy*

[2] *Dipartimento di Scienze Fisiche, Università degli Studi di Napoli Federico II, Italy*

INTRODUCTION

CUMAS (Cabled Underwater Module for Acquisition of Seismological data) is an underwater module that is equipped with different types of sensors that have been developed for the acquisition of geophysical signals on the shallow seafloor, for geohazard monitoring in volcanic areas. It was conceived for the specific application in the Campi Flegrei caldera (southern Italy), where the main features of the present volcanic activity consist of slow soil movements (bradyseism) accompanied by intense and shallow seismic activity.

The aim of CUMAS is to:
– continuously acquire geophysical and oceanographic data on the seafloor according to a single time reference, and to store them on hard disk;
– transmit the acquired data in real time to an acquisition centre on land;
– receive commands from the land centre and modify its acquisition configuration accordingly.

The sensors installed in the module comprise: a broad-band seismometer and hydrophone to record local earthquakes related to volcanic activity and artificial explosions; and physical oceanographic sensors for the long-term monitoring of the water current system, which are also useful for seafloor seismic microtremor studies. A further task consists of testing the feasibility of the use of water pressure measurements at the seafloor to detect changes in the water column pressure that are potentially related to bradyseismic activity.

The module is connected via an electromechanical cable to a previously deployed buoy (elastic beacon) equipped with an electrical supply and a Wi-Fi communication system to ensure the transfer of the seafloor data to the land acquisition centre in Naples.

CUMAS has been developed for the system to be installed within the sea sector of the Campi Flegrei caldera, at 97 m depth, from 2 to 3 km from shore and about 4 km from the land acquisition centre (Figure 1).
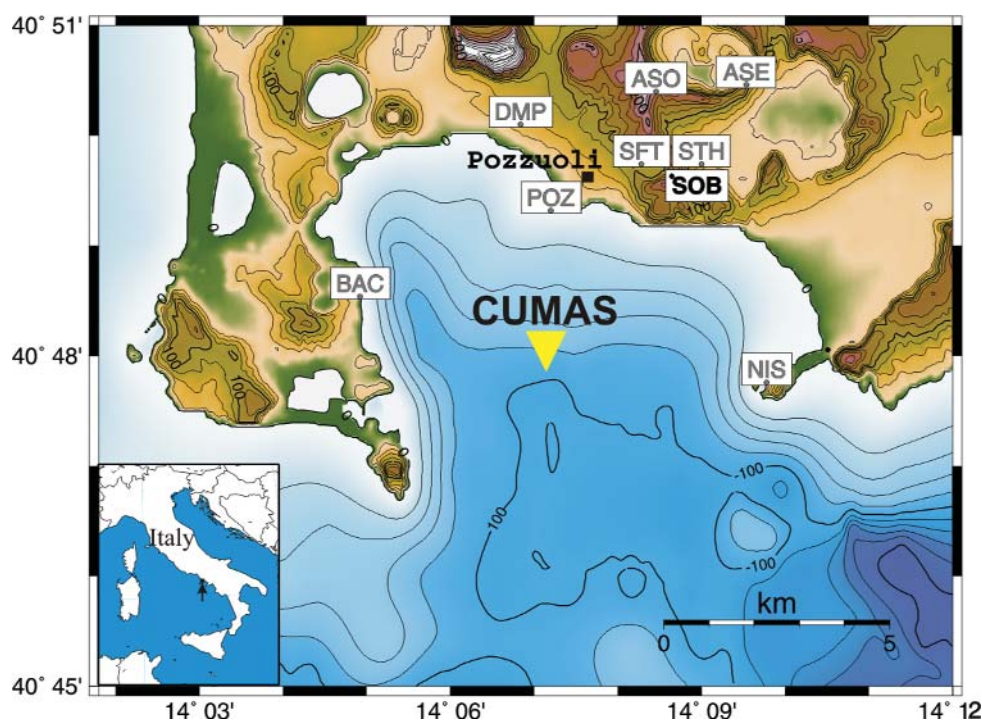
Fig. 1. The Gulf of Pozzuoli area and the site (yellow triangle) selected for the deployment of CUMAS. White rectangles represent seismic stations of the monitoring system managed by Osservatorio Vesuviano.

All these features ensure that CUMAS is fully integrated into the centralised monitoring system of the Neapolitan volcanic areas (Vesuvio, Campi Flegrei and Ischia Island) that are managed by the Osservatorio Vesuviano-INGV. It also represents the first step towards the extension of the present land-based Campi Flegrei monitoring networks that operate in the marine sector of the caldera, and which cover something over one third of the volcanic area.

The features of CUMAS

The CUMAS set-up consists of a steel frame in the shape of a truncated pyramid of about 1 m in height and with a square base of 1 m per side. The total

weight including the equipment is about 430 kg in air (320 kg in water) (Figure 2). The structure, which is made from welded open profiles, has a lower section with vertical mountings, surmounted by an upper section in the form of

Fig. 2. The fully equipped CUMAS set-up in the laboratory during tests; the acquisition system was kept out of its frame temporarily to check on its operation.

a truncated pyramid. In the middle section (between the vertical section and the pyramidal section), there are four ballast plates have the double function of stabilizing the structure during its release and to provide controlled sinking into the superficial sediment of the seabed, on the basis of our knowledge of the mechanical characteristics of the seabed itself.

The seismometer and the cylinder containing the electronics are located in the lower section of the structure, while the rest of the instrumentation is installed in the upper section. The container for the electronics is made of aluminium, type 6082 T6. Moreover, the structure is protected by 8 sacrificial anodes in zinc positioned on each horizontal element. The number of anodes needed was determined according to the DNV RP B401 "Cathodic Protection Design" Normative.

Sensors

The following sensors have been installed within the CUMAS' structure:
a) seismic sensor;
b) hydrophone;
c) current meter;
d) pressure gauge;
e) status and control sensors.

Seismic sensor

This comprises a three-component, broad-band seismometer, model Güralp CMG-40T OBS (30 s, 50 Hz), housed in a 16 cm glass sphere with an auto-leveling platform.
It is equipped with a ±30° microprocessor-controlled leveling system, with an internal three-axis magnetometer for orientation measurements and the automatic calibration and tilt compensation system.

Hydrophone

A broad-band hydrophone, model SQ03 Sensor Technology (1 Hz ÷ 65 kHz), equipped with an integrated pre-amplifier with 40-dB gain.
Our interest is concentrated around the acquisition of signals of very low frequencies (1-10 Hz) detected by the hydrophone.
The hydrophone has a nominal voltage sensitivity of 162.0 ±1 dBV, 1 µPa at 20 °C and an operating depth down to 650 m. Its typical horizontal-vertical directivity is of ±2 dB.

Current meter

A single-point, three-component acoustic wave/current meter, model 3D-ACM Falmouth Scientific, Inc.
The current meter ensures the acoustic measurement of vector-averaged current speeds and directions. It is also capable of high-accuracy temperature measurements (resolution, 0.01 °C), with an ASCII serial data output via an RS-232 interface.
The specifications of these sensors include:
– velocity range from 0 to 600 cm/s (resolution, 0.01 cm/s);
– direction and 0° to 30° two-axis tilt measurement (resolution, 0.01°);
– vector averaging period from 15 s to 1 h;
– MEMS pressure transducer (resolution, 0.01% FS).

Pressure gauge

The pressure gauge is a Series 8000 Paroscientific, Inc., 8CDP200-I model, characterised by:
– an accuracy better than 0.01% FS;
– 10-8 resolution (resolution/sample time depends on the integration time);
– low power.

Status and control sensors

These include tilt and heading sensors, for the measurement of the real module attitude on the seafloor, and status sensors for the monitoring of the internal status of the vessel (e.g., internal temperature, power absorption, water intrusion).

Data acquisition

Data from the broad-band seismic sensor and from the hydrophone are acquired by a Q330 Kinemetrics Quanterra digitiser at a rate of 100 sps, which is equipped with an external hard disk (Baler PB14F, 20GB) as the local mass storage. The digitiser is installed inside the electronics container. The Q330 consists of a six-channel, ultra-low-power $\Delta\Sigma$ 24-bit A/D resolution with DSP, 8 Mb of RAM memory, a GPS receiver, and a telemetry application for real-time data transmission. The Q330 datalogger has an integrated GPS receiver, for correct synchronization of the internal clock, and an external GPS antenna with a 5-m cable. With our system configuration, due to the more than 100-m distance between the GPS antenna installed on the buoy and the Q330 positioned in the vessel on the seabed, this set-up could not be used. Therefore, it was necessary to design two electronic boards (Guardato and Iannaccone, 2007) that allow the external use of the same remotely mounted GPS antenna-receiver combination of the Q330 datalogger (unplugged from this), via an RS-485 interface, allowing a much greater distance between the antenna and the recorder. The data from the external GPS transmission are sent over a 120-Ω-impedance, twisted-pair cable (length up to 3 km, at 9600 bps) via different transmitting-receiving lines, in addition to a 1 PPS marker from the GPS receiver and the power control line for the RS-485 interface.
The digital output from the sensors (current meter, pressure gauge, and status and control sensors) are acquired by an embedded computer (MOXA UC-7408) equipped with Linux OS, via an RS-232 port. This embedded CPU features eight RS-232/422/485 serial ports, an eight-channel digital input, an eight-channel digital output, dual 10/100 Mbps ethernet ports, and USB, PCMCIA and CompactFlash interfaces.

Cable

The electromechanical cable connecting CUMAS to the buoy has a diameter of 23 mm and weighs 630 g/m; its length is 140 m. It is dedicated to the transportation of the overall signals (ethernet 10/100 Mbps, four differential pairs of RS-485 ports for the GPS) and the power distribution (48 V DC). The cable was designed also to be used for the installation and later recovery of the system. To simplify these operations, the cable was divided into two sections with underwater electrical connectors: 16-pin, wet-mateable, MCIL16M and MCIL16F connectors.

TECHNICAL CHARACTERISTICS OF THE BUOY

The elastic beacon is a semi-rigid structure with a metallic pole of 20 m in height (diameter, 0.25 m) that is fixed to the sea bottom by an antitorsion steel cable (diameter, 40 mm), to a ballast of 17 tons. The pole is kept vertical by a plastic submerged float (diameter, 2.1 m; length 3.2 m) that can be adjusted to a pear shape, according to the local sea conditions. The buoy is equipped with a two square platforms mounted at 2 and 4 m above the level of the sea, which are equipped with ten batteries that are recharged by six solar panels (110 W each). For the charging of the solar panels, the reduced possibility of torsional movement around the vertical axis of the elastic beacon still allows a precise placing of the equipment on the tower where it is best exposed to the sun at a precise angle, therefore ensuring a powerful supply. On the space (1.5 m2) of the square tower, there is a 400-W aeolic generator (Air-X Marine). A meteorological station is also mounted on the tower, providing local meteorological measurements (e.g., barometric pressure, wind velocity and direction, rain-meter, thermometer), to allow the correlation of the air and seafloor data. A 19-inch enclosure for the rack-mountable electronic equipment contains an 802.11g wireless WLAN bridge (Cisco Aironet 1300 series) equipped with an omni-directional antenna, for the data transmission to the land, and other added equipment, including the RS-485 interface with the Q330 GPS receiver and antenna, an embedded CPU, an interface board connected to the CPU with electronic switches used to enable/ disable the power to the overall set-up and to the instrumentation, an Ethernet 10/100 Mbps hub, and a DC/DC power converter (12 V to 48 V, 50 W).

POWER REQUIREMENTS

The power requirements of CUMAS

The power requirements for the devices (voltage range specifications included) embedded in the vessel and for the sea bottom sensors are shown in Table 1.

Tab. 1. Sea-bottom power requirements.

Device	Voltage (V)	Power (W)
Q330 datalogger	10÷18	1.0
PB14F Baler	10÷18	6.0 max.
RS-485 GPS interface	10÷18	0.3
CPU Moxa UC-7408	12÷48	6.0 max.
10/100 Mbps hub	10÷18	2.0
Tilt & heading Ostar-Compass	6÷16	0.5
Status card	12	0.2
CMG-40T-OBS seismometer	10÷18	1.7
Pressure gauge transducer	6÷16	0.2
SQ03 hydrophone	10÷18	0.1
3DACM current-meter	7÷24	0.4
Total		**18.4 max.**

The total consumption of the system is therefore around 12 W, with peaks to 18.4 W due to the disc unit of the PB14F Baler.

To minimize the drop in resistance along the electromechanical cable, the whole length of the cable has a continuous tension of 48 V, which satisfies the basic security criteria. In the electrical panel at the surface on the tower of the buoy, a DC/DC step-up converter is installed with 12 V in and a nominal 48 V out. Considering an additional peak power margin of 20%, which corresponds to about 4 W, the DC/DC step-down in the underwater module should have a nominal power of around 23 W; on this basis, a DC/DC converter with a nominal power of 50 W was chosen (model PS50-48S12 PowerSolve).

Power requirements of the buoy

The power requirements for the various loads included on the 19-inch rack enclosure on the tower of the buoy are shown in Table 2.

All of the power supplies pass through the switching board and are protected by a 2-A rapid fuse, while a 1.5-A fuse has been inserted on the main power line of 48 V. The minimum entry tension of the underwater module instrumentation was obtained considering the maximal fall in tension along the cable that can be generated by the maximum current, which must be able to guarantee a transfer of 20 W. Considering this peak power that is needed to run the cable and the underwater module, and the ca. 20 W that is needed for the DC/DC power supply of the control panel on the platform of the buoy, the maximum output power needed by the main power supply system comprising the battery rechargers with charge regulators and by the ten back-up batteries is a little over 40 W.

Tab. 2. Surface power requirements.

Device	Voltage (V)	Power (W)
CR200 meteorological datalogger	7÷16	0.03
Pressure transducer	9÷33	0.01
Wind direction & speed sensor	10÷15	0.1
Rain meter	n/a	none
Temperature sensor	10÷16	0.01
RS-485 GPS interface (including GPS receiver and active antenna)	10÷18	1.5
UC-7408CPU Moxa	12÷48	6.0 max.
10/100 Mbps hub	10÷18	2.0
Tilt & heading Ostar compass	6÷16	0.5
Status card	12	0.2
Bridge Cisco WLAN	10÷18	10.0
Total		20.4 max.

The electrical power supply chain of the system was designed according to the expected consumption by the various users, and comprises:
– 11 Haze-Sonnenshein back-up batteries of 12 V, 110 Ah (one of which is for the exclusive use of the sea light as a visual warning);
– electromechanical cable with its resistance fall (about 4 Ω);
– step-down DC/DC converter for the power supply to the underwater module.

Under these conditions, it is possible to guarantee continuous autonomous functioning for more than 48 h in the case of a total absence of solar or wind energy; indeed, the continuous consumption that needs to be supplied corresponds to a current of around 600 mA at 48 V DC. The nominal capacity of 110 Ah of each of the batteries (when fully charged) allows the continuous functioning in the absence of sunlight for at least three days. To all of this, there should also be added the energy provided by the wind generator, meaning that it is possible to guarantee about a week of autonomy of the system under all atmospheric conditions.

EXPECTED RESULTS

CUMAS represents the first marine node of an integrated land-sea network for geo-hazard monitoring in the Campi Flegrei volcanic area. The CUMAS data, which is continuously sent to the land acquisition center, will be integrated with those from to the whole of the surveillance system. In particular, the seismological data will be used jointly with the land seismic network and will contribute towards improvements to the localization of earthquakes occurring

in the sea sector of the caldera. Furthermore, and as demonstrated by Vassallo et al. (2007) this use will enhance the seismic detection capabilities for low energy earthquakes that are usually masked by the high level of anthropic seismic noise seen in this area. The pressure gauge measurements, which are corrected for tidal effects and complemented with coastal tide gauge network data, can for the first time estimate the vertical seafloor bradyseismic movement, which until now has only been measured on land.

REFERENCES

Vassallo M., Bobbio A., Iannaccone G., 2006. Analysis of broad band seismic data acquired under the sea of Pozzuoli Gulf (Southern Italy). European Geophysical Union General Assembly, Vienna (Austria), April, 2-7, 2006.

Vassallo M., Nisii V., Zollo A., Iannaccone G.. Morphology and depth of reflectors from 2D non-linear inversion of seismic data. Geophysical Exploration of the Campi Flegrei (Southern Italy) Caldera' Interiors: Data, Methods and Results (edited by A. Zollo, P. Capuano and M. Corciulo) Publisher Doppiavoce ed., Napoli., 2006.

Use of Forward Looking InfraRed thermal cameras at active volcanoes

L. Lodato[1], L. Spampinato[1], A.J.L. Harris[2], J. Dehn[3], M.R. James[4],
E. Pecora[1], E. Biale[1], A. Curcuruto[5]

1 Istituto Nazionale di Geofisica e Vulcanologia, Sezione di Catania, Catania, Italy

2 HIGP/SOEST, University of Hawaii, Honolulu, Hawaii, USA

3 University of Alaska Fairbanks, Alaska, USA

4 Environmental Science Department, Institute of Environmental and Natural Sciences, Lancaster University, Lancaster, United Kingdom

5 Department of Engineering, University of Catania, Catania, Italy

INTRODUCTION

Nowadays, thermal imaging has become a common remote sensing tool for monitoring active volcanoes. The study of temperature variations within open-conduit systems, at eruptive fissures, active vents, domes, lava lakes, lava fields and other volcanic features has proven fundamental to better understand volcanic system behaviour over the short and long terms (Harris and Stevenson, 1997; Oppenheimer and Yirgu, 2002; Calvari et al., 2004; Wadge et al., 2006). At INGV Catania Section, thermal imaging has been applied at Mt Etna, Stromboli, Vulcano and Panarea since 2001.

The instruments used are thermal cameras manufactured by FLIR (Forward Looking InfraRed) and consist in uncooled bolometers that are sensitive within 7.5 and 13 μ wavelengths. Thermal cameras are based on the capability to detect radiation emitted by bodies according to Planck's Law.

In particular, the camera we used is a FLIR thermal camera A 40 M Ethernet with a focal plane array uncooled bolometer (320 x 240 pixels), and a spectral range between 7.5 and 13 micrometers (Figure 1.). It has a standard optics 24° with spatial resolution (IFOV, instantaneous field of view) of 1.3 mrad, a horizontal view of 24° and a vertical view of 18°. This camera has also been equipped with optional filter to measure temperature values up to 1500°C with the possibility of setting up different temperature ranges.

The thermal camera can record and transfer in real time via wi-fi radiometric frames in JPG format of the observed eruptive activity according to some environmental parameters, such as external temperature, air humidity and emissivity and allows the vision of volcanic activity both day and night. Temperature range varies between 0 e 500° C and the emissivity value $\varepsilon = 1$. To correct the temperature of all pixels from the atmospheric attenuation

Fig. 1. Thermal camera FLIR A 40 M.

effects, we considered atmospheric parameters, such as air temperature and air humidity, in addition to the introduction of the path length (400 m) in the camera software. In fact, the radiations detected by the FLIR thermal cameras, that work in the spectral band between 7.5 e 13 μm, are affected by the absorption factor from the water spectrum, which is predominant in this band; particularly at La Fossa crater where the water content in the fumaroles is higher than the other gas species.

Because of the necessity to correct the radiometric data from the atmospheric factors in real-time, we installed a meteorological station able to interface with the camera to provide atmospheric parameters for the auto-calibration.

THERMAL CAMERA INSTALLATION AT LA FOSSA CRATER, VULCANO (AEOLIAN ARCHIPELAGO)

Between 18 and 20 July 2005, L. Lodato and L. Spampinato from INGV-Catania, A.J.L. Harris from SOEST, University of Hawaii, and J. Dehn University of Fairbank, Alaska, carried out two days of thermal measurements at La Fossa crater (Vulcano Island) (Figure 2).

The survey had a dual purpose:

1. to continue thermal measurements at fumaroles performed by Harris since 1994, using infrared handheld thermometers and thermocouples (Harris and Stevenson, 1997; Harris and Maciejewski, 2000);
2. to repeat the same measurements by using FLIR thermal cameras, to test their ability for monitoring La Fossa's fumarole field.

Measurements involved four FLIR thermal cameras imaging the Lower fumarolic zone (Figure 2). Cameras were aligned in a NE-SW direction on the opposite inner flank (southern) of the crater, at distances of 50, 100, 200 and
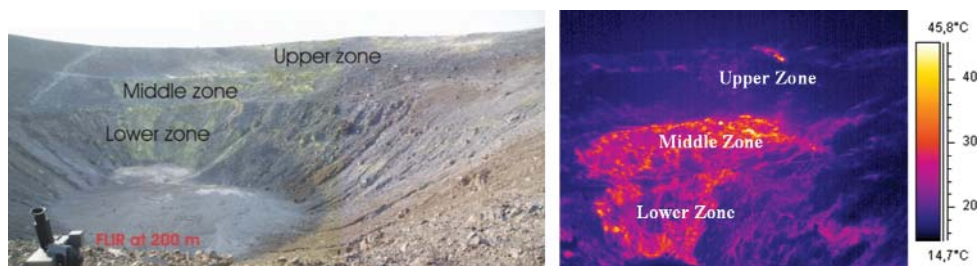
Fig. 2. Photo and thermal imaging of La Fossa's fumarole field taken from the opposite inner flank of the crater. Three main fumarolic zones, Lower, Middle and Upper zone are distinguished according to Harris and Maciejewski (2000).

400 m from the Lower zone. Thermal cameras were tripod mounted and synchronized with GMT time. GPS points for each measurement station were recorded.

For applying thermal cameras, internal calibration for atmospheric corrections of temperature for all pixels, air temperature and relative humidity were measured in situ using handheld hygrometers. Emissivity used was 0.9751, according to Harris and Maciejewski (2000) and the acquisition frequency chosen was 10 seconds.

Additionally, a 12-degree lens was also applied to the 400 m distant FLIR. This lens increased the camera magnification by a factor of two, corresponding to half of the real pathlength (Harris et al., submitted to Bulletin of Volcanology in 2007).

During the second day of measurements, a fifth thermal camera located at ~ 350 m distance from the Lower zone was used. The instrument was a FLIR A 40 M thermal camera, the kind used at Mt Etna and Stromboli permanent stations.

The analysis of thermal images collected during the entire survey proved the reliability of thermal cameras for monitoring La Fossa fumarole field. This provided us the input to develop a methodology to improve thermal data collection and the monitoring system at Vulcano fumaroles.

Indeed, the opportunity to install a permanent thermal camera could haveenabled us the possibility to:
1. record thermal images in continuous and real-time,
2. acquire images with the same easily comparable geometry,
3. control the whole system from INGV Catania main site.

Thermal camera installation

A year later, in June 2006, an A 40 FLIR thermal camera was installed at almost the same 400 m distant site from the Lower zone, chosen during the

thermal survey of the previous year. For this distance, the effective pixel size resulted ~ 50 x 50 cm. This location allowed imaging the Lower, Middle and Upper zone, and part of the fumaroles located at the northeastern crater rim (Figure 3).
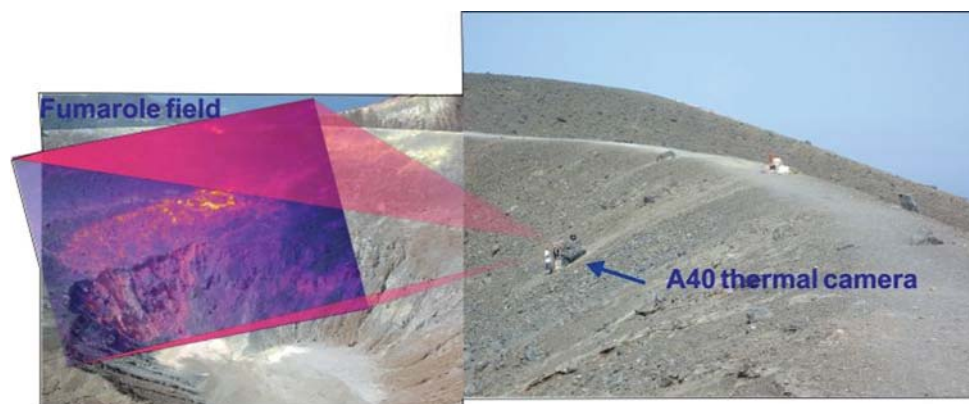
Fig. 3. Photo of La Fossa inner crater taken from the southwestern crater rim showing the A 40 location. The overlapped thermal image represents the camera field of view.

The thermal camera began acquisition at the end of September 2006 with a frequency of 30 minutes.
The installation occurred in two main phases:
– *First phase:* thermal camera installation.
– *Second phase:* weather station installation and mainboard for the interface between the thermal camera and the weather station.

First phase: thermal camera installation

In June 2006, thanks to the support of the helicopter of DPC (Dipartimento di Protezione Civile Nazionale), the thermal camera station was installed (Figure 4). This comprised an A 40 M FLIR thermal camera, photovoltaic power system and wi-fi system for radiometric data transmission.
The A 40 camera was located within a polycarbonate box supported by a steel inox structure, whereas the battery was put into a Gewiss resin box (Figure 5). To protect the thermal camera lens from alteration by volcanic gases, the polycarbonate box was equipped with an additional germanium lens. Moreover, due to high air temperatures occurring during Summer (temperatures > 60° C), the thermal station was equipped with a chronothermostat.

Fig. 4. Photo taken from La Fossa southern crater rim 24 June 2006. Helicopter of DPC Nazionale transporting the thermal station components.

Fig. 5. Polycarbonate box containing the A 40 M FLIR thermal camera.

Radiometric data transfer and thermal camera remote control are controlled by an access point equipped with a serial and Ethernet connection.

The serial connection creates the interface between the thermal camera and the weather station, while the Ethernet connection links the thermal camera with the access point.

Radiometric data are transferred by wi-fi to Lipari (INGV Catania) site, sent to Catania (CUAD, Centro Unificato Acquisizione Dati, Catania) by Garr network (2 Mbps), where they are stored on a personal computer and analyzed in real-time by IDL software. In detail, the access point, located within the Gewiss resin box, communicates with the Lipari system through a directional antenna (Figure 6).

Fig. 6. Directional antenna for wi-fi data transmission to Lipari Island.

At Lipari (Osservatorio della Marina), another access point (Alvarion) was installed for the acquisition of radiometric and atmospheric data transmitted by the thermal station in Vulcano.

The feeding system comprised two photovoltaic Kyocera panels with a steel inox structure, linked to a charge regulator through an electric cable (Figures 7a,b).
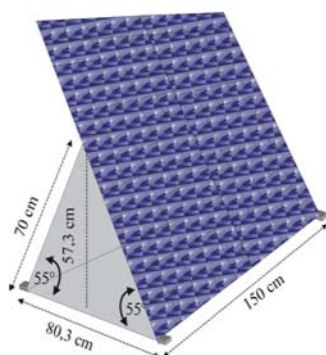
Fig. 7. Left **(a)**, Kyocera photovoltaic panel project; right **(b)**, photo showing the photovoltaic panel installation.

Energy necessary to supply the thermal station was calculated by considering that:

a. the thermal camera has to work 24 hours per day,
b. an average of three hours of sun light taking into account Winter and Summer,
c. without sun light, the battery has almost two days of autonomy, and
d. the whole system needs an average of 550 W/day.

Second phase: weather station installation

In January 2007, to apply corrections for the atmospheric parameters within the thermal camera internal software in real-time, a weather station close to the thermal camera was installed. The remote control, the atmospheric parameter acquisition and the interface between the A 40 and the weather station is managed by a mainboard.

The weather station is a La Lacrosse WS 2305 (Figure 8) provided of a hygrometer, anemometer, rain gauge and a temperature sensor.

The microcontroller used to create the interface between the components of the entire system (Figure 8), is a Microchip Pic (Peripheral Interface Controller) 18F258. In particular, the microcontroller reads the atmospheric parameters recorded by the weather station and sends them to the access point. Additionally, it periodically sends values of air temperature and relative humidity to the thermal camera for the autocalibration (Figure 9).

The whole system was tested in Catania before the installation.
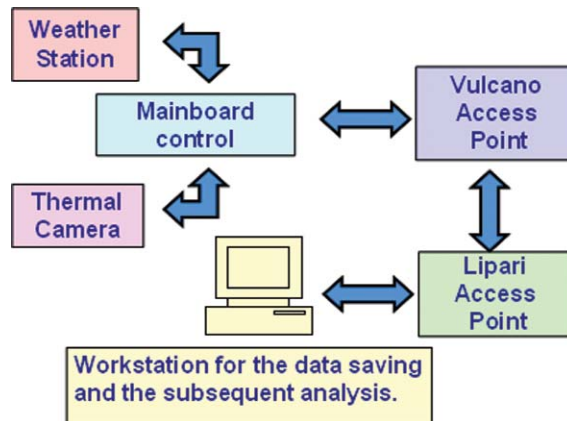

Fig. 8. La Lacrosse WS 2305 weather station.

Fig. 9. Block diagram of the system.

Future development

During a survey two months after the installation of the station, we observed that it shows very clear corrosion traces due to highly corrosive gases emitted by Vulcano, even more marked than those observed at Stromboli stations (Figure 10).

For this reason, we are performing a study to carry out special protection for future installations in this kind of environment.

The polycarbonate case well preserved the thermal camera from the acid gas corrosions.

Fig. 10. Gas corrosion effects at Vulcano station.

REFERENCES

Calvari, S., Lodato, L., Spampinato, L., 2004. Monitoring active volcanoes using a hand-held thermal camera. Thermosense XXVI-SPIE, The International Society for Optical Engineering 5405, 199-209, DOI: 10.1117/12.547497.

Harris, A.J.L., Stevenson, D.S., 1997. Magma budgets and steady-state activity of Vulcano and Stromboli volcanoes. Geophys Res Lett 24:1043-1046.

Harris A.J.L., Maciejewski A.J.H., 2000. Thermal survey's of the Vulcano Fossa fumarole field 1994-1999: evidence for fumarole migration and sealing. J Volcanol Geotherm Res 102:119-147.

Harris, A.J.L., Lodato L., Dehn J., Spampinato L., 2007. Thermal Characterization of Fumarole Fields. Submitted to Bulletin of Volcanology in 2007.

Oppenheimer, C., Yirgu, G., 2002. Thermal imaging of an active lava lake: Erta 'Ale volcano, Ethiopia. Int. J. Remote Sens. 23(22), 4777-4782.

Wadge, G., Macfarlane, D.G., James, M.R., Odbert, H.M., Applegarth, L.J., Pinkerton, H., Duncan, A.R., Loughlin, S.C., Strutt, M., Ryan, G., Dunkley, P., 2006. Imaging a Growing Lava Dome with a Portable Radar. EOS, Trans. AGU 87, 23.

A multiparametric low power digitizer: project and results

M. Orazi, R. Peluso, A. Caputo, M. Capello, C. Buonocunto, M. Martini

Istituto Nazionale di Geofisica e Vulcanologia, Sezione di Napoli, Osservatorio Vesuviano, Italy

INTRODUCTION

In the past decade systems and techniques for geophysics monitoring activities have rapidly improved. Monitoring itself is moving to a multi-matter scientific field. The systems under studies often require the collection and analysis of several geophysical parameters. This is, for example, the case of volcano monitoring: volcanoes produces many kind of signals as seismic and acoustic waves, variations in gas composition, deformation of the structure etc. Another example is given by Ocean Bottom Systems (OBS) used as multiparametric geophysics systems: they may be equipped with seismic sensors, hydrophones, electromagnetometers, pressure sensors etc.

The acquisition of all these data (both for experimental and monitoring activities) are usually performed using systems developed by commercial companies. These systems are often conceived only for a single specific application so they may have characteristics not fully satisfying the requirements of such a multiparametric data collection. A typical seismic data recorder provide a number of channels in multiples of three since it is supposed that the system should acquire data only from tri-axial sensors (velocimeters, accelerometers, etc.). Even the sampling rate of such systems may be only set in ranges useful to acquire seismic data. A multiparametric system should satisfy requirements for different sensors (tilt, seismic, magnetic, etc.) needing different acquisition specifications.

Volcano monitoring often needs instruments installation in remote places, where the only power source is the energy provided by solar panels stored in accumulators. In this case it is important to have electronic instruments requiring very little power consumption in order to minimize the number of solar panels and accumulators to be transported and installed. In the same way low power consumption is an absolute requirement in the case of OBS systems.

Moreover commercial systems are often conceived as closed "black boxes" for which the final user has only limited possibilities to adapt the hardware to his particular needs. For instance the necessity to add some channel in a seismic system is often only possible buying and deploying a new complete system. In some installations is necessary to locate the Global Positioning System (GPS) receiver far from the sensors site (for example an OBS with a moored buoy

link or a sensor in a cave) and this may only be done by the manufacturer.

In this context a project named "GILDA" (Geophysical Instrument for Low power Data Acquisition) led by the Istituto Nazionale di Geofisica e Vulcanologia (INGV), sezione di Napoli, "Osservatorio Vesuviano" (OV), has been promoted to develop a new data acquisition system that will be able to give an effective answer to these issues for both multiparametric volcanic and OBS monitoring.

The targets of this system are a very low power consumption, modularity and flexibility in order to be adaptable to the specific requirements for different kinds of data acquisition. Good sampling resolutions with an high dynamic range and the possibility to monitor system status parameters (for example the environment temperature) have been took into account. With this project, the INGV also follows the strategic long-term target to autonomously develop the technology necessary for future instrumental applications.

SYSTEM ARCHITECTURE AND PROJECT

The first development step in the GILDA project has been the realization of the basic digitizer system presented in this report. It has been conceived as a collection of small subsystems each one dedicated to a specific task following the general requirements presented in section "Introduction".

The project of the digitizer has been greatly simplified by this approach, making the development of the basic system and the testing of the single sub-pieces a simpler work. This approach results in a little higher production costs offering on the other hand the advantage to improve or change a single sub-board without redesigning everything. The basic system, as schematized in Figure 1, is composed by an ADC board with 24bit resolution, a microcontroller board, a GPS and a PLL board all mounted on a "mother board".
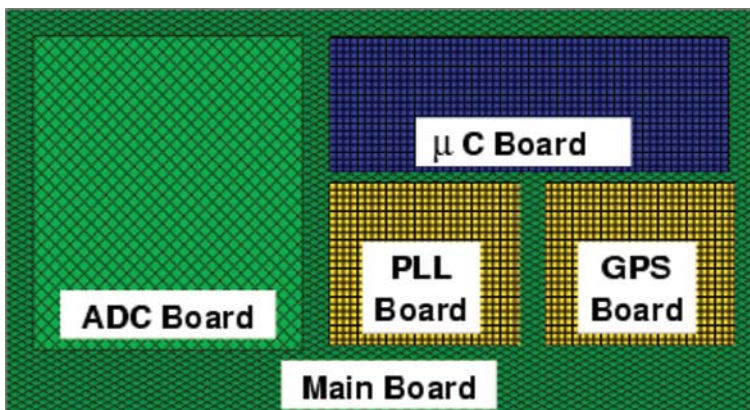
Fig. 1. Block schematic of GILDA system.

The ADC board

The ADC board is based on the CS3301, CS5372 and CS5376A chipsets produced by CIRRUS LOGIC. CS5372 is a dual channel fourth order, high dynamic range, $\Delta\Sigma$ modulator designed for geophysical and sonar applications. The CS5376A is a chip which realizes the DSP functions (essentially a filtering) on the data stream produced by the modulator. When used together they provide an high resolution and an high dynamic range ADC system (nominally 24bit with a bandwidth of 124dB@411Hz). They offer a low total harmonic distortion, low power consumption per channel and an unique flexibility in geophysical applications so resulting in a valid choice for an ADC board.
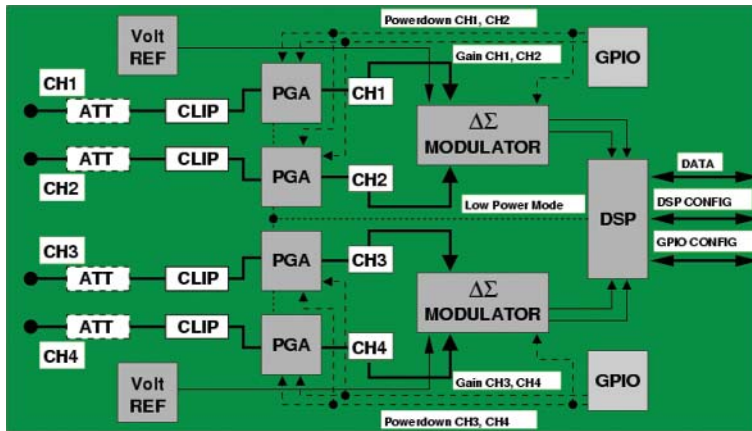
Fig. 2. Block schematic of the ADC board.

The CS3301 is a low-noise, differential input, differential output Programmable Gain Amplifier (PGA). The gain settings are binary weighted (×1, ×2, ×4, ×8, ×16, ×32, ×64) and may be selected by pin settings. These devices provide a low power running mode which reduces the channel power requirements lowering, in the meanwhile, the dynamic range of about 3dB. They also provide an individual power down pin to switch off a single channel. The ADC was realized with a 4 channels configuration in order to preserve the symmetry in the Printed Circuit Board (PCB), when needed one or more of these channels may be turned off using the power down mode. The realized ADC board uses a pair of General Purpose Input Output device (GPIO) used to set up the configuration sent by the microcontroller via the SPI bus. A functional block schematic of the ADC board is shown in Figure 2 while in Figure 3 there is a picture of an ADC board.

The signal levels of the sensors connected to the board must be adapted to the maximum values tolerated by the ADC chip so it was necessary to introduce in the signal path an input attenuator. A passive resistor attenuator was implemented to avoid a decrease in noise performances due to active circuits. The full scale attenuation ratio is settled by the impedance values of a pair of resistors. A signal line protector and a clipper was placed after the input attenuator to protect the PGA from the destructive effects of overvoltages or transients.
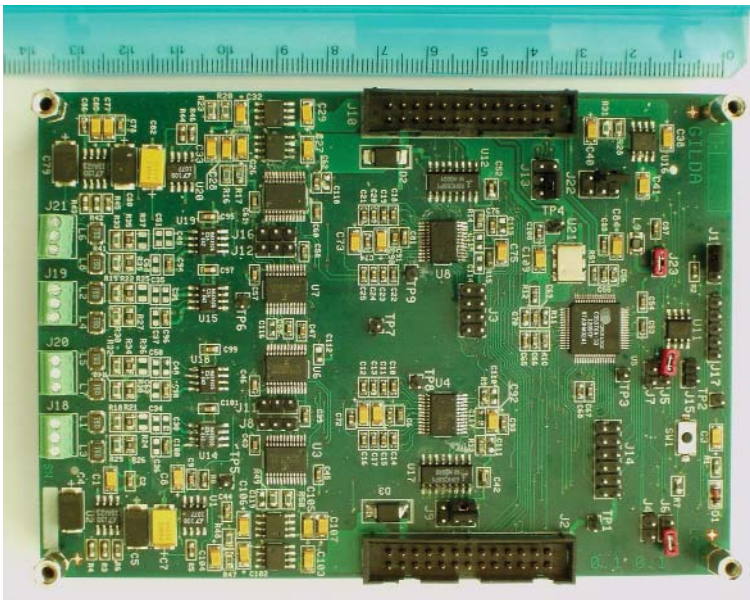
Fig. 3. ADC board picture.

Several low noise design procedures was strongly taken into account to reach the maximum performances of the high resolution ADC. In particular a 4 layer PCB was conceived reserving one of them entirely for the ground plane, one for the power lines and the other two for the signals. The ground plane was partially split into and analog and a digital signals domain connecting them only in one single point under the bottom of the mixed signals components (modulators and PGA). This allows an accurate and separate routing between analog and digital signals avoiding any coupling noise from digital into analog "world".

It is not possible to avoid analog and digital signal proximity in the bottom of the mixed signals components: it may happen that a small amount of digital

noise is injected into the analog ground plane. These currents, however, should be quite small since those components do not drive a large fanout. The minimization of fanout on the converter's digital port will also keep its logic transitions relatively free from ringing and it will minimize digital switching currents. This reduces any potential coupling into the analog port of the component. As an extreme caution an optional RC net was reserved in the electrical design of the ADC. This circuit allows cleaning of the digital signals as it works as a shape formator.

The used routing rule is well reported in Figure 4 which is a PCB CAD view of the board layers. In brown it is highlighted the ground plane and in black the splitting areas. Red and green shows the signal lines on the top and bottom layers. In the center of the image is possible to view a group of digital (red) lines reaching the target components without crossing the analog ground domain. The separation in the central area of the board prevents the usage of an unique voltage reference for the modulators requiring two separate references for each of the two pairs of channels.

The ADC board communicates with the external world via a pair of 26 poles connectors. Data are taken from the DSP via a dedicated serial bus. When solicited on a given line (SDTKI) the DSP will communicate the availability of ready data that must be read as soon as possible. Its internal buffer, in fact, is an 8-deep data FIFO: to avoid any data lost the rate of the SDTKI signal must be equal or greater than the word data rate of the ADC. It is also required to guarantee that the rate of data reading will be high enough.
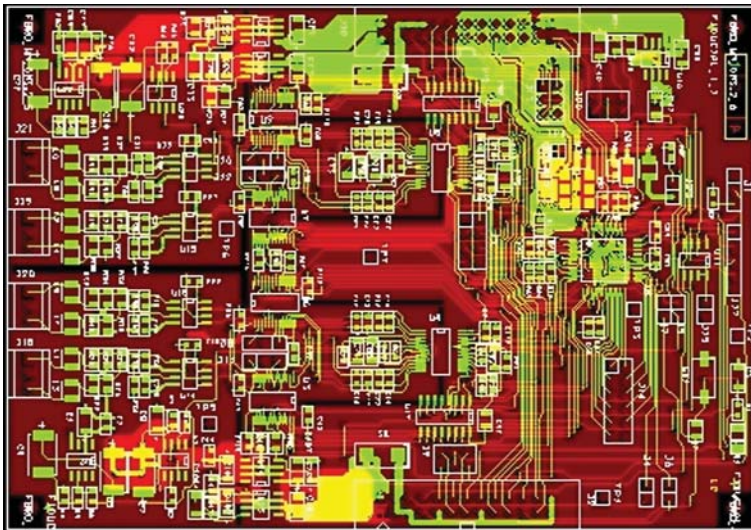

Fig. 4. PCBCAD view of the ADC board.

The PLL board

The correct time labeling of each data sample can be reached correlating the CLK clock to the GMT absolute time. This task is accomplished by the PLL board (Figures 5 and 6a) which operates in a digital controlled phase loop. The external microcontroller modifies the output voltage of the 16bit DAC changing in this way the frequency of the voltage controlled oscillator. The output clock at 32.768MHz is scaled by three onboard counters generating five different synchronous clock speeds. 2, 4, 8 or 16kHz clocks may be selectively (via a jumper) sent to the ADC board as the SDTKI signal (see Section "The ADC board"). The 1Hz internal Pulse Per Second (PPS) is sent back to the microcontroller and is matched with the PPS generated by the GPS receiver. The microcontroller uses a Proportional-Derivative (PD) algorithm (see section "GPS configuration") to modify the DAC value and thereby the frequency of the oscillator. This loopback algorithm is able to keep the CLK clock synchronized with the GMT time guaranteeing the correct time labeling of data samples.
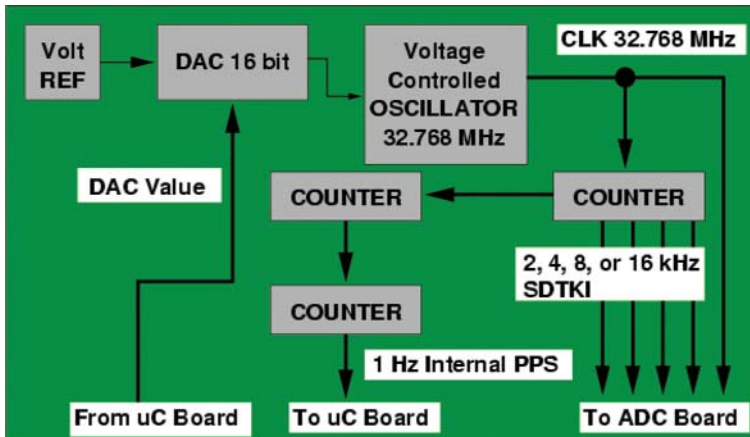

Fig. 5. Block schematic of the PLL board.

It is possible to periodically toggle the power of the GPS receiver further reducing the power requirements of the board. This needs some sort of stability in the clock of the 1 Hz internal PPS. If the oscillator frequency is not an exact submultiple of the PPS (and thus of GMT time) the system adds a constant error in time determination of the samples. Without any correction this error accumulates itself and should not exceed a maximum tolerated value. When the PLL loop is turned off there are many sources of this kind of errors. Changes in the external temperature may make the oscillator drift

its frequency, influencing in the same time the voltage reference of the DAC. Fluctuations in the power source may have similar effects. Another source arises from the discretization of the analog values produced by the DAC: their number directly depends on its bit resolution. Together with the tuning sensibility of the oscillator this determines the minimum frequency difference.

A   B
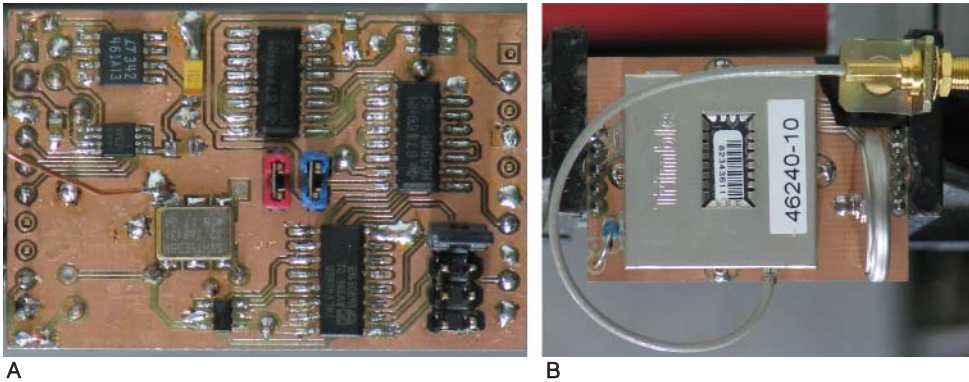
Fig. 6. Auxiliary boards pictures. A, PLL board; B, GPS board.

The GPS board

The GPS board shown in Figure 6b is no more than a socket adapter for the complete GPS module. The TRIMBLE LASSEN IQ has been chosen for the GILDA system due to its compact dimensions and very low power requirements. The module receives a set of commands from the microcontroller via its UART interface and sends back informations about time and satellites locking status. It also generates the PPS impulse which is used to synchronize the CLK clock (see section "The PLL board").

The microcontroller board

The microcontroller board is equipped with a 16/32bit ARM core LPC2129 which accomplish all the supervisor and control logic functions of the system. It synchronizes the GPS PPS with the internal PPS, reads the status of the GPS board via its first UART, reads the data from the ADC board via a dedicated SPI bus and outputs them as a stream on its second UART.

This 32bit microcontroller has been chosen in order to reduce the consumption of the system. The dynamic power consumption in a logic device is tied to the supply voltage by the relation:

$$P = \frac{1}{2}nCV^2f$$

that represents the power needed to toggle *n* logic gates switching once per cycle at a frequency *f*. *C* is the capacitance of the single CMOS gate powered at voltage *V* (note that there is a square dependence on the power voltage). The LPC2129 uses a power core voltage of 1.8V against the typical 3.3V used by other 8 and 16 bit microcontroller architectures. It follows that a power save factor greater than 3 can be achieved on equal computational logic resources.

The LPC2129 may work at five different core frequencies (12, 24, 36, 48 and 60MHz) driven by an internal PLL circuit. Higher clock frequencies are required to reach the highest baudrates of the UART ports. It has two power saving modes realized by shutting down the computational core alone or together with any internal devices. It may be awaken from these idle states by any kind of interrupt requests. The second shutdown mode also turns off the internal counters used to measure lags between events and it has too long awakening times. For these reasons it is unuseful for our kind of application. Using just the first shutdown mode allows the system to save a nice amount of power as the microcontroller spends many time idling in this state. As the core is completely shut down, the power consumption of the microcontroller becomes quite independent from the controller clock.

The firmware running on the controller and some of the used algorithm are briefly described in section "Firmware description".

The main connection board

The main board of the GILDA system interconnects all the other boards previously described. It contains the main power source section that feeds all the other ones (see Figure 7). DC-DC converters have been used to drop down battery voltage from the input value (9÷18V) to 3.3 and 5V. The 3.3V power line serves all the logic devices with the exception of the microcontroller core which requires 1.8V generated by another DC-DC. Two low-noise power rails are needed for the mixed signals section of the main ADC board. A low noise dropout linear regulator gives the +2.5V from the 3.3V regulated power while a charge pump voltage inverter first produces the -3.3V which is then raised to the required -2.5V. With the exception of these last lines all the other ones are directly accessible by reserved connectors on the main board. Some of them are under relay control in order to toggle the power of externally connected devices.

A 12bit ADC is also present on the main board. It is used to obtain device status informations, such as temperature, power consumption, battery voltage, solar panel current or any other auxiliary low-rate acquisition. This ADC in
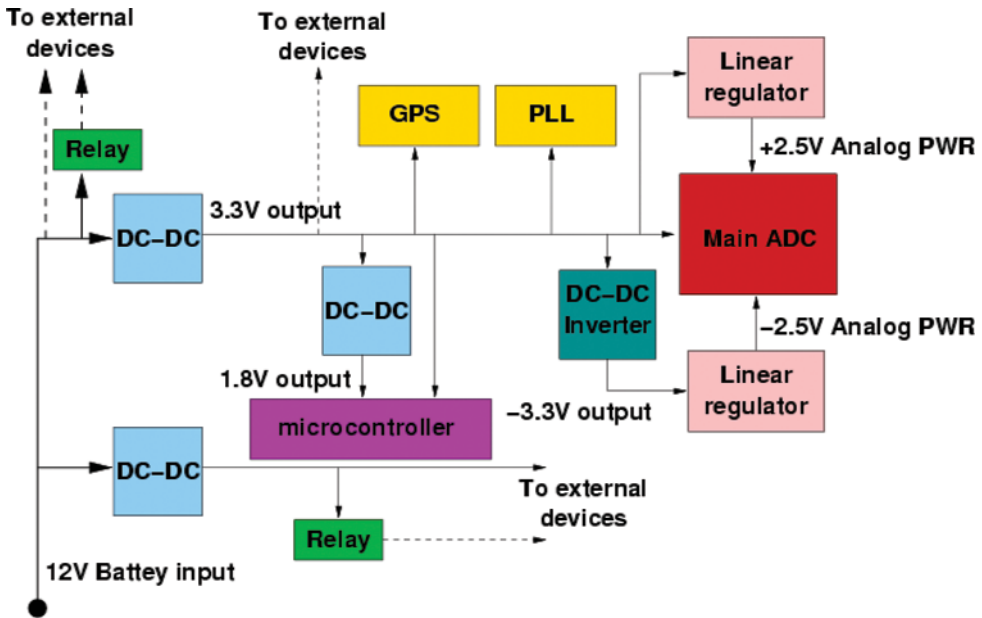
Fig. 7. Schematic block of the power net of the GILDA system.

fact is used at a maximum rate of 1 sample per second. It has single ended inputs with maximum range selectable at 12V, 5V or 3.3V.

In addition the board has an expansion serial port to connect other general purpose cards for future applications. One will probably be a middle-resolution 16bit ADC for low-rate data acquisition.

FIRMWARE DESCRIPTION

The system firmware is written in standard ANSI C using the GNU GCC ARM toolchain (version 3.3.1 using uClib 0.9.20). Some small GCC extensions to the ANSI C were required to handle interrupt functions. The use of ARM machine language has been kept to the possible minimum: only few lines were used to enable/disable interrupt requests. The uLINK JTAG (Joint Test Action Group) interface is currently used to download and debug the program into the internal microcontroller Flash memory. This method will not be used in production boards as the LPC2129 allows its programming through the first UART interface.

Care has been taken during the development to keep the firmware divided into big functional blocks. In this way both the development and the debugging of the code was simpler and faster. Adding new features to the code is also sim-

plified by a well factorized code. In Figure 8 there is a rough block description of the firmware tasks and of their interconnections.
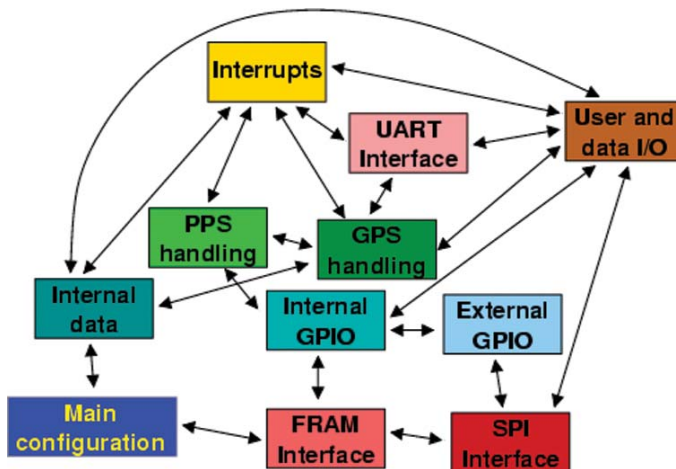

Fig. 8. Logical blocks of the GILDA firmware.

The board has three main different modalities of operation. Each of them performs specific tasks and has been written having in mind the maximum ease of use and the minimum possible power consumption. This has been achieved, for example, turning off any unused device, or avoiding idle loops on the microcontroller making it to enter shutdown mode when possible. Currently active modes are:
1. The boot sequence.
2. The acquisition loop.
3. The configuration and control menu.

The main interface of the firmware is the second UART port of the LPC2129 (being the first one reserved to GPS communications). By default the station starts at 57600baud but it may be configured to work at any known standard serial speed. Non standard speeds (230400baud and 460800baud) are currently supported for devices that may use them, while the 921600baud speed is not supported by the current hardware. No special program is needed to configure and handle the station: a simple serial terminal emulator on the serial line is pretty good.
During the boot sequence or the acquisition loop the station will answer to simple commands sent on the serial line. For example three 'c' characters in a row (ASCII value 0x63 hexadecimal) will make the station switch to the con-

figuration menu. Other commands may be sent, a complete list is reported in Table 1.

Tab. 1. Command strings available during the boot sequence and the acquisition loop. Each command must be sent within one second.

Commands	ASCII equivalents (hexadecimal)	Actions
ccc	0x63 0x63 0x63	Enter configuration mode
rrr	0x72 0x72 0x72	Perform soft reset
hhh	0x68 0x680 x68	Perform an hard reset[a]
bbb	0x62 0x62 0x62	Enter binary configuration mode[b]

[a] Hard reset is only available using an external circuit. When the extra board is not present it will revert to a soft reset.
[b] Binary configuration is not yet implemented in the firmware, but the board already answers to this command.

The boot sequence

The program enters this state when turned on or after a reset. This phase is devoted to the initialization and configuration of the board hardware. It performs many tasks, for example the measurement of the internal microcontroller clock and the first phase lock between the clock generated by the PLL board (see section "The PLL board") and the PPS impulse coming from the GPS receiver.
Figure 9 shows a schematic flux diagram of the boot procedure. The only interrupt routine active during the procedure is the handler of user inputs on the second UART interface. It parses the input characters checking for one of the commands of Table 1. When a command is recognized it halts the boot sequence and enters the requested firmware state.

GPS configuration

Communications with the GPS receiver go through the first UART interface using the binary Trimble Standard Interface Protocol (TSIP). This has been used instead of the standard NMEA protocol because it contains packets for both configuring the receiver and acquiring GPS navigation data.
The receiver configuration is compared with the one it should have for a correct work. Only if it mismatches (for example for a newly mounted receiver) it is sent again and stored in the GPS internal Flash memory.
After checking (or sending) the configuration, the microcontroller waits for the first fix of the GPS position with more than three used satellites. Only
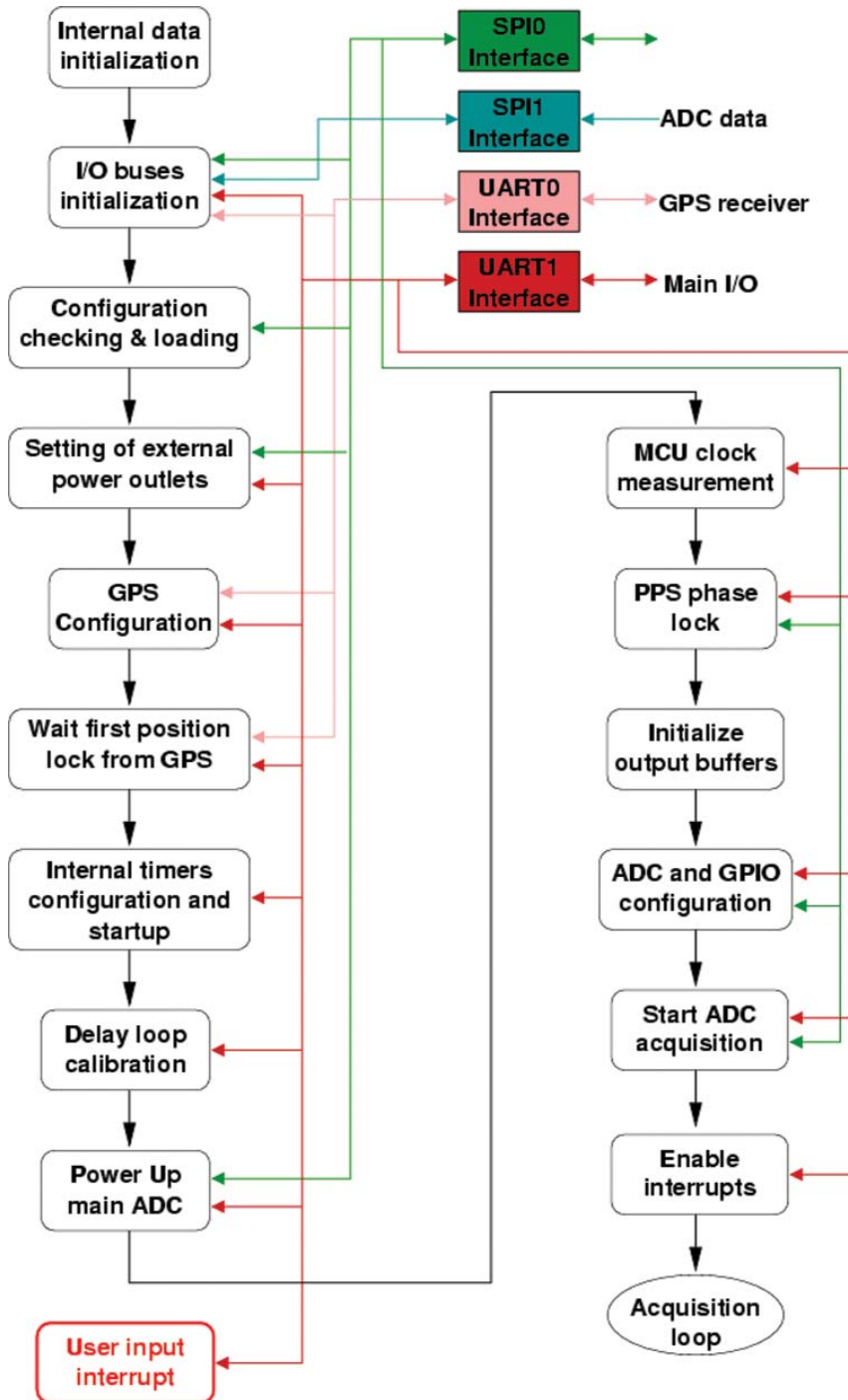
Fig. 9. Schematic flux diagram of the boot sequence.

when correctly locked, in fact, the PPS signal from the receiver is guaranteed to be stabilly related to the absolute GMT time. The MCU use these pulses also to make a more precise measure of its internal clock. This is required to correct the group delay introduced by the ADC in the data samples (see section "The acquisition loop".).

PPS locking

The first phase lock between the CLK clock and the PPS sent by the GPS is performed during the board boot. It may last for many minutes (up to ten) in order to reach the required locking precision needed by the board. The lock may be done between the external PPS and the SDTKI clock or between the external PPS the one generated by the PLL board. This can be selected by configuration options and by some switches on the mother board of the station.

An internal timer of the MCU runs freely incrementing at each clock of the core. Each rising edge on the PPS's (or on the external PPS and the SDTKI signal) triggers a snapshot of the counter value. The difference between two consecutive snapshots gives a measure of the phase difference of the two signals (with the resolution given by the clock).

The PPS locking loop uses a Proportional-Derivative (PD) algorithm to keep this phase as little as possible. The measured phase difference is used to calculate the next value sent to the 16bit DAC using the following recursive equation:

$$D_i = D_{i-1} + \alpha P_i + \beta(P_i - P_{i-1})$$

where D_i are the values sent to the DAC, P_i are the measured phases, α and β two experimentally determined constants. The lock is considered good when the measured phase remains under a given threshold for 60 consecutive times. The best values for the two constants have been experimentally determined as those that make the locking procedure as fast as possible while remaining stable. Using the actual hardware they are:

$$\begin{cases} \alpha = -0.5 \\ \beta = -2 \end{cases}$$

The same algorithm is used during the following acquisition loop where phase measurement and DAC settings are made into dedicated interrupt routines. In Figure 10 is reported a schema of the currently used PLL loop.
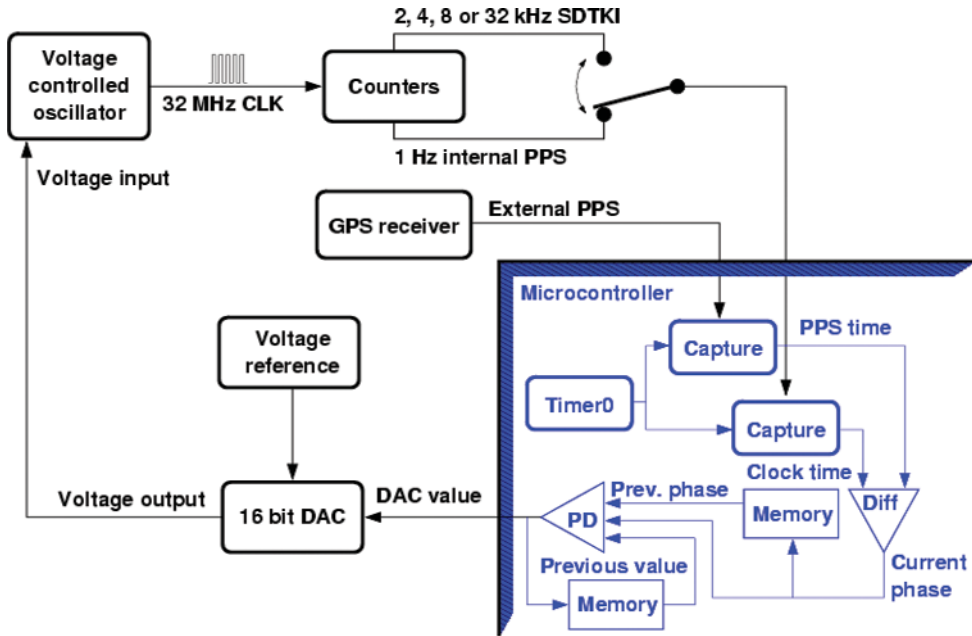
Fig. 10. PLL schema.

Boot ending

When the PPS signal is locked the firmware sends the configuration to the ADC board via the SPI bus and then the start command. Interrupts are temporarily disabled, the interrupt vector is cleared and the new interrupt mask for the acquisition loop is loaded. Then the boot procedure exits and the acquisition loop is entered.

The acquisition loop

This is the main operational mode of the digitizer system. A schematic flux diagram is shown in Figure 11. Here the data are read from the ADC, packed and sent on the serial line. Most of the operations are done via interrupt requests (IRQ). The main loop of the firmware just waits for new data to be available and sends them as soon as they are ready. The microcontroller is then put in its first power saving mode (see section "The microcontroller board"). Each interrupt request awakes the core and a new loop is done. The firmware never exits from this loop until turned off, reset or when sent in the configuration menu continuing to output the data stream at a rate of one packet per second.
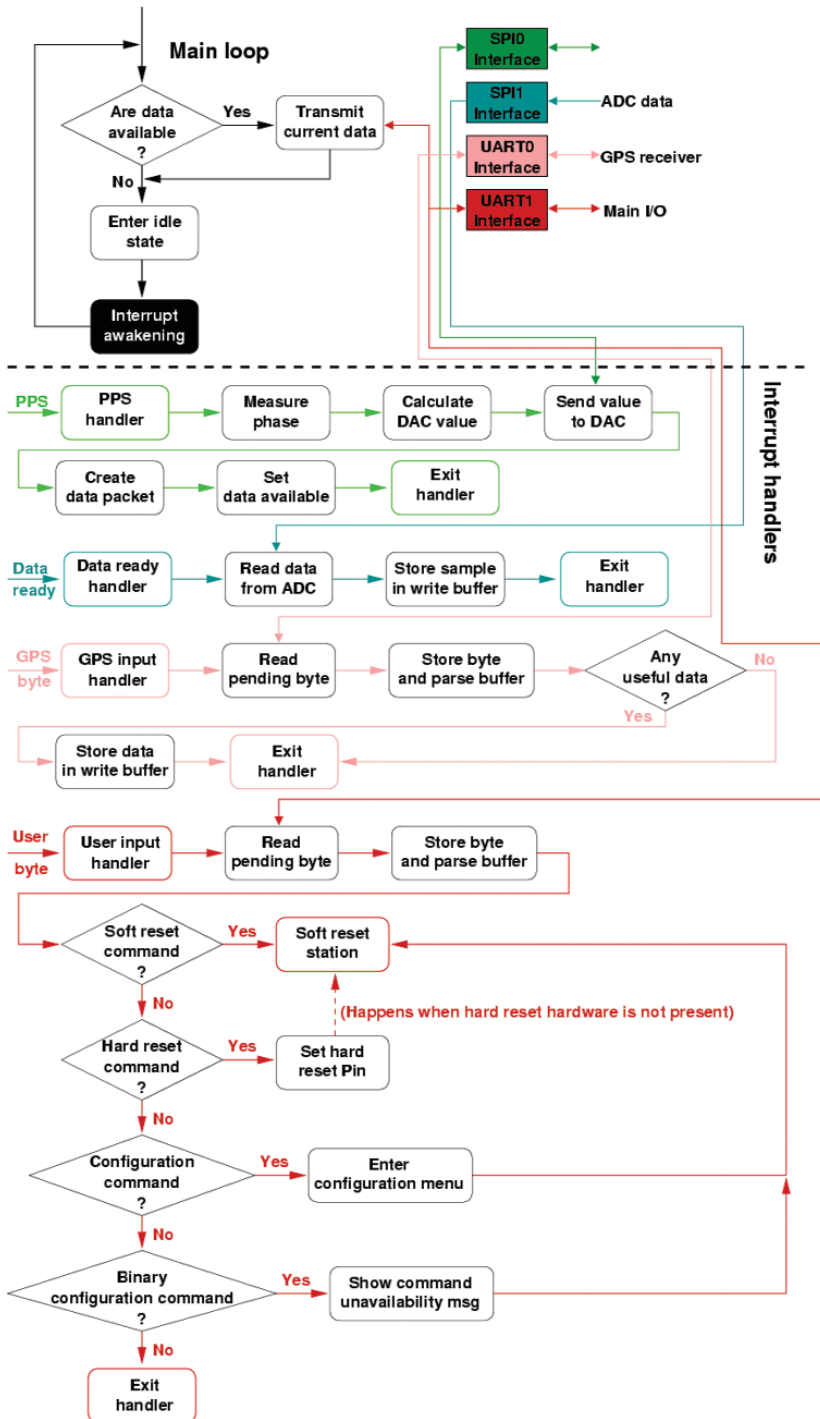
Fig. 11. Schematic flux diagram of the acquisition loop.

The most important IRQ active in this phase is the one answering to the PPS's. The board may be configured to react both to the GPS impulse or to the PLL board impulse. In this second case (which is the default one) the firmware can also perform temporary shutdowns of the GPS receiver.

The first PPS interrupt is used to send the SYNC signal to the ADC. This signal resets all its internal buffers and forces the acquisition to restart. The signal is sent some time before the next PPS in order to correct the ADC group phase delay. Subsequent interrupts are used to correct the CLK clock frequency in the same way described in the "PPS locking" section. Also, using the informations got from the GPS receiver, the time of the last packet is calculated and the "data available" flag is set for the main loop.

The ADC, stimulated by the SDTKI signal, sends a data ready signal (SDRDY) each time it has data to be read. This signal is connected to an external interrupt request of the microcontroller. The interrupt routine extracts data via the second dedicated SPI interface. They are then packed in a write buffer in the controller RAM.

The last two interrupts are active on the two serial lines. The one on the first UART reads and parses the data coming from the GPS receiver setting all the needed flags and data in the currently written packet. The second one is active on the other UART interface and answers to user inputs as it does during the boot procedure.

Board configuration

When the board enters configuration mode, all the external devices are shut down. Only the GPS receiver, the main SPI bus and the two UART lines are kept on. Configuration is done through easy to use number driven menu. In Figure 12 is shown a screenshot of the main configuration menu. Note that the menus described in this article are related to the current version of the firmware, namely 0.12.x.

Briefly, the item **'1'** will show the current board configuration as eventually modified. Item **'2'** allows to modify many board parameters: a new menu, shown in Figure 13, is then entered. Changes do not become effective until item **'6'** is used which then exits from the configuration menu. Item **'3'** is used to revert any change done and come back to the previous board configuration. Item **'7'** discards the modification done and exits from the configuration menu. Item **'5'** is used to turn on and off the auxiliary power outputs (5V or 12V) acting on some relais present on the mother board (into another menu not shown there).

All the configuration parameters of the board are contained into a Ferromagnetic RAM (FRAM). Item **'8'** is used to format this FRAM and to write into it the default ("factory") configuration. Item **'9'** resets the micro-controller and restarts the firmware from the boot sequence. Item **'10'** will only work if the external hard reset circuit is mounted. In this case the power

```
****************************************************************
GILDA-Controller v.0.12.0 "Lilith"
****************************************************************

Main configuration menu:
        1 - Show current configuration.
        2 - Modify configuration.
        3 - Restore previous configuration.
        4 - GPS module handling.
        5 - Configure power outputs.
        6 - Save configuration and exit.
        7 - Discard configuration and exit.
        8 - Factory reset.
        9 - Perform a soft reset.
       10 - Perform an hard reset.

Select:
```

Fig. 12. Screenshot of the main configuration menu.

```
*******************************************************************
GILDA-Controller v.0.12.0 "Lilith"
*******************************************************************

Alter configuration:
1. Name of station: GLD0                2. Samples per second: 100
3. Number of channels: 4                4. Serial baud rate: 57600
      1 - CH01        2 - CH02      3 - CH03        4 - CH04

5. Filter clock frequency: 16384 kHz    6. Master clock frequency: 2048 kHz
7. MDATA clock frequency:  512 kHz      8. MCU frequency: 12 MHz
9. Output get at: FIR2 output          10. Low power mode: DISABLED

11. GPS mode: ENHANCED   12. Wait first GPS fix: YES (Ignored after: 120)

13. Data transmission: BINARY          14. Boot mode: NORMAL
15. Lock mode: PPS                     16. PPS Source: PLL board

17. Auxiliary ADC: ENABLED (using 2 channels)
Channels: 1 - AUX0/1 (1) 2 - AUX1/2 (2)

18. Previous menu.

Select:
```

Fig. 13. Screenshot of the modification menu.

```
*******************************************************************
GILDA-Controller v.0.12.0 "Lilith"
*******************************************************************
GPS handling menu (38400 baud):
        1 - Identify GPS serial speed.
        2 - Retrieve and check GPS configuration.
        3 - Acquire GPS statuses.
        4 - Send configuration to GPS.
        5 - Store configuration to GPS flash.
        6 - Power cycle GPS unit.
        7 - Soft reset GPS.
        8 - Hard reset GPS.
        9 - Factory reset GPS.
       10 - Return to previous menu.

Select:
```

Fig. 14. Screenshot of the GPS control menu.

is temporarily shut down to all the board. When not present the microcontroller will "manually" shut down the power to the external devices and then perform a soft reset.

Item **'4'** enters another menu (Figure 14) where you can handle the GPS receiver. Here it is possible to check and send the configuration of the receiver, look for its current lock status, turn off and on the receiver or make it perform one of the supported resets.

CONCLUSIONS AND RESULTS

The basic digitizer system is shown in the photo in Figure 15 where is possible to see all the boards described in section "System architecture and project".
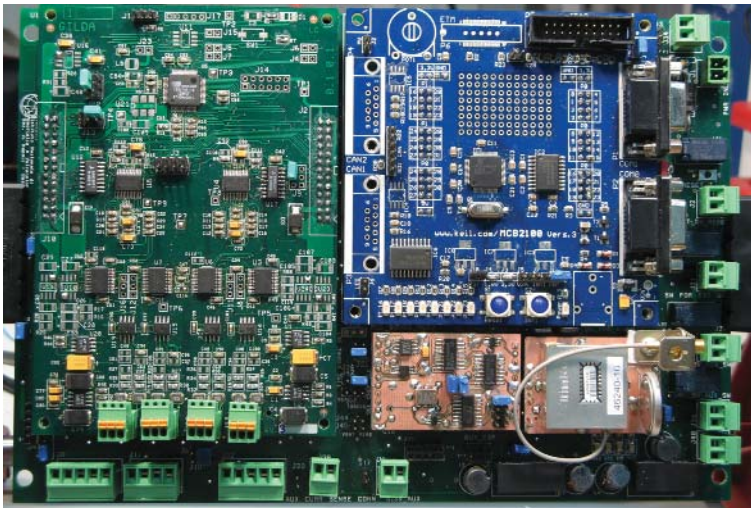
Fig. 15. Photo of the first GILDA digitizer prototype.

Power consumption

Power consumption of the realized digitizer depends on many configurable settings: active channels, DSP filter clock and power modality. Even the configurable 5V power output (see "The main connection board") drains an additional current when turned on, raising the total consumption of the board. When this line is turned off the total absorbed current lies in the range from $\simeq 44.55$mA to $\simeq 70$mA (@12V) depending on the configuration. A complete list of the measured power consumptions is in Table 2.

The used CS5376A, however, does not support any DSP clock at any output word rate. There are some limitations on the minimum power consumption at those rates due to the minimum value of the clock. The supported DSP clock frequencies are shown in Table 3.

Tab. 2. Summary of power consumptions for the GILDA.

Low power mode	OFF				ON			
Active channels	1	2	3	4	1	2	3	4
DSP clocks	Power consumption (mW)							
16 MHz	624	696	768	840	600	642	678	720
8 MHz	588	660	732	804	564	600	642	684
4 MHz	570	642	708	786	540	582	624	666
2 MHz	558	630	696	768	534	576	618	660

Tab. 3. Supported DSP clock rates.

Word rates	DSP clocks (MHz)			
	2048	4096	8192	16384
40 Hz	NA	NA	NA	OK
50 Hz	OK	OK	OK	OK
100 Hz	NA	NA	OK	OK
125 Hz	OK	OK	OK	OK
200 Hz	NA	NA	NA	OK

Noise characteristics

Noise characteristics and dynamic range of the ADC system (DSP + modulator) are directly related to the oversampling ratio. The modulator oversamples the signal at 512kHz, then the DSP decimates and filters it giving the requested Output Word Rate (OWR). Increasing the OWR makes the oversampling ratio (512kHz / OWR) to decrease and, consequently, the noise level to increase.

This can be view comparing Figures 16, 17 and 18. They represent three noise acquisitions of the same ADC channel shorted on a 50Ω[1] resistor at three dif-

---

[1] This is needed to simulate the typical output impedance of an active sensor.
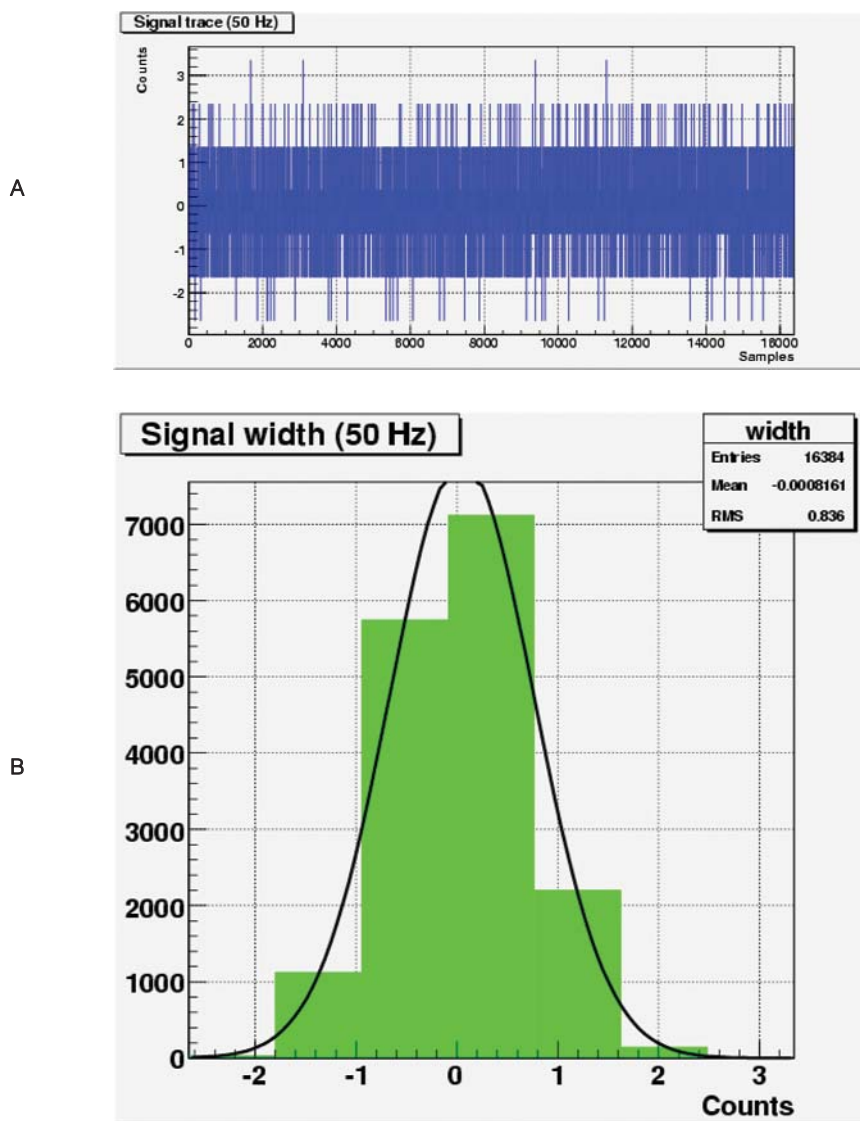
Fig. 16. Shorted input noise recorded at 50Hz. **(a)** trace. **(b)** signal histogram.

ferent sampling rates (50Hz, 100Hz and 200Hz respectively) in the non low-power mode.

In the Figures 19, 20 and 21 are shown the same acquisitions made in low-power mode. They have been done using the maximum DSP clock frequency and using the idle tones removal pin setting of the modulator. This introduces a fixed offset on the signal that has been removed in the figures. Noise appears to be gaussian distributed around its mean (random noise). The width
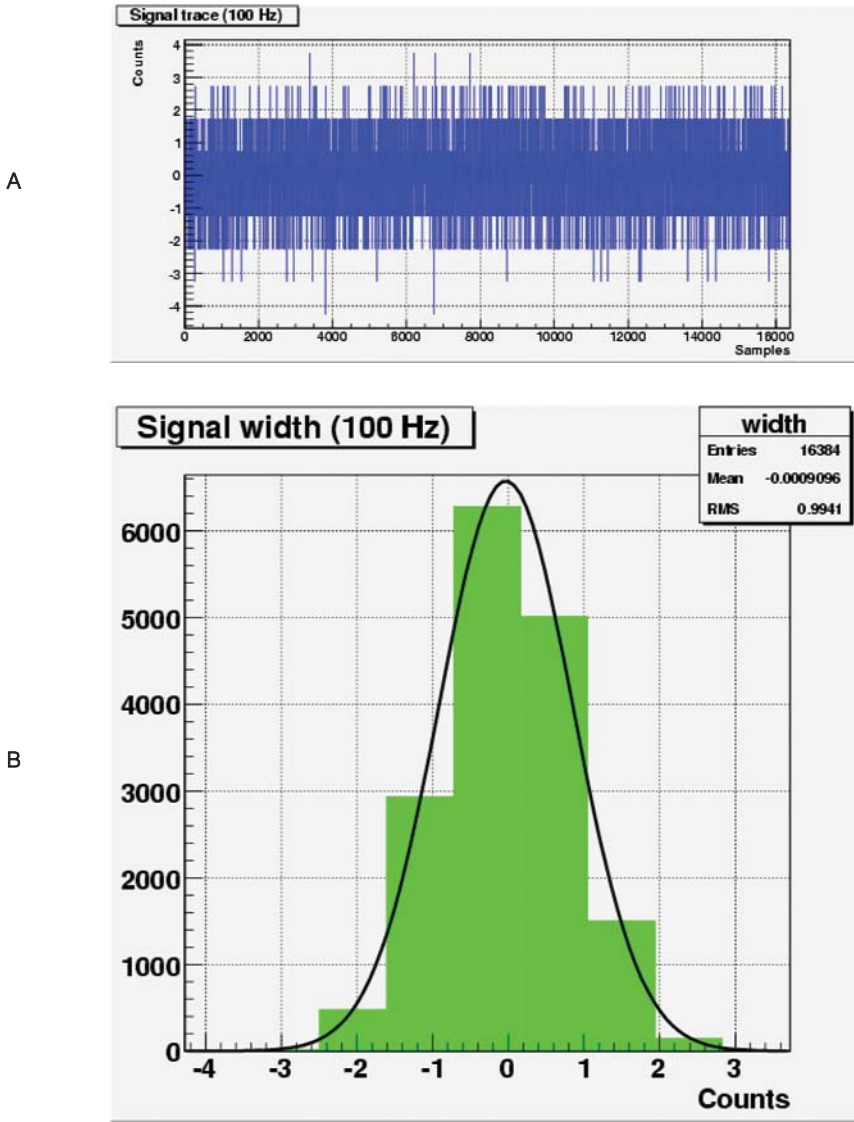
Fig. 17. Shorted input noise recorded at 100Hz. **(a)** trace. **(b)** signal histogram.

of the gaussian distributions increases as the output word rate increases. The Signal-to-Noise Ratio (SNR), expressed in dB, is given by:

$$\mathrm{SNR}_{dB} = 20 \log_{10} \left(\frac{C_{\mathrm{FS}\ rms}}{C_{\mathrm{NOISE}\ rms}} \right)$$
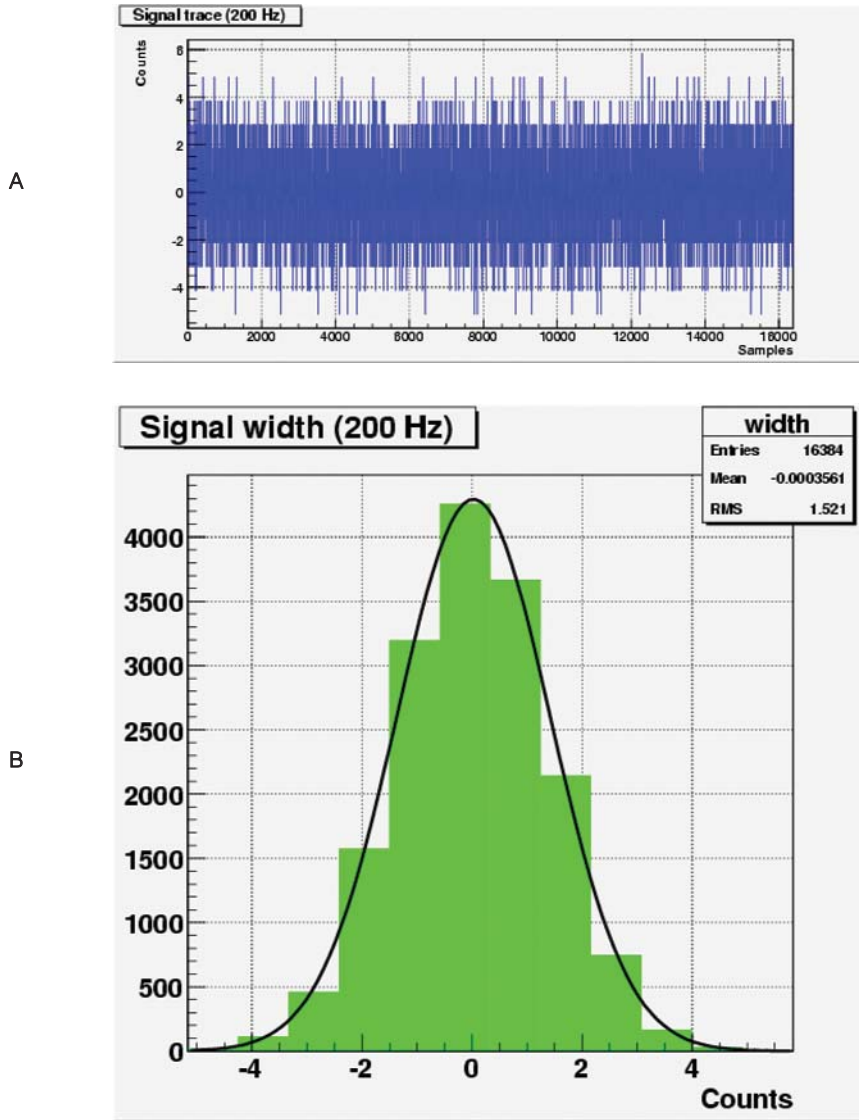
Fig. 18. Shorted input noise recorded at 200Hz. **(a)** trace. **(b)** signal histogram.

where $C_{FS\ rms}$ is the *rms* of the full scale input, while $C_{NOISE\ rms}$ is the *rms* of the noise both expressed in digitizer counts. SNR measurement are usually performed using a fixed frequency sine wave as input signal. In such case, the *rms* is given by:

$$C_{FS\ sine\ rms} = \frac{C_{pp}}{2\sqrt{2}}$$
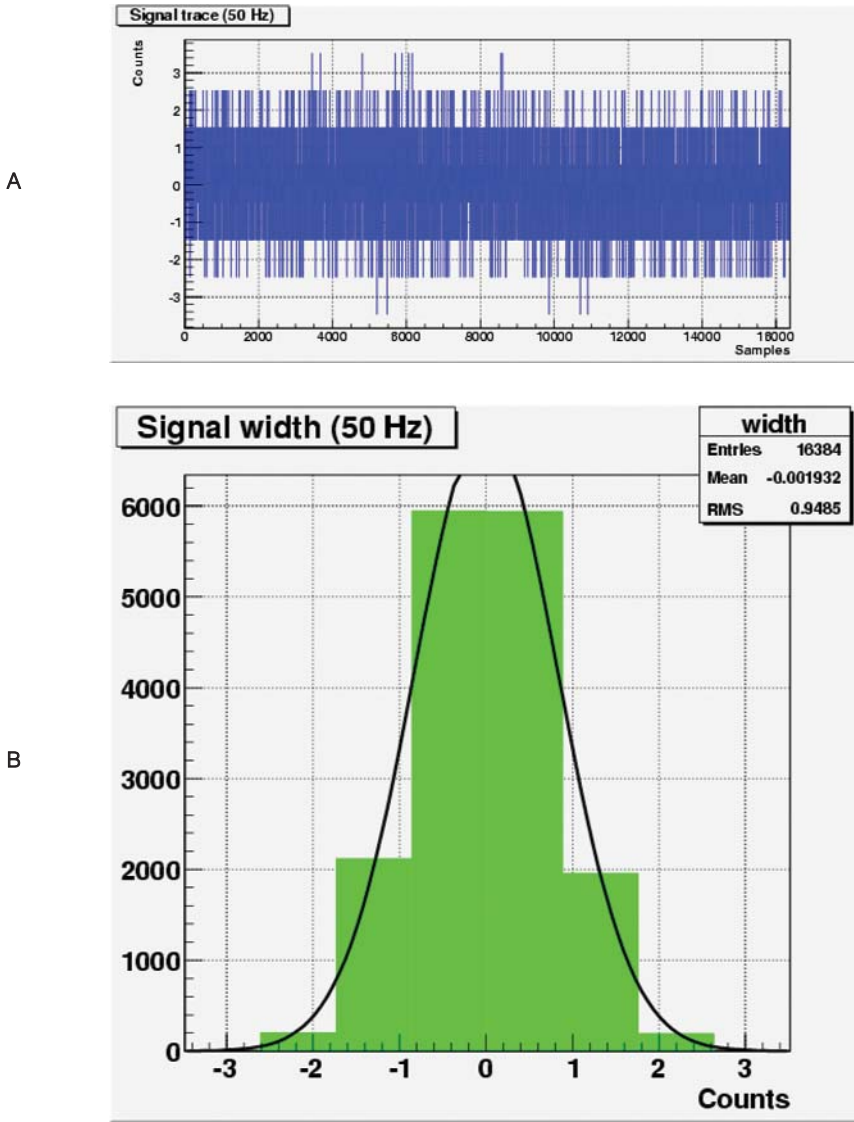
Fig. 19. Shorted input noise recorded at 50Hz in low power mode. **(a)** trace. **(b)** signal histogram.

being C_{pp} the peak-to-peak value of the signal. As reported by the data sheets of the modulator a full scale differential input signal will be translated in the interval [6291455,-6291455]. This will give to a theorical full scale sine wave input signal an *rms* of:

$$C_{FS\ rms} = \frac{6291455}{\sqrt{2}} \simeq 4448730$$
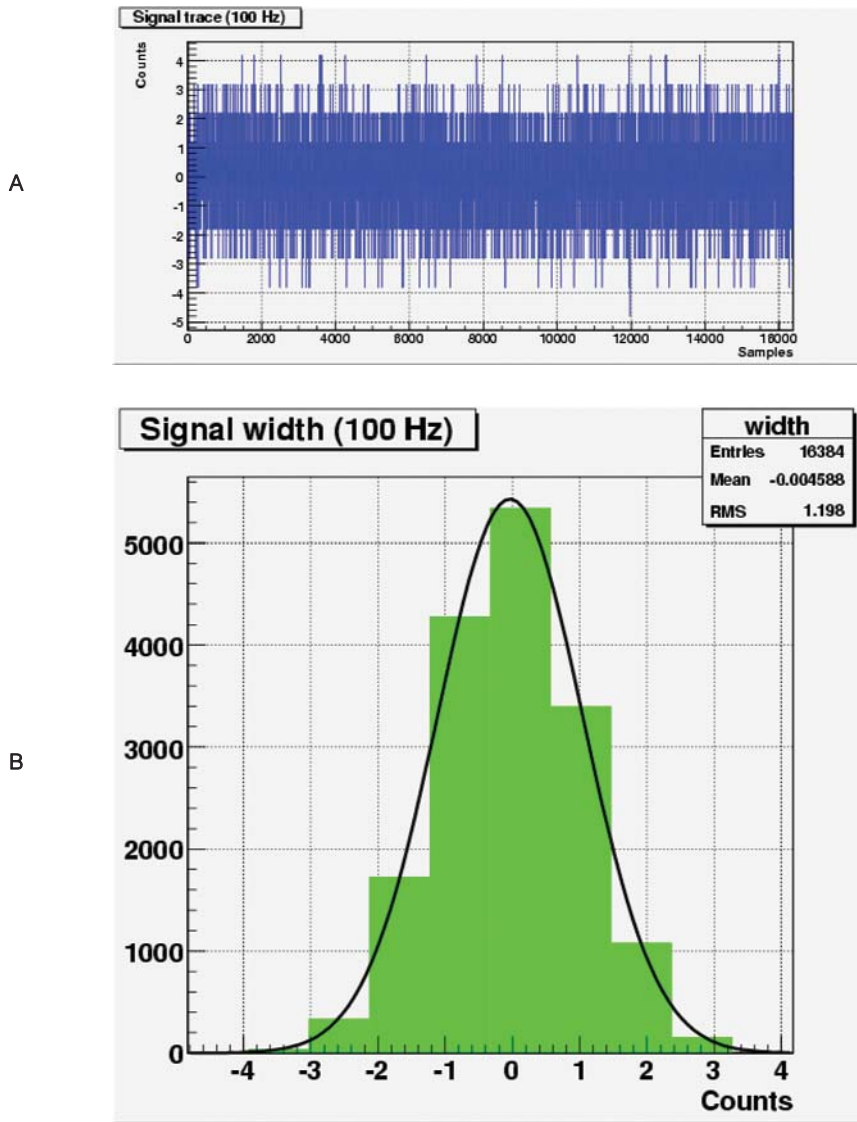
Fig. 20. Shorted input noise recorded at 100Hz in low power mode. **(a)** trace. **(b)** signal histogram.

expressed in digitizer counts. Table 4 summarizes the measured *rms* noise and the SNR_{db} of the digitizer.

The ADC system has been conceived to be interfaced to different sensors with different output voltages changing the input attenuator value (see section "The ADC board"). So it is not possible to give a fixed relation between input voltage and output counts. This can be only done using the maximum modulator input, which is fixed by its voltage reference in the interval [-2.5V, 2.5V].
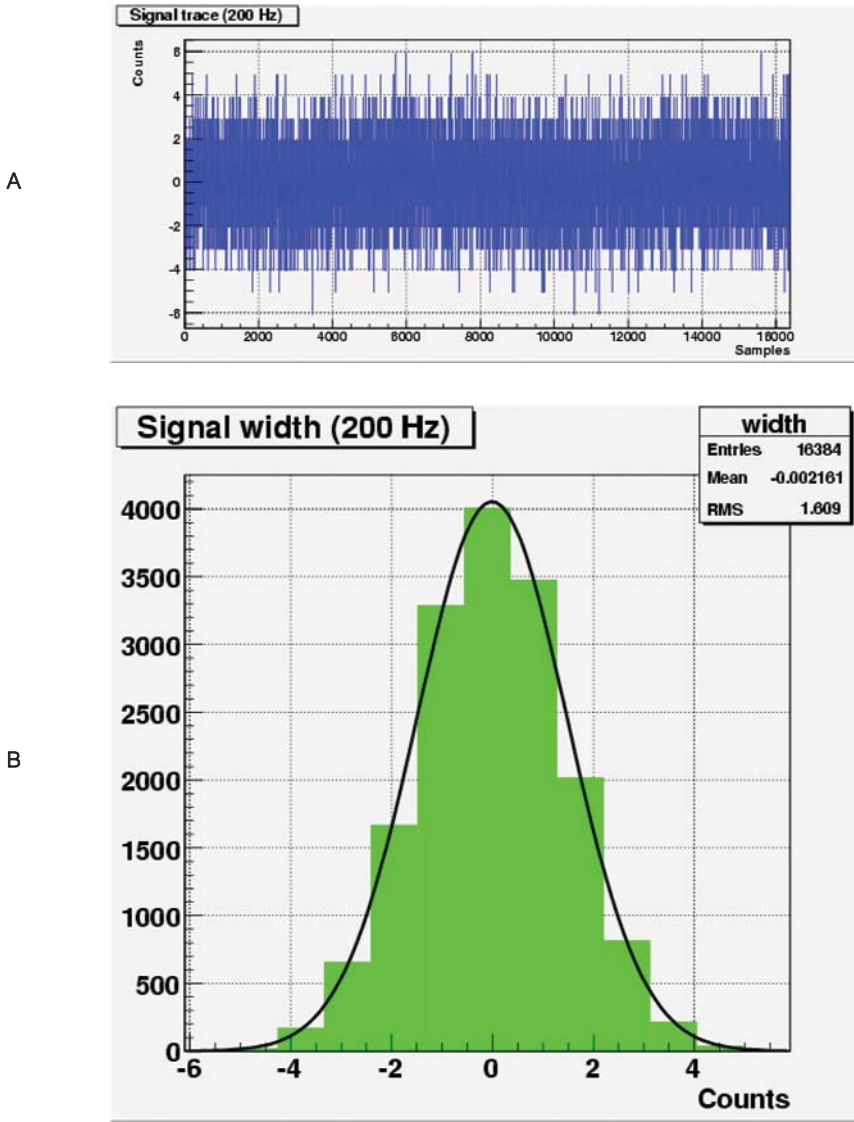
Fig. 21. Shorted input noise recorded at 200Hz in low power mode. **(a)** trace. **(b)** signal histogram.

The single count conversion value is then:

$$V_{\text{count}} = \frac{2.5V}{6291455} \simeq 397.4nV$$

that can be reported to the effective maximum input signal multiplying it by the input attenuator factor. For example, the ADC used in the reported tests

Tab. 4. *rms* noise (shorted input) and relative SNR$_{db}$ at several output word rates.

Acquisition	C$_{NOISE\ rms}$	SNR$_{dB}$
50 Hz normal	0.8	134.9
50 Hz low power	0.9	133.8
100 Hz normal	1.0	132.9
100 Hz low power	1.2	131.4
200 Hz normal	1.5	129.4
200 Hz low power	1.6	128.9

has a 4x attenuator, resulting in an accepted input in the interval [-10V, 10V] with a voltage per counts factor of:

$$V_{\text{count } 4\times} = 4 \times V_{\text{count}} \simeq 1.590 \mu V$$

Thermal gradiometer's array: mechanical and electrical design and first field test results

G. Romeo[1], S. Bello[2], P. Benedetti[1], M. Mari[1], G. Urbini[1]

[1] *INGV, Roma1*

[2] *Scienze Matematiche, Fisiche e Naturali, Università La Sapienza*

1-WIRE DESIGN

Gradiometer's array is based on the Maxim-Dallas 1-wire sensors. The most appetizing characteristic of these devices is the multidrop capability and the cheapness. All de 1-wire devices are single chip, directly connectable to a 1-wire net: no special interface is required. Although originally designed for short single-wire connection to a microprocessor port and a peripheral (i.e. battery chip supervisor, NV-ram etc.) 1-wire may be used (with some difficult) for small instrument DAQ network.

The most part of 1-wire devices offers a parasitic power capability: the power is supplied through the data wire: so just one wire (plus the reference) is required to establish a connection. Some of them (like the thermometers) give the designer the possibility to choose the kind ova power to use. Net performance increases by using the power wire.

1-wire limitations are the speed, the network length, the number of sensors you can drop on a single net branch. A unique identification number (memorized in every 1-wire chip) can identify every 1-wire device. This represents a difficult when several 1-wire devices of the same kind are connected in the same network: every device must be directly identified, and no identical nets are possible. Number of sensors and wire length are tied. Using a class5 twisted pair cable Maxim-Dallas claims the 1-wire net can be 300 meters long. A 1-wire device loads the net like 1 meter of wire:

$$300 = l + n \qquad \text{l=length, n=number of device}$$

These characteristics and the availability of nice performance 1-wire thermometer brought us to design the thermal gradiometer using such kind of devices.

GRADIOMETER PROTOTYPES: ELECTRICAL AND LOGIC DESIGN

The original idea (**design 1**) of the gradiometer was shown in Figure 1. A laptop controlled a long string of paralleled devices through a DS2480 serial -to-

Fig. 1. Left: extremely simple electrical wiring: just paralleled devices. Bottom: a look of the prototype head.

1-wire interface. Unfortunately the number of sensors and the line length is the limitations of such design. The other severe limitation is that a malfunction of a single device (i.e. a short-circuit) may affect the entire net. A second, not functional but annoying limitation is that the controller must know identifiers, order (and calibration curves) of the thermometers used inside the gradiometers. So, in case of a new device the controller needs a descriptive file to operate it.

The formula $300=l+n$ an optimistic consideration, because it doesn't take care of connectors, PCB and all ancillary needs that may affect the net performance. This simple architecture allows the connection of just few sensors.

Figure 2 (**design 2**) shows the first upgrade of the original idea: this improves the number of gradiometers in the net and allows the controller to read the descriptive file from the gradiometer itself. Gradiometers are not just paralleled, but are connected in a daisy-chain architecture. A 1-wire controlled switch connects the net to the present gradiometer thermometers array or to the next gradiometer.

During a field-test the **design 2** shown a weakness that has been corrected in **design 3**. Although **design 2** is not a classical multi-drop design, it still suffers of typical multi-drop connection disease if a node is malfunctioning (i.e. shorted) this affects the entire net connection. A net malfunction avoids the master to issue any command, included the network reset command. There is a way to bypass this condition, ad is to disconnect and connect the net. Since the 1-wire couplers, after reset, establish the connection to the outgoing connector, the network may work again, if the controller (taking in account the error condition) skips the malfunctioning gradiometer. Of course the net connection cannot be controlled with a 1-wire device, because the net is ino-
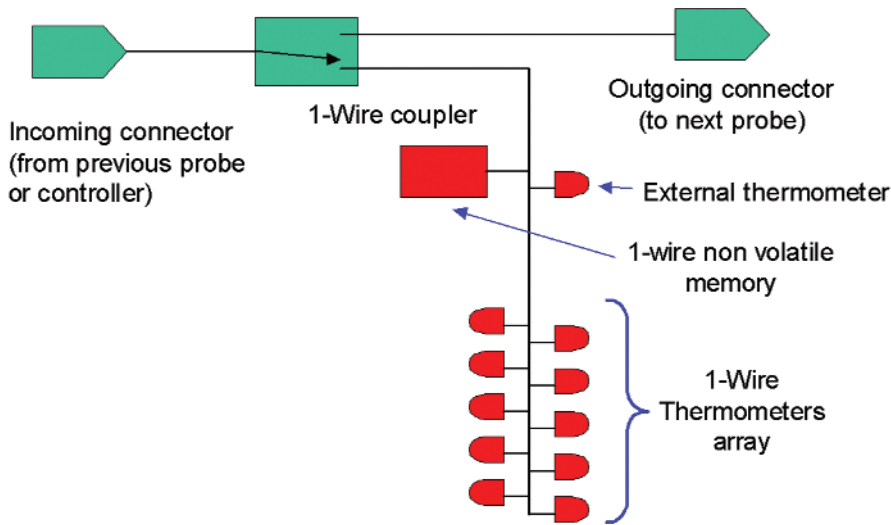
Fig. 2. The design 2 architecture. A built-in switch (1-wire coupler) connects the net to the next gradiometer or to the thermometers array. Since the 1-wire coupler is the only device visible regardless the switch position, each probe is identified by the 1-wire coupler address. The memory contains the thermometers calibration curves and position inside the probe, offering to the control software all the necessary information, and there is no need for a descriptive file to be stored in advance in the controller.

perative when we need to issue this command. To solve the problem we designed a new version of the gradiometer (**design 3**). Figure 3 illustrates the third design where a timer regulates the internal connection to the thermometers. The connection is active for 2 seconds after operating the one-wire coupler. The controller has this time to read the thermometers content. In case of failure, after the time the malfunctioning net branch is insulated, ant this restores the net functionality.

MECHANICAL DESIGN

Like the electrical design, the mechanical design evolved from the first proto (Figure 4). The role of the mechanical design is to protect the electronics against the harsh environment e to ensure, at the same time, a good quality thermal coupling sensors-terrain. The design moved from an initial realization in aluminium and sealing glue to a high quality especially built Teflon case, which ensures a long-term protection. The thin walled stainless steel tube, with the copper thermal couplers, ensures a good thermal coupling to the terrain and a high sensor-to-sensor insulation (the lengthwise thermal conductivity is comparable to a dry terrain one).
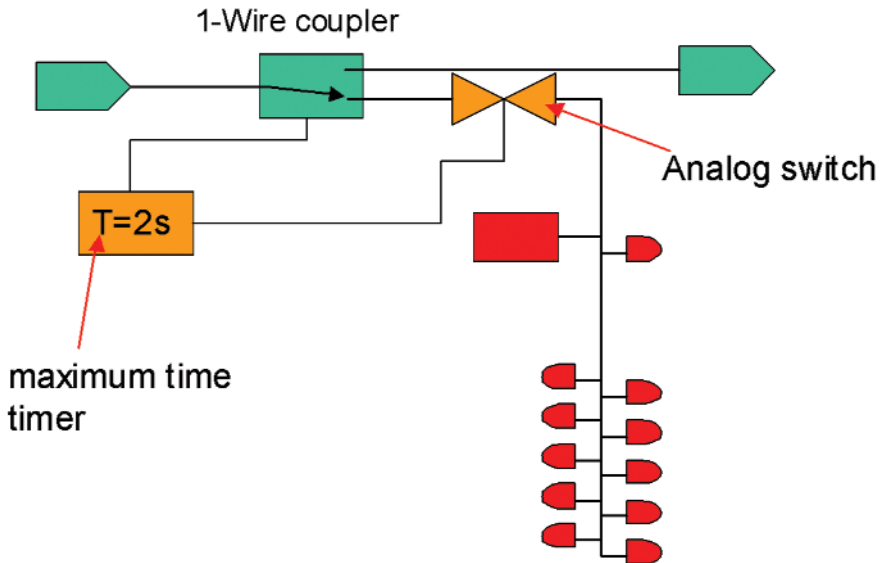
Fig. 3. Faultless gradiometer (design 3). The (T=2s) timer closes the analog switch as the 1-wire coupler is operated. The computer must read the thermometers in 2 seconds. After this time the analog switch insulates the thermometers array, avoiding malfunction in the branch to affect the entire net.
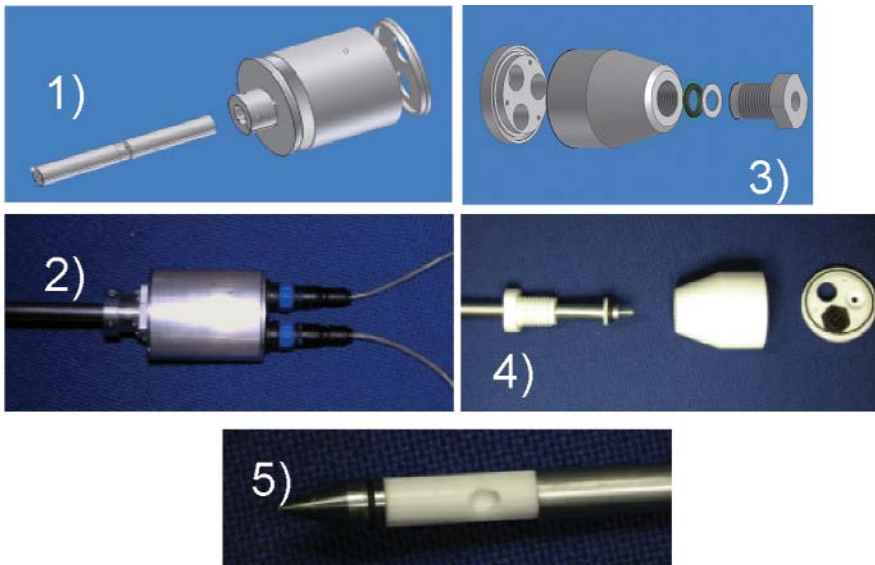

Fig. 4. Mechanical design evolution. 1) 3D drawing of the head in aluminium. 2) aluminium head prototype. 3) 3D drawing of the Teflon head. 4) disassembled Teflon head. 5) disassembled gradiometer apex.

Figure 5 shows a particular of the rod during the working process. Figure 6 shows the head PCB, associating the visible parts to the block diagram.
Although the stainless steel offers a good thermal coupling and protection, a long exposition to a corrosive environment may be harmful even for it. In this case a further protection should be used. For this purpose was successfully used a high-temperature Teflon-fiberglass tape. This, unfortunately, increases the response time.
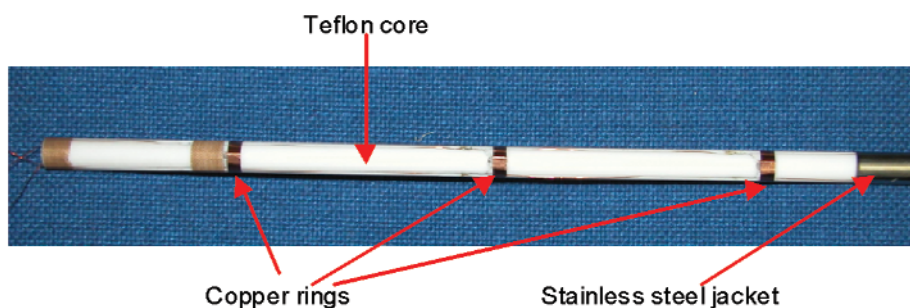
Fig. 5. Inside the gradiometer rod. Copper ring increase the thermal coupling between the sensors ant the jacket wall.
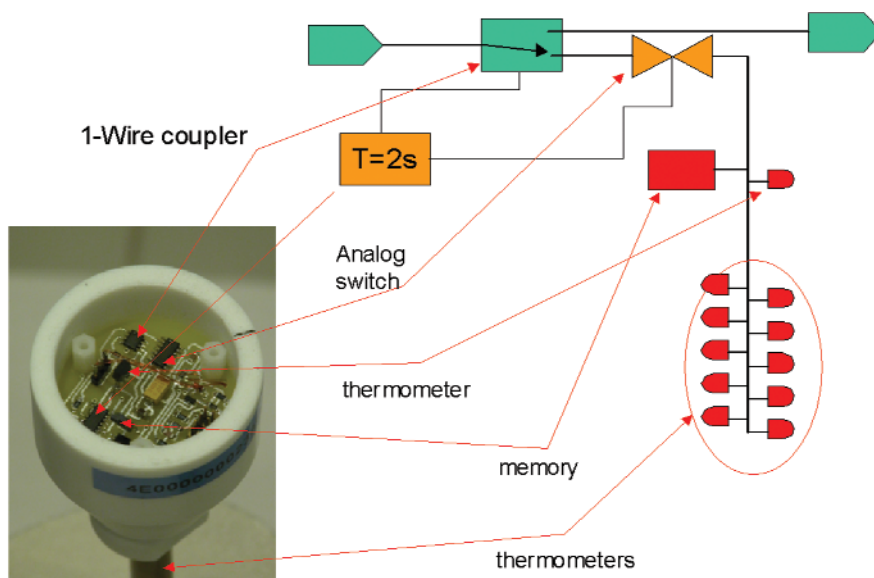
Fig. 6. Inside the gradiometer head.

GRADIOMETERS CONNECTION

Gradiometer array uses a daisy chain connection, as shown in Figure 7.
This configuration takes several advantages both physical and logic.
The physical advantage is the electric presence of one gradiometer's thermo-
meters at time on the net: this reduces the number of 1-wire devices, allowing
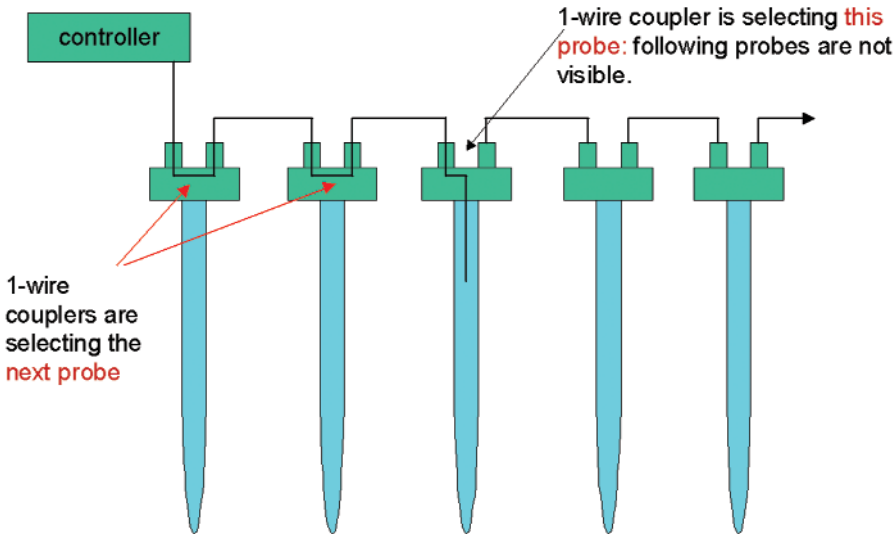a longer wiring.

Fig. 7. The gradiometers daisy-chain connection. In this picture the controller can reach: 3 1-wire couplers and memory and sensors of the 3rd probe.

The logic advantages are: gradiometer may be simply identified by the control-
ler, and may contain a calibration memory; gradiometer's can be directly under-
stood by the controller: during the installing procedure the operator doesn't
need to keep track of the sensor's order: it comes from the wiring order. The
lab test of the gradiometer's array showed some communication malfunction
when we attempted to use a chain with more than 10 gradiometers. The solu-
tion adopted was to change the connection topology to make the system to see
no more than 5 sensors chain at time. This is realized using a 1-wire hub to split
a single, 25 gradiometers chain, into 5 shorter chains (Figure 8)

DATA LOGGING

Data acquisition operations are shown in Figure 9.
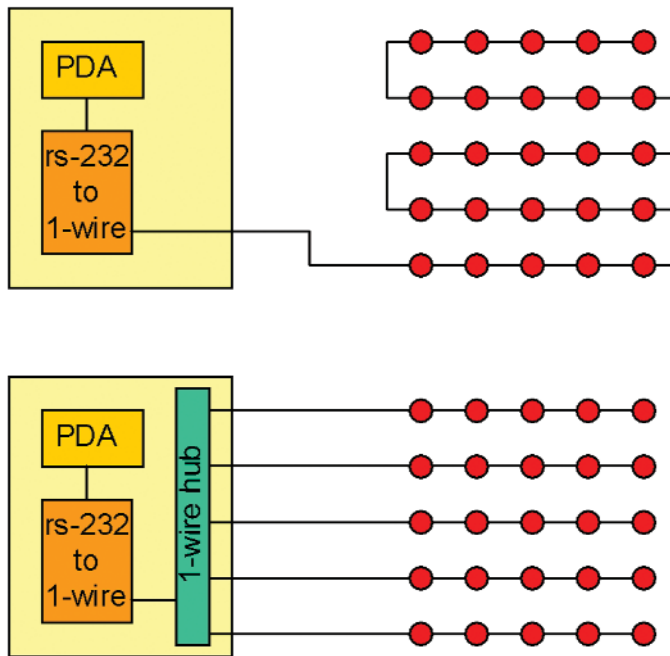
Fig. 8. Two different strategies to connect thermal gradiometer to the data logger. The upper connection uses a single wire to connect all the gradiometers (represented by red circles). The lower connection uses a 1-wire hub. Using the hub allows to keep net branches much shorter (6 times) than the single branch net. This ensures more reliable data transmission. The PDA (Personal Digital Assistant) is used as data logger.

After an initial attempt to base the remote acquisition on a notebook size PC, the design moved to a PDA. Recent devices offer a great connectivity (GSM, GPRS), easy local interface (USB, UART, IRDA, Bluetooth), GPS localization and timing. A further useful performance is built-in power handling: just plug a power jack, and the PDA controls the correct charge, keeping the battery in good health. The user interface may be nicely programmed using the built-in TFT touch screen. The use of memory cards brings the non-volatile memory available up to 4 gigabytes.

Interfacing the 1-wire net is a very simple task, from hardware point of view: a 3-state microprocessor port can do that. The software point of view presents more difficulties. Maxim-Dallas helps in this task offering free windows dlls and java libraries. Some routines have been written to check and acquire gradiometers on windows based laptop PC and on Windows Mobile based PDA.

The acquisition program uses a main module written in C# and a secondary one, written in Java. The main module implements all the system needs (user interface, timing, GPS reading), except the 1-wire interface, that is operated by
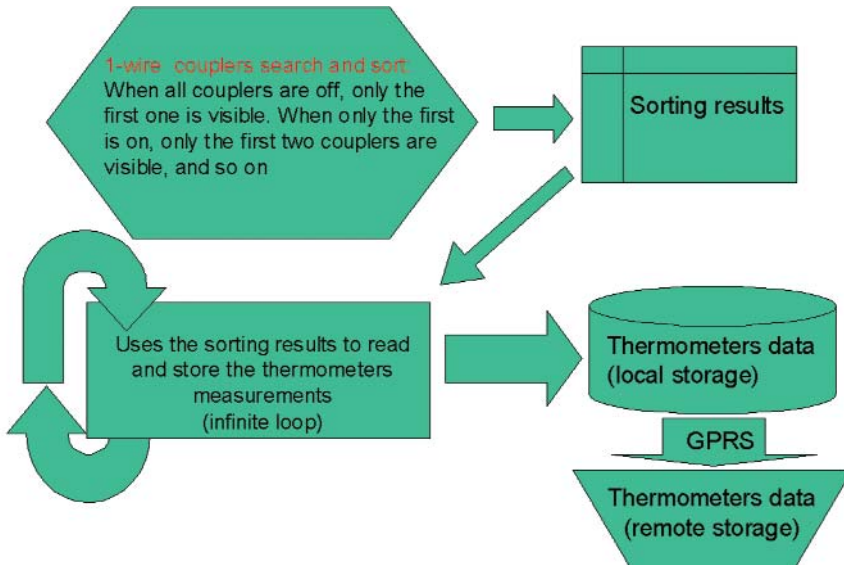
Fig. 9. PDA data acquisition block diagram. After the first net exploration, to understand the configuration (number of gradiometer, order, calibration parameter) the system starts the acquisition at the time interval defined by the operator. Data are temporarily stored in a local memory, waiting to be e-mailed using GPRS. After a successful transmission, data are removed from the temporary memory.

the Java program. The Java module, started by the C main at a selectable time interval reads the gradiometers and writes an XML file containing the GPS position (if selected), and the thermometer's reading. It produces a file per reading. A temporised task performs a periodic scan of the memory, looking for files. If a file is detected the program starts a GPRS connection and sends an e-mail to a predefined address. In case of successful transmission the data file is cleared. A sample of a two 6-sensors gradiometer is shown below.

```
Da:      palmito@ingv.it
Inviato:        mercoledì 16 maggio 2007 18.05
A:      undisclosed-recipients:
Oggetto:        Invio dati tramite email dal palmare

\temperature\20070516173726.xml
-------------------------------
<?xml version="1.0" encoding="utf-8" ?>
<DS9097U_COM1>

<stecche>
<stecca>
<term id="47000000BF98B428">24.875</term>
```

```
<term id="50000000BF926628">23.875</term>
<term id="8B000000BFCDCA28">27.75</term>
<term id="07000000BF3BEA28">24.625</term>
<term id="E5000000BF779C28">23.125</term>
<term id="22000000BF9A5E28">23.0</term>
</stecca>
<stecca>
<term id="64000000BF32D628">24.625</term>
<term id="C7000000BF640428">23.625</term>
<term id="75000000BFBD6028">25.5</term>
<term id="F4000000BF368E28">23.875</term>
<term id="93000000BFBBDC28">22.875</term>
<term id="34000000BF297628">22.75</term>

</stecca>
</stecche>
</DS9097U_COM1>
```

It's actually a logorrheic file, useful for debug that can be shorted in the future.

## Hardware implementation

Data logger

The data logger consists of a HP9015 PDA, some ancillary electronics, a whether proof enclosure, a solar power supply. Figure 10 shows the connection PDA-1wire. The cable supplied by Hewlett-Packard ends with a female db9; the adapter rs232 1-wire ends with the same kind of connector. Moreover the ds9097u uses the DTR and RTS signal to power the adapter internal circuitry, but HP doesn't implement these signals. The circuit shown in Figure 9 shows a gender exchanger to connect the HP cable to the Maxim-Dallas adapter that supplies also the power. Although invisible in the simplified schematics, the ds9097u uses a few Ohms resistor to connect the internal ground to the 1-wire reference ground. We found a better net performance shorting this resistor. A DC/DC 12 to 5 volts supplies the power to the PDA and to the gradiometer's array.

A further circuit was introduced to allow the PDA to insulate the external circuitry in the time between two different measurements. This is shown in Figure 11.

This circuit was introduced to disconnect power and signal in the time between 2 measurements. This helps saving power and (more important) keeps the external long line (source of electrical disturbance) disconnected from the data logger. We found some sporadic 1-wire malfunction disappeared using this circuit. Figure 12 shows the 1-wire hub schematic diagram. The use of this circuit is described in Figure 9. The purpose is to shorten the 1-wire bran-
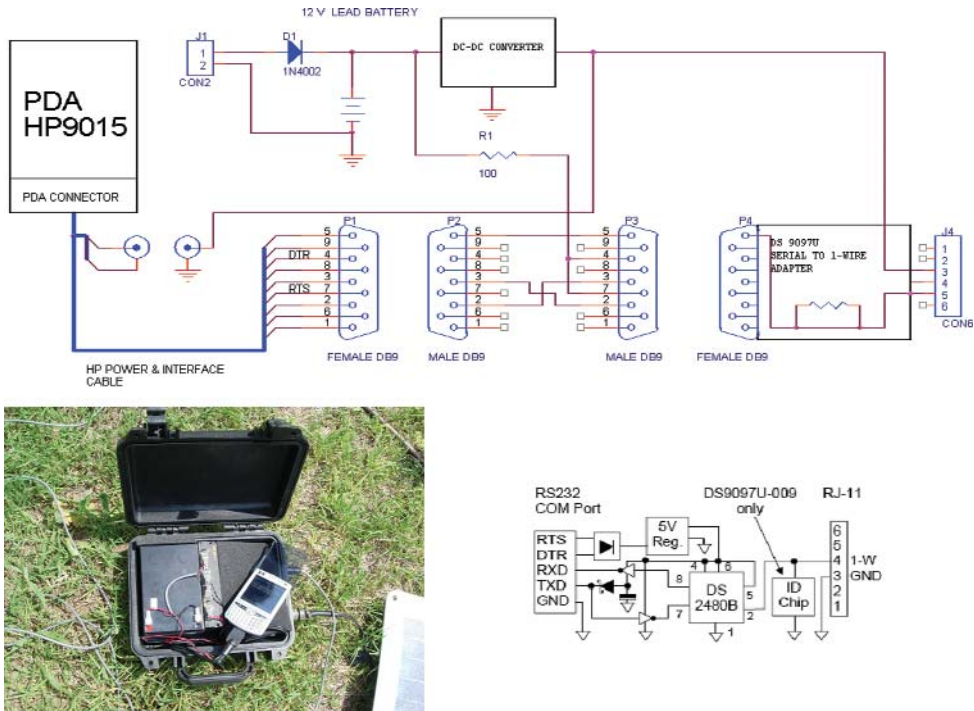
Fig. 10. The PDA connection inside the whether-proof box (top) and the data logger box during a field-test (bottom, left). A simplified schematic of the ds9097u adapter,1-wire ⇔ rs232 (bottom, right) is also shown.
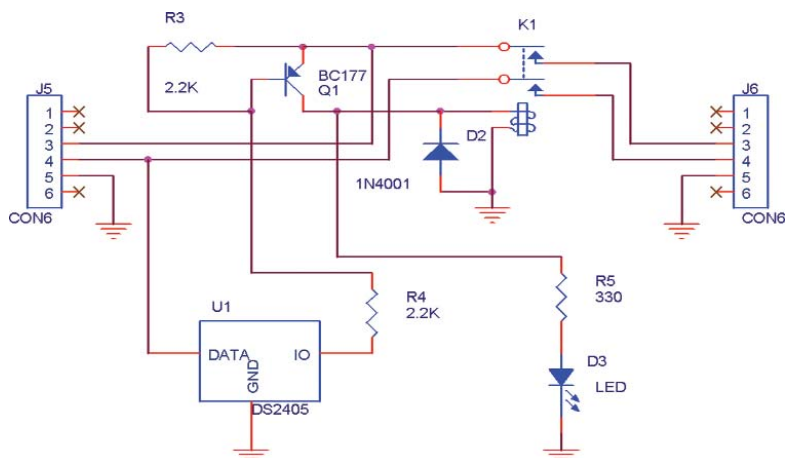
Fig. 11. This circuit uses a 1-wire DS2505 open drain switch to connect the gradiometer data and power line just for the time required for a measurement.
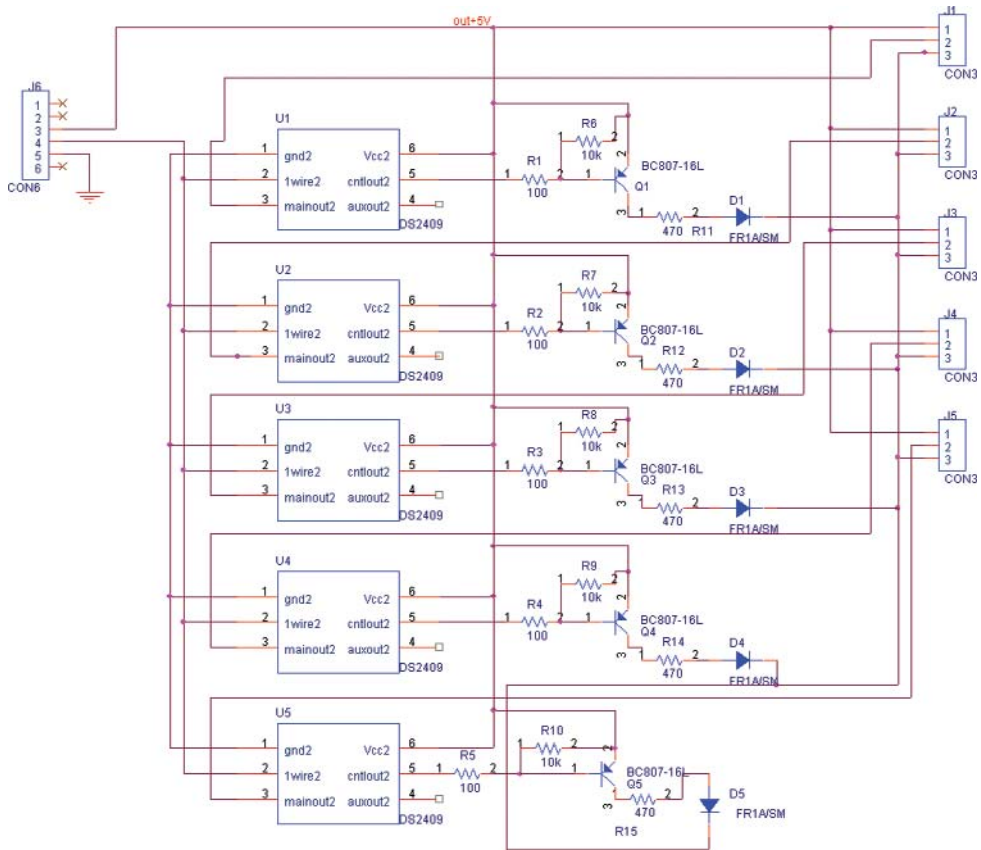
Fig. 12. 1-wire hub. Five 2409 chips are used to activate a single net branch, one at time. When a branch is select the associated led lights.

ches to get a more reliable connection. Using the hub the maximum line length is shorten of 5 times.

Gradiometer

Figure 13 shows the schematic diagram of the circuit inside each gradiometer. At power on the ds2409 output branches are disabled, and the only chip visible by the net is the 2409 itself. If the controller selects the auxiliary branch the LED lights, the timer (555) activates the (4066) analog switch and thermometers and memory are connected. The will stay connected until the time expires or the 2409 is switched to the main branch. In this case even the 2409 of the next gradiometer became visible and so on.
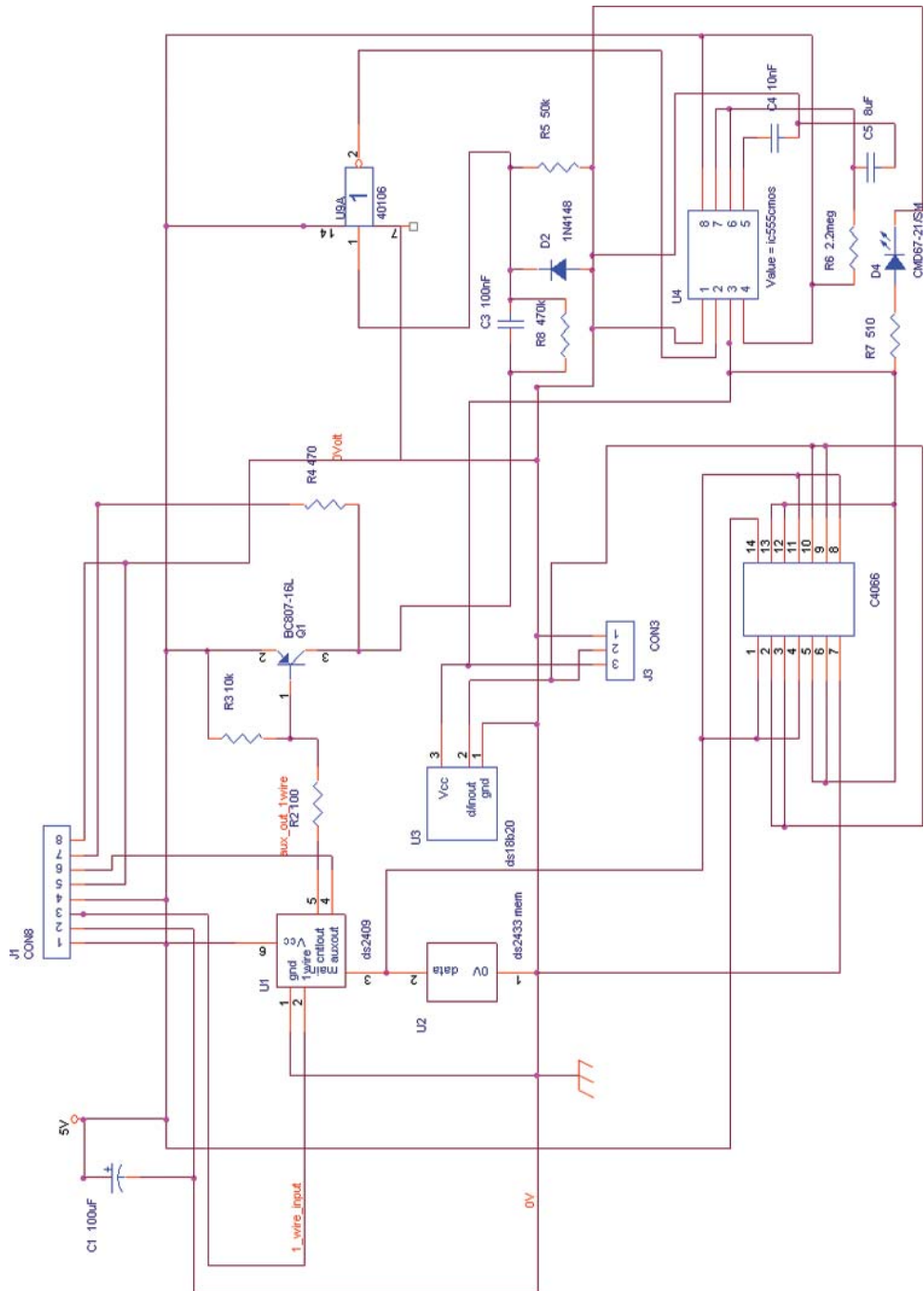
Fig. 13. Electronic circuit inside the gradiometer's head. Connector J1 brings signal to the connectors installed on the top cover and to the LED. J3 connects the 1-wire thermometers array inside the rod.

FIELD TESTS

The system has been testes in the INGV lab in Pozzuoli (Solfatara), and in the Vulcano island and showed an acceptable performance. Figure 14 shows a 8-days recording of a gradiometer installed in La Fossa di Vulcano.
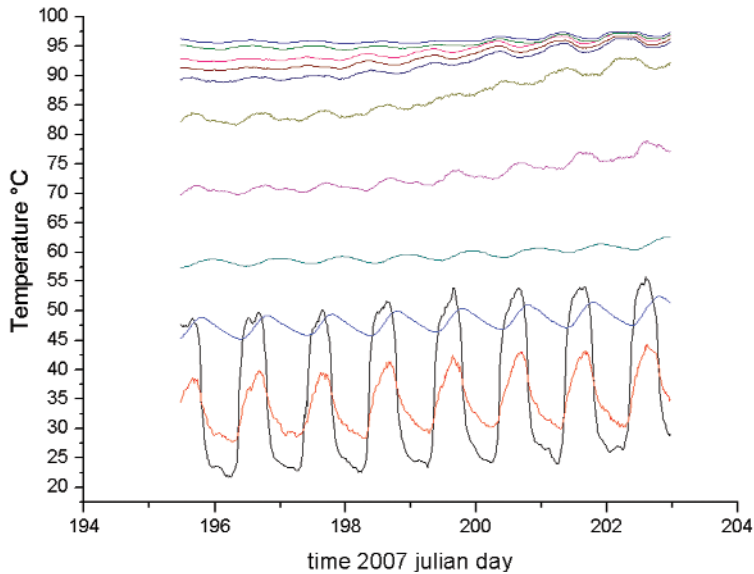
Fig. 14. Eight days of continuous temperature recording La Fossa di Vulcano.

REFERENCES

Macedonio and Chiodini (2001) Observation and modelling natural CO2 emissions in Italy. Geophysical Research Abstracts, 3, EGS. 26th GA, Nice, March 2001, p. 1080.

Aubert, M., Diliberto, S., Finizola, A., Chebli, Y. Double origin of Hydrothermal convective flux variation in the Fossa of Vulcano (Italy). Bull Volcanol DOI 10.1007/s00445-007-0165y.

Avino et al. (2000) Heat flow from diffuse degassing structures of active volcanoes Eos Trans. AGU, 81 (48), Fall Meet. Suppl., Abstract V62C-01.

Thermal gradiometer:
purposes, design and performance

G. Romeo[1], G. Chiodini[2], F. Pongetti[1]

[1] *INGV, Roma1*
[2] *INGV, Napoli*

INTRODUCTION

Direct thermal gradient measurement is a powerful instrument to investigate volcanic areas. It allows measurements about thermal emission, thermal transportation mechanisms and degassing.

The goal of this project is to produce an instrument able to deliver a complete, real-time, thermal measurement of a ground slab. This instrument will offer a way for thermal cameras calibration, since the surface temperature is a measured observable and the instumented area may be uses as calibration target.

Installing several thermometers in the ground slab to investigate, in a well-known geometry may perform thermal gradient measurement. The geometry, the measured temperature and the thermal conductivity knowledge allow calculating the thermal gradient and heat flow.

Although the gradient may be directed in any direction, we expect the ground temperature to increase with de deepness, with an average of roughly 2.5°C/m. In volcanic areas this gradient increases tremendously. The vertical temperature gradient, directly tied to the heat flow, has the maximum interest to volcanolologists.

A simple way to build a vertical thermal gradiometer is to instrument a rod with thermometers. The ratio between the temperature difference of two thermometers and their distance gives the thermal gradient. Increasing the number of high quality thermometers improves the measurement performance. Figure 1 shows a vertical gradiometer's array instrumenting a terrain slab.

The rod insertion must not perturb the terrain. This may be obtained with small rod diameter and using material with a poor thermal conductivity.

TEMPERATURE MEASUREMENTS

Temperature measurements are, in principle very simply: a substance changes some physical properties with temperature (may be length, electrical resistivity, color). After placing it in contact with the object to measure and waiting for thermal equilibrium, you can get your temperature information. Of course
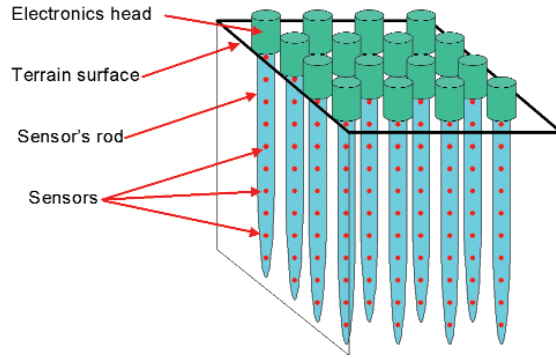
Fig. 1. A 3-d thermal gradiometer obtained by installing an array of vertical gradiometers. A gradio-meter is a rod filled with temperature sensor connected to a data acquisition system.

electric properties (resistivity first) are preferred because of the simplicity electric signals may be handled, converted and stored.

Figure 2 shows some methods of electrical temperature measurement.

The first one (upper left) is the good one: a current source forces a well-known current to the sensing platinum resistor: we do not have to worry about the voltage drop in the wires because the generator operates in current mode. We use two separated wires to pick up the voltage on the resistor, and still we don't worry about the voltage drop because the current on the pick up wires is very near to 0 so the voltage drop is negligible. Unfortunately connecting several sensors in this way has an unpractical complexity because of the huge number of wires.
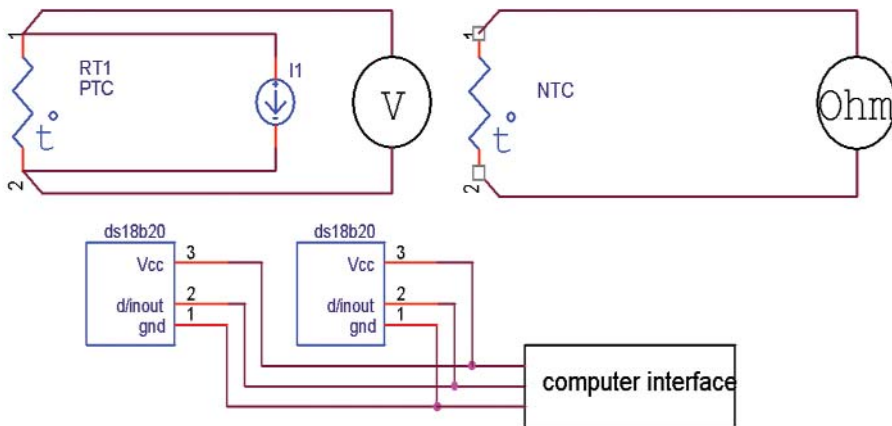
Fig. 2. Upper left: High quality temperature measurement: Platinum resistor and 4 wires connection. Upper right: poor temperature measurement: NTC resistor and 2 wires connection. Bottom: nice temperature measurement: digital sensors with a network connection: 2 or 3 wires for multiple sensors.

The second (upper right) one is a very poor one: NTC are age changing devices, with an exotic calibration curve.

We may skip the error induced by wires (NTC are available with a very high resistance, but we earn several other error's sources).

The third method (bottom) is a nice one. Digital communication allows connecting several sensors and does not suffers of the errors induced by wires. This method, chosen for the thermal gradiometers construction, allows fitting several thermometers inside the measurement rod without increasing the wiring complexity.
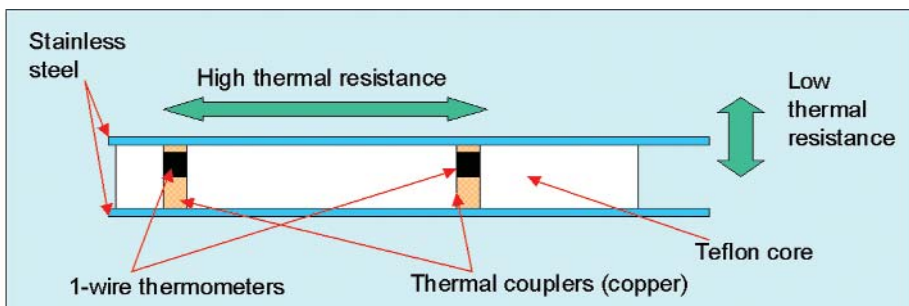
THERMAL GRADIOMETER ASSEMBLY

A good gradiometer assembly must offer a good coupling thermometer-terrain and a poor lengthwise thermal conductivity. This has been obtained in the assembly shown in Figures 3 and 4.

A thin walled stainless steel tube houses the thermometers, thermally connected to the tube wall by copper rings. Insulation between thermometers is obtained by a Teflon core, which also keeps in place thermometers thermal couplers and connection wires.

1-WIRE THERMOMETERS

The digital thermometer shown in Figure 1 is an interesting integrated circuit, produced by Dallas-maxim semiconductor. It's a part of the 1-wire family.

1-wire is an electrical and logical method to build a master slave network where all components are connected on a multi-drop bi-directional serial line capable to carry the power. In our case the master is the data logger, and the

Fig. 3. Section of a thermal gradiometer. Sensors are housed in a thin walled stainless steel tube filled wit a Teflon core. The core avoids convection inside the tube. The lengthwise/widthwise thermal resistance ratio depends of the 1/(wall tube thickness)^3. With the chosen values the lengthwise resistivity approximates the dry terrain one.
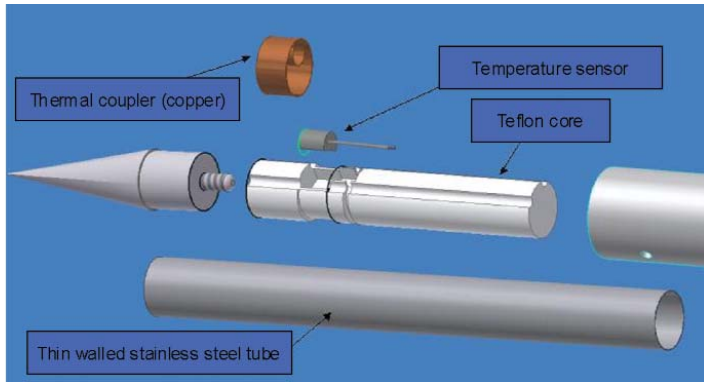
Fig. 4. A mechanical sketch of the first gradiometer prototype.

slaves are the thermometers. A 1-wire thermometer integrates in a single chip, containing a unique identification number, a net handler (protocol and so on), a semiconductor thermometer and its a/d converter. They can be dropped on a single 2 or 3 wires line and their number is limited only by electrical consi-derations. The chosen thermometers offer a temperature range from -55 C to +125 C with a maximum resolution of 12 bits. Despite the poor declared accuracy (1 degree), 1-wire thermometers show a precision only limited by the internal A/D converter resolution. An experiment has been conducted to eva-luate the 1-wire sensors performance. Some 1-wire thermometers have been tested for two months, comparing the measured temperature to a well-known pt1000 (Figure 5).

Te left diagram in Figure 5 shows a one-day temperature recording obtained with a pt100 (red trace) and with a 1-wire sensor (blue trace).

The left diagram in Figure 5 shows some difference between the two signals. The most part of this difference may be ascribed to the sensor's time response. The PT100 has a bigger thermal capacity, and it is slower than the 1-wire fol-
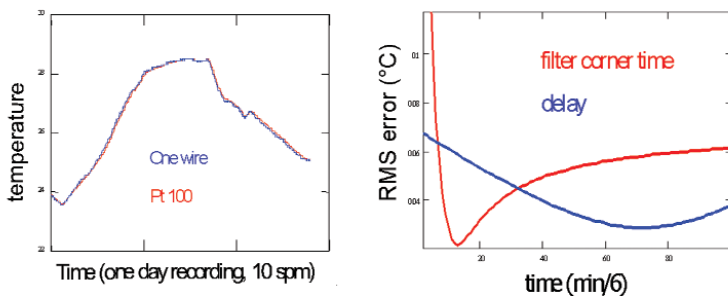

Fig. 5. Left: a one-day recording using a pt100 and a 1-wire sensor. Right: the RMS error between the two sensors calculated for a time-filtered and time-delayed 1-wire signal.

lowing the temperature changing. This can be correct wit a simple time shift (delaying the faster 1-wire response) or with a true 1-pole low-pass filter (it's a good approximation of the reality). In this diagram we may see the RMS error between the two signals after such treatment. The low pass approach brings the error very near to the limit given by the sensor resolution.

PROTOTYPE TEST

A prototype with 14 thermometers has been build to check the design goodness. A first field occurred in the Solfatara (Pozzuoli, NA) and consisted in the vertical temperature profile measurement, and in a comparison with a PT100 thermometer. The comparison showed the expected agreement between 1-wire and pt100 inside the error gap.

Figure 6 shows the temperatures measured by the prototype after the insertion of the instrument in the terrain. After a settling time of few minutes the gradiometer reaches the equilibrium and returns stable readings. Figure 7 shows two thermometers temperature-time diagram after the insertion.

Both diagrams can be fitted using the logistic function:

$$y(x) = \frac{a}{1 + be^{-cx}}$$

Using interpolated data allows speeds up the measurement allowing determining the final temperature analysing only the initial values, without waiting for the thermal equilibrium. This is useful for a quick single-point measurement. The agreement between extrapolated and measured data calculated on the whole a prototype is shown in Figure 8. The error increases near the terrain surface. This has been attributed to the fast variation of the surface temperature, which invalidates the method.
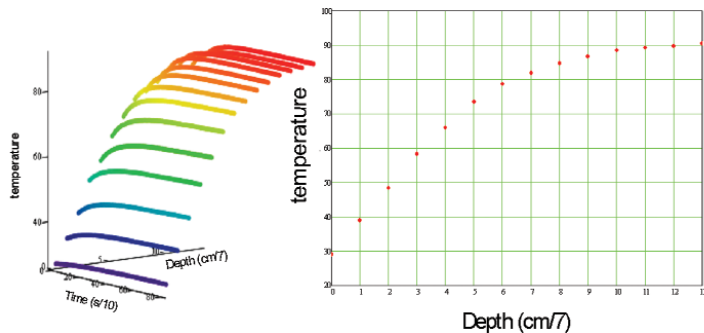
Fig. 6. The left diagram shows the temperature behaviour after the instrument insertion, during the settling time. The right diagram shows the temperature profile.
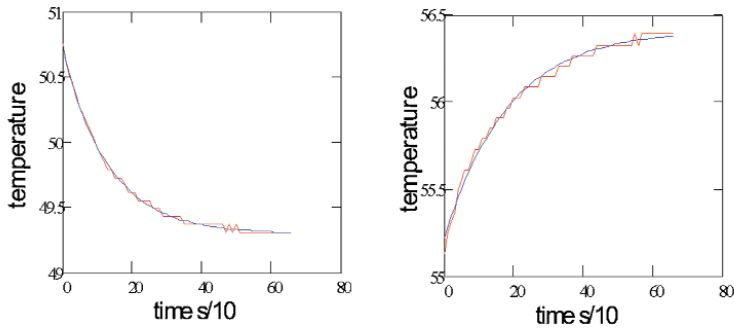
479

Fig. 7. The shown diagram illustrates the temperature changing in two thermometers after installation. The red curves show the measured values, the blue ones show a fit with a logistic function.
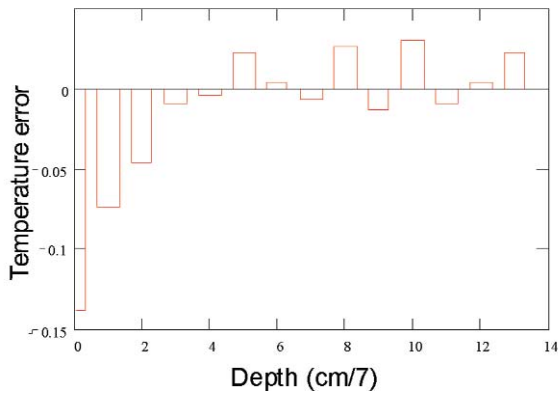

Fig. 8. Error between the measured data and the interpolated data. The interpolation comes from 6 minutes data, and the error is calculated after 12 minutes.

DS18B20 Programmable Resolution 1-Wire Digital Thermometer, http://datasheets.maxim-ic.com/en/ds/DS18B20.pdf.

REFERENCES

Macedonio and Chiodini (2001) Observation and modelling natural CO2 emissions in Italy. Geophysical Research Abstracts, 3, EGS. 26th GA, Nice, March 2001, p. 1080.

Aubert, M., Diliberto, S., Finizola, A., Chebli, Y. Double origin of Hydrothermal convective flux variation in the Fossa of Vulcano (Italy). Bull Volcanol DOI 10.1007/s00445-007-0165y.

Avino et al. (2000) Heat flow from diffuse degassing structures of active volcanoes Eos Trans. AGU, 81 (48), Fall Meet. Suppl., Abstract V62C-01.

The permanent thermal infrared network for the monitoring of hydrothermal activity at the Solfatara and Vesuvius volcanoes

G. Vilardo, G. Chiodini, V. Augusti, D. Granieri, S. Caliro,
C. Minopoli, C. Terranova

Istituto Nazionale di Geofisica e Vulcanologia, Osservatorio Vesuviano, Italy

Abstract: In this paper we describe the activities carried out for the realization of an image surveillance systems, in the thermal infrared (TIR) wavelengths range, for the continuous long-term monitoring of the shallow thermal structure of the Solfatara (Campi Flegrei) and Vesuvius volcanoes. The system implementation was pursued by both acquiring and integrating all the technological instruments necessary to operate an instrumental system constituted by: a network of remote monitoring stations; a transmission system for the image data centralization; a control unit for both the remote stations control and the acquired data processing. The analysis of two-years long series of IR images collected at the Solfatara allowed us to evaluate, in the observation period, the main thermal features of the major fumarole field located in the SE inner slope of the Solfatara crater.

INTRODUCTION

In recent years, following the hand-held thermal imaging cameras development, increasing use is being made of ground-based thermal IR measurements to map and investigate lava flow field structures, to estimate active lava flow parameters, to analyze the evolution of active eruption plumes (Pinkerton et al., 2002; Calvari and Pinkerton, 2004; Lautze et al., 2004; Calvari et al., 2005; Johnson et al., 2005; Harris et al., 2005; Vaughan et al., 2005; Lodato et al., 2006).

With respect to previous IR applications, most of which regarded the study of relatively quick processes associated to volcanic eruptions, our experiment was finalized to detect and quantify over long periods slow temperature changes of the shallow thermal structure of quiescent volcanoes. Any increase in the flux of fluid expulsed by the volcanoes will be accompanied by an increase in the temperature of the rocks hosting the fumarolic vents or in the size of the fumarolically heated areas (Oppenheimer et al., 1993; Kaneko and Wooster,

G. Vilardo, G. Chiodini, V. Augusti, D. Granieri, S. Caliro, C. Minopoli, C. Terranova

1999). Moreover it is our opinion that also relatively slow variations in the amount of thermal energy flux can help to define the level of activity of the volcano and that possible major changes in surface temperature can mark the transition from a quiescent stage to an eruptive phase. For this reason our experiment was designed to monitor a significant portion of the Solfatara fumarolic field and the inner slope of the Vesuvius crater with the periodical, systematic acquisition of IR images from permanent stations.

In the first part of the paper we described the experiment design including the technical aspects of the IR camera, the remote control system and the main characteristics of monitored scene. In the second part of the paper we present the analyses performed on a comprehensive time series of 2175 nighttime IR images acquired by the station located at Solfatara in the period October 2004-January 2007 with the double purpose to evaluate the thermal features in the observation period and to determine whether IR information can be useful in the long period monitoring of a volcanically active area. To our knowledge, this is the more comprehensive of such datasets available for a volcanic area.

## EXPERIMENT DESIGN AND SYSTEM DEVELOPMENT

The development and the operating assembling of the whole surveillance system have been characterized by a heavy technological integration activity and specific tools development that has not previous noteworthy example to which refers. In fact, the thermal infrared image cameras with uncooled focal plane array measuring systems (microbolometer technology) are of recent availability for the civil market. Such systems find a massive use for process control and quality control in production line and the monitoring of systems in motion or electrical devices; therefore, such monitoring applications implies the use of the thermal cameras as laboratory instruments or just predisposed for indoor installations.

Up to now are not realized any applications for environmental monitoring by permanent stations, still less in extreme conditions as those affecting the volcanic areas; consequently the available thermal imaging cameras are commercialized without the availability of additional tools, like protective housing, data transmission devices or remote control systems.

For this reasons, the integration of the supplementary and necessary technological modules has required the execution of appropriate market surveys to look for special suppliers e\o producers, as well as, the conceiving of specific solutions.

The TIR monitoring network has been conceived in order to satisfy the requirements of continuous long-term volcanological surveillance and has been planned to install the image thermal cameras in two remote sites located on the top of the Vesuvius crater and in the Solfatara crater (Flegrei Fields) respectively (Figure 1).
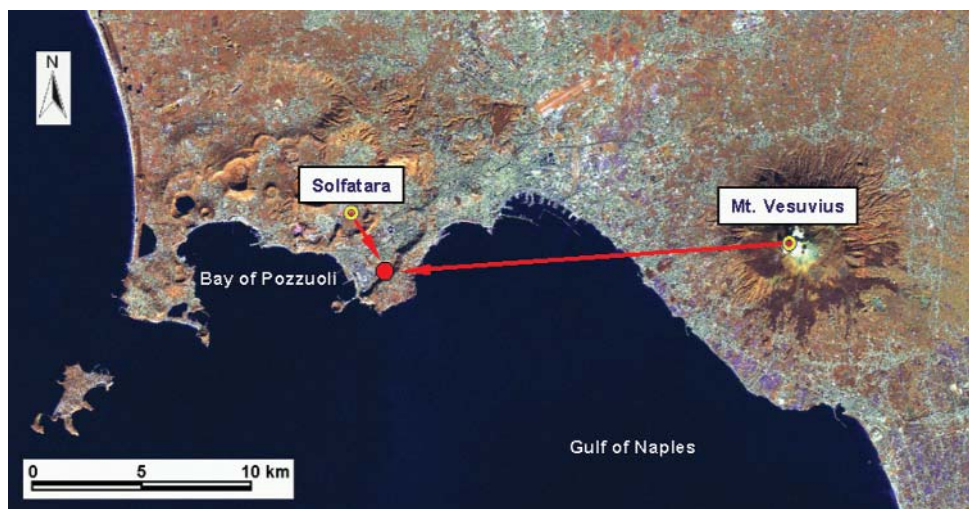
Fig. 1. Location of the Remote Monitoring Stations (RMS). Red dot represents the position of the Surveillance Center.

The whole system consists of two permanent remote monitoring stations, with remote control of the calibration and shooting functionalities of the microbolometric image sensors calibrated on the long thermal infrared wavelengths (Lwave TIR), and a control unit that manages the system by setting the measure session parameters for each single station.

The control unit is located at the surveillance center of the Vesuvius Observatory-INGV in Naples. Its main feature is the management of the remote stations network through a communication system based on two different technological solutions: a master transmission system via GSM frequency network and an emergency system on radio frequency network. The control unit communicates with the RMS's allowing to both configure times and shooting parameters for the image acquisition and run the automatic uploading of the remotely acquired thermal images. In addition, the control unit performs the storage of the transferred thermal images both in its proprietary graphic format for data visualization and, after real-time data conversion, in form of digital ASCII matrix containing the temperature values for further processing.

THE TIR REMOTE MONITORING STATION

The IR cameras used, are the NEC Thermo Tracer TS7302 with uncooled focal plane array measuring systems (microbolometer technology 320x240 pixel) that operates in the spectral range from 8 to 14 μm across a 29° (H) x

22° (V) field of view and a focusing range from 0.5 m to infinity with standard lens.

Up to the beginning of the experiment were not realized any applications for long period outdoor monitoring in extreme conditions as those affecting a volcanic area. For this reason, the first part of the experiment was devoted to integrate the station with protective housing and remote monitoring system (RMS) including data transmission devices. The protective housing, inside of which the camera is placed, has been realized in special stainless steel (Figure 2a) in order to operate in presence of corrosive elements. The shooting window is protected by a germanium glass (Figure 2b) that results transparent to the thermal wavelengths, and is equipped with a mechanical device for covering the germanium glass.

This cover has the dual function to allow the microbolometric sensor calibration and to preserve the integrity and the cleanness of the shooting window during the standby of the thermal camera. The RMS directly manages the phase of the image shots by running in succession the execution of the following actions: (1) turns the thermal camera on, (2) waits for the calibration of the microbolometric sensor, (3) opens the watertight cover, (4) sets the sensibility, the range levels and focus parameters, (5) waits for the image acquisition, (6) closes the watertight cover, (7) uploads the image data acquired by the thermal camera in numerical format through serial RS 232C interface, (8) turns the thermal camera off.
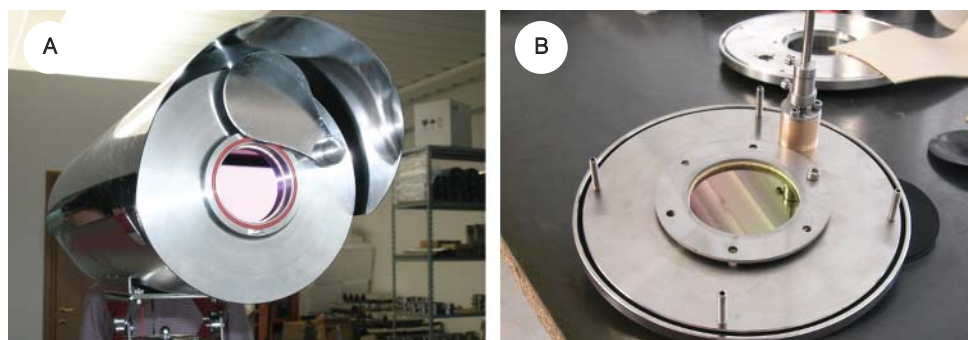
Fig. 2. **(a)** The protective housing realized in special stainless steel. **(b)** Detail of the frontal flange in which is located the germanium glass.

Following the RMS image storage, the control unit communicates with the RMS and runs the automatic uploading of the remotely acquired thermal images. Table 1 summarizes the time taken by each task from the thermo camera on, up to the image downloading carried out by the control unit.

Tab. 1. Time duration of each task involved in the image acquisition and transfer.

| Task		Time
Thermo camera	On	00 s
	Check	45 s
	Run	15 s
	Calibration	45 s
Shooting window opening		05 s
Sensibility, range levels and focus set up		10 s
Image acquisition		15 s
Shooting window shutting		05 s
Image transfer from the camera to the RMS		6 m 20 s
Image transfer from the RMS to the Control Unit		3 m 10 s
Total time		11m 50 s

THE TIR ACQUIRED SCENES

The installation of the remote monitoring stations at Vesuvius crater rim (Figure 3) and at Solfatara (Figure 4) ended at the mid of July 2004 and at the mid of September 2004 respectively. After tests performed on the whole
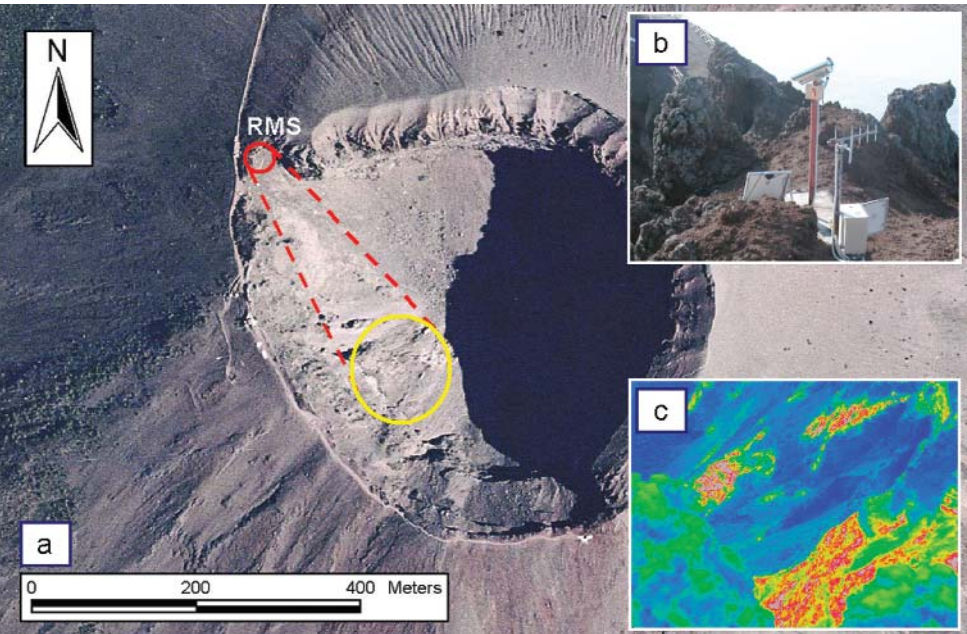
Fig. 3. Vesuvius thermal monitoring station. **(a)** viewing geometry, the yellow circle represents the target area; **(b)** the TIR station on the crater rim; **(c)** scene (320x240 pixel) acquired by the remote station in the spectral range of the IR wavelength.
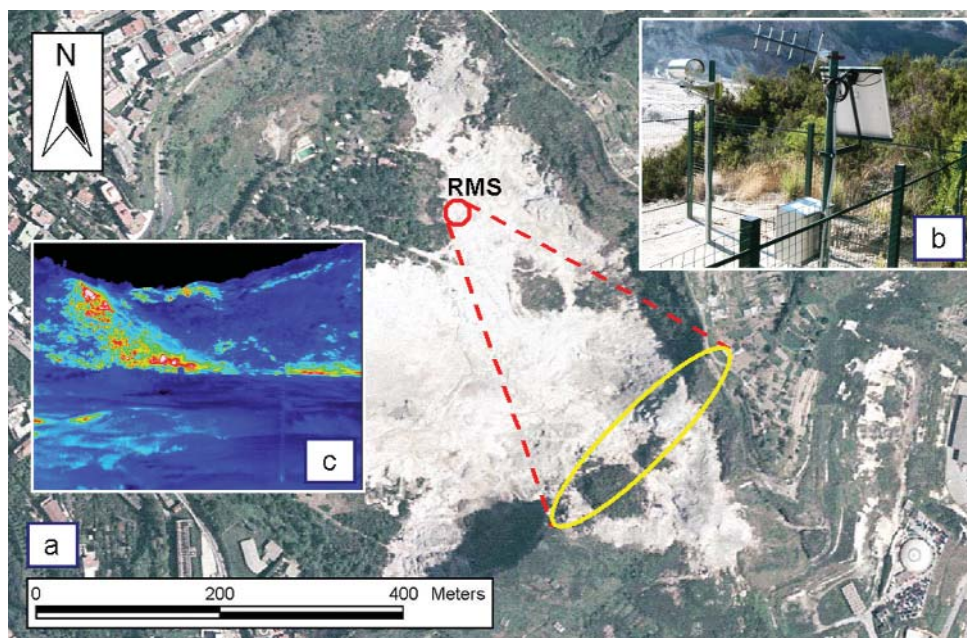
Fig. 4. Solfatara thermal monitoring station. **(a)** viewing geometry, the yellow ellipse represents the target area; **(b)** the TIR station in the field; **(c)** scene (320x240 pixel) acquired by the remote station in the spectral range of the IR wavelength.

system began the systematic thermal imaging acquisition. IR images were nighttime collected with the rate of three images per night (acquisition time: Vesuvius 23:00, 01:00, 03:00 UTC and Solfatara 00:00, 02:00, 04:00 UTC).

The acquired scene in the spectral IR range are shown in Figure 3c and 4c.

For the Vesuvius thermal monitoring station the scene includes part of the SW inner slope of the Vesuvius crater (Figure 3a). This area even if not affected by fumarolic activity shows a significant thermal anomaly depicted by the most radiant pixels in Figure 3c.

For the Solfatara thermal monitoring station the acquired scene includes part of the SE inner slope of the Solfatara crater (Figure 4a) where most radiant pixels correspond to the location of the major fumaroles (150°~160°C) (Figure 4c), which are sited at the intersection of two active, SW-NE and NW-SE, main faults of Campi Flegrei. This area is the most active sector of the crater. On the basis of previous investigations (Chiodini et al., 2001), can be evaluate that this area releases diffusively ~ 15% of the total CO_2 and heat released by Solfatara crater (i.e. ~ 250 t d^{-1} and ~ 13 MW respectively).

The Solfatara TIR image framing covers a viewing distance that ranges from 40 m up to a maximum of about 500 m, with the main fumaroles field located at an average distance of about 300 m. The Vesuvius TIR image framing

covers a viewing distance that ranges from 100 m up to a maximum of about 400 m, with the main thermal anomalies located at average distances of from about 150 m up to 300m. In both the cases, the increasing viewing distance produces an increase in the pixel size (Table 2) and consequently a decrease in the image resolution.

Tab. 2. Pixel size vs. viewing distance.

Distance (m)	10	30	100	300	500
Pixel size (mm)	16	48	160	480	800

The Solfatara TIR imagery was generally of good quality, though it suffers from two minor problems related to the weather conditions: (1) the occasional presence of wide blurred areas due to the condensation of the fumaroles plume and (2) the rare occurrence of heavy rain which caused the homogenization of the IR temperature. On the contrary, the Vesuvius TIR imagery strongly suffers from problems related to the cloudily weather conditions which frequently affect the top of the volcano (the station is located at 1165 m a.s.l.). Moreover, gaps in the GSM transmission often affect the Vesuvius area and this causes the lack of the image transfer to the control unit.

The Vesuvius monitoring station was also affected by two further problems related to: a) the electrostatic charges accumulation that damaged the electronic components of both the RMS and the thermal camera, and b) the failure of the washer impermeability of the protective housing in which the thermal camera is located. In order to restore the functionality of the Vesuvius monitoring station, the broken thermal camera and RMS were replaced and both the line protections and the ground conductor to dissipate the strike into the earth were improved.

Due to the gaps in the image acquisition, related to the operation restoration, the whole TIR image dataset acquired from the Vesuvius remote monitoring station up to 31st may 2007 consists of 1864 images; on the contrary the Solfatara monitoring station, which was not affected by any instrumental problems, acquired 3546 TIR images.

THE PORTABLE TIR MONITORING STATION

Further efforts have been dedicated to design and assemble a portable thermal infrared imagery instrumental system to be employed in temporary surveys in sensitive areas.

The portable station, named TITANO (Thermal Infrared Transportable Apparatus for Nearby Observation), is based on the same technological approach used to operate the permanent monitoring stations with the addition of a tripod necessary to keep up the protective housing containing the thermal camera. The tripod has been conceived and realized adequately solid in order to ensure a stable TIR scene acquisition and it was equipped with telescopic joints to facilitate the clamping on the ground in different field settings. The portable TIR imagery acquisition system was tested during a field survey carried out at Vulcano Island on June 2006 (Figure 5a). On that occasion was estimated in about two hours the time necessary for the installation of the whole acquisition and centralization system, as well as, was verified the right operation of both the GSM and radio transmission systems.

Following the satisfactory results obtained in the first field test, TITANO was used during the Major Emergencies Simulation Exercise (MESIMEX), which, coordinated by the Italian Civil Protection Department, took place from October 18th to October 23rd 2006 in the Vesuvian area. The exercise, which was focused on the preparedness phase for a major volcanic emergency in the area of Vesuvius, involved several Volcano Expert Teams (VET) which improved the existing monitoring systems with the deployment of added instruments.

Successively, in order to improve the thermal monitoring of the Campi Flegrei, affected by a general small terrain uplift phase started in autumn 2005 (Troise et al., 2007), TITANO station was installed on October 30th 2006 and up to now operative, at Pisciarelli (Figure 5b).

This area is located on the outer eastern flank of the Solfatara crater and is characterized by heavy water vapor and CO_2 emissions.

ANALYSIS OF THE SOLFATARA TIR IMAGE SERIES

The reliability of the acquired data was firstly tested with an in situ calibration procedure, performed by comparing IR temperatures with those given by a K type thermocouple.

The experiment consisted in the comparison between IR temperatures and temperatures measured with a K type thermocouple (hereafter named T_ther). The thermocouple connected with an automatic data logger was installed in an easily identified target (the wood wall of a cabin located in the central sector of the IR scene) whose IR temperature was estimated as the average temperature of 4 pixels, located in the center of the cabin wall (hereafter named T_target). The experiment started on the 1st August 2006 and ended on the 3rd January 2007 producing 434 couples of T_ther and T_target values ranging from 273 to 301 K. The temperatures registered by the two independent methods were then compared and, even if the IR measurements resulted systematically lower than T_ther, the results are very good: the two

Fig. 5. **(a)** Field test of TITANO equipment performed on June 2006 at the Vulcano Island. **(b)** From October 30th 2006 TITANO is operating at Pisciarelli (Phlegraean Fields).

temperatures strictly follow the same temporal pattern and show a very high correlation (R^2 = 0.989). The positive results allowed us to do not apply any instrumental corrections to the rough data. This chose was based also in the consideration that another source of uncertainty arises from viewing the surface at an oblique angle (Ball and Pinkerton, 2006), an effect which is difficult to be evaluated for every pixel of the image. The availability of a long time series of the same scene, allowed us to analyze the collected thermal imagery in terms of relative temperature variations without apply any correction for the oblique angle view whose possible effects remained unchanged at each location during the monitoring period.

Meteorological data were also specifically acquired during the experiment in order to investigate the dependence of IR data on environmental parameters. IR temperatures are controlled mainly by air temperature which alone explains 92%-97% of the IR temperature variance. This implies a strong seasonal control on the IR temperatures of both background and fumarolized hot areas of Solfatara. In order to remove the effect of ambient temperature variations, which masks the variation caused by endogenous changes, a simple background correction (T-T_target) was applied to all the data.

We investigated also the quality of the images (i.e. sharpness, contrast, etc.) which strongly affects the possibility to recognize temperature anomalies and which we found well quantified by the standard deviation (SD) of the IR temperatures of the images. The image quality resulted inversely correlated with the vapor concentration in air. In order to study the evolution in the time of the monitored thermal structure we thus adopted a simple 'quality image' filter based on SD values (7.7 < SD < 8.8).
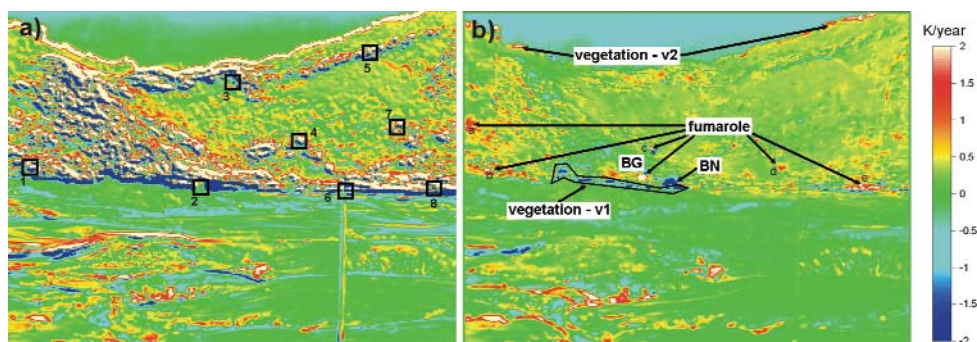

Fig. 6. (a) Map of the IR 10-days averaged temperature changes expressed in K/year. A series of contiguous positive and negative anomalies are evident. Eight boxes in the SE inner slope of Solfatara crater are selected to co register the image; (b) Co-registration of the image with the identification of the true temperature changes. Alternations of positive and negative anomalies are disappeared and a few cooling spots (V1 area) and heating spots (areas from a to e and BG area) are highlighted.

On a selected dataset of 2175 TIR images has been performed a pixel by pixel linear regression of T-T_target with respect to time in order to investigate local temperature changes of the scene. A 10-days average values of T-T_target at each pixel was considered in order both to reduce the computation time and to smooth high frequency variations. The results are graphically reported in the map of Figure 6a.

The map, which represents the temperature change expressed as K/year, highlights a series of positive and negatives structured anomalies. At any positive anomaly systematically corresponds a negative anomaly, located at left and below of few pixels, suggesting that a movement of the scene occurred during the monitoring period. This unexpected behavior complicates the identification of the real temperature change of the scene. In order to do a co registration of the images, a study of the correlations among selected portions of the scene (boxes from 1 to 8 in Figure 6a) was performed. Practically for each box were determined the shifts in the horizontal and in the vertical axis (DX and DY respectively, expressed as number of pixels) for which the best correlation with respect to a reference case (image n. 1200, 20-02-2006) is obtained. The results in terms of mean values are reported in the DX and DY chronograms of Figures 7a and 7b.

All the boxes are located in the SE inner slope of Solfatara crater in correspondence of hot spots where the contrast with the relatively cold nearby
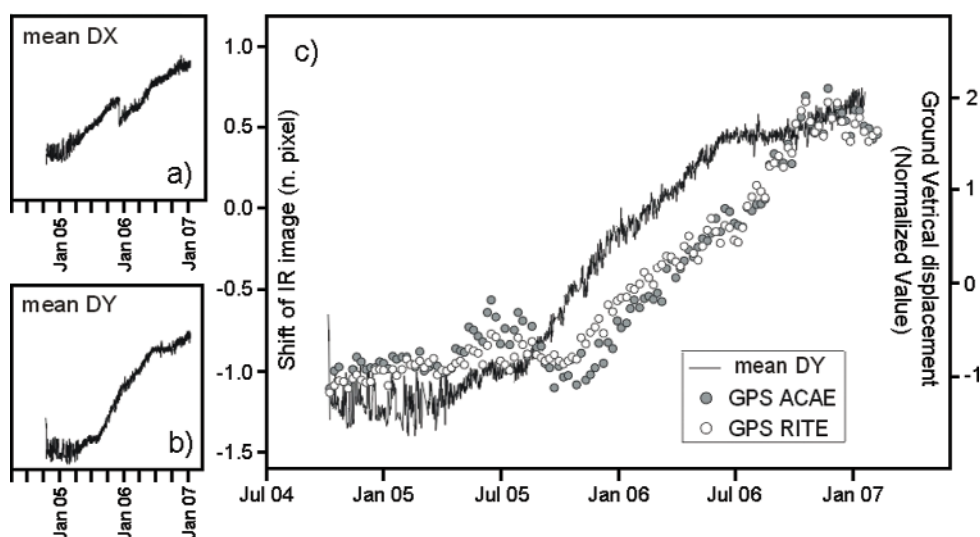
Fig. 7. **(a)** mean horizontal shift (DX) and **(b)** mean vertical shift (DY) represent the horizontal and the vertical displacement in number of pixels of the whole IR scene with respect to a reference case (image n. 1200, 20-02-2006). **(c)** Chronogram of the mean vertical displacement of the scene (mean DY) compared to the ground vertical movement recorded by the RITE and ACAE GPS stations (normalized values).

zones makes the computation more efficient and the best results, i.e. where the less noising DX and DY curves were obtained. The results evidenced that all the curves obtained in different portions of the scene show very similar temporal trend. On the base of this similitude it is assumed that the entire IR scene moved both synchronously and at the same velocity following the mean DX and DY vs. time patterns shown in Figures 7a and 7b. This homogeneous behavior of the entire scene suggests that a slow movement affected the camera.

The DY vs time curve shows an intriguing similitude with the ground deformation at CF as returned by GPS continuous monitoring stations located in the neighborhood of the Solfatara (Figure 7c). This observation lead us to suppose that a local deformation of the terrain would have caused the tilt of the pole where the camera is installed and the consequent movement of the scene. We can not exclude that this local deformation is linked to the general terrain uplift phase which occurred at Campi Flegrei in 2005-2006 (Troise et al., 2007).

The best correlation between DY and GPS measurements is obtained by back-shifting ACAE and RITE data of ~100 days. This similitude, if confirmed in the next years, would imply that Solfatara is in some way affected by a ground dynamic which anticipates the general deformation at CF. Solfatara would consequently result as an excellent site to study precursors of bradyseismic crisis.

The inferred DY and DX mean values (Figures 7 a and 7b) have been used to perform the co registration of all the images assuming as reference (DX=0, DY=0) the image n. 1200 (acquired on 20-02-2006). Practically for each pixel of each image was computed a new value of T-T_target as the average of the values of the 4 pixels located in the new position and weighted in function of the surface contribution. Successively, a pixel by pixel regression with respect to time of the corrected T-T_target data (averaged on a 10 days period) has been performed and the results are graphically shown in Figure 6b.

The map doesn't show any more the structured alternation of positive and negative anomalies which characterizes the analogue picture obtained from the uncorrected values (Figure 6a).

This suggests in general the efficiency of the adopted correction and that Figure 6b can be used to investigate temperature changes occurred at Solfatara during the monitoring period. The main thermal features observed in the map of Figure 6b show that temperature variations affected both the Solfatara crater wall and the areas of the plane nearest to the camera. We focus here our attention to the variations of the Solfatara crater wall being the second ones of smaller dimension and most probably linked to very local processes. The map of Figure 6b suggests that generally the SE inner slope of the Solfatara crater was not affected by important temperature changes, being these generally restricted in the interval from -0.5 K/year to 0.5 K/year. The map however highlights the presence of some spots characterized by higher temperatu-

re increases (red and white colors) and few spots which cooled (blue color). Figure 6b shows that the temperature increase, which is particularly evident at BG site (Bocca Grande: the main fumarole at Solfatara), didn't affect the entire fumarolic field where, contrary, some spots cooled (blue color in Figure 6b). This temperature increase did not regard the maximum temperature of BG fumarole which, in the period of IR monitoring, did not show such large variations remaining at a stationary value of 161 ± 2°C. The observed temperature increase regarded the nearby hot soils most probably affected by an increased flux of fumarolic fluids. It is worth noting that also steam velocity of BG fumarole, a parameter monitored since spring 2005, shows an increase in the flux of the fumarolic fluids, suggesting that the IR temperature anomaly detected in the observation period is caused by the increased fumarolic flux. On the contrary, the temperature decreases are not linked to the variation of the hydrothermal source rather they reflect anthropic jobs or vegetation growth. In particular the BN (Bocca Nuova) site, another high temperature fumarole (~ 150°C) shows a marked cooling. In this case the temperature variation registered by the automatic station was caused by the building in October-November 2006 of a tourist pathway that goes around the BN fumarole. The work caused a clear decrease of the temperature of the area, variation not linked to the activity of the volcano.

Other temperature decreases were observed in the area labeled 'vegetation-v1' in Figure 6b. In this case the temperature decrease reflects the fact that the relatively hot pixels of the Solfatara crater wall were progressively occupied by the colder vegetation growing in the spring season. The same process explains also the positive anomalies at the border between the sky and the ground ('vegetation-v2' in Figure 6b), being in this case the relatively cold pixels of the sky progressively occupied by the hotter vegetation.

CONCLUSIONS

The set up of Infrared (IR) automatic stations for the continuous long-term monitoring of the shallow thermal structure of hydrothermal zones was the main objective of this research. With respect to previous IR applications, most of which regarded the study of relatively quick processes associated to volcanic eruptions, our experiment was finalized to detect and quantify over long periods slow temperature changes of shallow thermal structures of quiescent volcanoes. In particular our experiment was designed to monitor a significant portion of the Solfatara fumarolic field and of the Vesuvius crater with the periodical, systematic acquisition of IR images from a permanent station. The analysis of two years of IR images acquired at the Solfatara gives a reliable picture, rich in particulars, of the temperature changes and important indications on the origin of the changes. The analysis of the data showed the occurrence of various processes, which were proved on the basis of inde-

pendent observations, such as anthropic jobs, vegetation growth and relatively low flux increases of hydrothermal fluids. It is note worth that these signs were detected in a system characterized at the present moment by a level of activity relatively low with respect to those systems affected by real volcanic crisis where more spectacular results will be expected.

An important point is that the images can be suitably filtered from ambient effects using simple corrections based on data belonging at the image itself. This makes the system independent from the availability of other data. Our filtering was based in fact on a background temperature defined in the scene, on the standard deviation of each image and on a procedure based on image data for the co-registration. These features make the system almost autonomous and able to work also in remote and impervious sites resulting as a suitable tool for volcanic surveillance.

ACKNOWLEDGMENTS

REFERENCES

Ball, M., and H. Pinkerton (2006), Factors affecting the accuracy of thermal imaging cameras in volcanology, J. Geophys. Res., 111, B11203.doi:10.1029/2005JB003829.

Calvari, S., and H. Pinkerton (2004), Birth, growth and morphologic evolution of the 'Laghetto' cinder cone during the 2001 Etna eruption, J. Volcanol. Geotherm. Res., 132, 225-239.

Calvari, S., L. Spampinato, L. Lodato, A. J. L. Harris, M. R. Patrick, J. Dehn, M. R. Burton, and D. Andronico (2005), Chronology and complex volcanic processes during the 2002-2003 flank eruption at Stromboli volcano (Italy) reconstructed from direct observations and surveys with a handheld thermal camera, J. Geophys. Res., 110, B02201.doi:10.1029/2004JB003129.

Chiodini, G., F. Frondini, C. Cardellini, D. Granieri, L. Marini, and G. Ventura (2001), CO_2 degassing and energy release at Solfatara Volcano, Campi Flegrei, Italy, J. Geophys. Res., 106, 16,213-216,221.

Harris, A. J. L., J. Dehn, M. R. Patrick, S. Calvari, M. Ripepe, and L. Lodato (2005), Lava effusion rates from hand-held thermal infrared imagery: an example from the June 2003 effusive activity at Stromboli, Bull. Volcanol., 68, 107-117.

Johnson, J. B., A. J. L. Harris, and R. P. Hoblitt (2005), Thermal observations of gas pistoning at Kilauea Volcano, J. Geophys. Res., 110, B11201.doi:10.1029/2005JB003944.

Kaneko, T., and M. J. Wooster (1999), Landsat infrared analysis of fumarole activity at Unzen Volcano: time-series comparison with gas and magma fluxes, J. Volcanol. Geotherm. Res., 89, 57-64.

Lautze, N. C., A. J. L. Harris, J. E. Bailey, M. Ripepe, S. Calvari, J. Dehn, S. K. Rowland, and K. Evans-Jones (2004), Pulsed lava effusion at Mount Etna during 2001, J. Volcanol. Geotherm. Res., 137, 231- 246.

Lodato, L., L. Spampinato, A. J. L. Harris, S. Calvari, J. Dehn, and M. Patrick (2006), The morphology and evolution of the Stromboli 2002-2003 lava flow field: an example of a basaltic flow field emplaced on a steep slope., Bull. Volcanol.doi: 10.1007/s00445-006-0101-6.

Oppenheimer, C., P. W. Francis, D. A. Rothery, R. W. T. Carlton, and L. S. Glaze (1993), Infrared image analysis of volcanic thermal features; Lascar Volcano, Chile, 1984-1992, J. Geophys. Res., 98, 4269-4286.

Pinkerton, H., M. James, and A. Jones (2002), Surface temperature measurements of active lava flows on Kilauea volcano, Hawai'i., J. Volcanol. Geotherm. Res., 113, 159-176.

Troise, C., G. De Natale, F. Pingue, F. Obrizzo, P. De Martino, U. Tammaro, and E. Boschi (2007), Renewed ground uplift at Campi Flegrei caldera (Italy): New insight on magmatic processes and forecast., Geophys. Res. Lett., 34, L03301.doi:10.1029/2006GL028545.

Vaughan, R. G., S. J. Hook, M. S. Ramsey, V. J. Realmuto, and D. J. Schneider (2005), Monitoring eruptive activity at Mount St. Helens with TIR image data, Geophys. Res. Lett., 32, L19305.doi:10.1029/2005GL024112.